Proceedings of the High Energy Density Matter (HEDM) Contractors' Conference held 4-7 June 1995 in Woods Hole MA

Patrick G. Carrick, editor
Simon Tam, editor

January 1996

Special Report

19960226 068

PHILLIPS LABORATORY
Propulsion Directorate
AIR FORCE MATERIEL COMMAND
EDWARDS AIR FORCE BASE CA 93524-7048

NOTICE

When U.S. Government drawings, specifications, or other data are used for any purpose other than a definitely related Government procurement operation, the fact that the Government may have formulated, furnished, or in any way supplied the said drawings, specifications, or other data, is not to be regarded by implication or otherwise, or in any way licensing the holder or any other person or corporation, or conveying any rights or permission to manufacture, use or sell any patented invention that may be related thereto.
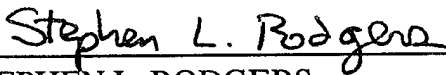
FOREWORD

This Conference Proceedings was compiled and edited by Dr. Patrick G. Carrick, OLAC Phillips Laboratory, Edwards AFB CA.
This report has been reviewed and is approved for release and distribution in accordance with the distribution statement on the cover and on the SF Form 298.

PATRICK G. CARRICK
Editor

STEPHEN L. RODGERS
Director
Propulsion Sciences Division

RANNEY G. ADAMS
Public Affairs Director

REPORT DOCUMENTATION PAGE

Form Approved
OMB No 0704-0188

1. AGENCY USE ONLY (LEAVE BLANK)	2. REPORT DATE JANUARY 1996	3. REPORT TYPE AND DATES COVERED Special Report 8 JUN 94-7 JUN 95

4. TITLE AND SUBTITLE
Proceedings of the High Energy Density Matter (HEDM) Contractors' Conference held 4-7 June 1995 in Woods Hole, MA

6. AUTHOR(S)
Patrick G. Carrick, editor
Simon Tam, editor

5. FUNDING NUMBERS
C:
PE: 62302F
PR: 3058
TA: 00N2

7. PERFORMING ORGANIZATION NAME(S) AND ADDRESS(ES)
Phillips Laboratory
OLAC PL/RKS
10 E. Saturn Blvd.
Edwards AFB CA 93524-7680

8. PERFORMING ORGANIZATION REPORT NUMBER

PL-TR-95-3039

9. SPONSORING/MONITORING AGENCY NAME(S) AND ADDRESS(ES)

10. SPONSORING/MONITORING AGENCY REPORT NUMBER

11. SUPPLEMENTARY NOTES Extended abstracts from the Ninth High Energy Density Matter Contractors' Conference
COSATI CODE(S): 2005; 2109

12a. DISTRIBUTION/AVAILABILITY STATEMENT

APPROVED FOR PUBLIC RELEASE
DISTRIBUTION IS UNLIMITED

12b. DISTRIBUTION CODE

13. ABSTRACT (MAXIMUM 200 WORDS)
This report documents the information presented at the ninth annual High Energy Density Matter (HEDM) Contractors' Conference held 4-7 June 1994 in Woods Hole, MA. This report contains the extended abstracts of the oral, workshop, and poster presentations given by the Air Force funded contractors and by the in-house researchers from the Phillips Laboratory.

14. SUBJECT TERMS
HEDM; High Energy Density Matter; propellant; solid hydrogen; cryogenic materials; potential energy surfaces

15. NUMBER OF PAGES

16. PRICE CODE

17. SECURITY CLASSIFICATION OF REPORT	18. SECURITY CLASSIFICATION OF THIS PAGE	19. SECURITY CLASSIFICATION OF ABSTRACT	20. LIMITATION OF ABSTRACT
Unclassified	Unclassified	Unclassified	SAR

TABLE OF CONTENTS

TABLE OF CONTENTS

TABLE OF CONTENTS

Extended Abstracts from Poster Session

TABLE OF CONTENTS

Introduction

The main purpose of the High Energy Density Matter (HEDM) program is to research and develop advanced high energy propellants containing increased energy densities (energy to mass ratio) to produce greater specific impulse (thrust per weight flow rate of propellant) which will enable significantly increased payloads for rockets and missles. With these advanced propellants, future space-bound payloads could be potentially four times greater than current systems for the same overall size and weight. Theoretical and experimental research is carried out by in-house researchers at the Phillips Laboratory, Propulsion Directorate, at Edwards Air Force Base and through Air Force funded contracts with numerous researchers in academic and industrial laboratories.

The HEDM program is administered by a steering group made up of representatives from the Phillips Laboratory Propulsion Directorate and the Air Force Office of Scientific Research (AFOSR). A technical panel administered by the National Research Council (NRC) assisted the steering group in ensuring the high technical content of the program.

Annual conferences, hosted by the AFOSR and the Phillips Laboratory, are arranged in order to allow in-house and contract researchers to report on their progress and new developments. The Ninth High Energy Density Matter Contractor's Conference was held 4-7 June 1995 at the "J. Erik Jonsson Woods Hole Center" of the National Academy of Sciences, Woods Hole, MA. The conference consisted of an overview of selected research areas on Sunday afternoon, a poster session Sunday night, and technical sessions on cryogenic solids, theory, synthesis, and advances concepts on Monday, Tuesday, and Wednesday morning. The conferecne also contained two special sessions - a Cryogenic Solid Propellants Workshop on Monday night and a "Round Table" discussion of Theory/Systhesis on Tuesday morning.

This report documents the information presented at this conference and contains extended abstracts of the oral presentations, special sessions, and poster session given at the conference. The next HEDM conference is scheduled for 2-5 June 1996 in Boulder, CO.

HIGH ENERGY DENSITY MATTER CONTRACTORS CONFERENCE

1995 AGENDA

Sunday, 4 June 1995

11:00 AM - 1:00 PM **Registration** (Carriage House) **and Lunch** (Main House)

1:15 PM	Introductory Remarks and Welcome Patrick G. Carrick, Phillips Laboratory and Michael R. Berman, AFOSR
1:30	*Advanced Propulsion Concepts*, Brice Cassenti
2:00	*Further Progress on Atom-Doped Cryogenic Solid Propellants*, Mario Fajardo
2:30 A.Voth	*Quantum Simulations of Potential High Energy Density Materials*, Gregory
3:00 - 3:30	**Break**
3:30	*Synthesis of High-Energy Density Materials Based on Strained-Ring Compounds*, William P. Dailey
4:00 Larson	*Lab Scale Test and Evaluation of Cryogenic Solid Rocket Fuels*, C. William
4:30 - 7:00	Dinner Break (dinner not provided)
7:00 - 10:00	**Poster Session** (*Main House*)

Monday, 5 June 1995

8:30	*Search for Metallization: Excitations, Order Parameters and Structure of High Pressure A-Phases of the Hydrogens*, Isaac F. Silvera
9:00	*Hopping Rates Determined from Models of Ortho-Para Conversion in the Solid Hydrogens*, James R. Gaines
9:30	*Zero Temperature Monte Carlo Studies of Solid Hydrogen and Impurity Species*, K. Birgitta Whaley
10:00 - 10:30	**Break**

10:30   *Experimental Studies of Hydrogen Clusters Doped with Alkali Metals*, Young K. Bae

11:00   *Spectroscopic Characterization of Non-Bonding Interactions of the Boron Atom*, Paul J. Dagdigian

11:30   *Structure and Energetics of $B(Ar)_n$ and $B(o-H_2)_n$ Clusters*, Millard Alexander

12:00 - 1:30   **Lunch** (Main House dining room)

1:30   *Spectroscopic Investigation of Alkali-Atom-Doped Hydrogen and Helium Clusters*, Giacinto Scoles

2:00   *Spectral Theory of Chemical Binding: Aggregates of Weakly Bound Atoms*, Peter W. Langhoff

2:30   *Monte Carlo Simulations of the Structure and Optical Absorption Spectra of Na/Ar Clusters and Solids: an Application of Spectral Theory of Chemical Binding*, Jerry Boatz

3:00 - 3:30   **Break**

3:30   *Electronic Structure Studies of Potential Energy Surfaces for HEDM Species*, Mark S. Gordon

4:00   *A Spectroscopic Study of the Jupiter - SL9 Comet Collision; High Energy Chemistry on a Grand Scale*, Takeshi Oka

4:30 - 7:00   **Dinner Break (not provided)**

7:00 - 10:00 **Cryo Solid Propellant Workshop** (Room to be announced)

Tuesday, 6 June 1995

8:30   *Improved routes for the Large-Scale Synthesis of 1,3,3-Trinitroazetidine*, Alan P. Marchand

9:00   *Several New HEDM Molecules- Challenges for Synthesis*, H. Harvey Michels

9:30   *Synthesis of Cubanes and Azacubanes*, Robert M. Moriarty

10:00 - 10:30 **Break**

10:30   *Current Status on ADN Chemistry*, Robert Schmitt

11:00   *Theory/Synthesis Workshop and Initiative Summary*, E. J. Wucherer

11:20 - 12:00 **"Round Table"** Discussion of Theory/Synthesis Area

12:00 - 1:30 **Lunch**

1:30   *Infrared Spectra of Boron-Ammonia Reaction Products in Solid Argon*
Lester Andrews

2:00   *Nonadiabatic Decay- a Key Aspect of Energetic Materials*, David R. Yarkony

2:30   *Cavity Ringdown Laser Absorption Spectroscopy of Catalytic Plasma Expansions*, R. J. Saykally

3:00 - 3:30 **Break**

3:30   *Metal Dimers and Metal Complexes: Model Systems for Metal Seeded Fuels*, Michael A. Duncan

4:00   *New Developments in Theory and Their Role in Studying High Energy and Density Matter*, Rodney J. Bartlett

4:30 - 6:00 **Break**

6:00 - 6:30 **Mixer** (Main House)

7:00 - 10:00 **Clam Bake** (<u>Outside</u>)

Wednesday, 7 June 1995

8:30   *Photodynamics of O and O_2 Isolated in Solid D_2 (H_2)*, V. Ara Apkarian

9:00   *Quantum Molecular Dynamics Simulations of Many-Atom Systems*, R. B. Gerber

9:30 - 10:00 **Break**

10:00   *Diffusion and Flow of Hydrogen Films*, Peter Taborek

10:30   *Progress Toward the Production of H_2 Clusters Containing Reactive Atoms*, Kenneth C. Janda

11:00 - 11:30 **WRAP-UP**

Expected Attendance List

Millard H. Alexander
Department of Chemistry
University of Maryland
College Park, MD 20742

W. Lester Andrews
Chemistry Department
University of Virginia
Charlottesville, VA   22901

V. Ara Apkarian
Department of Chemistry
University of California
Irvine, Ca 92717

Young K. Bae
10 E. Saturn Blvd.
Phillips Laboratory/RKS
Edwards AFB, CA 93524-7680

Rodney J. Bartlett
P.O. Box 118435
University of Florida
Gainesville, FL 32611-8435

Charles Bauschlicher
NASA Ames Research Center
RTC 230-3
Moffett Field, CA 94035

Dave Benard
Rockwell International Science Center
1049 Camino dos Rios
Thousand Oaks, CA 91360

Jerry Boatz
10 E. Saturn Blvd.
Phillips Laboratory/RKS
Edwards AFB, CA 93524-7680

Ellen Boehmer
Rockwell International Science Ctr
1049 Camino Dos Rios
Thousand Oaks, CA 91360

Chris Brazier
10 E. Saturn Blvd.
Phillips Laboratory/RKS
Edwards AFB, CA 93524-7680

Patrick Carrick
10 E. Saturn Blvd.
Phillips Laboratory/RKS
Edwards AFB, CA 93524-7680

Brice Cassenti
United Technologies Research Center
411 Silver Lane
East Hartford, CT 06108

Galina Chaban
Iowa State University
316 Wilhelm
Ames, IA 50011

Karl Christe
10 E. Saturn Blvd.
Phillips Laboratory/RKS
Edwards AFB, CA 93524-7680

Gilbert W. Collins
Lawrence Livermore National Lab
700 East Ave, L-482
Livermore, CA 94550

Paul J Dagdigian
Johns Hopkins University
Remsen Hall
Baltimore, MD 21209

William Dailey III
Dept of Chem, Univ of Pennsylvania
231 S. 34th St
Philadelphia, PA 19104-6323

Michelle DeRose
10 E. Saturn Blvd.
Phillips Laboratory/RKS
Edwards AFB, CA 93524-7680

Michael Duncan
Department of Chemistry
University of Georgia
Athens, GA 30602

Dr Robert L. Forward
Forward Unlimited
P.O. Box 2783
Malibu, CA 90265-7783

Mario Fajardo
10 E. Saturn Blvd.
Phillips Laboratory/RKS
Edwards AFB, CA 93524-7680

James Gaines
Dept of Chem, Univ of Hawaii at Manoa
2505 Correa Road
Honolulu, HI 96822

R. B. Gerber
Department of Chemistry
University of California
Irvine, CA 92717

Mark Gordon
Dept of Chem, Iowa State Univ
Gilman Hall
Ames, Iowa 50011

V.E. Haloulakos
McDonnel Douglas Aeronautics
5301 Bolsa Avenue, MS A3-Y833-13-3
Huntington Beach, CA 92647-2048

Marilyn Jacox
Molecular Spectroscopy Section
MS B-843, Physics Building
NIST
Gaithersburg, MD 20899

Kenneth C. Janda
Dept of Chemistry
University of California at Irvine
44 Ulrey Court
Irvine, CA 92717

Dan Katayama
PL/GP/LIM
29 Randolph Road
Hanscom AFB MA 01731-3010

John Kenney, III
Eastern New Mexico University
Station #33, Dept of Physics
Portales, NM 88130

Phil Kessel
10 E. Saturn Blvd.
Phillips Laboratory/RKS
Edwards AFB, CA 93524-7680

Michael L. Klein
Dept of Chem, Univ of Pennsylvania
3231 Walnut St
Philadelphia, PA 19104-6202

Peter W. Langhoff
Dept of Chemistry
Indiana University
Bloomington, IN 47405

Stephen R. Langhoff
NASA Ames Research Center
RTC 230-3
Moffett Field, CA 94035

C. William Larson
10 E. Saturn Blvd.
Phillips Laboratory/RKS
Edwards AFB, CA 93524-7680

Zhiming Li
Dept of Chemistry
Univ of California at Irvine
Irvine, CA 92717

W. Carl Lineberger
Department of Chemistry
University of Colorado, JILA Box 440
Boulder, CO 80309-0440

6

Michel Macler
10 E. Saturn Blvd.
Phillips Laboratory/RKS
Edwards AFB, CA 93524-7680

Alan P. Marchand
Department of Chemistry, Box 5068
University of North Texas
Denton, TX 76203-5068

Michele A. McMahon
Univ of California, Berkeley
Berkeley, CA 94720

Harvey Michels
United Technologies Research Center
411 Silver Lane
East Hartford, CT 06108

Jeffrey D. Mills
Indiana Univ and Phillips Lab
3615 South Leonard Springs Rd
Bloomington, IN 47403

Robert M. Moriarty
Uiniv of Illinois, Chicago
5417 SES Bldg
Chicago, IL 60680

Edward Murad
PL/WSSI
29 Randolph Road
Hanscom AFB, MA 01731-3010

Takeshi Oka
Department of Chemistry
The University of Chicago
5785 S. Ellis Avenue
Chicago, IL 60637

Mitchio Okumura
Depatment of Chemistry 127/72
California Institute of Technology
1201 E. Cal Blvd
Pasadena, CA 91125

Bryan Palaszewski
NASA Lewis Research Center
MS 500-219
21000 Brook Park Road
Cleveland, OH 44135

Leslie Perkins
10 E. Saturn Blvd.
Phillips Laboratory/RKS
Edwards AFB, CA 93524-7680

Mark Petrie
10 E. Saturn Blvd.
Phillips Laboratory/RKS
Edwards AFB, CA 93524-7680

Eric Rice
ORBITEC
402 Gammon Place
Madison, WI 53719

Stephen Rodgers
10 E. Saturn Blvd.
Phillips Laboratory/RKS
Edwards AFB, CA 93524-7680

James E. Rutledge
Dept of Physics
Univ of California, Irvine
Irvine, CA 92717

Roberta Saxon
SRI International
333 Ravenswood Avenue
Menlo Park, CA 94025

Richard Saykally
Department of Chemistry
University of California
Berkeley, CA 94720-1460

Henry Schaefer, III
Center for Computational
Quantum Chemistry
University of Georgia
Athens, GA 30602-2556

Robert Schmitt
SRI International
PS281
333 Ravenswood Ave
Menlo Park, CA 94025

Giacinto Scoles
Department of Chemistry
Prnceton University
Princeton, NJ 08544

George M. Seidel
Dept of Physics
Brown University
Providence, RI 02912

Jeff Sheehy
10 E. Saturn Blvd.
Phillips Laboratory/RKS
Edwards AFB, CA 93524-7680

Isaac F. Silvera
Department of Physics
Harvard University
Cambridge, MA 02138

Paul Sokol
Dept of Physics
Pennsylvania State Univ
University Park, PA 16802

William C. Stwalley
Dept of Physics, U-46
Univ of Connecticut
2152 Hillside Rd
Stoors, CT 06269-3046

Suresh Suri
10 E. Saturn Blvd.
Phillips Laboratory/RKS
Edwards AFB, CA 93524-7680

Peter Taborek
Dept of Chemistry
Univ of California at Irvine
Irvine, CA 92717

Gregory A. Voth
Department of Chemistry
University of Pennsylvania
Philadelphia, PA 19104-6323

Scott T. Weidman
National Research Council
2101 Constitution Ave., N.W.
Washington, D. C. 20418

Eric Weitz
Northwestern University
Department of Chemistry
2145 Sheridan Rd
Evanston, IL 60208-8113

Brigitta Whaley
Department of Chemistry
University of California
Berkeley, CA 94720-1460

William Wilson
10 E. Saturn Blvd.
Phillips Laboratory/RKS
Edwards AFB, CA 93524-7680

E. J. Wucherer
10 E. Saturn Blvd.
Phillips Laboratory/RKS
Edwards AFB, CA 93524-7680

Edward J. Yadlowsky
HY-Tech Research Corp
104 Centre Court
Radford, VA 24141

David R. Yarkony
Johns Hopkins Univ.,Dept. of Chem.
3400 N. Charles St
Baltimore, MD 21218

Advanced Propulsion Concepts

Brice N. Cassenti
United Technologies Research Center
East Hartford, CT 06108

Abstract

Advanced propulsion systems fall into two general categories: conventional rockets, and nonconventional systems. Conventional rockets include chemical, nuclear, and *in-situ* systems, while nonconventional systems systems include: tethers, gravity assists, radioactive thrust sheets, etc. Much of the recent work has concentrated on nuclear propulsion systems. In nuclear rockets, the energy is extracted from either fission, fusion or annihilation reactions. Each of these reactions have been examined for use in advanced space propulsion systems. Specific impulse for nuclear systems have been predicted to vary from about 850 seconds to over one million seconds. *In-situ* systems can reduce drastically the fuel required for interplanetary missions. Chemical systems are nearing their theoretical limits, and a major breakthrough will be required to increase performance to the level of nuclear systems. Free radicals, metastable (i.e., triplet) helium, and monatomic hydrogen are all possibilities, but most investigations have uncovered serious technical problems in these technologies. Under nonconventional systems only gravity assists, aeroassists, rail guns and the ram cannon have been pursued experimentally. Gravity assists are now routinely used in interplanetary missions. Both conventional rockets and nonconventional systems are discussed. Their promise and their technical problems are presented.

Conventional Propulsion Technologies

Conventional propulsion technologies include two major categories: chemical and nuclear. A third smaller group includes *in-situ* propellant production.

Nuclear Propulsion Systems

Advanced nuclear propulsion can take on several forms. Radioactive thrust sheets[1] directly use the decay of radioactive nuclei to provide propulsion. The fissioning of nuclei has been extensively studied for propulsion both analytically and experimentally.[2,3] Fusion has been analytically examined as a means for providing propulsion[4] during the last few decades. In the last decade serious attention has been given to the direct annihilation of matter.[5,6] Each of these technologies will be discussed below.

Radioactive Decay

A high specific impulse, low thrust rocket may be constructed using a sheet of radioactive material with an absorber on one side.[1] The escaping decay products will then provide thrust.

Fission

The use of fission can provide both high specific impulse and high thrust.[7] The NERVA solid core rocket is an example of an established technology.[8] Particle bed reactors appear to offer a definite improvement over NERVA derived nuclear rockets.[9] Smaller nuclear rockets will enable more missions but would provide slightly less performance for high energy manned Mars missions.[10] Zubrin[11] has examined methods for extending nuclear fission solid core rockets to the use of indigenous propellants. Nuclear electric propulsion[12] has been extensively examined for use in Mars missions. Advanced nuclear propulsion can: (1) make use of a gas core[13,14] to provide significantly higher specific impulse, or (2) use small explosions (nuclear pulse propulsion).[15] Nuclear fission pulse propulsion could provide a specific impulse as high as 10,000 sec at high thrust and will likely have a specific impulse between 3,000 and 10,000 seconds.

Fusion

Magnetic confinement fusion has been examined as a means for providing considerably better specific impulse than fission rockets. Borowski[4] has summarized this form of propulsion clearly presenting its advantages. Kammash and Galbraith[16,17] have recently proposed a form of magnetic and inertial confinement fusion that may allow significant increases in the magnetic fields. Fusion can also be used in a pulsed form by igniting pellets (i.e., inertial confinement

fusion). The Daedalus study[18] shows how nuclear fusion pulse propulsion may provide specific impulses as high as one million seconds with a few hundred thousand seconds being likely.

Direct Annihilation

Eugene Sanger first proposed using the direct annihilation of positrons and electrons into gamma rays for producing propulsion.[19] Unfortunately it is extremely difficult to store the positrons and to direct the gamma rays efficiently. It is far better to annihilate nucleons using antiprotons. This annihilation reaction primarily produces pions, with about five percent kaons. The neutral pions decay immediately into high energy gamma rays. Making about one third of the energy difficult to use. The charged pions can be directed by magnetic fields and will readily deposit kinetic energy in a fluid (propellant). The pions decay into muons and neutrinos. The energy in the neutrinos is lost but he muons can now be used. Finally the muons decay into electrons (or positrons) and neutrinos. The electrons can be again used. It has been shown that if the annihilation products are used to heat liquid hydrogen, then as much as forty-five percent of the annihilation energy will be captured.[19] It has also been shown that the amount of antimatter required for a mission can be minimized.[20]

Several types of propulsion systems, based on antiproton annihilation are possible. These include: solid core systems[21,22], solid propellant,[6] gas core,[23] plasma core,[24] pellets,[6,25], annihilations in heavy nuclei,[6] and the direct use of pions.[26,27] Specific impulses as high as 21 million seconds may be obtained. An interesting possibility that uses only two thousandths of a picogram of antiprotons for a Mars mission has been proposed by Lewis, Newton, Smith and Toothacker.[28] Antiprotons are annihilated in a spherical shell of uranium or plutonium surrounding fusion materials. The uranium or plutonium fission products provide the energy to trigger fusion. The propulsion system proposed uses a form of external nuclear pulse propulsion proposed by Solem.[29] Internal nuclear pulse propulsion has recently been shown to be an efficient propulsion form, and is closer to conventional rockets.[30] A combination of the concepts in References 16, 17, 28 and 30 may be feasible as proposed in References 31 and 32.

Many problems must be overcome before antimatter propulsion becomes a reality. Currently antiprotons are created by colliding protons with heavy element nuclei, but it would be more efficient to collide heavy nuclei head on. Other concepts for efficiently producing antiprotons can be found in papers by Cassenti.[33,34]

Once the antiprotons are collected they must be cooled and this an extremely difficult process to perform efficiently.[35] The cooled antiprotons must be neutralized, for high density storage, by combining with positrons[36] to create antihydrogen. The antihydrogen must be cooled and trapped. Here laser cooling may be useful.[37] It should be possible to store the antihydrogen by using cluster ions.[38] Long term storage will require an excellent vacuum; this should be

possible.[39] Several problems must also be overcome in the propulsion systems. LaPoint[24] has shown that the efficiencies in a plasma core engine may be as low as one percent. Morgan[26] has a calculated a low thrust for the high specific impulse pion rocket, and there is the problem of radiation from the neutral pion decay into gamma rays.[40,41] Finally annihilations in heavy nuclei, or annihilations in pellets, could provide high specific impulse at high thrust.[42]

Obviously antiproton annihilation rockets will not be ready for use tomorrow but heir potential performance is enormous. In fact, Forward, et al[43] have shown that antiproton annihilation propulsion will always cost less than other propulsion systems for a sufficiently high performance mission. The amount of antimatter required for a mission can be readily estimated. For example a 5.5 km/sec, 10 ton transfer from low earth orbit to geosynchronous orbit and back requires about 4 mg of antimatter.[20] A 500 ton transfer to Mars and back in 150 days requires about 31 g of antimatter (using the analysis in Ref. 20), and a 500 ton, 45 year flyby of Alpha Centauri (about 4 light years distance) requires about 12 kg of antimatter.[20]

Chemical Propulsion

Although chemical propulsion is a mature technology, there are improvements that could provide significant increases in performance. The July 1990 issue of Aerospace America had several brief articles describing 'New Directions in Propulsion'. Articles included: the STME, the ARSM, hybrid rockets, electric propulsion, and some specific international work. Wilhite, et al,[44] and Piland and Taly[45] consider several likely advances in chemical propulsion rockets. These include: multi-mode (e.g., airbreathing and rocket), variable mixture ratio, and slush hydrogen (which increases the propellant density). Below three general areas of advanced chemical propulsion will be summarized. These include extensions of current and fuel technologies, exotic chemical propellants, and *in-situ* propellant production.

Extensions

The use of multi-mode propulsion systems has a long history of theoretical development but was not pursued vigorously until the NASP development program.[46,47] Trade studies are necessary for multi-mode systems since the added weight of the airbreathing engine can decrease the overall performance. A dual mixture ratio system could provide engines that perform well as lower and upper stages.[48] Hybrid propulsion can simplify full liquid systems by using a solid fuel with a liquid oxidizer.[49] Tube-bundle rocket thrust chambers may provide higher reliability.[50]

Exotic Fuels

Several exotic fuels have been examined over the last few decades. Hydrogen stored in its monatomic form can provide a specific impulse as high as 1500 sec when it is recombined into diatomic hydrogen.[51] The technical problems here are storage in the monoatomic form, and recombination at high temperature. Triplet helium (where the two electrons in the helium atom have their spins aligned and hence one must move to a higher energy state) has been examined for many years,[52] but no convincing storage mechanism has yet been proposed. In fact many of the exotic propellants have serious problems that must be overcome before they can be considered for applications.[53]

HEDM

The Air Force HEDM (High Energy Density Matter) program[54] has as an objective the development of advanced chemical propellants that could increase the performance of conventional solid or liquid propellants by as much as 50 to 100 seconds.

In-Situ Propellants

Producing propellants at a destination will significantly reduce the propellant that would be carried in a round trip mission. Two sources for propellants have generally been examined: Lunar[55,56] and Martian.[57,58] Lunar and Martian soils both contain oxygen and materials for some low performance solid fuels. The Martian atmosphere contains carbon dioxide, at 7 mbar, which can be decomposed into a liquid carbon monoxide fuel and liquid oxygen. The north polar cap on Mars contains water (in the form if ice) which could provide a supply of hydrogen. The hydrogen could be used directly, or it could be combined with carbon to make methane. The ultimate *in-situ* propellant collection system is the interstellar ramjet[59,60] which collects the hydrogen in space, adds energy, possibly by fusion, and ejects the heated hydrogen to produce thrust.

Nonconventional Propulsion System

Nonconventional propulsion systems include, for example: 1) launchers, 2) tethers, 3) solar, laser or maser systems, 4) assists such as gravity or aerodynamic and ultimately 5) field effect propulsion. Although there are many other forms for nonconventional advanced propulsion techniques, only a small fraction will be summarized below.

Launchers

Several concepts have been proposed for launching payloads directly into space. Jules Verne's novel <u>From the Earth to the Moon</u> is well known for using a large cannon to shoot men to the moon. Other concepts include: rail guns,[61] light gas guns,[61] and coil guns.[61,62,63] Rail guns are particularly simple. They consist of two rails and a movable slide. When a d. c. voltage is placed across the rails the current moving through the slide interacts with the magnetic fields in the rails and accelerates the slide down the rails. Two problems must be overcome to make the rail guns a reality: wear on the slides and rapid power transfer to the slide. Coil guns avoid the wear problems, but the position of the projectile must be accurately controlled while the power transfer problem remains. A variation on launchers is to launch propellant to the spacecraft.[64] Here guidance of the pellets to insure that the spacecraft does collect them is a key problem. The pellets can be launched after the spacecraft, or before the spacecraft is launched. This second case provides a runway for the craft to use for acceleration.

Tethers

Tethers provide a broad range of capabilities,[65] but their greatest promise is propellantless propulsion. A rotating orbital tether can be used to grab a satellite and inject it into a higher energy orbit. Energy and momentum must be conserved, of course, and, hence, a conventional tether must be constantly boosted. Landis[66] has proposed a novel method for pumping up the orbital energy analogous to pumping a swing. Tethers suffer from dynamic and stability problems, and require enormous strengths. Forward[67] has noted that multi-strand tethers can significantly increase the operating stress of a tether, and Zubrin[68] has a clever method for reducing the loading. The cable catapult[69] is a unique idea Forward has proposed which uses a linear motor and cable to launch payloads in space. Here wave propagation in the cable is a primary concern.

Assists

Assists come in two forms: gravitational and aerodynamic. Gravitational assists have been used successfully for interplanetary missions since the 1970s and are now considered a common technique. Aeroassists have been routinely used for earth orbital re-entry, and for Venus and Mars landers. Recent papers on aeroassists are References 70 and 71. In Reference 72 tethers and aeroassists are combined. Aeroassist is an inexpensive technology that can provide enormous increases in payload that can be delivered.

Solar Energy

Solar energy can be used to provide propulsion for space vehicles. The earliest proposal was the solar sail which was first proposed by Tsander[72] in the 1920s. Solar sails use the momentum from reflected light to provide momentum and have been the subject of considerable work, (see, e.g., References 73, 74 or 75). Since the thrust is low, structural response[76] and trajectory optimization[77] are major concerns. Solar energy can also be used to heat propellant, and have recently been investigated both theoretically and experimentally.[78,79]

Zubrin and Andrews[80] have proposed and refined[81] a novel propulsion concept that would make use of the charged particles in the solar wind. A current carrying loop is placed in space. The magnetic field from the loop reflects a sizable fraction of the particles in the wind to provide thrust.

Electric Propulsion

Electric propulsion (see, for example, Deionges[82]) has been the subject of numerous investigations. Nuclear reactors are generally used, in design studies, to provide the power but solar power is also frequently considered.[83]

Lasers and Masers

Lasers and masers provide a means to direct a beam of energy to a spacecraft.[84] The energy can be used to heat a fluid, or the momentum can be used to propel the vehicle. Myrabo[85,86] has proposed using laser, and more recently microwave energy to drive vehicles in the atmosphere of the earth to high speed. Myrabo has shown that light and microwaves can provide most of the energy needed to place spacecraft in orbit about the earth. Forward[87,88] has also examined laser and maser pushed sails on to interstellar missions. The microwave sail consists of a extremely light wire mesh which will capture virtually all of the energy in the beam.

Field Effect Propulsion

The ultimate in propulsion systems are those that propose to change, in some manner, the space around the vehicle. Most such proposals are based on the General Theory of Relativity. Forward[89] summarizes general relativity theory while Alcubarre[90] proposes a specific local distortion of the space about a vehicle that would allow unlimited speeds. Unfortunately there is no known way to produce or maintain the distortion proposed. Bennett[91] has proposed examining particles that move faster than light, in addition to distorting the space, but faster than light particles, or signals, have never been observed. Finally, a frequent proposal has been to use

the zero-point energy of the vacuum (e.g., see Cox[92]). Using the zero-point energy is speculative, but it is the ultimate source of energy.

Conclusions

Proposals for advanced propulsion systems cover a wide range, from extensions of current technology to speculative. Some have been demonstrated and have been used successfully. It is this wide variety and the sure knowledge that some will succeed that make the search interesting, exciting and ultimately rewarding.

References

1. Berman, A.I.: The Physical Principles of Astonautics. John Wiley & Sons, Inc., New York, 1961.
2. Sutton, G. P.: Rocket Propulsion Elements. John Wiley & Sons, Inc., New York, 1963.
3. Oates, G. C.: Aerothermodynamics of Gas turbine and Rocket Propulsion. American Institute of Aeronautics and Astronautics, Washington, D.C., 1988.
4. Borowski, S. K.: A Comparison of Fusion/Antiproton Propulsion Systems for Interplanetary Travel. Paper No. AIAA-87-1814, presented at the AIAA/SAE/ASME/ASEE 23rd Joint Propulsion Conference, San Diego, June 29-July 2, 1987.
5. Forward, R. L.: Antiproton Annihilation Propulsion. Paper No. AIAA-84-1482, presented at the AIAA/SAE/ASME 20th Joint Propulsion Conference, Cincinnati, June 11-13, 1984.
6. Cassenti, B. N.: Conceptual Designs for Antiproton Space Propulsion Systems. Paper No. AIAA-89-2333, presented at the AIAA 25th Joint Propulsion Conference, Monterey, July 10-11, 1989.
7. Buden,D: Nuclear Thermal Rocket Propulsion. Paper No. AIAA-90-2755, presented at the AIAA/SAE/ASME/ASEE 26th Joint Propulsion Conference, Orlando, July 16-18, 1990.
8. Sievers, R. K., J. M. Livingston, and B. L. Pierce: NERVA Propulsion System Design Considerations. Paper No. AIAA-90-1951, presented at the AIAA/SAE/ASME/ASEE 26th Joint Propulsion Conference, Orlando, July 16-18, 1990.
9. Cerbone, R. J., and T. Lawrence: Nuclear Heating in the Upperstage of a Particle Bed Driven Nuclear Propulsion System. Paper No. AIAA-91-2055, presented at the AIAA/SAE/ASME 27th Joint Propulsion Conference, Sacramento, June 24-26, 1991.
10. Zubrin, R.: The Use of Practical Nuclear Thermal Rocket Stages to Support the Human Exploration of the Moon and Mars. Paper No. AIAA-92-3407, presented at the AIAA/SAE/ASME/ASEE 28th Joint Propulsion Conference, Nashville, July 6-8, 1992.
11. Zubrin, R. M.:Missions to Mars and the Moons of Jupiter and Saturn Utilizing Nuclear Thermal Rockets with Indigenous Propellants. Paper No. AIAA-90-0002, presented at the AIAA 28th Aerospace Sciences Meeting, Reno, Jan. 8-11,1990.

12. W. D. Deiningera and K. T. Nock: A Review of Electric Propulsion Spacecraft System Concepts. Paper No. AIAA-90-2553, presented at the AIAA/DGRL/JSASS 21st International Electric Propulsion Conference, Orlando, July 18-20, 1990.

13. Mensing, A., T. Latham and W. Roman: Gas Core Nuclear Rocket Technology - Revisted. Paper No. AIAA-90-3790, presented at the AIAA Space Programs and Technologies Conference, Huntsville, September 25-28, 1990.

14. Kuhrt, W. A.: Space Propulsion in the Fiscal Year 2001. Presented at the Fourth Goddard Memorial Symposium, American Astronautical Society, Washington, D.C., March 15-16, 1966.

15. Martin, A. R. and A. Bond: Nuclear Pulse Propulsion - A Historical Review of an Advanced Propulsion Concept. Journal of the British Interplanetary Society, 32, pp. 611-632, 1976.

16. Kammash, T. and D. L Galbraith: A High Gain Fusion Reactor Based on the Magnetically Insulated Inertial Confinement Fusion (MICF) Concept. Nuclear Fusion, 29, pp. 1079-1099, 1989.

17. Kammash, T. and D. L. Galbraith: Antimatter Induced Fusion Rocket Propulsion. Paper No. AIAA-90-2509, presented at the 26th AIAA/ASME/SAE/ASEE Joint Propulsion Conference, Orlando, 1990.

18. Martin, A. R. (ed.): Project Daedalus - The Final Report on the BIS Starship Study. Journal of the British Interplanetary Society - Supplement, 1978.

19. Cassenti, B. N: Design Considerations for Relativistic Antimatter Rockets. Journal of the British Interplanetary Society, 35, pp. 396-404, 1982.

20. Cassenti, B. N.: Optimization of Relativistic Antimatter Rockets. Journal of the British Interplanetary Society, 37, pp. 483-490, 1984.

21. Vulpetti, G.: A Further Analysis about the Liquid Propellant Thermal Antimatter Engine Design Concept. Acta Astronautica, 15, pp. 551-555, 1987.

22. Howe, S. D. and J. D. Metzger: Survey of Antiproton-Based Propulsion Concepts and Potential Impact on a Manned Mars Mission. Los Alamos Preprint LA-UR-87-2191, 1987.

23. Cassenti, B. N.: Antimatter Propulsion for OTV Applications. Journal of Propulsion and Power, 1, pp. 143-149, 1985.

24. LaPointe, M. R.: Antiproton Annihilation Propulsion with Magnetically Confined Plasma Engines. Ph.D. Dissertation, University of New mexico, May, 1989.

25. Vulpetti, G.: Antimatter Propulsion for Space Exploration. Paper No. IAA-85-491, presented at the 36th Congress of the International Astronautical Federation, Stockholm, October 7-12, 1985.

26. Morgan, D. L.: Concepts for the Design of an Antimatter Annihilation Rocket. Journal of the British Interplanetary Society, 35, pp. 405-412, 1982.

27. Hora, H. and H. W. Lob: Efficient Production of Antihydrogen by Laser for Space Propulsion. Zeitschrift fur Flugwissenshaften und Weltraumforschung, 10, pp. 392-400, 1986.

28. Lewis, R. A., R. Newton, G. A. Smith and W. S. Toothacker: An Antiproton Catalyst for Inertial Confinement Fusion Propulsion. Paper No. AIAA-90-2760 presented at the AIAA/ASME/SAE/ASEE 26th Joint Propulsion Conference, Orlando, July 16-18, 1990.

29. Solem, J. C.: Medusa: Nuclear Explosive Propulsion for Interplanetary Travel. Journal of the British Interplanetary Society, 46, pp. 21-26, 1993.

30. Parlos, A. G. and J. D. Metzger: Feasibility Study of a Contained Pulsed Nuclear Propulsion Engine. Journal of Propulsion and Power, 10, No. 2, pp. 269-278, 1994.

31. Cassenti, B. N., T. Kammash, and D. L. Galbraith: An Antiproton Catalyzed Inertial Fusion Propulsion System. Presented as Paper No. AIAA 94-3354 at the 30th Joint Propulsion Conference, Indianapolis, June 27-29, 1994.

32. Cassenti, B. N.: A Contained Antiprooton Catalyzed Pulse Nuclear Propulsion System. To be presented as Paper No. AIAA 95-2898 at the 31st Joint Propulsion Conference, San Diego, CA, July 10-12, 1995.

33. Cassenti, B., P. Mannheim and P. Gould: Concepts for the Efficient Production and Storage of Antimatter. Paper No. AIAA 93-2031, 1993.

34. Cassenti, B. N.: Concepts for the Efficient Production of Antimatter. Eleventh Symposium on Space Nuclear Power and Propulsion, AIP Conference Proceedings, Albuquerque, NM, Jan., pp. 1429-1434, 1994.

35. Larson, D. J.: Scaleup of Antiproton Production and Collection. Proceedings of the RAND Workshop on Antiproton Science and Technology, edited by B. W. Augenstein, B. E. Bonner, F. E. Mills, and N. M. Nieto, World Scientific, New Jersey, pp.202-219, 1988.

36. Mitchell, J. B. A.: Antihydrogen Production Schemes. Proceedings of the RAND Workshop on Anitproton Science and Technology, edited by B. W. Augenstein, B. E. Bonner, F. E. Mills, and N. M. Nieto, World Scientific, New Jersey, pp. 359-372, 1988.

37. Lett, P. D., P. L. Gould, and W.D. Phillips: Prospects for Electromagnetic Manipulation and Trapping of Anithydrogen. Hyperfine Interactions, 44, pp. 335-348, 1988.

38. Stwalley, W. C.: Bibliography of Hydrogen Cluster Ions. Proceedings of the RAND Workshop on Anitproton Science and Technology, edited by B. W. Augenstein, B. E. Bonner, F. E. Mills, and N. M. Nieto, World Scientific, New Jersey, pp. 393-433, 1988.

39. Gabrielse, G., et al.: Thousandfold Improvement in the Measured Anitproton Mass. Physical Review Letters, 65, pp. 1317-1320, 1990.

40. Cassenti, B. N.: Radiation Shield Anaslysis of Antimatter Rockets. Paper No. AIAA-87-1813, Presented at the AIAA/SAE/ASME/ASEE 23rd Joint Propulsion Conference, San Diego, June 29-July 2, 1987.

41. Bishop, R.: Gamma Radiation Shielding for Antiproton Annihilation Engines. Master of Science Thesis, Pennsylvania State University, PSU-LEPS-89/10, December, 1989.

42. Cassenti, B. N.: High Specific Impulse Antimatter Rockets. Paper No. AIAA-91-2548, presented at the AIAA/SAE/ASME 27th Joint Propulsion Conference, Sacramento, June 24-26, 1991.

43. Forward, R. L., B. N. Cassenti, and D. Miller: Cost Comparison of Chemical and Anithydrogen Propulsion Systems for High Delta-V Missions. Paper No. AIAA-85-1455, presented at the AIAA/SAE/ASME/ASEE 21st Joint Propulsion Conference, Monterey, July 8-10, 1985.

44. Wilhite, A. W., et al.: Advanced Technologies for Rocket Single-Stage-to-Orbit Vehicles. Paper No. AIAA-91-0540, presented at the 29th Aerospace Sciences Meeting, Reno, January 7-10, 1991.

45. Piland, W. M. and T. A. Talay: Advanced Manned Launch System Comparisons. Space Technology, 10, pp. 215-224, 1990.

46. Lepsch, R. A. and J. Christopher: The Perofrmance of a Winged Booster Powered by Combined Rocket and Airbreathing Propulsion. Paper No. AIAA-92-3500, presented at the AIAA/SAE/ASME/ASEE 28th Joint Propulsion Conference, Nashville, July 6-8, 1992.

47. Maurice, L. Q., J. L. Leinang, and L. R. Carreiro: Airbreathing Space Boosters Using In-Flight Oxidizer Collection. Paper No. AIAA-92-3499, presented at the AIAA/SAE/ASME/ASEE 28th Joint Propulsion Conference, Nashville, July6-8, 1992.

48. Limerick, C. D.: Dual Mixture Ratio H_2/O_2 Engine for SSTO Application. Paper No. AIAA-87-1942, presented at the AIAA/SAE/ASME/ASEE 23rd Joint Propulsion Conference, San Diego, June 29-July2, 1987.

49. Goldberg,, B. and J. Cook: Preliminary Results of NASA/Industry Hybrid Propulsion Program. Paper No. AIAA-92-3299, presented at the AIAA/SAE/ASME/ASEE 28th Joint Propulsion Conference, Nashville, July 6-8, 1992.

50. Kazaroff, J. M. and A. J. Pavli: Advanced Tube-Bundle Rocket Thrust Chambers. Journal of Propulsion and Power, 8, pp. 786-791, 1992.

51. Palaszewski, B. A.: Atomic Hydrogen as a Launch Vehicle Propellant. Paper No. AIAA-90-0715, presented at the 28th Aerospace Sciences Meeting, Reno, Janury 8-11, 1990.

52. Zumuidzinas, J. S.: Spin-Polarized Triplet Helium. AFRPL TR-84-027, Air Force Rocket Propulsion Laboratory (now the Phillips Laboratory), Edwards Air Force Base, 1984.

53. Kelly, J. D.: Free Radicals, Electronic Metastables, and Other Energetic Molecules as Potential Rocket Propellants. Paper No. AIAA-88-3172, presented at the AIAA/ASME/SAE/ASEE 24th Joint Propulsion Conference, Boston, July 11-13,1988.

54. Carrick, P. G.: Theoretical Performance of High Energy Density Cryogenic Solid Rocket Propellants, to be presented as Paper No. AIAA 95-2893, 31st Joint Propulsion Conference, San Diego, CA, July 10-12, 1995.

55. Rosenberg, S.: Concepts in Lunar Resource Utilization. Paper No. AIAA-91-2446, presented at the AIAA/SAE/ASME/ASEE 27th Joint Propulsion Conference, Sacramento, June 24-26, 1991.

56. Brower, D., et al: Conceptual Design of Hybrid Rocket Engine Utilizing Lunar-Derived Propellant. Paper No. AIAA-90-2114, presented at the AIAA/ASME/SAE/ASEE 26th Joint Propulsion Conference, Orlando, July 16-18,1990.

57. Colvin, J., P. Schallborn and K. Ramohalli: Propellant Production on Mars: Single Cell Oxygen Production Test Bed. Papere No. AIAA-91-2444, presented at the AIAA/SAE/ASME/ASEE 27th Joint Propulsion Conference, Sacramento, June 24-26, 1991.

58. Bowles, J. V. et al.: Propellant Production from the Martian Atmosphere. Journal of Propulsion and Power, 8, pp. 907-909, 1992.

59. Bussard, R. W.:Galactic Matter and Interstellar Flight. Acta Astronautica, VI, pp. 179-195, 1960.

60. Cassenti, B. N.: Design Concepts for the Interstellar Ramjet. Journal of the British Interplanetary Society, 46, pp. 151-160, 1993.

61. Lcanos, D. and I. Brownville: Hypervelocity Coil Guns, Rail Guns and Light Gas Guns. Paper No. AIAA-94-4627, AIAA Space Programs and Techniques Conference, Huntsville, AL, September 27-29, 1994.

62. Escher, W. I. D.: The View from Space: Applications of Electromagnetic Launch Technologies in Space. Paper No. AIAA 94-4630, AIAA Space Programs and Technologies Conference, Huntsville, AL, September 27-29, 1994.

63. Mankins, John C.: Electromagnetic Earth-to-Orbit Launch Concepts: One Strategy in Achieving Reductions in Launch Costs Beyond the Next Generation, Paper No. AIAA 94-4625, AIAA Space Programs and Technologies Conference, Huntsville, AL, September 27-29, 1994.

64. Singer, C. E.: Interstellar Propulsion Using a Pellet Stream for Momentum Transfer. Journal of the British Interplanetary Society, 33, pp. 107-116, 1980.

65. Harrison, J. K.: Tethers in Space: A Broad Perspective. AIAA 26th Aerospace Sciences Meeting, Reno NV, January 11-14, 1988.

66. Landis, G. A.: Reactionless Orbital Propulsion Using Tether Deployment. Acta Astronautica, 26, pp. 307-312, 1992.

67. Forward, R. L.: Failsafe Multistrand Tether Structures for Space Propulsion. 28th Joint Propulsion Conference, Nashville, TN, July 6-8, 1992.

68. Zubrin, R.: The Hypersonic Sky Hook. Journal of the British Interplanetary Society, 48, pp. 123-128, 1993.

69. Forward, R. L., et al.: The Cable Catapult: Putting It There and Keeping It There. Paper No. AIAA 92-3077, 28th Joint Propulsion Conference, Nashville, TN, July 6-8, 1992.

70. Lewis, M. I.: The Use of Hypersonic Waveriders for Aero-Assisted Orbital Manoeuvring. Journal of the British Interplanetary Society, 46, pp. 11-20, 1993.

71. Longuski, J. M., et al.: Optimal Mass for Aerobraking Tethers. Acta Astronautica, 35, pp. 489-500, 1995.

72. Tsander, F. A.: On Using the Force of Light Pressure for Flight Into Interplanetary Space. The Problem of Flying Rocket Devices: Interplanetary Flights. (Russian) 2nd Edition, Oborongcz, Moscow, pp. 361-368, 1961.

73. Forward, R. L.: Grey Solar Sails. The Journal of the Astronautical Society, 38, pp.161-185, 1990.

74. Forward, R. L.: The Solar Photon Thruster, Journal of Spacecraft and Rockets, 27, pp. 411-416, 1990.

75. Matloff, G. L. and E. Mallove: Solar Sail Starships - The Clipper Ships of the Galaxy. Journal of the British Interplanetary Society, 34, pp. 371-380, 1981.

76. Cassenti, B. N., G. L. Matloff and J. Strobl: The Structural Response and Stability of Interstellar Solar Sails. Presented at the conference on "Practical Robotic Interstellar Flight: Are We Ready?" New York City, NY, August 29- September 1, 1994, submitted to the Journal of the British Interplanetary Society.

77. Subra Rao, P. V. and P. V. Ramanan: Optimal Three-Dimensional Heliocentric Solar Sail Rendezvous Transfer Trajectories. Acta Astronautica, 29, pp. 341-345, 1993.

78. Emrich, W.: Design Considerations for Space Transfer Vehicles Using Solar Thermal Propulsion. Paper No. AIAA 95-2634, to be presented at the 31st Joint Propulsion Conference, San Diego, CA, July 10-12, 1995.

79. Bonmetti, J. and C. Hawk: Solar Thermal Concentrator. Paper No. AIAA 95-2637, to be presented at the 31st Joint Propulsion Conference, San Diego, CA, July 10-12, 1995.

80. Zubrin, R. M. and D. G. Andrews: Magnetic Sails and Interplanetary Travel. Paper No. AIAA 89-2441, 25th Joint Propulsion Conference, Monterey, CA, July, 1989.

81. Zubrin, R. M.: The Use of Magnetic Sails to Escape from Low Earth Orbit. Journal of the British Interplanetary Society, 46, pp. 3-10, 1993.

82. Deinonges, W. D. and K. T. Nock: A Review of Electric Propulsion Spacecraft System Concepts. Paper No. AIAA 90-2553, AIAA/DGLR/ISASS 21st International Electriv Propulsion Conference, Orlando, FL, July 18-20, 1980.

83. Stuhlinger, E.: Comet Nucleus Sample Return Missions with Electrically Propelled Spacecraft. Journal of the British Interplanetary Society, 39, pp. 273-281, 1986.

84. Keefer, D., et al.: Laser Propulsion Using Free Electron Lasers. AIAA Journal, 30, pp. 2478-2482, 1992.

85. Myrabo, L. N. and Yu P. Raizer: Laser Induced Air Spike for Advanced Transatmospheric Vehicles. Paper No. AIAA-94-2451, 25th AIAA Plasmadynamics and Laser Conference, Colorado Springs, CO, June 20-23, 1994.

86. Myrabo, L. N., et al.: Thermal Management System for an Ultralight Microwave Propelled Transatmospheric Vehicle. Paper No. AIAA 94-2924, 30th AIAA/ASME/SAE/ASEE Joint Propulsion Conference, Indianapolis, IN, June 27-29, 1994.

87. Forward, R. L.: Roundtrip Interstellar Travel Using Laser-Pushed Lightsails. Journal of Spacecraft and Rockets, 21, pp. 187-195, 1984.

88. Forward, R. L.: Starwisp: An Ultralight Interstellar Probe. Journal of Spacecraft and Rockets, 22, pp. 345-350, 1985.

89. Forward, R. L.: SpaceWarps: A Review of One Form of Propulsionless Transport. Journal of the British Interplanetary Society, 42, pp. 553-542, 1989.

90. Alcubarre, M.: The Warp Drive: Hyper-fast Travel Within General Relativity. Classical and Quantum Gravity, 11, pp. L73-L77, 1994.

91. Bennett, G. L. and H. B. Knowles: Boundary Conditions on Faster-Than-Light Transportation Systems, Paper No. AIAA 93-1995, AIAA/SAE/ASME/ASEE 29th Joint Propulsion Conference, Monterey , CA, June 28-30, 1993.

92. Cox, L. T., Jr.: Calculation of Resonant Values of Electromagnetic Energy Incident Upon Dielectric Spheres. Report No. PL-TR-93-3002, Phillips Laboratory, Edwards AFB, CA, February, 1994.

HIGH ENERGY DENSITY MATTER CONTRACTORS CONFERENCE
Wood's Hole, MA 4-7 June 1995

Further Progress on Atom Doped Cryogenic Solid Propellants

Mario Fajardo, Simon Tam, Michel Macler, Jerry Boatz,
Janet Petroski, Michelle DeRose, Young Bae, and Chris Brazier
Emerging Technologies Branch, Propulsion Directorate, Phillips Laboratory
(OLAC PL/RKFE Bldg. 8451, Edwards AFB, CA 93524-7680)

ABSTRACT

I will present the highlights from our past year's efforts at trapping energetic atomic species in cryogenic van der Waals solids.

Our novel, compact, non-mechanical velocity selection technique, Temporally and Spatially Specific PhotoIonization (TASSPI), has now been demonstrated for fast laser ablated Al, Ga, and In atoms [see poster by M. Macler]. We are still working on extending this technique to other atoms, *e.g.* Li and B, which do not exhibit convenient single photon photoionization absorptions. We will ultimately combine the TASSPI method with our matrix isolation experiments to determine optimum metal atom doped sample preparation conditions.

We have completed our preliminary experiments on depositing electrically discharged $N/N_2/He$ gas mixtures directly onto "superfluid" lHe II surfaces [see poster by M. DeRose]. Our observations confirm the presence of novel features in the $N(^2D) \rightarrow N(^4S)$ matrix induced emission spectrum previously reported by E.B. Gordon, *et al.* [Chem. Phys. **189**, 367 (1994)]. We have also observed sudden and spectacular releases of visible radiation and thermal energy upon warming of these gram-scale samples, as previously reported by Gordon's group. We are still examining various models for the microscopic structure of these rapidly quenched materials, including Gordon's proposed "Impurity Stabilized Solid Helium Phase" concept. We are currently redesigning our cryostat to provide better access to, and control over, the sample preparation process.

We have also made further progress on our methods for simulating the optical absorption lineshapes for $P \leftarrow S$ transitions of matrix isolated metal atoms [see poster by M. Fajardo, and talk by J. Boatz]. Our latest results include predicted lineshapes for Na atoms in liquid, and critical point fluid, Ar systems. I will offer speculations as to why the simulated $Na/Ar_{(l)}$ spectrum resembles our experimental Li/Ar/Xe mixed matrix spectrum, and why the simulated $Na/Ar_{(fluid)}$ spectrum resembles our Li/H_2 matrix spectrum. These similarities have prompted us to attempt (with modest initial success) to simulate Li/H_2 matrices by applying the Monte Carlo method to "fictitious" classical ensembles.

Quantum Simulations of Potential High Energy Density Materials

Gregory A. Voth

Department of Chemistry, University of Pennsylvania, Philadelphia, Pennsylvania 19104-6323

Introduction

Solid hydrogen doped with atomic impurities (e.g., Li, B) is a potential high energy density material (HEDM) for use in rocket propulsion.[1] Quantum computer simulation techniques have been shown to yield important information on the structure of impurity trapping sites in quantum solids such as *para*–hydrogen.[2-5] However, an even more challenging problem is the explicit simulation of dynamical diffusion and recombination. Such simulations of impurity mobility in quantum solids are particularly difficult because the solid is so strongly influenced by quantum effects, thereby requiring a *quantum dynamical* method. Such a method has been developed[6] and applied in our group and will be described below.

Quantum Dynamical HEDM Simulations

The rate constant k_r for recombination of two impurities in a low temperature solid can be approximately described by the equation

$$\frac{1}{k_r} \approx \frac{1}{k_{in}} + \frac{1}{k_D} \quad , \tag{1}$$

where k_{in} is the intrinsic recombination rate for the two impurities (i.e., when at the contact distance r_c) and k_D is the rate at which the two impurities diffuse into proximity with one another. The latter rate is related to the diffusion constant D such that $k_D \approx 4\pi r_c D$. If the intrinsic rate of recombination is very fast and/or the diffusion rate is slow, it is clear from Eq. (1) that the overall rate of recombination will be limited by the impurity diffusion. In order to trap impurities in a quantum solid, one would obviously like their diffusion constant to be small in order to obtain a stable material.

Computer simulation can be invaluable in determining the factors which influence impurity diffusion in quantum solids. The diffusion constant can be obtain from one of two formulas:

$$D = \frac{1}{6} \lim_{t\to\infty} \frac{d}{dt} \langle |\mathbf{q}(t) - \mathbf{q}(0)|^2 \rangle \tag{2}$$

or

$$D = \frac{1}{3} \int_0^\infty dt \langle \dot{\mathbf{q}}(t) \cdot \dot{\mathbf{q}}(0) \rangle \quad , \tag{3}$$

where the notation $A(t) \equiv e^{iHt/\hbar} A e^{-iHt/\hbar}$ denotes a quantum Heisenberg operator for any operator "A". Both of the above functions are quantum dynamical correlation functions. Therefore, the simulation of impurity diffusion in quantum solids requires a quantum dynamical simulation method which will now be described.

Our method revolves around the intriguing properties of the path centroid variable in the Feynman path integral formulation of quantum statistical mechanics.[6,7] The multidimensional centroid of a Feynman path $\mathbf{q}(\tau)$ is defined by[7]

$$\mathbf{q}_0 = \frac{1}{\hbar\beta} \int_0^{\hbar\beta} d\tau \, \mathbf{q}(\tau) \quad , \tag{4}$$

which can be used to define a classical-like equilibrium "centroid density" $\rho_c(\mathbf{q}_c)$ at the point in space $\mathbf{q}_c$. The latter quantity is given by the "imaginary time" (i.e., equilibrium) Feynman path integral expression[6,7]

$$\rho_c(\mathbf{q}_c) = \int \cdots \int D\mathbf{q}(\tau) \delta(\mathbf{q}_c - \mathbf{q}_0) exp\{-S[\mathbf{q}(\tau)]/\hbar\} \quad , \tag{5}$$

where the preceding expression is a multidimensional functional integral and $S[\mathbf{q}(\tau)]$ is the action functional in imaginary time.[7] Note that the path centroid is defined, and seemingly has meaning, only within the context of equilibrium statistical mechanics. However, insight into the *dynamical* role of the centroid variable in the computation of quantum time correlation functions has been uncovered, resulting in a method called "Centroid Molecular Dynamics" (CMD).[6]

The basic result of CMD is that the position or velocity correlation function for quantum particles in many-body systems is related to a centroid correlation function obtained by running *classical-like trajectories* on an effective quantum potential.[7] With the CMD method, one can directly and efficiently calculate the quantum dynamical properties of condensed matter systems as they are described by time correlation functions. In fact, the quantum centroid potential can be represented by an effective pairwise pseudopotential,[7] allowing for *extremely efficient* quantum dynamical simulation of large systems (i.e., once the potential is in this form, the simulation is no more time-consuming than a classical MD simulation). Shown in Fig. 1 is the effective centroid pseudopotential between two p–H_2 molecules at 25 K as compared to the classical one. Shown in Fig. 2 are the classical and centroid velocity autocorrelation functions. The centroid-based calculation gives a liquid phase self-diffusion constant via Eq. (3) which is in excellent agreement with the experimental result as well as an exact (and very time-consuming) CMD calculation.[9] This result confirms the validity of both the theoretical methodology and the pairwise pseudopotential approach, at least for the liquid density. The solid phase centroid potential will be more challenging to model in a pairwise form by simple considerations alone. It seems clear at this point, however, that the CMD breakthrough will allow us to accurately simulate impurity diffusion in quantum solids and liquids in order to probe the microscopic factors which influence the stability of potential HEDMs.
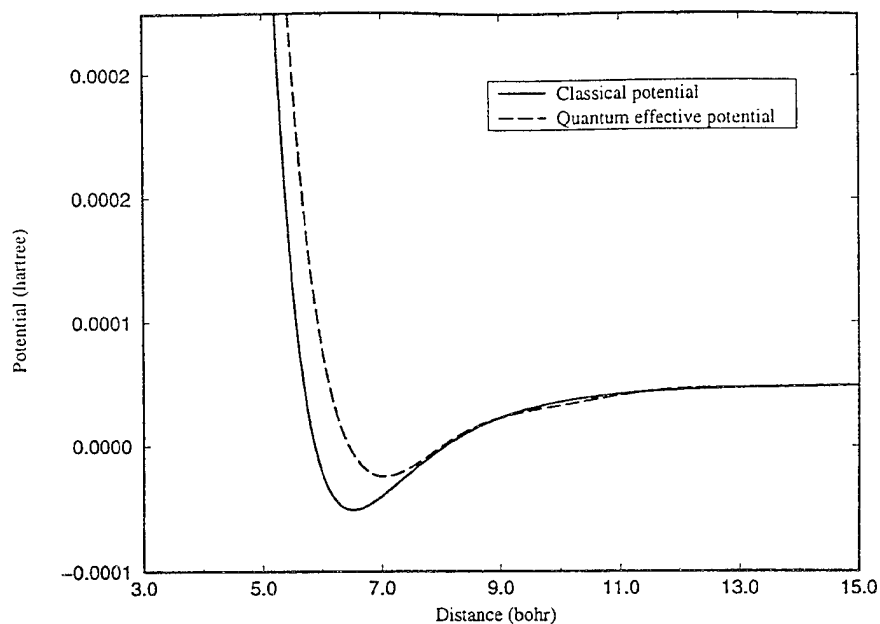
Figure 1: A comparison of the classical pair potential for p-H_2 with the effective quantum centroid pair potential obtained numerically at 25 K (Ref. 8). The shallowness of the centroid potential effectively reflects the zero-point quantization of the hydrogen molecules, while its minimum is shifted outward from the combined effect of the quantization and the potential anharmonicity.

Normalized liquid H_2 velocity autocorrelation function at 25 K
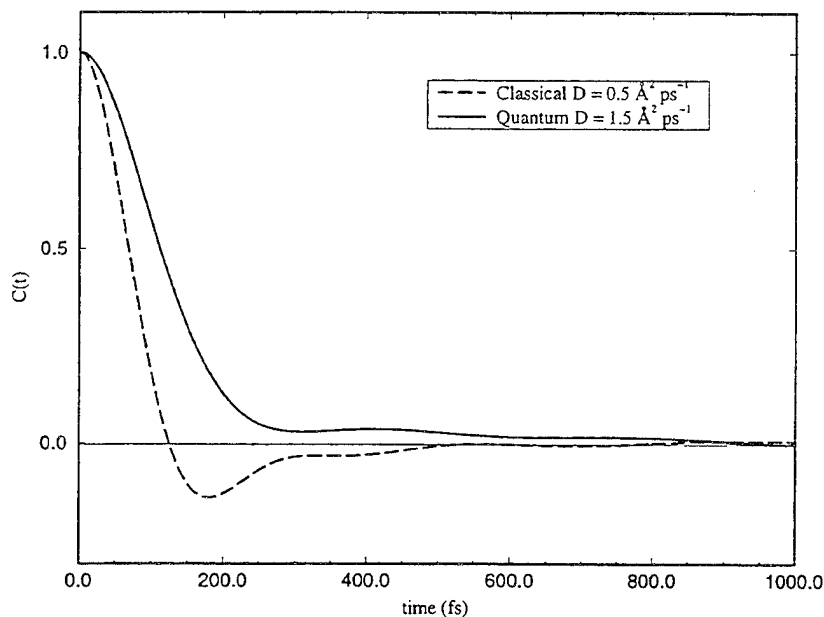
Figure 2: Plots of the classical (dashed line) and CMD (solid line) velocity autocorrelation functions for liquid p-H_2 at 25 K and V = 31.7 cm^3 mol^{-1} (Ref. 8). The self-diffusion constant in the classical case is calculated to be 0.5 Å^2 ps^{-1}, while the quantum CMD value is found to be 1.5 Å^2 ps^{-1}. The experimental value is 1.6 Å^2 ps^{-1}. Calculations at other densities give similar agreement between CMD and experiment (Ref. 9).

References

(1) M. E. Fajardo, in *Proceedings of the High Energy Density Matter Conference*, edited by M. E. Cordonnier (USAF Phillips Laboratory, Edwards AFB, CA, 1991); J. Chem. Phys. **98**, 110 (1993).

(2) D. Scharf, G. J. Martyna, D. H. Li, G. A. Voth, and M. L. Klein, J. Chem. Phys. **99**, 9013 (1993).

(3) D. H. Li and G. A. Voth, J. Chem. Phys. **100**, 1785 (1994).

(4) D. H. Li and G. A. Voth, J. Chem. Phys. **96**, 5340(1992); J. Chem. Phys. **98**, 5734 (1993).

(5) D. Scharf, G. J. Martyna, and M. L. Klein, J. Chem. Phys. **99**, 8997 (1993); D. Scharf, M. L. Klein, and G. J. Martyna, J. Chem. Phys. **97**, 3590 (1992); D. Scharf, G. J. Martyna, and M. L. Klein, Chem. Phys. Lett. **197**, 231 (1992); Low Temp. Phys. **19**, 364 (1993).

(6) J. Cao and G. A. Voth, J. Chem. Phys. **99**, 10070 (1993); J. Chem. Phys. **100**, 5093 (1994); J. Chem. Phys. **100**, 5106 (1994); J. Chem. Phys. **101**, 6157 (1994); J. Chem. Phys. **101**, 6168 (1994).

(7) R. P. Feynman, *Statistical Mechanics*, (Addison–Wesley, Reading, MA, 1972).

(8) M. Pavese and G. A. Voth, (to be published).

(9) G. J. Martyna (private communication).

SYNTHESIS OF HIGH-ENERGY DENSITY MATERIALS BASED ON STRAINED-RING COMPOUNDS

William P. Dailey
Department of Chemistry
University of Pennsylvania
Philadelphia, PA 19104-6323

On a per carbon basis, cyclopropene is one of the most energetic hydrocarbons that can be synthesized and manipulated. Cyclopropene itself has $\Delta H_f = 66$ kcal/mol and a strain energy of 55 kcal/mol. The parent compound and substituted derivatives which have fewer than two substituents on the methylene carbon tend to be unstable. They undergo polymerization via an ene reaction. However, cyclopropenes that have two groups at the methylene carbon can be quite robust. For instance, 3,3-dimethylcyclopropene can be heated to 100 °C for extended periods without decomposition. We are investigating these compounds as potential high energy fuels and fuel additives.

Two of the new compounds that we have prepared are shown below.

1

$\Delta H_f = 120$ kcal/mol
$I_{sp} = 310.2$ sec

2

$\Delta H_f = 184$ kcal/mol
$I_{sp} = 306.3$ sec
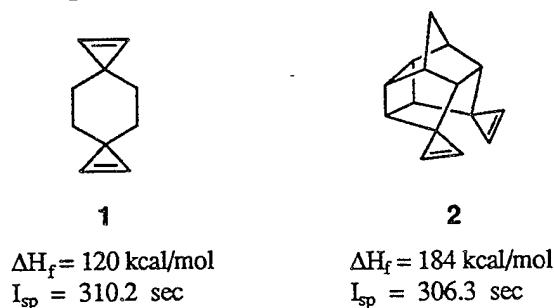
The synthesis of **1** is shown below. The bisdiene was prepared using modifications of literature preparations. Addition of dibromocarbene using phase transfer conditions produced the bis(dibromocyclopropane). Tin hydride reduction followed by base induced elimination produced the biscyclopropene **1** in good overall yield. The compound is a liquid at room temperature and is moderately sensitive to oxygen or Lewis acids.
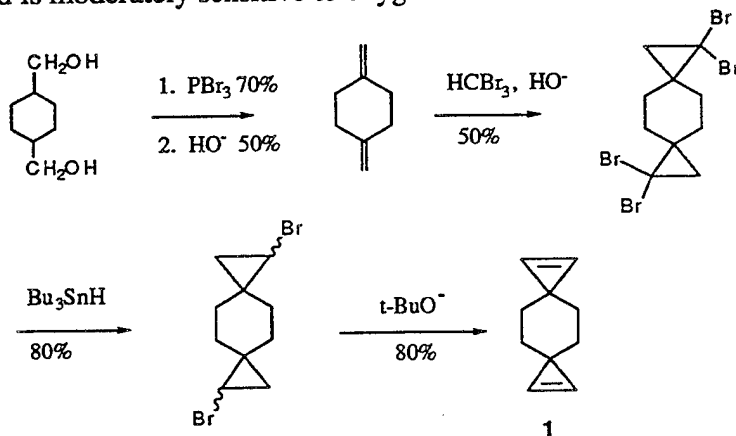
A conformational study of **1** was undertaken by dynamic ¹H NMR. At room temperature the 1H NMR for 1 consists of 2 sharp peaks. Upon cooling, each of these peaks broadens and resharpens into two peaks. At 500 MHz, the coalescence temperature for the methylene protons was -70 °C. The spectra are shown below.
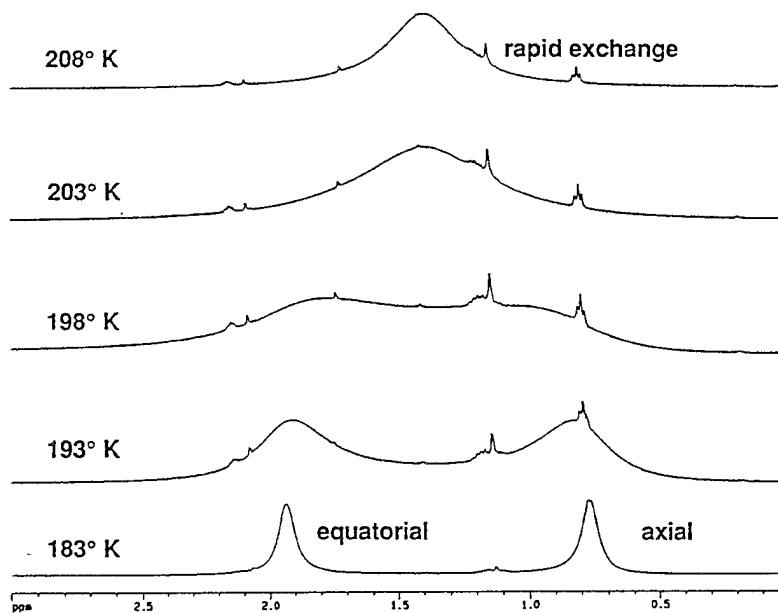
The free energy of activation for the site exchange process in **1** is 8.8 kcal/mol. This can be compared with cyclohexane (10.8 kcal/mol) and 1,1,4,4-tetramethylcyclohexane (11.4 kcal/mol). The transition structure for conversion of the chair form of cyclohexane to give the twist boat form, the half twist chair form, was located using HF/6-31G* calculations. The barrier is calculated to be 12.2 kcal/mol. In a similar manner, the analogous transition structure was calculated for the biscyclopropene **1**. The barrier is calculated to be 9.8 kcal/mol, in good agreement with our value derived from dynamic NMR measurements. A diagrammatic representation of this process is shown below.

$$\Delta G^{\ddagger} = \quad 8.8 \text{ kcal/mole}$$

Cyclohexane $\Delta G^{\ddagger}$ = 10.8 kcal/mole

1,1,4,4-Tetramethylcyclohexane $\Delta G^{\ddagger}$ = 11.4 kcal/mole[8]
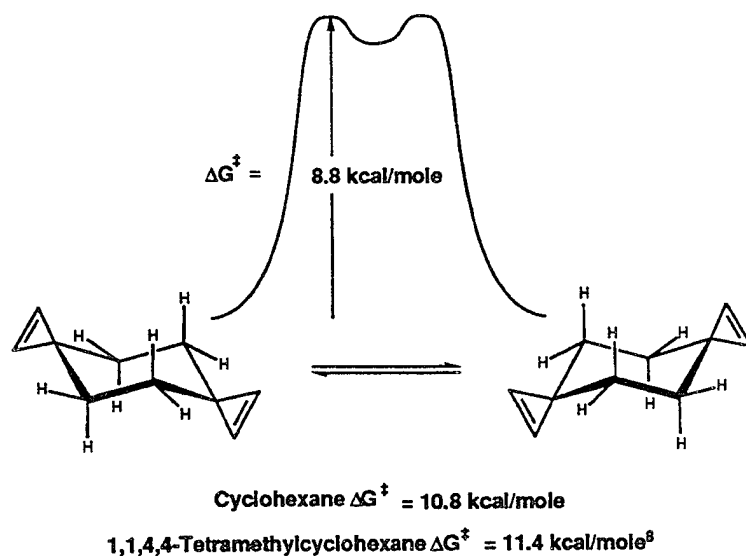
In collaboration with Professor Gleiter, we obtained the photoelectron spectrum of compound **1**. It is shown below. The appearance potential (8.9 eV) is in good agreement with calculated values.
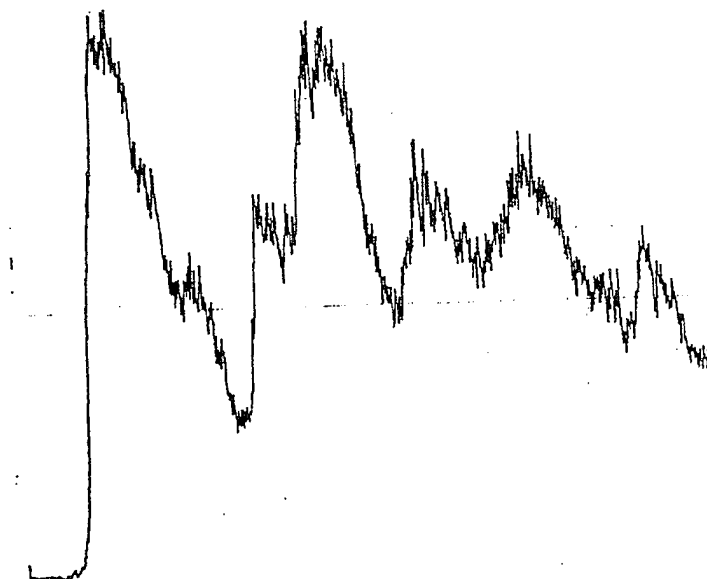
The caged-ring compound **2** was prepared in a manner similar to that of **1**. We found that the precursor diene could be prepared much more easily using the Lombardo reagent than the literature method (3 steps, 52% yield). Dibromocarbene addition followed by reduction and base induced elimination produced the biscyclopropene **2** which was a crystalline solid with mp 44 - 46 °C. This biscyclopropene was much more sensitive to oxygen than compound **1**.

30

Zn-CH$_2$Br$_2$-TiCl$_4$
THF-CH$_2$Cl$_2$
62%

CHBr$_3$
NaOH
TEBA
40%

Bu$_3$SnH
92%

t-BuOK
76%

2
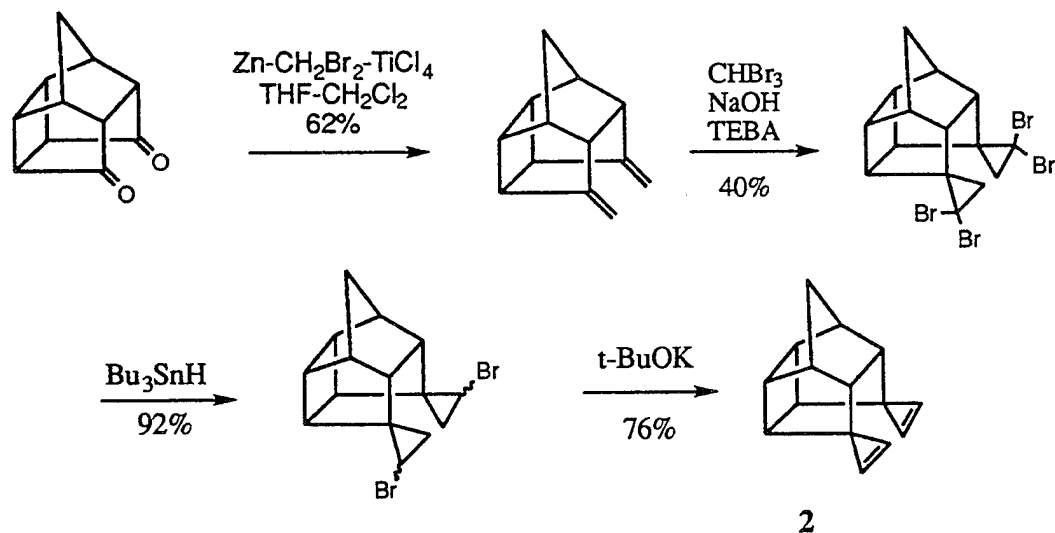
The structure of **2** was confirmed by single crystal x-ray analysis. An ORTEP is shown in below. A comparison of the experimental and HF/6-31G* calculated structure is also included. The agreement is outstanding. The calculated density is 1.26 g/cc
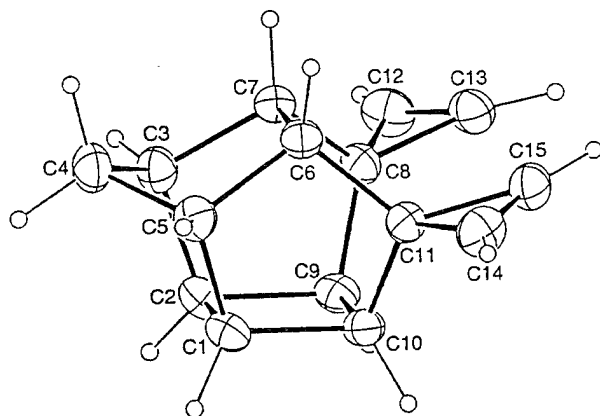
Comparison of Experimental and Calculated Structure of Caged Biscyclopropene

Bond	Observed Distance (Å) (X-ray)	Calculated Distance(Å) (HF/6-31G*)
C(1)-C(2)	1.554	1.553
C(1)-C(5)	1.543	1.551
C(1)-C(10)	1.559	1.556
C(2)-C(3)	1.539	1.551
C(2)-C(9)	1.560	1.556
C(3)-C(4)	1.525	1.528
C(3)-C(7)	1.545	1.549
C(4)-C(5)	1.520	1.528
C(5)-C(6)	1.542	1.549
C(6)-C(7)	1.582	1.582
C(6)-C(11)	1.521	1.527
C(7)-C(8)	1.515	1.527
C(8)-C(9)	1.511	1.522
C(8)-C(12)	1.503	1.494
C(8)-C(13)	1.500	1.488
C(9)-C(10)	1.567	1.568
C(10)-C(11)	1.515	1.522
C(11)-C(14)	1.505	1.494
C(11)-C(15)	1.488	1.488
C(12)-C(13)	1.280	1.281
C(14)-C(15)	1.273	1.281

Cryogenic Hybrids, A New Kind of Rocket

Patrick G. Carrick and C. William Larson
Phillips Laboratory
Propulsion Directorate
Edwards AFB, CA 93524-7680

ABSTRACT

We have investigated the preparation and combustion of solid cryogenic fuel (ethylene and n-pentane) for use in rockets that utilize the hybrid geometry. In this investigation we prepared a variety of fuel grain cylinders, by fast and slow condensation of hydrocarbons, at 77K. The vaporization/oxidation of the fuel grain cylinders was analyzed through measurement of the instantaneous combustion chamber pressure that resulted from burning with a measured oxidizer mass flow rate. Video recordings of the combusting fuel grain and exit nozzle were acquired and analyzed. The burning rate of the cryogenic fuels was about 5-10 times faster than polymethyl methacrylate. Cryogenic solids may have burning rates approaching or exceeding those found in solid rocket motors. Thus, for missions that require the high burning rates of solid rocket motors and the advantages of the hybrid rocket configuration, cryogenic solid hybrid rocket motors may be suitable. Cryogenic solid fuels may also offer additional advantages in propulsion applications because they are more dense than liquids and because the cold solid fuel matrix offers an environment to stabilize high energy density fuel additives.

INTRODUCTION

In propulsion, the use of high energy density matter (HEDM) for fuel promises to improve rocket performance, specific impulse. Tremendous engineering problems need to be solved before the quintescential HEDM, solid hydrogen at 4 degrees Kelvin, seeded with up to 8% atomic additive, may become useful[1]. One approach envisions burning this cryogenic solid fuel in the hybrid rocket configuration. To demonstrate its feasibility, and to further the understanding of combustion in hybrid rockets, we designed a laboratory scale experiment to evaluate combustion of cryogenically solidified (with liquid nitrogen) lightweight hydrocarbons, fuels that are gases or liquids at ambient temperature and pressure. In this preliminary report, results of a study of combustion of solid ethylene and solid n-pentane are described.

Compared to conventional hybrid rocket fuels, these cryogenic solids are expected to have much faster burning rates since they require ten to twenty times less energy to vaporize into the oxidizer stream. Whereas the conventional fuels (solid polymeric materials at room temperature, e.g., polymethyl methacrylate or PMMA, commonly known as Plexiglas) must be pyrolyzed and vaporized, the cryogenic solid hydrocarbon fuels need only be vaporized. The thermal diffusivity of the solid hydrocarbons is expected to be very small and similar to the conventional polymer fuels, around 0.001 cm^2/sec. The time scale for melting to a depth where liquified fuel would slough off would be long compared to the burning rate, thus precluding the loss of the cryogenic solid's integrity and premature melting during burning, viz., time-scale for melting = (melting depth)^2/(thermal diffusivity), $t_{melt} = \delta^2/\alpha$. Thus, for a melting depth of 1mm, t_{melt} is 10 seconds, which is ten to one-hundred times longer than the burning time of 1mm of cryogenic fuel grain depth.

The history of the hybrid rocket was described recently by Altman[2]. Marxman[3] and co-workers, in a series of percipient papers published in the early sixties, described a two-dimensional model in which the instantaneous radial regression rate of the fuel, r' = dr/dt, in an axisymmetric hybrid rocket geometry was given by

(1) $r' = (0.036/\rho_f) (G)^{0.8} (\mu/x)^{0.2} B^{0.23}$
        for 5 < B < 10

In the Marxman Equation[3], G is the total mass flux (oxidizer plus fuel mass flow per unit port area, G = m' $/\pi r^2$), μ and x are the free stream viscosity and distance from the fuel grain's oxidizer entrance port, respectively. B is the blowing coefficient, which had both a fluid dynamic and a thermodynamic definition:

(2) $B = G_{ox} /(G_{fuel} C_f/2)$ fluid dynamic

(3) $B = \Delta h/ h_v$ thermodynamic

where G_{fuel} is the mass flux from the surface of the fuel and C_f is the skin friction coefficient with blowing into a stream of oxidizer of mass flux G_{ox}. In the thermodynamic analog, h_v is the energy to pyrolyze and vaporize unit mass of fuel, and Δh is the enthalpy difference between a unit mass of fuel grain and the hot, fully oxidized free stream gas mixture of oxidation products produced by oxidation of a unit mass of fuel. Thus, the cryogenic solid fuels are expected to have higher burning rates because their h_v are ten to twenty times smaller than the h_v of conventional hybrid fuels. The thermodynamic blowing coefficient[4] for PMMA is 5, compared to ethylene's value of 85.

Sutton's textbook[5] summarizes this and other approaches for modeling the fuel regression rate along with experimental results.

EXPERIMENTAL

An axisymmetric laboratory scale experiment to measure the gross overall average burning properties of conventional and cryogenic solid hybrid rocket fuel is presented in figure 1. The definition and values of the experimental variables are defined below.

P_a is the ambient pressure in the laboratory, around 91.0 kPa (13.2 psia)

m'_{ox} is the instantaneous mass flow rate of gaseous oxygen, which is the principal experimental control variable. It was measured with a precision thermistor/laminar bypass flow sensor obtained from Omega, model FMA-876-V, which had a maximum flow measurement of 500 standard liters per minute (11.9 g/s) oxygen, and an accuracy of 2%. The start-up transient response time required to reach steady state from zero flow was 0.5 to 0.8 seconds. Thereafter, the flow sensor responded to small changes in flow in a few tens of milliseconds. Experiments to date have been limited to $m'_{ox} < 20$ g/s, and varied by about 10% during the burns because pressure buildup in the combustion chamber fed back into the oxygen supply system.

L is the height of the fuel grain. Most of the cryogenic solid ethylene and n-pentane fuel grains had L = 15.7 cm (6-inches). Most PMMA standard burns had L = 10.1 cm (4-inches).

r_c is the radius of the combustion chamber, which was the inside radius of a 1-inch diameter, 0.049-inch wall, stainless steel tube: $r_c = 1.14$ cm (0.450-inch).

r_o is the initial radius of the fuel grain, which for most runs was 1.27 cm (1/2-inch).

L_p is the length of the post combustion chamber, which was designed to be as small as possible: $L_p = 10.1$ cm (4-inches).

$m_{ox,post}$ is the mass flowrate of oxygen that enters the post combustion chamber, below the fuel grain. At this point in time, we have not carried out experiments with post combustion oxidizer, $m_{ox,post} = 0$ g/s. It may be necessary to use post combustion oxygen to achieve complete fuel combustion.

P_c is the instantaneous combustion chamber pressure during the burn, which was acquired at the rate of 100 Hertz with a computer, and was measured with a diaphragm pressure transducer with a frequency response around 100 Hertz. The maximum pressures measured to date are around 2.06 MPa (260 psia).

A_n is the area of the nozzle/orifice, which for the experiments reported here were $A_n = .247$ cm^2, $A_n = 0.203$ cm^2, and $A_n = .178$ cm^2. The nozzle choked the flow[6], $P_a/P_c < 0.52$. Under these conditions the rocket equation applies, in which the characteristic exhaust velocity, c^*, is a simple function of total mass flux through the nozzle, m', A_n, and P_c, as well as the chamber temperature, T_c, average molecular weight of combustion gases, M_{av}, and the specific heat ratio, γ, viz:

(4) $c^* = P_c A_n/m' = (R\ T_c/M_{av})^{1/2}\ \{\gamma[2/(\gamma+1)]^{(\gamma+1)/(\gamma-1)}\}^{-1/2}$.

where R is the universal gas constant. Thus the experimental c^* velocity is a measure of the efficiency of combustion because it it is related to the chamber temperature per unit average molecular weight. The function $\{\gamma[2/(\gamma+1)]^{(\gamma+1)/(\gamma-1)}\}^{-1/2}$ has a limit of about 1.65 as γ approaches unity, which occurs for molecules with more than about 5 to 10 atoms.

m'_f is the instantaneous total mass flow rate (g/s) of fuel into the vapor phase. In these experiments we compute a gross overall average mass flow rate of fuel, $m'_{f,ave}$, based on the time required to burn all of the cryogenic solid fuels, t_b, or, in the case of plexiglass standard, on the mass of PMMA burned over the duration of the run. In either case, the burn time is a gross estimate that is based on the P_c-time history of the experiment, as described later in this report.

r' is the instantaneous radial regression rate of fuel. A gross overall average experimental r', r'_{ave}, was computed from the total thickness of the cryogenic solids, $r_c - r_o$, and the burn time: $r'_{ave} = (r_c - r_o)/\Delta t_b$. Similarly, for the PMMA standard burns, r'_{ave} was computed from the weight loss, Δw, and the burn time: $r'_{ave} = (1/\Delta t_b)([\Delta w/\pi r_f L + r_o^2]^{1/2} - r_o)$. The experimental r'_{ave} values are thus averages over the fuel grain length and radius and the burn time.

The "uniform burn" approximation

In the "uniform burn" approximation, the fuel burns uniformly along the axis, and the instantaneous fuel regression rate, $r' = dr/dt$, is independent of the axial distance along the port. A mass balance in terms of the fuel density, ρ_f, and the cylindrical volume element, dV, of thickness dr, results from $dV = \pi L[(r + dr)^2 - r^2]$, $= 2\pi L r dr$ and may be written:

(5) $\quad m'_f = dm_f/dt = 2\rho_f \pi L r \, dr/dt$

The mass balance equation may be used to derive other quantities and relationships. The instantaneous mass flux of oxygen through the port, G_{ox}, and the instantaneous average mass flux of fuel G_f (averaged over the fuel grain height, L) , are given by:

(6) $\quad G_{ox} = m'_{ox}/\pi r^2$

(7) $\quad G_f = \rho_f r' = m'_f/2\pi r L$

The instantaneous oxidixer to fuel mass ratio, $R = m'_{ox}/m'_f$, is given by:

(8) $\quad R = (r/L)(1/2\rho_F)(1/r') G_{ox} = (1/2\pi r L \rho_F r') m'_{ox}$

which may be rearranged to the familiar form where r' is given explicitly as a function of the oxygen mass flux or mass flow rate:

(9) $\quad r' = (r/L)(1/2\rho_F)(1/R) G_{ox} = m'_{ox}/2\pi r L \rho_F R$

Two idealizations of combustion experiments that are carried out at constant m'_{ox} may be defined: (1) constant R burn, or constant m'_f burn, and (2) constant G_f burn, or constant r' burn. Thus, for the uniform burn approximation with constant R (or equivalently, constant m'_f), Eq(9) may be integrated to obtain the fuel port radius and fuel flux as functions of time:

(10) $\quad r = (r_o^2 + Ft)^{1/2}$

(11) $\quad G_f = \rho_F F/[2(r_o^2 + Ft)^{1/2}]$

where F is a constant of the burn: $F = m'_{ox}/\pi L \rho_F R$. F has dimensions of a diffusion coefficient, and may be thought of as the mass diffusivity of the evaporating liquid fuel surface. Thus, in time t, the evaporating surface dissappears to a depth given by $(Ft)^{1/2}$.

For the case where a burn occurs at constant fuel flux (or equivalently at constant regression rate), Eq (7) may be integrated to produce:

$$(12) \quad r = Mt + r_o$$

$$(13) \quad R = m'_{ox} /[2\pi L \rho_f M(Mt + r_o)]$$

where M is a constant of the burn: $M = G_f/\rho_f = r'$. Equation (13) shows that R must decrease during a constant r' burn.

When the fuel flux or regression rate are constant during a burn, the temperature of the evaporating liquid fuel surface, T_S, is also a constant of the burn. T_S may be related to the surface evaporation flux by application of the detailed balance principle to the liquid-vapor eqilibrium[7]:

$$(14) \quad G_f = \rho_{gas} c_{av}/4 = (p_v/RT_S)(8kT_S/\pi m)^{1/2}$$

where ρ_{gas} is the density of vapor in equilibrium with liquid at T_S, c_{av} is the average velocity of the Maxwellian gas molecule of molecular mass m, k is Boltzman's constant, and where p_v is the vapor pressure of the liquid at T_S. The Clausius-Clapeyron[7] equation gives the vapor pressure as a function of temperature: $p_v = p_{v,o} \exp(-h_v/RT_S)$, where h_v is the heat of vaporization and R is the gas constant. Thus, an experimental measurement of r' (or G_f) may be used to infer an effective instantaneous temperature at the surface of the evapoarating fuel that is an average over the L dimension of the experiment.

As pointed out by Sutton[5], useful engineering evaluations of hybrid fuels may be carried out by use of the general form for the regression rate,

$$(15) \quad r' = aG_{ox}^n = a(m'_{ox}/\pi r^2)^n$$

which lumps all of the complexities of hybrid combustion into two empirical parameters, a and n. In actual experiments the value of n has been found to vary between 0.4 and 0.7. Comparison of equations (9) and (15) shows:

$$(16) \quad R = (1/2\rho_F La)(m'_{ox}/\pi)^{1-n} r^{2n-1}$$

Thus, R is a constant of the burn only in the special case where n = 0.5. If n < 0.5, R decreases during the burn, and if n > 0.5, R increases during the burn.

The optimum R, $R_{\phi=1}$, occurs when the oxygen to fuel ratio is near its stoichiometric value, i.e., when the equivalence ratio, ϕ, is unity. For the fuels studied in this research, $R_{\phi=1}$ values are 3.43 for ethylene, 3.56 for n-pentane, and 1.92 for PMMA. Experiments completed to date include burns of ethylene and n-pentane where the instaneous R was as small as 0.3 throughout most of the burn. Average R values for PMMA burns ranged between 2 and 3.

Oxidizer flowfield at entrance to the fuel grain port

No effort was made to condition the oxidizer flowfield prior to entering the fuel port. Oxygen entered the combustion chamber at room temperature through a 0.48 cm diameter tube that was bent to impart a slight spiral trajectory. At m'_{ox} of 5 g/s, the Reynolds number was 65,000. Additional chaos and turbulence was imparted to the flowfield when the oxygen collided with the microtorch/spark ignitor assembly. Turbulence was enhanced by asymmetric high velocity injection onto an obstruction at the top of the fuel grain.

Video Recording

SVHS video tape recordings provided considerable surveillance and documentation. The SVHS format produces about 450 lines of video data at the rate of 30 frames per second, 2 subframes per frame, for a total of 60 frames per second, time resolution of 17 ms. Panasonic industrial micro SVHS CCD

cameras, tape recorders, and monitors were used. The cameras were positioned around the experiment to record four views of the burning events:

(1) The burning surface of the fuel grain was imaged through a window at the top of the combustion chamber (see Figure 1), located about 25 centimeters above the top of the fuel grain. A telephoto lens provided a 2 cm field of view of the burning surface, for a spatial resolution of about 60 μm. Generally, because this view looked directly into the chaotic conflagration, it required a pinhole iris, as well as a neutral density filter (1% transmittance). The pinhole iris maximized the depth of field to about $\pm$ 8 cm.

(2) A close-up, 10 cm field of view of the exhaust plume (see Figure 1) was obtained with a telephoto lens that stood off about 45 cm from the exhaust nozzle. This view was also bright, which enabled use of a pinhole iris. Up to six Mach diamonds were clearly visible in the exhaust plume, which varied from a highly luminous, sooty, underoxidized flame, to a clean and fully oxidized flame.

(3) A wide shot, 100 cm field of view of the exhaust plume was obtained with a telephoto lens, usually through a pinhole iris.

(4) A wide shot, 150 cm field of view was obtained with a Panasonic SVHS video camcorder.

PMMA Standard Fuel Grain

PMMA (polymethyl methacrylate, or Plexiglass) fuel grains measuring 2.28 cm (0.900-inch) outside diameter, 1.27 cm (0.500-inch) inside diameter, and 10.2 or 15.2 cm (4- or 6-inch) long were machined from commercially available 1-inch diameter solid rod. The measured density was 1.17 g/cm^3, which agreed with the literature.[8]

Cryogenic Fuel Grain Preparation

A vacuum Dewar containing the fuel grain area in Figure 1 was used to prepare cryogenic fuel grains of ethylene and n-pentane, with L = 15.2 cm (6-inches), and up to 5 mm thick. The process was monitored and recorded on videotape by positioning a camera/telephoto lens to view the inside wall of the combustion chamber. The three techniques used to prepare solid ethylene produced three distinct morphologies. (1) A porous, low density solid (about 0.4 g/cm^3) was produced by condensation below the triple point pressure (about 700 mTorr). The Dewar was filled with liquid nitrogen slowly, about 0.5 cm per minute, while ethylene vapor, flowing at about 0.5 g/min, condensed on the combustion chamber wall at the level of the surrounding LN$_2$. This condensation of gas directly to solid produced a precise, well defined fuel grain of uniform thickness in about 30-minutes. (2) A dense mixture of amorphous glassy solid and polycrystalline solid resulted when ethylene condensed from a fast flowing helium/ethylene mixture at atmospheric pressure. In this procedure, the Dewar was filled to a depth of 15 cm, and a helium/ethylene mixture was blown through the cold combustion chamber. The mixture ratio varied from pure ethylene to pure helium. The ethylene condensed out of the mixture as a liquid over the entire six-inch length of the cold wall. It would flow down the wall and freeze rapidly into a glassy amorphous solid. Pure helium was used to melt protuberances that would grow on the main body of the solid, which would then run down the wall and refreeze or drip out of the tube and be vented. About 80 to 90% of the ethylene was vented to the atmosphere. After freezing an excessive amount of solid with a crude irregular channel, a circular port could be sculpted somewhat by forcing a warm rod up the center. (3) A well defined accurate geometry of polycrystalline solid ethylene was produced when a mandril was positioned inside the combustion chamber. The dewar was filled at the rate of about 0.5 cm per minute while ethylene gas, flowing at about 1 g/min, liquified on the cold wall and collected at the bottom of the mandrel and slowly froze.

A well defined polycrystalline solid n-pentane fuel grain was produced using the mandril. In this procedure, the liquid was poured slowly into the mandrel, where it froze slowly, simultaneously with the raising of the LN$_2$ level in the Dewar.

Ignition

The fuel grain was ignited by synchronizing the Tesla coil ignition of a small methane/oxygen torch with a staged increase of the oxygen mass flow to the final m'$_{ox}$ of the experiment. Thus, the oxygen mass flow was programmed to ramp to the final maximum m'$_{ox}$ in about 0.3 seconds. The microtorch

contributed enough energy to melt and vaporize a small amount of fuel, which mixed with the initial slow flow of oxygen and provided a smoothe "soft" start to the burning of the fuel. Solonoid valves and gas flows were controlled remotely with a control program that worked within the Labview environment.

RESULTS AND DISCUSSION

PMMA

Figure 2 summarizes our results, and compares our PMMA standard burns to Bryant's[9] PMMA study. In Figure 2, we plot the average regression rate, r'_{av}, based on the overall change in fuel radius over the burn time, $r'_{av} = \Delta r/t_b$, versus the initial mass flux of oxidizer, $G_{ox,initial}$. We note that the constant control variable of these experiments is m'_{ox}, and that $G_{ox,initial} = m'_{ox} / \pi r_o^2$, where $r_o = 0.64$ cm (0.25-inch) in both sets of experiments. Our PMMA results lie on the extrapolation of Bryant's[9] PMMA results to low m'_{ox}. The pressure profiles of Bryant's burns were constant and steady, indicating that the O/F ratio throughout the burn, and therefore m'_f, were constants of the burn. Thus, in the uniform burn approximation, equations (10) and (11) would apply, and the regression rate decreases during the burn. Bryant fit his data to the form: $r'_{av} = a\, G^n_{ox, initial} = [a/(\pi r_o^2)^n][(m'_{ox})^n]$, and finds a = 0.0608 in/s, n = 0.61, when m'_{ox} is expressed in lbm/s. Bryant's study, like ours and others, involves a constant m'_{ox} experiment. G_{ox} is not a constant of the burn. A gross overall average oxidizer flux, $G_{ox,average}$, might be used to obtain the empirical constants in $r' = a\, G^n_{ox, average}$, but they would not be comparable to the constants in equation (15) that derive from direct real time measurements (by ultrasound and other techniques) of r during the burn.

When m'_f is constant, the characteristic c* velocity is constant, and easily computed from eq (4). Table 1 compares experimental variables and c* calculations of the two studies. Although our burns produced constant pressure profiles, they were accompanied by large instabilities that were symmetric around an average P_c. We used this average P_c in the calculation of the c* of our burns.

Table 1. Comparison of PMMA data from Bryant and 5-second PMMA burns from this study.

Bryant[9] ($A_n = 0.585$ cm^2, L = 30.5 cm, $r_o = 0.64$ cm)

m'_{ox} (g/s)	m'_f (g/s)	P_c (psia)	c* (cm/s)	R
12.7	7.68	85	168,000	1.65
19.0	10.7	120	163,000	1.76
24.9	13.5	155	163,000	1.84
31.3	14.6	185	163,000	2.14

This study ($A_n = 0.202$ cm^2, L = 10.1 cm, $r_o = 0.64$ cm)

5.0	1.68	53.0 ($\pm$13)[a]	113,000	2.98
5.0	1.67	53.8 ($\pm$3.5)[b]	111,000	2.99
3.1	1.57	51.0 ($\pm$11)	152,000	1.97

a) numbers in parenthesis are the measured instabilities in the pressure.
b) L = 15.2 cm, otherwise, L = 10.1 cm.

Table 1 shows agreement in c* at similar R values around the R = 1.92 stoichiometric value. Also, our L = 15.2 cm produced a relatively stable pressure profile with small instabiliy compared to the shorter fuel grains. The overoxidized experiments (R = 2.98) produced a substantially smaller c* in our study.

Solid Ethylene and Pentane

Figure 2 also compares our results for the cryogenic fuel grains that were prepared using the mandril technique. We estimated the time required to burn all of these fuel grains ($\Delta r = 0.5$ cm), and plotted the gross overall average regression rate at the two values of m'_{ox} (5 g/s and 3 g/s) to obtain "ball park" estimates for figure 2. The instantaneous r' values vary by about a factor of two around the

averages. These "ball park" estimates show that pentane and ethylene burn three and ten times faster than PMMA, respectively. Values of R around the maximum P_c were 0.6 to 0.8 for pentane, and 0.3 to 0.4 for ethylene. Based on observation of the exit plume, considerable soot was produced in these highly underoxidized experiments. Further, we observed that most of the fuel burned in the air after exiting the combustion chamber.

Figures 3, 4, 5, and 6 show the chamber pressure profiles for burning ethylene and pentane at high and low oxidizer mass flow rate, in addition to computed quantities that are based on the approximations described below. Although the pressure profiles were relatively stable, they were not constant. The profiles showed long tails, and decreasing from their maxima at the "top of the burn". In order to compute a time dependent characteristic velocity c^*, we require an estimate of the time dependent fuel mass flow rate, m'_f, to incorporate into equation (4). The excess pressure created when the fuel leaves the wall, mixes and burns, may be obtained directly from the P_c vs t profile: $P_{excess} = P_c - P_{c,background}$, where $P_{c,background}$ is the pressure in the chamber when cold oxidizer flows. We offer the expression:

(17) $m'_f = b \, (P_{excess})^i$

and suggest that the value of i should be about unity, because the mass flow of fuel is directly proportional to the heat release in the chamber, which is proportional to the temperature rise, which in turn is proportional to the pressure rise. The constant b is a normalizing factor, calculated from $b = (m_f/\Delta t)\Sigma(P_{excess}\Delta t)$, where Δt is the time step for our data acquisition, $\Delta t = 0.01$ sec. This leads to a time dependent evaluation of the characteristic velocity, c^*:

(18) $c^* = A_n P_c/[m'_{ox} + m'_f] = A_n P_c/[m'_{ox} + bP_{excess}]$

Using equation 18, the c^* curves vs. time were calculated for the two solid ethylene and two n-pentane experiments. These results are also presented in Figures 3 through 6. The total fuel mass was calculated based on the fuel volume, 43 cm³, and an estimated density $\rho_f = 0.7$ g/cm³ based on a 15% volume contraction when liquid freezes. Ideal c^* values were calculated using a standard specific impulse program.[10] The calculated ideal c^* values for fuel-rich burns (R = 0.6) of ethylene and pentane are 143,000 cm/s and 54,000 cm/s, respectively. are around A comparison of the c^* values for each experimental run shows good agreement for the pentane experiments but substantially low c^* values from the ethylene experiments. The low ethylene results may be due to several factors, such as poor mixing of the fuel/oxidizer gas stream for the fast ethylene combustion, or ethylene fuel densities considerably lower than deduced from the volume of the deposited fuel grain. In either case, additional experiments must be conducted to determine the optimum combustion conditions.

CONCLUSIONS

Cryogenic solid fuel grains produced from low molecular weight, volitile hydrocarbons have been sucessfully combusted with gaseous oxygen in a simple hybrid rocket configuration. The burning rate of solid ethylene and solid pentane, when compared to polymethyl methacrylate (PMMA), show increased blowing coefficients and average regression rates.

Current limitations in the mass flow delivery of the gaseous oxygen prevented experiments that reach the stoichiometric mixture ratio for most of the tests, expecially for ethylene. This limitation will be overcome in future experiments.

REFERENCES

1. Carrick, P. G., "Theoretical Performance of High Energy Density Cryogenic Solid Rocket Propellants", AIAA 31st Joint Propulsion Conference, July 1995, San Diego, CA; and USAF Technical Report PL-TR-93-3014.

2. Altman, D., "Hybrid Rocket Development History," AIAA/SAE/ASME/ASEE 27th Joint Propulsion Conference, June 24-26, 1991, Sacramento, CA, Paper AIAA 91-2515, American Institute of Aeornautics and Astronautics.

3. Marxman, G. A., "Boundary Layer Combustion in Propulsion," 11th International Symposium on Combustion, The Combustion Institute, August 1966, p. 269.

4. Lengelle, G., Fourest, B., Godon, J.C., and Guin, C., "Condensed Phase Behavior and Ablation Rate of Fuels for Hybrid Propulsion," AIAA/SAE/ASME/ASEE 29th Joint Propulsion Conference, June 28-30, 1993, Monterey, CA, Paper AIAA 93-2413, American Institute of Aeornautics and Astronautics.

5. Sutton, G. P., "Rocket Propulsion Elements," Sixth Edition, (John Wiley, New York, c1992) Chapter 15.

6. Zucrow, M. J., and Hoffman, J. d., "Gas Dynamics," Volume 1, (John Wiley, New York, c1977), p 277ff. ; and Welty, J.R., Wicks, C.E., and Wilson, R.E., "Fundamentals of Momentum, Heat, and Mass Transfer," (John Wiley, New York, c1969), Chapter 11.

7. Moelwyn-Hughes, E. A., "Physical Chemistry," The Macmillan Company, New York, c1961.

8. Wunderlich, W., "Physical Constants of Polymethyl methacrylate, PMMA," Polymer Handbook, Third Edition, J. Brandrup, E.H. Immergut, Eds., John Wiley, New York, c1989, p. V/77ff.

9. Bryant, Rodney, A., "An Experimental Investigation of a Hybrid Rocket Using Gaseous Oxygen and Polymethyl Methacrylate," Masters Thesis, Department of Aeronautics and Astronautics, University of Maryland, 1993.

10. USAF, AFAL Theoretical Isp Program, originally written by Curtis Selph and Robert Hall, adapted for microcomputers by C. Beckman, R. Acree, and T. Magee, Phillips Laboratory, Edwards AFB, CA.

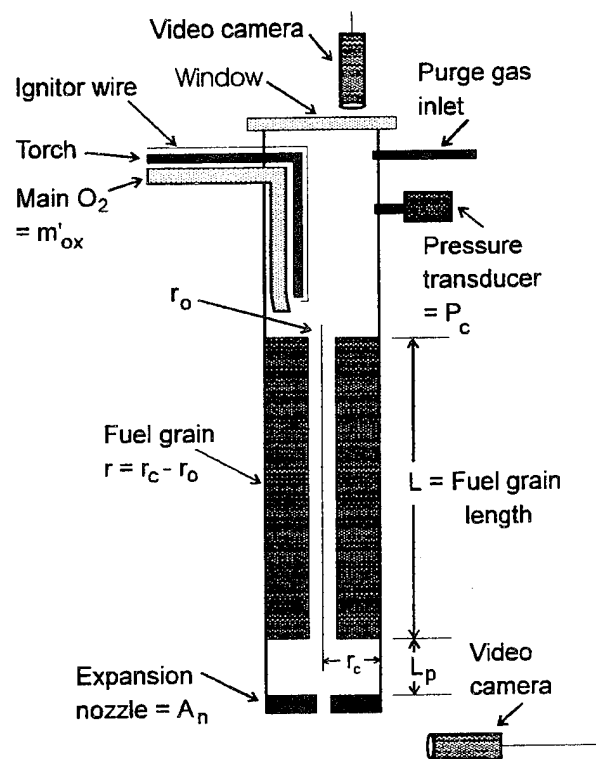**Figure 1. Experimental Cryogenic Hybrid Rocket Configuration**
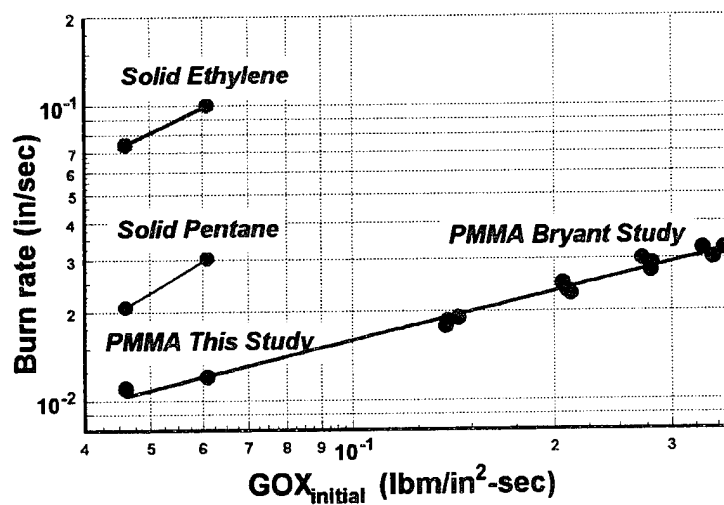

Figure 2. Comparison of Polymethyl methacrylate (PMMA) with pentane and ethylene
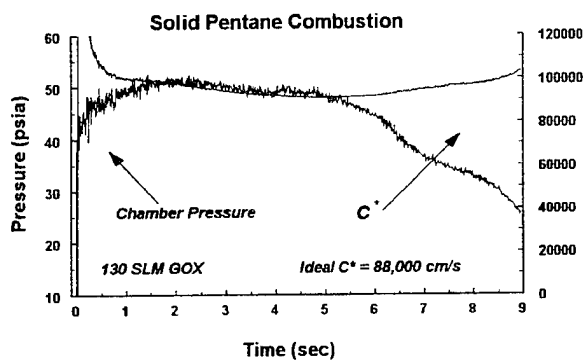
Figure 3. Combustion of Solid Pentane with 130 SLM GOX.
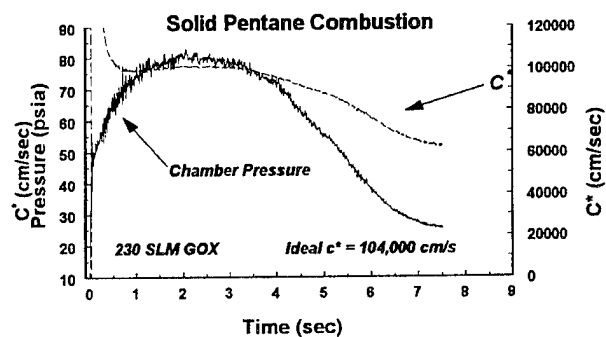

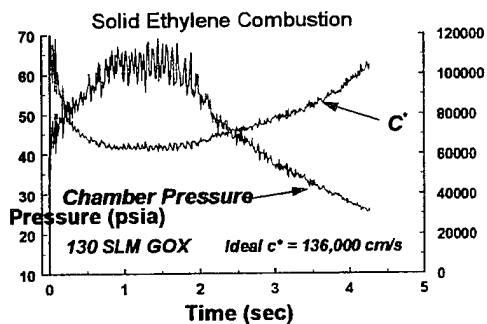**Figure 4. Combustion of Solid Pentane with 230 SLM GOX.**

Figure 5. Combustion of Solid Ethylene with 130 SLM GOX.
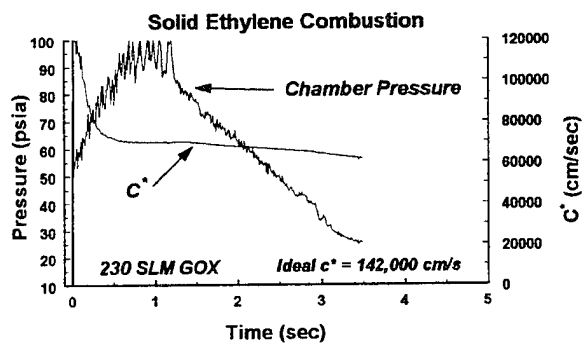

Figure 6. Combustion of Solid Ethylene with 130 SLM GOX.

41

Search for Metallization: Excitations, Order Parameters and Structure of High Pressure A-Phases of the Hydrogens

Isaac F. Silvera

Lyman Laboratory of Physics, Harvard University, Cambridge, MA 02138

Solid deuterium has been studied by high and low resolution spectroscopy using a tunable color center laser in the infrared. Spectra have been recorded to pressures approaching 200 GPa and down to liquid helium temperatures. The observed vibron absorption lines, combined with Raman scattering observations can be used to investigate the allowed structures of the various phases. In a search for metallization of the deuterium-A phase, the broad band absorption spectra are used to try to identify a Drude edge characteristic of metallization. The spectra show an interesting increase of absorption with decreasing frequency when in the A-phase. Even though these measurements are to the lowest energy yet for the hydrogens, still lower energy spectra are required to make a definitive statement as to the nature of the A-phase.

At sufficiently high pressures believed to be in the 150-400 GPa range, hydrogen and its isotopes are expected to become metallic. The hydrogens have rich and unusual phase diagrams at high pressure. In the megabar range the hydrogens are predicted to have a band overlap insulator-metal transition within the molecular phases. At still higher pressure, molecules should dissociate to form the atomic metallic state, also predicted to be a high temperature superconductor. At about 150 GPa both hydrogen and deuterium have transitions to a new phase called the A-phase, shown in Fig. 1. This phase has some unusual spectroscopic properties which will be discussed. Although the A-phase has been suspected to be the molecular metallic phase, there still exists no experimental evidence for this hypothesis. We have carried out infrared measurements to study the Drude behavior and find interesting results which depend on the ortho-para mixtures of the solids [1]. We have also made a detailed IR and Raman study of the of the excitations to determine the phase lines in solid ortho-D_2 down to liquid helium temperatures [2]. We find that the line for the A-phase meets a line for orientational order in the insulating phase at a triple point, as shown in Fig. 1.
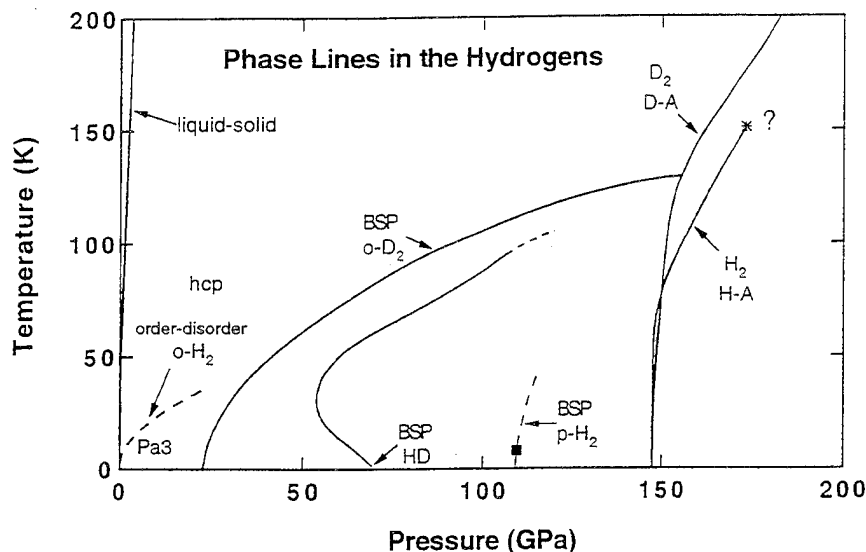
Fig. 1 The high pressure phase diagram of the hydrgogens.

A study of the IR and Raman active modes enables us to determine the order parameters and to narrow down the possible structures of the solid. Except for the low pressure hexagonal close packed structure, the structure of the various phases have not been identified. Crystal structures popular amongst theorists for calculations of electronic structure of the high pressure phases, such as the hcp and Pa3 space groups have been eliminated for the A-phases by our experimental observations.

In order to measure the spectra we used a Burleigh tunable color center laser with a useful spectral range from 0.37 to 0.55 eV. The chopped laser beam was split into a reference arm and a sample arm containing the diamond anvil cell, and detected with two independent cooled InSb detectors. The dual beam technique assures proper scaling of the absorption spectra and makes the signal independent of laser power fluctuations. Broad band spectra in the D-A phase were normalized by spectra taken in the low pressure phase. In this way we are very sensitive to small changes in the dielectric constant and relatively insensitive to systematic errors which could influence the final results. For high resolution spectra of vibrons, the spectra were often normalized by spectra in a high temperature disordered phase (hcp) as the absorption strength depends on the state of order and this procedure provides a sensitive method of observing weak absorption lines.

The normalized broad band spectrum is shown in Fig. 2. In Fig. 2a we see that with increasing pressure the absorption increases on the low energy side of the spectrum (in these figures the large peak at about 3150 cm^{-1}, corresponding to a vibron, should be ignored). It has been suggested that metallization in the hydrogens might be suppressed by Anderson
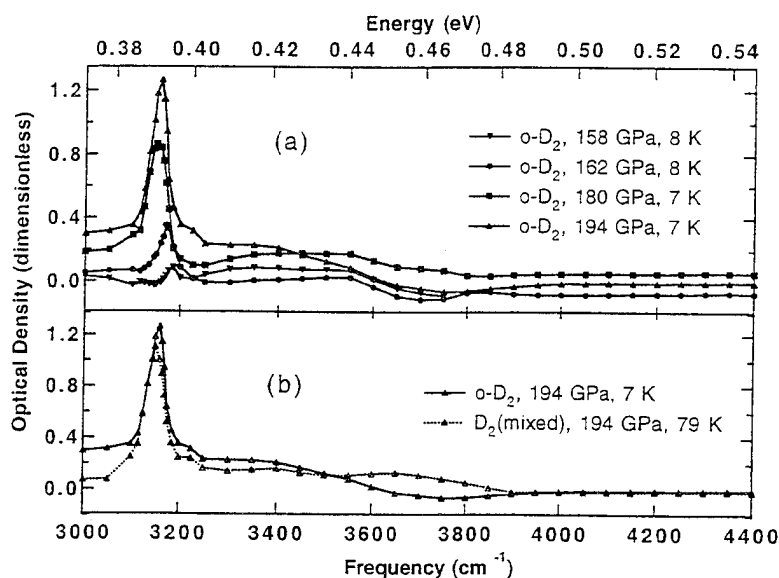
Fig. 2. IR absorption in deuterium at indicate pressures, normalized to the absorption at a pressure of about 150 GPa where deuterium is not in the A phase. a) shows absorption as a function of pressure and b) for mixed and pure ortho deuterium.

localization. If a mixed crystal of ortho-para deuterium is used then electrons will see different potentials for the different species and since these are randomly distributed, electrons might be localized. To study this possibility, we compared the absorption for a mixed crystal and for pure ortho-deuterium in Fig. 2b. Indeed we observe a change in the absorption spectrum with the pure crystal absorbing more in the low energy region. In Fig. 3 we compare all data to date, all of the older data being on hydrogen. The absorption bump represented by open circles from Hanfland et al [3] was presented as evidence of metallic behavior, but it has been argued that this interpretation is invalid [4]. Moreover, this peak rises and begins to fall, uncharacteristic of Drude behavior. In Fig. 3 the dashed lines represent the Drude
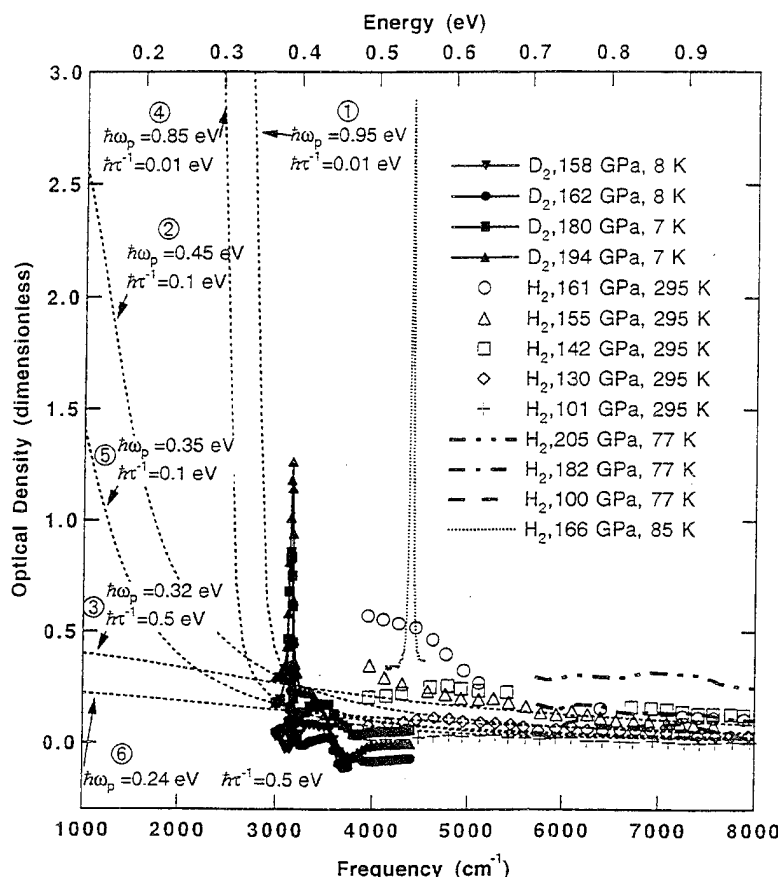
Fig. 3 A comparison of older data of IR absorption in hydrogen with our current measurements on deuterium, shown by the filled symbols. The dashed lines represent absorption for a Drude free electron model with several values of Drude parameters. The sharp peaks correspond to IR active vibrons and are not important for the Drude behavior.

absorption for models with differing Drude parameters, ω_p and τ. These were chosen as examples with a high frequency tail such as we observe. It is possible that metallization might be present, but clearly the current data is insufficient to make a determination . We conclude that the A phase might be metallic, but the data must be extended to substantially lower energy to search for a possible sharp rise of the Drude absorption.

One of the most important input parameters for theoretical analyses is the crystal structure of the A phase. Since X-ray diffraction determination is very difficult at megabar pressures, we have attempted to determine the structure from spectroscopy. A group theoretical

analyses of a crystal structure will give the number of lattice modes and which are IR or Raman active. This information can be correlated with the experimental observations to narrow down the possible structures. The high resolution data identified a number of IR active vibron modes in the various phases and these have been discussed in detail by Cui et al [2]. The results of the analyses and experiments are summarized in Table I. We see agreement between

Space Group	IR Vibron	Raman Vibron	IR Phonon	Raman Phonon	References
P63/mmc hcp-c	(0)	A_{1g} (1)	(0)	E_{2g} (1)	
Pa3	(0)	A_g+T_g (2)	$2T_u$ (2)	(0)	
P42/mnm rutile	(0)	$A_{1g}+B_{1g}$* (2)	E_u (1)	(0)	
Pca2₁	$A_1+B_1+B_2$ (3)	$A_1+A_2+B_1+B_2$ (4)	$2A_1+2B_1+2B_2$ (6)	$2A_1+3A_2+2B_1+2B_2$ (9)	
P2₁/c	A_u+B_u (2)	A_g+B_g (2)	$2A_u+B_u$ (3)	$3A_g+3B_g$ (6)	
Pmc2₁	A_1+B_1* (2)	A_1+B_1* (2)	A_1+B_1* (2)	$A_1+A_2+B_1$* (3)	
P2/m	B_u (1)	A_g (1)	(0)	$2A_g+B_g$ (3)	
Cmca	(0)	$A_{1g}+B_{3g}$ (2)	$B_{1u}+B_{2u}$ (2)	(0)	
P63/m	E_{1u} (1)	$2A_g+E_{2g}$ (3)	A_u+2E_{1u} (3)	$2A_g+E_{1g}+3E_{2g}$ (6)	

Experimental Observations for ortho-D_2

LP	0^	1^	--	1†	
BSP	3^	1^	--		
D-A	1^	1^	--		

^ This work

Table 1. Group theoretically allowed Raman and IR transitions for lattice modes in a number of crystal structures. The number of distinct modes is given in parenthesis. Experimental observations are shown at the bottom of the table.

experiment and theory for the known hcp structure at low pressure. Some of the structures popular with theorists have been eliminated for the A phase: hcp and Pa3. A good candidate was the P2/m phase. However our determination that the transition from the A phase to the hcp phase is a second order transition eliminates this structure. Using the Landau theory of phase transitions, we predict that for such a structure the transition must be first order. Thus, at this point the structure of the A phase is not yet determined, but our observations have eliminated a number of structures that were predicted by the latest theories.

References

1. L. Cui, N.H. Chen, and I.F. Silvera, Phys. Rev. Lett. **74,** 4011 (1995).
2. L. Cui, N.H. Chen, and I.F. Silvera, Phys. Rev. B **51,** 14987 (1995).
3. M. Hanfland, R.J. Hemley, and H.K. Mao, Phys. Rev. B **43,** 8767 (1991).
4. I.F. Silvera, *NATO ARW on Frontiers of High Pressure Research.* 1991. Plenum Press, New York.

"Hopping Rates and Ortho-Para Conversion Rates Determined for H_2 Molecules on Activated Carbon Fibers"

Steven Y. Song, Anupam Misra , Antonio Querubin, and J.R. Gaines
Department of Physics and Astronomy
University of Hawaii at Manoa
2505 Correa Road
Honolulu, Hawaii 96822

We have used pulsed NMR techniques to study H_2 and HD molecular monolayers absorbed on activated carbon fibers (ACF) over the temperature range from 4.6 K to 20 K. These fibers have an effective absorption area of 2000 m^2 per gram so that for monolayer coverage, 10^{19} molecules per m^2, one gram of ACF holds about one liter (STP) of hydrogen gas. We record the fourier transform of the NMR lineshapes (the FID) and the measured height of the FID immediately after the 90° pulse (a quantity that is proportional to the number of spins in the sample) as functions of time and temperature. The time dependence of the NMR signal in H_2 makes it possible to measure the ortho (spin 1) to para (spin 0) conversion time since only the ortho molecules have an NMR signal while the FID gives the lineshape and enables us to study the spin dynamics of the molecules. Our analysis of the NMR data is based on comparisons with that of oH_2-pH_2 mixtures of bulk (3D) solid hydrogen.

When the spins are confined to lattice positions, the NMR lineshape is essentially gaussian in nature (gaussian FID) and its width ($\Delta\omega$) is well characterized by the second moment, M_2, with $(\Delta\omega) \approx \sqrt{(M_2)}$. "Motion" of the spins results in a narrower line and a change in lineshape from gaussian to lorentzian (exponential FID), effects predicted by Anderson and Weiss[1]. If the motional frequency is Γ, the motionally narrowed linewidth is given by: $(\Delta\omega) \approx (M_2)/\Gamma$, a result valid so long as $\Gamma > \sqrt{(M_2)}$. The "motion" responsible for this narrowing can come from actual translational hopping, in which case the data can be used to infer diffusion coefficients, or it can be due to intramolecular interactions between neighboring oH_2 molecules that produce spin-flips, without any translational motion. *These latter interactions are absent in pure HD so that a narrowed HD resonance line is indicative of translational hopping.*

In our experiment with pure HD (about 1.9% H_2 and 0.3% D_2), we observe a lorentzian lineshape, indicative of motional narrowing, and the weakly temperature dependent observed widths (2.2×10^4 at 13.6 K to 4.4×10^4 rad/s at 5 K) are smaller than the width predicted from the second moment (5×10^4 rad/s). This is shown in Fig. 1. At 7.6 K, the hopping frequency calculated from our data is $\Gamma = 8 \times 10^4$ rad/s and the two dimensional (2D) diffusion coefficient is $D = <a^2>\Gamma/4 = 2.3 \times 10^{-11}$ cm^2/s, comparable to three dimensional (3D) H_2 at 11 K.
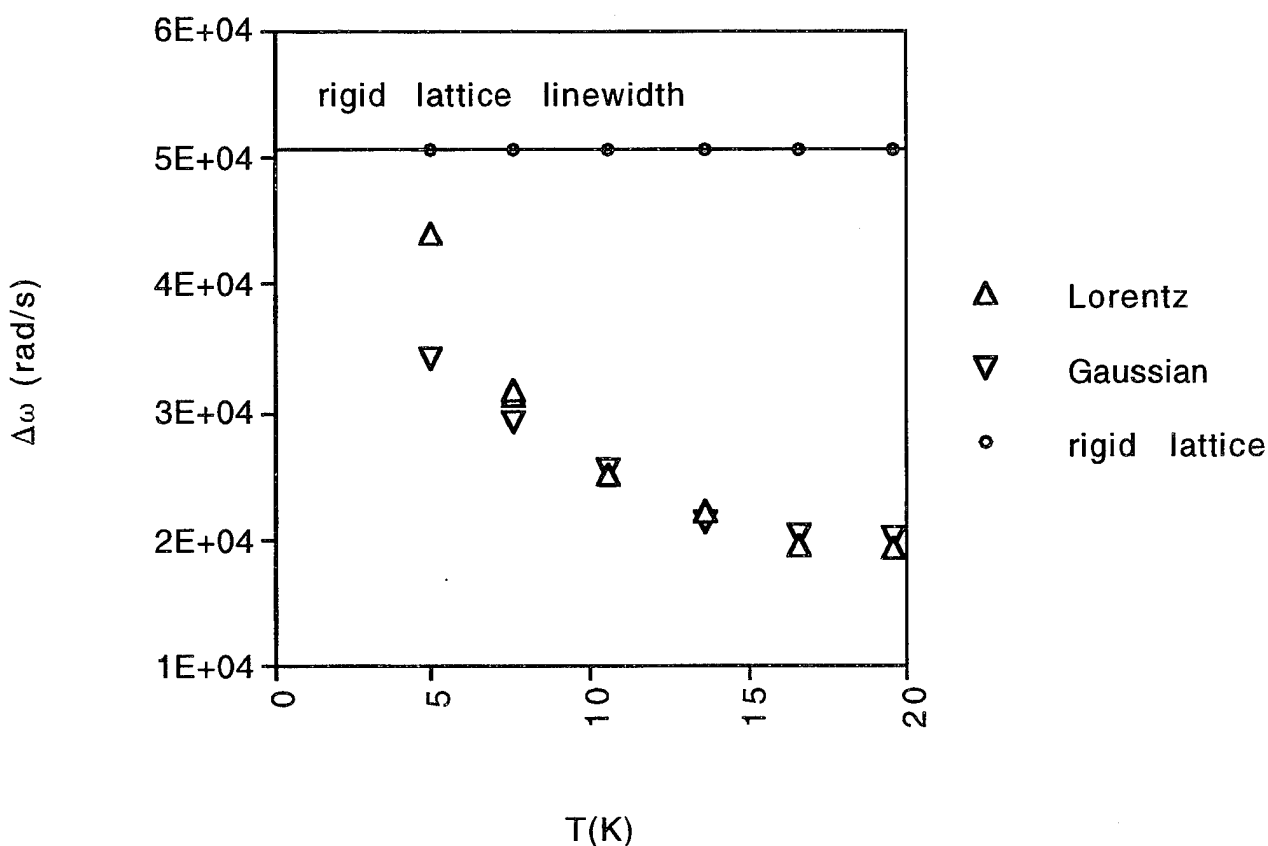
Figure 1. NMR linewidths for HD on ACF are shown. The predicted width for a rigid lattice is given by the solid line while the observed width, using both gaussian and lorentzian fits are shown.

The NMR lineshapes of H_2 molecules absorbed on ACF are also lorentzian and, at the starting oH_2 concentration of $x_1 = 0.75$, all widths are narrower than predicted from the calculated value of M_2. As the samples age, at fixed temperature, their linewidths increase, *exactly the opposite behavior expected from spins on a rigid lattice*. This is shown in Fig. 2. The increase in width as the concentration is reduced results from the electric-quadrupole-quadrupole interactions between J = 1 ortho H_2 molecules. These interactions are absent in HD at low temperatures as all molecules are in the J = 0 state.
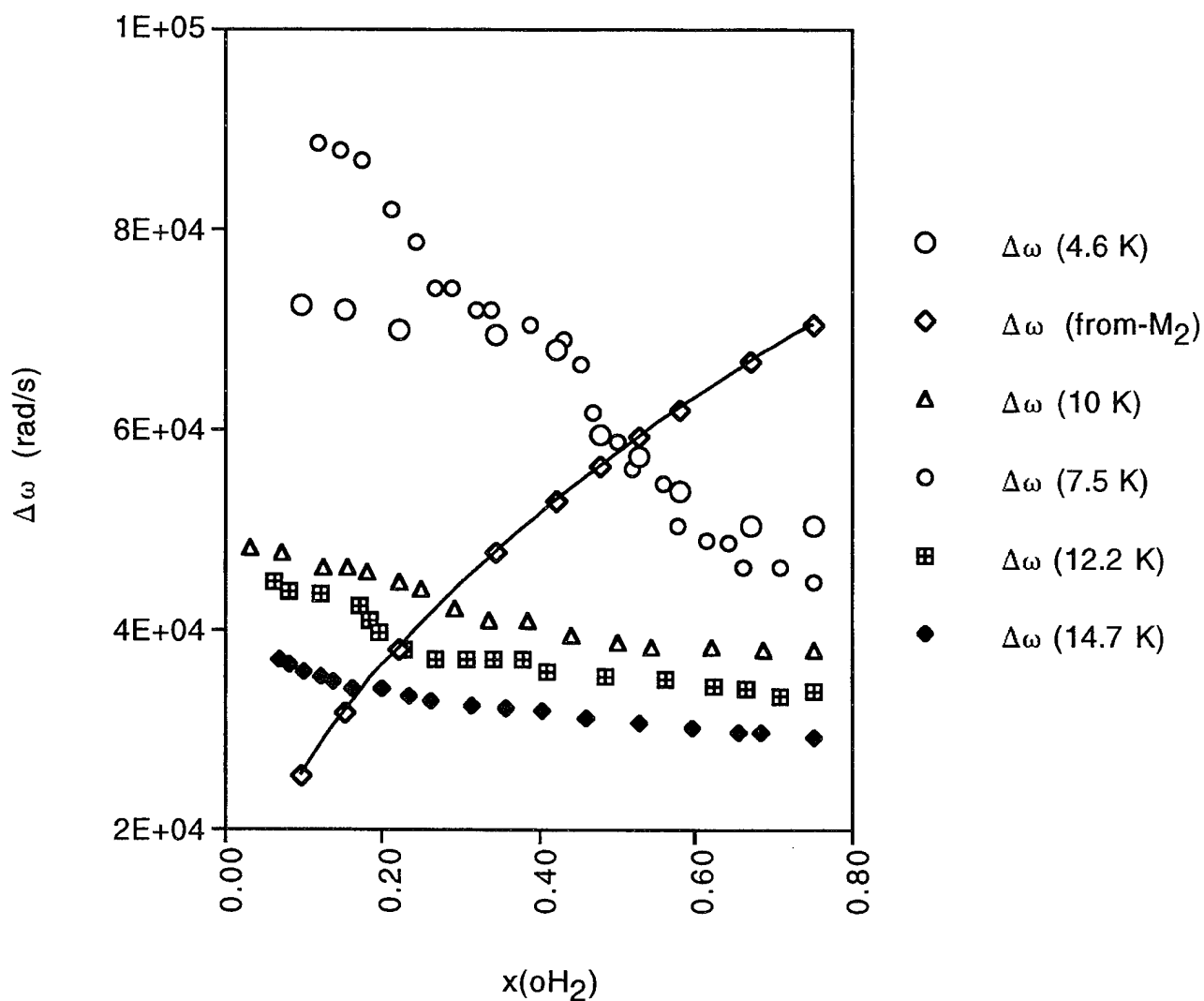
Figure 2. The observed NMR linewidths for H_2 on ACF are plotted vrs. the oH_2 concentration. The initial oH_2 concentration is assumed to be 0.75 although it may be smaller. The calculated "rigid lattice width" is shown for comparison.

This would indicate that the hopping frequency decreases with decreasing oH_2 concentration. Nevertheless, the hopping frequencies are comparable to those found in HD and the diffusion coefficients are of order of magnitude 10^{-11} cm^2/s. The weak temperature dependence of the hopping frequencies for $x_1 = 0.75$, is characteristic of an activation energy of 5.6 K.

Since the NMR signal height for H_2 is directly proportional to the number of oH_2 molecules, the decay of the signal at fixed temperature can be used to study the oH_2-pH_2 conversion process. Two types of conversion have been studied previously, intrinsic conversion where the intermolecular interaction between molecules provides the magnetic field gradient needed for conversion, and catalyzed conversion where a paramagnetic impurity such as an H (or O) atom or O_2 molecule provides the needed magnetic field gradient.

Using a "strong collision" approach to calculate the local transition probabilities, we obtain the following differential equations for intrinsic conversion:

(1)

$$(a) \frac{dN_1}{dt} = - (N_1)^2 (\frac{zv_0}{\tau}) f_c \quad \text{if } W_{10}\tau > 1$$

$$(b) \frac{dN_1}{dt} = - (N_1)^2 (zv_0 W_{10}) f_c \quad \text{if } W_{10}\tau < 1$$

where τ ($\tau = \Gamma^{-1}$) is the time to hop to any of the z nearest neighbor sites, v_0 is the volume per particle such that $v_0 N_T = 1$, and f_c is a correlation function that gives the fraction of near neighbor sites at the new site that were not near neighbor sites at the old site. For hcp lattice, $v_0 = a^3/\sqrt{2}$. To modify this for 2D, replace v_0 by A_0, the area per particle, where $A_0 = (\sqrt{3}/2)a^2$. For two dimensions f_c is approximately 0.50.

For intrinsic conversion, $(N_1)^{-1}$ is linear in time and the rate has been measured[2] for H_2 and found to be 1.9 % per hour or 5.3×10^{-6} s^{-1}. A careful calculation of the basic rate in H_2 has been done[3] finding a rate of 1.67% per hour.

Using the same procedure as above, we obtain the differential equations for catalyzed conversion (with c_a the concentration of unpaired electron spins):

(2)

$$(a) \frac{dN_1}{dt} = - (N_1) (\frac{zc_a}{\tau}) f_c \quad \text{if } W_c(a) \tau > 1$$

$$(b) \frac{dN_1}{dt} = - (N_1) (zc_a W_c(a)) f_c \quad \text{if } W_c(a) \tau < 1$$

In both cases, there is an exponential decay of the number of ortho molecules, $N_1(t) = N_1(0) \exp(-kt)$, where k depends on which of the above limits applies.

By using the factors in the calculation (but using the experimental value of the H_2 rate), it is possible to predict: (i) the intrinsic conversion rate for an H_2 monolayer (2D intrinsic rate $W_{10} \approx 1.7 \times 10^{-5}$ s^{-1}); and (ii) the transition probability per unit time due to

an unpaired electron spin at the nearest neighbor spacing (a). For 3D H_2, this is $W_c(a)$ = 5.46 x 10^{-2} s^{-1}(in agreement with the estimate of Shevtsov et al[4]). This latter rate can be adjusted to our monolayer spacing giving for 2D, ACF, the value $W_c(a)^{2D} \approx$ 0.177 s^{-1}. Our measured oH_2-pH_2 conversion rates are about a factor of 10 larger than the predicted intrinsic conversion rates and the signal decay is approximately (see below) exponential, indicative of catalyzed conversion. This is not surprising since O_2 contamination of the surface is assured given the transport and handling conditions of the ACF. Thus, we will ignore intrinsic conversion in our analysis.

There is an additional feature to the time decay of the NMR signal at fixed temperature, namely the conversion rate appears to change (increase), rather abruptly, with time, a phenomenon observed previously for 3D bulk H_2 by Schmidt[2] at 1.57 K and by Rall et al[5] for H_2 absorbed on zeolite. This is shown in Fig. 3.
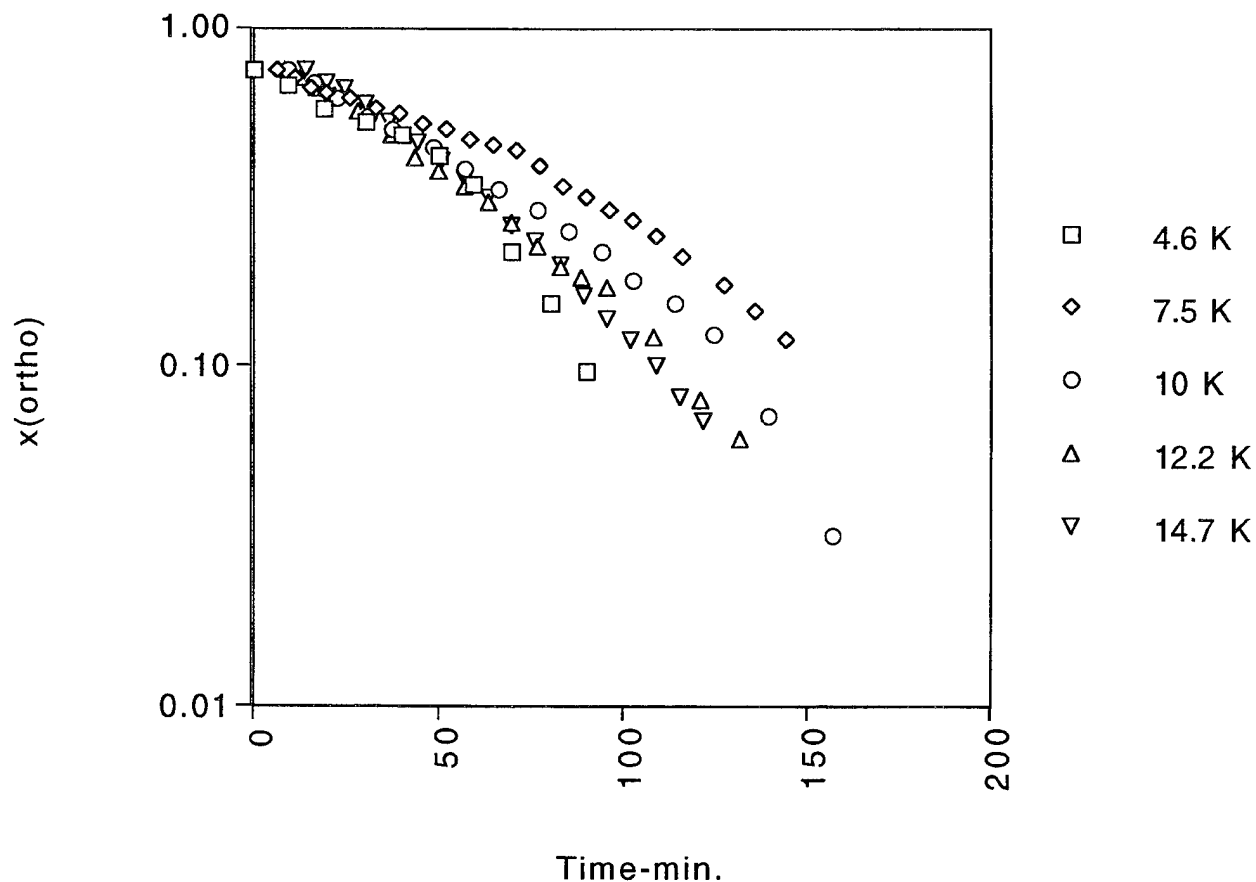

Figure 3. The oH_2 concentration (assumed 0.75 at the start) is plotted as a function of time at fixed T. The data cannot be fitted by a single exponential.

We have satisfactorily fitted the conversion rate data with two exponentials and extracted two rates, k_1 and k_2. There is a weak temperature dependence to these rates with k_1 increasing with T and k_2 decreasing with T so that they tend to converge to the same value at high T's. If we ignore the temperature dependence, the mean values are $\langle k_1 \rangle = (2.1 \pm .6) \times 10^{-4}$ s^{-1} and $\langle k_2 \rangle = (4.8 \pm 1.2) \times 10^{-4}$ s^{-1}. We will assume that k_1 is the "normal" rate based on the previous findings[2,5].

If we assume we are in the "fast diffusion" limit, then the rate k_1 is given in Eqn. 2b: $k_1 = zf_cc_aW_c(a)$. For $z = 6$, $f_c = 0.5$, and $W_c(a) = 0.177$ s^{-1}, we obtain from $\langle k_1 \rangle$ that $c_a = 4 \times 10^{-4}$ (or 400 PPM). This limit implies that Γ is larger than 0.177 rad/s. Our motionally narrowed NMR lineshapes require Γ's larger than 10^4 rad/s.

If we assume that we are in the slow diffusion regime, then $k_1 = zf_cc_a \Gamma$ and the mean rate implies that the product $c_a \Gamma = 7 \times 10^{-5}$ s^{-1}. We do not know c_a independently but choosing $\Gamma \approx 10^4$ rad/s, consistent with the NMR line narrowing, would imply that $c_a \approx 10^{-8}$, an unlikely value (much too small for samples exposed to air in shipping). Thus, we conclude that our data is in the "fast diffusion" limit and that the hopping frequencies can be determined from the NMR line narrowing but not the ortho-para conversion rates. The H_2 data is consistent with the HD data and yields diffusion coefficients of order $D \approx 10^{-11}$ cm^2/s.

We have no explanation for the increase in the conversion rate observed as the samples age at fixed temperature. Other workers[2,5] attributed the increase they observed to clustering of the ortho molecules driven by the electric quadrupole-quardupole (EQQ) interaction. While this might be true for their experiments, it is not a likely source of increased conversion when the conversion is catalyzed by unpaired electron spins. From our NMR lineshape narrowing, there is no indication of increased diffusion as the samples age, rather the opposite is true, the frequency Γ appears to decrease (and hence D) with decreasing ortho concentration (x_1) or increasing age.

REFERENCES

1. P.W. Anderson and P.R. Weiss, Rev. Mod. Phys. **25**, 269 (1953). There is a very clear description of this work in "Principles of Nuclear Magnetism" by A. Abragam, p. 447 ff., Oxford University Press 1961.

2. F. Schmidt, Phys. Rev. **B10**, 4480 (1974).

3. A.J. Berlinsky and W. N. Hardy, Phys. Rev. **B8**, 5013 (1973).

4. Shevtsov et al, Journal of Low Temperature Physics **95**, 815 (1994).

5. M. Rall, J.P. Brison, and N.S. Sullivan et al, Phys. Rev. **B44**, 9932 (1991).

Zero Temperature Quantum Monte Carlo Study
of Li Atoms in Solid H$_2$

E Cheng and K. Birgitta Whaley

Department of Chemistry, University of California, Berkeley, California 94720

1 Introduction

The trapping of atomic and molecular impurities in quantum matrices (solid and cluster) has attracted considerable attention lately. Particularly of interest is the possibility of improving chemical energy storage and rocket propulsion capabilities by trapping light metal impurities in solid H$_2$. [1, 2, 3] Theoretical calculations on the structure and spectra are essential to characterize the trapping sites and local environments of the impurity. While numerous studies, both experimental and theoretical, have been made for alkali impurities trapped in rare gas matrices, [4, 5] the full quantum calculations, which are necessary for H$_2$ matrices, have only recently been attempted. [6]

Theoretical evaluations of impurity spectra are crucially dependent upon the availability of accurate potentials for interaction of excited state Li* with the host H$_2$ species. Lack of such an accurate potential limited the previous quantum calculation. [6] An accurate Li*-H$_2$ potential has since become available. [7] In this extended abstract, we report the results of quantum Monte Carlo methods, both variational Monte Carlo (VMC) and diffusion Monte Carlo (DMC), using the potential of Konowalow to calculate the absorption spectra of Li atoms trapped in various sites of the H$_2$ solid. All H$_2$ in this work refer to para-H$_2$ and are treated as spherically averaged particles. A more detailed account will be published elsewhere. [8]

2 Theoretical Models and Methods

A Li atom in solid H$_2$ is described by the Hamiltonian:

$$H = -\frac{\hbar^2}{2M}\nabla^2_{R_{Li}} - \frac{\hbar^2}{2m}\sum_i \nabla^2_{R_i} + \sum_{i<j} V_{H_2-H_2}(\mathbf{R}_i - \mathbf{R}_j) + \sum_i V_{Li-H_2}(\mathbf{R}_{Li} - \mathbf{R}_i), \qquad (1)$$

where M and m are the masses of Li and H$_2$, respectively; the vectors $\mathbf{R}_{Li}$ and $\mathbf{R}_i$ denote the respective positions of Li atom and the i-th H$_2$ molecule. The spherical ground state interaction potentials between a pair of H$_2$ molecules, $V_{H_2-H_2}$, [9] and between a Li and an H$_2$, V_{Li-H_2}, are illustrated in Fig. 1 (a). The spherical ground state Li-H$_2$ potential was obtained by fitting the MRCI calculations of Konowalow [7] to analytical form. [8]

The ground state of this system can then be obtained by solving the Schrödinger equation with quantum Monte Carlo techniques, either at the variational (VMC) or the "exact" (DMC) level. [10] For this purpose, we model the solid with a finite number of lattice sites N in a rectangular simulation box. Standard periodic boundary conditions and "minimum imaging" method are applied to eliminate surface effects, and corrections are made for long range potential contributions. [11] Both FCC and HCP phases are considered. For the FCC phase, we use 108 lattice sites in a cubic box of size $L = 16.05$ Å, with the density of $\rho = 0.026$ Å^{-3}. For the HCP phase, 180 sites are employed in a slightly larger box with
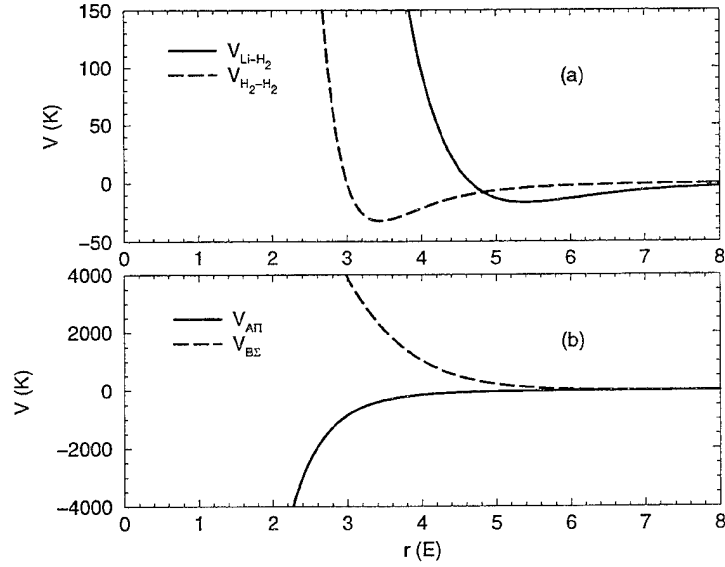
Figure 1: (a) The interaction potentials between H_2 molecules and between a Li atom and a H_2 molecule, all in their ground states. (b) The interaction potentials between an excited (p-state) Li* atom and a ground state H_2 molecule.

the same density. The Li impurity atom is introduced into the simulation box by replacing various numbers, n_v, of H_2 molecules. [8]

In the VMC, we use the following trial wavefunction: [12]

$$\Psi(\mathbf{R}_I, \mathbf{R}_1, ..., \mathbf{R}_N) = \prod_{i<j}^{N-n_v} \psi(R_{ij}) \prod_{i}^{N-n_v} \phi(|\mathbf{R}_i - \mathbf{S}_i|) \prod_{i}^{N-n_v} \psi_I(R_{iI}) \phi_I(|\mathbf{R}_I - \mathbf{S}_I|), \qquad (2)$$

$$\psi(r) = e^{-B/r^5}, \quad \psi_I(r) = e^{-B_I/r^5}, \qquad (3)$$

$$\phi(r) = e^{-\frac{1}{2}Ar^2}, \quad \phi_I(r) = e^{-\frac{1}{2}A_I r^2}. \qquad (4)$$

Here $R_{ij} \equiv |\mathbf{R}_i - \mathbf{R}_j|$, $\mathbf{S}_i$ is the position of the i-th lattice site, and $\mathbf{S}_I = \sum_{j=1}^{n_v} \mathbf{S}_j / n_v$. B, B_I, A, and A_I are parameters whose values are determined through the minimization of the total energy. Once optimized, we have the ground state of the system at the VMC level.

The VMC result is only approximate and is limited by the quality of the trial wavefunction form. A DMC walk is then performed to achieve the "exact" ground state of the system. [10] Residual bias may exist in the DMC results, however, from the following factors:

1. The use of the optimized VMC wavefunction as the "guiding function" in the DMC walk can introduce wavefunction bias from the form in Eq. (2), which violates the Bose symmetry and translational invariance;

2. The finite size and preset geometry of the simulation box impose a prefered lattice structure and inhibits long wavelength relaxation;

3. Computational limitations in the total imaginary propagation time, time step, and sample size.

We can usually eliminate 2 and 3, and we minimize 1 after comparison with VMC. [8, 10]

The VMC and DMC walks generate ground state configurations Q with quantum probability $\mathcal{P}(Q) \propto |\Psi(Q)|^2$ in VMC and $\Phi(Q)\Psi(Q)$ in DMC (Ψ is the VMC trial wavefunction and Φ is the true wavefunction). Generally, the ground state structures of quantum condensed phases such as H_2 and He do not differ much from those at low temperatures (a few K). Therefore, we can use the ground state probability densities to calculate the Li absorption spectra *via* the semi-classical Franck-Condon approach: [8, 13]

$$I(\omega) \propto \int dQ \mathcal{P}(Q)\delta\{[E_f(Q) - E_i(Q)]/\hbar - \omega\}, \tag{5}$$

where $E_f(Q)$ and $E_i(Q)$ are the energetic expectation values of the final and initial state Hamiltonian in configuration Q, respectively. In our case, $E_f(Q) - E_i(Q)$ can be well approximated by the energy difference

$$\Delta E = \sum_{k=1}^{3} E_{Li-H_2}^{e_k} - \sum_{i=1}^{N-n_v} V_{Li-H_2}^{g}(\mathbf{R}_{Li} - \mathbf{R}_i), \tag{6}$$

where $E_{Li-H_2}^{e_k}$ is an eigenvalue of the 3×3 potential matrix, $V_{\alpha\beta}^{e} = \sum_i \langle \chi_\alpha \left| V_{Li-H_2}^{e}(\mathbf{R}_{Li} - \mathbf{R}_i) \right| \chi_\beta \rangle$, $\chi_\alpha = p_{-1}, p_0, p_1$. [5] Here we have used superscripts to distinguish ground state and excited state potentials. The 3-fold degeneracy of the Li* p state is in general split by the presence of neighboring H_2 molecules. When the H_2 is spherically averaged, the interaction potential between Li* and H_2 has a doubly degenerate, mostly attractive, Π state, $V_{A\Pi}(r)$, and a singly degenerate, mostly repulsive, Σ state, $V_{B\Sigma}(r)$ (see Fig. 1 (b)). These potentials are obtained by spherically averaging and fitting the MRCI results of Konowalow. [7, 8] Diagonalization of the first order perturbation matrix V^e then yields the excited state energies $E_{Li-H_2}^{k}$ ($k = 1, 2, 3$), and hence $E_f(Q) - E_i(Q)$ and the spectra $I(\omega)$.

3   Results

We have performed both VMC and DMC simulations of Li in solid H_2 with various trapping sites ranging from $n_v = 1$ to 13. The $n_v = 1$ case corresponds to simply replacing one H_2 molecule by the Li atom at a lattice site. For $n_v > 1$, n_v neighboring molecules are taken out of the lattice. For $n_v = 13$, one H_2 molecule together with all 12 of its nearest neighbors are removed, leaving a large and near spherically symmetric cavity. The results of the HCP phase only show small quantitative differences from the corresponding ones of the FCC phase and are not included here. [8]

The zero temperature two-body correlation functions $g(r)$ are shown in Fig. 2. The Li-H_2 $g(r)$ is very sensitive to n_v, and thus to the size of the cavity. The Li absorption spectra are presented in Fig. 3. For smaller n_v, we clearly observe a split "triplet", with the split structures very sensitive to n_v, the local environment of the Li atom. The splitting generally becomes smaller as n_v gets larger and the triplet becomes unresolved for $n_v = 13$. Significant size dependent shifts in frequency are also observed, with the average shift decreasing as n_v increases. These shifts are found to be in good agreement with simple estimates based on knowledge of the interaction potentials and the interparticle distributions. [8]

The difference between the VMC and DMC results are relatively small. The DMC spectra have, in general, smaller shifts and widths than the VMC ones. This is consistent with the observation that the DMC $g(r)$ for Li-H_2 generally has more structure than those from VMC
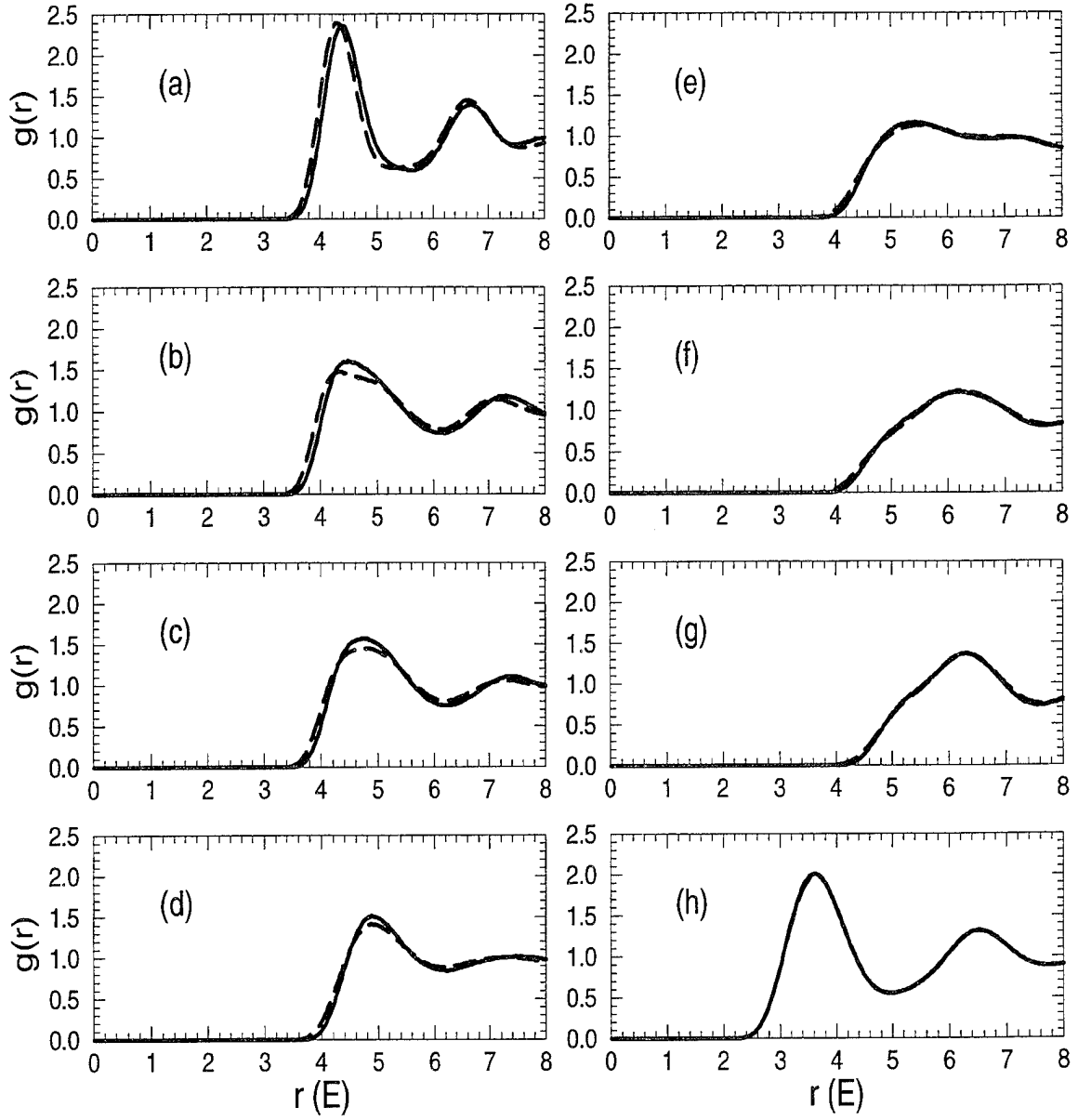
Figure 2: (a)-(g): The Li-H_2 two body correlation functions of a Li atom in an FCC H_2 solid. These are calculated with the Li impurity replacing 1 (a), 2 (b), 3 (c), 6 (d), 10 (e), 12 (f), and 13 (g) H_2 molecules in the lattice. The solid curves are the DMC results and the dashed curves are VMC ones. (h) is the H_2-H_2 correlation function, which is virtually identical in all above cases.
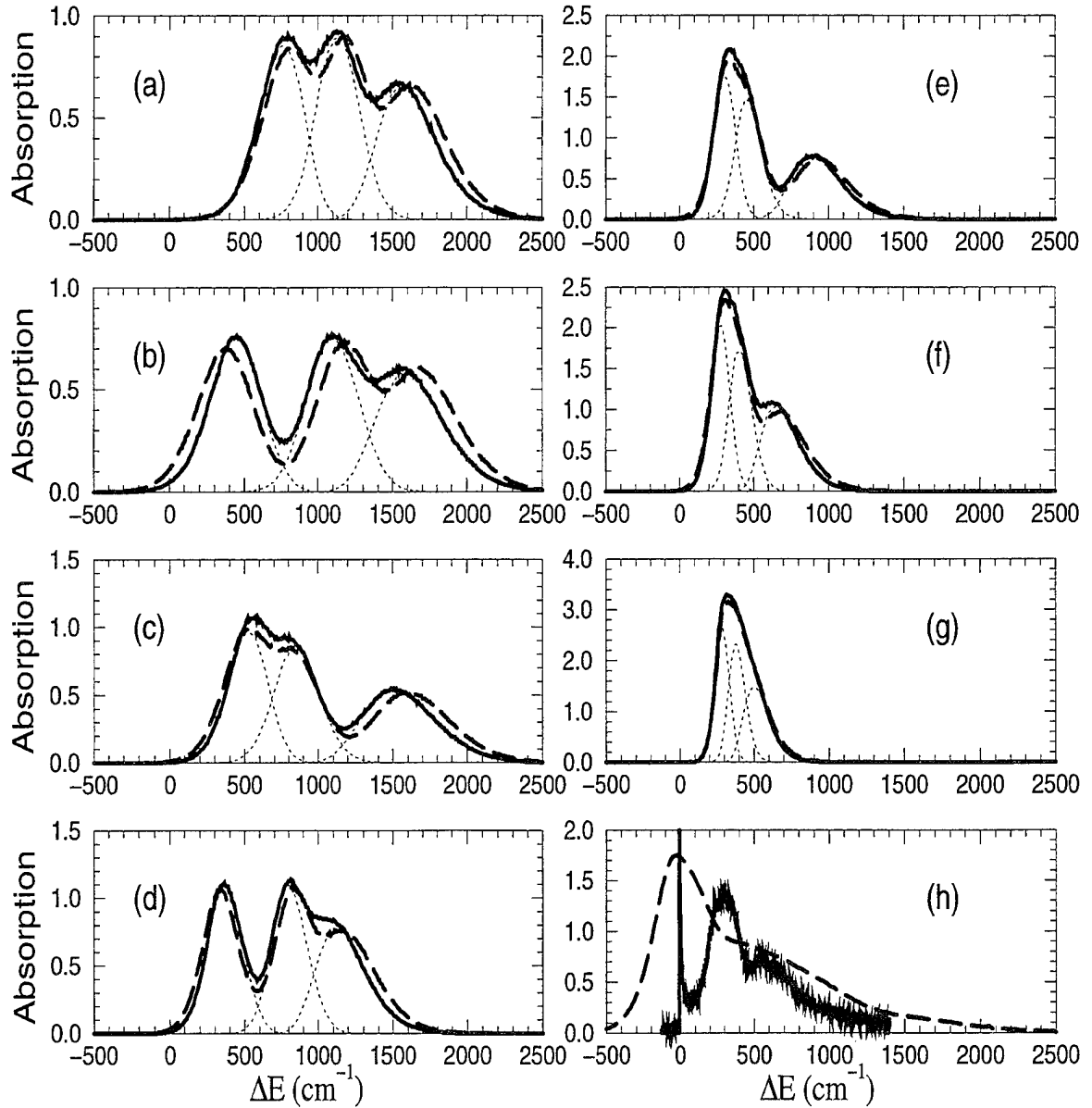
Figure 3: The Li absorption spectra in solid H_2, plotted as shifts relative to the atomic spectra. From (a) to (g) are our theoretical results calculated with an FCC lattice and the Li impurity replacing 1 (a), 2 (b), 3 (c), 6 (d), 10 (e), 12 (f), and 13 (g) H_2 molecules. The solid curves are the DMC results while the dashed curves are VMC ones. The dotted curves show the theoretical components of the "triplet" DMC spectra. All theoretical spectra have been normalized to have the same total intensity. (h): Experimental results. The solid curve is the cluster spectrum from Ref. [3] and the dashed curve is the solid spectrum from Ref. [2].

(Fig. 2); it reflects the fact that DMC is less biased by the preset lattice structure and allows more relaxation in the vicinity of the cavity. The general similarity between VMC and DMC results indicates that the VMC trial function, Eq. (2), is of high quality, and that little residual wavefunction bias is present in the DMC.

4 Discussions

Our spectra show considerable disagreement with the previous results of path-integral Monte Carlo (PIMC) simulation performed at finite temperature $T = 4$ K and constant pressure $P = 0$ for Li in HCP H_2. [6] While ours show a non-zero average shift dependent on n_v, the spectra in Ref. [6] do not appear to be sensitive to n_v, with the first peak consistently centered close to (the unshifted position) $\Delta E = 0$. This difference is attributed to the use of i) different excited state Li*-H_2 potentials, and ii) "liquid core" configurations as a startup in the PIMC. We have also performed VMC calculations mimicing the presence of a "liquid core". While these yield spectra with smaller blue shifts and more similarity to the PIMC results, they have higher total energy than the crystalline lattice and are consequently metastable states at best. These issues are discussed in more detail in Ref. [8]

As observed in Fig. 3, our results do *not* show overall agreement with the experimental data of Li in solid H_2 by Fajardo either. [2] Most importantly, we do not observe any signal in the unshifted position where the experimental data show a broadened peak. Using the Konowalow potentials, we estimate that an unshifted peak would indicate a "cavity" of at least 7 Å in radius. [8] This is much larger than the energetically favored sites (around $n_v = 3$). [6, 8] The existence of such large cavities can not be ruled out, however, under the experimental conditions of laser ablation and matrix accretion. [2] Defects and grain boundaries with large vacancies are quite likely. On the other hand, our spectra do coincide in the region where the data show a much broadened shoulder. Unfortunately the resolution in the experimental data here is unsufficient for quantitative comparison.

The recent high resolution LIF data of Li "attached" to H_2 clusters by a pickup process display quite different features however. [3] Apart from the extremely narrow unshifted peak, these data appear to closely agree with our results. In particular, the blue shifted structures match our spectra for $n_v = 12$. This is therefore strong evidence that these peaks originate from interior states of Li trapped *inside* the cluster. The narrow peak at the gas phase absorption is most likely due to surface attached Li. This raises the question of what energetic barriers control the relative intensities of absorption from different trapping sites. Furthermore, our calculations show that $n_v = 12$ is not an energetically favored trapping site in *bulk solid*. [8] On the other hand, the lattice structure and relative energetics of different sites in clusters may be influenced by the size and boundary effects. [6] We also note that the temperature is lower in the clusters than in the solids. It is also unclear whether the LIF spectra differ from the absorption because of extensive non-radiative quenching processes. [3]

In summary, we have performed VMC and DMC simulations of a Li impurity atom trapped inside solid H_2 at $T = 0$. The results show that these are indeed powerful theoretical tools to probe structural information in the vicinity of the impurity, provided accurate ground and excited state impurity-H_2 potentials are available. With pure samples and high resolution spectroscopy, these structures should also be characterizable in low temperature experiments. We also note that the VMC results appear to be quite accurate in comparison with the more reliable DMC ones, indicating both minimal wavefunction bias in the calculations and little

structure relaxation about the impurity.

Our results demonstrate the merit of further theoretical pursuit in this area. Work is underway to simulate the Li/H$_2$ cluster system, in which both the interior and exterior (surface) states will be investigated. We also plan to study the pressurized high density solid state, where the orientationally ordered H$_2$ molecules introduce anisotropic effects, which may have a non-negligible influence on the spectrum.

5   Acknowledgements

References

[1] *Proceedings of the High Energy Density Matter (HEDM) Conference, 1993*, ed. by T. L. Thompson (USAF Phillips Laboratory, Edwards Air Force Base, CA, 1993).

[2] M. E. Fajardo, J. Chem. Phys. **98**, 110 (1993); M. E. Fajardo, S. Tam, T. L. Thompson, and M. E. Cordonnier, Chem. Phys. **189**, 351 (1994).

[3] G. Scoles, these Proceedings.

[4] N. Schwentner, E. E. Koch, and J. Jortner, *Electronic Excitations in Condensed Rare Gases*, Springer-Verlag, Berlin, 1985.

[5] J. A. Boatz and M. E. Fajardo, J. Chem. Phys. **101**, 3472 (1994) and references therein.

[6] D. Scharf, G. J. Martyna, and M. L. Klein, J. Chem. Phys. **99**, 8997 (1993); D. Scharf, G. J. Martyna, D. Li, G. A. Voth, and M. L. Klein, *ibid.* **99**, 9013 (1993).

[7] D. D. Konowalow, in *Proceedings of the High Energy Density Matter (HEDM) Conference, 1993*, ed. by T. L. Thompson (USAF Phillips Laboratory, Edwards Air Force Base, CA, 1993); D. D. Konowalow, University of Dayton Research Institute, Internal Report, 1993.

[8] E Cheng and K. B. Whaley, J. Chem. Phys., to be submitted.

[9] I. Silvera and V. V. Goldman, J. Chem. Phys. **69**, 4209 (1978).

[10] R. N. Barnett and K. B. Whaley, Phys. Rev. A **47**, 4082 (1993); J. Chem. Phys. **99**, 9730 (1993).

[11] M. P. Allen and D. J. Tildesley, *Computer Simulation of Liquids*, Clarendon Press, Oxford, 1987.

[12] T. A. Bruce, Phys. Rev. B **5**, 4170 (1972).

[13] M. Lax, J. Chem. Phys. **20**, 1752 (1952).

Experimental Studies of Clusters towards Deposition of Doped Clusters with HEDM Species

M. Macler[a], C. R. Brazier[a], T. Presilla[b], C. W. Larson, D. S. Silver, and Y. K. Bae[a]

Phillips Lab/RKFE
10 E. Saturn Blvd.
Edwards AFB, CA 93524-7680

1. Introduction

In achieving the desired high concentrations[1] of HEDM additives in the hydrogen matrix for cryogenic propellant grains of advanced hybrid rockets, it is essential to able to predict physical and thermodynamic properties of highly doped hydrogen matrices. The doped hydrogen matrices that appear to be promising have binding energies between the guest and host much greater than those between the host and host. What is then the effect of the presence of the dopant guests on the properties of the doped matrices? Can the dopant guest be considered a binder that makes the matrix physically stronger and denser? How does the guest perturb the quantum behavior of the host hydrogen molecule? What is the relationship between the melting temperature and the activation threshold energy of the guest diffusion?

Fig. 1. shows the relationship between the melting temperature, T_m, and the Lennard-Jones potential energy depth, ε_{LJ}, of various van der Waals solids. For "classical" solids, such as Ne, Ar, Kr, and Xe matrices, the ratio of T_m to ε_{LJ} is ~0.7. However, the ratios for quantum matrices, such as He and H_2 matrices, are much different from 0.7. The difference is believed to result from the quantum behavior of the hosts. It is interesting to note that the melting temperature of matrices of H_2, D_2, T_2, and Ne, which have similar van der Waals potential depths, increases as the mass of the constituent element increases. A comparison of the melting temperatures of He and D_2 matrices of which constituent masses are equal reveals also that the quantum behavior depends also on the potential strength. Does the behavior possibly result simply from suppression of the zero point motion, as the constituent element becomes heavier? Or are there any other more complicated mechanisms, such as "tunneling", responsible for such behavior?

Recently, Gordon et al.[2] reported to produce a solid mainly composed of He in ambient pressure by heavily doping liquid He with heavy elements, such as N_2, Ar, Xe, etc. They reported that the melting temperature of the doped He solid was ~ 7 K. Because ε_{LJ} of He is ~10 K, the ratio of the melting temperature and ε_{LJ} is ~0.7, similar to those of those of other classical van der Waals solids. Based on this and other observations they proposed that the impurity element forms a core of a "snow ball" with a He shell that is radially confined. In this picture, the melting of the solid is proposed to be related with the "tunneling" of the core element through the He shell into the core of the neighbor "snow ball". The difference between the doped He solid and pure LHe lies, Gordon et al. proposed, in that the behavior of the heavy dopant elements is classical in

contrast with that of He atoms surrounded by He atoms in pure LHe. Such a model should, however, be both theoretically and experimentally verified.

If the model of Gordon et al. is correct, we predict that the melting temperature of the highly doped H_2 matrix may approach its "classical" value, ~$0.7\varepsilon_{LJ}$= 22 K, which is substantially higher than that of pure solid hydrogen (14 K). In this case, because the doped solid is in general very stable at temperatures up to 1/3 of the melting temperatuer of the matrix, we also predict that the highly doped solid hydrogen can be produced and kept at ~7 K which can be obtained with the closed cycle He refrigeration technology nowadays. We also predict that the molar density of the doped solid hydrogen should be higher than that of pure solid hydrogen. We are currently investigating the report and proposal of Gordon et al. in our lab.[3]

How can we produce the highly doped matrices? It appears that the conventional vapor deposition technique is not likely to succeed in producing them. Fig. 2 shows a result of an MD simulation result by Fraenkel and Haas[4], which elucidates an atomic level picture of the conventional vapor deposition processes. In this simulation, room temperature Ar gas was directly deposited on a 5 K fcc Ar solid. The four gray colored layers represent the initial substrate. The result shows defects, voids, and dendrite structures particularly in the accretion region. Because the guest elements are mostly trapped in the defects or voids of the accretion region, they are expected to have much larger diffusion rates than the ones trapped in the highly packed bulk structure. Therefore, recombination rates of the guest elements are expected to be high in the accretion region, and result in low concentrations of isolated guest elements.

Another issue is related with removal of the heat of condensation from the accretion region because the heat removal rate is a limiting factor on the deposition speed of the matrices. Because a loosely packed solid has much smaller thermal conductivity than a highly packed solid, the deposition techniques that produce high packing densities of the matrices are desirable. We propose cluster deposition for achieving the high doping concentrations. In the cluster deposition, the additive elements will be first encapsulated by clusters before deposition, thus the surface diffusion process will be suppressed and the isolation of the additive elements will be improved. Furthermore, there is theoretical evidence[4] that with a proper kinetic energy of the clusters a highly packed solid can be produced by cluster deposition.

Fig. 3 shows the salient features of an MD calculation performed by Mueller[5] using the van der Waals potential. The calculation assumes that the clusters are deposited on a O K surface. The left figure shows the result with the kinetic energy of clusters per the constituent atoms, E/N, is about 10 % of the van der Waals potential depth ε_{LJ}, representing deposition of very slow clusters. Similar to the conventional vapor deposition, it produces structures with voids and defects. However, when E/N is greater than ε_{LJ}, in this case, 1.5 ε_{LJ}, representing deposition of relatively fast clusters, the clusters are fused to form a highly packed solid structure. Therefore, cluster deposition is predicted to produce highly packed solid even under very cold deposition conditions through "self annealing" caused by the momentum carried by the clusters.

Other interesting aspect of the cluster deposition is that the heat of the solvation and the kinetic energy accompanied by the guest atoms in the clusters can be dissipated in the gas phase before deposition. For example, the result of a calculation simulating

hydrogen clusters capturing 2000 K B atoms is shown in Fig. 4. Here the solvation energy of B atoms was neglected. The temperature of the cluster rises to ~ 50 K immediately after the capture owing to the kinetic energy of the B atom, then decreases rapidly as a function of time. In ~ 1 msec, the time scale between capture and deposition of the clusters, the temperature of the cluster decreases to ~ 15 K dissipating ~ 2/3 of the initial heat of doping in the gas phase and the cluster size decreases from 38 to ~20 resulting in a doping concentration of ~ 5 %.

2. Proposed research topics

The research topics to solve problems anticipated in developing the cluster deposition technology are:

a. Doping studies of clusters with HEDM Species in the gas phase

- To achieve ~ 5 % doping concentration after deposition, we have to study doping processes with clusters of ~ 50 monomers, i.e. microclusters.
- Reactivity of the additive species with constituent monomers in clusters have to be investigated.
- Sticking coefficient and capture cross sections of the additive elements to the clusters should be measured.
- Solvation and/or encapsulation of the additive elements in the clusters should be studied.

b. Deposition studies of doped clusters

- The packing density and thermal conductivity of the doped matrices produced by cluster deposition should be investigated.
- The recombination threshold temperature and melting temperature of the matrices should be measured.
- The shock sensitivity and mechanical properties of the matrices should be investigated.
- The actual energy density of the matrices should be measured.

c. Scaling-up related issues

- The economically viable pathways to mass production of the doped clusters should be investigated.

3. Highlights of Recent Progress

We started our program late last year, and have finished construction of the source part, the doping part and the gas-phase diagnostic part. The schematic diagram of the apparatus that has been completed is shown in Fig. 5. The cluster source has a 0.17 mm

dia nozzle and is cooled by a cryostat that can cool the source to ~20 K. The cluster source chamber is pumped by a 900 l/s roots blower pump. The cluster beam is collimated through two skimmers with 1 and 2 mm dia nozzles respectively, then enters the additive chamber. The section between the skimmers is pumped by a 600 l/sec turbo pump.

In the additive chamber the clusters capture the additive atoms or molecules either in a super sonic beam or in a stagnant gas introduced to the additive chamber. In the latter case, the entire additive chamber is utilized as a pick-up cell similar to the one introduced by Prof. Scoles' group.[5] The additive chamber is pumped by a 3500 l/sec turbo pump which is backed by a 100 l/sec turbo pump and a 10 cfm mechanical pump. The cluster beam then enters the analysis chamber, and is electron-impact ionized. The cluster fragment ions resulted from the electron-impact ionization are mass analyzed by a quadrupole which has a mass resolution, $\Delta m/m$, of ~ 1/300 and a maximum mass range of 300 amu. The quadrupole chamber is connected to the additive chamber by an angle tuning device, so that the angular distribution of the doped clusters can be studied.

Fig. 6 shows a mass spectrum obtained by electron-impact ionizing argon clusters doped with oxygen molecules. The mean size of the Ar neutral clusters prior to the electron-impact ionization was estimated to be ~120±20 with the source temperature and pressure of 300 K and 3.4 bar respectively. The estimation was based on a reduced scaling law developed by Hagena,[6] which was improved by other groups.[7,8] The spectrum shown in the left figure was taken at a doping pressure of 1×10^{-5} Torr. All the major peaks of Ar cluster ions with up to 7 atoms are clearly shown here as peaks at masses of 40n, here n is an integer. It also shows satellite peaks at masses of 40n+32 resulted from Ar clusters doped with one O_2 molecule. The peaks at masses of 40n+16 resulted from dissociative ionization of dopant O_2 molecules on the doped Ar clusters. The spectrum taken at a higher doping gas pressure of 1×10^{-4} Torr shown in the right figure additional peaks at masses of 40n+24 appear. These peaks are attributed to fragment ions from clusters doped with two oxygen molecules. Also, the 40n+16 peaks became more prominent because of the additional contribution from clusters with three oxygen molecules.

Buck and Meyer have studied fragmentation of small Ar clusters upon electron impact ionization.[9] They found that the small clusters with up to 6 atoms, fragment mostly into dimer ions. However, electron impact induced fragmentation of the clusters with ~100 atoms is much less understood. We have investigated this issue by measuring the capture cross sections from the dopant gas pressure dependence of the cluster ion beam intensity. The cross section slowly increases as the number of Ar atoms, N, in the cluster ions increase, but levels off with N>3 at ~400 A^2. The radius and the cluster size estimated from the cross section are ~11.3 A and ~140 in agreement with the estimated cluster size ~120±20 based on the scaling law. Thus, it seems that the doped cluster ions with more than 3 Ar atoms mostly resulted from fragmentation of the doped parent neutral clusters of the mean cluster size.

We have also investigated multiple pick-up processes of Ar cluster doped with water molecules. Fig. 7 shows a result. The bottom curve shows the spectrum obtained with a water doping pressure of 5×10^{-6} Torr. The curve shows the pure Ar cluster ion peaks at masses of 40n. As the water pressure increases, the water doped cluster ion

peaks became more dominant as is shown in the middle curve with the water pressure of $2x10^{-5}$ Torr. At higher water pressures as shown in the upper curve with the water pressure of $1x10^{-4}$ Torr, all the peaks corresponding to doped and undoped cluster ions disappeared and pure water cluster ion peaks emerged. When the Ar cluster beam was turned off, the pure water cluster peaks disappeared, thus we concluded that these water clusters were grown on the Ar clusters. The growth of clusters in Ar cluster is not well understood now and remains an exciting subject of further studies.

(a) Hughes STX
(b) AFMC/PL NRC Postdoctoral Research Associate.

References

1. P. G. Carrick, Proc. of the HEDM Contractors's Conf. edited by T. L. Thompson (1993).
2. E. B. Gordon et al., Chem. Phys. 170, 411 (1993).
3. M. DeRose et al, in this proceeding.
4. R. Fraenkel, and Y. Haas, J. Chem. Phys. **100**, 4324 (1994).
5. K. Mueller, J. Appl. Phys. 61, 2516 (1987). See also H. Haberland, Z. Insepov, and M. Moseler, Phys. Rev. B 51, 11061 (1995).
6. T. Gough et al., J. Chem. Phys. 83, 4958 (1991).
7. OF. Hagena, Z. Phys. D4, 291 (1987).
8. J. Cuvellier et al., Z. Phys. D21, 265 (1991) and references therein.
9. A. J. Bell et al., Z. Phys. D26, 994 (1993).
10. U. Buck and H. Meyer, J. Chem. Phys. 84, 4854 (1986).
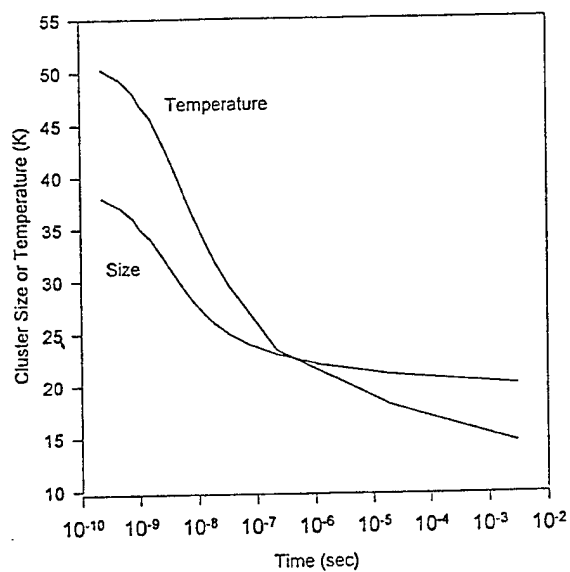
Figure 4. The size and temperature of a $(H_2)_{38}$ cluster doped with a 2000 K B atom as a function of time.
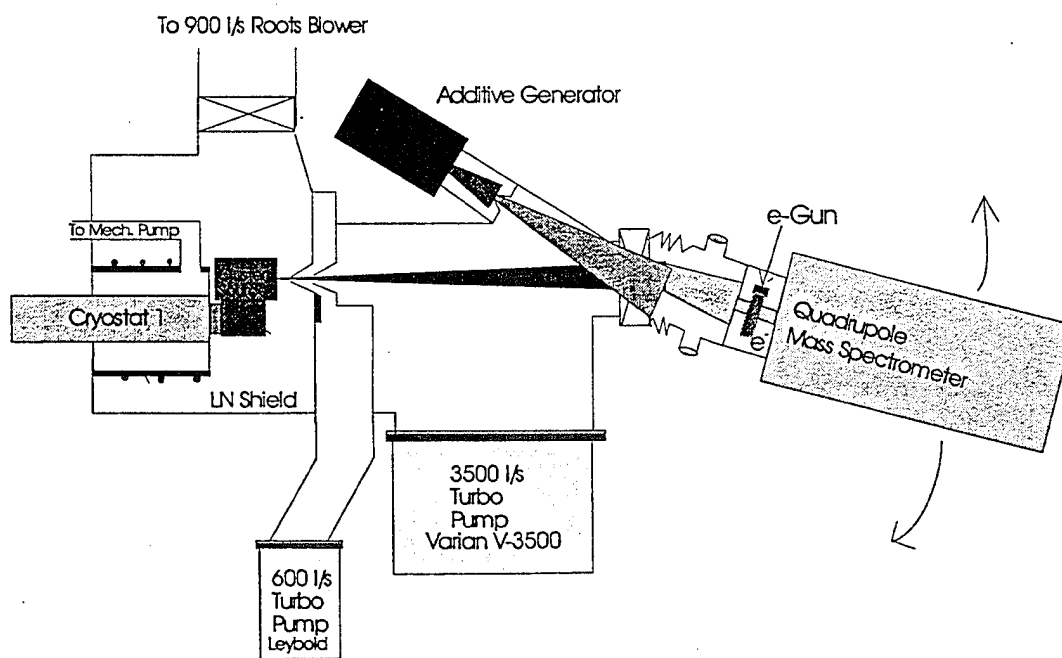
Figure 5. Schematic diagram of the experimental apparatus for gas-phase studies of doped clusters.
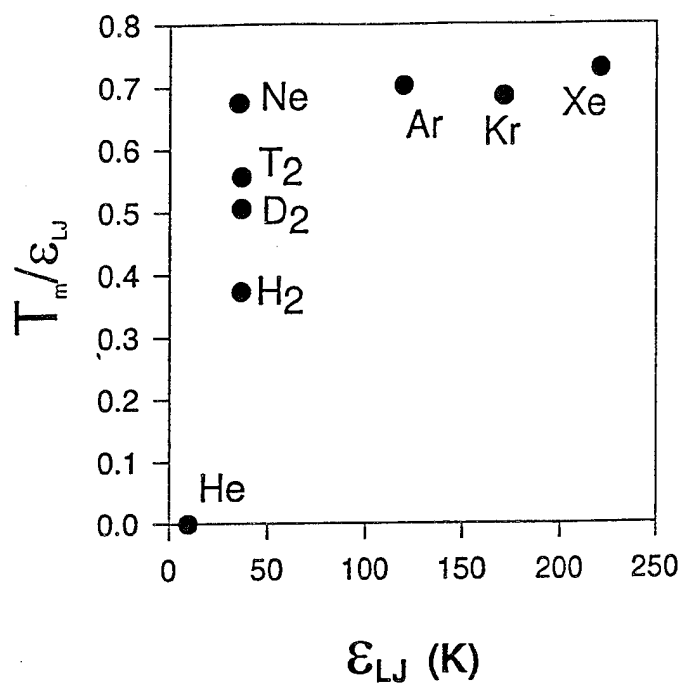
Figure 1. The ratio of the melting temperature to the Lennard-Jones potential depth of various van der Waals solids.
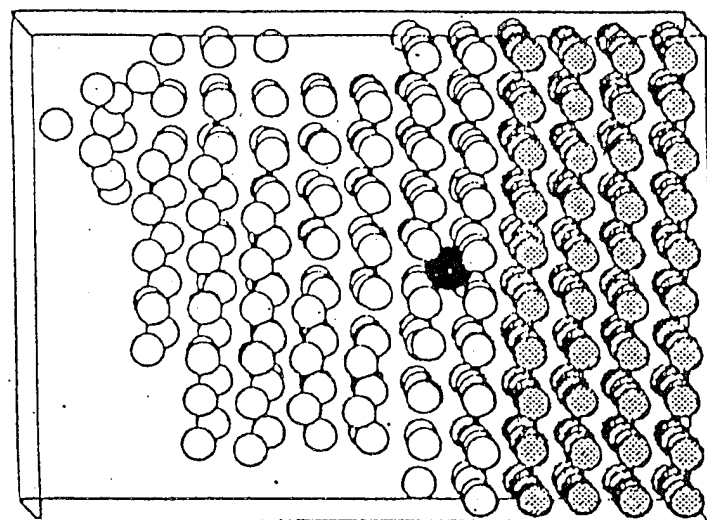
Figure 2. The result of molecular dynamics calculations of vapor deposition on a cold (5 K) surface by Fraenkel and Haas.

$$E_{K.E.}/N = 0.1\varepsilon_{LJ}$$

$$E_{K.E.}/N = 1.5\varepsilon_{LJ}$$
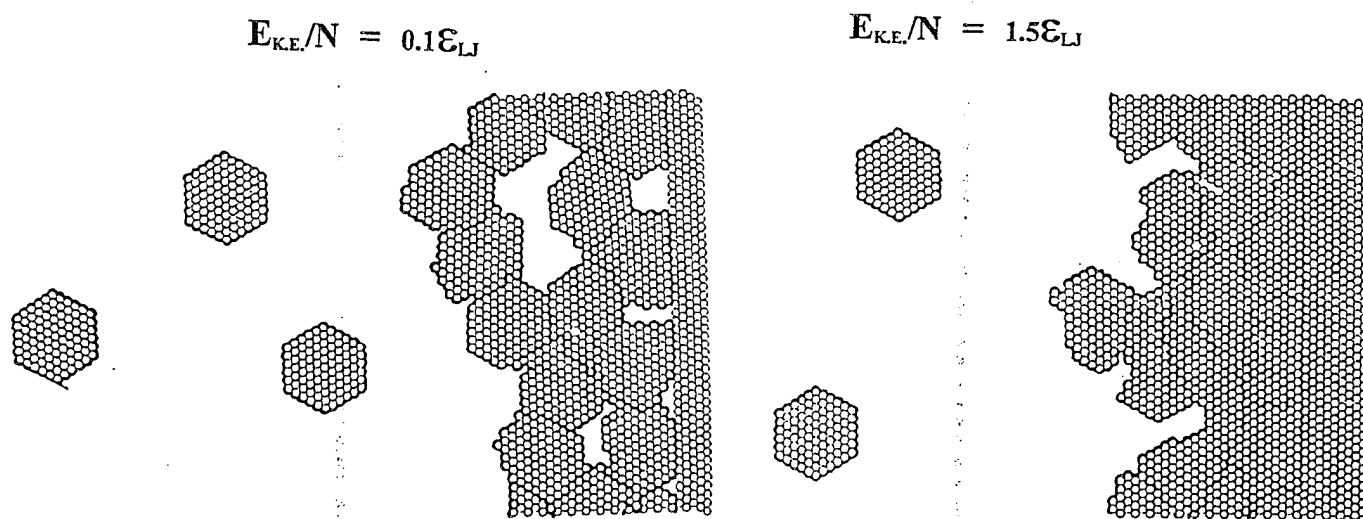
Figure 3. The result of 2-D molecular dynamics calculations of cluster deposition by Mueller.
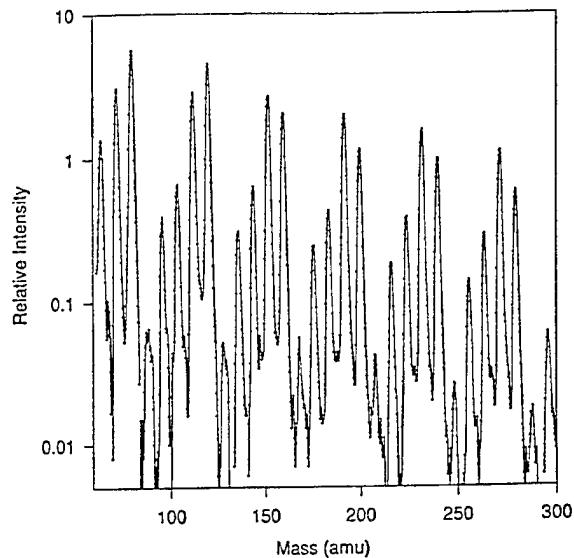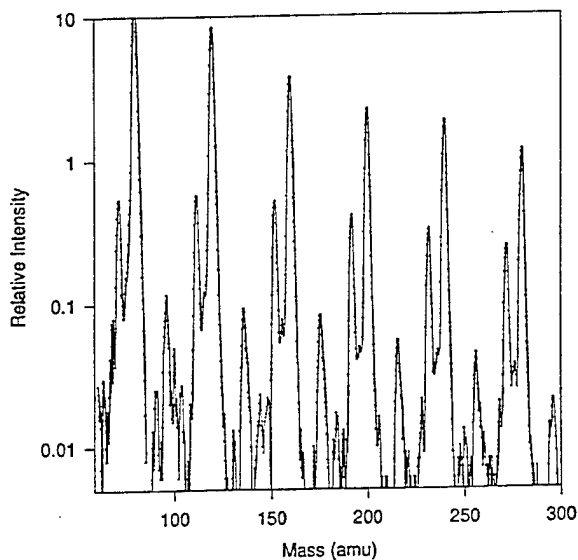
Figure 6. Mass spectra of electron impact ionized fragment ions of doped Ar clusters with oxygen. The estimated mean size of the Ar cluster is 120.
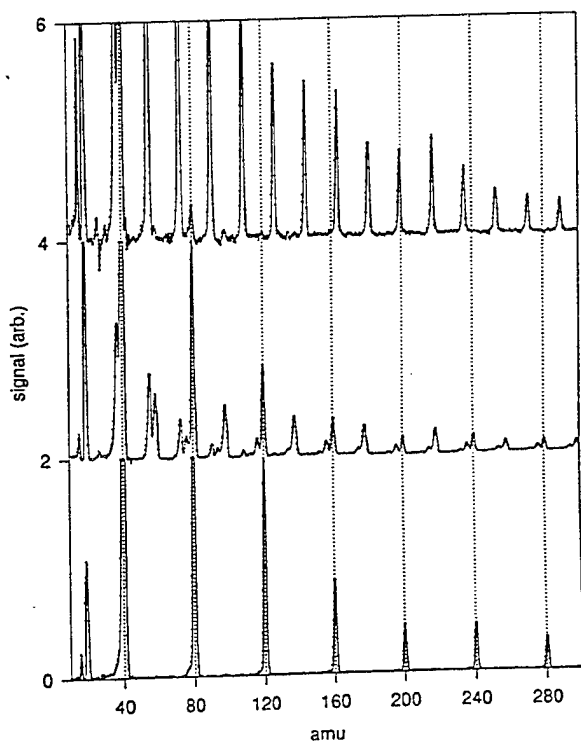
Figure 7. The evolution of mass spectra of electron impact ionized fragment ions of doped Ar clusters with H_2O molecules as the H_2O pressure increases.
At a very high H_2O pressure (the bottom curve) the spectrum only shows water cluster ions.

Spectroscopic Characterization of Non-bonding Interactions of the Boron Atom

Paul J. Dagdigian, Eunsook Hwang, and Xin Yang
Department of Chemistry, The Johns Hopkins University
Baltimore, MD 21218-2685

1. Introduction

In order to provide experimental data which can be used to characterize the non-bonding interactions of the boron atom, we have recorded and analyzed laser fluorescence excitation spectra of van der Waals complexes involving B atoms. Our experimental results have been interpreted in an extensive collaborative fashion with the Millard Alexander's group at the University of Maryland.[1] This group has calculated the interaction energies of the boron atom, in both its ground $2p \, {}^2P$ and excited $3s \, {}^2S$ electronic states, with several atom and molecular species. These interaction energies have then been used to compute binding energies of clusters of these species and compared with our experimental observations.

Over the past year, we have made significant improvements to our experimental apparatus. These modifications have allowed the observation of more weakly bound systems than previously possible. We present here a brief description and discussion of our recent observations on the BNe, B$\cdots$H$_2$, B$\cdots$D$_2$ complexes, as well as the spin-orbit excited level of BAr. We also present observations by laser fluorescence detection of polyatomic B–rare gas clusters, involving Ar and Kr.

2. Experimental Observations

In our experiments, we prepare complexes of the boron atom in a free jet expansion. The boron atoms are photolytically prepared by 193 nm photolysis of diborane, present at 0.5% of the total gas concentration, at the tip of the nozzle orifice. Boron atoms and complexes are detected by laser fluorescence excitation at wavelengths near to that of the B $3s \, {}^2S \leftarrow 2p \, {}^2P_J$ atomic transition at 249.8 nm.[2]

2.1. Boron–Neon. We have observed the laser fluorescence excitation spectrum of the BNe complex. We find a single broad, diffuse feature, which is displayed in Fig. 1. We interpret this transition as excitation to the repulsive portion of the $B^2\Sigma^+$ state, which correlates with the B($3s \, {}^2S$) + Ne
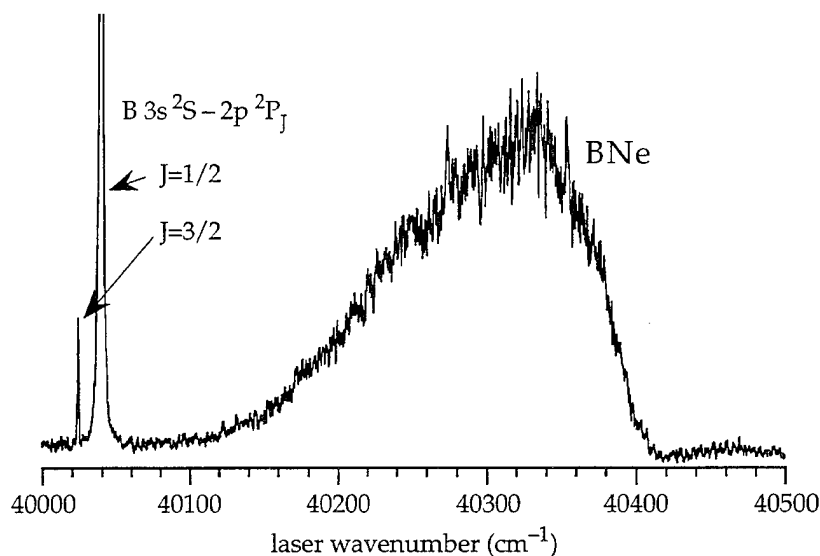
FIG. 1. Laser fluorescence excitation spectrum of BNe.

asymptote. The observed emission is thus due to fluorescence from B($3s$ ^2S) excited atoms formed by dissociation on the $B^2\Sigma^+$ potential energy curve. Since the maximum intensity in the BNe laser fluorescence excitation spectrum occurs approximately 270 cm^{-1} to the blue of the atomic resonance line, the BNe($B^2\Sigma^+$) potential energy curve can be estimated from the Franck-Condon principle to be repulsive by roughly this magnitude at the equilibrium separation of the BNe($X^2\Pi$) ground state.

This assignment as a free ← bound transition has been confirmed by comparison of the experimental spectrum with simulations computed with *ab initio* BNe potential energy curves calculated by Yang and Alexander.[1] In distinct contrast to the strong binding in BAr($B^2\Sigma^+$),[2] the $B^2\Sigma^+$ state of BNe is found to be entirely repulsive.

2.2. Boron–Hydrogen. In very recent experiments, we have also observed laser fluorescence excitation of the B···H$_2$ and B···D$_2$ complexes. In contrast to the B–rare gas complexes, reaction within the B···H$_2$(D$_2$) complex is energetically allowed and can lead to formation of BH + H, where the hydride can be in its ground or several low-lying electronic states, or B + 2H.[3] Rather surprisingly, we find no evidence for chemical reaction within the complex. We observe by laser fluorescence excitation a structureless feature akin to that observed for BNe to the blue of the atomic resonance line at 249.8 nm. This fluorescence spectrum is displayed in Fig. 2. This emission is detected in the wavelength range of the atomic transition. We also searched,

69
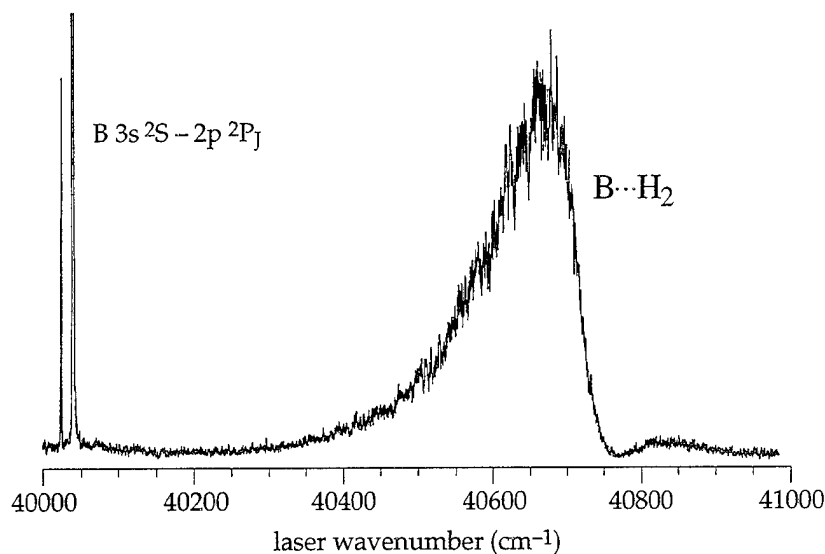
FIG. 2. Laser fluorescence excitation spectrum of B···H$_2$.

unsuccessfully, for BH $A - X$ chemiluminescence emission. The spectrum of the B···D$_2$ complex is similar to that shown for B···H$_2$. The main difference is that the intensity falls off more quickly on the red side of the maximum than for B···H$_2$. This behavior can be explained by the smaller zero-point energy, and hence larger binding energy, for the former.

The maximum intensity in the B···H$_2$ spectrum is *ca.* 600 cm^{-1} to the blue of the atomic resonance line; this indicates that the excited potential energy surface is more repulsive than for BNe. Our observations suggest that there is a significant barrier to the B($3s$ ^2S) + H$_2$ chemical reaction. We are in the process of interpreting our spectra for B···H$_2$ and B···D$_2$ with *ab initio* potential energy surfaces calculated by Millard Alexander and co-workers.[1]

2.3. Boron–Argon. For the BAr complex, for which we previously observed the $B^2\Sigma^+ - X^2\Pi_{1/2}$ (v′,0) progression of bands,[2] we have also now observed the spin-orbit excited $X^2\Pi_{3/2}$ manifold.[4] We have determined a value of 10.88 ± 0.08 (1σ) cm^{-1} for the spin-orbit constant A. This value is close to a simple estimate (2/3) ΔE, = 10.17 cm^{-1}, where ΔE is the boron $2p$ $^2P_{3/2} - {}^2P_{1/2}$ spin-orbit splitting. Consideration of the slight transition to Hund's case (c) coupling, through mixing with the low-lying $A^2\Sigma^+$ electronic state, yields a revised theoretical value of 10.62 cm^{-1}, which agrees even more closely with the experimental result. The good agreement of experimental and theoretical values for the BAr spin-orbit splitting suggests

that the boron $2p$ orbital is not strongly affected by the weak B–Ar interaction.

With the improvements to our experimental apparatus, we have been able able take spectra of boron-argon complexes at higher backing pressures than in our previous experiment on this system.[3] We have obtained spectra in which features due to higher BAr_n ($n > 1$) are present. Figure 3 compares spectra taken at low and high backing pressures. We clearly see a feature at 40400–40500 cm^{-1} due to a higher cluster. In addition, there may also be a
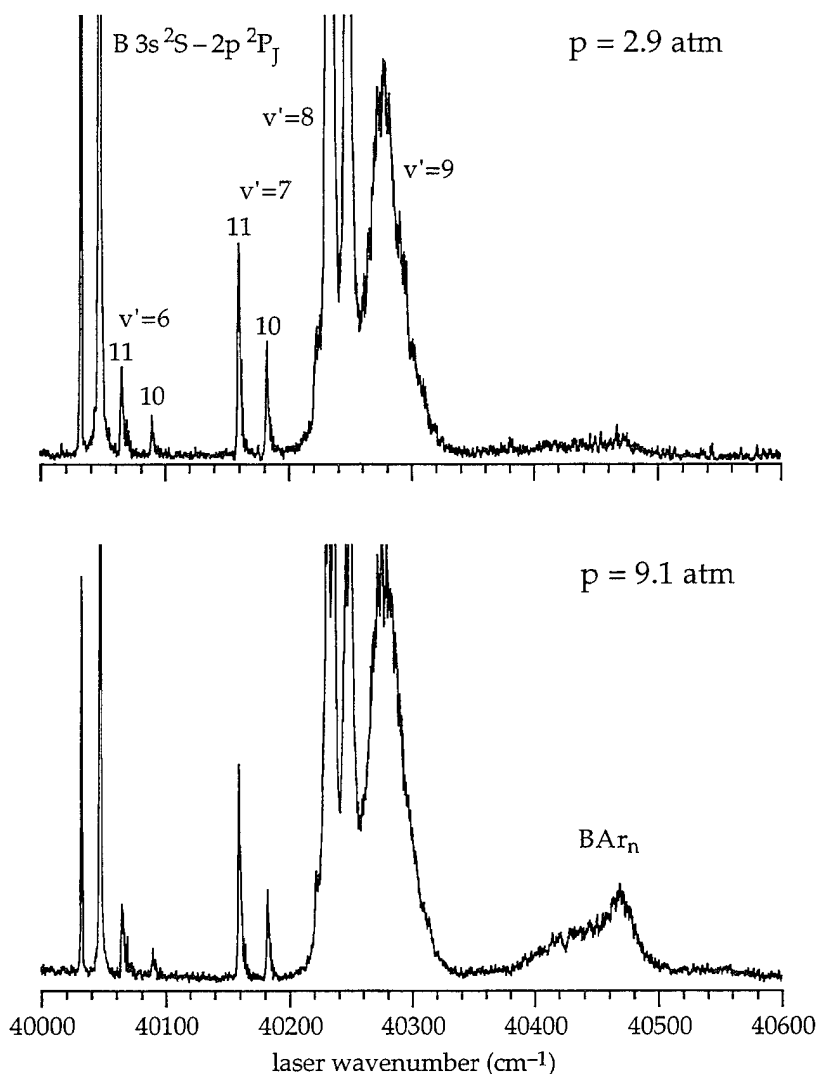

FIG. 3. Laser fluorescence excitation spectra of boron-argon complexes taken with different beam source backing pressures (80 : 20 argon–helium mix). The ^{11,10}BAr $B - X$ (v',0) bands to both bound and quasibound levels are marked.

transition due to a polyatomic cluster coincident with the transition wavenumber for excitation[2] of the BAr v'=9 quasibound level. We are in the process of interpreting these spectra with calculations of the structure and energetics of BAr_n clusters being carried out by Alexander and co-workers.[1] The spectra shown in Fig. 3 suggest that the blue shift of the transition wavenumber of BAr_n clusters increases with increasing size.

2.4. Boron–Krypton. We have been also attempted to observe the BKr complex. Even with low concentrations of Kr in the seed gas ($\geq 5\%$), we only observe features characteristic of polyatomic species. We believe that this implies that the BKr binding energy is less than that of Kr–Kr and that BKr_n clusters ($n \gg 1$) are being formed in the supersonic beam expansion.

3. Discussion. We see that complexation of boron atoms with rare gases and hydrogen leads to a blue shift of the boron $3s \leftarrow 2p$ atomic transition. Fajardo *et al.*[5] have observed that the first uv absorption of boron atoms in hydrogen, neon, and argon matrices occurs as a doublet below 220 nm, considerably to the blue of the gas-phase $3s \leftarrow 2p$ atomic transition. Using our previously determined[2] BAr potential energy curves, Boatz and Fajardo[6] carried out Monte Carlo simulations of solid B/Ar and did not find such a large blue shift. Fajardo and co-workers have tentatively concluded that the features below 220 nm should be assigned to the higher resonance transition in atomic boron, namely $2s2p^2\,{}^2D \leftarrow 2s^22p\,{}^2P$. Our results on BNe and $B\cdots H_2$ are consistent with this supposition and suggest that the $3s \leftarrow 2p$ atomic transition will be extensively broadened in Ne and H_2 matrices, probably to the point of undetectability.

---

1. M. H. Alexander etc., *these proceedings.*

2. E. Hwang, Y.-L. Huang, P. J. Dagdigian, and M. H. Alexander, J. Chem. Phys. **98**, 8484 (1993).

3. X. Yang and P. J. Dagdigian, J. Phys. Chem. **97**, 4270 (1993).

4. E. Hwang and P. J. Dagdigian, Chem. Phys. Lett. **233**, 483 (1995).

5. M. E. Fajardo, S. Tamm, T. L. Thompson, and M. E. Cordonnier, Chem. Phys. **189**, 351 (1994); M. E. Fajardo, S. Tamm, and M. Macler, in *Proceedings of the High Energy Density Matter Contractors' Conference* (Woods Hole, MA, 1993), p. 123.

6. J. Boatz and M. Fajardo, in *Proceedings of the High Energy Density Matter Contractors' Conference* (Woods Hole, MA, 1993), p. 351.

Investigation of Weakly-Bound Clusters of Atomic B with p-H$_2$, o-H$_2$, and Ne

Millard H. Alexander and Moonbong Yang
Department of Chemistry and Biochemistry, University of Maryland, College Park MD 20742-2021

I. Introduction

We have continued our investigation of weakly-bound clusters involving atomic B, concentrating on clusters with Ne, p-H$_2$ and o-H$_2$. Close contact continues with Dagdigian's group, who are reporting related experimental investigations of these clusters. Our theoretical work on the complexes most relevant to HEDM interest (BH$_2$) has benefited from the insight and understanding gained from work on less relevant complexes (BAr,[1, 2] ArBH,[3] ArAlH,[4] and NeOH[5]) which, however, were easier to investigate experimentally.

II. BNe Complexes

Ab initio calculations of the complexes of ground ($...2s^2 2p$) and electronically excited ($..2s^2 3s$) B with Ne were carried out. Coupled-cluster [CCSD(T)] calculations were done for the $X^2\Pi$ and $A^2\Sigma^+$ states and multi-reference, configuration-interaction (MRCI) calculations for the excited $B^2\Sigma^+$ state. The calculated potentials were adjusted by an additional scaling of the correlation energy.[6] The BNe X and A state potentials were qualitatively similar to those found earlier for BAr, although, the well in the X state is shallower.

In contrast to BAr, the potential curve for the B state, shown on the next page, has no well. The shoulder in this curve reflects the weak Pauli repulsion at long-range between Ne and the diffuse $3s$ orbital of B, and a steeper short-range repulsive interaction involving the core electrons. Simulation studies reveal[7] that the shape of this B state potential is responsible for the asymmetry in the observed lineshape of the photoexcited action spectrum of the BNe complex.

III. BH$_2$ Complexes

The first goal in the investigation of complexes of B with o- and p-H_2 is to develop the theoretical framework for the understanding of ongoing experiments. This task involves the determination of accurate PES's for the B$\cdots$H$_2$ complex and,
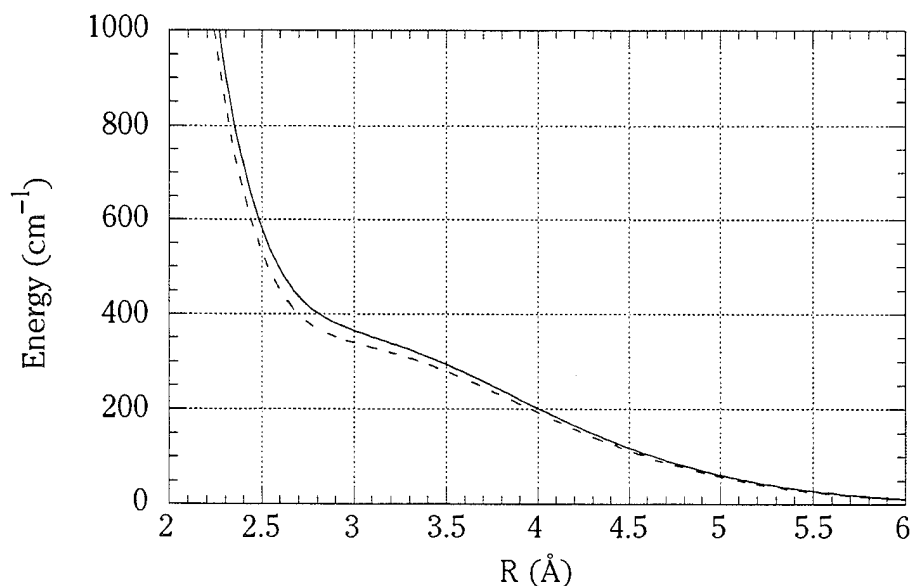
Fig. 1. *Ab initio* potential curves for the $B^2\Sigma^+$ state of BNe. The solid curve is the output of MRCI+Q calculations, while the dashed curve illustrates the effect of scaling the correlation energy to achieve a best fit to experiment (Ref. 7).

subsequently, the treatment of nuclear dynamics on these PES's including a full description of the coupling between the nuclear motion and the electronic and spin angular momenta of the B atom. The second goal is to provide a means to simulate larger $B(H_2)_n$ clusters, particularly those involving o-H_2. The quantum nature of the rotational motion of the light H_2 moiety and the electronic degree of freedom of the B atom, invalidate fully classical simulations.

A. Diabatic representation of the BH$_2$ complex

The interaction between B(^2P) and a closed-shell diatomic is described by three *adiabatic* electronic potential energy surfaces (PES's). Each of these PEF's are functions of the three Jacobi coordinates (R, θ, ϕ) which define the orientation of the H_2 molecule with respect to the B atom.[8, 9] In a diabatic representation, in which the states are defined by the orientation (x, y, or z) of the $2p$ orbital with

respect to $\bar{R}$, the Hamiltonian is a 3×3 matrix involving *four* potential energy functions (PEF's).

In previous work on the BH_2 cluster,[9] we followed the earlier work of Rebentrost and Lester,[8] and used matrix elements of the electronic orbital angular momentum, to determine the (approximate) diabatic → adiabatic transformation. We find this transformation to differ insignificantly from an alternate transformation, based on the configuration expansion coefficients in the CASSCF BH_2 wavefunctions,[10], Further, differentiation of the diabatic → adiabatic transformations from both these approximate diabatization schemes yields derivative coupling matrix elements ($< i \mid \partial/\partial q \mid j >$) which differ insignificantly from those computed by direct differentiation. This observation confirms the accuracy of our previous diabatic potential energy surfaces for BH_2.

B. Determination of bend-stretch levels of complexes of $B(^2P)$ with H_2

In our prior investigations of the binary clusters of $B(^2P)$ with o- and p-H_2[9,11] we assumed that the nuclear motion of the cluster occurred solely on the lowest electronic potential surface – the Born-Oppenheimer approximation. Within this "electronically adiabatic" limit, the unique potential energy surface corresponds to the lowest root of the 3×3 Hamiltonian discussed in Sec. III.A.

Using the general treatment of Dubernet and Hutson,[12] we have extended our prior work to determine the bend-stretch levels of $B(^2P)H_2$ with the full electronic Hamiltonian, including all *three* adiabatic electronic states. We can both ignore, or include, the electronic spin (and, concomitantly, the spin-orbit splitting) of the B atom. This is small (15 cm^{-1}) but not necessarily negligible compared to the anisotropy of the BH_2 PES's, which is also small.

For $B(^2P)\cdots p H_2$, within the electronically adiabatic limit the van der Waals stretching states are eigenstates of a one-dimensional potential. For $B(^2P)\cdots p H_2$ described by the full electronic Hamiltonian, and for the complexes of oH_2, the bend-stretch states are eigenstates of a multidimensional Hamiltonian, similar to the description of other weakly-bound complexes.[13] For complexes which are produced in supersonic expansions, only the lowest values of the total angular momentum are populated. Almost invariably the projection of the total angular momentum along the body axis $\bar{R}$ is a good quantum number.

We have shown,[3, 4, 14, 15] that the vibrational levels of these complexes are, further, well described within the "adiabatic bender" limit, in which the nuclear motion is described by one-dimensional potentials. These are the eigenvalues, as a function of R, of the full Hamiltonian expanded in a set of rotor states of the free diatomic moiety (H_2 in our case). In this adiabatic bender limit, the electronic degree of freedom of the atom and the internal motion (rotation and, if need be, vibration) of the diatomic moiety are coupled together correctly, and subsequently diagonalized. This is not necessarily the same description as the "electronically adiabatic" limit, in which the electronically Hamiltonian is first diagonalized, without any consideration of the nuclear motion.

To illustrate the accuracy of these various treatments of the $B(^2P)H_2$ complex, we present in Tables I – III the positions and assignments of the bending states corresponding to the lowest van der Waals stretch ($v_s = 0$). It is not accurate to completely decouple the electronic and nuclear motion, as was done in our earlier study,[16] in which we considered motion only on the lowest electronically adiabatic PES. However, it may be possible to ignore the spin, since the exact energies agree quite well (last columns of Tables II and III).

Table I. Positions of bending states of the $B(p\text{-}H_2)$ complex .

	electronically adiabatic	full electronic Hamiltonian	
		adiabatic bender	exact
P^a		$S = 0$ $\quad$ $S = 1/2$	
0.5	-30.1	-36.5	-34.5

a. Projection of total angular momentum along $\bar{R}$.

Table II. Positions of bending states of the $B(o\text{-}H_2)$ complex; $S = 0.$ [a]

n^c	P	electronically adiabatic [b]		full electronic Hamiltonian	
		adiabatic bender	exact	adiabatic bender	CD
1	0	-57.4	-59.4	-47.9	-47.9
2		n. a.	n. a.	-41.0	-40.0
1	1	-69.5	-71.9	-29.8	-29.1
1	2	n. a.	n. a.	-34.9	-34.9

a. The spin of the B atom is here ignored.
b. Nuclear motion occurs on just the lowest $1A'$ electronically adiabatic PES. See Ref. 16.

77

Table III. Positions of bending states of the B(o-H_2) complex; $S = 1/2$. [a]

		adiabatic bender		full Hamiltonian	
n [b]	P	fully adiabatic	crossed [c]	CD [d]	exact
1	0.5	− 50.7	− 46.2	− 47.8	− 47.9
2		− 37.8	− 37.8	− 36.7	− 36.7
3		− 24.4	− 34.3	− 30.9	−30.9
1	1.5	− 38.6	− 36.9	−37.7	−38.1
2		− 21.5	− 25.8	−22.1	−21.8
3	2.5	− 26.0	−26.0	−26.0	− 26.0

a. The spin of the B atom is here included.
b. Index of adiabatic bender state.
c. Spin-orbit avoided crossing ignored.
d. Centrifugal decoupling assumed.

Since the complexes involving o-H_2 are significantly more strongly bound, and since o-H_2 is more abundant, future simulations of larger $B(H_2)_n$ clusters should involve the o-H_2 molecule. The development of model interaction potentials, which include the rotational degree of freedom of o-H_2 and the electronic degree(s) of freedom of B, is now underway in our group.

C. Potential energy surface for complexes of $B(^2S)$ with p-H_2 and o-H_2

Since the first excited electronic state of B (... $2s^2 3s$) is nondegenerate, only one PES will be required to describe the complex of $B(^2S)$ with H_2. Following earlier calculations of complexes of $B(^2S)$ with Ar[1] and Ne,[7] we carried out MRCI calculations of the $B(^2S)H_2$ PES. The atomic orbital basis set used in our original $B(^2P)H_2$ calculations[9] was expanded to include diffuse s- and p-type functions to allow for the Rydberg nature of the B $3s$ orbital. In addition, the H_2 bond length was allowed to vary.

Despite the electronic excitation of the B atom (40,000 cm^{-1} [11]), the $B(^2S)H_2$ complex is non-reactive in the region of configuration space sampled by the vibrational motion of the $B(^2P)H_2$ complex. Figure 2 displays the dependence on R of both the anisotropic component and the largest anisotropic component of the $B(^2S)H_2$ PES. The isotropic component is reminiscent of the $B(^2S)$Ne potential curve (Fig. 1), with a broad shoulder and, inside, a steeply rising wall.
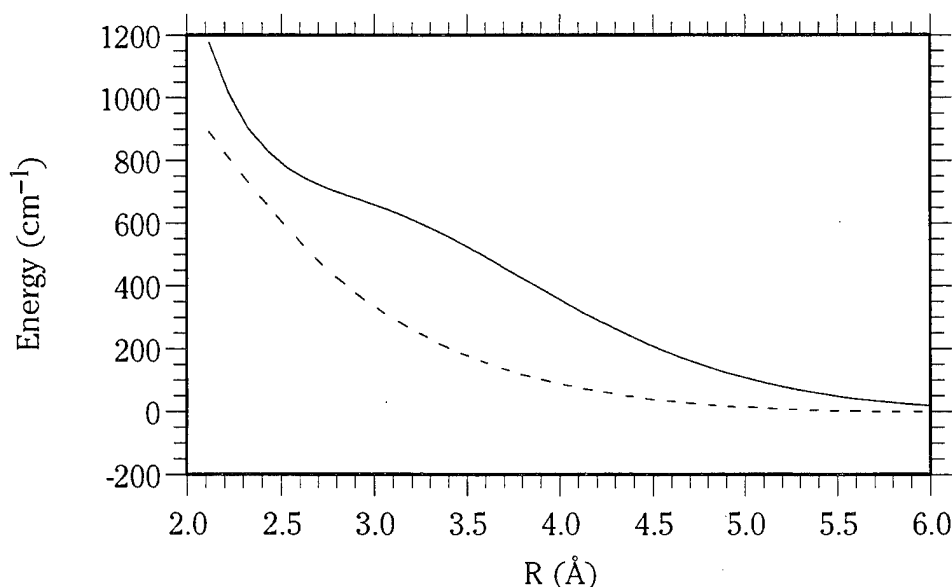
Fig. 2. MRCI+Q potential curves for $B(^2S)H_2$. The solid and dashed curves refer to the isotropic component and first { $P_2[\cos(\theta)]$ } anisotropy. All higher anisotropic terms are negligibly small. The PES has been averaged over the H_2 vibrational motion.

References

1. E. Hwang, Y.-L. Huang, P. J. Dagdigian, and M. H. Alexander, J. Chem. Phys. **98**, 8484 (1993).

2. E. Hwang, P. J. Dagdigian, and M. H. Alexander, Can. J. Chem. **72**, 821 (1994).

3. M. H. Alexander, S. Gregurick, and P. J. Dagdigian, J. Chem. Phys. **101**, 2887 (1994).

4. M. Yang, M. H. Alexander, S. Gregurick, and P. J. Dagdigian, J. Chem. Phys. **102**, 2413 (1994).

5. M. Yang and M. H. Alexander, J. Chem. Phys. **102**, xxxx (1995).

6. A. Degli Esposti, A. Berning, and H.-J. Werner, J. Chem. Phys. **102**, xxxx (1995).

7. X. Yang, P. J. Dagdigian, M. Yang, and M. H. Alexander, J. Chem. Phys. **102**, xxxx (1995).

8. F. Rebentrost and W. A. Lester, Jr., J. Chem. Phys. **63**, 3737 (1975).

9. M. H. Alexander, J. Chem. Phys. **99**, 6014 (1993).

10. H.-J. Werner, B. Follmeg, and M. H. Alexander, J. Chem. Phys. **89**, 3139 (1988).

11. C. E. Moore, *Atomic Energy Levels, NSRDS-NBS 35* (U. S. Government Printing Office, Washington, 1971).

12. B. Pan, J. M. Bowman, and B. Gazdy, Chem. Phys. Lett. **221**, 117 (1994).

13. J. M. Hutson in *Advances in Molecular Vibrations and Collision Dynamics*, edited by J. M. Bowman and M. A. Ratner (JAI Press, Greenwich, CT, 1991) 1A, p. 1.

14. M. H. Alexander, S. Gregurick, P. J. Dagdigian, G. W. Lemire, M. J. McQuaid, and R. C. Sausa, J. Chem. Phys. **101**, 4547 (1994).

15. M. Yang, M. H. Alexander, C.-C. Chuang, R. W. Randall, and M. I. Lester, J. Chem. Phys. **102**, xxxx (1995).

16. A. Vegiri, M. H. Alexander, S. Gregurick, A. McCoy, and R. B. Gerber, J. Chem. Phys. **100**, 2577 (1994).

SPECTROSCOPIC INVESITGATION OF ALKALI-ATOM-DOPED HYDROGEN AND HELIUM CLUSTERS

F. Stienkemeier*, J. Higgins, C. Callegari, W. Ernst‡ and G. Scoles
Department of Chemistry, Princeton University, Princeton, N. J. 08544

1_ Introduction

In view of the possible application to improving the propellant properties of solid hydrogen (by seeding in it light metal atoms) the mobility and other properties of atomic and molecular species dispersed in condensed hydrogen need to be studied. While the theoretical description of both static interactions and dynamics of "impurities" in highly quantum condensed matter (mostly solid H_2 and liquid He) is making steady improvement, we are still very far from being able to predict the needed properties by calculating them and, therefore, an experimental approach is necessary. While solid matrices are being studies at the Phillips Laboratory and elsewhere, we proposed to approach the problem by using large clusters instead of bulk solids and liquids.

The use of clusters is made possible by the pick-up cluster-doping technique introduced by us ten years ago (1). This technique consists of passing the beam of clusters to be doped through a scattering box which contains a small pressure (about 10^{-2} Pa) of the substance to be loaded into the clusters. If the clusters are sufficiently large (n $\simeq$ 1000 or larger) they collide with the atoms or molecules which reside in the pick-up cell and emerge on the other side practically undeflected. Since, because of evaporative cooling, the clusters are generally quite cold, the atoms (or molecules) in the cell stick to them with very high probability.

Using large clusters as host matrices for spectroscopic measurements offers several advantages over bulk solids and liquids. First, by controlling the pressure in the pick-up cell one can control the average number of "impurities" which attach to the cluster.

Second, due to their small size and to the mobility of their surface atoms (or molecules), clusters reach internal equilibrium (i.e. anneal) rather easily. Third, by using two pick-up cells, different atoms (or molecules) can be loaded in the same cluster producing mixed "impurities" with only a small population of dimer of the same impurity species. Disadvantages include the need for molecular beams and the difficulties connected with the presence of an imprecisely known size distribution in the cluster beam.

---

* Present address: Fakultät für Physik, Universität Bielefeld, D-33615 Bielefeld, Germany
‡ Permanent address: Department of Physics, Penn State University, State College, PA. 16802

2_ Spectroscopy of Na-doped liquid helium clusters using laser induced fluorescence detection

2.1_ Experimental apparatus

A schematic diagram of the experimental arrangement used to introduce LIF detection is displayed in Fig.1. Expanding He from a 10μm nozzle, at temperatures down to 12K and stagnation pressures up to 10^4KPa, this apparatus can produce a beam of helium clusters ranging in average size up to 10^4 atoms/cluster. Doping the clusters with chromophores is achieved by placing a heated pick-up cell directly downstream of the collimating skimmer. A heated tube connecting the pick-up cell to an alkali reservoir establishes the necessary Na partial pressure of 10^{-3} - 10^{-1} Pa inside the cell. The latter is normally kept at a temperature 100K higher than the reservoir to avoid alkali atom distillation and to keep the alkali vapor free of dimers. According to the value of the alkali pressure in the cell, the clusters pick up one or more alkali atoms without being appreciably deflected from their path. For each alkali pick-up, about 150 He atoms evaporate from the cluster. A few centimeters downstream of the scattering cell, at the center of a two-mirror laser induced fluorescence (LIF) detector of standard design, the clusters are crossed with the well baffled output beam of a tunable dye laser. The fraction of the photomultiplier signal which is phase related to the chopped cluster beam, is measured using a lock-in amplifier. A Langmuir-Taylor surface ionization detector, located beyond the LIF detector, is used to monitor the presence of the alkali atoms in the beam. It also aids in establishing the optimum cluster source and pickup cell conditions for maximum cluster flux and desired alkali dopant concentration in the clusters.

2.2_ Na$_2$ spectroscopy on He clusters: singlet molecules

The results obtained with Na atoms will be described later (together with those obtained using Li atoms). Hereafter we describe the results obtained for Na$_2$. A paper based on this work has just appeared in Phys. Rev. Letters (Vol.74 (1995) 3592). Molecular sodium spectra have been obtained in the frequency range between 14500 and 16500 cm^{-1} by using initially a Spectra Physics 380 tunable ring dye laser at 5GHz resolution. Fig. 2 shows a spectrum at a cluster source temperature of 19K and a He stagnation pressure of 7 MPa. The spectrum consists of three main groups of spectral features that will be discussed separately.

The first very strong group is detected between 15800 and 16500 cm^{-1} with a sharp intensity threshold near 15800 cm^{-1}. This spectrum is about a hundred times more intense than the bands observed at lower frequencies, which can be unambiguously identified as being produced by sodium dimers (see below). The intensity of this structure shows a higher order dependence on
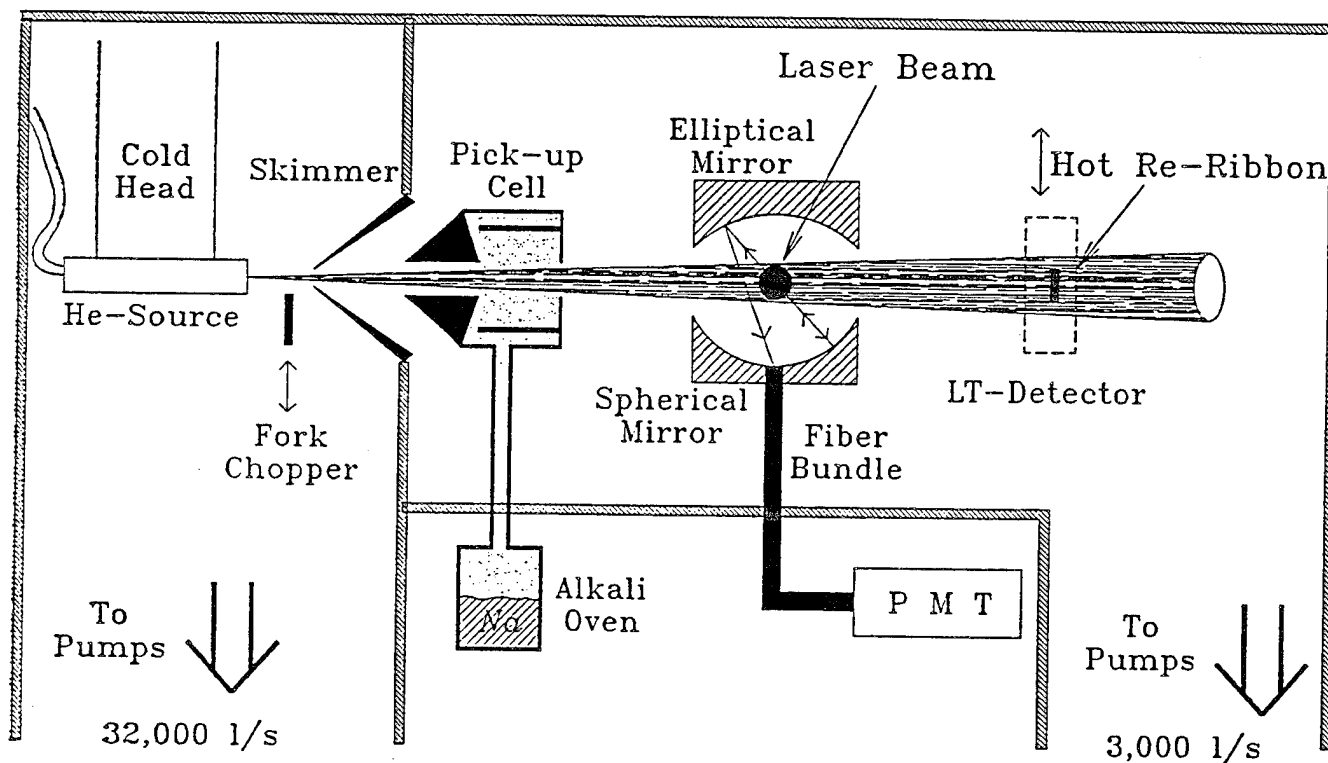
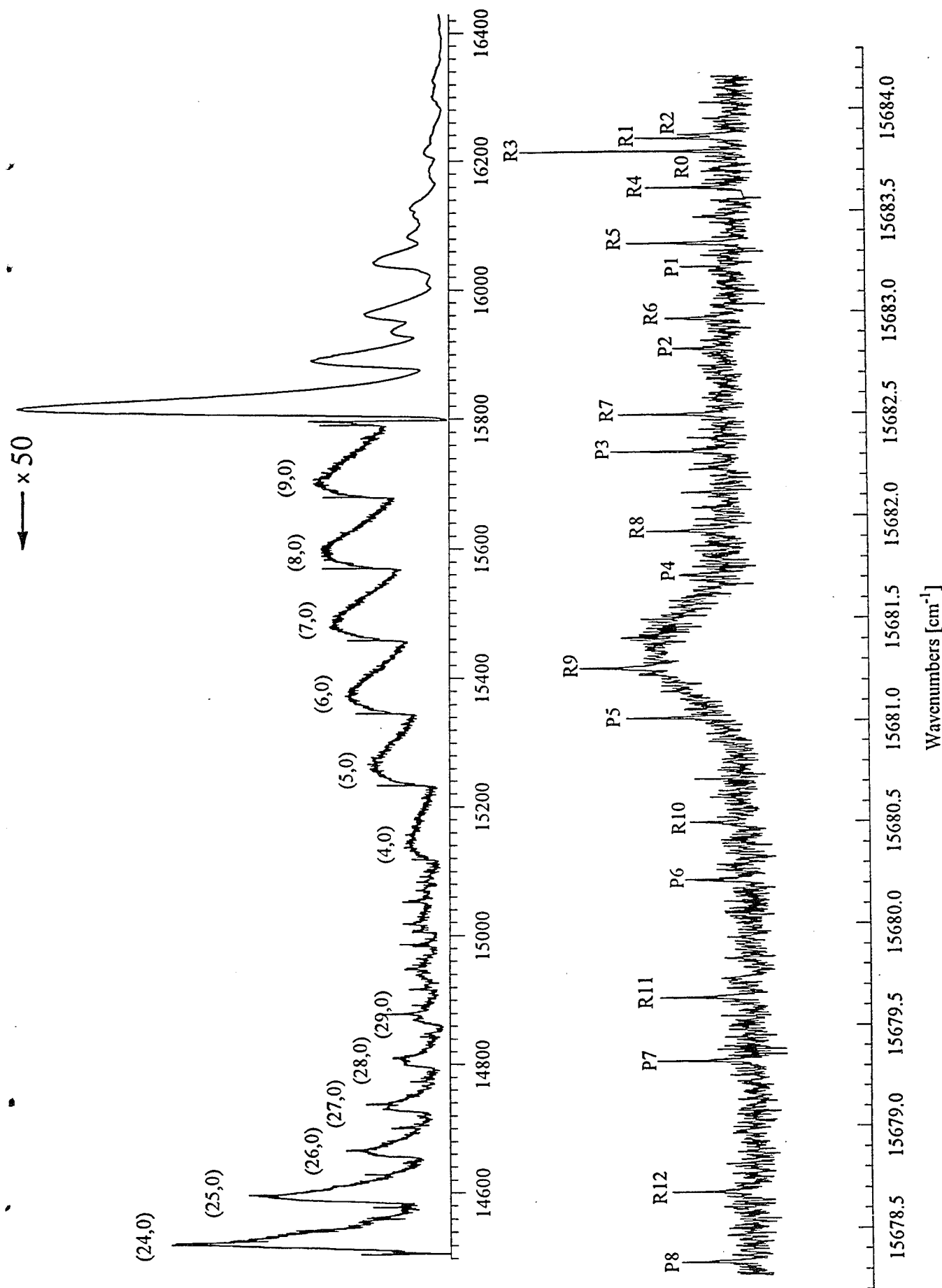Fig. 1 Experimental apparatus for laser induced fluorescence spectroscopy of alkali doped He or H_2 clusters.

Fig. 2 LIF spectrum of Na doped helium clusters. a) Upper panel) Source stagnation conditions: P = 6 MPa, T = 18.5 K. The features between 14,600 and 15,000 cm^{-1} are due to $^3\Sigma_g^+ \leftarrow ^3\Sigma_u^+$ transitions of Na$_2$ while those between 15,100 and 15,800 are due to A $\leftarrow$ X transitions also of Na$_2$. The unlabeled transitions above 15,800 cm^{-1} are unassigned transition of a species which is likely to contain three Na atoms. b) (Lower panel) Source conditions: P=4 MPa, T = 17.6 K. High resolution scan of a small region near the beginning of the (9, 0) band (see text). The nozzle diameter is 10 μm.

the Na partial pressure inside the pick-up cell than the dimer bands. This suggests that the measured intensities may be due to a process involving three or more Na atoms. The B - X system of the trimer lies in this region, but has a completely different ro-vibrational structure.

The second group of features one encounters the first moving towards the red, can be identified as due to Na_2 $A^1\Sigma_u^+ - X^1\Sigma_g^+$ transitions. The threshold frequency of each sub-band and the spacings between these (center of Fig.2) agree well with the corresponding quantities for gas phase Na_2. The absence of a large blue shift, typical for species located inside liquid or solid helium, indicates that the Na_2 molecules are, as the atoms, located on the cluster surface. In contrast to the gas phase, where the width of a sub-doppler line is limited only by its lifetime to 13MHz, each of the bands measured here consists of a _relatively_ narrow (1cm^{-1} or 30 GHz) line and an 80 cm^{-1} broad feature extending toward the blue. Decreasing the cluster size by raising the nozzle temperature to 22.5K narrows the latter width to 25cm^{-1}. The observation of these spectra is strictly correlated to the production of He clusters and the bands disappear for nozzle temperatures T$\geq$ 25K.

Since the low resolution scans indicated the presence of higher resolution structures, a Coherent 699-21 ring dye laser ($\sim$ 1MHz bandwidth) was used to scan over a 6cm^{-1} interval of the $A^1\Sigma_u^+ - X^1\Sigma_g^+$ (9,0) vibrational band. The results are shown in Fig. 2b. A very large fraction of the observed lines can be assigned as rotational lines of the (9,0) band as indicated in the figure. The absolute line positions agree with those of the free sodium dimer within the 0.01cm^{-1} accuracy of the frequency measurement. The intensity of the narrow lines scales with the intensity of the broad band envelopes and the lines disappear under the same conditions as the envelopes ruling out the pick-up cell as a possible source of free dimers. The linewidth of the (Lorentzian) rotational lines narrows with decreasing laser intensity to a value of 80MHz obtained at 50mW/cm^{-2} where some power broadening is still likely to be present. A plot of the degeneracy corrected line intensities versus rotational quantum number revealed that a unique rotational temperature cannot be derived. The relative intensities of the four lowest states are consistent with a temperature of 3K, but higher rotational states (up to J = 12) show intensities which are much greater than those expected for such a temperature.

Since the identified rotational lines exhibit no shift compared to the gas phase molecular line positions of Na_2 (and therefore the molecular constants have not changed) but the spectrum disappears in the absence of He clusters, the Na atoms must be first picked up by the He clusters and must form sodium dimers on the cluster surface. The weak binding to the He cluster, the presence of large quantities of angular momentum from the pickup and the recombination process,

together with the disposal of the recombination energy, cause the desorption of a fraction of the molecules from the cluster surface. These molecules desorb at a velocity which may be quite low due to the extreme softness of the helium surface and its low temperature. A fraction of these dimers then travels to the detector with the clusters and gives rise to features that reflect their gas phase nature.

The broad line shown at the center of Fig 2b corresponds to the "narrow" peaks located at the beginning of each vibrational band mentioned before. The red shift with respect to the gas phase band origin is constant for each vibrational band ($2.4 cm^{-1}$ independently of cluster size). This indicates that the vibrational constants of the sodium dimer attached to the cluster are equal to those of the free molecule. If the line at the origin of each vibronic envelope is taken as a "zero phonon" line, then the $80 cm^{-1}$ band extending toward the blue can be attributed to a phonon sideband arising from an inelastic Stokes process involving the combined excitation of the Na_2 and the phonons of the helium cluster.

2.3_ Na₂ spectroscopy on helium clusters: triplet molecules

Below $15000 cm^{-1}$, another vibrational progression is observed which is due to the presence on the clusters' surface of van der Waals bound triplet dimers which form with 3 times larger probability than the singlet molecules. The assignment of this progression to the $5 2. \Sigma_g^+ \leftarrow 1^3 \Sigma_u^+$ transition of the triplet dimer, can be done (and initially we had indeed followed this procedure) on the basis of the comparison between the experimental separations of the vibronic bands and the energy level separations calculated from the $1^3 \Sigma_g^+$ potential of ref. 2, in the region located vertically above the ground state of the $1^3 \Sigma_u^+$ state.

However, the appearance of a paper by Demtröder and collaborators [3] has made this task easier and more precise even if the sets of level covered in the two experiments do not overlap. Table 1 shows a comparison between the positions and spacings of the transitions predicted on the basis of the assignments made in ref. 3 with our experimental values. Since our transitions are broadened and possibly shifted by the interaction with the He clusters, the comparison of the transition positions should be done carefully and was carried out as follows. We have first arbitrarily identified the experimental transition positions with the beginning of the steep rise in each band (see fig.2a). Secondly, for the 0-24 transition we have calculated the small shift ($4.8 cm^{-1}$ to the red) which would make this transition coincide with the corresponding transitions as predicted on the basis of the data of ref.3. Finally, the positions reported in Table 1 are the experimental positions, each shifted by the same amount as the 0-24 transition. The agreement for both positions and spacings is very good confirming both our assignments and those of ref.3.

Table 1

Positions ν term differences ΔG and Franck-Condon factors (FCF) for the $1^3\Sigma_g^+ \leftarrow 1^3\Sigma_u^+$ spectrum of Na$_2$ extrapolated from the work of Demtröder and collaborators compared with the measurements reported in this work.

Transition v' ← v"	ν (cm⁻¹) (ref. 5b)	ν (cm⁻¹)[a] (this work)	ΔG (cm⁻¹) (ref. 5b)	ΔG (cm⁻¹) (this work)	FCF[b,c] (ref. 5b)	FCF [b] (this work)
24 ← 0	14,508.5	14,508.5			1	1
25 ← 0	14,580.9	14,579.9	72.4	71.4	0.61	0.69
26 ← 0	14,652.0	14,651.4	71.1	71.5	0.38	0.31
27 ← 0	14,722.0	14,720.8	70.0	69.4	0.23	0.22
28 ← 0	14,790.9	14,790.1	68.9	69.3	0.15	0.16
29 ← 0	14,858.7	14,857.6	67.8	67.5	0.08	0.12

a_ All experimental values have been shifted to the red by 4.8 cm⁻¹ to make the position of the 24 ← 0 transition coincide with the position of the same transition extrapolated from the data of ref. 3

b_ All values have been normalized to the value of the 24 ← 0 transition.

c_ Calculated values. (Table 1 of ref. 3.

Table 1 also shows a comparison of the intensity of each transition (relative to the 0-24 band) and the Franck-Condon factors calculated in ref.3.

It is remarkable that the spectrum does not appear to be shifted (a least no more than a relatively small fraction of the vibrational spacing). This, however, is in keeping with our findings for the spectra of the atoms and the singlet molecule, under the same conditions. A detailed analysis of the spectrum and attempts at resolving the fine structure which appears to be present in the data are in progress in our laboratory. A preliminary account of these results has appeared in ref. 4.

3_ Laser induced fluorescence of Li and Na atoms on liquid helium clusters

The spectra obtained by doping the helium clusters with a relatively small amount of Na or Li (in order to avoid the formation of too many dimers) are shown in fig.3 and 4 respectively. The regions where the intensity goes out of scale coincide, of course, with the gas phase absorptions for the two $3(2)\,^2P_{\frac{3}{2},\frac{1}{2}} \leftarrow 3(2)^2S_{\frac{1}{2}}$ free atom transitions. Notable are the very small shifts and he substantial blue tails which are much more pronounced for Na than for Li.

The Na (Li) atom interactions with atomic He are extremely weak (well depths of the order of one cm^{-1}) and the atoms are expected to be expelled by the clusters (5). If this is the case, it is natural that the Li atom being lighter would be also more delocalized and be less perturbed by the helium cluster.

Information on the cluster size dependence of the spectra has beFn obtained by changing the temperature of the nozzle producing the clusters. Because the atomic spectra lack the signatures introduced by the rovibronic structure (which is instead present in the dimer spectra) their analysis is more difficult and is presently in progress. We are here collaborating with Dr. S. Kanorsky of the Max Planck Institute of Garching who is presently extending a line-broadening type of model to the cluster-perturbed atomic spectra.

4_ Laser induced fluorescence spectroscopy of Li and Na atoms in hydrogen clusters

The spectra obtained from hydrogen clusters doped with Na and Li atoms are shown in Fig.5. Contrary to the helium case most of the intensity is now coming from absorptions which are substantially blue shifted (500 and 300 cm^{-1} respectively) with respect to the gas phase absorptions. This seems to indicate that in the case of hydrogen the atoms are located inside the clusters as opposed to on their surface.
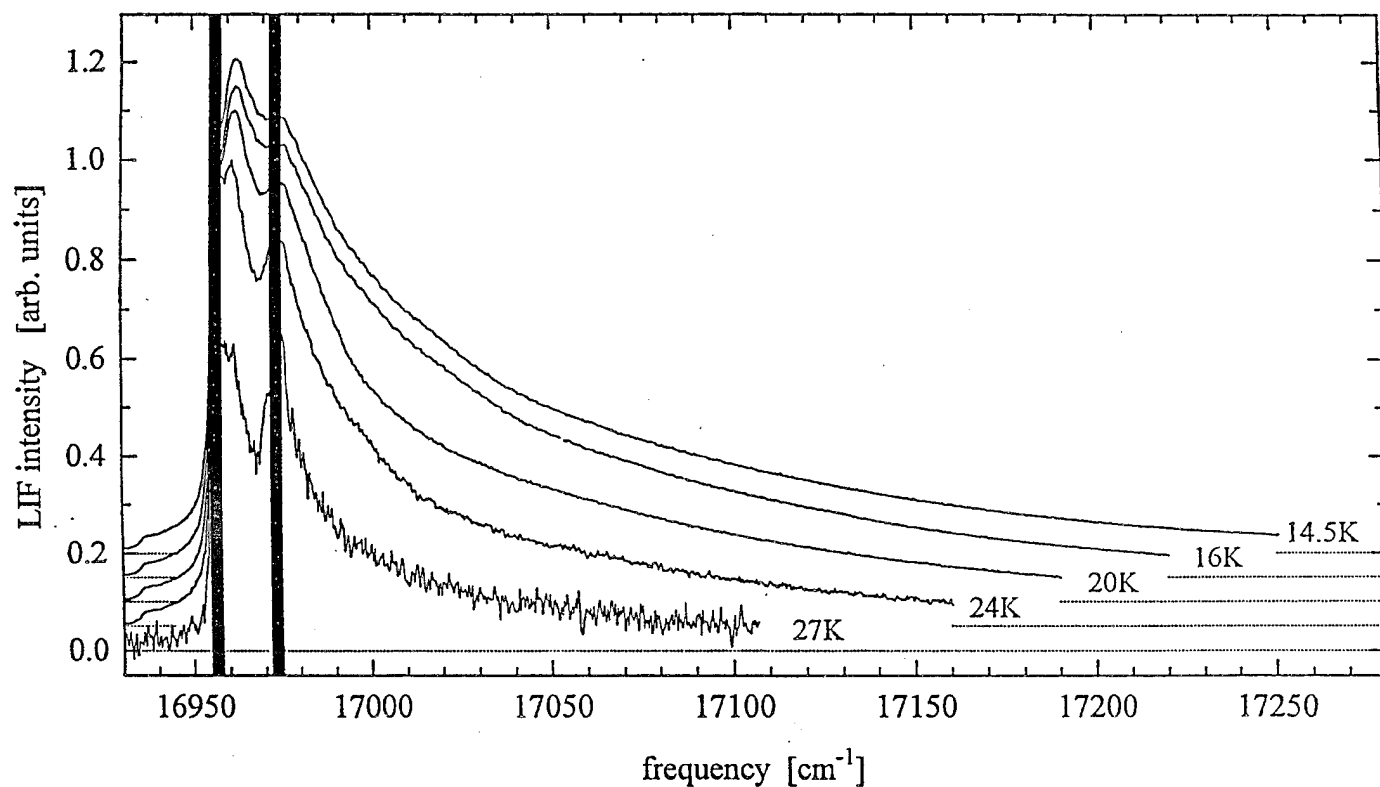
Fig. 3 LIF spectrum of Na doped helium clusters in the vicinity of the gas phase Na atom absorptions. The temperature of the nozzle is indicated at the end of each curve which, for sake of clarity is shifted upwards by a constant incremental amount. The stagnation pressure is 5 MPa for all nozzle temperatures. The nozzle diameter is 5 μm.
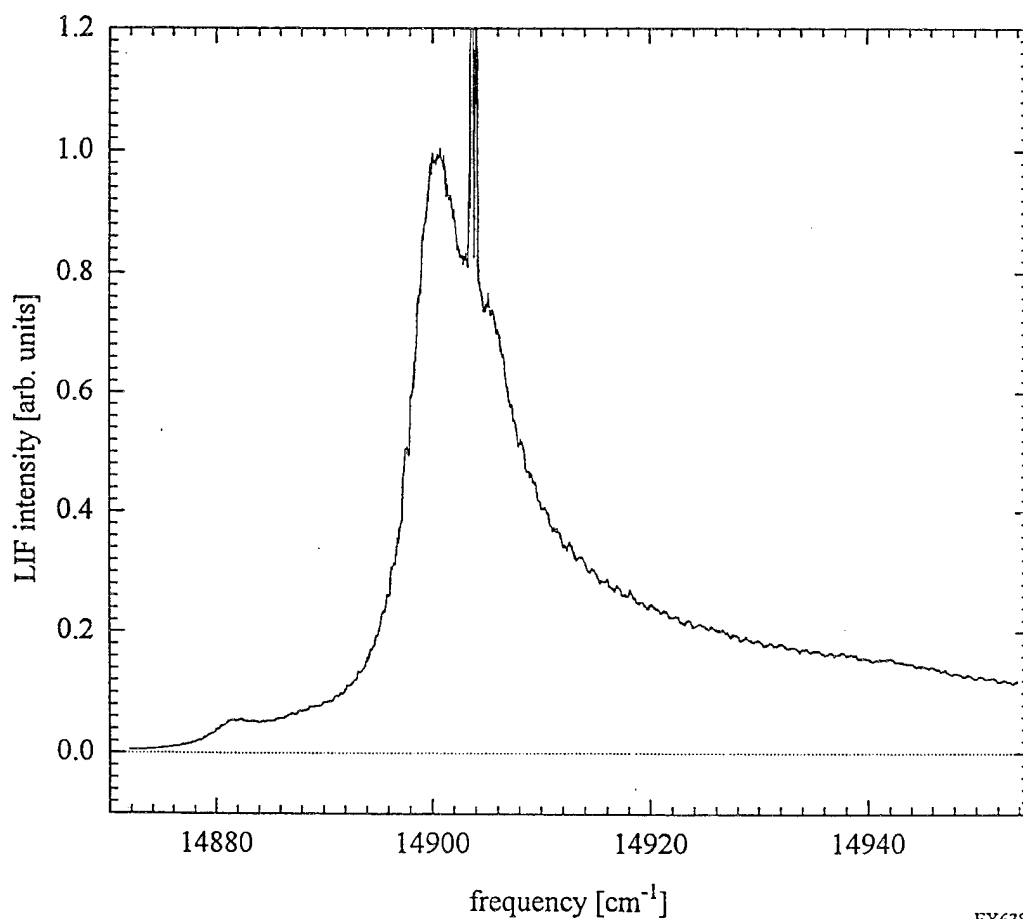

FX638.ORG

Fig. 4 LIF spectrum of Li doped helium clusters in the vicinity of the gas phase Li atom absorptions. The nozzle temperatures is 19 K. The stagnation pressure is 5 MPa.
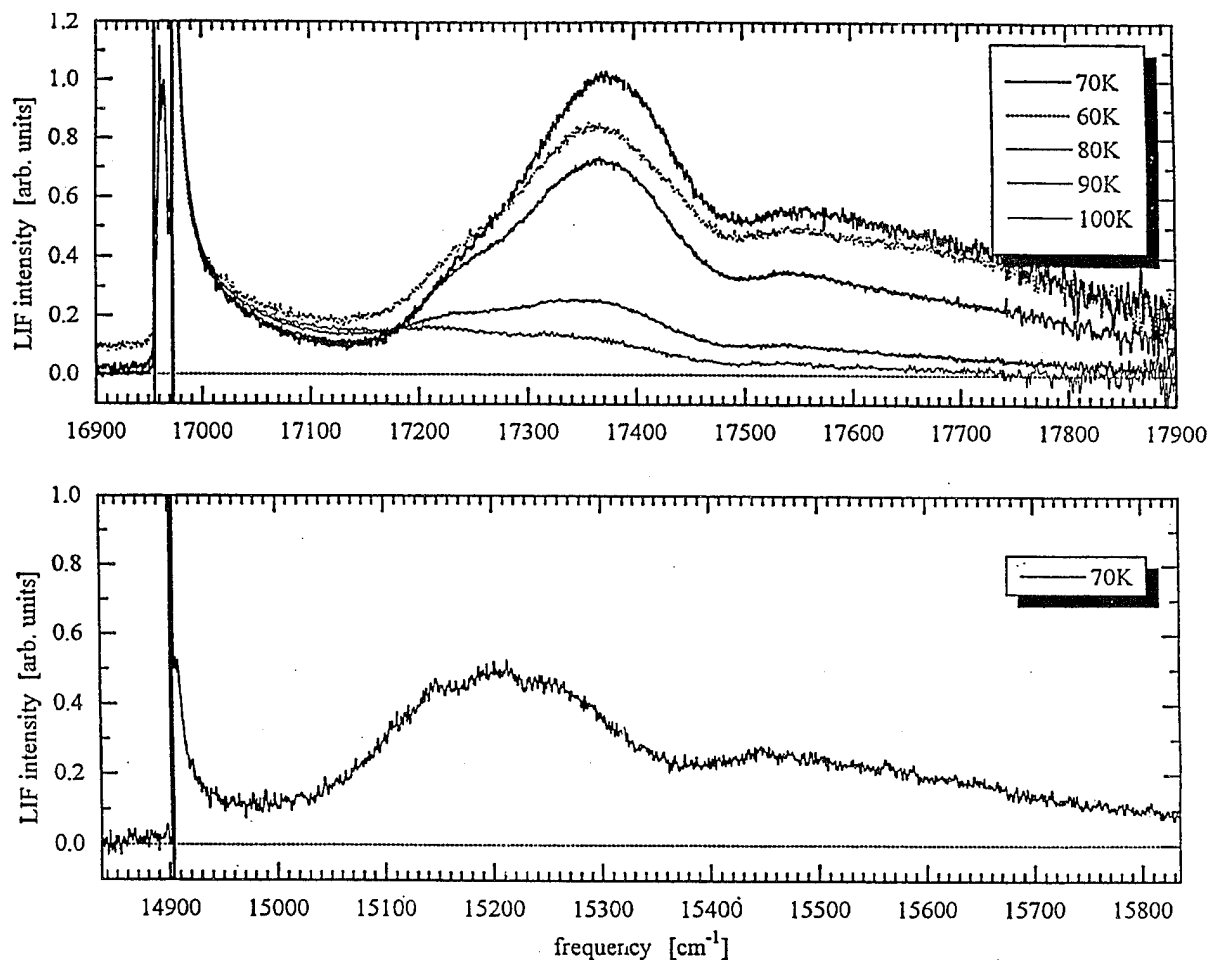
88

Fig. 5 LIF spectra of Na (upper panel) and Li (lower panel) doped hydrogen clusters. The nozzle temperatures are indicated in the insets. The stagnation pressure is 2.1 MPa in all cases. The nozzle diameter is 10 μm.
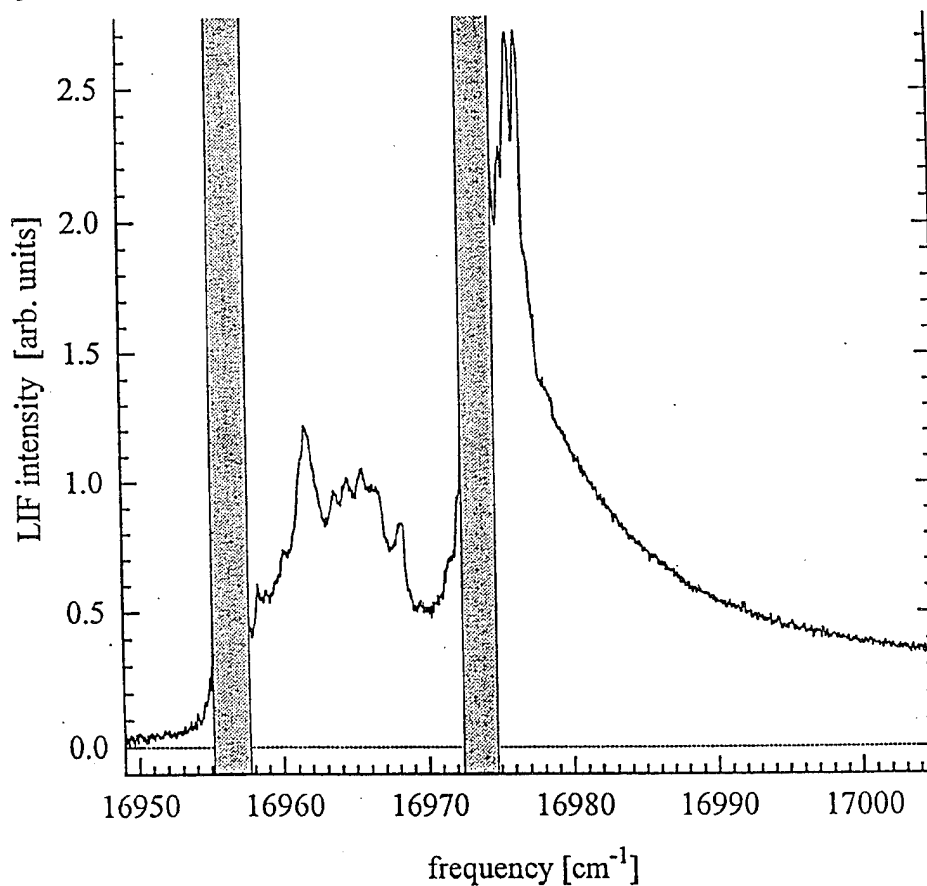

Fig. 6 Expanded view of the LIF spectrum of Na atoms in hydrogen clusters reported in fig. 7. The nozzle temperature is 60 K and the stagnation pressure is 2.1 MPa.

The Li results disagree with the calculations of Scharf, Martyna and Klein [6]. The Na results turned out to be particularly interesting since they reveal (in the region near the gas phase absorption) high frequency oscillations (see fig.6) which may be due to an oscillatory behavior of the H_2/Na quenching probability as a function of the frequency of the exciting laser. We note that in spite of the very good S/N ratio the Na(Li) measurement in hydrogen give rise to much lower counting rates (by a couple of orders of magnitude) than the corresponding spectra on helium. This decrease in LIF is quite likely a consequence of the quenching action of the H_2 molecule on the atomic excited species. Finally, in Fig.7 we show a comparison between helium and hydrogen cluster spectra for Na atoms. Whether or not the residual absorption near the gas phase line values is due to the smallest clusters in the cluster size distribution (which in this case will need to be bimodal) or to the presence of two residence states (surface and bulk) on the large clusters (which could be populated according to the different energies prevailing in the pick-up collision) will be the subject of further investigation.

5_ Summary and outlook

With respect to the Air Force main interest of studying the interactions between light metals and condensed hydrogen we can say that the spectra reported here are likely to be an excellent testing ground for a) the static interaction energy calculations carried out under USAF Sponsorship by Konowalow and coworkers (7), b) the approach of Gerber and coworkers (8) which has been designed for calculating the dynamical interactions between Li atoms and H_2 clusters and c) the Quantum Montecarlo calculations of Klein and coworkers (6). In addition, it is now possible for us to dope the hydrogen clusters with other metals, intermetallic compounds or other radical species and obtain their spectra with relative ease. We have now a tool in our hands for attacking the problem of the mobility of foreign species in condensed hydrogen. A substantial amount of work remains to be done to fully understand and predict the mobility of "impurities" in condensed hydrogen, but a firm first step towards the solution of this problem has been taken.

To summarize our results, we have doped both hydrogen and helium clusters with variable amount of alkali (Na and Li) atoms and obtained the spectra of the following combinations: Na $(He)_N$, $Na_2(He)_N$, $Na_3 (He)_N$, Na $(H_2)_N$, Li $(He)_N$ and $Li(H_2)_N$. Spectra for both singlet to singlet and triplet to triplet transitions have been obtained for Na_2 showing that the He clusters provide a cold surface environment on which stable and unstable molecules can be formed and studied with either vibrational (on the cluster) and rotational (after evaporation) resolution.
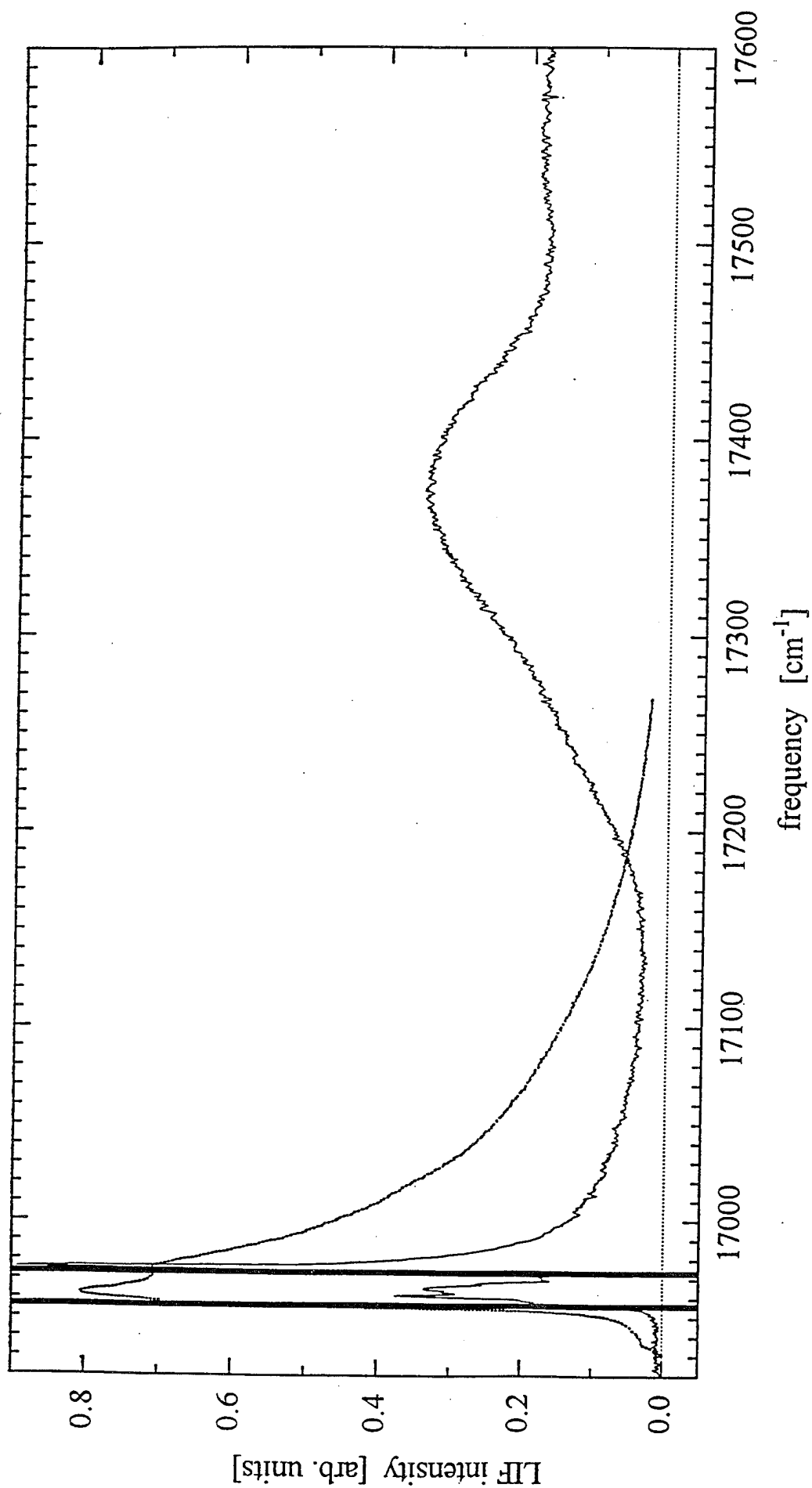
Fig. 7   Comparison between the LIF spectra of Na-doped helium and hydrogen clusters. The arb. units scales for the intensity are different in the two spectra. Because of quenching, the intensities in the case of hydrogens are orders of magnitude lower than in the case of helium.

Looking at the future, we can say that the investigation of alkali trimers formed at the surface of a cold He cluster in their doublet state can reveal if the small interaction with the He neighbors affects the strong coupling of electronic and nuclear motion in these molecules. Furthermore, the study of the Na_3 quartet state may give us very detailed insight into the 3-body component of the physical part of intermolecular forces. By using a second pick-up cell, it will be possible to form mixed clusters of predetermined composition. For instance, mixed singlet and triplet dimers can be prepared, the latter being nearly impossible to form using the presently available methods. The new "matrix-isolation" technique described here has the advantage over bulk-matrix methods, of providing to the spectroscopist all the flexibility of molecular beam based methods. Photoionization spectroscopy can be applied and large electric fields can be used without interference from electrical discharges and breakdown.

Acknowledgements

References

(1) T. E. Gough, M. Mengel, P. A. Rowntree and G. Scoles, J. Phys. Chem. 83, 4958 (1985).

(2) S. Magnier et al., J. Chem. Phys. 99 7113 (1993).

(3) A. Farbert, J. Koch, T. Platz and W. Demtröder, Chem. Phys. Lett. 223, 546 (1994).

(4) F. Stienkemeier, W. E. Ernst, J. Higgins and G. Scoles, J. Chem. Phys. 102 615 (1995).

(5) F. Dalfovo, Z. Physik D 29, 61 (1994).

(6) D. Scharf, G. Martyna and M. L. Klein, J. Chem. Phys. 99, 8997 (1993).

(7) D. D. Konowalow, Report, October 1993.

(8) Z. Li and R. B. Gerber, J. Chem. Phys. 102, 4056 (1995).

SPECTRAL THEORY OF CHEMICAL BINDING:
AGGREGATES OF WEAKLY BOUND ATOMS†

P. W. Langhoff

Department of Chemistry
Indiana University
Bloomington, IN 47405-4001

ABSTRACT

Applications are reported of recently devised theoretical methods for study of dilute metal (Na) radicals trapped in rare-gas (Ar) cryogenic matrices. Potential energy surfaces obtained following these procedures are described for $NaAr_2$ aggregates in C_{2v} symmetry employing ten-term $(3S, 3P_{\pm1,0}, 4S, 3D_{\pm2,\pm1,0})_{Na} \otimes (\,^1S_0)_{Ar}$ atomic-product-state representations of the corresponding $(X\Sigma^+, A\Pi_{\pm1}, B\Sigma^+, C\Sigma^+, D\Delta_{\pm2}, E\Pi_{\pm1}, F\Sigma^+)$ $NaAr$ pair states. Large non-pair-wise-additive contributions to the four lowest-lying ($\,^2A_1$, $\,^2B_1$, $\,^2B_2$, $\,^2A_1$) potential energy surfaces are obtained which are attributed to the "near" $3S$-$3P$ Na atomic state degeneracy, a circumstance expected to be common to alkali-metal/rare-gas interactions more generally. The predicted energy surfaces for larger aggregates are seen to depend sensitively upon the detailed angular arrangement of rare-gas perturbers around the metal radical seedant, providing a caging effect that is largely missing from perturbative and related approaches widely employed for this purpose. The relevance of these effects to calculated optical absorption spectra and aggregate radial distriution functions are illustrated here for $NaAr_6$ clusters, and for larger clusters and solids in an accompanying report also appearing in this Proceedings.

1. Introduction

Recent reports describe new theoretical foundations [1-3] for a class of theories which attempt to construct many-body potential energy surfaces from individual fragment information [4-13]. The general formulation described is based on use of a direct product of complete sets of atomic spectral eigenstates [5] and the exact pair-wise-additive nature of the total Hamiltonian matrix in this representation [8,9]. A separation therorem is obtained from the development which expresses the interaction energy of an arbitrary aggregate in terms of response matrices which can be determined once and for all for atoms and other fragments of interest. In the present report, a pair-interaction-based version of the development, which employs diatomic potential energy curves and related pair information and is expected to be particularly suitable for semi-empirical (renormalized) approximations [3], is applied to studies of dilute metal (Na) radicals trapped in rare-gas (Ar) cryogenic matrices. The results obtained are seen to contain in lowest order the widely employed pair-wise-additive approximation to interaction energies in N-body clusters [14], to clarify and extend rigorously various diatomics-in-molecules approaches to potential-surface construction [8,9], to include the effects of configuration mixing and charge distortion missing from semi-empirical and perturbation approximations [10-13] commonly employed in calculations of trapped-radical optical spectra [15-17], and to encompass and demonstrate equivalences among these approaches in appropriate limits. The computational application reported for dilute (Na) metal radicals trapped in (Ar) rare-gas cryogenic matrices employs available $NaAr$ pair potential energy curves $(X\Sigma^+, A\Pi_{\pm1}, B\Sigma^+, C\Sigma^+, D\Delta_{\pm2}, E\Pi_{\pm1}, F\Sigma^+)$ [18-20] in a semi-empirical construction of the required configuration-mixing transformation matrix in a ten-atomic-product state $(3S, 3P_{\pm1,0}, 4S, 3D_{\pm2,\pm1,0})_{Na} \otimes (\,^1S_0)_{Ar}$ approximation. Additional computational results for Na-seeded Ar_N clusters and solids obtained employing this approach are also reported separately elsewhere in this Proceedings [21].

2. Sodium-Argon Aggregate Interactions

Equations are provided here for the interaction of a single Na atom with an N-body aggregate of Ar atoms arranged in an arbitrary configuration specified by the vector $\mathbf{R} \equiv (\mathbf{R}_1, \mathbf{R}_2,... \mathbf{R}_N)$ in a coordinate system centered at the Na atom. The Na-Ar_N atomic-product states are given by the 10-term row vector

$$\mathbf{\Phi} = \left(3S, 3P_{+1}, 3P_0, 3P_{-1}, 4S, 3D_{+2}, 3D_{+1}, 3D_0, 3D_{-1}, 3D_{-2}\right)_{Na} \otimes \prod_{k=1}^{N} \left(^1S_0\right)_{Ar_k},$$

where $(^1S_0)_{Ar_k}$ refers to the ground state of the kth Ar atom. The molecular $NaAr_k$ pair states are given by the corresponding 10-term row vectors

$$\mathbf{\Psi}^{(k)} = \left(X\Sigma^+, A\Pi_{+1}, B\Sigma^+, A\Pi_{-1}, C\Sigma^+, D\Delta_{+2}, E\Pi_{+1}, F\Sigma^+, E\Pi_{-1}, D\Delta_{-2}\right)_{NaAr_k},$$

which are connected to the atomic-product-basis by the transformation [1-3]

$$\mathbf{\Phi}^{(k)} = \mathbf{\Psi}^{(k)} \cdot \mathbf{U}^{(k)}(R_k) \cdot \mathbf{R}^{(k)}(\phi_k, \theta_k),$$

where $\mathbf{\Phi}^{(k)}$ refers to the atomic-product-basis component for the kth Ar atom, $\mathbf{U}^{(k)}(R_k)$ is the required transformation matrix, and $\mathbf{R}^{(k)}(\phi_k, \theta_k)$ is a rotation operator [1-3].

The total 10x10 Hamiltonian matrix in the atomic-product basis is

$$\mathbf{H}(\mathbf{R}) = \mathbf{H}^{(A)} + \sum_{k=1}^{N} \mathbf{V}^{(k)}(\mathbf{R}_k) + (1/2)\sum_{k=1}^{N}\sum_{k'=1}^{N} (k \neq k')\mathbf{V}^{(k,k')}(R_{k,k'}),$$

where $\mathbf{H}^{(A)}$ is the 10x10 total atomic Hamiltonian matrix, and

$$\mathbf{V}^{(k)}(\mathbf{R}_k) = \mathbf{H}^{(k)}(\mathbf{R}_k) - \mathbf{E}^{(k)}(\infty),$$

is the 10x10 pair-interaction matrix for the Na metal radical and the kth Ar atom located at $\mathbf{R}_k$ $(= R_k, \phi_k, \theta_k)$ measured from the Na atom position,

$$\mathbf{H}^{(k)}(\mathbf{R}_k) = \mathbf{R}^{(k)}(\phi_k, \theta_k)^\dagger \cdot \mathbf{U}^{(k)}(R_k)^\dagger \cdot \mathbf{E}^{(k)}(R_k) \cdot \mathbf{U}^{(k)}(R_k) \cdot \mathbf{R}^{(k)}(\phi_k, \theta_k),$$

is the transformation of the 10x10 diagonal pair-potential-energy matrix $\mathbf{E}^{(k)}(R_k)$, $\mathbf{E}^{(k)}(\infty) = \mathbf{E}^{(k)}(R_k \to \infty)$ is its asymptotic form, and $\mathbf{V}^{(k,k')}(R_{k,k'})$ are the (pair-wise-additive) ground-state Ar-Ar interactions.

In order to complete evaluation of the total Hamiltonian matrix, explicit expressions are required for the matricies $\mathbf{U}^{(k)}(R_k)$ and $\mathbf{R}^{(k)}(\phi_k, \theta_k)$. The 10x10 rotation matrix $\mathbf{R}^{(k)}(\phi_k, \theta_k)$ in the present case is

$$\mathbf{R}^{(k)}(\phi_k, \theta_k) = \begin{pmatrix} \mathbf{D}^{(0)}(\phi_k, \theta_k) & 0 & 0 & 0 \\ 0 & \mathbf{D}^{(1)}(\phi_k, \theta_k) & 0 & 0 \\ 0 & 0 & \mathbf{D}^{(0)}(\phi_k, \theta_k) & 0 \\ 0 & 0 & 0 & \mathbf{D}^{(2)}(\phi_k, \theta_k) \end{pmatrix},$$

where the $\mathbf{D}^{(L)}(\phi_k, \theta_k)$ are the rotation matrices of indicted angular momentum $(L = 0, 1, 2)$ [22,23]. The (real) 10x10 configuration mixing matrix $\mathbf{U}^{(k)}(R_k)$ employed in the present case contains twenty-six coefficients which are determined by only seven independent values as a consequence of the constraining orthogonality conditions,

$$\mathbf{U}^{(k)}(R_k)^\dagger \mathbf{U}^{(k)}(R_k) = \mathbf{U}^{(k)}(R_k)\mathbf{U}^{(k)}(R_k)^\dagger = \mathbf{I},$$

employed in the development, with $\mathbf{U}^{(k)}(R_k)^\dagger$ $(=\mathbf{U}^{(k)}(R_k)^T)$ the transpose of the (real) $\mathbf{U}^{(k)}(R_k)$ matrix and $\mathbf{I}$ the 10x10 unit matrix. The transformation coefficients are determined in the present development by requiring the atomic product basis to reproduce the calculated pair-dipole and transition-dipole moments as functions of internuclear separation [18-20]. More generally, the transformation matrix can be calculated employing *ab initio* procedures which demonstrate its unitarity by convergence.

3. Computational Results

In Figures 1 and 2 are shown potential energy curves (cm^{-1}) obtained for the four lowest-lying ($^2A_1$, $^2B_1$, $^2B_2$, $^2A_1$) electronic states of a simple C_{2v} $NaAr_2$ aggregate. Depicted are energies as a function of the angle between the directions to the two Ar atoms from the Na atom employing fixed Na-Ar distances of 4 Angstrom (Å) units each for the indicated computational approximations. The ground-state Na and Ar atomic energies are arbitrarily set to zero, and the Ar-Ar interaction energy, having a well depth of ≈ 100 cm^{-1} [20], has been deleted to better exhibit the non-pair-wise additive Ar-Na-Ar contributions to the potential surfaces obtained from the present development.

Referring first to the ground-state $^2A_1$ results of Figure 1, the values labelled 1x1 refer to the pair-wise-additive approximation, whereas the 4x4, 5x5, and 10x10 values show the effects of adding additional ($3P, 4S, 3D$) atomic Na states to the ground state in the development. These results (4x4, 5x5, 10x10) are seen to be smoothly convergent and to contribute significantly to the total energy, a circumstance which can be attributed to the "near" $3S - 3P$ degeneracy of the Na atom energy levels. Specifically, the ground-state potential energy surface for a Na-Ar_N aggregate is obtained from perturbation theory to 2nd order following a two-state ($3S$, $3P_0$) approximation to the present development in the form [2,3]

$$E_g(\mathbf{R}) \approx E_{3\,^2S}^{(Na)} + NE_g^{(Ar)} + \sum_{k=1}^{N} \left\{ E_X(R_k) - (E_{3\,^2S}^{(Na)} + E_g^{(Ar)}) \right\}$$

$$+\frac{1}{(E_{3\,^2S}^{(Na)} - E_{3\,^2P}^{(Na)})} \sum_{k=1}^{N} \sum_{k'=1}^{N} (k \neq k') H_{12}(R_k) H_{21}(R_{k'}) cos\, \omega_{k\,k'},$$

where $H_{12}(R_k) = H_{21}(R_k) = <X\Sigma^+|3P_0> (E_X(R_k) - E_B(R_k)$, $<X\Sigma^+|3P_0>$ gives the Na $3P_0$ contribution to the $X\Sigma^+$ $NaAr$ ground state, and $\omega_{k\,k'}$ is the angle between the vectors $\mathbf{R}_k$ and $\mathbf{R}_{k'}$. Evidently, the development includes the pair-wise additive approximation and also gives non-additive interaction terms involving the Na atom and the two distinct Ar atoms. The latter terms introduce an angular dependence in the ground-state potential surface missing in the additive approximation. Since all the alkali metals exhibit "near" $S - P$ degeneracy, the non-additive angular-dependent "caging" effect - higher energy in collinear Ar-Na-Ar configuration - depicted in Figure 1, the magnitude of which arises from the energy difference appearing in the denominator of the second-order approximation, may be a common occurrence in alkali metals trapped in or on rare-gas aggregates more generally. Of course, the computational results shown are obtained from diagonalization of the indicated matrices, and do not involve a perturbation theory approximation.

Referring to Figure 2, the non-additive angle-dependent contributions to the $^2B_1$ surface are seen to be zero for the 4x4 and 5x5 results and very small for the 10x10 results. This is a consequence of the largely out-of-plane ($3P_x$) atomic Na nature of the $^2B_1$ state, to which the $3S$ (4x4) and $4S$ (5x5) Na-atom states do not contribute, with the potentially contributing $3D_{xz}$ (10x10) Na-atom state evidently giving a very small shift. These results are seen to be in accordance with the C_{2v} symmetry of the aggregate. The energy variations of the $^2B_2$ and excited $^2A_1$ states in Figure 2 are seen to be relatively large even in the lowest (3x3) approximation. Of course, these variations refer to the degeneracy lifting and splitting associated with the atomic $3P$ Na states, which actually gives non-additive effects associated with the diagonalization of the relevant 3x3 matrix [10-13]. The origin of these effects are clarified by writing the excited-state energy matrix in a four-state ($3S$, $3P_0$, $3P_{\pm 1}$) approximation to 2nd-order in perturbation theory in the form

$$\mathbf{H}_{3\,^2P}^{(A)}(\mathbf{R}) \approx (E_{3\,^2P}^{(Na)} + NE_g^{(Ar)})\mathbf{I}_{bb} + \sum_{k=1}^{N} \left\{ \mathbf{V}_{bb}(\mathbf{R}_k) - (E_{3\,^2P}^{(Na)} + E_g^{(Ar)})\mathbf{I}_{bb} \right\}$$

$$+\frac{1}{(E_{3\,^2P}^{(Na)} - E_{3\,^2S}^{(Na)})} \left\{ \sum_{k=1}^{N} \sum_{k'=1}^{N} (k \neq k') \mathbf{H}_{ba}(\mathbf{R}_k) \cdot \mathbf{H}_{ab}(\mathbf{R}_{k'}) \right\}.$$

Here, $\mathbf{V}_{bb}(\mathbf{R}_k)$ is the familiar 1st-order perturbation-theory approximation to the $3P$ Na atom level splitting [10-17], whereas the terms in the double sum ($k \neq k'$) give angular-dependent corrections to these results

95

[3]. The additional non-additive angle-dependent contributions shown in Figure 2, which are obtained from diagonalization of the matrices of indicated dimension, are seen to be small but not negligible. Specifically, the 4x4 and 5x5 results for the $^2B_2$ state are small and should be identically zero at all angles - failure to achieve exact unitarity in the $\mathbf{U}^{(k)}$ matrix employed accounts for the discrepancy. The 10x10 results in this case are seen to give an ≈ 200 cm^{-1} splitting from the 3x3 results that removes the exact degeneracy of the two states at 90 degrees. The 4x4, 5x5, and 10x10 results for the excited $^2A_1$ state all correctly give additional non-additive angle-dependent contributions, with the 10x10 results giving a caging effect for $\approx$ 180 degrees, as in the ground state, associated with the contribution from the $3D_0$ Na-atom function.

In Figures 3 and 4 are shown Na-Ar radial distribution functions and optical absorption spectra for a $NaAr_6$ aggregate obtained from classical Monte Carlo calculations at 10 K [17], constructed employing the indicated potential energy surfaces. Referring first to Figure 3, the 3x3 results correspond to use of perturbation theory for the excited states and the additive approximation for the ground state, whereas the three other approximations involve the introduction of additional atomic product states in the development, as in Figures 1 and 2. Examination of the geometries of these aggregates (not shown) finds the Na atom on the periphery of the aggregate in every case, consequent of the more attactive nature of the ground-state Ar-Ar interaction relative to the Na-Ar interaction [18-20]. Evidently, the introduction of additional states in Figure 3 gives rise to a noticeable contraction of the Na-Ar distances, which can be attributed to the attractive nature of the non-additive contributions to the Na-Ar potential for acute angular Ar-Na-Ar configurations, as indicated in Figure 1. Referring to Figure 4, which results are obtained from Monte-Carlo-determined dipole autocorrelation functions [17,21], small but discernable shifts are evidently present in the spectra as additional states are added to the development. Of particular interest is the blue shift in the highest lying absorption feature, which can be understood by inspection of the trends shown in the states of the simpler $NaAr_2$ system depicted in Figures 1 and 2. The results of Figures 3 and 4 are in general accord with earlier predictions for $NaAr_6$ clusters based on one-electron potentials which also take into account the effects of Na atom charge distortion or state mixing upon aggregate formation [24].

4. Concluding Remarks

Dilute (Na) metal radicals trapped on physically bound cryogenic (Ar) rare-gas clusters are studied employing available potential energy curves and related information in an illustrative application of the spectral method reported recently [1-3]. The effects of state mixing and charge distortion missing from commonly employed semi-empirical and perturbation-theory studies of trapped-radical spectra are examined on basis of the spectral development to display the explicitly non-additive contributions to the potential surfaces. The predicted adiabatic electronic energy surfaces are seen to depend more sensitively upon the detailed angular arrangement of rare-gas perturbers around the radical metal than do results inferred from perturbation approaches due to angular-dependent caging effects present in the spectral development that are missing from earlier approaches. The calculations show large non-additive contributions to the lowest-lying potential surfaces, as manifested in the Na-Ar radial distribution functions and optical absorption spectra obtained for low-temperature $NaAr_6$ aggregates. The relevance of these results to interpretations of experimentally determined trapped-radical spectra is also reported separately elsewhere in this Proceedings [21].

References

[1] P.W. Langhoff, "Theoretical Methods for Cryogenically Trapped Metal Radical Spectra," in *Proceedings of the HEDM Contractor's Conference* (1994), PL-TR-94-3036, T.L. Thompson and S.L. Rogers, Editors.

[2] P.W. Langhoff, "Spectral Theory of Physical and Chemical Binding," J. Phys. Chem. (accepted for publication).

[3] P.W. Langhoff, "Spectral Theory of Weakly Bound Atomic Aggregates," Phillips Laboratory Report, Edwards AFB, CA, June 1995 (unpublished).

[4] H. Eisenschitz and F. London, Z. Physik **60**, 491 (1930).

[5] W. Moffit, Proc. Roy. Soc. (Lond.) **A210**, 245 (1951).

[6] A.T. Amos and J.I. Musher, Chem. Phys. Letters **1**, 149 (1967).

[7] J.I. Musher and A.T. Amos, Phys. Rev. **164**, 31 (1967).

[8] F.O. Ellison, J. Am. Chem. Soc. **85**, 3540 (1963).

[9] J.C. Tully in, *Modern Theoretical Chemistry*, Edited by G.A. Segal, (Plenum, NY, 1977), Vol. 7, pp. 173-200.

[10] W.E. Baylis, J. Phys. B **10**, L477 (1977).

[11] K.M. Sando, G.J. Erickson, and R.C. Binning, J. Phys. B **12**, 2697 (1979).

[12] J.F. Dawson and L.C. Balling, J. Chem. Phys. **71**, 836 (1979).

[13] L.C. Balling and J.J. Wright, J. Chem. Phys. **79**, 2941 (1983).

[14] J.P. Visticot, P. de Pujo, J.M. Mestdagh, A. Lallement, J. Berlande, and J. Cuvellier, J. Chem. Phys. **100**, 158 (1994).

[15] A.V. Danilychez and V.A. Apkarian, J. Chem. Phys. **100**, 5556 (1994).

[16] W.G. Lawrence and V.A. Apkarian, J. Chem. Phys. **101**, 1820 (1994).

[17] J.A. Boatz and M.E. Fajardo, J. Chem. Phys. **101**, 3472 (1994).

[18] R.P. Saxon, R.E. Olson, and B. Liu, J. Chem. Phys. **67**, 2692 (1977).

[19] B.C. Laskowski, S.R. Langhoff, and J.R. Stallcop, J. Chem. Phys. **75**, (1981).

[20] R. Düren, W. Gröger, E. Hasselbrink, and R. Liedtke, J. Chem. Phys. **74**, 6806 (1981).

[21] J.A. Boatz, M.E. Fajardo and P.W. Langhoff, "Monte Carlo Simulations of the Structure and Optical Absorption Spectra of Na/Ar Clusters and Solids," in this Proceedings.

[22] A.R. Edmonds, *Angular Momentum in Quantum Mechanics* (Princeton, NJ, 1957).

[23] D.A. Varshalovich, A.N. Moskalev, and V.K. Khersonskii, *Quantum Theory of Angular Momentum*, (World Scientific, Singapore, 1988).

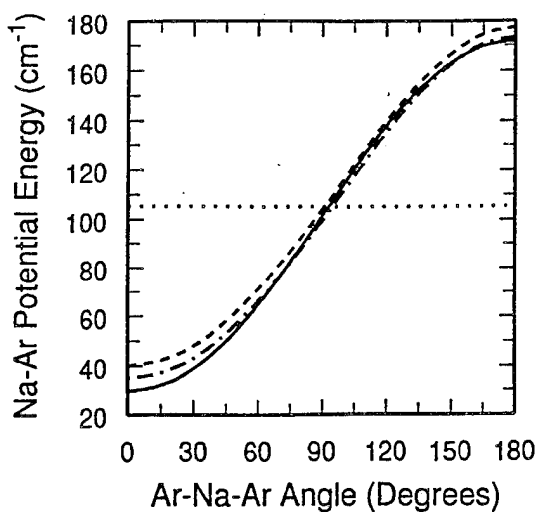[24] C. Tsoo, D.A. Estrin, and S.J. Singer, J. Chem. Phys. **96**, 7977 (1992).

Figure 1. Ground ($^2A_1$) state energy surface for C_{2v} $NaAr_2$ as a function of the Ar-Na-Ar apex angle at fixed Ar-Na distances of 4 Å: ($\cdots$) - 1x1 pair-wise additive; (- - -) - 4x4 matrix; (- $\cdot$ -) - 5x5 matrix; (—) - 10x10 matrix approximation.
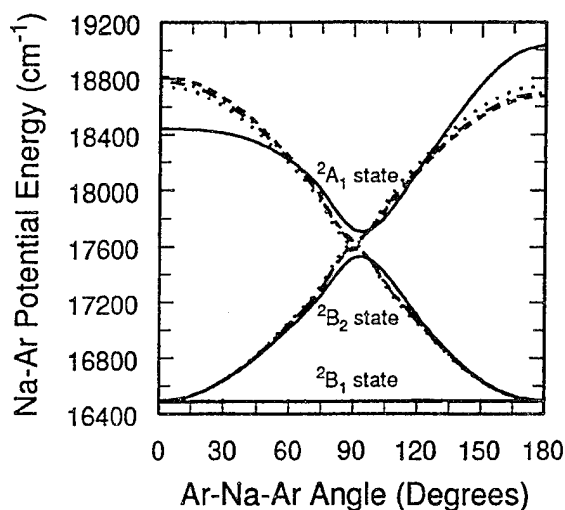
Figure 2. As in Figure 1, for the excited $^2B_1$, $^2B_2$, and $^2A_1$ state energy surfaces for a $NaAr_2$ cluster in C_{2v} symmetry: ($\cdots$) - 3x3 matrix; (- - -) - 4x4 matrix; (- $\cdot$ -) - 5x5 matrix; (—) - 10x10 matrix approximation.
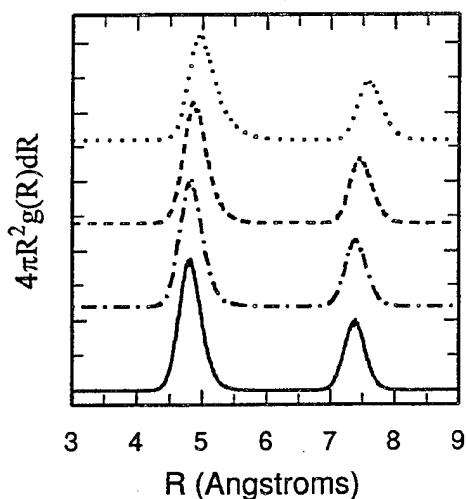

Figure 3. Radial distribution functions for $NaAr_6$ aggregate constructed employing the indicated potential energy surfaces and classical Monte Carlo calculations at 10 K [17]: ($\cdots$) - 3x3 matrix; (- - -) - 4x4 matrix; (- $\cdot$ -) - 5x5 matrix; (—) - 10x10 matrix approximation.
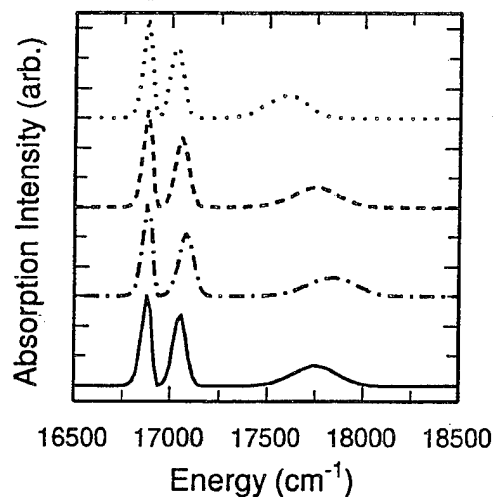
Figure 4. Optical absorption spectra for $NaAr_6$ aggregate constructed employing the indicated potential energy surfaces and classical Monte Carlo calculations at 10 K [17]: ($\cdots$) - 3x3 matrix; (- - -) - 4x4 matrix; (- $\cdot$ -) - 5x5 matrix; (—) - 10x10 matrix approximation.

Monte Carlo Simulations of the Structures and Optical Absorption Spectra of Na/Ar Clusters and Solids: An Application of Spectral Theory of Chemical Binding

Jerry A. Boatz and Mario Fajardo
Phillips Laboratory
OLAC PL/RKFE
Edwards AFB, CA 93524-7680

and

Peter W. Langhoff
Department of Chemistry
Indiana University
Bloomington, IN 47405-4001

ABSTRACT

Classical Monte Carlo simulation techniques have been used in conjunction with a recently developed spectral theory of chemical binding to predict the structures and optical absorption spectra of Na/Ar clusters and solids. The new spectral theory, which is a broad generalization of the Balling and Wright model (B&W) for predicting the ^2P excited state potential energy surfaces of alkali atoms in the presence of an arbitrary number and arrangement of rare gas perturbers, is based on the use of a direct product of complete sets of atomic eigenstates. This technique extends the approximation of simple pairwise additivity to include interactions between multiple diatomic potential energy curves. An important consequence of the interactions between multiple surfaces is a more sensitive dependence of the predicted transition energies on the angular arrangement of rare gas perturbers in comparison to the first-order degenerate perturbation theory-based B&W theory. Specifically, an angular dependence of the shift of the centroid of the absorption band is obtained which is absent in the B&W treatment. Diatomic potential energy curves, configuration interaction coefficients (or approximations thereof), and the transformation properties of atomic angular momentum eigenstates under rotations are used in the computational implementation of this theory.

I. Introduction

The fundamental behavior of light atoms trapped in condensed phase matrices has been a topic of long-standing interest in the HEDM program. In particular, atomic sodium in argon, which is a classical prototype of proposed HEDM systems such as atomic lithium in hydrogen, has been the focus of several experimental[1] and theoretical[2] efforts, due in part to the relative ease in which it can be studied from both experimental and theoretical standpoints. Of particular interest are the spectral features of this model system since they offer insights to the nature of the sodium atom trapping sites.

The experimental optical absorption spectra of Na/Ar solids show the presence of up to three sets of "triplet" peaks, which are thought to arise from the $^2S \rightarrow {}^2P$ (3s -> 3p) electronic transition of sodium atoms trapped in distinct sites in the argon matrix. The so-called "red", "blue", and "violet" triplets are centered at approximately 17020, 18350, and 19530 cm^{-1}, respectively.[1] The extent to which each triplet absorption is blue-shifted from the gas-phase sodium 3s -> 3p transition (16968 cm^{-1}) is presumably related to the volume of the trapping site, with larger blue shifts arising from tighter sites.

Considerable effort has been expended in the development of theoretical models for predicting the optical absorption spectra of sodium atoms in condensed phase argon[2,3] and related systems.[4-6] While our initial theoretical models[2] have been qualitatively successful in reproducing the experimental absorption spectra of this system, they have fallen short of the level of accuracy which will ultimately be required to connect the observed spectra with the structures of the trapping sites. For example, the predicted centroid shift of the most crowded trapping sites considered in our earlier simulations[2] (1-atom substitutional and interstitial sites) was approximately 1000 cm^{-1} to the blue, far short of the experimentally observed violet triplet, which has a centroid blue shift of about 2560 cm^{-1}. While the discrepancy between the predicted and observed centroid shift could be due in part to failure of our idealized trapping sites to accurately represent the actual metal atom trapping site environment in the matrix, it is not unreasonable to expect that the B&W treatment is incapable of giving quantitative accuracy in the prediction of the excited

state levels of atomic sodium in the presence of rare gas perturbers. The current work is an attempt to improve upon the accuracy of our earlier spectral simulation models as well as to extend the applicability of these models to a wider variety of HEDM systems.

II. Theoretical Methods

The core of our spectral simulation model is the combination of the classical Metropolis Monte Carlo method[7] with the recently developed[8] spectral theory of chemical binding. The latter theory, of which the B&W first-order degenerate perturbation theory model[3] is a special case, is similar in approach to the diatomics-in-molecules technique[9] and provides a systematic method for obtaining an increasingly accurate manifold of eigenstates of a dopant atom in the presence of an arbitrary number and arrangement of rare gas perturber atoms. The spectral theory is formulated in terms of a diatomic basis[8b] and is therefore limited in accuracy only by the availibility and accuracy of the underlying ground and excited state diatomic potentials and "configuration interaction" (CI) coefficients describing the atomic state contributions to the diatomic potentials as a function of internuclear distance. Alternatively, in the absence of such ab initio CI data, approximate state mixings can be derived from diatomic dipole and transition moment functions, as is done in the present work (see Appendix A for details.)

The current study examines the effects on the predicted absorption spectra of Na/Ar clusters and solids as successive Na-Ar diatomic potential curves are included in the spectral theory computation of the matrix-perturbed ground ("3s") and excited state ("3p") levels. The B&W model may be regarded as a "zeroth" level implementation of this theory, where no matrix-induced mixing of the 3p levels with other atomic states is considered. The next level of sophistication accounts for mixing of the 3s and 3p states, followed by inclusion of mixings involving the sodium 4s Rydberg state, and finally addition of the 3d manifold. The four levels of treatment are for convenience denoted as 3x3, 4x4, 5x5, and 10x10, respectively, in reference to the dimensions of the "U" matrix, which is the unitary transformation matrix connecting the diatomic basis with the atomic-product basis.[8b]

The Na-Ar diatomic potential curves used in the present study are taken from the *ab initio* calculations of Saxon, Olson, and Liu[10] (X $^2\Sigma^+$, A $^2\Pi$, and B $^2\Sigma^+$ states) and Laskowski, Langhoff, and Stallcop[11] (C $^2\Sigma^+$, (1) $^2\Delta$, and (2) $^2\Pi$ states). Furthermore, the calculated A $^2\Pi$ and B $^2\Sigma^+$ dipole moment functions of Saxon et al.[10] and the calculated X $^2\Sigma^+$ dipole moment function and X $^2\Sigma^+$ - A $^2\Pi$, X $^2\Sigma^+$ - B $^2\Sigma^+$, and X $^2\Sigma^+$ - C $^2\Sigma^+$ transition moment functions of Laskowski et al.[11] were used to derive approximate values for the atomic state mixing terms used in constructing the U matrix. It should be noted that the use of calculated diatomic potentials and moment functions from two separate theoretical studies (which employed different computational methods) limits the present results to being only suggestive in nature, rather than of predictive quality. Although the spectral theory places no such limit on its implementation, contributions arising from the Ar_2 excited state potentials are not considered in this study. Therefore, the common assumption of pairwise additivity is used in computing the Ar-Ar interaction energies, for which the "HFDB-2" ground state Ar_2 potential of Aziz and Slaman[12] is used.

Solid fcc argon is simulated by imposing periodic boundary conditions[13] on a cubic "chunk" of an argon lattice containing 108 atoms. The sodium atom trapping sites are simulated by replacing varying number of adjacent argon atoms with a single sodium atom and then allowing the system to equilibrate at the specified simulation temperature (10 K in the present study.)

III. Results and Discussion

Na/Ar clusters: The structures and absorption spectra of several $NaAr_n$ clusters (n=1,2,3,6,11,12) were predicted using the 3x3 (which is equivalent to the B&W method), 4x4, 5x5, and 10x10 "levels" of the spectral theory. The fundamental characteristics of all the cluster spectra include a "doublet" peak (which may be partially or wholly resolved into two individual peaks) close to the gas-phase transition energy plus a single blue-shifted, broad "satellite" peak. The magnitude of the blue shift of the latter peak is determined primarily by the number of nearest-neighbor argon atoms.[2] For all clusters considered here, the radial distribution functions (not shown) show only minor changes as a function of spectral

theory level. Thus, the variation in predicted absorption spectra (see below) are primarily due to differences in the computed ground and first excited state levels of the trapped sodium atom.

With the exception of the diatomic (for which all 4 levels necessarily give identical results), the predicted cluster spectra all exhibit the same qualitative behavior as a function of spectral theory level. Because of this, only the predicted spectra for the $NaAr_{12}$ cluster are shown (Figure 1) and discussed in detail. While the "doublet" peak varies only slightly in position and in the extent to which the underlying peaks are resolved, the most noticeable difference in the computed spectra is the location of the satellite peak. This peak is centered at about 17700 cm^{-1} in the 3x3 spectrum but moves further to the blue (~18000 cm^{-1}) when mixing of the 3s and 3p states is accounted for (i.e., the so-called 4x4 spectral theory level.) Inclusion of the 4s state (i.e., 5x5) moves this peak even further to the blue to about 18250 cm^{-1}. At the 10x10 level, however, where the contributions from the 3d states of sodium are additionally present, the satellite peak is shifted to about 18200 cm^{-1}; i.e., slightly to the red of the corresponding peak computed at the 5x5 level. This suggests that the spectral theory energy levels are "converging" to a stable solution that will show only minor changes upon inclusion of additional higher-lying states. Of course, to verify this one needs to use a consistent set of Na-Ar diatomic data (rather than a "mixed" set as in the present case) and to include states above the sodium 3d manifold and/or excited states of argon.

Na/Ar solids: The structures and absorption spectra of 1-, 4-, and 6-atom substitutional trapping sites of sodium in solid argon have been predicted using the 3x3, 4x4, 5x5, and 10x10 spectral theory levels. As in the Na/Ar cluster simulations, the radial distribution functions (not shown) show little variation as a function of spectral theory level; thus the variation in simulated spectra are due mostly to differences in the predicted ground state and first excited state levels of the trapped sodium atom. Since the results for all three trapping sites are qualitatively similar, only the results for the 1-atom substitutional site are presented in detail (see Figure 2.) Note that long-range corrections[13b] have not been applied to any of the Na/Ar solid spectra.

Figure 2 shows the simulated absorption spectra of a sodium atom in a single substitutional trapping site, as a function of spectral theory level. All four simulated spectra show a symmetric triplet pattern, although the degree of resolution of the three underlying peaks varies somewhat with the spectral theory level. Clearly the dominant effect of varying the spectral theory level is in the location of the absorption centroid. While the centroid of the 3x3 absorption spectrum is located at about 18000 cm^{-1}, inclusion of 3s-3p state mixings (4x4 level) actually shifts the absorption centroid to a lower energy (~17400 cm^{-1}.) However, the 5x5 level reverses the shift of the absorption centroid to lower energies and results in a centroid location of about 18100 cm^{-1}, slightly more blue-shifted than in the 3x3 case. Finally, the 10x10 absorption centroid is shifted even further to the blue, located at approximately 18700 cm^{-1}.

Since the 1-atom substitutional site is the most crowded of the trapping sites considered in this work, it presumably should most closely resemble the trapping site of the experimentally observed "violet" triplet centered at 19530 cm^{-1}. Therefore, the increase in centroid blue shift at the 10x10 level relative to our earlier B&W prediction[2] is an encouraging indication that the spectral theory method is more quantitatively accurate relative to the B&W model. Also, the progressive increase in centroid blue shift with successive addition of atomic state mixings in the spectral theory treatment (4x4 -> 5x5 -> 10x10) suggests that inclusion of additional higher-lying sodium states and/or excited argon states may continue to shift the predicted absorption spectrum of the 1-atom substitutional site to higher energies, thus bringing the predicted spectrum into even closer agreement with the observed violet triplet.

However, the simulated spectra in Figure 2 show little evidence of approaching convergence of the spectral theory energy levels. This suggests that atomic levels beyond the 3d manifold and/or argon excited states must be included to reach a converged solution. This is in contrast with the Na/Ar cluster simulations where the simulated spectra appeared to be approaching convergence at the 10x10 level. This is likely due in part to the closer nearest-neighbor Na-Ar distance in the solid (4 angstroms) relative to the cluster (5 angstroms.) Thus, it appears that contributions

from higher-lying atomic states are more important at shorter Na-Ar separations.

IV. Conclusions

The newly developed spectral theory of chemical binding[8] has been applied to the study of the structures and optical absorption spectra of Na/Ar clusters and solids. The geometries of both the Na/Ar clusters and solids show little variation as a function of spectral theory level, and thus the differences in predicted spectra arise primarily from changes in the calculated ground state ("3s") and the first manifold of excited states ("3p") of the Na/Ar systems.

The most noticeable difference in the cluster spectra as a function of spectral theory level is the location of the blue-shifted "satellite" peak. The predicted cluster spectra suggest that the spectral theory is nearing convergence at the 10x10 level, and therefore inclusion of additional Na and/or Ar excited states is expected to have minimal effect on the predicted spectra.

For the simulation of sodium in a 1-atom substitutional site in solid argon, the absorption centroid is increasingly blue-shifted as the number of atomic state mixings included in the spectral theory is increased. Although this increase in absorption centroid blue shift brings the simulated spectra in closer agreement with the experimentally observed violet triplet, the calculated "3s" and "3p" energy levels show little sign of converging with respect to the number of atomic state mixings included in the spectral theory, thus indicating that additional Na and/or Ar state mixings must be included.

Finally, all of the above conclusions are contingent upon the validity of using Na-Ar potential energy curves and moment functions from two different sets of ab initio calcuations.[10,11] Efforts are currently udnerway to generate a consistent set of diatomics potentials, dipole moments, and transition moments for several states of Na-Ar.[14]

References

1. Tam, S.; Fajardo, M. *J. Chem. Phys.* **1993**, <u>99</u>, 854.

2. Boatz, J.A.; Fajardo, M.F. *J. Chem. Phys.* **1994**, <u>101</u>, 3472-2487.

3. Balling, L.C.; Wright, J.J. *J. Chem. Phys.* **1983**, <u>79</u>, 2941-2944.

4. a) Scharf, D.; Martyna, G.J.; Klein, M.L. *J. Chem. Phys.* **1993**,
   <u>99</u>, 8997-9012.
   b) Scharf, D.; Martyna, G.J.; Li, D.; Voth, G.A.; Klein, M.L. *J. Chem. Phys.*
   1993, <u>99</u>, 9013-9020.

5. Whaley, K.B., "Zero Temperature Quantum Monte Carlo Study of Li Atoms
   In Solid H_2", these proceedings.

6. Boatz, J.A.; Fajardo, M.F. "Proceedings of the High Energy Density Matter
   (HEDM) Contractors' Conference", T.L. Thompson, ed., 1993.

7. Metropolis, N.; Rosenbluth, A.W.; Rosenbluth, M.N.; Teller, A.H.; Teller, E.
   J. Chem. Phys. **1953**, <u>21</u>, 1087-1092.

8. a) Langhoff, P.W. *J. Phys. Chem.*, submitted.
   b) Langhoff, P.W., "Spectral Theory of Chemical Binding: Aggregates of
   Weakly Bound Atoms", these proceedings.

9. Tully, J. "Modern Theoretical Chemistry", G.A. Segal, ed., Plenum, NY, 1977,
   Vol. 7, 173-200.

10. Saxon, R.P.; Olson, R.E.; Liu, B. *J. Chem. Phys.* **1977**, <u>67</u>, 2692-2702.

11. Laskowski, B.C.; Langhoff, S.R.; Stallcop, J.R. *J. Chem. Phys.* **1981**,
    <u>75</u>, 815-827.

12. Aziz, R.A.; Slaman, M.J. *Mol. Phys.* **1986**, <u>58</u>, 679-697.

13. See, for example:
    a) Gibbons, T.G.; Klein, M.L. *J. Chem. Phys.* **1974**, <u>60</u>, 112-126.
    b) Allen, M.P.; Tildesley, D.J. "Computer Simulation of Liquids",
    Oxford University Press: New York (1989).

14. Sheehy, J., private communication.

15. Weise, W.L.; Smith, M.W.; Glennon, B.M. *Atomic Transition Probabilities*,
    Nat. Stand. Ref. Data Ser., Nat. Bur. Stand. Circ. 4, (U.S. G.P.O.,
    Washington, DC, 1966), Vol I.

16. Edmonds, A.R. *Angular Momentum in Quantum Mechanics* (Princeton, NJ, 1957).

17. Condon, E.U.; Shortley, G.H. *Theory of Atomic Spectra* (Cambridge
    University Press, New York, 1935).

NaAr₁₂ Absorption Spectra
T=10K
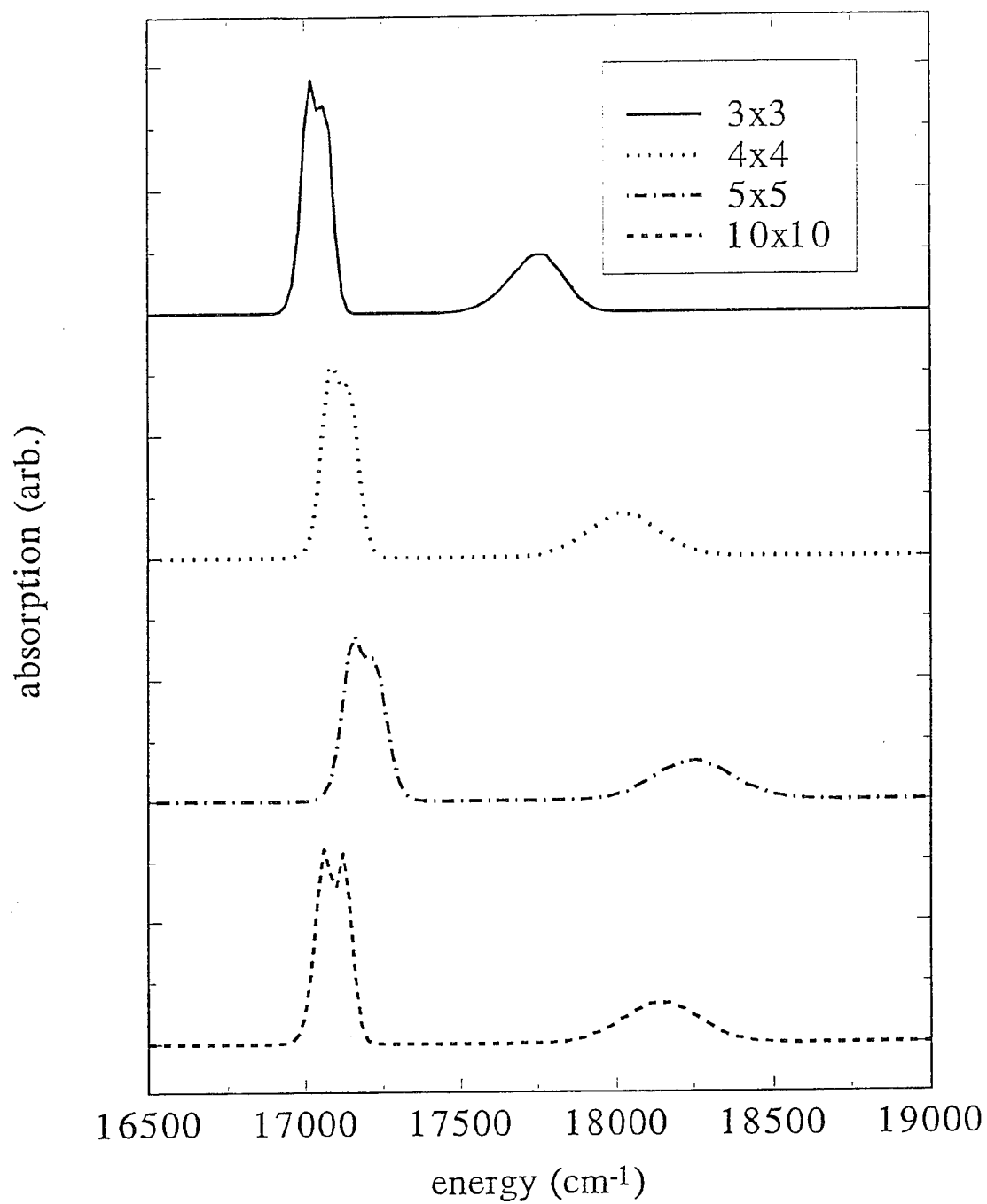
NaAr₁₀₇ (Solid) Absorption Spectra
T=10K

absorption (arb.)

energy (cm⁻¹)

3x3
4x4
5x5
10x10
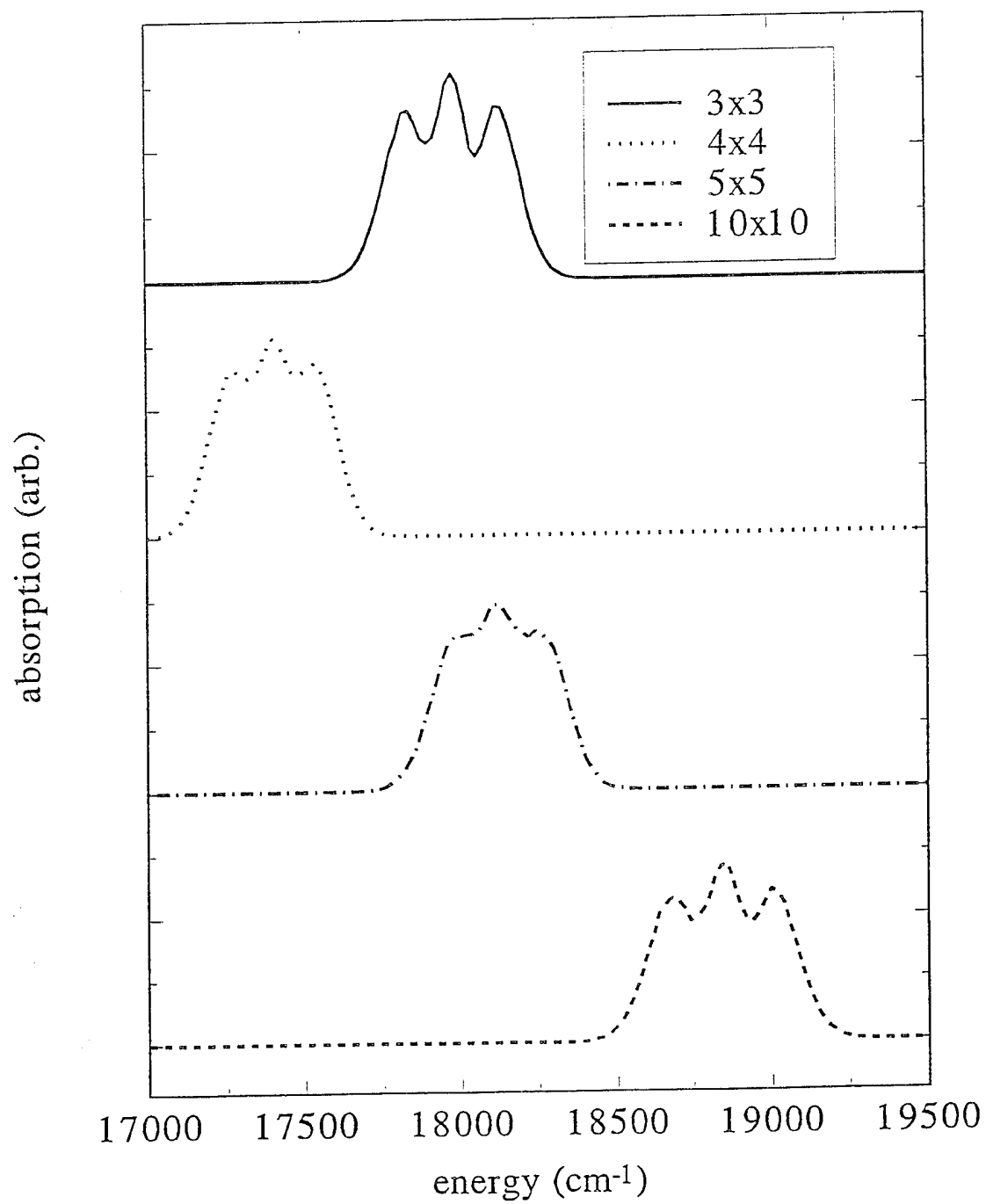
Appendix A - Spectral Equations for Na-Ar$_N$ Interactions

Equations are provided here for the interaction of a single Na atom with an N-body aggregate of Ar atoms arranged in an arbitrary configuration specified by the vector $\mathbf{R} \equiv (\mathbf{R}_1, \mathbf{R}_2,... \mathbf{R}_N)$ in a coordinate system centered at the Na atom.

The order of $Na\text{-}Ar$ atomic product pair states [Eq. (10)] employed is given by the 10-term row vector

$$\mathbf{\Phi}^{(k)} = \left(3S, 3P_{+1}, 3P_0, 3P_{-1}, 4S, 3D_{+2}, 3D_{+1}, 3D_0, 3D_{-1}, 3D_{-2} \right)_{Na} \otimes \left({}^1S_0 \right)_{Ar_k}, \tag{A1}$$

where $\left({}^1S_0 \right)_{Ar_k}$ refers to the ground state of the kth Ar atom. The corresponding order of molecular $NaAr_k$ pair states is given by the 10-term row vector

$$\mathbf{\Psi}^{(k)} = \left(X\Sigma^+, A\Pi_{+1}, B\Sigma^+, A\Pi_{-1}, C\Sigma^+, D\Delta_{+2}, E\Pi_{+1}, F\Sigma^+, E\Pi_{-1}, D\Delta_{-2}, \right)_{NaAr_k}. \tag{A2}$$

The total 10x10 Hamiltonian matrix in the atomic product basis is

$$\mathbf{H}(\mathbf{R}) = \mathbf{H}^{(A)} + \sum_{k=1}^N \mathbf{V}^{(k)}(\mathbf{R}_k) + (1/2) \sum_{k=1}^N \sum_{k'=1}^N \mathbf{V}^{(k,k')}(\mathbf{R}_{k,k'}), \tag{A3}$$

where

$$\mathbf{H}^{(A)} = \begin{pmatrix} (E_{3S}^{(Na)} + NE_g^{(Ar)})\mathbf{I}_{aa} & 0 & 0 & 0 \\ 0 & (E_{3P}^{(Na)} + NE_g^{(Ar)})\mathbf{I}_{bb} & 0 & 0 \\ 0 & 0 & (E_{4S}^{(Na)} + NE_g^{(Ar)})\mathbf{I}_{cc} & 0 \\ 0 & 0 & 0 & (E_{3D}^{(Na)} + NE_g^{(Ar)})\mathbf{I}_{dd} \end{pmatrix} \tag{A4}$$

is the 10x10 total atomic Hamiltonian, with $\mathbf{I}_{aa}$(1x1), $\mathbf{I}_{bb}$(3x3), $\mathbf{I}_{cc}$(1x1), and $\mathbf{I}_{dd}$(5x5) unit matrices of indicated dimensions, and

$$\mathbf{V}^{(k)}(\mathbf{R}_k) = \mathbf{H}^{(k)}(\mathbf{R}_k) - \mathbf{E}^{(k)}(\infty), \tag{A5}$$

is the 10x10 pair-interaction matrix for the Na metal radical and the kth Ar atom located at $\mathbf{R}_k$ $(= R_k, \phi_k, \theta_k)$ measured from the Na atom position. The (pair-wise-additive) ground-state $Ar\text{-}Ar$ interactions given by the last term in Eq. (A3) are not written out explicitly in the present development.

In Eq. (A5)

$$\mathbf{H}^{(k)}(\mathbf{R}_k) = \mathbf{R}^{(k)}(\phi_k, \theta_k)^\dagger \cdot \mathbf{U}^{(k)}(R_k)^\dagger \cdot \mathbf{E}^{(k)}(R_k) \cdot \mathbf{U}^{(k)}(R_k) \cdot \mathbf{R}^{(k)}(\phi_k, \theta_k), \tag{A6}$$

is the transformation of the 10x10 diagonal pair-potential-energy matrix

$$\mathbf{E}^{(k)}(R_k) = \begin{pmatrix} E_X(R_k) & 0 & 0 & 0 & 0 & 0 & 0 & 0 & 0 & 0 \\ 0 & E_A(R_k) & 0 & 0 & 0 & 0 & 0 & 0 & 0 & 0 \\ 0 & 0 & E_B(R_k) & 0 & 0 & 0 & 0 & 0 & 0 & 0 \\ 0 & 0 & 0 & E_A(R_k) & 0 & 0 & 0 & 0 & 0 & 0 \\ 0 & 0 & 0 & 0 & E_C(R_k) & 0 & 0 & 0 & 0 & 0 \\ 0 & 0 & 0 & 0 & 0 & E_D(R_k) & 0 & 0 & 0 & 0 \\ 0 & 0 & 0 & 0 & 0 & 0 & E_E(R_k) & 0 & 0 & 0 \\ 0 & 0 & 0 & 0 & 0 & 0 & 0 & E_F(R_k) & 0 & 0 \\ 0 & 0 & 0 & 0 & 0 & 0 & 0 & 0 & E_E(R_k) & 0 \\ 0 & 0 & 0 & 0 & 0 & 0 & 0 & 0 & 0 & E_D(R_k) \end{pmatrix}, \tag{A7}$$

where the twenty-six indicated coefficients are determined by only seven independent values as a consequence of the constraining orthogonality conditions,

$$\mathbf{U}^{(k)}(R_k)^\dagger \mathbf{U}^{(k)}(R_k) = \mathbf{U}^{(k)}(R_k)\mathbf{U}^{(k)}(R_k)^\dagger = \mathbf{I}, \tag{A14}$$

with $\mathbf{U}^{(k)}(R_k)^\dagger$ ($=\mathbf{U}^{(k)}(R_k)^T$) the transpose of the (real) $\mathbf{U}^{(k)}(R_k)$ matrix and $\mathbf{I}$ the 10x10 unit matrix.

It is convenient to rewrite the configuration-mixing matrix employing a temporary re-ordering of the atomic product and molecular states in the forms

$$\Phi_r^{(k)} = \left(3S, 3P_0, 4S, 3D_0, 3P_{+1}, 3D_{+1}, 3P_{-1}, 3D_{-1}, 3D_{+2}, 3D_{-2}\right) \otimes \left(^1S_0\right)_{Ar_k}, \tag{A15}$$

$$\Psi_r^{(k)} = \left(X\Sigma^+, B\Sigma^+, C\Sigma^+, F\Sigma^+, A\Pi_{+1}, E\Pi_{+1}, A\Pi_{-1}, E\Pi_{-1}, D\Delta_{+2}, D\Delta_{-2},\right)_{NaAr_k}. \tag{A16}$$

This temporary re-ordering serves to bring the $\mathbf{U}^{(k)}(R_k)$ matrix to the block-diagonal form

$$\mathbf{U}^{(k)}(R_k) = \begin{pmatrix} \mathbf{U}_{11}(R_k) & \mathbf{0} & \mathbf{0} & \mathbf{0} \\ \mathbf{0} & \mathbf{U}_{22}(R_k) & \mathbf{0} & \mathbf{0} \\ \mathbf{0} & \mathbf{0} & \mathbf{U}_{33}(R_k) & \mathbf{0} \\ \mathbf{0} & \mathbf{0} & \mathbf{0} & \mathbf{U}_{44}(R_k) \end{pmatrix}, \tag{A17}$$

where

$$\mathbf{U}_{11}(R_k) = \begin{pmatrix} <X\Sigma^+|3S> & <X\Sigma^+|3P_0> & <X\Sigma^+|4S> & <X\Sigma^+|3D_0> \\ <B\Sigma^+|3S> & <B\Sigma^+|3P_0> & <B\Sigma^+|4S> & <B\Sigma^+|3D_0> \\ <C\Sigma^+|3S> & <C\Sigma^+|3P_0> & <C\Sigma^+|4S> & <C\Sigma^+|3D_0> \\ <F\Sigma^+|3S> & <F\Sigma^+|3P_0> & <F\Sigma^+|4S> & <F\Sigma^+|3D_0> \end{pmatrix}, \tag{A18}$$

$$\mathbf{U}_{22}(R_k) = \begin{pmatrix} <A\Pi_{+1}|3P_{+1}> & <A\Pi_{+1}|3D_{+1}> \\ <E\Pi_{+1}|3P_{+1}> & <E\Pi_{+1}|3D_{+1}> \end{pmatrix} \tag{A19}$$

$$\mathbf{U}_{33}(R_k) = \begin{pmatrix} <A\Pi_{-1}|3P_{-1}> & <A\Pi_{-1}|3D_{-1}> \\ <E\Pi_{-1}|3P_{-1}> & <E\Pi_{-1}|3D_{-1}> \end{pmatrix} = \mathbf{U}_{22}(R_k) \tag{A20}$$

$$\mathbf{U}_{44}(R_k) = \begin{pmatrix} <D\Delta_{+2}|3D_{+2}> & 0 \\ 0 & <D\Delta_{-2}|3D_{-2}> \end{pmatrix}. \tag{A21}$$

The individual elements of the configuration-mixing matix are chosen to satisfy orthogonality conditions and to reproduce three calculated dipole moments [10,11]

$$\mu_X(R_k) = <X\Sigma^+|\hat{\mu}_z|X\Sigma^+> \tag{A22}$$

$$\mu_A(R_k) = <A\Pi_{+1}|\hat{\mu}_z|A\Pi_{+1}> \tag{A23}$$

$$\mu_B(R_k) = <B\Sigma^+|\hat{\mu}_z|B\Sigma^+> \tag{A24}$$

and three calculated transition dipole moments [10,11]

$$\mu_{X\to A}(R_k) = <X\Sigma^+|\frac{1}{\sqrt{2}}(\hat{\mu}_x - i\hat{\mu}_y)|A\Pi_{+1}> \equiv <X\Sigma^+|\hat{\mu}_-|A\Pi_{+1}> \tag{A25}$$

$$\mu_{X \to B}(R_k) = < X\Sigma^+|\hat{\mu}_z|B\Sigma^+ > \tag{A26}$$

$$\mu_{X \to C}(R_k) = < X\Sigma^+|\hat{\mu}_z|C\Sigma^+ > . \tag{A27}$$

The matrix elements of Eq. $(A21)$ are determined from orthogonality alone in the forms

$$< D\Delta_{+2}|3D_{+2} > = < D\Delta_{-2}|3D_{-2} > = 1, \tag{A28}$$

whereas those of Eqs. $(A19)$ and $(A20)$ are obtained from orthogonality and Eq. $(A23)$ in the forms

$$< A\Pi_{+1}|3D_{+1} > = - < E\Pi_{+1}|3P_{+1} > = < A\Pi_{-1}|3D_{-1} > = - < E\Pi_{-1}|3P_{-1} >$$

$$= \frac{\mu_A(R)}{2 < 3D_{+1}|\hat{\mu}_z|3P_{+1} >} \tag{A29}$$

for the off-diagonal elements, and

$$< A\Pi_{+1}|3P_{+1} > = < E\Pi_{+1}|3D_{+1} > = < A\Pi_{-1}|3P_{-1} > = < E\Pi_{-1}|3D_{-1} >$$

$$= \{1 - < A\Pi_{+1}|3D_{+1} >^2\}^{1/2}, \tag{A30}$$

for the diagonal elements, where the numerical value of the atomic transition matrix element $< 3P_{+1}|\hat{\mu}_z|3D_{+1} >$ is given below.

A perturbative approach is employed to construct the (diagonally dominated) $\mathbf{U}_{11}$ matrix employing Eqs. $(A22)$ and $(A24)$ to $(A27)$. Specifically, orthogonality is enforced to first-order in the (small) off-diagonal matrix elements by writing $\mathbf{U}_{11}$ in the form

$$\mathbf{U}_{11} = \mathbf{D}_{11} + \Delta\mathbf{U}_{11}, \tag{A31}$$

where $\mathbf{D}_{11}(\approx \mathbf{I})$ is diagonal, and the (small) off-diagonal matrix $\Delta\mathbf{U}_{11}$ is made to satisfy

$$\Delta\mathbf{U}_{11}^\dagger \equiv \Delta\mathbf{U}_{11}^T = -\Delta\mathbf{U}_{11}, \tag{A32}$$

so that

$$\mathbf{U}_{11}^T\mathbf{U}_{11} = \mathbf{U}_{11}\mathbf{U}_{11}^T = \mathbf{I} + O(\Delta\mathbf{U}_{11}^2). \tag{A33}$$

Since Eqs. $(A22)$ and $(A24)$ to $(A27)$ provide only five conditions, and there are six independent elements in the orthogonal (4x4) $\mathbf{U}_{11}$ matrix, two of the off-diagonal elements are arbitrarily set to zero. These are chosen to be $< C\Sigma^+|3D_0 >$ and $< F\Sigma^+|4S >$, since they are found to enter into the moment values of Eqs. $(A22)$ to $(A27)$ only in second order. Accordingly,

$$< C\Sigma^+|3D_0 > = < F\Sigma^+|4S > = 0. \tag{A34}$$

Employing expressions for the $NaAr$ molecular functions ($X\Sigma^+$, $B\Sigma^+$, $C\Sigma^+$, $F\Sigma^+$) in terms of the $\mathbf{U}_{11}$ matrix elements and the atomic-produce spectral functions ($3S$, $3P_0$, $4S$, $3D_0$) $\otimes$ ($^1S_0$) in the dipole and transition moments of Eqs. $(A22)$ and $(A24)$ to $(A27)$, neglecting second-order terms in off-diagonal elements, and setting the diagonal elements of $\mathbf{U}_{11}$ to unity in the resulting equations (only) gives the expressions

$$\mu_X(R_k) \approx 2 < X\Sigma^+|3P_0 > < 3S|\hat{\mu}_z|3P_0 >, \tag{A35}$$

111

$$\mu_B(R) \approx -2 <X\Sigma^+|3P_0><3S|\hat{\mu}_z|3P_0> +$$

$$2 <B\Sigma^+|4S><4S|\hat{\mu}_z|3P_0> +2 <B\Sigma^+|3D_0><3P_0|\hat{\mu}_z|3D_0>, \qquad (A36)$$

$$\mu_{X\to B}(R) \approx <3S|\hat{\mu}_z|3P_0> + <X\Sigma^+|4S><4S|\hat{\mu}_z|3P_0> + <X\Sigma^+|3D_0><3D_0|\hat{\mu}_z|3P_0>, \qquad (A37)$$

$$\mu_{X\to C}(R) \approx - <B\Sigma^+|4S><3S|\hat{\mu}_z|3P_0> + <X\Sigma^+|3P_0><4S|\hat{\mu}_z|3P_0>, \qquad (A38)$$

$$\mu_{X\to A}(R) \approx <3S|\hat{\mu}_-|3P_{+1}> + <X\Sigma^+|4S><4S|\hat{\mu}_-|3P_{+1}> + <X\Sigma^+|3D_0><3D_0|\hat{\mu}_-|3P_{+1}> . \qquad (A39)$$

Finally, solution of these equations provides the off-diagonal $\mathbf{U}_{11}$ matrix elements in the forms

$$<X\Sigma^+|3P_0> = - <B\Sigma^+|3S> = \frac{\mu_X(R)}{2 <3S|\hat{\mu}_z|3P_0>}, \qquad (A40)$$

$$<B\Sigma^+|4S> = - <C\Sigma^+|3P_0> = \frac{<X\Sigma^+|3P_0><4S|\hat{\mu}_z|3P_0> -\mu_{X\to C}(R)}{<3S|\hat{\mu}_z|3P_0>} \qquad (A41)$$

$$<B\Sigma^+|3D_0> = - <F\Sigma^+|3P_0>$$

$$= \frac{\mu_B(R) + 2 <X\Sigma^+|3P_0><3S|\hat{\mu}_z|3P_0> -2 <B\Sigma^+|4S><4S|\hat{\mu}_z|3P_0>}{2 <3P_0|\hat{\mu}_z|3D_0>} \qquad (A42)$$

$$<X\Sigma^+|3D_0> = - <F\Sigma^+|3S> = \frac{\mu_{X\to B}(R) + \mu_{X\to A}(R)}{3 <3D_0|\hat{\mu}_-|3P_{+1}>}, \qquad (A43)$$

$$<X\Sigma^+|4S> = - <C\Sigma^+|3S> = \frac{\mu_{X\to B}(R) - <3S|\hat{\mu}_z|3P_0> - <X\Sigma^+|3D_0><3D_0|\hat{\mu}_z|3P_0>}{<4S|\hat{\mu}_z|3P_0>}, \qquad (A44)$$

whereas enforcing orthogonality in the final $\mathbf{U}_{11}$ diagonal matrix elements gives the expressions

$$<X\Sigma^+|3S> = \{1- <X\Sigma^+|3P_0>^2 - <X\Sigma^+|4S>^2 - <X\Sigma^+|3D_0>^2\}^{1/2} \qquad (A45)$$

$$<B\Sigma^+|3P_0> = \{1- <B\Sigma^+|3S>^2 - <B\Sigma^+|4S>^2 - <B\Sigma^+|3D_0>^2\}^{1/2} \qquad (A46)$$

$$<C\Sigma^+|4S> = \{1- <C\Sigma^+|3S>^2 - <C\Sigma^+|3P_0>^2 - <C\Sigma^+|3D_0>^2\}^{1/2} \qquad (A47)$$

$$<F\Sigma^+|3D_0> = \{1- <F\Sigma^+|3S>^2 - <F\Sigma^+|3P_0>^2 - <F\Sigma^+|4S>^2\}^{1/2}. \qquad (A48)$$

Numerical values (a.u.) for the required atomic transition moments are given in the forms

$$<3S|\hat{\mu}_-|3P_{+1}> = \mu_{X\to A}(R\to\infty) = 2.58 \qquad (A49)$$

$$< 3S|\hat{\mu}_z|3P_0 >= \mu_{X\to B}(R \to \infty) = -2.58 \tag{A50}$$

$$< 4S|\hat{\mu}_-|3P_{+1} >= 2.48 \tag{A51}$$

$$< 4S|\hat{\mu}_z|3P_0 >= -2.48 \tag{A52}$$

$$< 3D_0|\hat{\mu}_z|3P_0 >= -2(1.50) = -3.00 \tag{A53}$$

$$< 3D_0|\hat{\mu}_-|3P_{+1} >= -1.50 \tag{A54}$$

$$< 3D_{+1}|\hat{\mu}_z|3P_{+1} >= -\sqrt{3}(1.50) = -2.60, \tag{A55}$$

obtained employing the calculated molecular moments [10,11] and tabluated atomic f-numbers [15]. The $U^{(k)}(R_k)$ matrix elements given by Eqs. $(A28)$ to $(A30)$ and $(A39)$ to $(A48)$ when employed in Eq. $(A13)$ complete the evaluation of the Hamiltonian matrix of Eqs. $(A3)$ to $(A13)$. It should be noted the sign convention [16,17] employed in the present development requires that the reported [10,11] numerical values of z-component transition and dipole moments be changed in sign uniformly, whereas the x-component moments reported should be employed as given.

# POTENTIAL ENERGY SURFACES FOR HIGH ENERGY SPECIES

AFOSR HEDM MEETING
JUNE 4-7, 1995

MARK S. GORDON, NIKITA MATSUNAGA, AND GALINA CHABAN
DEPARTMENT OF CHEMISTRY
IOWA STATE UNIVERSITY
AMES, IOWA 50011

JERRY A. BOATZ
PHILLIPS LABORATORY
EDWARDS AFB, CA

EXTENDED ABSTRACT

The potential energy surfaces for several types of high energy species have been investigated using *ab initio* electronic structure theory, with the ultimate goal of using a combination of electronic structure theory and dynamics as a synthetic tool, to lead the way toward new high energy species. Considerable use in this design process has been made of isoelectronic relationships An important example of such relationships centers around the molecule bicyclobutane:
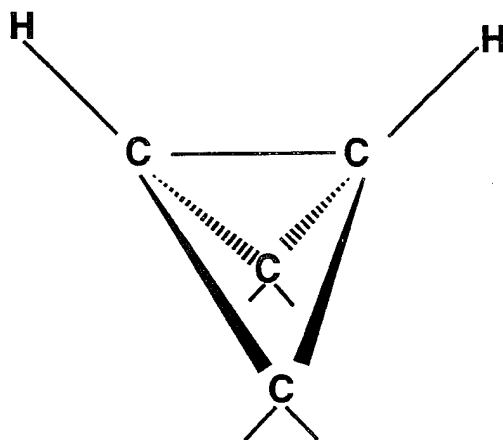
This highly strained organic molecule has several potentially interesting isoelectronic and valence isoelectronic analogs. For example, the tetrasila analog is valence isoelectronic with bicyclobutane, as is the compound in which only the two bridgehead carbons are replaced by silicons. Previous calculations by us and others have predicted both of these molecules to exhibit bond stretch isomerism, in which two isomers, differing primarily in the bridgehead Si-Si distance, are connected by a transition state. The silicon compounds are highly strained and therefore also highly energetic.

More exotic analogs of bicyclobutanes can also be imagined. Since CH is isoelectronic with N and CH_2 is isoelectronic with O, there may well exist a high energy isomer of N_2O_2 that has a bicyclobutane-like structure. Similarly, FN_3 is isoelectronic with these compounds as well. All of these isoelectronic species are considered below.

In addition to bicyclobutane analogs, several other potentially important high energy species have been investigated in our group. The anions NH_4^- and PH_4^- have been used to illustrate how electronic structure theory and dynamics can be merged to determine routes to high energy species. This is also discussed below. Extensive studies have also been performed on high energy isoelectronic analogs of prismane (a high energy isomer of benzene) and on Van der Waals complexes of main group metal atoms with clusters of molecular hydrogen. Each of these last two species are discussed in separate abstracts.

The *tetrasila-analog of bicyclobutane* has been of interest for several years, since it has been predicted by electronic structure theory to exist as two isomers that differ primarily in the length of the bridgehead Si-Si distance, a normal 2.35Å in the sort bond (SB) isomer and a much longer 2.9Å in the long bond (LB) isomer. In the unsubstituted compound, the LB isomer is predicted to be lower in energy. The only analog that has been synthesized is highly substituted, with t-butyl groups replacing the hydrogens at both bridgehead positions. In contrast to the theoretical predictions, only the SB isomer is found for this substituted compound. This difference between theory and experiment is important to understand, since the unsubstituted compound (which has not yet been synthesized), when used as an additive to LOX/LH2 in 2.5 mole % is found to increase the specific impulse by 11 seconds. Therefore, GVB/6-31G(d) calculations were performed on the SB->LB isomerization as a function of the group R in the bridgehead positions. As shown in Figure 2, increasing the size of the bridgehead substituents, destabilizes the LB isomer, relative to the LB isomer. This explains why only the SB isomer is found experimentally. Of particualr interest is our prediction that the two isomers of the dimethyl analog are nearly isoenergetic, separated by about a 6 kcal/mol barrier. This suggests that both isomers of the dimethyl compound may be synthesized.

In order to determine the effect of increasing the sophistication of the calculations on the predictions summarized in the previous paragraph, both the basis set and the level of theory used for these calculations have been systematically improved. The result is that we find second order perturbation theory (MP2), coupled cluster theory including triples (CCSD(T)), and second order perturbation theory based on a two configuration reference (CASPT2) all predict (for a range of basis

sets from 6-31G(d) to 6-311G(2df,2pd)) that the transition state falls below the short bond isomer. This suggests that the short bond isomer disappears when dynamic correlationis included in the calculation. Subsequent optimization of the geometry of the short bond isomer using MP2/6-31G(d) verified this. So, the appropriate target molecule is the long-bond isomer.

Because the bicyclobutane analog with Si atoms in the bridgehead positions and C atoms in the peripheral positions may be easier to synthesize, this species was also reinvestigated. At the GVB/3-21G* level of theory[1], long and short bond isomers are again found on the ground state potential energy surface, with the long bond isomer lower in energy by 23 kcal/mol. Two different transition states (TSA and TSB) connecting the two isomers were found. Because of the unusual nature of this potential energy surface, we are again exploring the affect of improving both the basis set and the level of theory. All four points (two isomers and two transition states) remain stationary points on the MP2/6-31G(d,p) level of theory (See Figure 1). The short bond isomer is much higher in energy (25 kcal/mol at this level of theory) than the long bond isomer, and it is separated from the lower energy isomer by barriers of 4 and 11 kcal/mol. So, the long bond isomer is probably the most sensible target molecule, although the short bond isomer should be isolable at low temperatures.

Several high energy isomers of N_2O_2 have been identified on the MCSCF(10,10)/6-31G(d) potential energy surface. Four of these are shown in Figure 2. The most reliable energies are those calculated with multi-reference second order perturbation theory (CASPT2) and the 6-311+G(2d) basis set. At this level of theory, all four isomers are predicted to be about 50-80 kcal/mol higher in energy than 2 NO. It is important to recognize, however, that unusual metastable species frequently have low-lying excited states, and these excited states may well be repulsive. If this is the case, an apparently stable species my be non-adiabatically unstable. Indeed, it has been shown that isomer 4 is non-adiabatically unstable to dissociation to $O + N_2O$[2]. The non-adiabatic stability of other N_2O_2 isomers is currently under investigation by Yarkony and co-workers and is discussed in a separate abstract. Our most recent calculations have focused on that part of the potential energy surface corresponding to decomposition of isomer 1 to 2 NO. The transition state for this decomposition has been identified, and the minimum energy path determined at both the MCSCF and CASPT2 levels of theory. At the highest level of theory, CASPT2(10,10)/6-311+G(2d)//MCSCF(10,10)/6-31G(d), the barrier to the decomposition is predicted to be 52 kcal/mol with an exothermicity of 49 kcal/mol. The potential energy surfaces for dissociations of the other high energy isomers are currently being explored.

There have been several previous calculations on the potential energy surface for *fluorine azide*

and its decomposition to $N_2 + NF$. We have recently found a new, higher energy isomer of this compound, in which the three nitrogen atoms form an isosceles three-membered ring. At the CASPT2 level of theory, based on an MCSCF(10,10) wave function and the 6-31G(d) basis set, the new isomer is found to lie 15 kcal/mol higher in energy than the open isomer. The isomerization barrier is higher in energy than the barrier for dissociation. As a result, the cyclic structure dissociates before it can isomerize. The calculated dissociation barrier is predicted to be 17 kcal/mol, with an exothermicity of 8.4 kcal/mol. A triplet cyclic isomer is predicted to be 61 kcal/mol higher than the singlet. It's dissociation barrier, to $N_2 + NF$ ($^3\Sigma^-$), is 16 kcal/mol, with an overall exothermicity of 45.2 kcal/mol. So, the higher energy, cyclic isomer could provide considerable energy gain. The nature of the surface crossings and non-adiabatic interactions are discussed in Professor Yarkony's abstract.

References

1. 127. J.A. Boatz and M.S. Gordon, J. Phys. Chem., <u>93</u>, 2888 (1989).

2. K.A. Nguyen, M.S. Gordon, J.A. Montgomery, Jr., H.H. Michels, and D.R. Yarkony, J. Chem. Phys., <u>98</u>, 3845 (1993).

BOND STRETCH ISOMERISM IN DISILABICYCLOBUTANE

MP2/6-31G(d,p) OPTIMIZED STRUCTURES

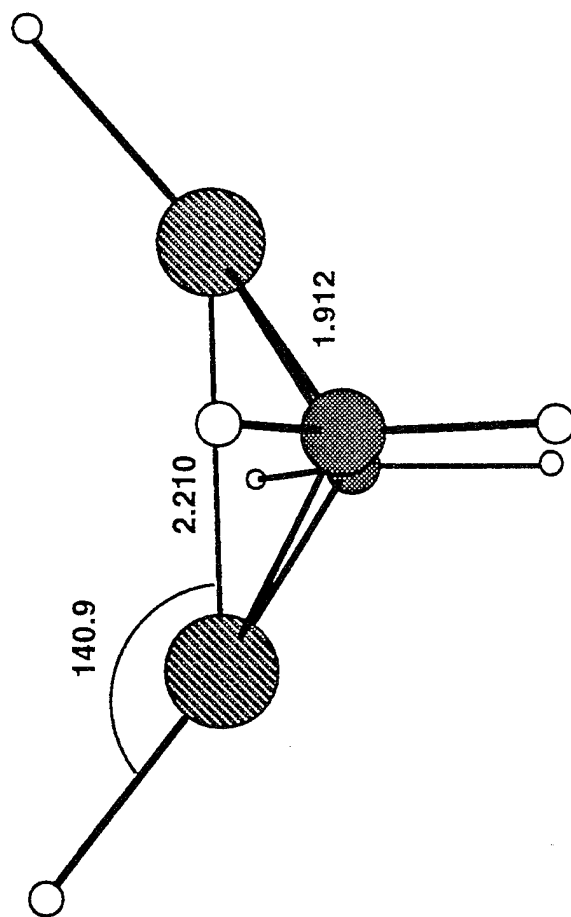
92.1

2.471

1.913

Long Bond (LB)

0.0

165.1
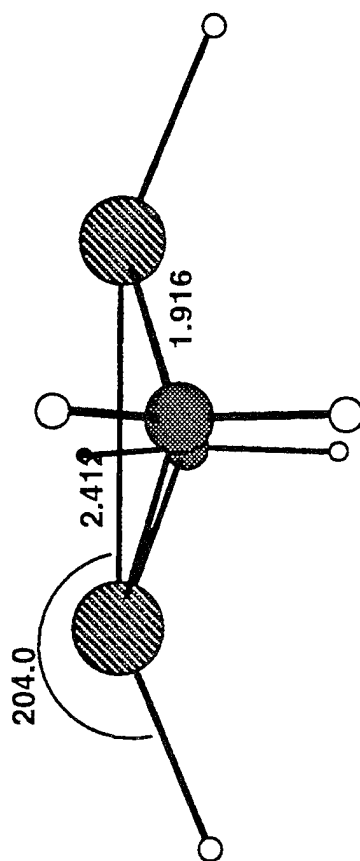
2.162

1.919
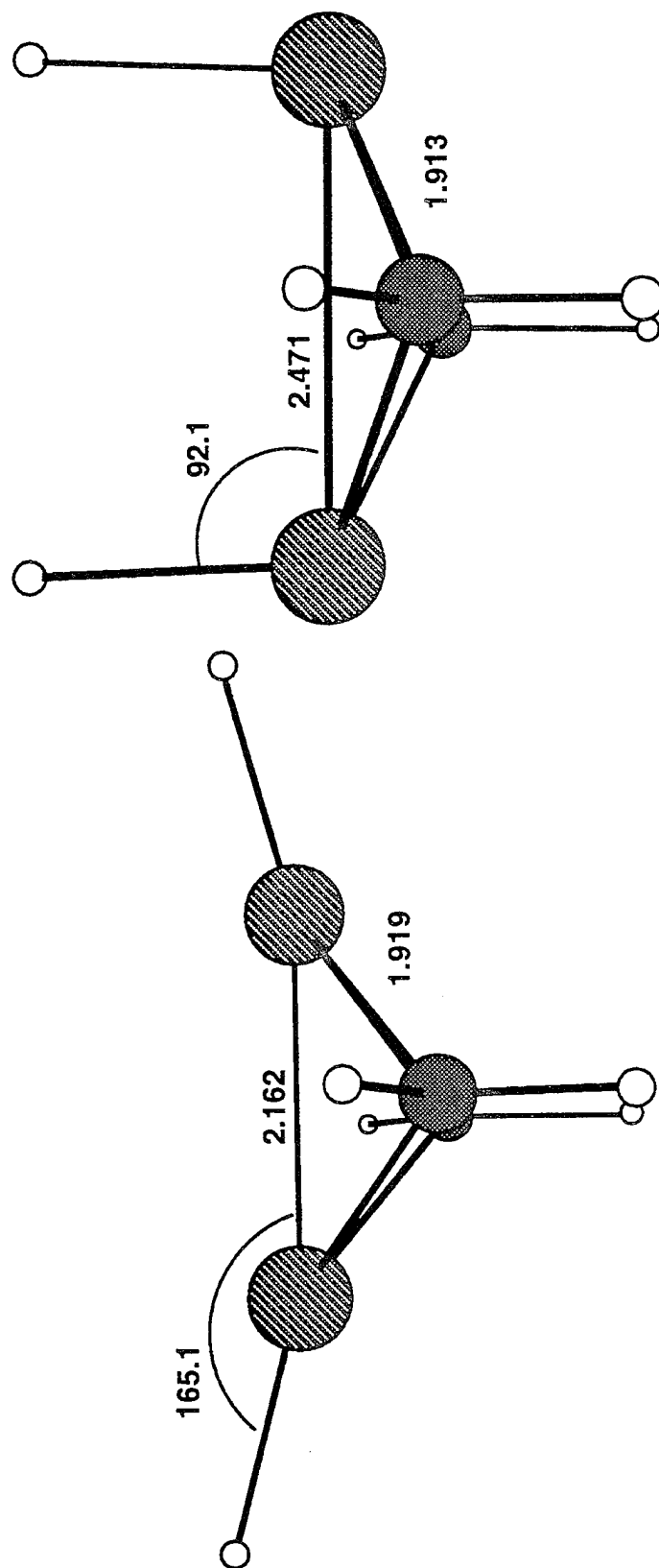
Short Bond (SB)

25.2 kcal/mol

BOND STRETCH ISOMERISM IN DISILABICYCLOBUTANE

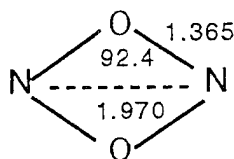## MP2/6-31G(d,p) OPTIMIZED TRANSITION STATES

TSA: 29.6 kcal/mol

TSB: 36.6 kcal/mol

N_2O_2 HIGH ENERGY ISOMERS

MCSCF(10,10)/6-31G(d) geometries (A,deg.) and relative energies (kcal/mol) with reference to 2 NO

1. D_{2h}

2. C_{2v}

E rel.

	1. D_{2h}	2. C_{2v}
MCSCF/6-31G(d)	71.0	71.2
CASPT2/6-31G(d)	49.0	77.3
MCSCF/6-311+G(2d)	71.7	73.2
CASPT2/6-311+G(2d)	48.7	81.9

3. C_{2v}

4. C_s
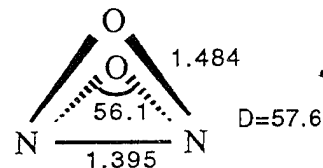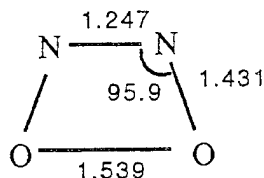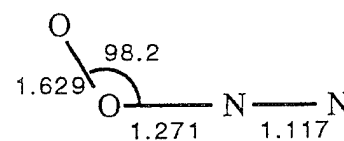
	3. C_{2v}	4. C_s
MCSCF/6-31G(d)	43.4	60.3
CASPT2/6-31G(d)	49.4	79.3
MCSCF/6-311+G(2d)	44.4	57.1
CASPT2/6-311+G(2d)	52.9	75.5

A Spectroscopic Study of the Jupiter-SL9 Comet Collision:

High Energy Chemistry on a Grand Scale*

Takeshi Oka

Department of Chemistry and Department of
Astronomy and Astrophysics

The University of Chicago and The Enrico Fermi Institute

Chicago, IL   60637

My contracts with the Air Force HEDM grant has been on two fronts of my research -- spectroscopy and dynamics of (i) hydrogen molecule, and ionic and neutral impurities in parahydrogen crystals and (ii) highly-excited H_3^+ ion. The former is to study radiative, intermolecular, and many body interactions in solid hydrogen and possibly to find application in high energy density materials, and the latter is to study behavior of the H_3^+ molecular ion in high temperature plasmas, both in the laboratory and in space. Both fronts developed into directions which were totally unexpected in my original proposal. In the former, the observation of very sharp spectral lines and thus the possibility of high resolution laser spectroscopy of solid hydrogen evolved, and in the latter the observation of extremely pure spectrum of H_3^+ in Jovian ionosphere. While the former project occupies a major part of our effort, today I would like to talk exclusively on the latter subject for three reasons: (a) I have not discussed this subject in HEDM meeting, (b) I discussed the former subject at the Irvine meeting on "The Physics and Chemistry of Quantum Solids, Fluids, Films and Clusters" in February, which many of you attended, and last but not least (c) the SL-9 comet-Jupiter encounter occurred last summer; that was surely a very rare event to stay in the history of observational astronomy which left us with much enigmatic observational data.

1. Laboratory Studies of H_3^+ in High Rovibrational States

Recent observation of the H_3^+ infrared emission in Jupiter in the $2\mu m$ $2v_2$ overtone band[1] and in the 4 μm v_2 fundamental[2] band have demonstrated that the H_3^+ ions, which exist abundantly in polar regions of Jupiter, are in approximate thermal equilibrium corresponding to a high temperature of ~1100K.[3] The highest emitting states so far identified are the $2v_2$, $1 = 2$ (J, G, U) - 10, 12, +2 level for the $2v_2$ overtone

emission band[1], and the $\nu_1 + \nu_2$ $l = 1$ (J, G, U) = 7, 6, -1 level for the $\nu_1 + \nu_2 - \nu_1$ hot band[4] that are 6669 cm^{-1} and 6985 cm^{-1} above the lowest state, respectively. Obviously, these levels at energies of ~10,000K are well populated. The high translational temperature of 1150K was also reported from the observed line width of Jovian emission lines.[5] Observations of the H_3^+ emission from Uranus[6] and Saturn[7] also showed similar high temperature of their ionospheres. The recent claim[8] of detection of the H_3^+ emission in *super nova* 1987A introduced the possibility that there are objects in which H_3^+ are populated with much higher temperature.

Spectroscopy and dynamical studies of H_3^+ in high rovibrational levels were done in two ways. The first method was to produce rovibrationally hot plasmas and observe spectral lines starting from high rovibrational levels. For this purpose, we used water-cooled He dominated hydrogen plasmas using a gas mixture of He/H_2 ~5 torr/0.6 torr.[9] The high ionization potential of He (24.6 eV as opposed to 15.4 eV of H_2) causes high electron temperature and thus highly-excited molecular states, while the low ionization potential of He (1.9 eV as opposed to 4.4 eV of H_2) keeps the proton in H_3^+ intact. The high vibrational temperature of H_3^+ in such a plasma is known.[10] High rotational temperature has been achieved by using water-cooled plasmas with a specially designed jet-type plasma tube.[9] Such plasmas allowed us to observe transitions starting from rotational energy levels up to 5092 cm^{-1} (7918K). Rotational levels reached by this method are shown in Fig. 1. The rotational distribution was found to be thermal corresponding to the rotational temperature of ~1000K as shown in Fig. 2.

The second method to observe high rovibrational levels is to use overtone spectrum.[11] The vibrational states we have reached by this method as well as by the method of hot plasmas are shown in Fig. 3.

A considerable number of theoretical works[12-24] and reviews[25-28] on this subject have recently been published.

2. Spectroscopic Observation of the Jupiter-SL9 Comet Collision

A. *Background*

The inside of Jupiter is composed dominantly of hydrogen and helium which are in the state of supercritical fluid under the condition of high temperature and pressure. From the center of the core to ~4/5 of the radius of Jupiter, hydrogen are under sufficient gravitational pressure to be metallic. The resulting electric conductivity inside Jupiter together with the rapid rotation (9 hours and 55.5 minutes per rotation) makes Jupiter a strong magnet, whose moment is larger than that of the earth by four orders of magnitude. This large magnetic field rotate with Jupiter and collect charges in the Jovian magnetosphere. Being trapped, the charges correlate with Jupiter; they are accelerated along the magnetic field lines of the electric field generated through magnetic perturbation and result in an enormous electric current (Birkeland current) which is focused at the polar regions and generate colossal plasmas. It is in these auroral regions where H_3^+ emission is most strongly observed.

The beautiful Fourier transform infrared recording by Maillard et al.[29] shown in Figure 4 gives the best panoramic view of the strong and pure H_3^+ emission lines corresponding to the ν_2 fundamental band. The H_3^+ spectrum appears in the wavelength region which is above the C-H stretch vibration of CH_4 and other hydrocarbons and below vibrations of heavier molecules such as CO_2 and hence the

remarkable purity. The spectrum is also amazing in that the background infrared radiation is almost nonexistent. In particular, in the region of 2600 to 2900 cm^{-1}, the background is almost completely flat and virtually zero. This is because infrared radiation coming from the inside of the cooling planet and from the reflection of the sun light is almost completely wiped out by the pressure broadened CH_4 spectrum in the low altitude, low temperature Jovian atmosphere. Only the H_3^+ emission occurring at the high altitude of the ionosphere reaches us unabsorbed.

More recently we found[30,31] that the H_3^+ emission is not localized in polar regions but are observed less intensely across the whole surface of Jupiter. Figure 5 shows our observation of the quartet lines at 2830 cm^{-1} (see Fig. 4). It is noted that the lines are extremely strong and free of background. The lower picture of Figure 5 shows Jupiter's spectral image from the South Pole to the North Pole. It is clear that the emission is all across the surface of Jupiter. This purity and the universality of the H_3^+ emission spectrum makes it a powerful general vehicle to monitor plasma activities of Jovian ionospheres. We planned to monitor variation of this spectrum during the SL-9 impact.

We also attempted to observe spectra of free radicals and molecular ions that are produced from CH_4, NH_3, and H_2O in Jovian atmosphere through the chemical reaction during the impact such as CH_2, CH_3, CH_3^+, NH_2, NH_3^+, OH, OH^+, H_2O^+, etc. for which we accumulated considerable information over the years.

B. *Observation*

The 20 comet fragments named alphabetically from A to W impacted Jupiter from July 16 to 22, 1994. We were granted six observation nights at the United Kingdom Infrared Telescope (UKIRT) in Mauna Kea Hawaii on July 15 (pre-impact) 17,

19, 22 (during impact) and 25 and 27 (post impact). It turned out that the night of the 11, when the observation of fragments V and W were planned, was wiped out because Emilia, one of the most violent hurricanes ever recorded, passed 300 miles south of Hawaii. Thus our direct observation of the effect of impact was limited to that of fragment C on July 17.

The fragment C impacted Jupiter at 7h:13m:51s ± 3 min. U.T. (Universal Time) on July 17.[32] The impact latitude was 43.4 south and behind Jupiter but was very close to the edge. Several minutes later, the plume generated by the impact came into view and the infrared flux reached maximum at about 7h:23m U.T. After the climax infrared intensity waned rapidly and in 20 minutes settled back to the pre-impact value.[33]

We used the high resolution cooled grating spectrometer CGS4 in echelle mode attached to the UKIRT 3.8m reflecting telescope. The spectrum was detected by using a 56 x 62 InSb detection array with pixel size of 2.12″ x 1.1″ (Jupiter diameter is ~40″). One dimension of the array was used for wavelength while the other dimension was used to monitor position-dependent variation of the spectrum from east (rising side) to west (setting). The spectral scan was from the wavelength of 3.529μ to 3.547μ, the same region as shown in Fig. 5.

The spectral image of Jupiter at 6:54 U.T., 20 minutes before the impact is shown in Fig. 6. The row 37 corresponds to the east edge of Jupiter (rising side) and row 24 the west edge (setting side). The quartet H_3^+ lines are clearly seen. It is noted that the wavelength of the spectral lines red shift from east to west due to Doppler effect caused by the fast Jupiter rotation. At the time this spectrum was taken, I had no idea about the magnitude of the effect of impact. While I was praying that the impact causes enormous chemical reaction and gives us strong new spectra, I was also prepared to see

very small effect. (Back in my mind was the case of Comet Kahoutec which ended up as a disappointment in spite of the publicity that it was going to be the brightest comet.)

After a long waiting of 25 minutes, we obtained at 7:19 U.T. the spectrum shown on Fig. 7. which caused enormous excitement among the observing crews. The enormous infrared emission of the plume has been recorded! The rising side rows 37 and 38 are whited out due to saturation of detectors in the color code used. The weaker infrared emission in rows 35 and 36 shows many new emission lines that are obviously not due to H_3^+. Thus began the analysis of the new emission lines which varies depending on time and position.

For a day and a half or so we were carried away by the hurrah of the observation and the spectrum was eagerly compared with laboratory data of numerous free radicals and molecular ions. It was soon found, to our disappointment, that the observed lines did not quite match the spectra of those exotic species and the stronger lines can be explained as due to CH_4, which was likely to be blown up from lower altitude. Of course, CH_4 spectrum had been the first to be suspected, but I forgot that the CH_4 spectrum at high temperature (~1500K) looks entirely different from that at room temperature. The vibration rotation spectrum of CH_4 has been continually studied in the last 60 years and we are equipped with the Air Force HITRAN data compilation (kindly provided by Dr. Linda Brown of JPL), but our knowledge of the spectrum was not sufficient to completely understand the observed spectrum. A laboratory experiment is being conducted by Dr. P. Bernath to take spectrum of high temperature CH_4.

Thus our second project of hunting for spectra of exotic species was switched to the study of temporal and spatial variation of the CH_4 spectrum. What we have here is a 3 dimensional spectroscopy, i.e., in wave number, time, and position, each with resolution of ~0.1 cm^+, 90 seconds, and 2.1". Out of the enormous amount of data accumulated we extracted information on the variation of luminosity, temperature, Doppler-shift etc. of the spectrum. They will be published in a comprehensive paper.

We have also obtained considerable amount of data on H_3^+. An example is shown in Fig. 8. The figure shows variations of the H_3^+ spectrum <u>before</u> the impact. The spectrum shows that the ionosphere was heated several minutes before the impact. Note in particular that the spectral line at 3.543μ increases its intensity drastically. A small part of it (<1/3) may be due to CH_4 but this feature is mainly due to H_3^+ hot band $2v_2^\circ \rightarrow v_2^1$ [8,9], which is very weakly seen in Fig. 5. It shows that the H_3^+ is heated to very high temperature (~5000K). There are other interesting post-impact effects on H_3^+ spectra.[33,34]

References

1. P. Drossart, J.-P. Maillard, J. Caldwell, S.J. Kim, J.K.G. Watson, W.A. Majewski,
J. Tennyson, S. Miller, S.K. Atreya, J.T. Clarke, J.H. Waite, Jr., and R. Wagener, *Nature*
340, 539 (1989).

2. T. Oka and T.R. Geballe, *Astrophys. J.* 351, L53 (1990).

3. T. Oka, *Rev. Mod. Phys.* 64, 1141 (1992).

4. T.R. Geballe, M.-F. Jagod and T. Oka, to be published.

5. P. Drossart, J.-P. Maillard, J. Caldwell, and J. Rosenqvist, *Astrophys. J.* 402, L25 (1993).

6. L.M.Trafton, T.R. Geballe, S. Miller, J. Tennyson, and G.E. Ballester, *Astrophys. J.* 405,
761 (1993).

7. T.R. Geballe, M.-F. Jagod, and T. Oka, *Astrophys. J.* 408, L1091 (1993).

8. S. Miller, J. Tennyson, S. Lepp and A. Dalgarno, *Nature* 355, 420 (1992).

9. D. Uy, C.M. Gabrys, M.-F. Jagod, and T. Oka, *J. Chem. Phys.* 100, 6267 (1994).

10. M. G. Bawendi, B.D. Rehfuss, and T. Oka, *J. Chem. Phys.* 93, 6200 (1990).

11. B.F. Ventrudo, D.T. Cassidy, Z.Y. Guo, S.W. Joo, S.S. Lee, and T. Oka, *J. Chem.
Phys.* 100, 6262 (1994).

12. M.J. Bramley, J.R. Henderson, J.Tennyson, and B.J. Sutcliffe, *J.Chem. Phys.* 98, 10104
(1993).

13. J.R. Henderson, J. Tennyson, and B.J. Sutcliffe, *J. Chem. Phys.* 98, 7191 (1993).

14. Q. Zhang, P.N. Day, and D.G. Truhler, *J. Chem. Phys.* 98, 4948 (1993).

15. R. Röhse, W. Klopper, and W. Kutzelnigg, *J. Chem. Physl.* 99, 8830 (1993).

16. S. Carter and W. Meyer, *J. Chem. Phys.* 100, 2104 (1994).

17. M.J. Bramley, J.W. Tromp, T. Carrington, Jr., and G.C. Corey, *J. Chem. Phys.* 100, 6175
(1994).

18. R. Röhse, W. Kutzelnigg, R. Jacquet, and W. Klopper, *J. Chem. Phys.* 101, 2231 (1994).

19. L. Wolniewicz and J. Hinze, *J. Chem. Phys.* 101, 9817 (1994).

20. B.M. Dinelli, S. Miller, and J. Tennyson, *J. Mol. Spectrosc.* 163, 71 (1994).

21. W.A. Majewski, A.R.W. McKellar, D. Sadovskii, and J.K.G. Watson, *Can. J. Phys.* 72, 1076 (1994).

22. R. Jacquet and R. Röhse, *Mol. Phys.* 84, 291 (1995).

23. J.K.G. Watson, *Chem. Phys.* 190, 291 (1995).

24. B.M. Dinelli, C.R. LeSuer, J. Tennyson, and M. D. Adams, *Chem. Phys. Lett.* 232, 295 (1995).

25. A. Dalgarno, *Adv. Atom. Mol. and Opt. Phys.* 32, 57 (1994).

26. S. Miller, H.A. Lam, and J. Tennyson, *Can. J. Phys.* 72, 760 (1994).

27. I.R. McNab, *Adv. Chem. Phys.* LXXXIX 1 (1995).

28. J. Tennyson, *Rep. Prog. Phys.* 57, 421 (1995).

29. J.-P. Maillard, P. Drossart, J.K.G. Watson, S.J. Kim, and J. Caldwell, *Astrophys. J.* 363, L37 (1990).

30. T.R. Geballe, M.-F. Jagod, and T. Oka, *unpublished*.

31. T. Oka and M.-F. Jagod, *J. Chem. Soc. Faraday Trans.* 89, 2147 (1993).

32. H.B. Hammel et al., *Science* 267, 1288 (1995).

33. G. Orton et al, *Science* 267, 1277 (1995).

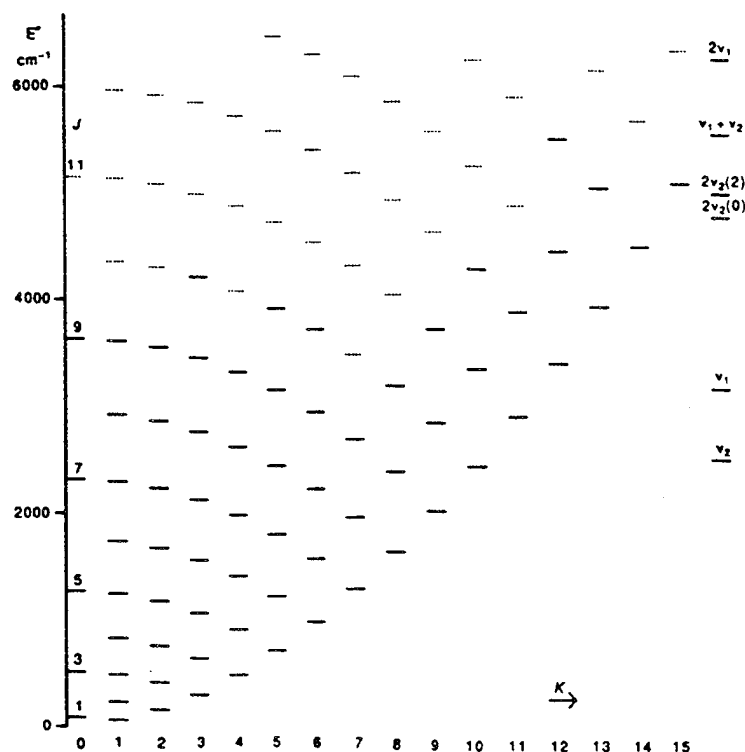34. S. Miller et al., *Geophys. Res. Lett.* 22, 1629 (1995).

Figure 1. Rotational energy levels of H_3^+ in the ground vibrational state. Solid lines show levels from which transitions were observed.
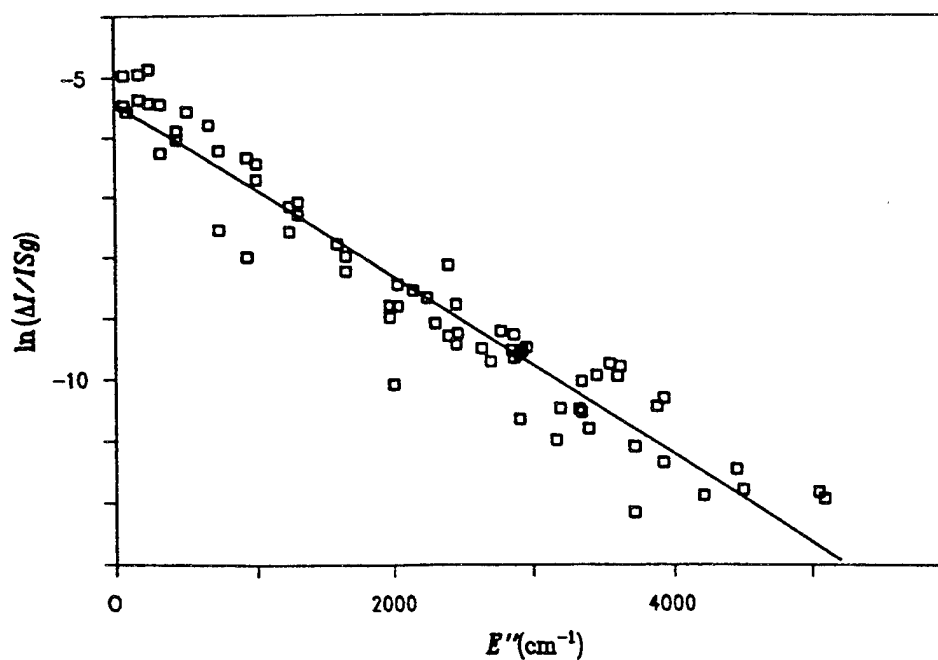

Figure 2. Observed ln [$\Delta I/ISg$] versus E'' where S and g are transition strength and degeneracy, respectively and E'' is the energy rotational levels in cm^{-1}. The results show that H_3^+ are thermal corresponding a temperature of ~1000K.

131

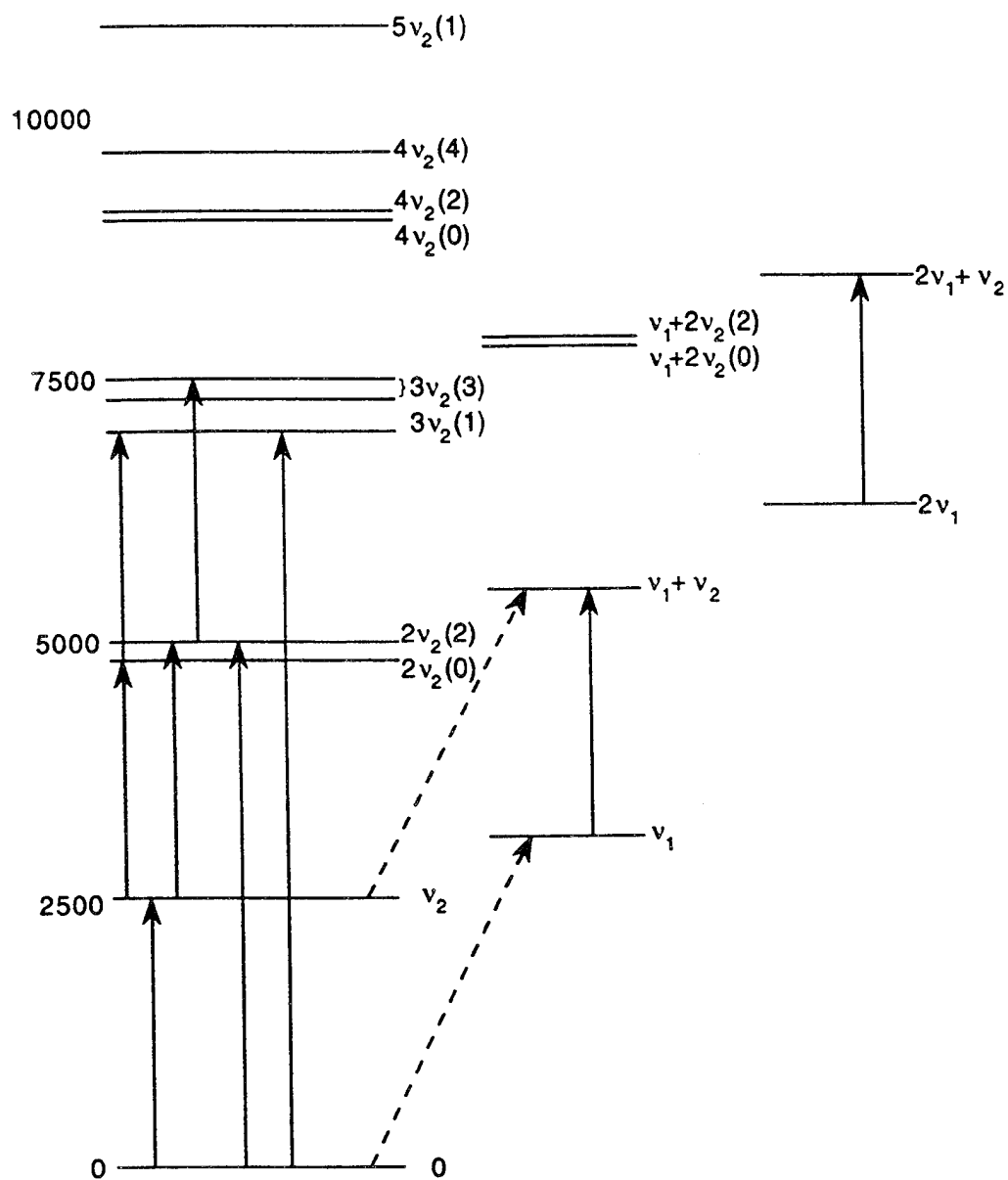**Figure 3.** Rovibrational transitions of H_3^+ so far observed in the laboratory. Broken lines indicate forbidden transitions.
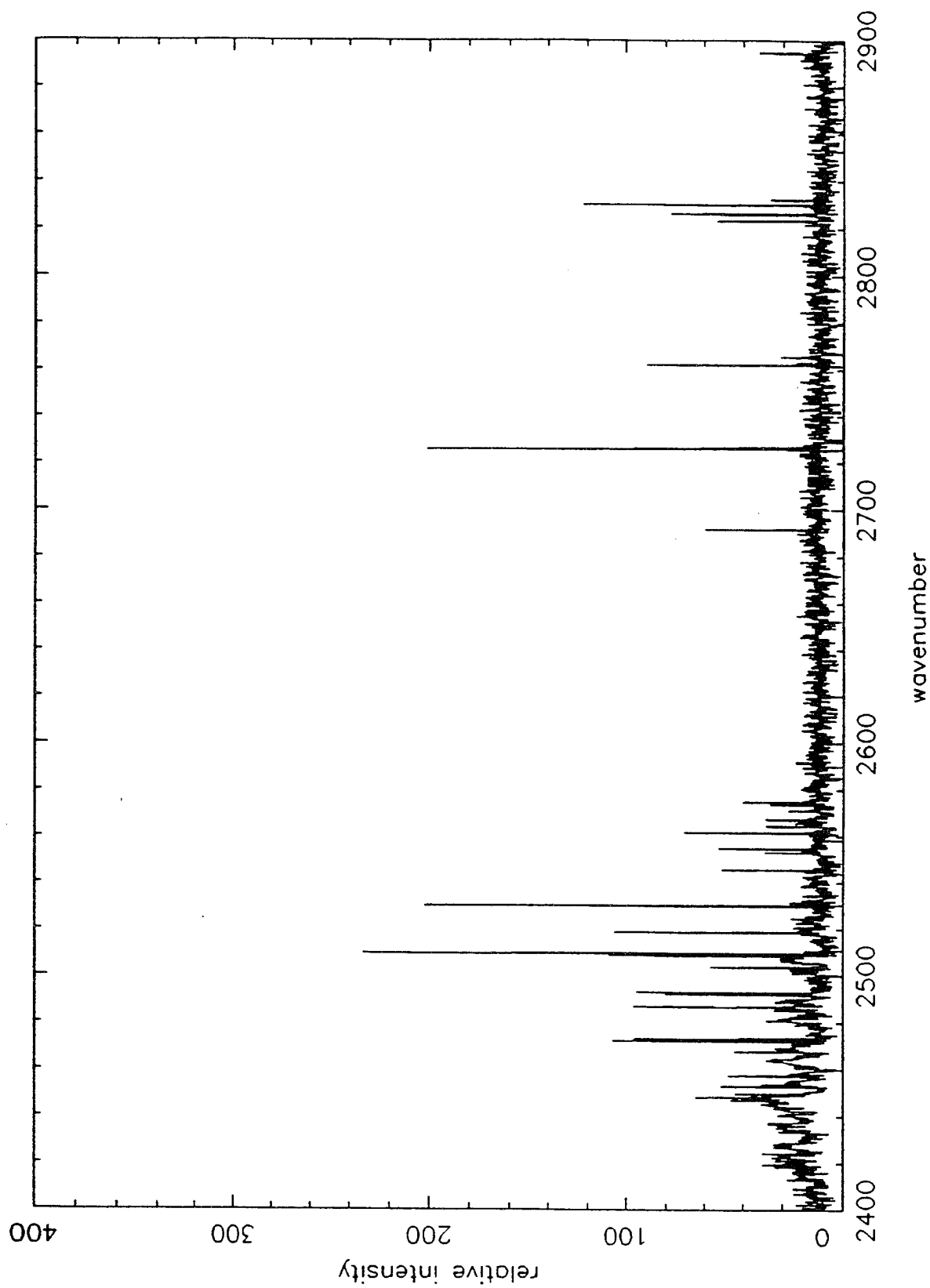
JUPITER H3+ EMISSION

Figure 4. The H_3^+ emission spectrum from the southern auroral zone of Jupiter recorded by Maillard et al.[29] All of the observed strong lines are assigned to H_3^+ v_2 vibration-rotation band. The purity of the spectra is remarkable.
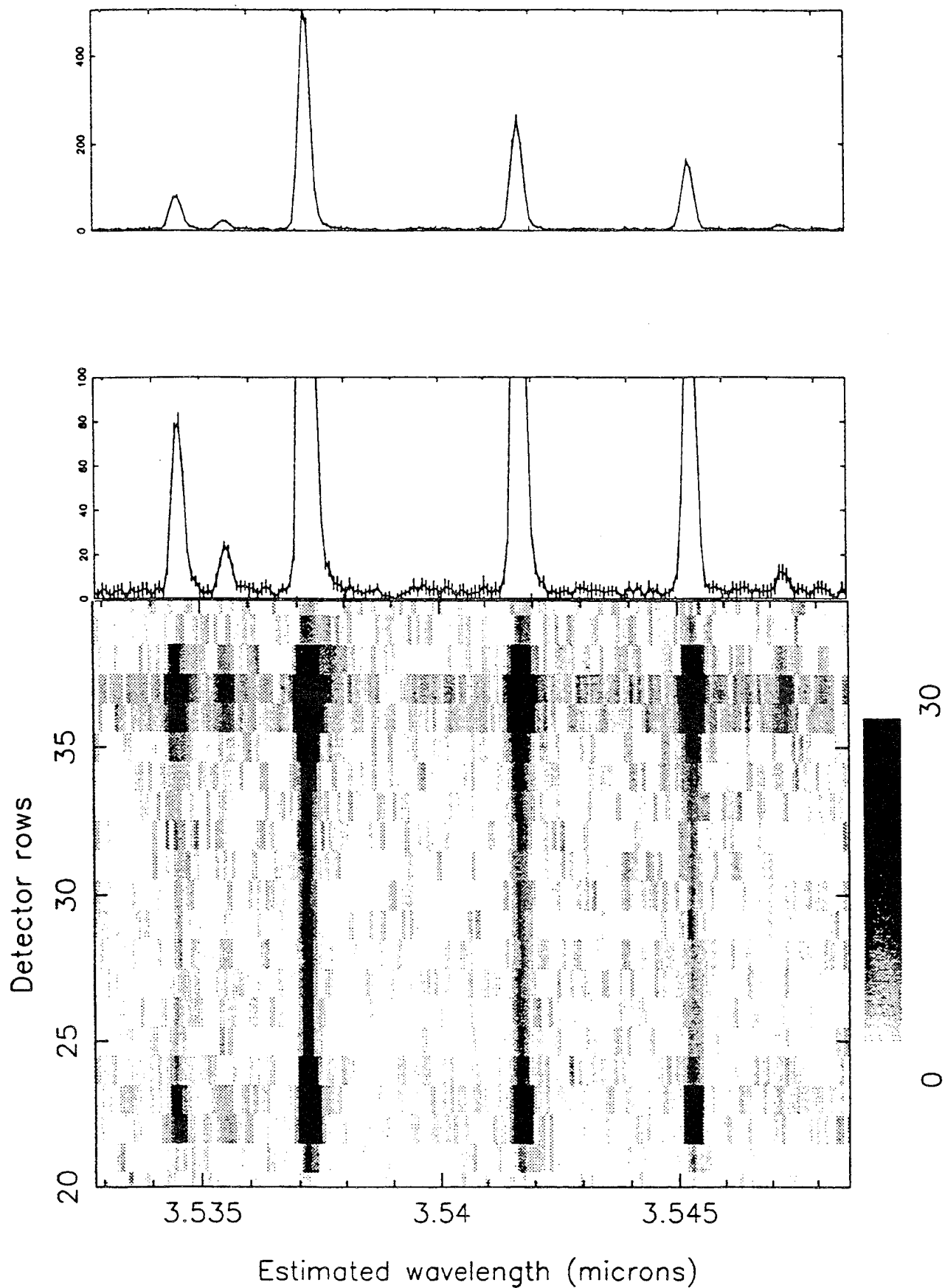
Figure 5. The H_3^+ quartet lines at 3.54 μm observed by UKIRT CGS4 grating spectrometer and Jupiter's spectral image. The spectral lines are amazingly free of infrared background. Jupiter's image from the South Pole (row 37) to the North Pole (row 22) shows that H_3^+ are emitting across the surface of Jupiter.
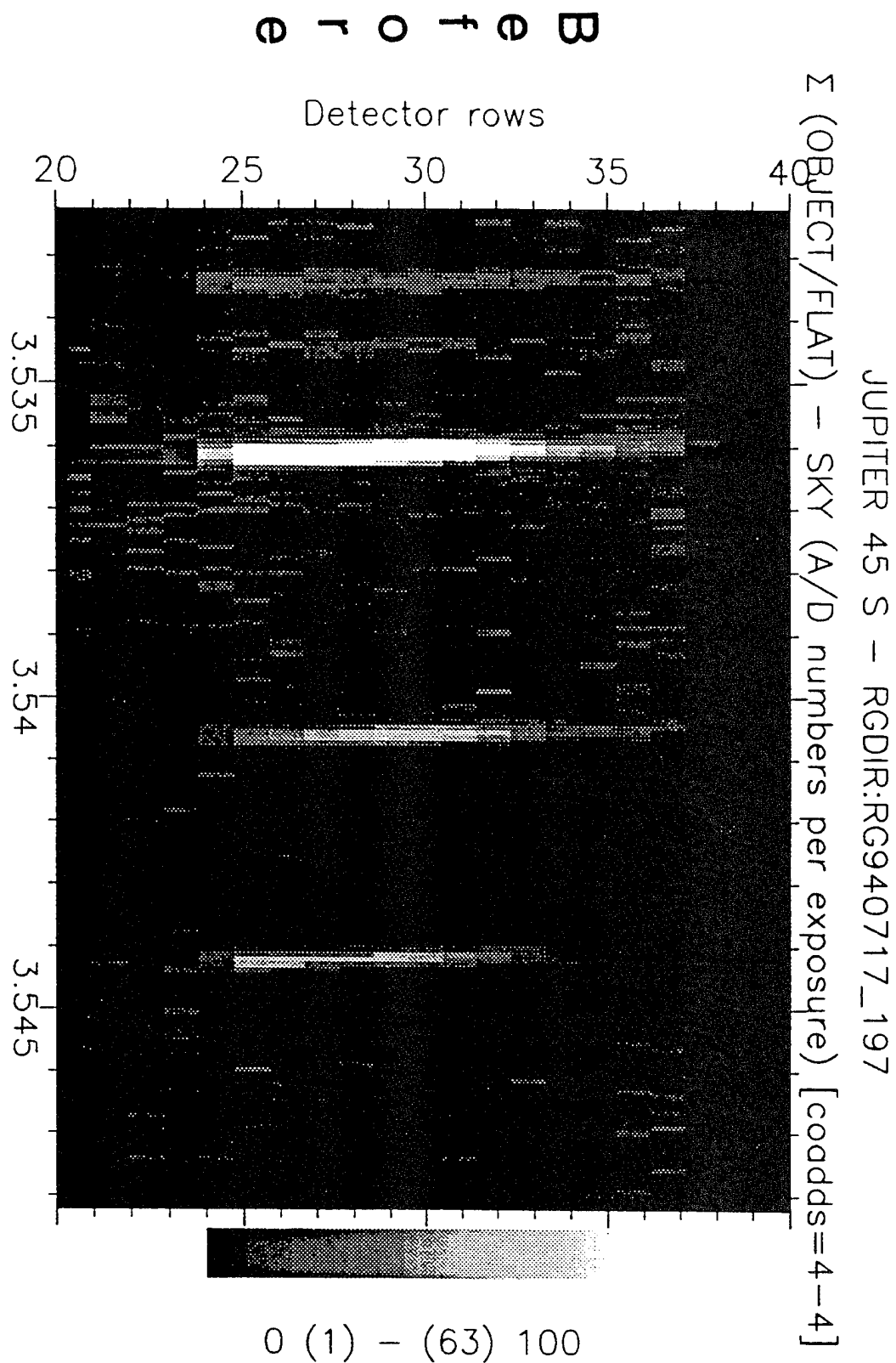
Figure 6. Jupiter's spectral image before the impact at time 6:54 U.T. The four spectral lines are due to H_3^+, the same lines as shown in Fig. 5. The vertical variable is positioned from east to west of Jupiter. Row 37 corresponds to the eastern edge and row 23 to the western edge. Each row corresponds approximately the distance of the radius of Earth.
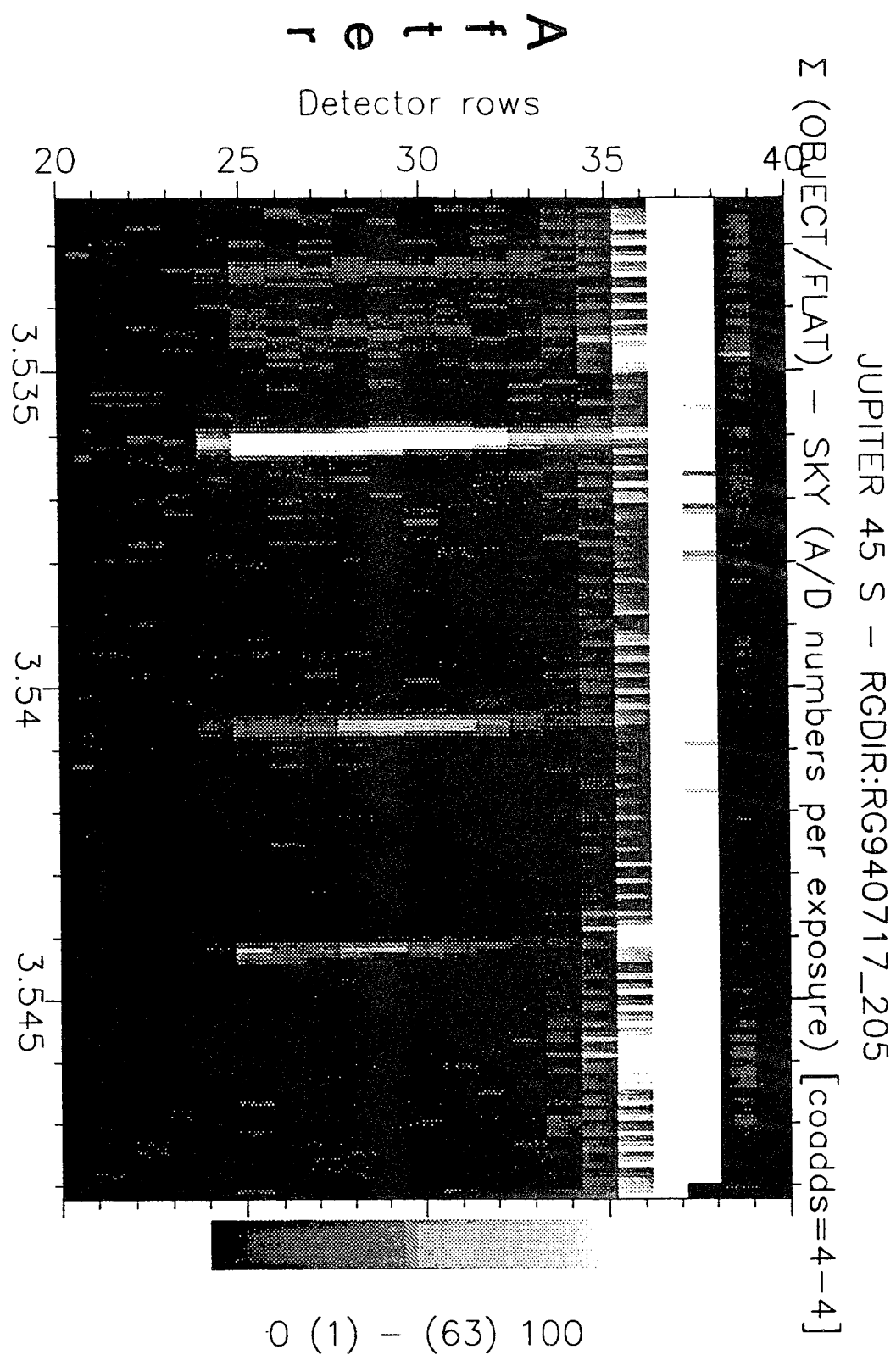
Figure 7. Jupiter's spectral image after the impact at time 7:19 U.T. Note the saturated rows 37 and 38, and the enormous number of spectral lines in rows 35 and 36.

FIGURE 8

H$_3^+$ Gets Excited by a Comet
Jupiter 45S row 0 17 July 1994 UT
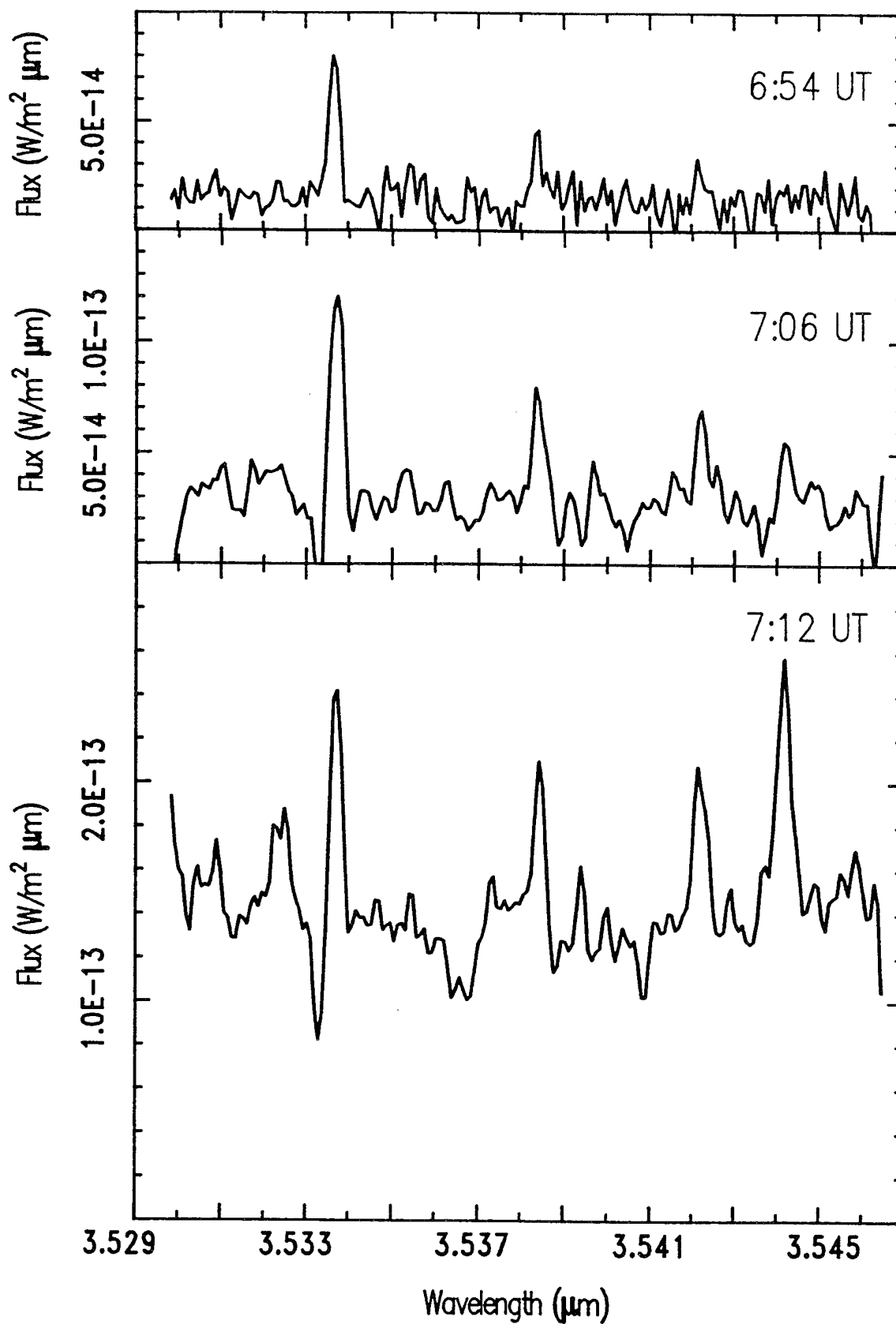
HEDM Contractors' Conference, Woods Hole, MA, 4-7 June 1995

IMPROVED METHODS FOR THE LARGE-SCALE SYNTHESIS OF 1,3,3-TRINITROAZETIDINE
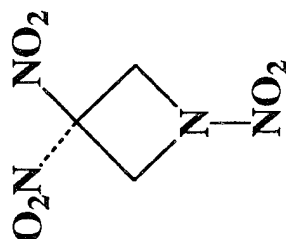
PART I: Additions of X-Y Across the C(3)-N σ-Bond in 1-Aza-3-ethylbicyclo-[1.1.0]butane. Novel Routes to 3-Substituted Azetidines

Alan P. Marchand*, D. Rajagopal, and Simon G. Bott*

PART II: A Novel Approach to the Synthesis of 1,3,3-Trinitroazetidine

Thomas G. Archibald*

Department of Chemistry, University of North Texas, Denton, Texas 76203-0068

Aerojet, Propulsion Division, P. O. Box 13222, Sacramento, California 95813-6000

Improved Routes for the Large-Scale Synthesis of 1,3,3-Trinitroazetidine

Alan P. Marchand*, D. Rajagopal, and Simon G. Bott*
Department of Chemistry, University of North Texas, Denton, Texas 76203-0068

Thomas G. Archibald*
Aerojet, Propulsion Division, P. O. Box 13222, Sacramento, California 95813-6000

LONG ABSTRACT

PART I. Additions of X-Y Across the C(3)-N σ-Bond in 1-Aza-3-ethylbicyclo-[1.1.0]butane. Novel Routes to 3-Substituted Azetidines

Figure 1.
Title Page

Figure 2.
Dintrogen tetroxide has been reported to add across carbon-carbon σ-bonds in highly strained carbocyclic systems to afford in each case the corresponding dinitroalicyclic compound.

Figure 3.
In connection with our interest in developing improved methods for the large-scale synthesis of 1,3,3-trinitroazetidine (TNAZ), we sought ways to add the elements of N_2O_4 across the C(3)-N σ-Bond in 1-azabicyclo[1.1.0]butane. The parent azabicyclobutane is not readily available; however, 3-ethyl-1-azabicyclo[1.1.0]butane, first prepared by Funke in 1969, is a stable compound which can be prepared readily and thus serves as a model compound for our study.

Figure 4.
3-Ethyl-1-azabicyclo[1.1.0]butane was synthesized in our laboratory by using a modification of the route described by Funke, W. *Chem. Ber.* **1969**, *102*, 3148.

Figure 5.
The reaction of 3-ethyl-1-azabicyclo[1.1.0]butane with N_2O_4 was studied under a variety of experimental conditions. The results of these studies are summarized herein. Although N_2O_4 adds smoothly across the highly strained C(3)-N σ-bond in this substrate, the data shown in this plate confirm the fact that this addition occurs in a manner that does not result in the introduction of both a new N-NO_2 and a new C-NO_2 into the resulting azetidine. (*Reference*: Marchand, A. P.; Rajagopal, D.; Bott, S. G.; Archibald, T. G. *J. Org. Chem.* **1994**, *59*, 1608.)

Figure 6.
X-ray crystal structure drawings of 3-ethyl-3-*O*-nitratoazetidinium nitrate and *N*-nitroso-3-*O*-nitratoazetidine.

Figure 7.
Reactions of 3-ethyl-1-azabicyclo[1.1.0]butane with a variety of electrophilic reagents were studied. Thus, the modes of the addition of ethyl chloroformate, methanesulfonic acid anhydride, and triflic anhydride to this substrate are shown herein.

Figure 8.

We utilized *N*-nitroso-3-ethyl-3-*O*-nitratoazetidine, the major product formed via reaction of 3-ethyl-1-azabicyclo[1.1.0]butane with N_2O_4, as starting material for the synthesis of *N*-nitro-3-ethyl-2-azetine. Interstingly, base promoted elimination of the elements of MsOH from *N*-nitro-3-ethyl-3-mesyloxyazetidine proceeds with exclusive formation of the azetidine. No trace of the corresponding 3-ethylidene isomer was detected among the reaction products. (*Reference*: Marchand, A. P.; Rajagopal, D.; Bott, S. G.; Archibald, T. G. *J. Org. Chem.* **1994**, *59*, 1608.)

Figure 9.

By way of contrast, we observed that the reaction of triflic anhydride (Tf_2O) with 3-ethyl-1-aza-bicyclo[1.1.0]butane produced exclusively *N*-[(trifluoromethane)sulfonyl]-3-ethylideneazetidine. Ozonolysis of this alkene afforded the corresponding ketone, which could be converted into the corresponding oxime. Reaction of this oxime with 100% HNO_3 in CH_2Cl_2 afforded two products: *N*-triflyl-3,3-dinitroazetidine (28%) and *N*-triflylazetidin-3-one (23%). (*Reference*: Marchand, A. P.; Rajagopal, D.; Bott, S. G.; Archibald, T. G. *J. Org. Chem.* **1994**, *59*, 5499.)

Figure 10.

X-ray crystal structure drawing of *N*-triflylazetidin-3-one oxime.

Figure 11.

X-ray crystal structure drawing of *N*-triflyl-3,3-dinitroazetidine.

Figure 12.

More recently, we have studied the reactions of 3-ethyl-1-azabicyclo[1.1.0]butane with NaN_3-$NaNO_2$, with NaN_3-$ClCO_2Et$, and with aqueous $NaNO_2$-HCl. The first reaction resulted in the formation of *N*-nitroso-3-azido-3-ethylazetidine. The second reaction afforded N-carboethoxy-3-azido-3-ethylazetidine, while the third reaction produced *N*-nitroso-3-ethyl-3-nitroazetidine. Subsequent oxidation of *N*-nitroso-3-ethyl-3-nitroazetidine afforded *N*,3-dinitro-3-ethylazetidine, thus pointing the way for a novel approach to the synthesis of TNAZ. (*Reference*: Marchand, A. P.; Rajagopal, D.; Bott, S. G.; Archibald, T. G. *J. Org. Chem.* **1994**, *59*, 5499.)

Figure 13.

N-Nitro3-ethylideneazetidine was prepared in two ways. First, this compound was obtained in 40% yield via reaction of 3-ethyl-1-azabicyclo[1.1.0]butane with $(n\text{-Bu})_4N^+$ NO_3^- and Tf_2O. In addition, it could be prepared via reaction of *N*-nitro-3-ethylazetidin-3-ol with Tf_2O in the presence of tertiary amines. Subsequent ozonolysis of *N*-Nitro3-ethylideneazetidine afforded *N*-nitroazetidin-3-one, which is of interest as a potential precursor to TNAZ. (*Reference*: Marchand, A. P.; Rajagopal, D.; Bott, S. G.; Archibald, T. G. *J. Org. Chem.* **1994**, *59*, 5499.)

Figure 14.

Summary of Part 1.

Part 2. A Novel Approach to the Synthesis of 1,3,3-Trinitroazetidine (TNAZ)

Figure 15.

Title page and Abstract.

Figure 16.

Success in completing the model study through which 3-ethyl-1-azabicyclo[1.1.0]butane was converted into N,3-dinitro-3-ethylazetidine pointed the way toward a novel TNAZ synthesis. The key step in this new approach, shown herein, involves the formation of 1-azabicyclo-[1.1.0]butane, which is removed rapidly from the reaction medium via azeotropic distillation. This unstable intermediate is trapped *in situ* in the distillation receiver via its reaction with aqueous $NaNO_2$-HCl, thereby affording N-nitroso-3-nitroazetidine in low yield.

Figure 17.

Two potentially serious limitations to the use of this approach are noted.

Figure 18.

In an attempt to address the issues raised in Figure 16, we studied an alternative reaction sequence which preserves the unique approach of formation and trapping of an intermediate 1-azabicyclo[1.1.0]butane. Thus, 1-aza-3-(bromomethyl)bicyclo[1.1.0]butane was generated and subsequently trapped by *in situ* generated HNO_2. Application of this procedure results in the formation of two N-nitrosoazetidines, **14** and **15** (see Figure 17), each of which was oxidized subsequently to the corresponding N-nitro derivative (i.e., **16** and **17**, respectively). Hydrolysis of **17** produced the corresponding alcohol, **18**, in good yield. Finally, under the reaction conditions shown herein, **18** underwent retro-Henry reaction, and the resulting α-nitro anion subequently suffered oxidative nitration *in situ*, thereby affording TNAZ (37% yield from **18**).

Figure 19.

Work in progress during Spring, 1995 includes the formation of N-substituted 3-bromo-3-nitro-azetidines and their subsequent reductive dimerization. Ultimately, we hope to be able to convert this compound into N,3-dinitro-3-(N',3'-dinitroazetidinyl)azetidine and related compounds. (*Reference:* Archibald, T. G.; Marchand, A. P.; Sharma, G. V. M., unpublished.)

Figure 20.

Finally, we hope to be able to synthesize N,3-dinitro-2-azetine and a dimeric analog of this compound, both of which are of interest as starting materials for preparing more highly nitrated analogs of TNAZ. (*Reference:* Archibald, T. G.; Marchand, A. P.; Sharma, G. V. M., unpublished.)

Figure 21.

Acknowledgment.

Addition of N_2O_4 to strained carbon-carbon σ-bonds has been performed successfully in highly strained carbocyclic systems:
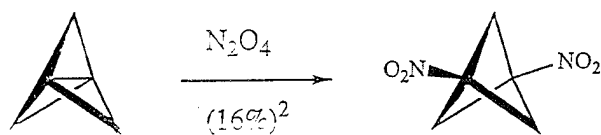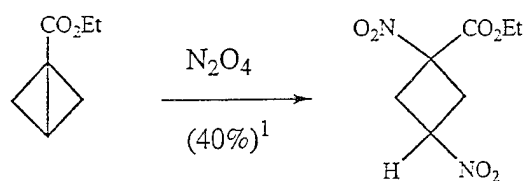
Literature Cited:

1. Archibald, T. G.; Garver, L. C.; Baum, K.; Cohen, M. C.
J. Org. Chem. 1989, *54*, 2869.

2. Wiberg, K. B.; Ross, B. S.; Isbell, J. J.; McMurdie, N.
J. Org. Chem. 1993, *58*, 1372.

FIGURE 2

FIGURE 3

142
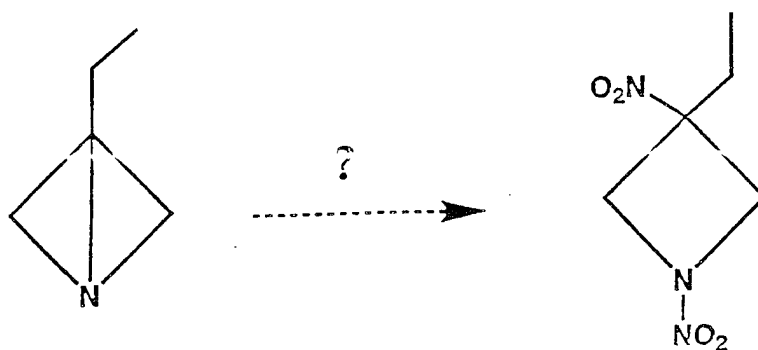
SYNTHESIS OF 3-ETHYL-1-AZABICYCLO[1.1.0]BUTANE

HBr-HOAc
sealed tube
170 °C, 12 h
(73%)

KOH
tetraethylene glycol
220 °C, 1 h (79%)

^{13}C NMR (CDCl$_3$) δ 9.68 (q), 20.26 (t), 31.02 (s), 52.86 (t)
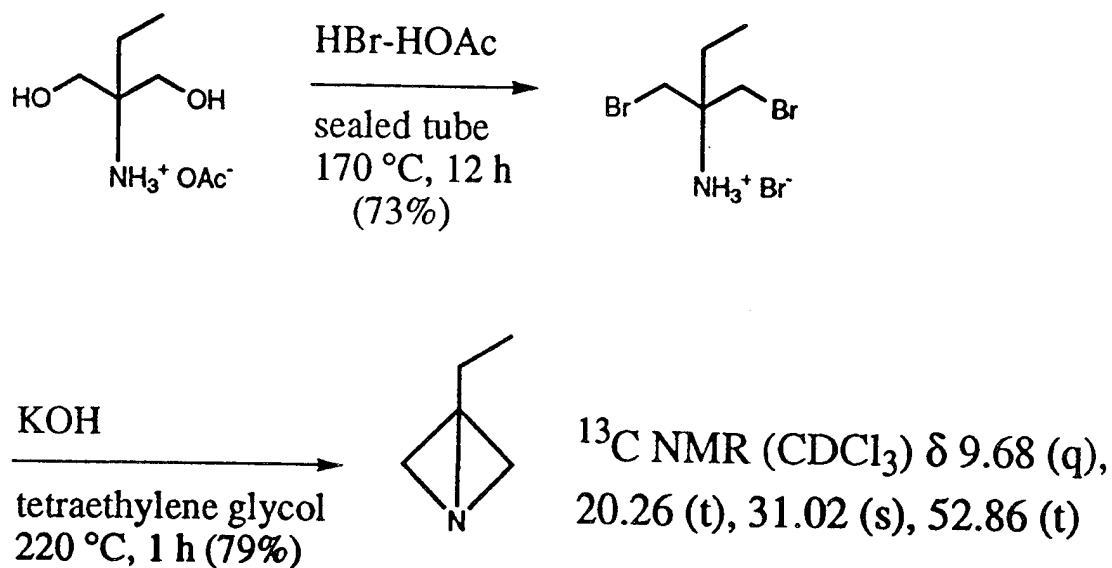
Synthesis: Dr. Alan P. Marchand, Dr. D. Rajagopal
Department of Chemistry, University of North Texas

Reference: Funke, W. *Chem. Ber.* **1969**, *102*, 3148.

FIGURE 4

Results

	1	2	3	4
1. Et$_2$O : THF : Pentane (1:1:1), -50°C, Ar Non aqueousworkup	30 %	23 %	----	----
2. CH$_2$Cl$_2$, 0°C, Ar	----	70 %	----	----
3. Et$_2$O, 0°C, Ar	----	72 %	----	----
4. CH$_2$Cl$_2$, 0°C, Atmospheric Oxygen	----	36 %	----	4%
5. Et$_2$O, 0°C, hν, 450 W Hg lamp	----	20 %	21 %	----
6. Et$_2$O, 0°C, O$_2$ Bubbling	----	68 %	----	----
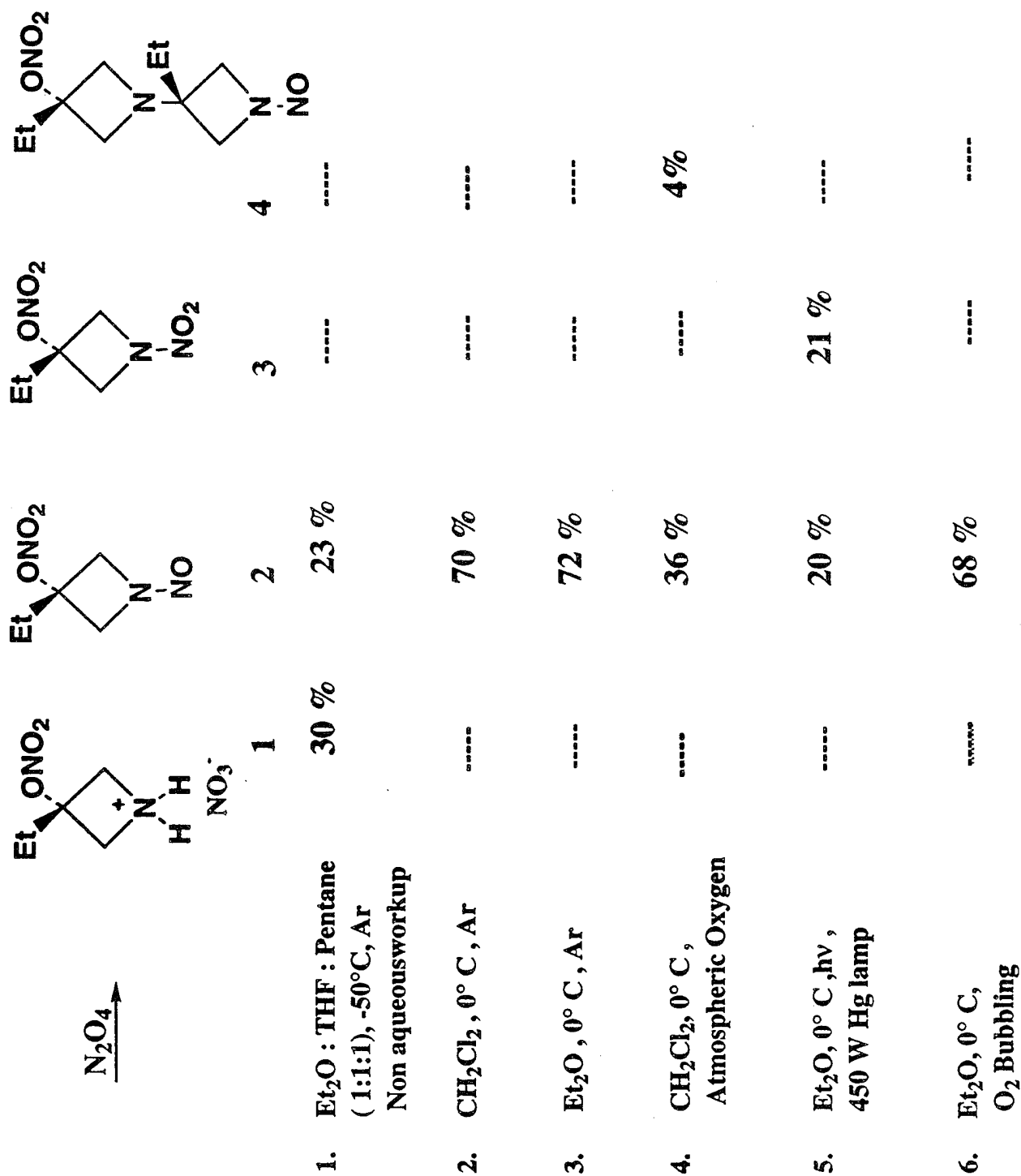
FIGURE 5

X-RAY CRYSTAL STRUCTURES
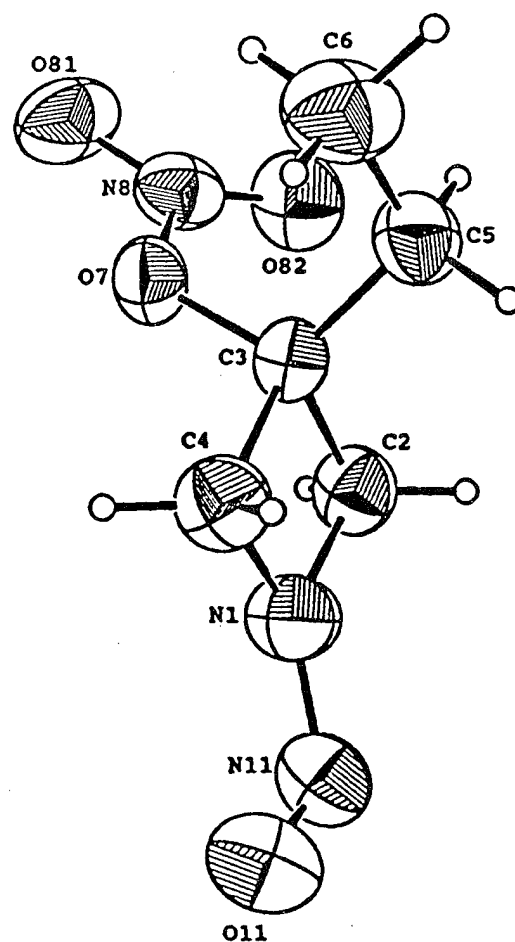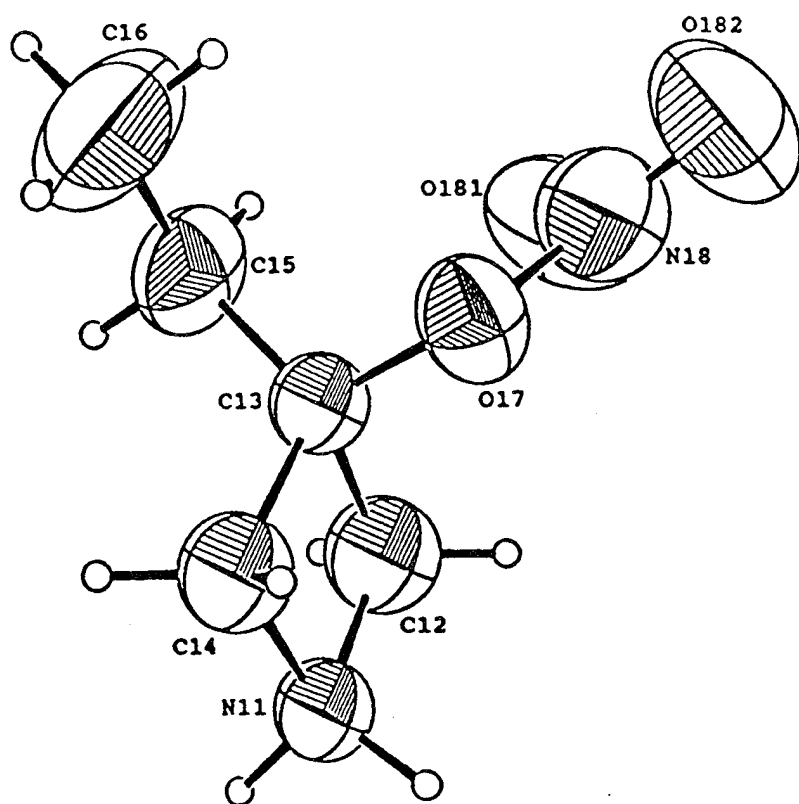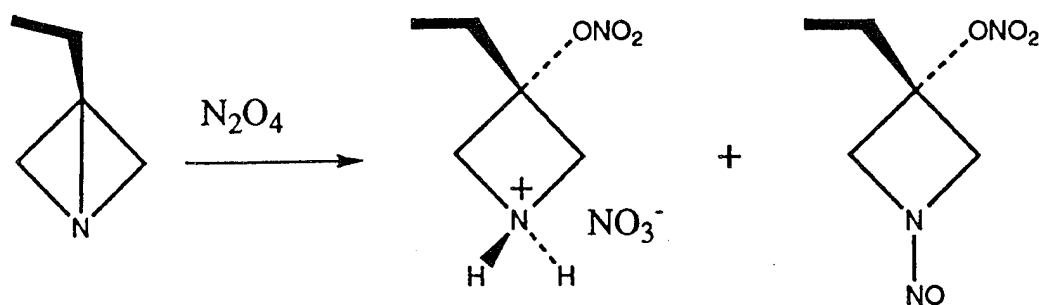
Synthesis: Prof. Alan P. Marchand, Dr. D. Rajagopal
X-ray Structures: Professor Simon G. Bott
Department of Chemistry University of North Texas

FIGURE 6   145

Scheme 2
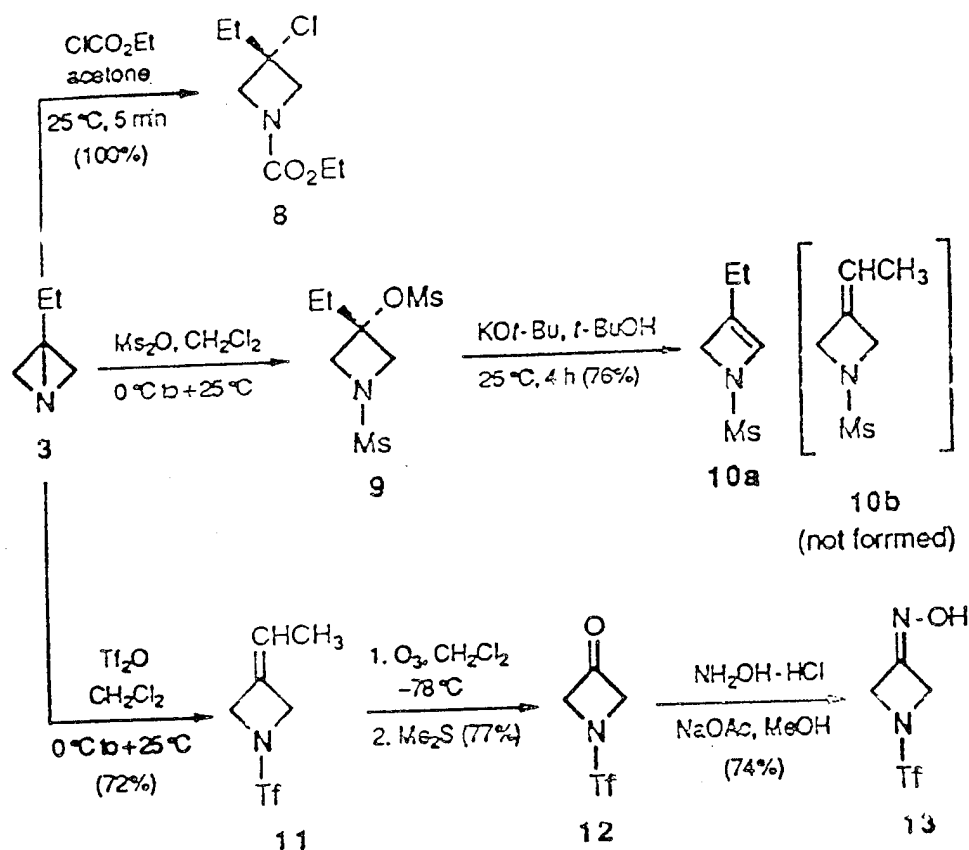
FIGURE 7

Synthesis of *N*-Nitro-3-ethyl-2-azetine

Synthesis: Dr. D. Rajagopal, *UNT Chemistry*

FIGURE 8   146
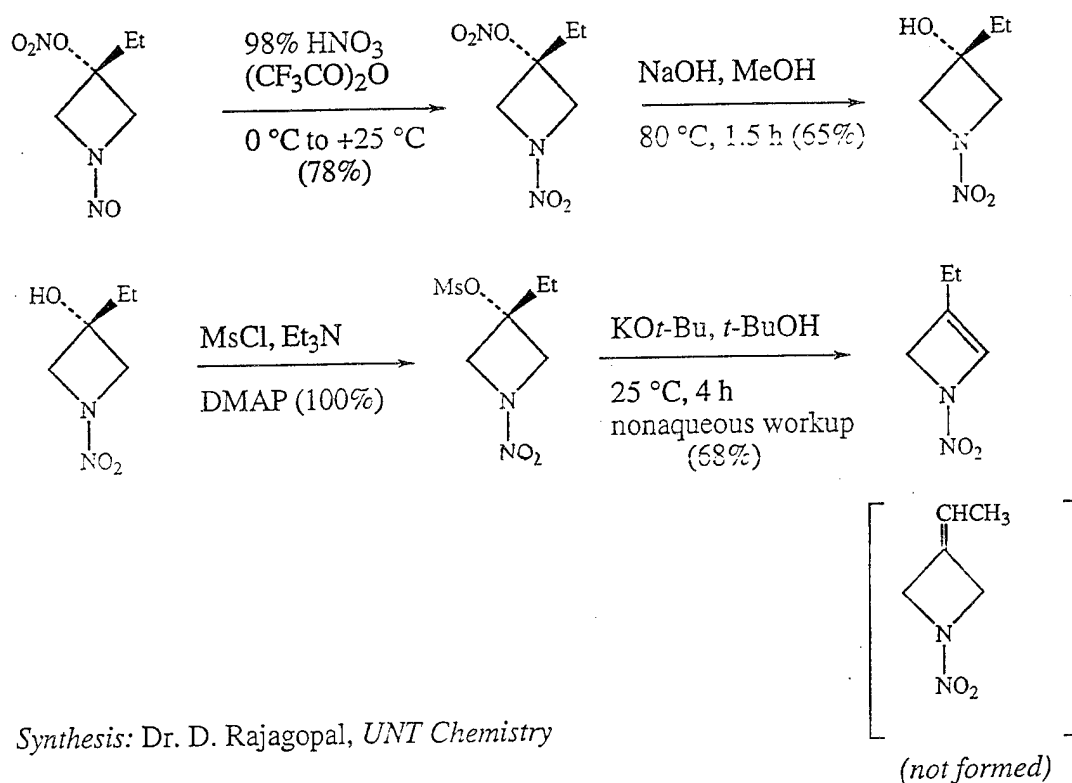
Synthesis of N-[(Trifluoromethane)sulfonyl]-3,3,-dinitroazaetidine

Synthesis: Dr. D. Rajagopal, UNT Chemistry

FIGURE 9

Synthesis:
Dr. D. Rajagopal

X-ray Structure:
Professor Simon G. Bott
Department of Chemistry
University of North Texas

FIGURE 10

147
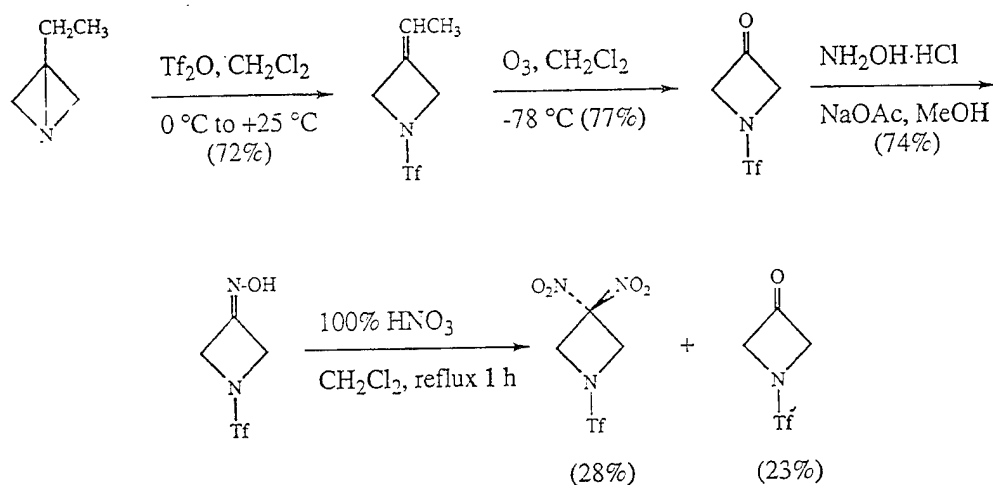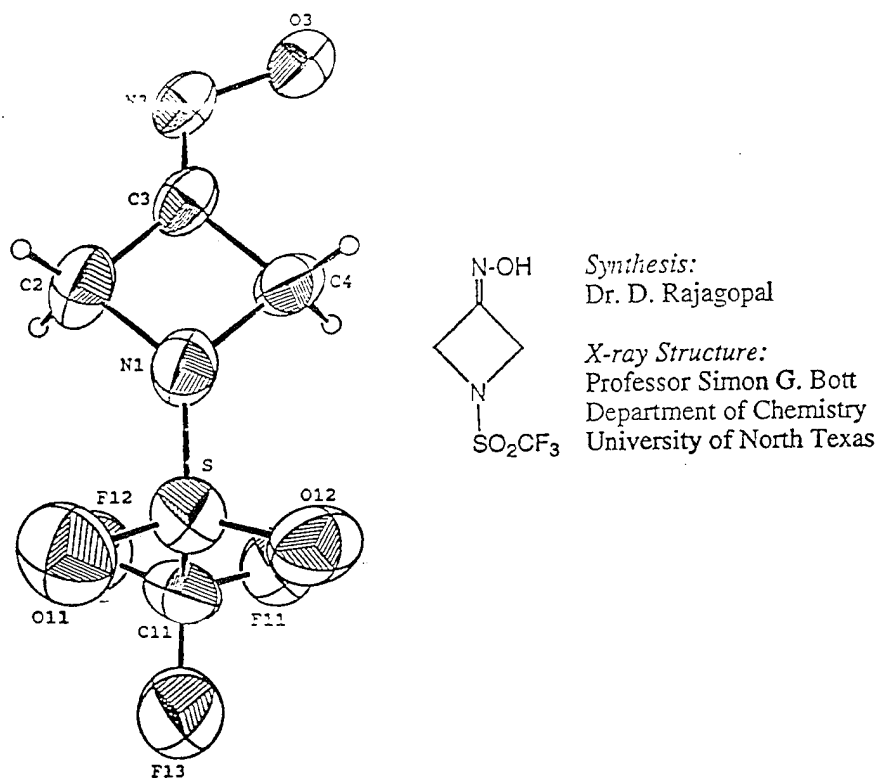
X-ray Crystal Structure of

N-Trifluoromethanesulfonyl-3,3-dinitroazetidine
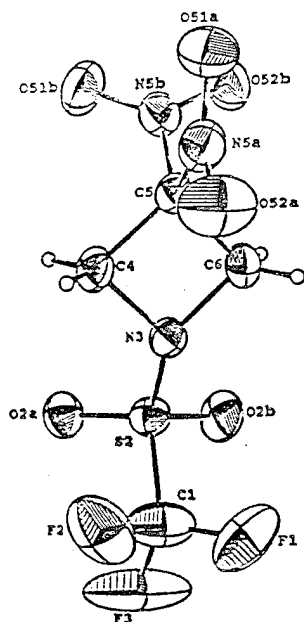
Synthesis:

X-ray Crystallography

Dr. D. Rajagopal

Professor Simon G. Bott
Department of Chemistry
University of North Texas
Denton, TX 76203-0068

FIGURE 11

Scheme 1
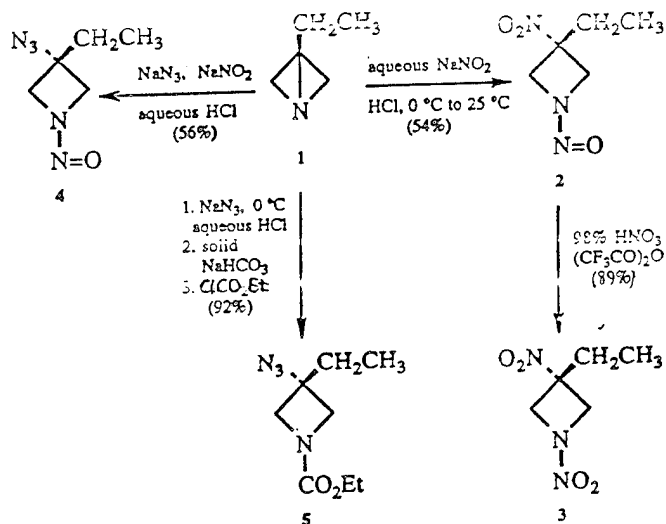
FIGURE 12

Scheme 2
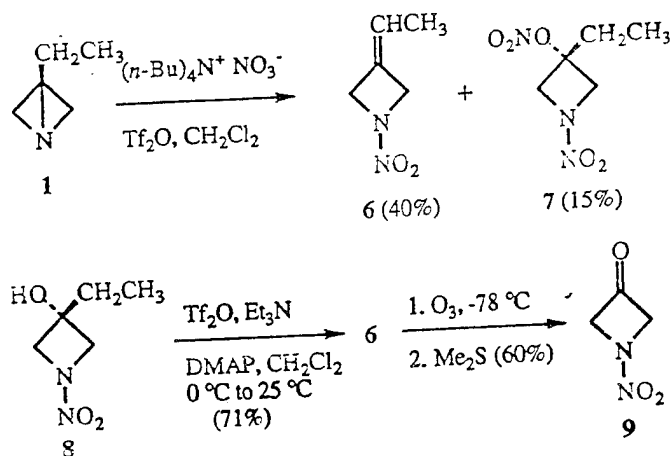
FIGURE 13

SUMMARY AND CONCLUSIONS

1-Aza-3-ethylbicyclo[1.1.0]butane (**1**) reacts with a variety of reagents, X-Y, to form products which result via addition across the highly strained C(3)-N σ-bond in the substrate.

X = NO$^+$, Y = N$_3^-$

X = NO$^+$, Y = NO$_2^-$

X = CO$_2$Et (from ClCO$_2$Et, Y = N$_3^-$

X = NO$_2^+$, Y = OTf
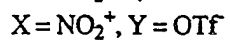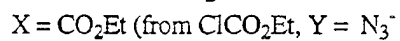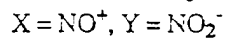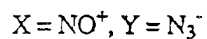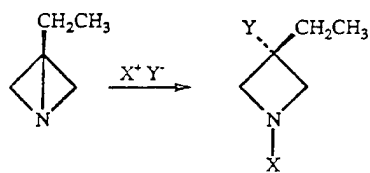
FIGURE 14

A Novel Approach to the Synthesis of 1,3,3-Trinitroazetidine

Alan P. Marchand*, D. Rajagopal, and Simon G. Bott*

Department of Chemistry, University of North Texas, Denton, Texas 76203-0068

Thomas G. Archibald*

Aerojet, Propulsion Division, P. O. Box 13222, Sacramento, California 95813-6000

ABSTRACT

Two novel syntheses of 1,3,3-trinitroazetidine (TNAZ, 1) are reported herein. A key step in each synthesis involves electrophilic addition of the elements of N_2O_3 (as NO^+ NO_2^-) across the highly strained C(3)-N σ-bond in a 1-azabicyclo[1.1.0]butane. Thus, 1-azabicyclo[1.1.0]butane (8) was generated and trapped *in situ* by $NaNO_2$-aqueous HCl, thereby affording N-nitroso-3-nitroazetidine (9) in low yield. Oxidation of 9 to N,3-dinitroazetidine (10, 72%) followed by oxidative nitration of 10 gave 1(40%). Similarly, 1-aza-3-(bromomethyl)bicyclo[1.1.0]butane (13) was generated and trapped *in situ* by $NaNO_2$-aqueous HCl to produce N-nitroso-3-nitro-3-bromomethylazetidine (14, 10%) along with N-nitroso-3-hydroxy-3-bromomethylazetidine (15, 3%). Subsequent oxidation of 14 to the corresponding dinitroazetidine, 17 (81%), followed by hydrolysis of the CH_2Br group therein produced N,3-dinitro-3-hydroxymethylazetidine (18, 78%). Finally, treatment of 18 with $NaNO_2$-$K_2S_2O_8$-$K_3Fe(CN)_6$ in the presence of base afforded 1 (37%).

Introduction. 1,3,3-Trinitroazetidine (TNAZ, 1) has received attention in recent years as a new energetic material that is of considerable interest to U. S. Military agencies.[1-4] Previously reported routes for synthesizing 1 generally proceed via intermediate N,3-substituted azetidines, which in each case requires subsequent conversion of the various substituents to $C(NO_2)_2$ groups. We now report a novel approach to the synthesis of 1 which involves electrophilic addition of NO^+ NO_2^- across the highly strained C(3)-N σ-bond in 1-azabicyclo[1.1.0]butane and in 3-(bromomethyl)-1-azabicyclo-[1.1.0]butane.

In 1969, Funke reported the synthesis of substituted 1-azabicyclo[1.1.0]butanes and some aspects of their chemistry.[5] Since that time, relatively little interest has been shown in this unusual ring system. Recently,[6] we investigated reactions of 2 with a variety of electrophiles, e.g., N_2O_4, $ClCO_2Et$, Tf_2O, and Ms_2O. In each case, the observed reaction product(s) resulted via addition of the reagent, X-Y, across the highly strained C(3)-N σ-bond in the substrate, thereby affording new N-,3-disubstituted azetidines. In the present study, we have used this approach to synthesize N-NO- and C-NO_2- containing intermediates which serve as useful synthetic precursors to 1.

Results and Discussion. Compound 2, synthesized by using a previously published modification[6] of a literature procedure,[5] was employed as substrate in a model study.[6b] In our hands, reaction of 2 with *in situ* generated aqueous HNO_2 resulted in addition of the elements of HNO_2 across the C(3)-N σ-bond with concomitant N-nitrosation of the resulting intermediate azetidine, thereby affording 3 (54% yield, Scheme 1). Subsequent oxidation of the N-NO functionality by using 98% HNO_3-$(CF_3CO)_2O$ afforded the corresponding N-nitramine (4, 89% yield).[6b]

Scheme 1
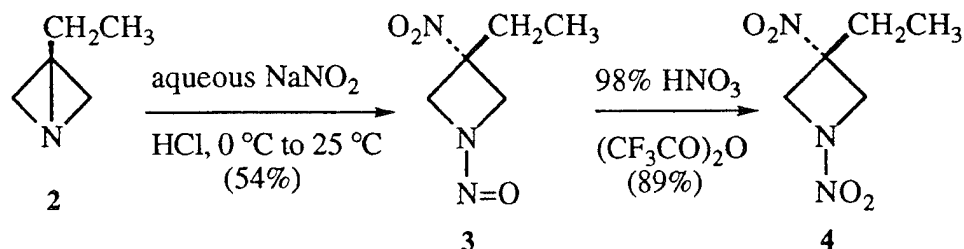
Our success in achieving the synthesis of **4** via the route shown in Scheme 1 pointed the way toward a novel TNAZ synthesis. The key step in this synthesis, shown in Scheme 2, is the formation of 1-azabicyclo[1.1.0]butane, **8**, which is removed rapidly from the reaction medium via azeotropic distillation and is trapped *in situ* in the distillation receiver via its reaction with aqueous $NaNO_2$-HCl, thereby affording *N*-nitroso-3-nitroazetidine (**9**) in low yield. The method by which **9** is converted subsequently into **1** is outlined in Scheme 2. The structure of 1,3-dinitroazetidine (**10**), an intermediate in the conversion of **9** to **1**, was established unequivocally via application of X-ray crystallographic methods. It should be noted that the formation and trapping of **8**, the key intermediate in the reaction sequence shown in Scheme 2, proceeds in poor yield (*ca.* 1%). In addition, the starting material, 2-amino-1,3-propanediol (**5**), although available commercially, nevertheless is very expensive.

Scheme 2
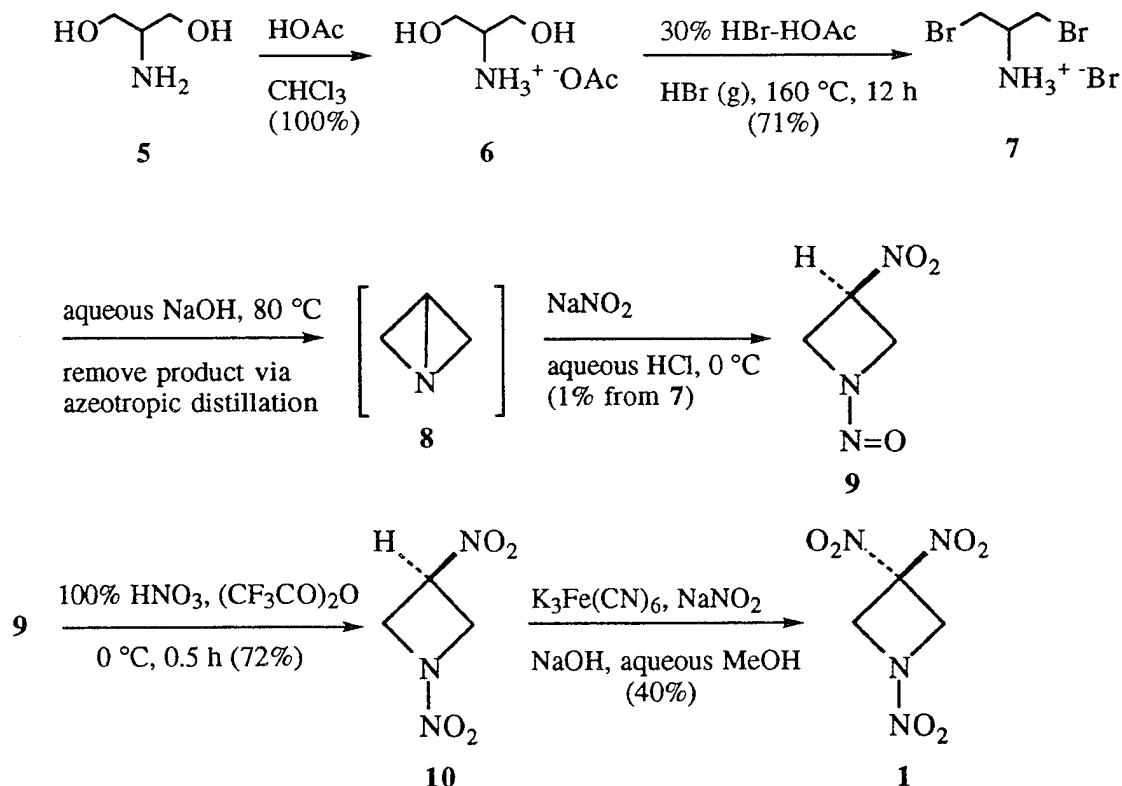
In attempting to address these issues, we studied an alternative reaction sequence which like the method shown in Scheme 2 preserves the unique approach of formation and trapping of an intermediate 1-azabicyclo-[1.1.0]butane. Pertinent results in this regard are outlined in Scheme 3. Thus, 1-aza-3-(bromomethyl)-bicyclo[1.1.0]butane (13) is generated by the method shown in Scheme 3 and subsequently is trapped by *in situ* generated HNO_2. This results in the formation of two *N*-nitrosoazetidines, 14 and 15, each of which was oxidized[6b,7] subsequently to the corresponding *N*-nitro derivative (i.e., 16 and 17, respectively). The structures of 16 and 17 have been established unequivocally via application of X-ray crystallographic methods. Hydrolysis[8] of 17 produced the corresponding alcohol, 18, in good yield. Finally, under the reaction conditions shown in Scheme 3,[1] 18 undergoes retro-Henry reaction,[9] and the resulting α-nitro anion subsequently suffers oxidative nitration *in situ*, thereby affording 1 (37% yield from 18).

Scheme 3
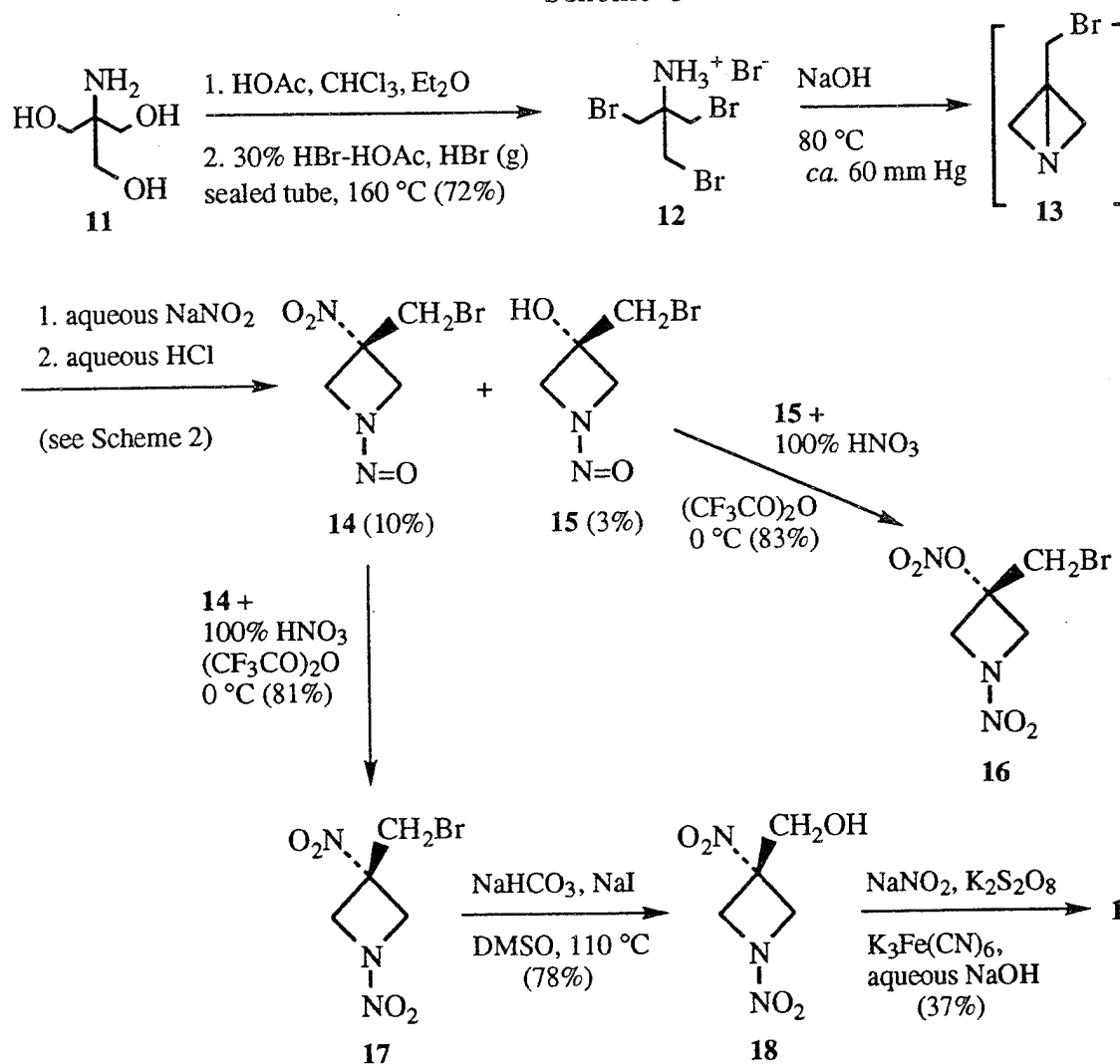
Some important features of the reaction sequence shown in Scheme 3 should be noted. Thus, formation and trapping of the key intermediate in this reaction sequence, i.e., **13**, proceeds in *ca.* 7% overall yield from the starting material, a significant improvement in yield *vis-à-vis* that of the corresponding reaction sequence shown in Scheme 2. In addition, the route shown in Scheme 3 offers the distinct advantage that the 3-bromomethyl functionality in **17** can easily be replaced by NO_2 via a two-step reaction sequence that employs the retro-Henry reaction with concomitant oxidative nitration of a carbanionic intermediate. Finally, in contrast to the prohibitively high cost of **5** (Scheme 2), the starting material for the reaction sequence shown in Scheme 3 [i.e., tris(hydroxymethyl)aminomethane, **11**] is relatively inexpensive. We are continuing to pursue new high-yield routes to appropriately functionalized 1-azabicyclo[1.1.0]butanes and to study the chemistry of these new systems as a potentially important class of alkylating agents.

Experimental Section

Melting points are uncorrected. Elemental microanalyses were performed by M-H-W Laboratories, Phoenix, AZ. Compounds **5** and **11** were purchased from the Aldrich Chemical Co. and used as obtained, without further purification.

1,3-Dibromo-2-ammonium Bromide (7). To a solution of 2-amino-1,3-propanediol (**5**, 20.0 g, 0.219 mol) in warm $CHCl_3$ (400 mL) was added dropwise with stirring glacial HOAc (60.0 g, 1.0 mol), and the resulting mixture was stirred at ambient temperature for 1 h. The reaction mixture was diluted with Et_2O (500 mL), and the resulting mixture was cooled to 5 °C by application of an external ice-water bath for 2 h. During this time, a colorless solid slowly precipitated from solution. This solid was collected by filtration, and the residue was washed with Et_2O (3 x 100 mL). The residue was dried thoroughly *in vacuo*, thereby affording 1,3-dihydroxypropyl-2-ammonium acetate (**6**, 33.0 g, 100%): mp 64-66 °C. This material was used as obtained in the next step without further purification.

Compound **6** (10.0 g, 11.2 mmol) was dissolved in a solution of 30% HBr-HOAc (50 mL), and the resulting solution was cooled to 5 °C via application of an external ice-water bath. Dry HBr gas was passed into this cooled solution until the reaction mixture had become saturated with HBr. The resulting thick syrup was heated in a sealed tube at 160 °C for 12 h. The reaction mixture was allowed to cool slowly to room temperature and then was diluted with MeOH (200 mL). The resulting solution was concentrated *in vacuo*. The residue was dissolved in MeOH (100 mL), and the resulting solution was clarified with Norite and then filtered. The filtrate was concentrated *in vacuo*, thereby affording a thick syrup which solidified upon prolonged drying under high vacuum. Compound **7** (13.4 g, 71%) was thereby obatined as a colorless microcrystalline solid: mp 157-159 °C (lit.[5b] mp 158-159 °C).

N-Nitroso-3-nitroazetidine (9). A 1000 mL round-bottom flask was fitted with an addition funnel, a distillation condenser and a receiver. The reaction vessel was charged with a solution of NaOH (80.0 g, 2.0 mol) in water (400 mL), and the resulting solution was heated to 80°C (internal reaction temperature). To this hot solution was added a solution of **7** (40.0 g, 0.13 mol) in water (80 mL) dropwise during 45 minutes. The reaction product was removed continuously during this period

via azeotropic distillation with water at reduced pressure (60 mm Hg, water aspirator). An aqueous solution of **8** distilled over continuously and was collected in a receiver that was maintained at -78 °C by application of an external dry ice-acetone bath. The water distillation process was continued for 30 minutes after the addition of **7** had been completed. A total of 3 mL of distillate was thereby collected. Water (5 mL) was added to the distillate followed by addition of $NaNO_2$ (2.07 g, 30.0 mmol). The resulting mixture was cooled to 0 °C via application of an external ice-water bath. Concentrated aqueous HCl (3 mL) was added dropwise with stirring to the cold reaction mixture, and the resulting mixture was stirred at 0 °C for 10 minutes. An additional quantity (5 mL) of concentrated aqueous HCl was added dropwise, and the resulting mixture was stirred at 0 °C for 30 minutes. Water (25 mL) was added, and the resulting suspension was extracted with EtOAc (3 x 15 mL). The organic layer was washed sequentially with 10 % aq $NaHCO_3$ (25 mL), water (25 mL) and brine (25 mL). The organic layer was dried (Na_2SO_4) and filtered, and the filtrate was concentrated *in vacuo*. The residue, a pale yellow oil, was purified by column chromatography on silica gel by eluting with 10% EtOAc-hexane. Pure **9** (168 mg, 0.96 %) was obtained as a pale yellow microcrystalline solid: mp 77-78°C ; IR (KBr) 2992 (w), 2902 (w), 1555 (s), 1370 (vs), 1301 (vs), 1159 (sh, m), 831 cm^{-1} (w) ; ^1H NMR ($CDCl_3$) δ 4.56 (d, J = 4.0 Hz, 2 H), 5.30-5.42 (m. 3 H); ^{13}C NMR ($CDCl_3$) δ 57.35 (t), 59.25 (t), 70.93 (d). Anal. Calcd for $C_3H_5N_3O_3$: C, 27.49; H, 3.84. Found: C, 27.25; H, 4.00.

1,3-Dinitroazetidine (10). A mixture of trifluoroacetic anhydride (500 mg, 2.4 mmol) and 100% HNO_3 (500 mg, 7.9 mmol, freshly prepared[7] via distillation from a 1:1 mixture of concentrated H_2SO_4 and fuming HNO_3) was cooled to 0 °C via application of an external ice-water bath. To this cooled solution was added with stirring **9** (50 mg, 0.38 mmol) in one portion. The resulting mixture was stirred at 0 °C for 30 minutes. The reaction mixture then was poured over crushed ice (20 g), and the resulting aqueous suspension was extracted with EtOAc (3 x 15 mL). The combined extracts were washed sequentially with water (30 mL), 10% aqueous $NaHCO_3$ (25 mL) and brine (25 mL). The organic layer was dried (Na_2SO_4) and filtered, and the filtrate was concentrated *in vacuo*. The residue, a pale yellow oil, was purified via column chromatography on silica gel by eluting with 10% EtOAc-hexane. Pure **10** (40 mg, 72%) was thereby obtained as a colorless microcrystalline solid: mp 62-63° C; IR (KBr) 1631 (sh, m), 1558 (vs), 1372 (s), 1323 (s), 1264 (s), 1216 (m), 1157 (m), 991 (w), 854 cm^{-1} (w) cm^{-1}; ^1H NMR ($CDCl_3$) δ 4.70 (m, 4 H), 5.08-5.24 (m, 1 H); ^{13}C NMR ($CDCl_3$) δ 60.56 (t), 68.70 (d). Anal. Calcd for $C_3H_5N_3O_4$: C, 24.50; H, 3.43. Found: C, 24.43; H, 3.25. The structure of **10** was established unequivocally via single crystal X-ray structural analysis (*vide infra*).

Oxidative Nitration of 10.[10] To a stirred solution of NaOH (16 mg, 0.34 mmol) in 40% aqueous MeOH (4.5 mL) was added **10** (50 mg, 0.32 mmol), and the resulting solution was stirred at ambient temperature for 30 minutes. This solution was added rapidly with stirring to a mixture of $K_3Fe(CN)_6$ (520 mg, 0.32 mmol), $NaNO_2$ (220 mg, 3.2 mmol), water (5 mL) and Et_2O (25 mL). Stirring was continued for 30 minutes after the addition of these reagents had been completed. The layers then were separated, and the aqueous layer was extracted with CH_2Cl_2 (3 x 10 mL). The

combined extracts were washed sequentially with water (25 mL) and brine (25 mL). The organic layer was dried (Na$_2$SO$_4$) and filtered, and the filtrate was concentrated *in vacuo*. The residue thereby obtained was placed onto a small pad of silica gel and eluted with 25% EtOAc-hexane, thereby affording **1** (25 mg, 40%) as a colorless waxy solid: mp 97-100 °C (lit.[1] mp 103-104 °C); ^{1}H NMR (CDCl$_3$): δ 5.20 (s, 4 H).

Tris(bromomethyl)aminomethane Hydrobromide (12). A solution of tris(hydroxymethyl) aminomethane (**11**, 60.5 g, 0.5 mol) in CHCl$_3$ (500 mL) was cooled to 5°C by application of an external ice-water bath. To this cooled solution was added portionwise with stirring glacial HOAc (120 g, 2.0 mmol). After the addition of HOAc had been completed, the external cold bath was removed, and the stirred reaction mixture was allowed to warm gradually to room temperature during 2.5 h. Diethyl ether (300 mL) was added, and the resuting mixture was filtered. The residue was washed with Et$_2$O (3 x 100 mL) and then dried *in vacuo*. The product, (HOCH$_2$)$_3$C-NH$_3$$^+$ $^-$OAc (90.5 g, 100%), was thereby obtained as a colorless microcrystalline solid: mp 117-118 °C. This material was used as obtained in the next synthetic step.

A suspension of this salt (40 g, 0.22 mol) in 30% HBr-HOAc (175 mL, excess) was cooled to 10°C by application of an external ice-water bath. Dry HBr gas was passed into this cooled suspension until the reaction mixture had become saturated with HBr. The resulting thick, syrupy suspension was divided into two equal portions, and each portion (*ca.* 90 mL) was placed in a sealed tube (capacity 180 mL) and heated at 160°C for 12 h. The reaction vessels were cooled to room temperature and then opened. The contents of the two reaction vessels were poured into EtOAc (300 mL). The resulting suspension was filtered, and the residue was washed sequentially with EtOAc (100 mL) and Et$_2$O (2 x 100 mL) and then dried *in vacuo*. Compound **12** (62.3 g, 72%) was thereby obtained as a colorless microcrystalline solid: mp 256-257°C; IR (KBr) 3226-2477 (br, s), 1567 (m), 1508 (m), 1420 (m), 1274 cm^{-1} (m); ^{1}H NMR (DMSO-d_6) δ 3.85 (s, 6 H), 4.62 (br s, 3 H); ^{13}C NMR (DMSO-d_6) δ 33.43 (t), 57.53 (s); Anal. Calcd for C$_4$H$_9$NBr$_4$: C 12.30, H 2.32; Found C 12.24, H 2.34.

Generation and Trapping of 3-(Bromomethyl)-1-azabicyclo[1.1.0]butane (13).[6b] A solution of NaOH (80.0 g, 2.0 mol) in water (400 mL) was placed in a 1000 mL 3-neck round-bottom flask. The reaction vessel was fitted with a pressure-equalized dropping funnel and a distillation condenser, and the reaction vessel was connected to a water aspirator. A solution of **12** (39.0 g, 0.10 mol) in 1% aqueous NaHCO$_3$ (100 mL) was placed in the dropping funnel, and the reaction vessel was evacuated to *ca.* 60 mm Hg. The reaction vessel then was heated to 80 °C. The contents of the dropping funnel were added dropwise to the reaction mixture during 45 minutes. During this time, the product which distilled from the reaction mixture was collected in a receiving flask that was cooled externally to -78°C. After the addition of **12** had been completed, the distillation was continued for an additional 2 h. The flask which contained the distillate (250 mL) was removed from the cold bath and allowed to warm gradually to room temperature. Solid NaNO$_2$ (69.0 g, 1.0 mol) was added to the distillate, and the resulting aqueous mixture was cooled in an external ice-water bath. To this cooled

155

mixture was added dropwise with stirring 50% aqueous HCl. After the addition of aqueous HCl had been completed, the resulting mixture was stirred for an additional 30 minutes. The reaction mixture then was poured over crushed ice (250 g), and the resulting slurry was extracted with EtOAc (3 x 50 mL). The combined organic extracts were washed sequentially with water (100 mL) and brine (100 mL), dried (Na_2SO_4) and filtered, and the filtrate was concentrated *in vacuo*. The residue thereby obtained, a yellow-green oil, was purified via column chromatography on silica gel by eluting with 20% EtOAc-hexane. Workup of the inital chromatography fractions afforded *N*-nitroso-3-(bromo-methyl)-3-nitroazetidine (**14**, 2.26 g, 10% yield based on **12**): mp 74-75 °C; IR (KBr) 3013 (w), 1549 (m), 1396 (s), 1333 (vs), 1285 (vs), 1243 (s), 1169 (m), 857 cm^{-1} (m); ^{1}H NMR (CDCl$_3$) δ 4.05 (s, 2 H), 4.37 (dd, J = 13.5, 2.1 Hz, 1 H), 4.63 (dd, J = 13.5, 2.1 Hz, 1 H), 5.12 (dd, J = 11.9, 2.0 Hz, 1 H), 5.45 (dd, J = 11.9, 2.0 Hz, 1 H); ^{13}C NMR (CDCl$_3$) δ 31.11 (t), 60.61 (t), 62.42 (t), 81.94 (s); Anal. Calcd for $C_4H_6N_3O_3Br$: C, 21.45; H, 2.70. Found: C, 21.55; H, 3.00.

Continued elution of the chromatography column with 30% EtOAc-hexane afforded *N*-nitroso-3-(bromomethyl)-3-hydroxyazetidine (**15**, 630 mg, 3% yield based on **12**) as a pale yellow oil; IR (neat): 3336 (s), 2948 (w), 1639 (w), 1395 (m, sh), 1338 (s), 1282 (m, sh), 1238 (m), 1169 (m), 1056 cm^{-1} (m); ^{1}H NMR (CDCl$_3$) δ 3.00 (bs, 1 H), 3.71 (s, 2 H), 4.05-4.25 (m, 2 H), 4.77-4.92 (m, 2 H); ^{13}C NMR (CDCl$_3$) δ 39.47 (t), 62.93 (t), 65.34 (t), 70.09 (s). Compound **15** was further characterized via the corresponding *N*-nitro-*O*-nitrato derivative (i.e., **16**; *vide infra*).

1-Nitro-3-(bromomethyl)-3-nitratoazetidine (16). A mixture of 100% HNO$_3$ (freshly distilled from a 1:1 mixture of H_2SO_4 and fuming HNO$_3$,[7] 1.00 g, 15.8 mmol) and (CF$_3$CO)$_2$O (TFAA, 1.0 g, 4.8 mmol) was cooled to 0°C via external application of an ice bath. To the cooled reaction mixture was added with stirring **15** (80 mg, 0.41 mmol). After the addition had been completed, the reaction mixture was stirred for an additional 30 minutes. The reaction mixture then was poured over crushed ice (50 g), and the resulting slurry was extracted with EtOAc (3 x 10 mL). The combined organic layers were washed sequentially with water (25 mL) and brine (25 mL), dried (Na_2SO_4) and filtered, and the filtrate was concentrated in vacuo. The residue, a pale yellow oil, was purified by column chromatography on silica gel by eluting with 40% EtOAc-hexane. Pure **16** (87 mg, 83%) was thereby obtained as a colorless microcrystalline solid: mp 91-92°C; IR (KBr): 3039 (w), 2965 (w), 1650 (vs) 1507 (s), 1343 (s), 1296 (s), 1285 (s), 1217(s), 1021 (w), 831 cm^{-1} (m); ^{1}H NMR (CDCl$_3$) δ 3.91 (s, 3 H), 4.57 (AB, J_{AB} = 12.0 Hz, 2 H), 4.64 (A*B*, J_{AB}= 12.0 Hz, 2 H); ^{13}C NMR (C$_6$D$_6$) δ 31.01 (t), 62.89 (t), 75.31 (s); Anal. Calcd for $C_4H_6N_3O_5Br$: C, 18.77; H, 2.36. Found: C, 19.00; H, 2.41. The structure of **16** was established unequivocally via X-ray crystallographic methods.

1,3-Dinitro-3-(bromomethyl)azetidine (17). *WARNING: Solutions of 100% HNO$_3$ and TFAA, which contain in situ generated trifluoroacetyl nitrate, are extremely hazardous and potentially explosive. Such solutions should be handled with extreme caution, and appropriate safeguards (e.g., explosion shield, protective clothing and protective eyewear) should be employed by persons who work with this material.* A solution of TFAA (1.05 g, 5.0 mmol) was cooled externally to 0 °C. To the

cooled TFAA was added with stirring 100% HNO_3 (freshly distilled from a 1:1 mixture of H_2SO_4 and fuming HNO_3,[7] 315 mg, 5.0 mmol), and the resulting mixture was stirred for 5 minutes at 0 °C. Compound **14** (100 mg, 0.44 mmol) then was added in one portion. The reaction mixture was stirred for 30 minutes and then was poured over crushed ice (50 g). The resulting aqueous suspension was extracted with EtOAc (3 x 10 mL). The combined organic layers were washed sequentially with water (50 mL) and brine (50 mL), dried (Na_2SO_4) and filtered, and the filtrate was concentrated *in vacuo*. The residue, a yellow oil, was purified via column chromatography on silica gel by eluting with 20% EtOAc-hexane. Pure **17** (85 mg, 81%) was thereby obtained as a colorless microcrystalline solid: mp 96-97°C; IR (KBr) 3034 (w), 2971 (w), 1650 (sh, m), 1544 (s), 1428 (s), 1343 (vs), 1280 (s), 1227 (s), 1132 (m), 857 cm^{-1} (m); ^{1}H NMR ($CDCl_3$) δ 4.01 (s, 2 H), 4.58 (dd, J = 11.2, 1.1 Hz, 2 H), 4.93 (d, J = 12.0 Hz, 2 H); ^{13}C NMR ($CDCl_3$) δ 30.99 (t), 63.57 (t), 79.26 (s); Anal. Calcd for $C_4H_6N_3O_4Br$: C, 20.02; H, 2.52. Found: C, 20.10; H, 2.25. The structure of **17** was established unequivocally via X-ray crystallographic methods.

1,3-Dinitro-3-(hydroxymethyl)azetidine (18).[8] A mixture of **17** (100 mg, 0.41 mmol), NaI (122 mg, 0.82 mmol) and $NaHCO_3$ (68 mg, 0.82 mmol) in DMSO (2 mL) was heated in an external oil bath at 110°C. The reaction was monitored by thin layer chromatographic (tlc) analysis. After all of the starting material had reacted (*ca.* 0.5 h), the oil bath was removed and the reaction was allowed to cool gradually to room temperature. Water (25 mL) was added, and the resulting aqueous suspension was extracted with EtOAc (3 x 10 mL). The combined organic layers were washed sequentially with water (25 mL) and brine (25 mL), dried (Na_2SO_4) and filtered, and the filtrate was concentrated *in vacuo*. The residue, a dark yellow oil, was purified by column chromatography on silica gel by eluting with 30% EtOAc-hexane. Pure **18** (58 mg, 78%) was thereby obtained as a colorless oil; IR (neat) 3480 (m), 2966 (vw), 2895 (vw), 1542 (vs), 1445 (m), 1344 (s), 1282 (m), 1063 cm^{-1} (m); ^{1}H NMR ($CDCl_3$) δ 4.13 (s, 2 H), 4.63 (AB, J_{AB} = 12.0 Hz, 2 H), 4.81 (AB, J_{AB} = 12.0 Hz, 2 H), 4.86 (br s, 1 H, disappears upon addition of D_2O); ^{13}C NMR ($CDCl_3$) δ 61.90 (t), 63.41 (t), 80.21 (s); Anal. Calcd for $C_4H_7N_3O_5$: C, 27.13; H, 3.98. Found: C, 27.30; H, 4.16.

1,3,3-Trinitroazetidine (1).[1] To a suspension of **18** (100 mg, 0.56 mmol) in water (1 mL) was added crushed NaOH pellets (27 mg, 0.67 mmol), and the resulting mixture was stirred for 10 minutes. The reaction mixture then was cooled to 10 °C via application of an external ice-water bath. To the cooled reaction mixture were added sequentially (i) a chilled (10°C) solution of $NaNO_2$ (380 mg, 5.6 mmol) in water (1mL), (ii) a chilled (10 °C) solution of $K_3Fe(CN)_6$ (184 mg, 0.56 mmol.) in water (1 mL), and (iii) solid $K_2S_2O_8$ (210 mg, 0.78 mmol). The external cold bath was removed, and the reaction mixture was stirred at room temperature for 48 h. Water (25 mL) was added, and the resulting aqueous suspension was extracted with EtOAc (3 x 10 mL). The combined organic layers were washed sequentially with water (25 mL) and brine (25 mL), dried (Na_2SO_4) and filtered, and the filtrate was concentrated *in vacuo*. The residue thereby obtained, a yellow oil, was purified via column chromatography on silica gel by eluting with 15% EtOAc-hexane. Pure **1** (40 mg, 37%) was thereby obtained as

a colorless microcrystalline solid: mp 98-99°C (lit.[1] mp 103-104 °C); ^1H NMR (CDCl$_3$) δ 5.20 (s, 4 H). Further elution of the chromatography column with 25% EtOAc-hexane allowed for recovery of unreacted starting material (i.e., **18**, 20 mg, 20%).

X-ray Structures of 10, 16, and 17.[11a] Data were collected on an Enraf-Nonius CAD-4 diffrac-tometer by using the ω–2θ scan technique, Mo Kα radiation (λ = 0.71073 Å) and a graphite mono-chromator. Standard procedures in our laboratory that have been described previously were used for this purpose.[11b] Pertinent details are presented in Table 1. Data for **10** were corrected for Lorentz and polarization effects but not for absorption. Data for **16** and **17** were corrected for Lorentz and polar-ization effects and also for absorption (DIFABS).[12] The structure of **10** was solved by direct methods (SIR[13]), and the model was refined by using full-matrix least-squares techniques. The structures of **16** and **17** were solved by using Patterson techniques, and the models were refined by using full-matrix least-squares techniques. The treatment of thermal parameters was based upon the number of observed data. All non-hydrogen atoms in **10** were treated with anisotropic thermal parameters. Anisotropic parameters were incorporated for the Br and nitro-group oxygen atoms in **16** and all non-hydrogen atoms in **17**. For all three structures, hydrogen atoms were located on difference maps and then included in the model in idealized positions [U(H) = 1.3 B$_{eq}$(C)]. All computations other than those specified were performed by using MolEN.[14] Scattering factors were taken from the usual sources.[15] The various bond lengths in the X-ray crystal structures of all three compounds are consistent with those which have been reported previously for similar systems.[16]

Table 1. X-ray structure data for **10**, **16**, and **17**.

Compound	**10**	**16**	**17**
Formula	C$_3$H$_5$N$_3$O$_4$	C$_4$H$_6$BrN$_3$O$_5$	C$_4$H$_6$BrN$_3$O$_4$
Size (mm)	0.11 x 0.13 x 0.44	0.22 x 0.42 x 0.44	0.40 x 0.51 x 0.61
Space Group	Pnma	P2$_1$/n	P2$_1$
a (Å)	9.2950 (8)	6.892 (1)	7.3333 (6)
b (Å)	6.8145 (5)	9.645 (2)	5.9374 (4)
c (Å)	9.5088 7)	13.130 (2)	9.3702 (5)
α (°)	90	90	90
β (°)	90	100.62 (1)	101.423 (6)
γ (°)	90	90	90
V (Å^3)	602.29 (8)	857.9 (8)	399.93 (5)
Z	4	4	2
D$_c$ (g-cm^{-3})	1.622	1.982	1.994
μ (cm^{-1})	1.41	47.39	50.71
(2θ$_{max}$)	50	44	60
Total refl.	2101	1230	1757
Unique refl.	649	1134	1275
R$_{int}$	0.024	0.041	0.035
I ≥ 3σ(I)	406	521	1096
Parameters	55	78	108
R, wR	0.0431, 0.052	0.0485, 0.0507	0.0395, 0.0453
(Δ/σ)$_{max}$	<0.01	<0.01	<0.01
ρ$_{min}$; ρ$_{max}$	0.25, -0.21	0.43; -0.32	0.58; -0.40

References and Footnotes

1. Archibald, T. G.; Gilardi, R.; Baum, K.; George, C. *J. Org. Chem.* **1990**, *55*, 2920.

2. (a) Axenrod, T.; Watnick, C.; Yazdehkasti, H.; Dave, P. R. *Tetrahedron Lett.* **1993**, *34*, 6677. (b) Axenrod, T.; Watnick, C.; Yazdehkasti, H.; Dave, P. R. *J. Org. Chem.* **1995**, *60*, 1959.

3. Katritzky, A. R.; Cundy, D. J.; Chen, J. *J. Heterocyclic Chem.* **1994**, *31*, 271.

4. Hiskey, M. A.; Coburn, M. D. U. S. Patent 5,336,784; *Chem. Abstr.* **1994**, *121*, 300750s.

5. (a) Funke, W. *Chem. Ber.* **1969**, *102*, 3148. (b) Funke, W. *Angew. Chem., Int. Ed. Engl.* **1969**, *8*, 70.

6. (a) Marchand, A. P.; Rajagopal, D.; Bott, S. G.; Archibald, T. G. *J. Org. Chem.* **1994**, *59*, 1608. (b) Marchand, A. P.; Rajagopal, D.; Bott, S. G.; Archibald, T. G. *J. Org. Chem.* **1994**, *59*, 5499.

7. Bull, J. R.; Jones, E. R. H.; Meakins, G. D. *J. Chem. Soc.* **1965**, 2601.

8. Dave, P.; Byun, H.-S.; Engel, R. *Synth. Commun.* **1986**, *16*, 1343. This paper reports the use of NaI-DMSO-NaHCO$_3$ to oxidize primary alkyl halides to aldehydes. In our hands, application of this regimen to **17** resulted simply in hydrolysis to afford the corresponding primary alcohol (**18**) without concomitant oxidation.

9. For a review of the Henry reaction, see: Baer, H. H.; Urbas, L. In: Feuer, H. (ed.) "The Chemistry of the Nitro and Nitroso Groups", Wiley-Interscience: New York, 1970, Part 2, pp 76-117.

10. Kornblum, N.; Singh, H. K.; Kelly, W. J. *J. Org. Chem.* **1983**, *48*, 332.

11. (a) The author has deposited atomic coordinates for these structures with the Cambridge Crystallographic Data Centre. The coordinates can be obtained, on request, from the Director, Cambridge Crystallographic Data Centre, 12 Union Road, Cambridge CB2 1EZ, UK. (b) Mason, M. R.; Smith, J. M.; Bott, S. G.; Barron, A. R. *J. Am. Chem. Soc.* **1993**, *115*, 4971.

12. Walker, N.; Stuart, D. *Acta Crystallogr., Sect. A* **1983**, *39*, 159.

13. Burla, M. C.; Carnalli, M.; Cascarano, G.; Giacovazzo, C.; Polidori, G.; Spagna, R.; Viterbo, D. *J. Appl. Cryst.* **1989**, *22*, 389.

14. *MolEN, An Interactive Structure Solution Program*; Enraf-Nonius: Delft, The Netherlands; 1990.

15. Cromer, D. T.; Waber, J. T. *International Tables for X-ray Crystallography*; Kynoch Press: Birmingham; Vol. IV, 1974, Table 2.

16. Allen, F. H.; Kennard, O.; Watson, D. G.; Brammer, L.; Orpen, A. G.; Taylor, R. *J. Chem. Soc., Perkin Trans 2* **1987**, S1.

Several New HEDM Molecules - Challenges for Synthesis

H. H. Michels and B. N. Cassenti
United Technologies Research Center
East Hartford, CT 06108

Donald D. Tzeng and Edmund Lee
United Technologies Chemical Systems
San Jose, CA 95150

ABSTRACT

Environmental concerns and the requirements for increased payload delivery into earth orbit have brought about the need for development of new chlorine-free propellants with improved performance. Since a costly redesign of current propulsion systems is unlikely in the near future, an incremental improvement in Isp, mainly through development of more energetic propellants, appears to be a necessary goal.

Ab initio calculations have been carried out to characterize the structure and stability of several new H, N, C, O target molecules that may exhibit a high energy content. Members of the nitramide family: $NH_4N(NO_2)_2$, $N(NO_2)_3$, $[N(NO_2)_2]_2$, $NON(NO_2)_2$, and the alkyldinitramines, $R-N(NO_2)_2$, are potential chlorine-free replacements for AP, exhibiting equivalent or superior density Isp. Several new members of this family of compounds have been examined: $[N-NO_2]_2$, $N(N-NO_2)_3$, $ON(N-NO_2)_2$ and the highly energetic diazidonitronium cation, $ON(N_3)_2^+$. The diazidonitronium cation exhibits remarkable stability as a $[C_2]$ structure and is an attractive candidate for synthesis. In contrast, we are unable to locate a stable structure for the nitramine dimer, $[N-NO_2]_2$. Tetranitrohydrazine, $[N(NO_2)_2]_2$, with an estimated heat of formation of $+128$ kcal/mol and typical composite propellant density equal to that for AP, remains the main target compound for synthesis in this group.

Studies have been initiated on the structure and stability of several substituted triazoles and tetrazoles. We find stability for several nitrotriazole structures, including 1-fluoro-3-nitrotriazole and 1-amino-3-nitro-1,2,4-triazole. Synthesis of this last compound has recently been reported. Comparisons of the calculated thermochemistry indicate improvement over a baseline compound, 3-nitro-1,2,4-triazole-5-one (NTO).

Discussion

There has been an increasing interest in the development of chlorine-free oxidizers and high energy compounds for use in advanced propellant formulations. Nitramines, which contain one or more covalently bonded $N-NO_2$ groups, constitute a promising class of chlorine-free energetic molecules. Examples of such compounds are the well-known explosives RDX and HMX,[1,2] and the recently synthesized hydrogen and ammonium dinitramide.[3,4,5] Other examples of energetic molecules are those containing the azide (N_3) group such as FN_3 [6] and ClN_3.[7] Halogen azide compounds, which exhibit a 15-20 kcal/mol barrier to decomposition, have high positive heats of formation (~100 kcal/mol) owing to their conformational stability as a local minimum on a potential surface that lies significantly higher in energy than dissociation to NF(Cl) + N_2. Polynitrogen azides (n>0), which are derived from the basic diazidamide anion, $N(N_3)_2^-$, have recently been reported[8] and exhibit remarkable stability with energy content of ~ 100 kcal/mol for each azide group present in the molecule. These open chain compounds should be experimentally more accessible than the cyclic or polycyclic N_n structures [9-13] which require synthetically very difficult ring closing methods.

Recently, Bottaro and Schmitt[3] have synthesized several new compounds that exhibit a dinitramide anion [$N(NO_2)_2^-$] structure. These compounds form as salts similar to ammonium nitrate or ammonium perchlorate, rather than as the less stable organic alkyldinitramines.[9] In previous studies, we have examined the structure of this new inorganic anion and have reported estimates of its vibrational spectra and thermodynamic stability.[5] The dinitramide anion exhibits exceptional stability and several new members of the inorganic dinitramide family have been examined for structural stability and energy content. *Ab initio* calculations were carried out for several new dinitramide oxidizers at the HF/6-31G* and MP/6-31G* levels of theory. Hydroxyammonium dinitramide [HADN] is stable as a C_1 ionic structure with a calculated heat of formation of ~ -30 kcal/mol. Recent synthesis and characterization studies of this compound[3] indicate that it is a liquid under normal conditions of temperature and pressure.

Two covalent compounds that could be formed by NO^+ and NO_2^+ addition to the central nitrogen atom in the dinitramide anion have been examined for stability. Nitrosyldinitramide, $ON-N(NO_2)_2$, is stable as a C_1 structure with an equilibrium ON-N bond length of 1.36 Å. Nitryldinitramide, (trinitramine) is found to have C_3 symmetry[14] with an extended O_2N-N bond of 1.42 Å owing to crowding of the nitro groups. Both of these molecules have recently been synthesized[3] but exhibit stability only at low temperatures, <0° C.

The nitration of hydrazine has been examined since the chemistry parallels that of the nitramides. Three vibrationally stable compounds are found from systematic nitration of hydrazine: 1,1-dinitrohydrazine [aminodinitramide], 1,2-dinitrohydrazine and tetranitrohydrazine [dinitramide dimer]. The first and last of these compounds are clearly in the dinitramide family.

1,2-dinitrohydrazine exhibits the highest stability in this group with a central N-N bond length of 1.36 Å. All of these compounds are highly energetic and are suggested target molecules for synthesis activities. The structure of these molecules is illustrated in Fig. 1.

We have initiated studies of the structure and stability of several substituted triazoles and tetrazoles. The baseline compound for comparison is 3-nitro-1,2,4 triazol-5-one [NTO] which is a shock insensitive explosive. We find a stable structure with C_s symmetry for 1-amino-3-nitro-1,2,4-triazole and a planar structure with C_s symmetry for 1-fluoro-3-nitro-1,2,4-triazole. Both of these compounds are highly energetic relative to NTO.

Several nitro-substituted alkynes have also been examined. We find stability for nitroacetylene, dinitroacetylene and 1-nitropropylene. All exhibit high positive heats of formation. Synthesis of 1-nitropropylene has been reported.[15] These structures are illustrated in Fig. 2. Finally, nitration of HCN results in a stable and energetic nitrylcyanide structure with C_{2v} symmetry.

Performance Characteristics

Although several of the compounds discussed above have not yet been synthesized, it is of interest to compare their relative value in improving the performance characteristics of solid propellant formulations. Heats of formation for all of these compounds have been calculated at the MP2/6-31G* level of theory from isodesmic reactions. or, for large molecules, from the atom equivalents method of Ibrahim and von Schleyer.[16] The use of isodesmic reactions permits cancellation of errors that can otherwise accumulate if heats of formation are based on atomization energies. Solid densities were estimated using Cady's method[17] for evaluating explosives. These calculated data are given in Table 1.

The performance characteristics of the new dinitramide compounds have been evaluated using a formulation optimized with R45M as the binder. The baseline oxidizer is ammonium perchlorate (AP) which has an I_{sp} of 253 sec. for sea level applications and an I_{sp} of 274 sec. for space applications. In Tables 2 and 3, we compare the performance gained by completely substituting these new oxidizers for AP. All exhibit equal or superior performance to AP. The dinitramide compounds aminodinitramide, 1,2-dinitrohydrazine and tetranitrohydrazine have predicted density impulse greater than 18 lb-sec/in^3 and are the optimum challenges for synthesis resulting from our studies of this class of compounds.

References

1. G. F. Adams and R. W. Shaw, Jr., Annu. Rev. Phys. Chem. **43**, 311 (1992).
2. Chemistry and Physics of Energetic Materials, Ed. S. N. Bulusu, Kluwer: London, (1990).
3. R. J. Schmitt and J. C. Bottero: private communication.
4. R. J. Schmitt, M. Krempp and V. M. Bierbaum, Int. J. Mass Spectrom. **117**, 621 (1992).
5. H. H. Michels and J. A. Montgomery, Jr., J. Phys. Chem., **97**, 6602 (1993).
6. D. J. Benard, B. K. Winkler, T. A. Seder and R. H. Cohn, J. Phys. Chem. **93**, 4790 (1989).
7. D. J. Benard, M. A. Chowdhury , B. K. Winkler, T. A. Seder and H. H. Michels, J. Phys. Chem. **94**, 7507 (1990).
8. H. H. Michels, J. A. Montgomery, Jr., K. O. Christe and D. A. Dixon, J. Phys. Chem. **99**, 187 (1995).
9. L. V. Cherednichenko, B. A. Ledebev and B. V. Gidaspov, Zh. Org. Khim. **14**, 735 (1978).
10. P. Saxe and H. F. Schaefer III, J. Am. Chem. Soc. **105**, 1760 (1983).
11. R. Engelke, J. Phys. Chem. **93**, 5722 (1989).
12. M. T. Nguyen, J. Phys. Chem. **94**, 6923 (1990).
13. W. J. Lauderdale, J. F. Stanton and R. J. Bartlett, J. Phys. Chem. **96**, 1173 (1992).
14. J. A. Montgomery, Jr. and H. H. Michels, J. Phys. Chem. **97**, 6774 (1993).
15. D. D. Tzeng: private communication.
16. M. R. Ibrahim and P. von R. Schleyer, J. Comp. Chem. **6**, 157 (1985).
17. H. H. Cady, "Estimation of the Density of Organic Explosives from their Structural Formulas", LA-7700-MS, Univ. of Cal., LASL, Los Alamos, NM (1979).

Table 1. Thermochemistry of Advanced Oxidizers

Compound	Formula	Mol. Wt.	Density gm/cm^3	$\Delta H_f(25°C)$ kcal/mol
ammonium dinitramide [ADN]	$H_4N_4O_4$	124.056	1.80 1.75	-36.0 +8.3 (g)
nitrosyldinitramide	N_4O_5	136.023	1.94	49.8
trinitramine	N_4O_6	152.022	2.15	+80.4
1,1-dinitrohydrazine (aminodinitramide)	$H_2N_4O_4$	122.040	2.04	+58.6
1,2-dinitrohydrazine	$H_2N_4O_4$	122.040	2.04	+44.3
tetranitrohydrazine	N_6O_8	212.034	2.17	+128.2
diazidamine	H_1N_7	99.057	1.56	+199.0
triazidamine	N_{10}	140.070	1.58	+302.0
diazidonitronium cation	N_7O^+	114.048	1.65	+397.1
nitrosylazide	N_4O	72.027	1.54	+115.4
nitrylazide	N_4O_2	88.026	1.76	+95.1
3-nitro-1,2,4-triazol-5-one [NTO]	$C_2H_2N_4O_3$	130.063	1.75	-10.5
1-amino-3-nitro-1,2,4-triazole	$C_2H_3N_5O_2$	129.079	1.61 [1.70]	+55.6 [+50.0] (exp.)
1-fluoro-3-nitro-1,2,4-triazole	$C_2HFN_4O_2$	132.054	1.68	+60.0
nitroacetylene	C_2HNO_2	71.035	1.51	+71.7
dinitroacetylene	$C_2N_2O_4$	116.032	1.79	+94.8
1-nitropropylene	$C_3H_3NO_2$	85.062	1.37	+57.8
nitrylcyanide	CN_2O_2	72.023	1.82	+58.0

Table 2. Theoretical Performance - Advanced Oxidizers

Specific Impulse, sec

Compound		ISP	IVC	% OX	DEN	Specific Impulse, sec
Oxidizer	Binder					
AP	R45M	253	274	90	1.76	
ADN		265	287	92	1.68	
$NON(NO_2)_2$		301	327	79	1.58	
$N(NO_2)_3$		298	324	78	1.67	
$NH_2N(NO_2)_2$		298	323	85	1.73	
$[NH(NO_2)]_2$		292	317	86	1.75	
$[N(NO_2)_2]_2$		299	325	79	1.70	
NON_3		318	345	89	1.44	
NO_2N_3		302	328	86	1.57	

Table 3. Theoretical Performance - Advanced Oxidizers

Density Impulse, lb-sec/in^3

Compound		ISP	IVC	% OX	DEN	10 12 14 16 18 20 22
Oxidizer	Binder R45M					
AP		16.1	17.4	90	1.76	
ADN		16.0	17.3	92	1.68	
NON(NO$_2$)$_2$		17.2	18.6	79	1.58	
N(NO$_2$)$_3$		18.0	19.5	78	1.67	
NH$_2$N(NO$_2$)$_2$		18.6	20.2	85	1.73	
[NH(NO$_2$)]$_2$		18.4	20.0	86	1.75	
[N(NO$_2$)$_2$]$_2$		18.3	19.9	79	1.70	
NON$_3$		16.5	17.9	89	1.44	
NO$_2$N$_3$		17.1	18.6	86	1.57	
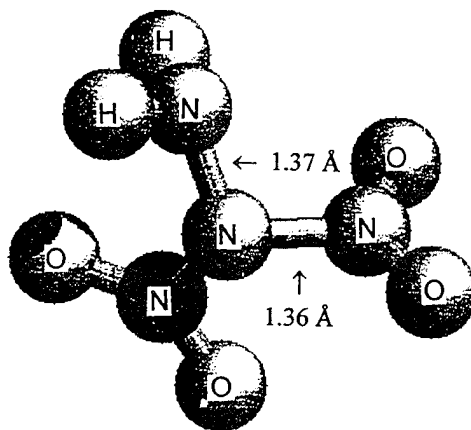
1,1-dinitrohydrazine [aminodinitramide]
[^{1}A] - C$_1$ Symmetry
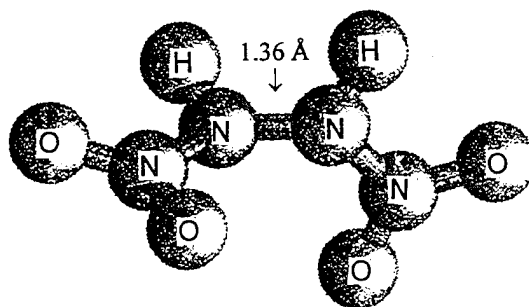
1,2-dinitrohydrazine
[^{1}A] - C$_2$ Symmetry
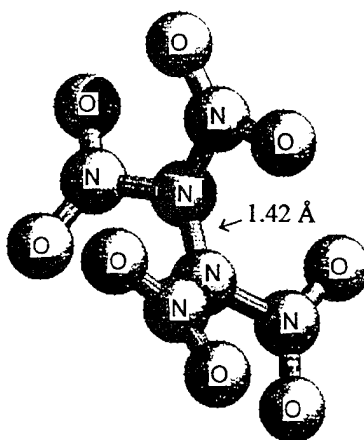
Tetranitrohydrazine
[^{1}A] - C$_2$ Symmetry

Fig. 1. Nitro-Hydrazine Compounds

Nitroacetylene
[$^1A_1$] - C_{2v} Symmetry

← 1.40 Å

← 1.18 Å
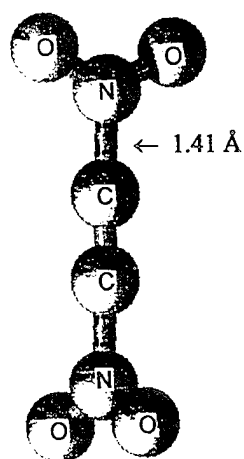
Dinitroacetylene
[$^1A_1$] - D_{2d} Symmetry

← 1.41 Å
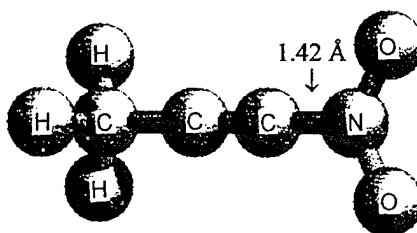
1-nitropropylene
[$^1A'$] - C_s Symmetry

1.42 Å

Fig. 2. Nitro-Substituted Compounds

Extended Abstract
Synthesis of Cubanes and Azacubanes

Robert M. Moriarty and M. Rao
Department of Chemistry, University of Illinois at Chicago
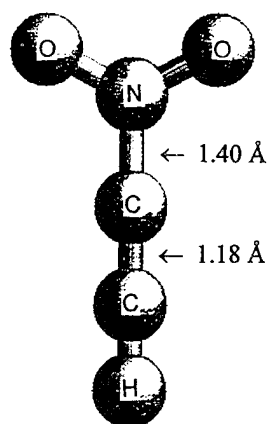Chicago Illinois 60680
AND
Steroids Ltd.
Chicago Technology Park
2201 West Campbell Park Drive
Chicago Illinois 60612

Introduction

As shown in Table I cubane possesses very attractive properties as a high density high energy material.

Table 1   Properties of Cubane
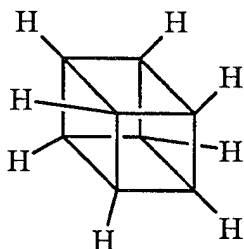
Vapor Pressure	1.1 Torr at 25°C
Solubility	18 wt–% in hydrocarbons
Melting Point	120–131°C (easily depressed)
Stability	Inert to light, water, air
Decomposition	>220°C (very slow)
Density	1.29 g/cm^3
Heat of Formation	+149 kcal/mole
Strain Energy	+166 kcal/mole
ΔH_c	204,450 BTU/gallon

Cubane is extremely energy "rich" with a heat of formation of +149 kcal/mole, density of 1.29 g/cm^3 and strain energy of +166 kcal/mole.

Table II   Cubane Compared to RJ–4 as an Air–Breathing Fuel

Cmpd	Formula	Density g/cc(lb/In^3)	ΔH_f kcal/m(cal/g)	ΔH_c cal/g(cal/cc)	% Increase by wt.	by vol.
RJ–4	$C_{12}H_{20}$	0.92 (0.0332)	–32.5 (–198.0)	10,114 (49,305)	–	–
Cubane	C_8H_8	1.29 (0.0468)	+149 (+1190.6)	10,517(13,567)	4.2	45.8
			[+137.6(+1321.6)	11,674(15,058)	4.7	50.8]

(using new estimate of cubane's heat of formation)

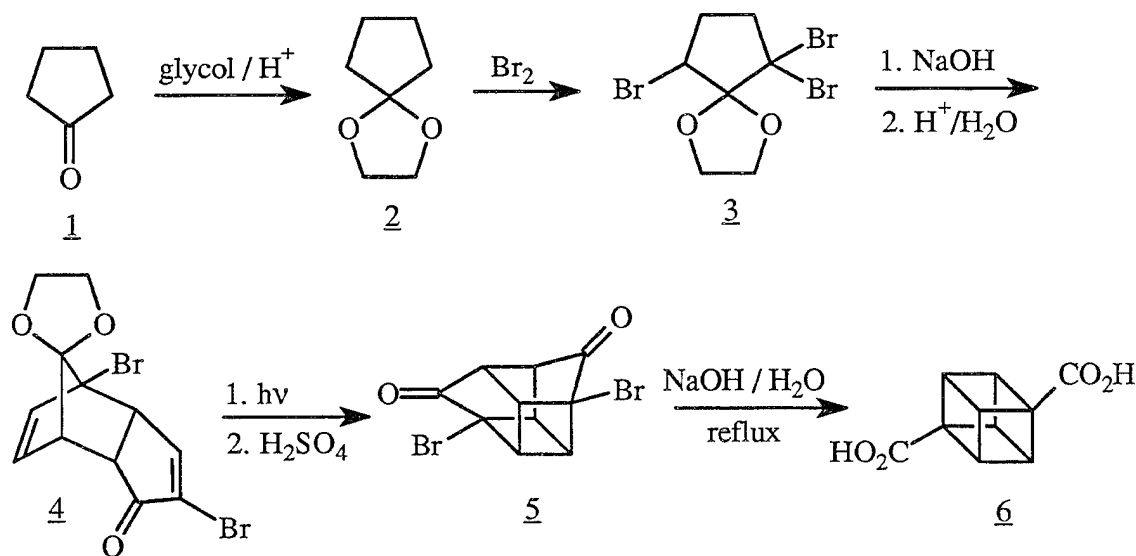The comparison of cubane to RJ-4 as an air–breathing fuel (Table II), likewise, demonstrates its promise in propulsion.

Under an SBIR Phase II contract, a two year program is underway aimed at the production of pound quantities of cubane 1,4-dicarboxylic acid which is the product of the Eaton cubane synthesis (Scheme 1).[1]

SCHEME 1   EATON CUBANE SYNTHESIS

Currently, the synthesis up to compound 4 has been standardized. Also the photocyclization (4 → 5) has been effected in high yield.

In the 6-month phase I project the key photochemical step was optimized using light of > 3000Å. This greatly improves the photocyclization in terms of operation, and also gives cleaner product in higher yield. In the Phase II project we aim to produce 10 pounds of 1,4-cubane dicarboxylate production rate of 1 pound/cycle.

Current Research

Cubane 1,4-dicarboxylic acid (6) plays a pivotal role in cubane syntheses because the carboxyl groups can be converted to a wide range of derivative functionality.
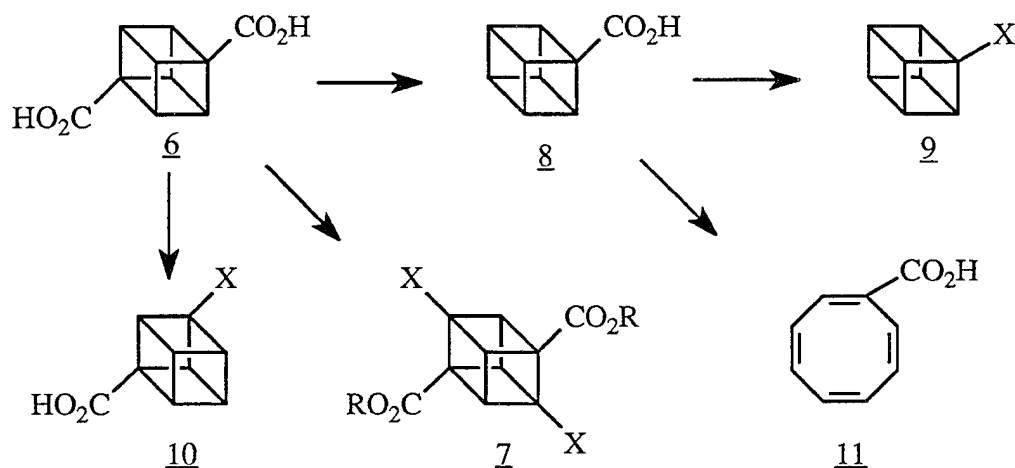
$$X = \text{alkyl, amino, halogen, nitro, } CH(NO)_2, CN, CONH_2$$

For conversion to the monocarboxylic acid the Barton decarboxylation has been very useful in obtaining cubane carboxylic acid (8) as well as cubane itself. Furthermore the CO_2H group is a useful precursor for a wide range of functional groups. Also the cubyl ring system undergoes an essentially quantitative conversion to cyclooctatetraene upon rhodium catalyzed ring opening.

The problem of carrying out displacement reactions upon cubane is illustrated in Scheme 2.

SCHEME 2   SYNTHETIC PROBLEM. NUCLEOPHILIC DISPLACEMENT UPON
CUBYL IODIDE
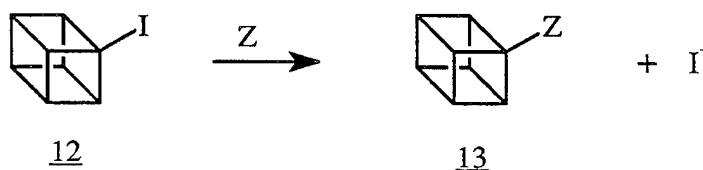
Impossibility of Sn 2 Displacement

Implausibility of Sn 1 (cubyl cation)

A solution to this problem was discovered using hypervalent iodine oxidative displacement as shown in Scheme 3.

SCHEME 3 HYPERIODINATIVE PATHWAY
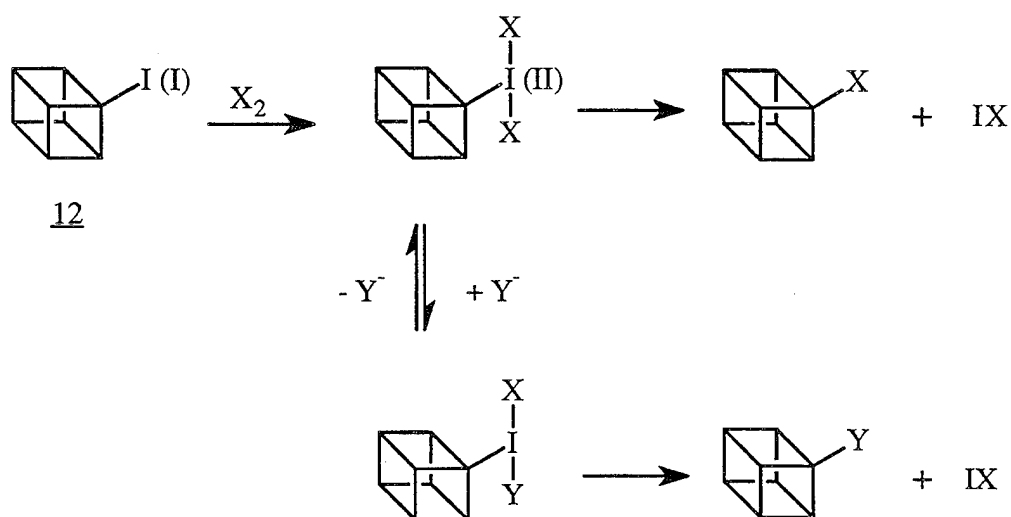
Thus a series of 1-substituted-4-carbomethoxy cubanes were obtained (Scheme 4).

SCHEME 4   OXIDATIVE DEIODINATON OF 1-IODO-4-CARBOMETHOXY CUBANE WITH HYPERVALENT IODINE REAGENTS.
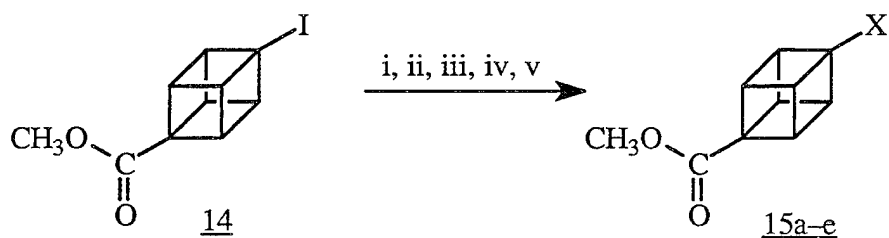
i) $C_6H_5I(Cl)_2$ / CH_2Cl_2, Δ

ii) $C_6H_5I(OH)OTs$ / CH_2Cl_2, Δ

iii) $C_6H_5I(OH)OMs$ / CH_2Cl_2, Δ

iv) $(C_6H_5IO)_n$, TMSOTf / CH_2Cl_2, Δ

v) $C_6H_5I(OCOCF_3)_2$ / CH_3Cl_2, Δ

X = Cl, OTs, OMs, OTf, $OCOCF_3$

Using the Barton decarboxylation iodocubane was obtained (Scheme 5).

171a

SCHEME 5 SYNTHESIS OF IODOCUBANE
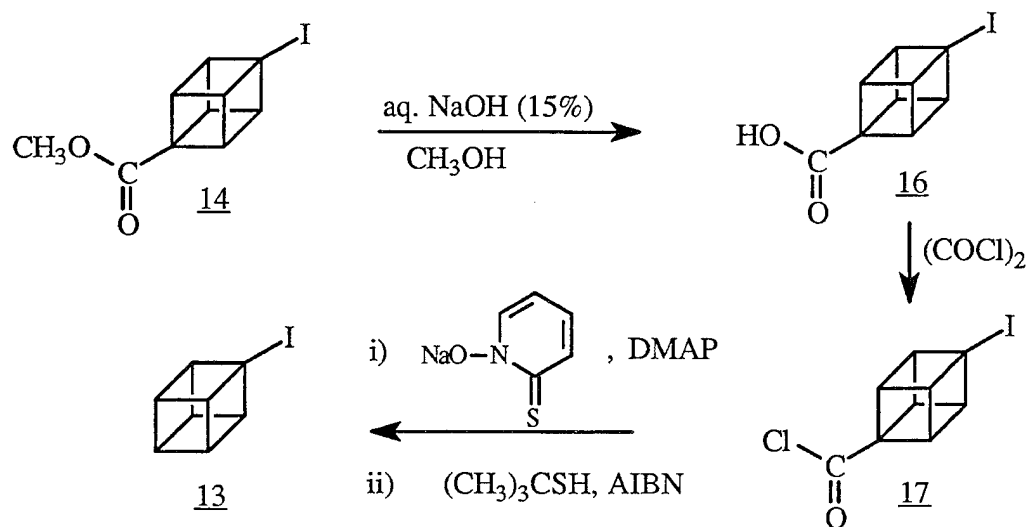
Iodocubane served as a precursor of a number of monosubstituted cubanes as shown below (Scheme 6).

SCHEME 6   OXIDATIVE DEIODINATION OF IODOCUBANE WITH HYPERVALENT IODINE REAGENTS.

i) $C_6H_5(Cl)_2$, CH_2Cl_2, Δ

ii) $C_6H_5I(OH)OSO_2C_6H_4CH_3R$ / CH_2Cl_2, Δ

iii) $C_6H_5I(OH)OSO_2CH_3$ / CH_2Cl_2, Δ

iv) $(C_6H_5IO)_n$, $(CH_3)_3SiOSO_2CF_3$ / CH_2Cl_2, Δ

X = Cl, OTs, OMs, OTf, OCOCF$_3$
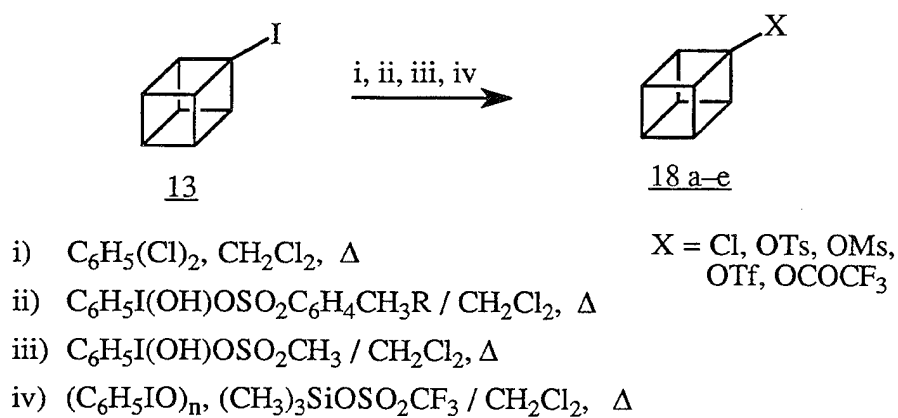
Using hypervalent iodine oxidative iododecarboxylation we were able to obtain mono and disubstituted cubanes (Scheme 7).

SCHEME 7
SYNTHESIS OF MONO AND DIHALOCUBANES FROM CUBANE CARBOXYLIC ACIDS UTILIZING HYPERVALENT IODINE METHODOLOGY.

19

20 a: X = I
b: X = Br

21 a: R = H
b: R = COOH
c: R = COOCH$_3$

22 a: R = H; X = I
b: R = H; X = Br
c: R = X = I
d: R = X = Br
e: R = COOCH$_3$; X = I
f: R = COOCH$_3$; X = Br
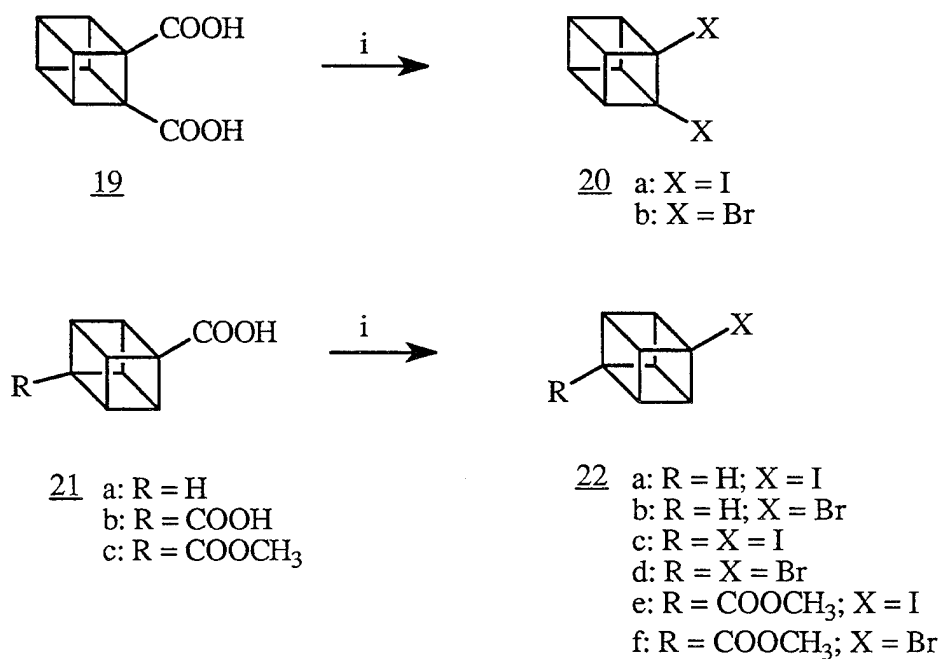
i) PhI(OAc)$_2$ or Br$_2$, C$_6$H$_6$ reflux

A series of 4-substituted cubyl triflates were synthesized and solvolyzed with the result that cubyl triflates undergo S$_N$1–type nucleophilic displacement (Schemes 8 and 9).

SCHEME 8   SYNTHESES OF 4-SUBSTITUTED CUBYL TRIFLATES

23

(PhIO)$_n$, TMSOTf
CH$_2$Cl$_2$

24

X = H, CH$_3$, COOCH$_3$, I, Br, Cl

SCHEME 9   SYNTHESIS OF 4-SUBSTITUTED CUBYL TRIFLATES

25

25a: X = H; 25b: X = CH3; 25c: X = CO2CH3
25d: X = I; 25e: X = Br

26   (OCD3)

26a–f

- No detectable rearrangement.

Cubyl triflates also act as an alkylating agent toward amines (Scheme 10).

SCHEME 10   CUBYLATION OF PYRROLIDINE

27

28
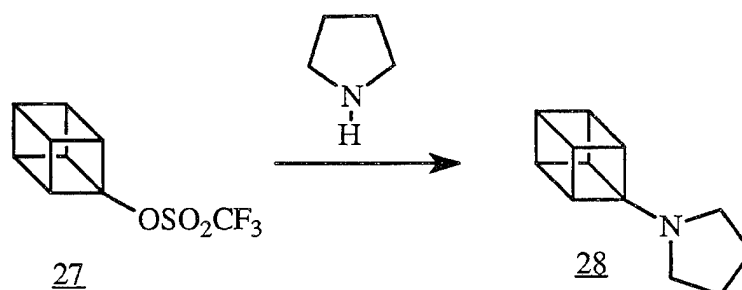
Azacubanes

Azacubanes stand for the basic cubane ring-system with progressive replacement of one or more carbon atoms by nitrogen atoms. In spite of the high strain energy of cubane (ca. 166 kcal/mole) it is thermally quite stable.[2] Cubane slowly decomposes when heated above 200°C. The high thermal stability may result from the forbiddeness of its reversion to smaller molecular components (i.e., retro 2+2 thermal cycloreversion). A priori, one might predict on the basis of the isoelectronic relationship between $(CH)_8$ and azacubanes that these latter compounds might show analogous stability. As mentioned above recent theoretical calculations have indicated that progressively introducing nitrogen, in place of carbon, into the cubane system has a profound effect upon the properties of cubane.

Based on thermodynamic calculations of heats of formation, Balaban et al[2] predict that azacubanes should be stable materials and feasible targets for organic synthesis. Politzer et al[3] and Engelke and Stine[4,5] have calculated that azacubanes are kinetically stable and decompose with the release of considerable amounts of energy. Rodney Bartlett has also published high level calculations on octaazacubane[4b] and has calculated ΔH_f of diaza– and tetra–azacubane.[4c] Fig. I shows calculated heats of formation (ΔH_f, kcal/mol[-1]) for azacubanes relative to cubane itself.

Figure I: HEATS OF FORMATION (ΔH_f, kcal mol^{-1}) of 22 ISOMERS of CUBANE and AZA ANALOGS

1 99.06	2 115.73	3 142.68	4 131.03	5 133.65	6 168.25
7 159.34	8 145.16	9 204.03	10 192.84	11 158.35	12 183.91
13 186.71	14 195.25	15 230.15	16 221.58	17 207.76	18 266.89
19 255.94	20 258.50	21 303.41	22 350.74		● = N
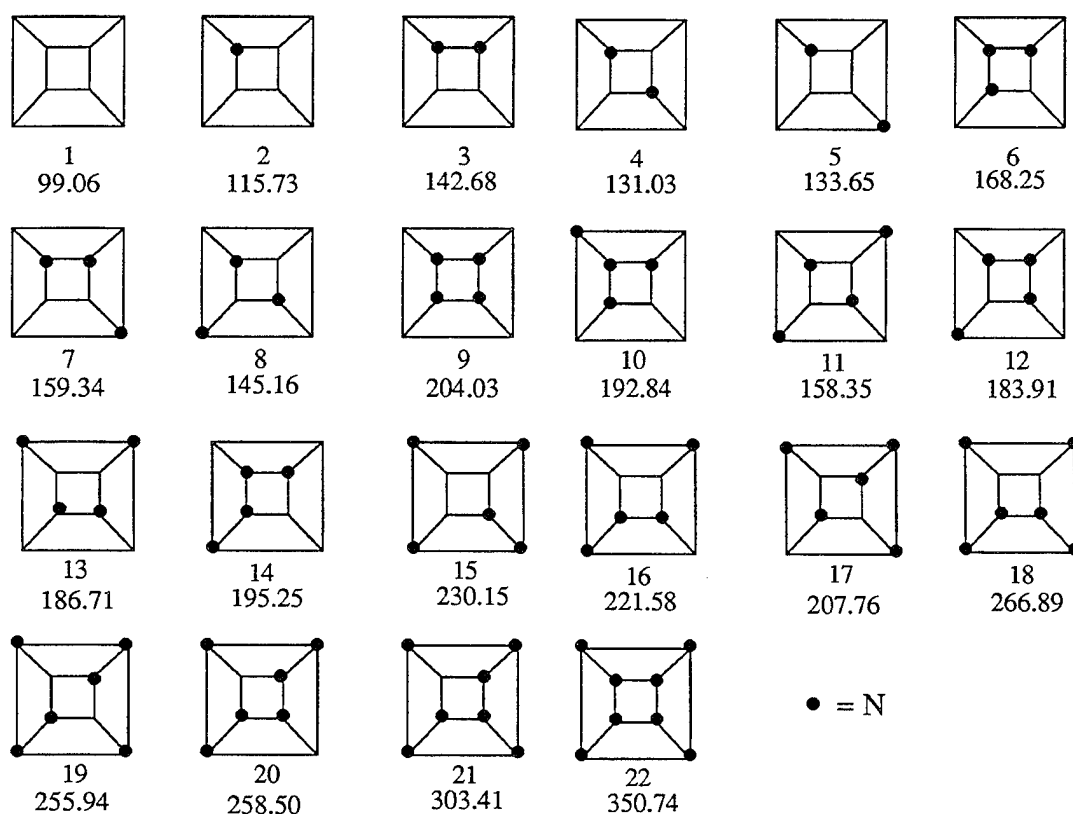
From: I. Alkorta, J. Elguero, I. Rozas and A.T. Balaban, "Theoretical Studies of Aza Analogues of Platonic Hydrocarbons", *J.Mol.Structure*, 206, 67-75 (1990).

Several synthetic approaches have been initiated during the past four years. The most promising is one which is patterned on the Eaton cubane synthesis.[1]

175
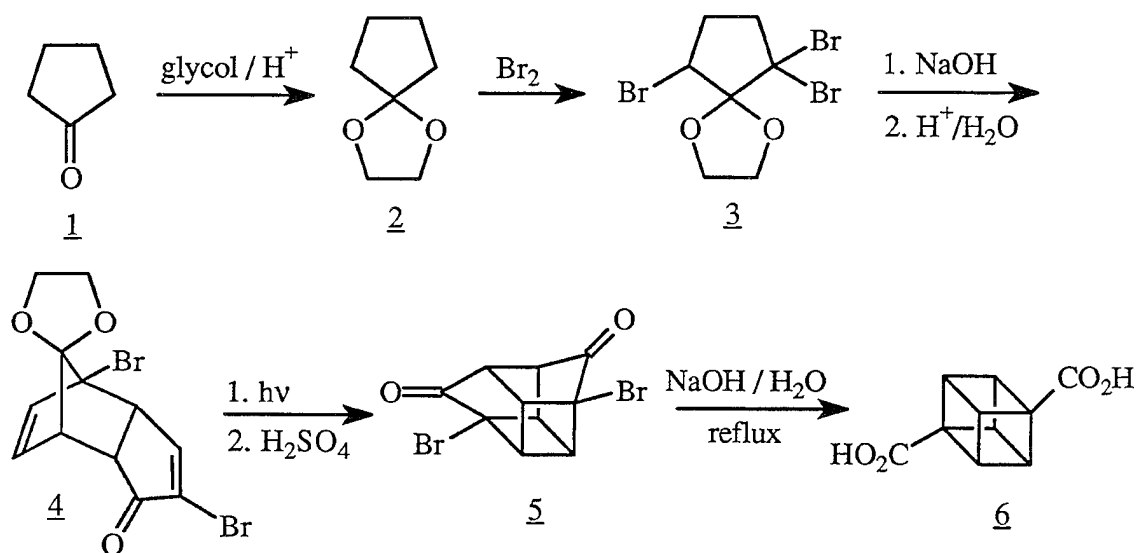
Basically, this process involves the dimerization of 2–bromocyclopentadienone ketal (**29**). The analogous nitrogen substituted analog is **30**.
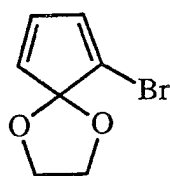
29
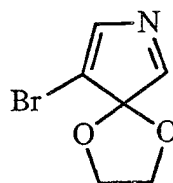
30

Compound **30** is related to 3–oxo–1–pyrrolidine. 1–Acetyl–3–oxo–1–pyrrolidine is well known and is synthesized in the following way:

31

32

33

34

34

35
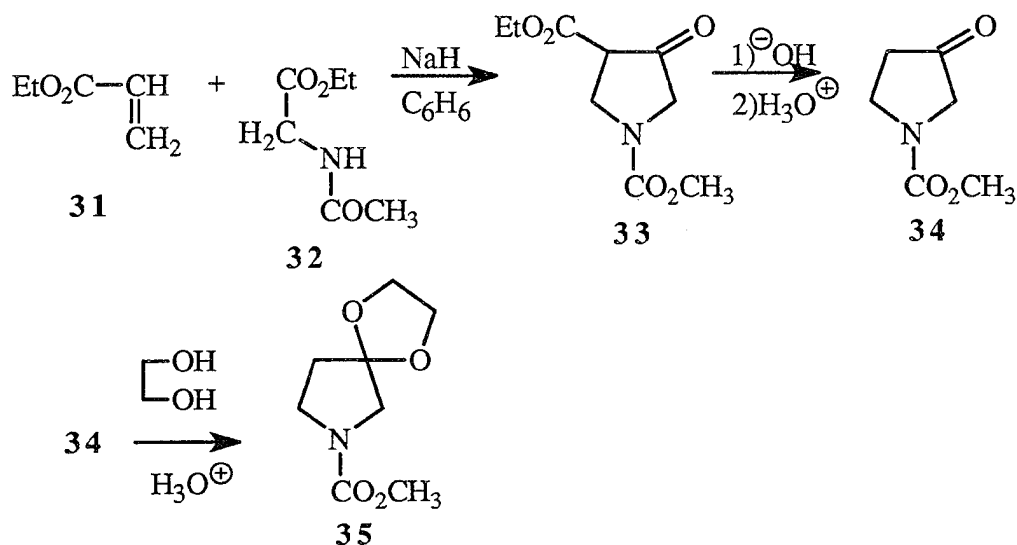
Bromination of **35** followed by treatment with NaOH proceeds in the sense of **35-->36 -->37**:

35

36

37
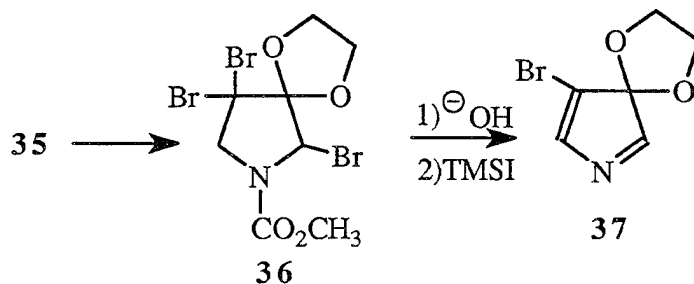
The Diels–Alder dimerization of **37** proceeds to yield adduct. The regiochemistry of this cycloaddition is in accord with the predictions of FMO theory. Using the numbering system designated in **37**, the dimer **38** should undergo an intramolecular photocyclization to form the N_1–C_8 and C_5–C_7 bonds.

176
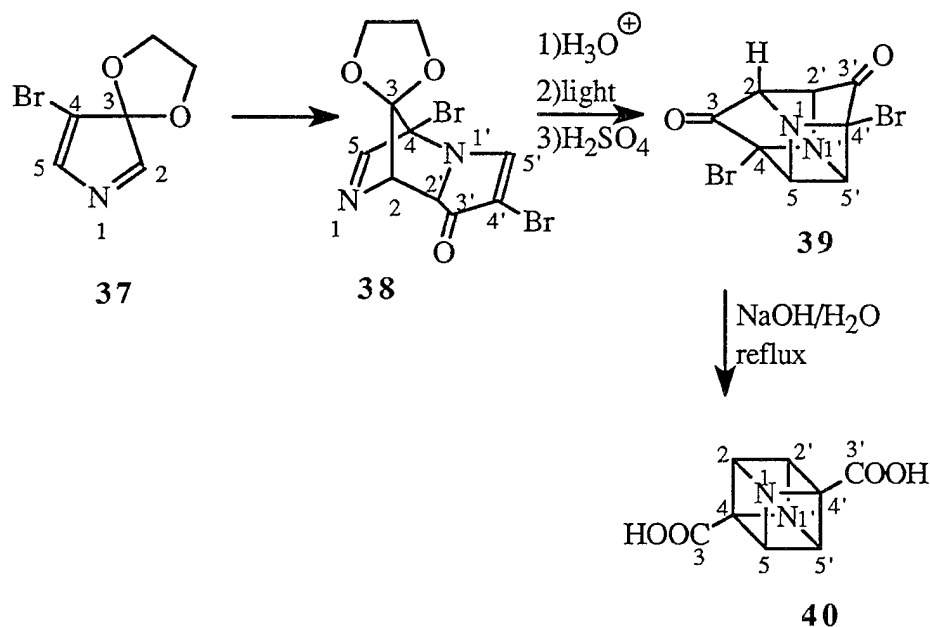
The caged dimer **39** can be hydrolyzed, then subjected to the Favorskii ring contraction to yield **40** in a manner completely analogous to the Eaton cubane synthesis. Carbonyl carbon atoms C_3 and C_{10} become exocyclic to the cubane system as the carbonyl carbon atoms of the carboxyl groups.

Acknowledgement

References

1. P. E. Eaton, T. W. Cole, *J. Am. Chem. Soc.*, **86**, 3157 (1964).

2. I. Alkorta, J. Elguero, I. Rozas, and A. T. Balaban, *J. Molec. Structure*, **206**, 67 (1990).

3. P. Politzer and J. M. Seminario, *J. Phys. Chem.*, **93**, 588 (1988).; P. Politzer and J. M. Seminario, *Structural Chemistry*, **1**, 29 (1989).

4. a. R. Engelke and J. R. Stine, *J. Phys. Chem.*, **94**, 5689 (1990).

   b. W. J. Lauderdale, J. F. Stanton, R. J. Bartlett, *J. Am. Chem. Soc.*, **96**, 1173 (1992).

   c. Personal communication, 1995.

5. R. Engelke, *J. Am. Chem. Soc.*, **115**, 2961 (1993) and summary references contained therein.

Title: Current Status of ADN Chemistry

By: Robert Schmitt and Jeffrey Bottaro
SRI International

Abstract:

We will present details about the current status of ammonium dinitramide (ADN), it's synthesis, application, and use. ADN is an advanced high energy oxidizer. As an oxidizer for solid propellants. ADN is known to increase the specific impulse of propellants by 15%. It is estimated that the use of ADN to replace ammonium perchlorate (AP) can reduce the size of some rockets by up to 60%. ADN is environmentally benign, chlorine-free, insensitive, and easy to demil.

Potential Applications for ADN are:
- Enhanced performance rockets
- Environmentally benign oxidizer for solid rocket
  propellants (AP replacement, HCl free exhaust)
- Extra high energy, low vulnerability gun propellants
  having improved range, large and small caliber
- Stealthy/minimum signature high energy boosters for
  aircraft and submarines
- Phase transfer catalyst for extracting heavy metals and
  organics from waste streams

Reactions of B Atoms with NH_3 to Produce HBNH, BNBH and B_2N

Craig A. Thompson and Lester Andrews

Department of Chemistry

University of Virginia

Charlottesville, Virginia 22901

Abstract

Pulsed-laser ablated boron atoms were reacted with ammonia in excess argon during condensation at 10 ± 1 K. Products were identified from infrared spectra, isotopic substitution and ab initio calculations of isotopic vibrational spectra. The major primary product was the reactive iminoborane molecule HBNH, which is isoelectronic with acetylene. Secondary B atom reactions followed by hydrogen elimination gave the cyclic azadiboriridine addition radical B_2N and the linear insertion product BNBH, which are analogous to reaction products observed with B atoms and acetylene.

Laser ablation has proven to be valuable for studying boron atom reactions with small molecules such as O_2, H_2O, N_2, H_2, CH_4 and C_2H_2 to produce and characterize new molecules and to understand reaction mechanisms.[1-9] Boron-methane studies identified novel $HBCH_2$ and HBCH products of the insertion reaction followed by dehydrogenation; the reaction of a second boron atom gave HBCBH.[6,7] In the case of acetylene, boron atom $C\equiv C$ addition and $C-H$ insertion products were observed and characterized.[8,9]

The simplest iminoborane HBNH is isoelectronic with acetylene and similar reactions with boron atoms are expected. However, HBNH is extremely reactive and only two experimental observations of HBNH have been reported, a matrix photolysis of H_3BNH_3 and a gas phase discharge of B_2H_6/NH_3 mixtures.[10,11] The boron-methane studies predict that the elusive HBNH molecule will be a major product of the boron-ammonia reaction and the boron-acetylene work suggests further reactions will give linear and cyclic secondary reaction products, which will be reported here.

The pulsed-laser ablation matrix-isolation technique has been described.[1-4] Mixtures of argon/ammonia (1% and less) were codeposited with laser ablated boron atoms onto a 10 ± 1 K optical window. Natural abundance ($^{14}NH_3$, 80.4% $^{11}B-19.6\%$ ^{10}B) and isotopically enriched precursors ($^{15}NH_3$, ND_3, 93.8% $^{10}B-6.2\%$ ^{11}B) were employed. Infrared spectra were recorded at 0.5 cm^{-1} resolution using a Nicolet 750 with MCT detector.

Figure 1 shows spectra of the major product absorptions in the diagnostic spectral regions. The sharp ^{n}B doublet at 1788.7, 1782.8 cm^{-1} with weaker (1:4) counterpart at 1826.3, 1819.9 cm^{-1} (Fig. 1c) are due to the $B-N$ stretching fundamental of $H^{11}BNH$ and $H^{10}BNH$ in natural abundance site split by the matrix. Fig. 1a shows spectra for the ^{10}B reaction and the latter doublet is enhanced, but the former doublet is still observed owing to 6.2% ^{11}B in the ^{10}B enriched sample. The spectrum for ^{10}B and $^{14}NH_3/^{15}NH_3$ is illustrated in Fig. 1b, and new bands were observed at 1804.6, 1798.3 cm^{-1} for $H^{10}B^{15}NH$. Analogous bands were observed at 1766.2, 1760.3 cm^{-1} for $H^{11}B^{15}NH$ in a ^{n}B isotopic experiment. Stronger bands were observed at 3710.5, 3700.5 cm^{-1} (NH stretch) and 463.3, 461.0 cm^{-1} (NH bend) for HBNH in agreement with earlier work; the assignments are confirmed by ^{15}N shifts and ab initio frequency calculations.

The strongest feature in the spectrum exhibits a 1:8:16 triplet at 901.5, 891.1, 882.1 cm^{-1} with ^nB (absorbance 0.4−0.7) and a mixed $^{14}N/^{15}N$ doublet at 901.5, 881.8 cm^{-1} with ^{10}B (not shown). This band system has been produced from ablated BN and from ablated B + N$_2$ reactions and identified as the cyclic azadiboriridine radical B$_2$N with 2 equivalent B atoms.[3] A weaker 1:8:16 triplet at 1769.1, 1753.4, 1736.4 cm^{-1} is due to the linear BNB radical.[3] The weaker C and F bands are due to minor reaction products that will be identified in a complete experimental and theoretical report.

The next strongest band gives a new 1:4:4:16 quartet at 1876.4, 1871.8, 1851.5, 1846.3 cm^{-1} with ^nB (Fig. 1c) denoting the vibration of 2 inequivalent B atoms; in the ^{10}B experiment (Fig. 1a) the former 3 bands were observed as a 88/6/6 triplet with lower weights for the 10,11-boron isotopic species. A mixed $^{14}N/^{15}N$ doublet (Fig. 1b) showed the involvement of a single N atom, and displacement with ND$_3$ verified the presence of hydrogen in this new species. Observed isotopic frequencies for this antisymmetric B−N−B stretching fundamental and weaker symmetric B−N−B stretching, B−H stretching and bending modes associated by common photolysis behavior (5% growth) are listed in Table 1.

The identification of linear BNBH from isotopic infrared spectra is confirmed by SCF calculations[12] of isotopic frequencies and intensities, which are also listed in Table 1. Typically SCF calculations produce frequencies that are about 10% higher than observed values as is the case for BNBH. However, the excellent agreement between observed and calculated isotopic frequencies is found in the observed/calculated frequency ratios given in the table for four isotopic BNBH molecules. First, note that the ratios are extremely close (0.928 − 0.941) for the three stretching modes (all isotopes) but slightly lower for the linear bending mode (0.881) as the latter mode is more anharmonic. Second, note that the deviation in isotopic frequency

ratios for the N−H stretch (±0.0002) gives a ±0.6 cm^{-1} frequency fit. The deviations in ratios for the antisymmetric B−N−B stretch (±0.0004) and symmetric counterpart (±0.0007) show ±0.8 cm^{-1} frequency agreement. The deviation (±0.0003) in ratios for the N−H bending mode produces ±0.3 cm^{-1} agreement. The observed band absorbances, relative to one another, agree well with the calculated infrared intensities except for the B−H stretch, which is weaker than predicted at the SCF level of theory. Finally, the observed/calculated frequency ratios for BNBD are slightly different owing to differences in anharmonicity and normal coordinate vibrational motion.

The matrix chemistry reported here is significant since the simplest and most reactive iminoborane, HBNH, and its further reactions with the simplest boron reagent, atomic B, have been examined. Scheme 1 outlines the major reactions observed here. The insertion of boron into a N−H bond requires activation energy provided by the hyperthermal ablated B atoms; the [HBNH$_2$]* species formed contains excess energy, which activates hydrogen elimination to give HBNH. Iminoborane, the acetylene analog, trimerizes to give borazine, $H_3B_3N_3H_3$, the benzene analog under normal conditions,[13] but here the condensing argon matrix prevents this reaction. However, secondary reactions with B atoms proceed as expected following addition and insertion reactions with B + HCCH to give H_2C_2B and CCBH.[8,9] Based on band intensities the major secondary reaction is addition followed by H_2 elimination to give the azadiboriridine radical B_2N; no evidence was found for H_xB_2N (x = 1,2) species absorbing near B_2N. In contrast the HCCH reaction yielded the borirene radical H_2C_2B and not C_2B; the latter has been observed from ablation of graphite/boron pellets.[14] The difference here is presumably the greater strength of C−H bonds compared to N−H and B−H bonds since the isoelectronic C_2B and B_2N rings should be of comparable stability.

The N−H insertion reaction followed by H and H_2 elimination produces the linear BNBH and BNB species. In contrast to HBCBH in the methane reaction,[6] there was no evidence for HBNBH; the former is a stable, allene-like species, whereas the latter is a radical precursor to the more stable BNBH molecule observed here. The yield of B_2N and BNBH in the present experiments is higher than the yield of H_2C_2B and CCBH in similar acetylene reactions,[8,9] based on band intensities. Considering the obvious fact that HCCH reagent concentration in earlier work surely exceeded HBNH concentration here by at least two orders of magnitude, the reactivity of HBNH toward B atoms is substantially greater than the reactivity of HCCH. This is in accord with the ready formation of borazine from HBNH and the slow formation of benzene from HCCH. Iminoborane, HBNH, is clearly a stable but highly reactive molecule that can be formed in the exothermic reaction of B and NH_3 and trapped in a condensing argon matrix.

References

(1)   Burkholder, T.R.; Andrews, L.; *J. Chem. Phys.* **1991**, *95*, 8697.

(2)   Andrews, L.; Burkholder, T.R. *J. Phys. Chem.* **1991**, *95*, 8554.

(3)   Andrews, L.; Hassanzadeh, P.; Burkholder, T.R.; Martin, J.M.L., *J. Chem. Phys.* **1993**, *98*, 922.

(4)   Hassanzadeh, P.; Andrews, L. *J. Phys. Chem.* **1992**, *96*, 9177.

(5)   Tague, T.J. Jr.; Andrews, L. *J. Am. Chem. Soc.* **1994**, *116*, 4970.

(6)   Hassanzadeh, P.; Andrews, L. *J. Am. Chem. Soc.* **1992**, *114*, 9239.

(7)   Hassanzadeh, P.; Hannachi, Y.; Andrews, L. *J. Phys. Chem.* **1993**, *97*, 6418.

(8)   Martin, J. M. L.; Taylor, P. R.; Hassanzadeh, P.; Andrews, L. *J. Am. Chem. Soc.* **1993**, *115*, 2510.

(9)   Andrews, L.; Hassanzadeh, P.; Martin, J. M. L.; Taylor, P. R. *J. Phys. Chem.* **1993**, *97*, 5839.

(10)   Lory, E.; Porter, R. *J. Am. Chem. Soc.* **1973**, *95*, 1767.

(11)   Kawashima Y.; Kawaguchi, K.; Hirota, E. *J. Chem. Phys.* **1987**, *87*, 6331.

(12)   Stanton, J.F.; Gauss, J.; Watts, J.D.; Lauderdale, W.J.; Bartlett, R.J. ACESII, an Ab Initio System, *Quantum Theory Project*; University of Florida: Gainesville, FL 1994.

(13)   Paetzold, P. *Pure and Appl. Chem.* **1991**, *63*, 345.; *Adv. Inorg. Chem.* **1987**, *31*, 123.

(14)   Martin, J. M. L.; Taylor, P. R.; Yustein, J. T.; Burkholder, T. R.; Andrews, L. *J. Chem. Phys.* **1993**, *99*, 12.

Table 1. SCF Calculated and Observed Isotopic Frequencies (cm^{-1}) for Linear BNBH.

	ν(B–H)	ν_a(B–N–B)	ν_s(B–N–B)	δ(N–B–H)	δ(B–N–B)
^{11}B^{14}N^{11}BH	2981.4	1988.9	1159.3	847.0	158.2
observed	2805.6	1846.3	1089.3	746.2	-
ratio	0.9410	0.9283	0.9396	0.8810	
I (km/mol)[b]	[94]	[947]	[118]	[2x24]	[2x.3]
I (observed)[c]	[0.004]	[0.160]	[0.014]	[0.009]	-
^{10}B^{14}N^{11}BH	2981.4	1993.9	1196.1	847.0	159.9
observed	2805.6	1851.5	-	746.2	-
^{11}B^{14}N^{10}BH	3004.9	2016.0	1173.7	857.0	158.9
observed	2826.9	1871.4	-	754.5	-
^{10}B^{14}N^{10}BH	3004.9	2020.5	1210.9	857.0	160.6
observed	2826.9	1876.4	1136.4	754.5	-
ratio	0.9408	0.9287	0.9385	0.8804	
I (km/mol)	[114]	[957]	[133]	[2x26]	[2x.3]
^{11}B^{15}N^{11}BH	2980.3	1951.1	1157.5	846.0	155.1
observed	2805.1	1812.3	1087.2	745.2	-
ratio	0.9412	0.9289	0.9393	0.8809	
I (km/mol)	[88]	[903]	[121]	[2x24]	[2x.3]
^{10}B^{15}N^{11}BH	2980.3	1956.0	1194.7	846.0	156.8
observed	2805.1	1817.2	-	-	
^{11}B^{15}N^{10}BH	3003.5	1979.5	1171.4	855.9	155.9
observed	2826.2	1838.8	-	-	
^{10}B^{15}N^{10}BH	3003.5	1983.9	1209.0	855.9	157.5
observed	2826.2	1843.3	1134.2	753.5	-
ratio	0.9409	0.9291	0.9381	0.8804	
^{11}B^{14}N^{11}BD	2368.8	1833.3	1134.9	677.4	150.6
observed	2218.7	1717.6	1062.4	596.4	-
ratio	0.9366	0.9369	0.9361	0.8804	
I (km/mol)	[447]	[615]	[97]	[2x25]	[2x0]
^{10}B^{14}N^{11}BD	2369.3	1839.7	1169.9	677.4	152.4
observed	2219.7	1723.8	-	-	-
^{11}B^{14}N^{10}BD	2418.6	1837.5	1147.4	689.9	150.9
observed	2262.3	1723.2	1074.0	-	-
^{10}B^{14}N^{10}BD	2419.1	1843.6	1182.8	689.9	152.6
observed	2263.2	1729.0	-	-	-

[a]Using 6-311G* basis sets, [b]calculated infrared intensities, [c]observed band absorbances.
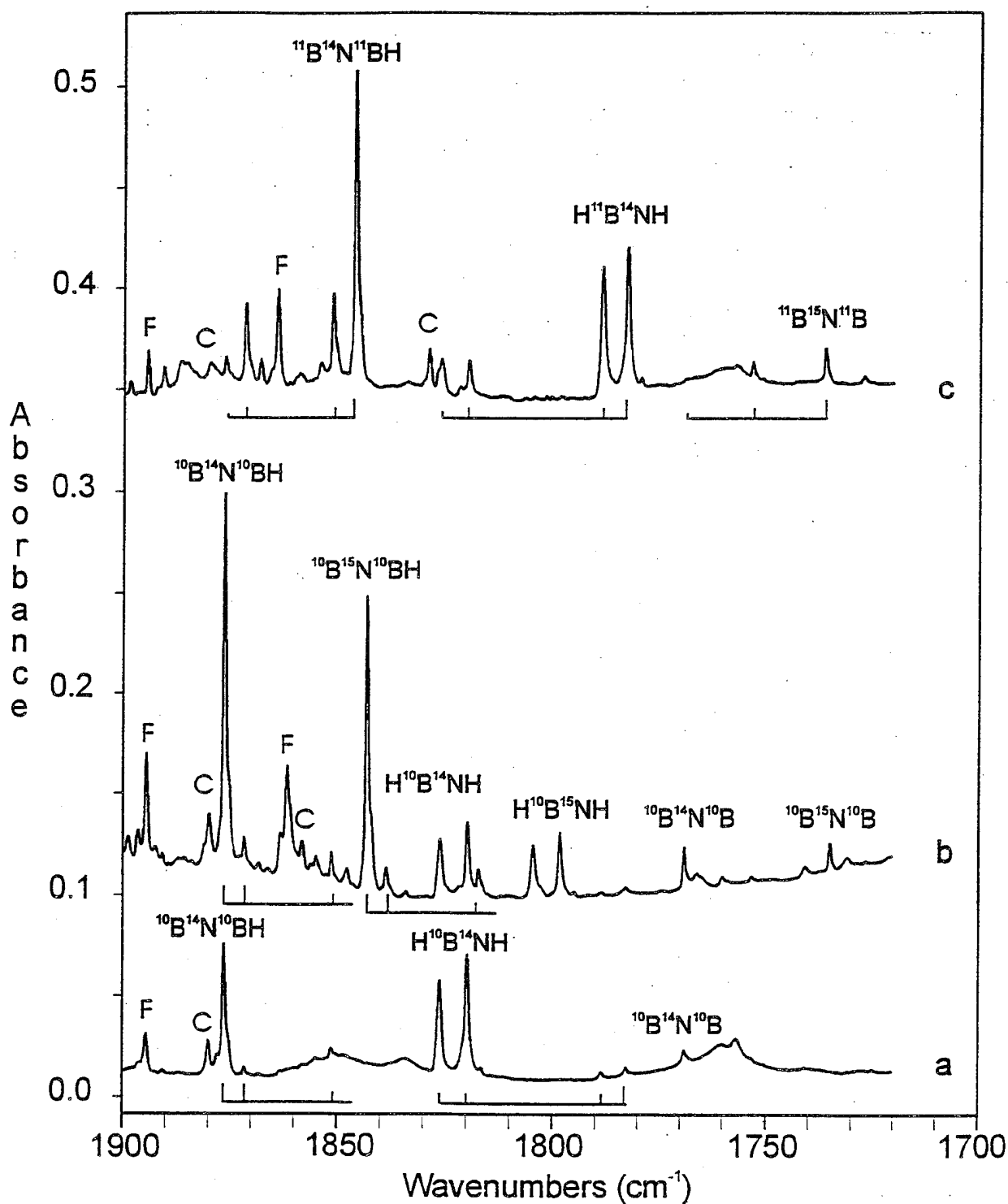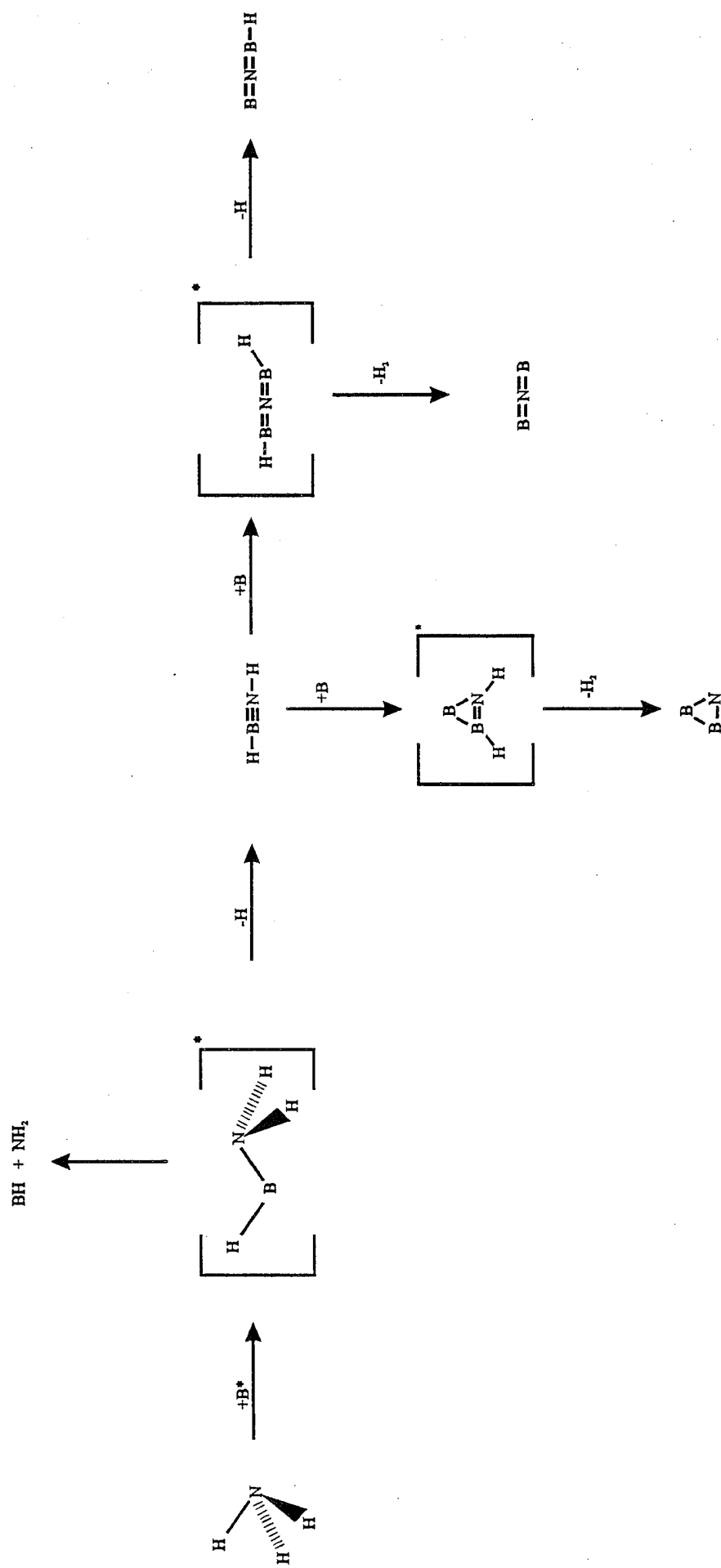
Figure Caption

Figure 1. Infrared spectra in the $B-N$ stretching region 1900-1725 cm^{-1} for pulsed-laser ablated boron atom-ammonia-argon samples condensed at $10\pm1K$. (a) $^{10}B+^{14}NH_3$, (b) $^{10}B+^{14}NH_3/^{15}NH_3$, and (c) $^nB+^{14}NH_3$. Horizontal lines indicate boron isotopic multiplets.

Scheme 1. Laser-ablated Boron Plus Ammonia Reaction Mechanism

187

Theoretical Studies of Nonadiabatic Processes Relevant to the Stability and Detection of Energetic Species

David R. Yarkony
Department of Chemistry
Johns Hopkins University
Baltimore, MD 21218

I. Radiationless decay of cyclic N_3F

Motivation

Recently M. Gordon's group at Iowa State University has identified an isomer of fluorine azide NNNF as a potential high energy density material (HEDM).[1] This isomer, denoted cyclic N_3F, can be described as an $NF(a^1\Delta)$ moiety bonded to ground state N_2. It is energetic by approximately 15kcal/mol relative to fluorine azide and has the structure indicated below.
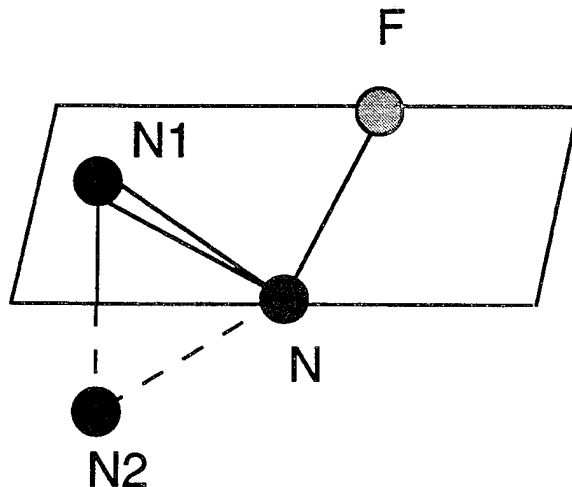
While there is a signifcant barrier (~10kcal/mol) to the dissociation to $N_2(X^1\Sigma_g^+) + NF(a^1\Delta)$ the possibility of predissociation to $N_2(X^1\Sigma_g^+)+NF(X^3\Sigma^-)$ could not be ruled out. In a related situation we had shown[2] that the asymmetric isomer of NO dimer, a-N_2O_2, described in 1988 by Michels and Montgomery[3] as potential HEDM is in fact rapidly predissociated to $N_2O + O(^3P)$ through an intersystem crossing with a triplet state. Thus computations to address the possibility of spin forbidden radiationless decay of N_3F were undertaken.[1]

Computational Studies

The following figure illustrates three possible situations that may arise for the minimum energy crossing point on the surface of intersection:
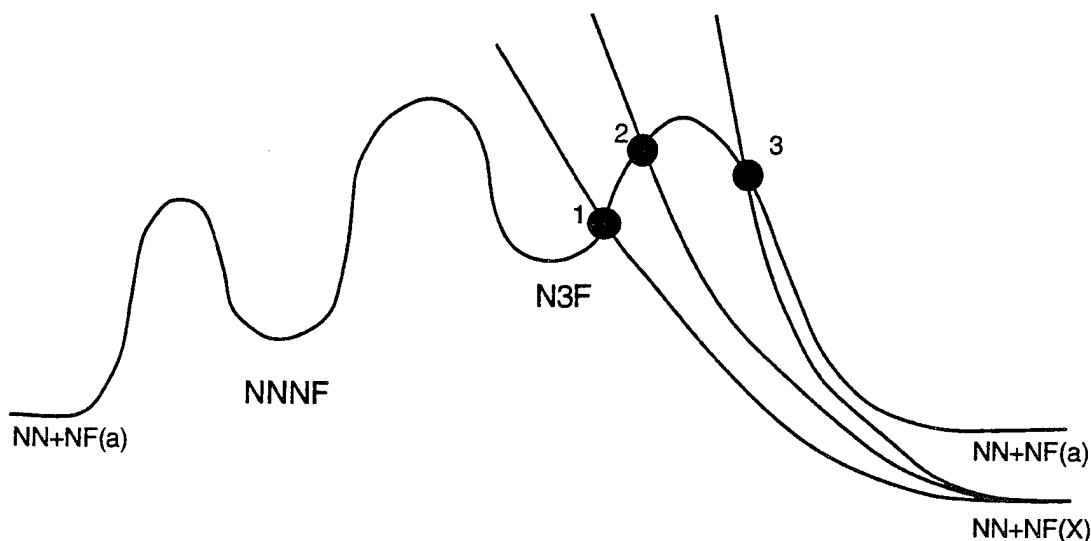
(1) rapid predissociation, (2) slow predissociation of lowest vibrational levels and rapid predissociation of higher vibrational levels and (3) slow predissociation of all levels. The third possibility is perhaps the most challenging. In that case the HEDM will certainly be detectable. However a more complete characterization of the relevant singlet-triplet surface of intersection is required to enable a determination of the lifetime of the vibrational levels which in this case are narrow resonances.

The electronic ground state for the cyclic isomer is the $1^1A'$ state and the relevant triplet wave function has symmetry $^3A''$. The wavefunctions for the $1^1A'$ and $1^3A''$ states were described at the multireference CI level. The results summarized below were obtained with a 5s4p1d basis and CSF expansions of dimension: 1126950 ($^1A'$) and 1868660 ($^3A''$).

	R(NF) (Å)	R(N-N1) (Å)	R(N1-N2) (Å)	$\angle$F-N-N12	E (kcal/mol)
Eq	1.383	**1.468**	1.181	101.6	0
TS	1.379	**1.760**	1.116	100.4	11.3
MEX	1.371	**1.869**	1.089	99.3	5.3
X1	1.381	1.826	1.058	117.7	17.5
X2	1.410	**1.757**	1.060	134.2	37.3

Eq=equilibrium structure, TS=transition state, MEX=minimum energy crossing, XN= additional crossings with R(N-N1)=R(N-N2) fixed at indicated value. Crossings degenerate to <0.5cm^{-1}.

Comparing the values of R(N-N1)=R(N-N2), an approximate reaction coordinate, it is seen that cyclic N$_3$F represents a type (3) situation, that is the crossing surface lies behind the barrier to spin-allowed decay. Thus cyclic N$_3$F is expected to be detectable. The additional calculations that are required to determine the lifetime of the vibrational levels (resonances) will be the object of a future investigation.

II. Quantitative Detection of BH(a$^3\Pi$) via BH(a$^3\Pi$) - BH(b$^3\Sigma^-$) LIF

Motivation

Benard and coworkers have suggested BH(a$^3\Pi$) as a possible energy source in an energy transfer chemical laser.[4] The metastable a$^3\Pi$ state stores approximately 1.3 eV of energy for use in a collisional energy transfer chemical laser system analogous to the oxygen-iodine laser system. Quantitative detection of BH(a$^3\Pi$) is desirable in design of this laser and can be accomplished through BH(a$^3\Pi$) - BH(b$^3\Sigma^-$) laser induced fluorescence. The BH(b$^3\Sigma^-$) state however can be predissociated by a spin-orbit induced interaction with a repulsive 1$^3\Sigma^+$ state (see figure below). Thus quantitative detection of BH(a$^3\Pi$) requires knowledge of the vibrational level dependence of the BH(b$^3\Sigma^-$) predissociation rate. Computational studies were undertaken to determine both the radiative and radiationless decay rates of the b$^3\Sigma^-$ state.[5]

Computational Studies

The spin-orbit induced radiationless decay process b$^3\Sigma^-$ → 1$^3\Sigma^+$ in BH was characterized. The spin-orbit coupling was determined within the Breit-Pauli approximation using MCSCF/CI wave functions. The relevant potential energy curves and spin-orbit interaction are presented below.
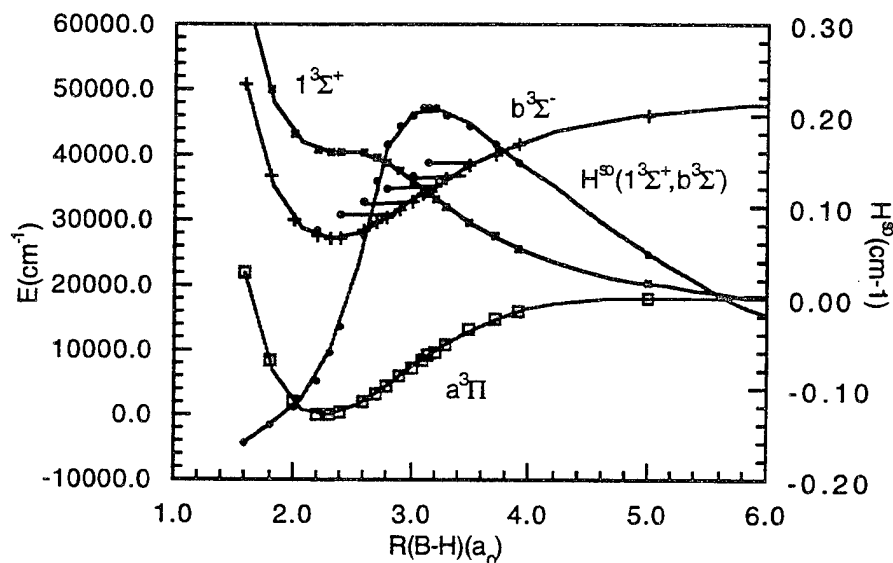
The radiationless decay lifetimes of the (b$^3\Sigma^-$,v,N, F$_i$) fine structure levels were determined in a Hund's case (b) approximation. The (b$^3\Sigma^-$,v=0-2, N = 0-15) levels are not significantly predissociated. However a spin-orbit induced perturbation b$^3\Sigma^-$ ~ 1$^3\Sigma^+$ of magnitude approximately

0.2 cm^{-1} within the crossing region of the $b^3\Sigma^-$ ~ $1^3\Sigma^+$ states results in appreciable predissociation of the v'=3 (v'=2) level in BH for low N (high N). The shortest calculated nonradiative lifetime τ=277ns corresponding to the $(b^3\Sigma^-, v=3, N=15, F_2)$ level is comparable to the radiative lifetime $(b^3\Sigma^- \rightarrow a^3\Pi)$ of τ=260ns of that level (case (a) approximation).

III. Nonadiabatic Effects in the Electronic Spectra of B_2
Motivation

The spectrum of B_2 is relevant to the study of boron containing HEDMs. Brazier and Carrick[6] observed significant deviations from the expected isotopomer relations in the $(2^3\Pi_g, v=0)$ – $(A^3\Pi_u, v= 0)$ band, deviations they attributed to perturbations in the $2^3\Pi_g$ state arising from an avoided crossing of the $1,2^3\Pi_g$ states. More recently these workers have reported a detailed analysis of the $(2^3\Pi_g, v")$ – $(A^3\Pi_u, v')$ band system[7] observing a sudden loss fluorescence signal for v" >1 and a significant rotational dependence in the interstate perturbations that they regard as highly unusual. A goal of our research program is to provide a theoretical underpining for these results.

Theoretical Approach

The adiabatic potential energy curves for the $1,2,3^3\Pi_g$ states of B_2 are pictured below.
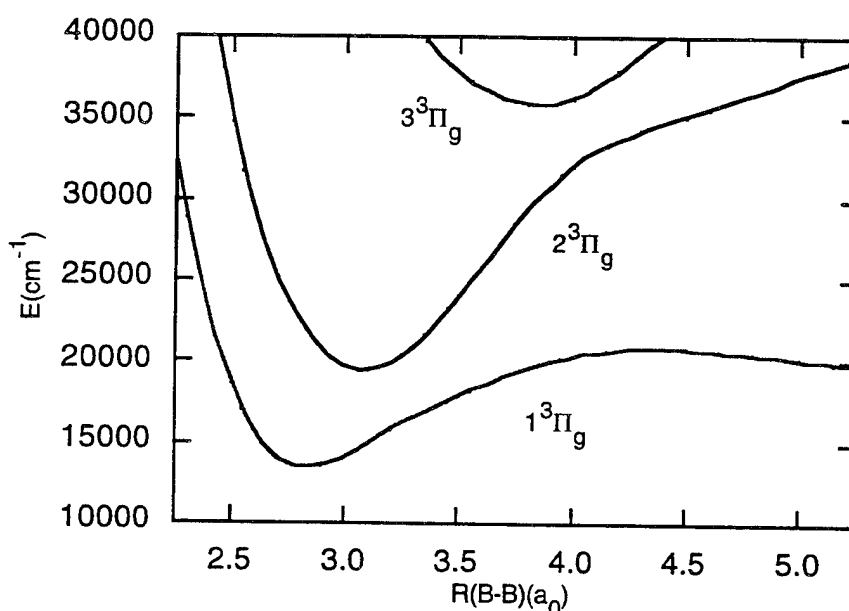
From this figure it is seen that the vibrational levels of the $2^3\Pi_g$ state, for v > 0, are resonances, predissociated by nonadiabatic interactions with the $1^3\Pi_g$ adiabatic state. Although only two

adiabatic states are required to describe these vibrational level <u>three</u> rigorous diabatic states are required to describe these levels and their radiationless decay. Our computational experience with the analogous states in Al_2[8] has shown that a nonperturbative, multichannel resonance theory would be required to provide quantitative a description of these resonances.

We are in the process of developing the computational tools to treat resonances involving several coupled electronic states in a numerically efficient manner. To date we have developed an approach valid for the description of a single dissociative electronic state coupled nonadiabatically to an arbitrary number of bound states.[9] Our approach has the advantage that both broad and narrow resonances are described with equivalent computational effort. Preliminary applications to the Al_2 system have been reported.[9] This approach is currently being extended to treat mulitchannel resonances.[10] The resulting computational approach will be used to described the quasi bound vibrational levels of the $2^3\Pi_g$ state of B_2.

REFERENCES

1. G. Chaban, D. Yarkony, and M. Gordon, to be submitted.

2. K. A. Nguyen, M. S. Gordon, J. A. Montgomery, H. H. Michels, and D. R. Yarkony, J. Chem. Phys. **98**, 3845 (1993).

3. H. H. Michels and J. A. Montgomery Jr., J. Chem. Phys. **88**, 7248 (1988).

4. D. J. Benard *Abstracts of the High Energy Density Materials Contractors Meeting,* **1993** .

5. L. A. Pederson and D. R. Yarkony, Molec. Phys. **84**, 611 (1995).

6. C. R. Brazier and P. G. Carrick, J. Chem. Phys. **96**, 8683 (1992).

7. C. R. Brazier and P. G. Carrick, J. Chem. Phys. **100**, 7928 (1994).

8. S. Han, H. Hettema, and D. R. Yarkony, J. Chem. Phys. **102**, 1955 (1995).

9. S. Han and D. R. Yarkony, J. Chem. Phys.submitted.

10. S. Han and D. R. Yarkony, manuscript in preparation

Cavity Ringdown Laser Absorption Spectroscopy of Catalytic Plasma Expansions

J.J. Scherer, J.B. Paul, C.P. Collier, and R.J. Saykally

Department of Chemistry, University of California, Berkeley, CA 94720-1460

The goal of this project is to synthesize and characterize several interesting HEDM species which have been shown through *ab initio* calculations to be metastable, but for which no credible experimental evidence exists. We have chosen the ring (D_{3h}) form of ozone[1] and the cyclic N_4 molecule[2] as initial targets, representative of larger classes of such molecules. The principal difficulty in this endeavor is that of finding a suitable means for producing and detecting these species. Because of their extreme fragility, "standard" diagnostic methods of mass spectroscopy, electronic spectroscopy, etc. are likely to fail.

We have chosen to generate O_3 and N_4 by two different methods in supersonic free jets, anticipating that the rapid collisional quenching that occurs in these medial can trap such metastable species in local potential minima. A pulsed corona discharge was first employed for generating the HEDM species, but subsequent experiments with a supersonic catalytic plasma reactor have appeared more promising. These are described below.

Detection of the metastable molecules was initially attempted through VUV (118 nm) photoionization in a time of flight mass spectrometer. However, it appears that even this – the shortest conveniently available wavelength – is nevertheless too long to effect a sufficiently gentle ionization, and no evidence for either cyclic O_3 or cyclic N_4 has been obtained using this method. Current efforts are directed toward the development of infrared cavity ringdown laser absorption spectroscopy (IRCRLAS) for this purpose, as infrared excitation of HEDM species is less likely to induce decomposition than are viable alternatives.

The laser vaporization supersonic plasma reactor is shown in Figure 1. Our source consists of a steel body designed to accept a 0.5 in. target metal rod, which is continuously rotated and translated using a screw drive. The pulse of gas is supplied from a General Valve Series 9 solenoid valve (0.060 inch orifice), with a backing pressure of 15 - 300 psi. The clustering channel can be removed from the body and interchanged, however the most successful is fan shaped. There are two reasons for this: the first is to allow the vaporization laser, which comes in 22° off normal to the surface of the target rod, access to the rod. This angle is necessary because the first skimmer of a time-of-flight mass spectrometer is located directly in front of the source. The second reason is this geometry increases the interaction length of the supersonic expansion and the probe laser of the direct absorption (CRLAS) spectrometer, resulting in higher sensitivity. The vaporization laser is a 248 nm excimer (Questek 2460) supplying typically 320 mJ/pulse. It is often necessary to attenuate the laser flux by shuttering and/or adjusting the focus onto the target.

We have tested this catalytic plasma approach for cluster production and compared the results with those obtained using standard laser vaporization for the molecules C_3 and Si_2. Monitoring the 4050 Å C_3 (comet) band, the maximum signal was obtained by seeding 1% CH_4 in helium, and using a backing pressure of 80 psi. By far the best catalytic metal proved to be either copper or silver, however, C_3 could be generated using a variety of other metals, including gold, niobium, aluminum, and nickel. When carbon was used as the target material, the C_3 signal strength did not change whether or not CH_4 was present in the carrier gas. This implies that the plasma resulting from the vaporization of graphite is in some way insufficient to atomize the CH_4

in the carrier gas. The plasma reactor method was found to produce an order of magnitude more C_3 signal than that from laser ablation of a graphite rod (Figure 2). Because we use a direct absorption technique (CRLAS) for detection, these results should accurately reflect the relative number density of C_3 in the jet expansion, and therefore show that the plasma reactor method in certain cases is considerably superior to standard laser vaporization for the generation of clusters.

As a means of generating HEDM species, we have tried seeding N_2, NH_3, or O_2 in the carrier gas of the plasma reactor source. We used the mass spectrometer with the 118 nm ionization as the method of detection. Several different target rod metals were tried. Figure 3 shows a mass spectrum taken with 355 nm light as the ionizing wavelength with a copper target rod. The presence of copper nitride clusters shows that free nitrogen atoms are most likely available to form new clusters. Unfortunately, no pure nitrogen or oxygen clusters were observed with the 118 nm ionization under any conditions. The main reason for this is probably the relatively low sensitivity of this apparatus as a whole due to the low conversion efficiency of the frequency tripling process.

By seeding silane into the carrier gas, metal silicide clusters were found to be produced very effectively. As these are important in a variety of problems involving semiconductor processing, a set of mass spectroscopic and electronic spectroscopy studies were carried out for the three coinage metal silicides[3,4,5] as well as for platinum slicides.[6] The first characterization of the diatomic species is presented in the references.

Electronic spectra of species produced in the catalytic plasma expansions were measured by the CRLAS method. A detailed description of the technique is presented in Reference 7. The Berkeley Cavity Ringdown Laser Absorption Spectrometer and Time-of-Flight mass spectrometer (TOFMS) are diagrammed in Figure 4. The design incorporates three stages of differential pumping, consisting of a main source chamber evacuated by a large Roots pump (2500 cfm Edwards EH4200), and two diffusion pumped regions. Each of the three regions are separated by electroformed molecular beam skimmers each having a 2 mm diameter (Beam Dynamics). The tandem design of the apparatus allows characterization of the molecular beam source while simultaneously measuring absorption features, which greatly aids in the maximization of cluster concentrations and also allows correlation studies to be performed.

The ringdown laser pulse consists of a few mJ of narrowband (.04 cm^{-1}) excimer pumped dye laser light which is coupled into the cavity with the use of a telescope. Roughly 1 part in 10^8 of this light passes through the exit mirror of the cavity and is detected with a photomultiplier (Hammamatsu R912). Proper timing of the ringdown laser pulse with respect to the transient molecular beam assures maximum temporal overlap between the two events. In fact, one of the primary advantages of employing CRLAS for pulsed molecular beams is the similar time scales of both the molecular beam and ringdown events (5-25 μs), allowing a probe duty cycle near unity to be achieved. The resultant ringdown decay waveform is amplified, digitized with a 12-bit, 20 MHz transient digitizer, and sent to a computer for analysis. Because the amount of light which transmits the exit mirror is linearly proportional to the amount of light still trapped inside the cavity, the intensity decay monitored at the photomultiplier follows the expression

$$I(t) = I_0 e^{(-Tt2L/c)}, \qquad (1)$$

where T is the transmission coefficient of the two mirror cavity, L is the mirror spacing, and t is time. Measurement of the cavity "ringdown" time (t, wherein $I = I_0 e^{-1}$) allows the transmissivity of (or absorption inside) the cavity to be determined, if the mirror spacing (cavity length) is known. This cavity "transmissivity" represents the total losses experienced by the light pulse

while traversing the cavity, including mirror transmissivity, optical scattering, mirror coating absorption, and molecular absorption for species located between the two mirrors. Measurement of the cavity "ringdown time" at a given wavelength gives a direct measurement of the total losses experienced by the circulating light over a single cavity round trip pass. A plot of cavity losses verses wavelength allows an absorption spectrum to be obtained for species placed in the cavity. Accurate relative absorption intensities for molecular transitions (in the limit of weak absorption) are readily determined by comparing cavity losses with and without the sample present. Typically, 16 laser shots are averaged per wavelength step in order to reduce noise introduced by fluctuations in the pulsed molecular beam.

We are presently extending the CRLAS method into the infrared region for application to detecting HEDM species. Vibration-rotation transition of molecules generated in the pulsed catalytic plasmas should be detected very efficiently by this approach. Preliminary results have been obtained for measurements near 1.5 μm and 3.3 μm.

References

1. S.S. Xantheas et al., *J. Chem. Phys.* **94**, 8054 (1991).

2. W.J. Lauderdale, J.F. stanton, and R.J. Bartlett, *J. Phys. Chem.* **96**, 1173 (1992); T.J. Lee, *J. Chem. Phys.* **94**, 1215 (1990).

3. J.J. Scherer, J.B. Paul, C.P. Collier, and R.J. Saykally, "Cavity Ringdown Laser Absorption Spectroscopy and Time-of-Flight Mass Spectroscopy of Jet-cooled Copper Silicides," *J. Chem. Phys.* **102**, 5190 (1995).

4. J.J. Scherer, J.B. Paul, C.P. Collier, and R.J. Saykally, "Cavity Ringdown Laser Absorption Spectroscopy (CRLAS) and Time of Flight Mass Spectroscopy of Jet-cooled Silver Silicides," *J. Chem. Phys.* (in press 1995).

5. J.J. Scherer, J.B. Paul, C.P. Collier, and R.J. Saykally, "Cavity Ringdown Laser Absorption Spectroscopy (CRLAS) and Time of Flight Mass Spectroscopy of Jet-cooled Gold Silicides," *J. Chem. Phys.* (submitted 1995).

6. J.B. Paul, J.J. Scherer, C.P. Collier, and R.J. Saykally, "CRLAS and TOF Mass Spectroscopy of Jet-Cooled Platinum Silicides," *J. Chem. Phys.* (submitted 1995).

7. J.J. Scherer, J.B. Paul, A. O'Keefe, and R.J. Saykally, "CRLAS: A New Analytical Technique for Cluster Science," in *Advances in Metal and Semiconductor Cluster, Volume III*, M.A. Duncan, editor (in press 1995).
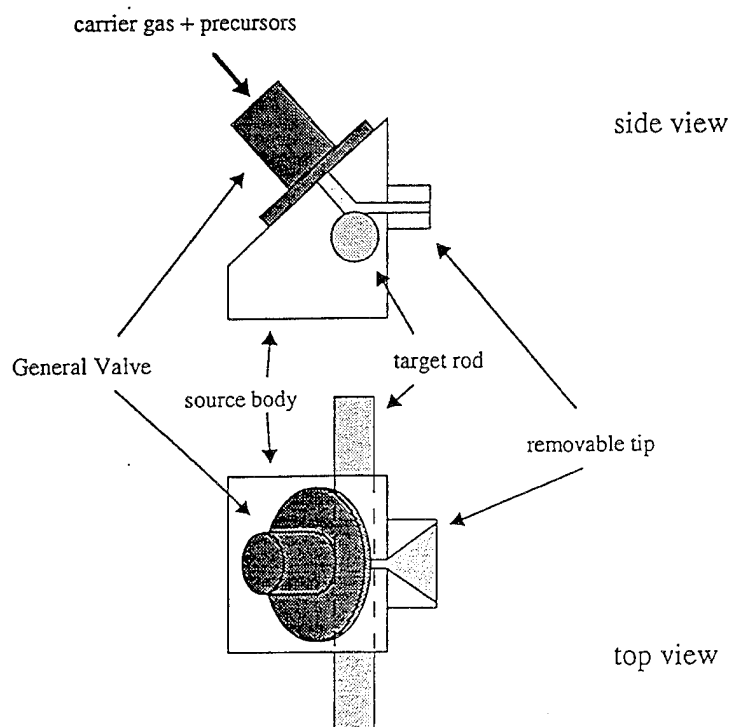
figure 1: the laser vaporization plasma reactor

$$C_3 \quad A^1\Sigma - X^1\Pi \quad (0,0)$$
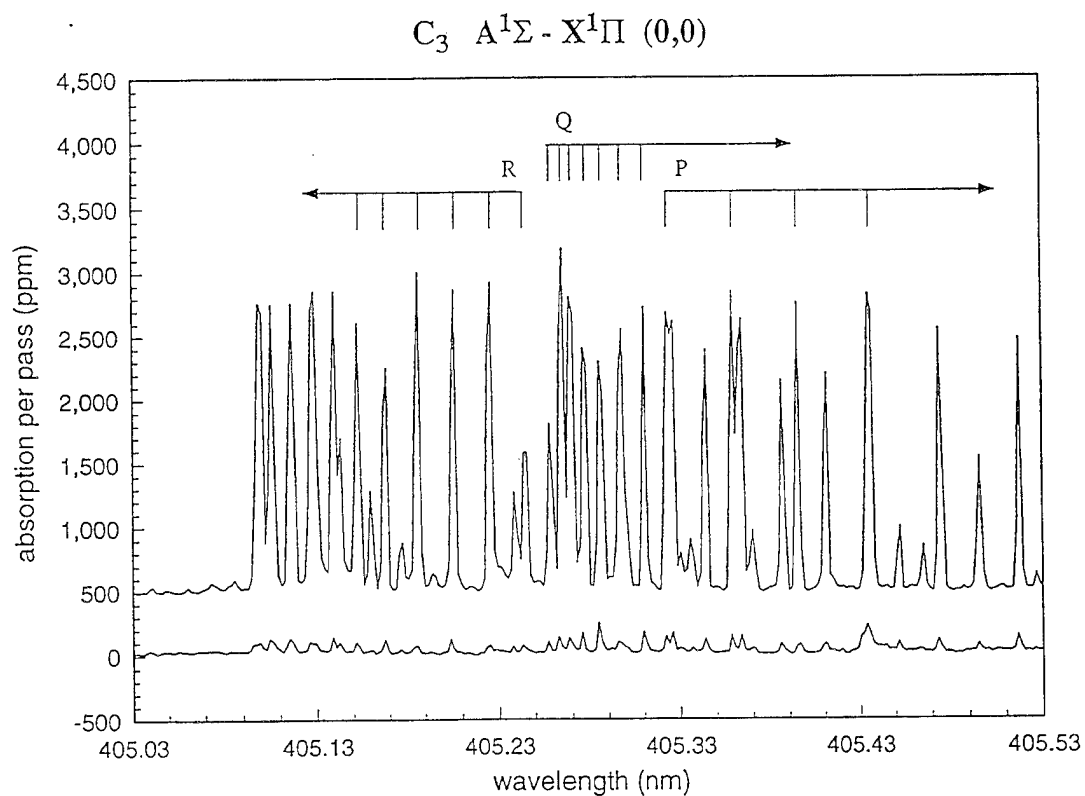
figure 2. The upper trace corresponds to C_3 generated by flowing CH_4 over a silver rod. The lower trace is from laser vaporization of a graphite rod.
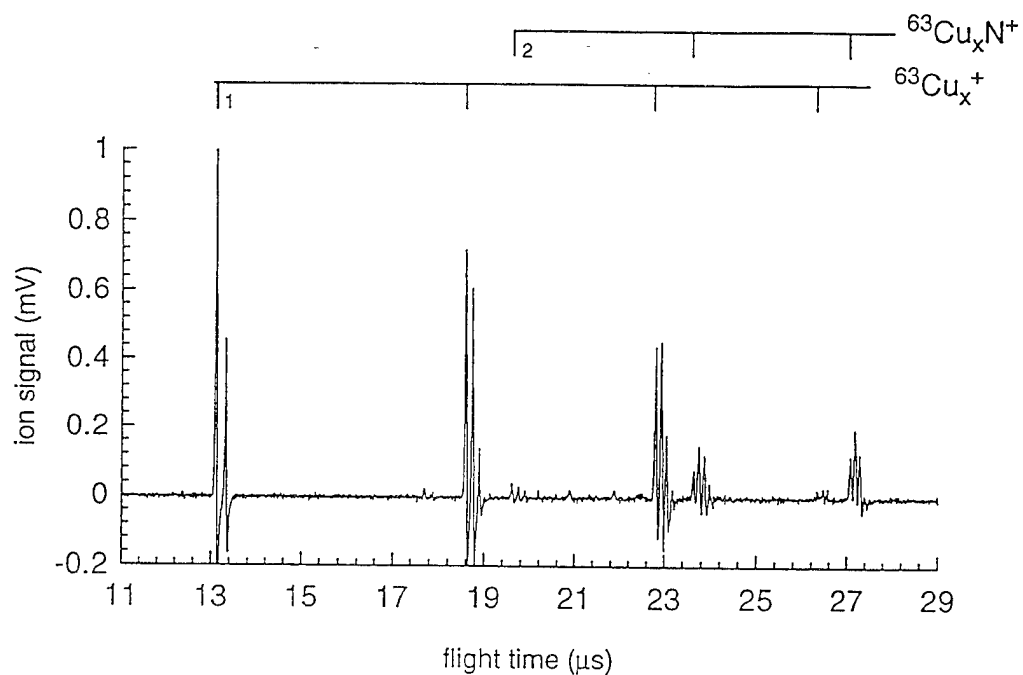
figure 3: Time-of-flight mass spectrum of copper and copper nitride clusters using 355 nm (multi-photon) ionization.

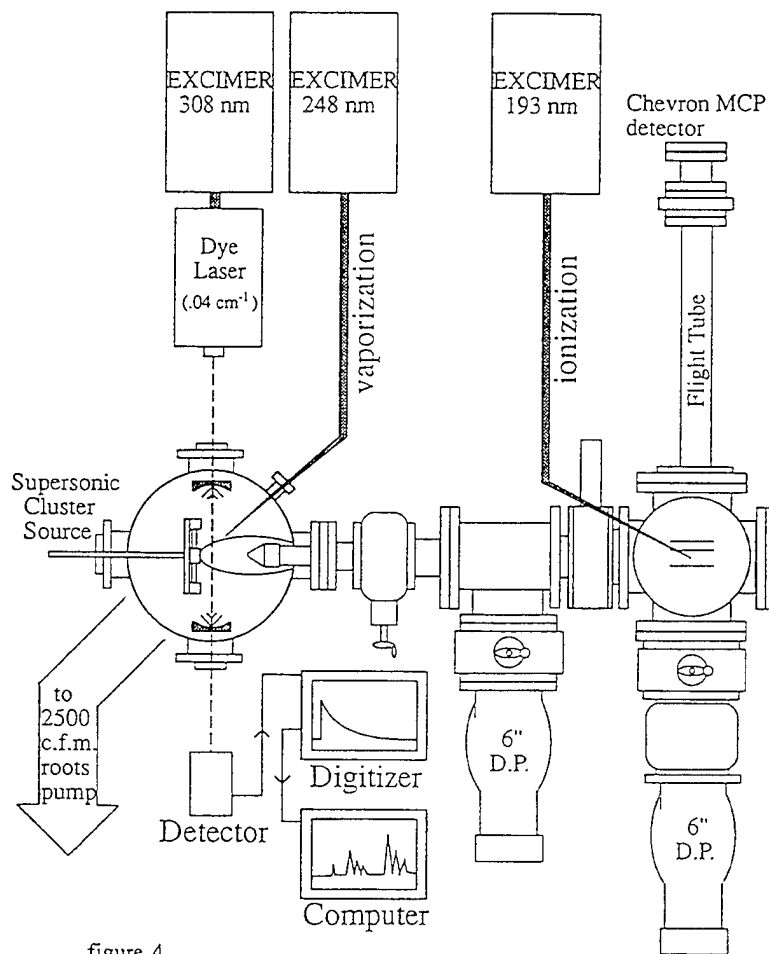## CRLAS: The Berkeley Cavity Ringdown Spectrometer

figure 4.

197

METAL DIMERS AND METAL COMPLEXES:
MODEL SYSTEMS FOR METAL- SEEDED FUELS

Michael A. Duncan

Department of Chemistry, University of Georgia, Athens, GA 30602

We are studying a variety of metal dimers and weakly bound complexes containing the metals lithium, aluminum and magnesium. These complexes are produced in supersonic molecular beams using a laser vaporization cluster source. Metal dimers and neutral complexes are studied with photoionization spectroscopy and "mass analyzed threshold ionization spectroscopy" (MATI). We will describe our latest results in this area, including new photoionization spectroscopy of the metal dimer LiAl, spectroscopic searches for MgC and MgAl dimers, and ongoing threshold photoionization experiments on lithium and aluminum complexes with rare gases and small molecules (N_2, CO_2, H_2, etc.).

The metal dimer LiAl is produced by laser vaporization using a XeCl excimer laser (Lumonics) at 308 nm on an alloy sample containing 5% lithium and 95% aluminum (Goodfellow). Photoionization is accomplished with a Nd:YAG pumped dye laser system (Spectra-Physics PDL-2 or Lambda Physik "Scanmate" system). The ionization scheme is two-color two-photon, with an tunable ultraviolet laser generated by frequency doubling in a KDP crystal as the first photon and a second dye laser with fixed red wavelengths used to complete the ionization. The isotopic species of the parent ion ($^6Li^{27}Al$ and $^7Li^{27}Al$) are detected in a homemade time-of-flight mass spectrometer.

Two excited electronic band systems have been measured for LiAl with electronic origins at 29,391 and 29,888 cm^{-1}. Both ground and excited state progressions and sequence bands are observed. The vibrational constants determined for the ground and excited states are shown in Table 1. The ground state is of particular interest for comparison to previous theoretical studies. The ground state vibrational frequency is ω_e=317 cm^{-1}, and the ground state dissociation energy is D_e=0.867 eV (determined from a Morse potential fit to the v=0 to v=5 ground state vibrational levels observed). As indicated in the table, these data are in good agreement with theory.[1,2]

Spectroscopic searches of the same type which were successful for LiAl have been

unsuccessful for MgAl and MgC diatomics. In the case of MgC, we believe that the strong bonding in C_2 causes formation of this diatomic to compete with MgC formation. MgAl studies were limited by the low concentration of Mg in the available alloy samples.

Resonance enhanced photoionization and threshold photoionization has been applied to investigate a variety of van der Waals complexes with the aluminum atom. Resonant two-photon photoionization (R2PI) studies reproduce the known spectroscopy of Al-Ar, but we are unable to obtain corresponding spectra for Al-N_2, Al-CO_2 or Al-H_2 by this method. Single photon ionization at deeper ultraviolet wavelengths near 210 nm are successful in producing strong signals for Al-$(N_2)_x$ and Al-$(CO_2)_x$, but not Al-H_2. Instead, deep UV photoionization on a beam containing hydrogen and aluminum produces a strong signal for Al-H. We suspect that aluminum atom may insert into H_2 instead of forming the weakly bound van der Waals complex. We have measured ionization potentials as a function of size for nitrogen complexes up to x=14 and for CO_2 complexes up to x=12. In the case of Al-N_2, the ionization potential appears with a sharp onset at 5.805 eV. The ionization potential of aluminum atom is 5.986 eV. The dissociation energy of Al^+-N_2 has been measured in a high pressure mass spectrometry experiment by Bouchard and McMahon to be 0.234 eV. These parameters can be combined in a simple energetic cycle to obtain the *neutral* Al-N_2 bond energy:

$$D_0(Al\text{-}N_2) = IP(Al\text{-}N_2) + D_0(Al^+\text{-}N_2) - IP(Al)$$

This procedure results in a van der Waals bond energy for Al-N_2 of 430 cm^{-1}.[4] Because the ionization onset is sharp, Al-N_2 is expected to have the same structure that its ion does. By analogy with other related metal ion-nitrogen complexes, and the charge-quadrupole interaction present, Al^+-N_2 is expected to be linear. Therefore, we believe that Al-N_2 van der Waals complex is also linear.

In experiments closely related to the threshold ionization studies, we have performed threshold photo-electron studies on some of these same complexes using the MATI technique. We have measured new and improved MATI spectra for Al-Ar, which we reported previously, and we have measured the first MATI spectrum for Al-Kr. The ground state vibrational frequencies for the Al^+-Ar and Al^+-Kr cations are determined from these spectra (69.7 and 85.3 cm^{-1}) as are the fundamental frequencies ($\Delta G_{1/2}$) for the respective neutral van der Waals complexes (33.6 and 45.1 cm^{-1}) in their ground electronic states.

References

1) L.R. Brock, J.S. Pilgrim and M.A. Duncan, Chem. Phys. Lett. **230**, 93 (1994).

2) A.I. Boldyrev, J. Simons and P.v.R. Schleyer, J. Chem. Phys. **99**, 8793 (1993).

3) M.E. Rosenkrantz, Air Force Systems Command Interim Report No. PL-TR-91-3088 (1992).

4) L.R. Brock and M.A. Duncan, J. Phys. Chem., in preparation.

Table 1. Spectroscopic constants (cm^{-1}) for the ^{7}Li-Al (A), <B> and ground states, and the comparison to the theory.

	Observed	Theory	
ground state		$^1\Sigma^+$	
ω_e''	318	322^1	
		$331.47^{2,a}$	$304.78^{2,b}$
$\omega_e x_e''$	4.05	$4.19^{2,a}$	$3.29^{2,b}$
D_e	6242	$6557.7^{2,a}$	$7098.1^{2,b}$
(A) state			
v_{00}	29383.9		
ω_e	233		
$\omega_e x_e$	2.55		
<B> state			
v_{00}	29882.3		
ω_e	261		
$\omega_e x_e$	0.802		

(a)MCSCF, (b)MRCI

1.   A.I. Boldyrev, J. Simons and Paul von R. Schleyer, *J. Chem. Phys.*, **99**, 8793 (1993)
2.   Marcy E. Rosenkrantz, Air Force Systems Command Interim Report No. PL-TR-91-3088 (1992)

Analogues of Tetrahedral N_4 as Potential High-Energy Molecules

Rodney J. Bartlett
Quantum Theory Project
University of Florida
Gainesville, Florida 32611–8435

ABSTRACT

We proposed and studied tetrahedral N_4 as a potential high-energy metastable system several years ago,[1] and then investigated several other nitrogen-based metastable molecules.[2-4] However, another route is to consider the many isoelectronic systems that share similar characteristics to N_4. This talk will survey what we know from theoretical studies about the related systems, N_2CO, N_2BF, C_2O_2, B_2F_2, $OCBF$, C_2FN and BNO_2,[5] as potential HEDM candidates that might be embedded in matrices.

REFERENCES

1. Rodney J. Bartlett, "Metastability in Molecules," Proposal to Air Force Office of Scientific Research, December 1987.

2. W.J. Lauderdale, J.F. Stanton and R.J. Bartlett, "Stability and Energetics of Metastable Molecules: Tetraazatetrahedrane (N_4), Hexaazabenzene (N_6), and Octaazacubane (N_8)," J. Phys. Chem. **96**, 1173 (1992).

3. D.H. Magers, E.A. Salter, R.J. Bartlett, C. Salter, B.A. Hess, Jr., and L.J. Schaad, "Do Stable Isomers of N_3H_3 Exist?" J. Am. Chem. Soc. **110**, 3435 (1988).

4. K. Ferris and R.J. Bartlett, "Hydrogen Pentazole: Does It Exist?" J. Am. Chem. Soc. **114**, 8302 (1992).

5. A.A. Korkin, A. Balkova, R.J. Bartlett, R.J. Boyd and PvR. Schleyer, J. Am. Chem. Soc., submitted.

Most high-energy materials contain nitrogen as a critical element, as groups like -NO_2 and -N_3 are capable of large amounts of energy storage, particularly if the molecule can be decomposed all the way to the unusually stable N_2 molecule. From another viewpoint, N also plays a role as the lone pairs on adjacent N atoms tend to cause high-energy, metastable structures to form — like tetrahedral N_4 and octahedral N_8.[1,2] Also, having multiple N atoms in ring structures benefit from similar lone-pair repulsions.[3,4] At the same time, to store the large amounts of energy that such structures contain, there must be electronic bonding leading to adequate barriers to decomposition. Tetrahedral N_4 is comparatively well-suited to these requirements, as it can store about 186 kcal/mol. Yet its barrier to unimolecular decomposition is 50–60 kcal/mol,[2] although due to spin forbidden decay on a triplet surface, the barrier is reduced to about 28 kcal/mol.[5] The reaction path and pertinent decomposition paths are illustrated in Figs. 1 and 2a.

In an effort to retain the attractive properties of N_4, just as T_dN_4 is suggested to be metastable by its isovalent relationship to stable P_4, we can consider other species isoelectronic to N_4. These include N_2CO (2), N_2BF (3), C_2O_2 (4), B_2F_2 (5), OCBF (6), C_2FN (7) and BNO_2 (8).[6]

The first modification is to relax the non-polar aspect of N_4 by replacing one N_2 with the barely polar CO unit. CO has a comparable energy to N_2, ensuring good energy storage properties. The global minimum is structure 2a, diazirinone. Nitrosyl cyanide, 2b, alone, is known experimentally. However, it is a less suitable energetic material than 2a, since its dissociation into NO and CN is endothermic by ~47–50 kcal/mol, while 2a dissociates exothermically by ~96–100 kcal/mol. The barrier to dissociation is 27 kcal/mol. This example illustrates the distinction between the synthesizable species and the preferred high energy species, or between kinetics and thermodynamics. We have to bear this in mind when proposing synthetic routes.

The relative energies of various stable forms of N_4 and N_2CO and of the remaining molecules are shown in examples 1–8.

BFN_2 can at most store only 18.7 kcal/mol. The most stable form of OCCO is an open shell $\left(^3\Sigma_g^-\right)$ state, with a storage capacity of 63.4 kcal/mol, but its open-shell character would likely cause degradation. The corresponding singlet state is not found as it is apparently repulsive. B_2F_2 is, similarly, a triplet $\left(^3\Sigma_g^-\right)$ in its lowest energy linear or C_{2h} $\left(^3B_g\right)$ form, but like the N_2BF molecule, does not benefit from decomposition to very stable diatomic species, and can only store ~11 kcal/mol. CBFO, too, seems to prefer a triplet ground state; and it, too, has little energy storage capacity (21 kcal/mol), assuming decomposition to CO and BF.

The molecule C_2NF once again has a singlet (C_{2v}) minimum, although several other isomers are possible. Similarly, OBNO, has comparable singlet and triplet states, both ~40 kcal/mol higher than BO and NO. The unusual feature of OBNO is its very small separation (~2 kcal/mol) between its lowest singlet and triplet state.

REFERENCES

1. Rodney J. Bartlett, "Metastability in Molecules," Proposal to Air Force Office of Scientific Research, December 1987.

2. W.J. Lauderdale, J.F. Stanton and R.J. Bartlett, "Stability and Energetics of Metastable Molecules: Tetraazatetrahedrane (N_4), Hexaazabenzene (N_6), and Octaazacubane (N_8)," J. Phys. Chem. **96**, 1173 (1992).

3. D.H. Magers, E.A. Salter, R.J. Bartlett, C. Salter, B.A. Hess, Jr., and L.J. Schaad, "Do Stable Isomers of N_3H_3 Exist?" J. Am. Chem. Soc. **110**, 3435 (1988).

5. D. Yarkony, J. Am. Chem. Soc. **114**, 5406 (1992).

Fig. 1

Fig. 2a

206

Fig. 2b
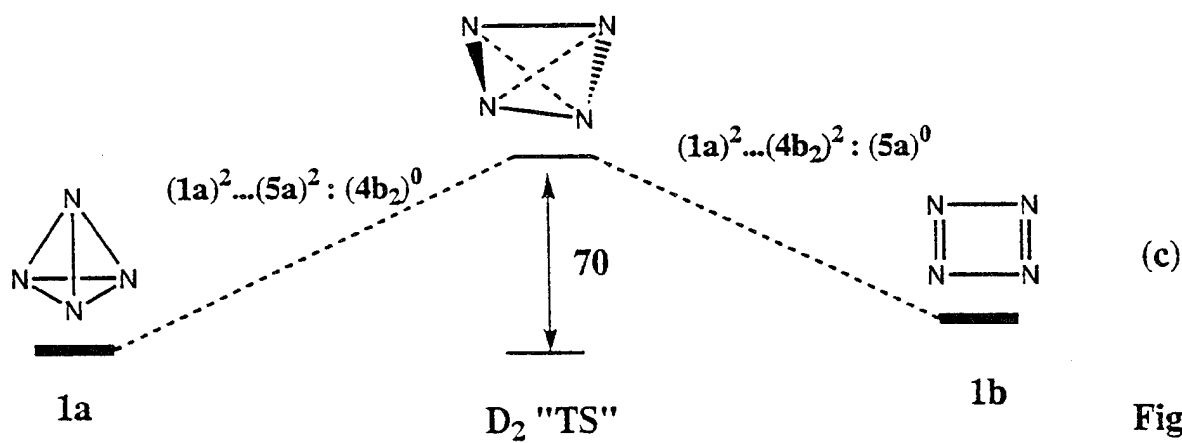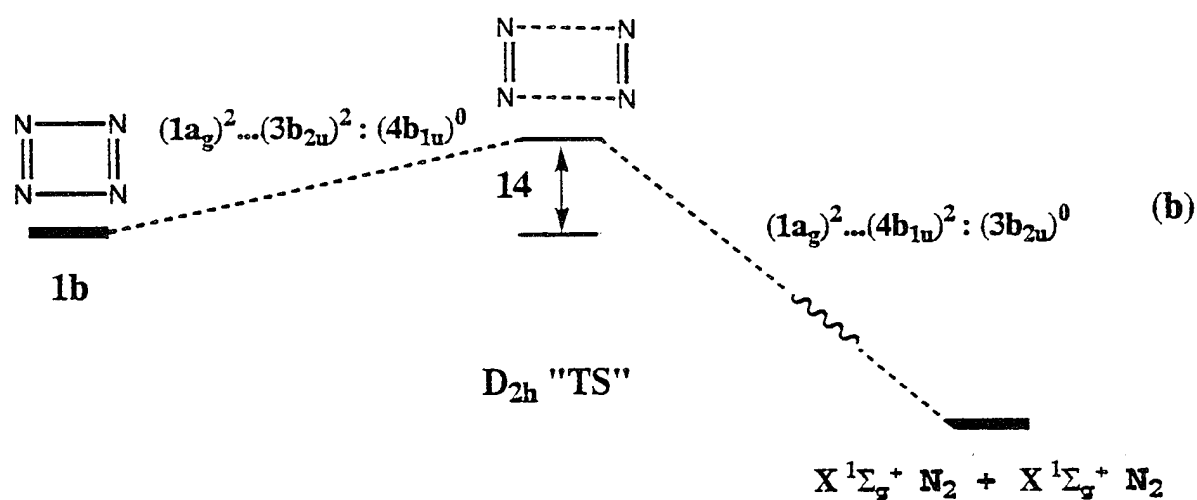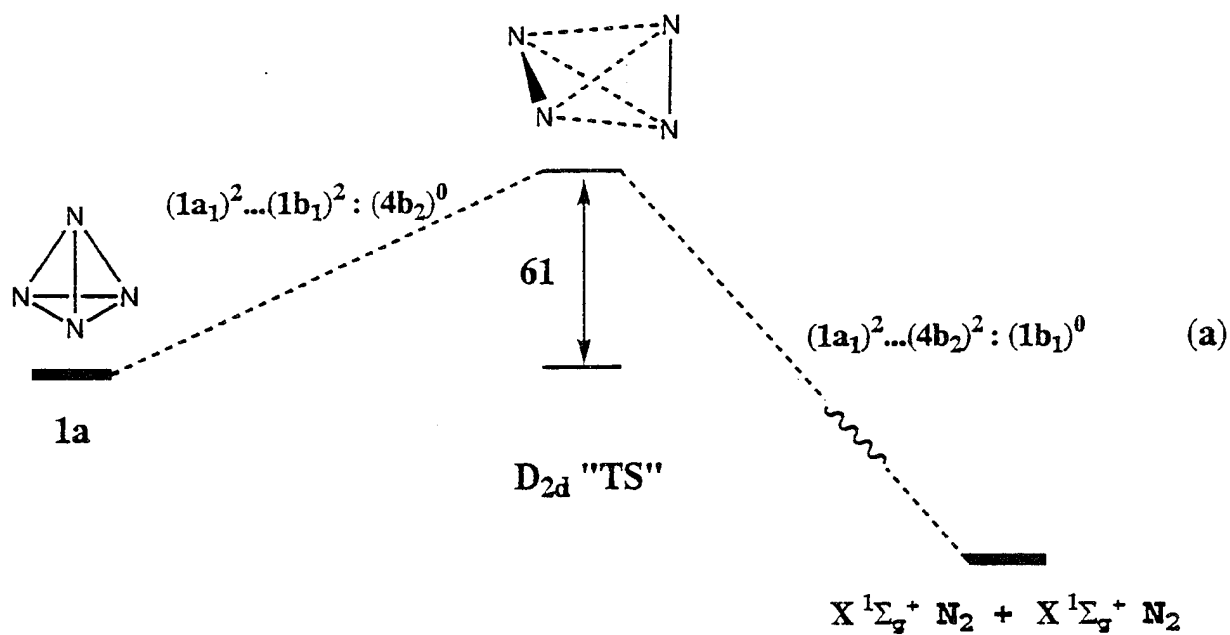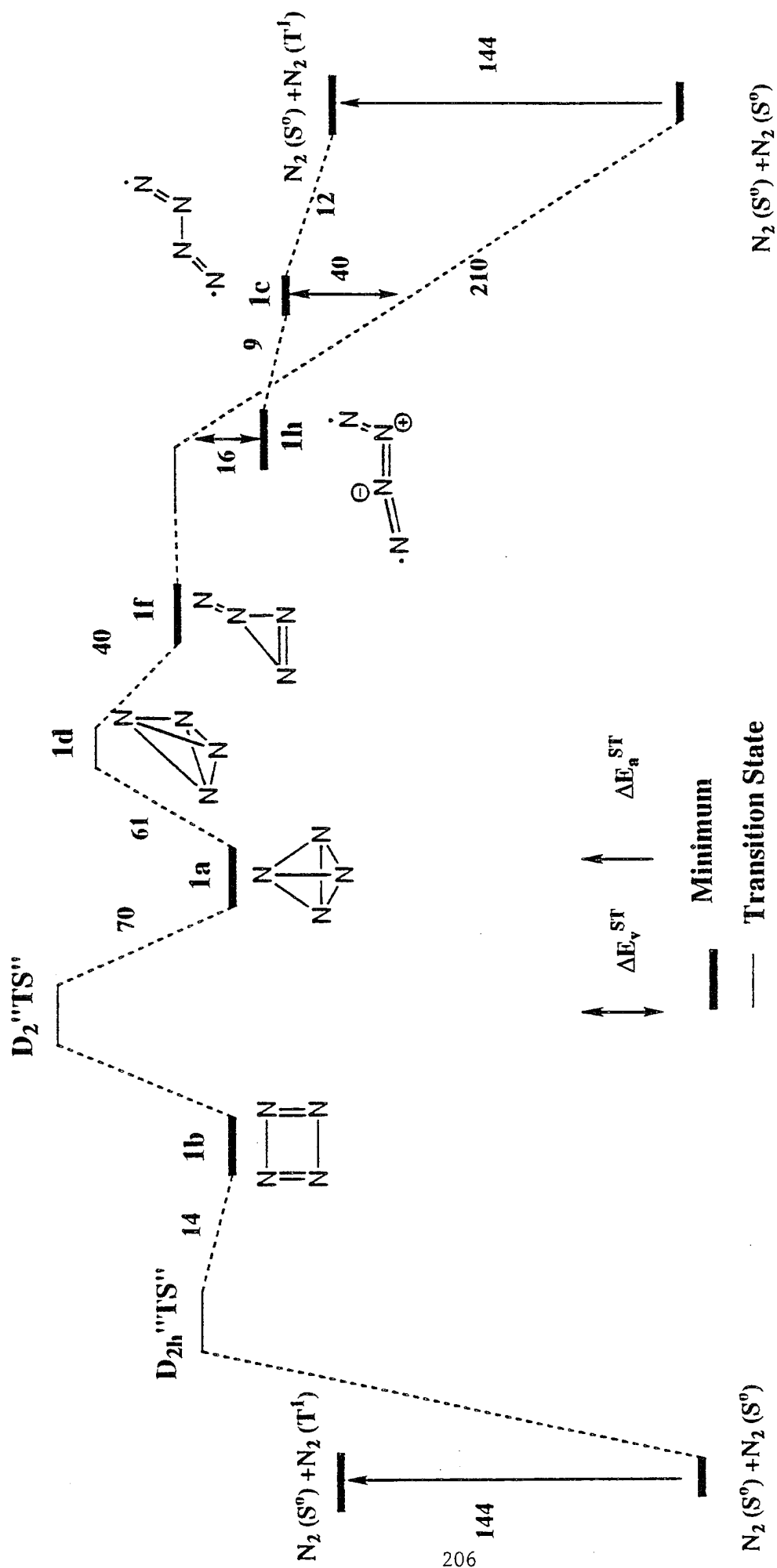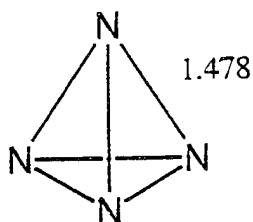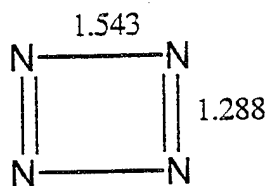
1a, T_d: 0.0 kcal/mol   **1b**, D_{2h}: -2.9 kcal/mol   **1c**, C_{2h} (^3B_u): -23.5 kcal/mol
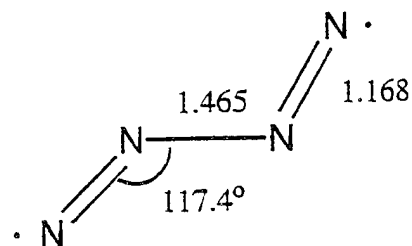
Scheme I-1
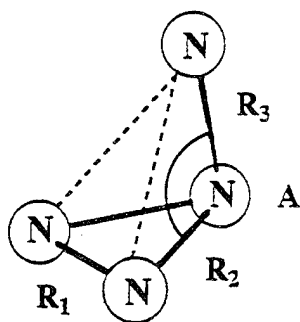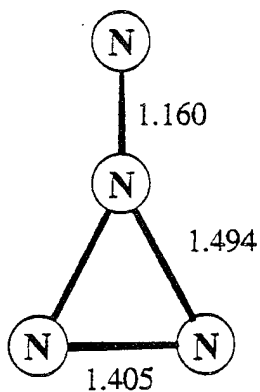
1d, C_s: 58.6 kcal/mol   **1e**, C_{2v}: 18.2 kcal/mol (MP2)   **1f**, C_s: 10.8 kcal/mol
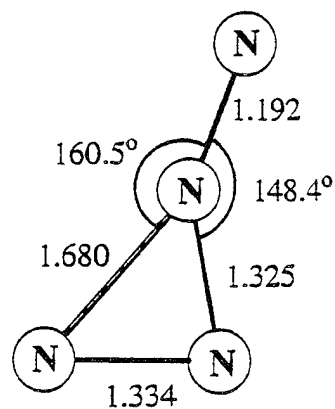
Scheme R-1
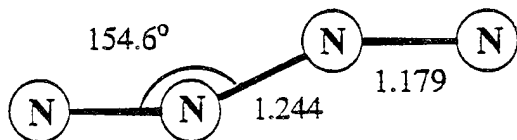
1g, C_{2h} (^3B_g): 18.6 kcal/mol (MP2)   **1h**, C_s ($^3A''$): -15.0 kcal/mol
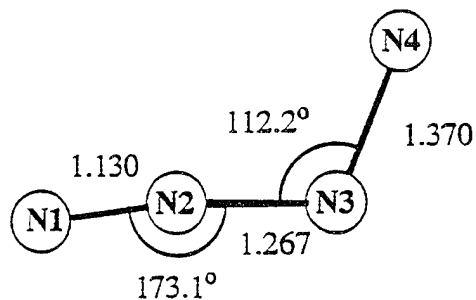
Scheme R-2

208
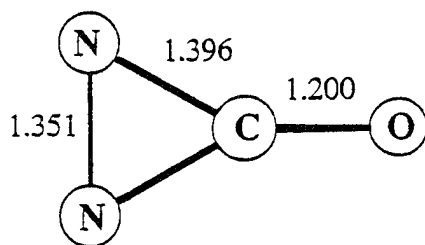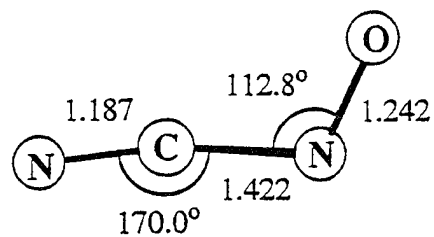
2a, C$_{2v}$: 0.0 kcal/mol

2b, C$_s$: 15.9 kcal/mol
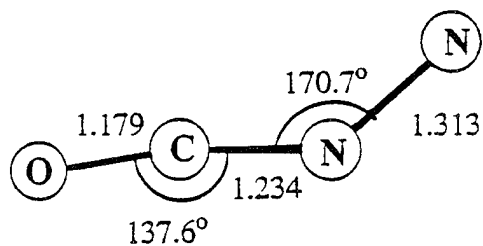
2c, C$_s$ (^{3}A"): 7.0 kcal/mol
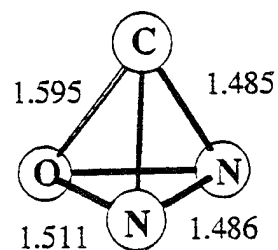
2d, C$_s$: 115.9 kcal/mol
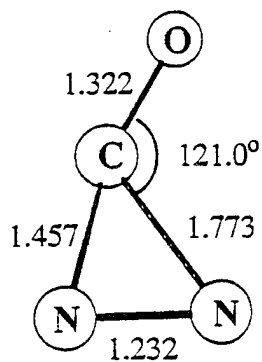
2e, C$_s$: 26.5 kcal/mol
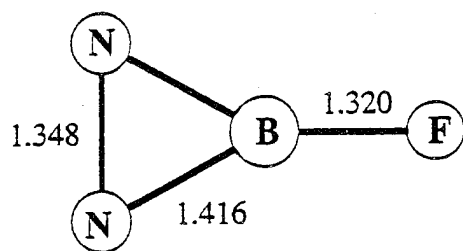
3a, C$_{2v}$: 0.0 kcal/mol
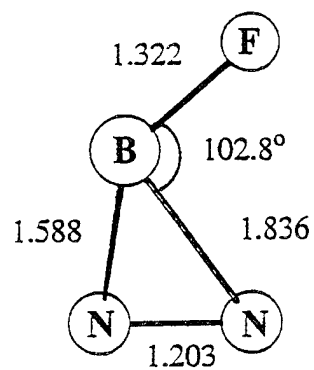
3b, C$_s$: 39.6 kcal/mol
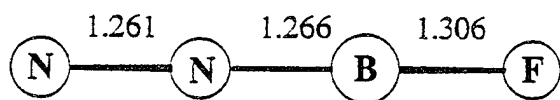
3c, C$_{*v}$ ($^3\Sigma^-$): 26. 4 kcal/mol
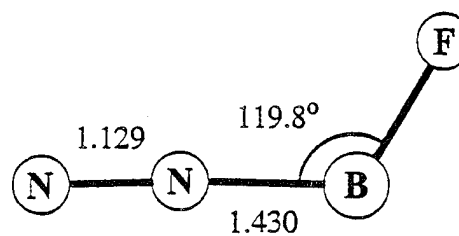
3d, C$_s$ (^{3}A"): 27.7 kcal/mol

Scheme R-5
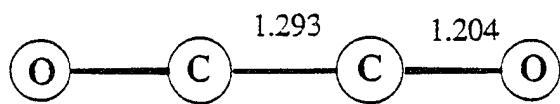
4a, D_{*v} ($^3\Sigma_g^-$): 0.0 kcal/mol
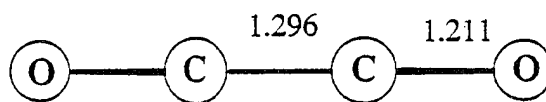
4b, D_{*v} ($^1\Delta_g$): 12.4 kcal/mol

Scheme R-6
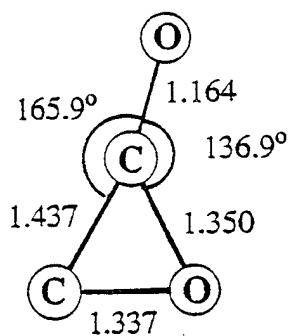
4d, C_s: 40.6 kcal/mol (HF)
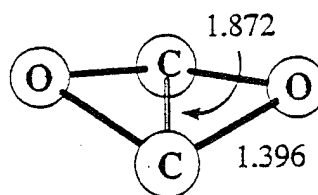
4d, C_s: 69.6 kcal/mol (MP2)
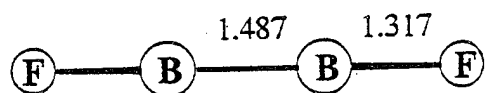
5a, D_{*v} ($^3\Sigma_g^-$): 0.0 kcal/mol
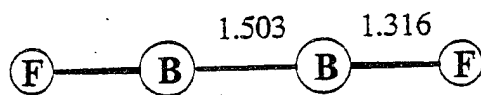
5c, D_{*v} ($^1\Delta_g$): 12.4 kcal/mol
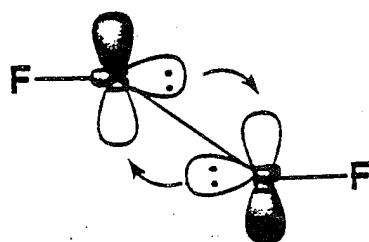
5d, C_{2h}: 5.0 kcal/mol

Scheme R-8
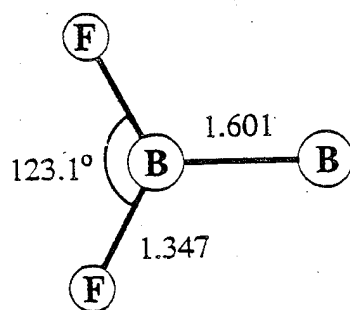
5f, C_{2v}: 92.0 kcal/mol (MP2)
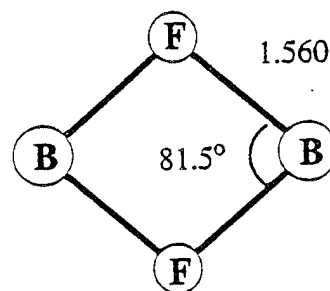
5g, C_{2v}: 81.1 kcal/mol (MP2)
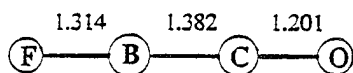
6a, C∗ᵥ (³Σ⁻): 0.0 kcal/mol
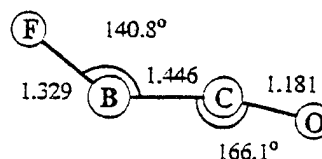
6b, Cₛ (³A"): −0.5 kcal/mol
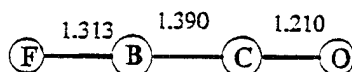
6b, C∗ᵥ (¹Δ): 16.5 kcal/mol

Scheme R-10
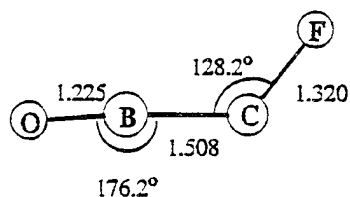
6d, Cₛ (³A"): 19.8 kcal/mol
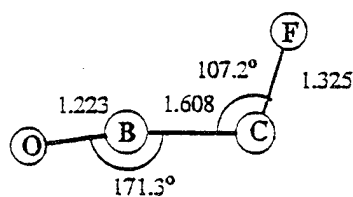
6e, Cₛ: 22.6 kcal/mol
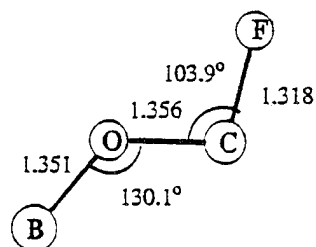
6f, Cₛ: 53.5 kcal/mol (MP2)
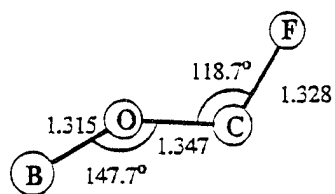
6g, Cₛ (³A"): 98.5 kcal/mol (MP2)

Scheme R-11
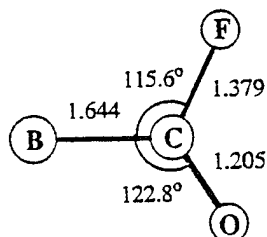
6h, Cₛ: 53.2 kcal/mol (MP2)
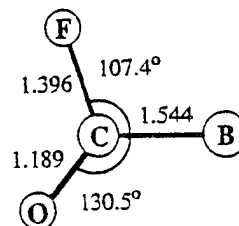
6i, Cₛ (³A"): 69.5 kcal/mol (MP2)

Scheme R-12
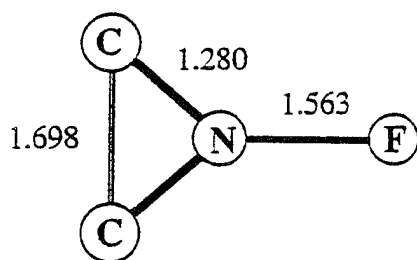
7a, C$_{2v}$: 84.2 kcal/mol (MP2)
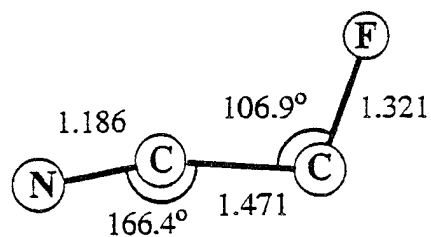
7b, C$_s$: 0.0 kcal/mol
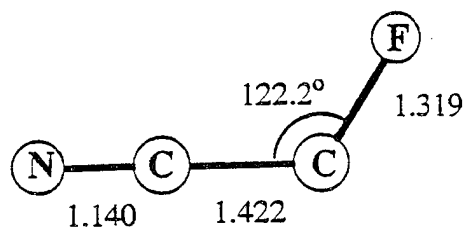
7c, C$_s$ (^{3}A"): 14.7 kcal/mol
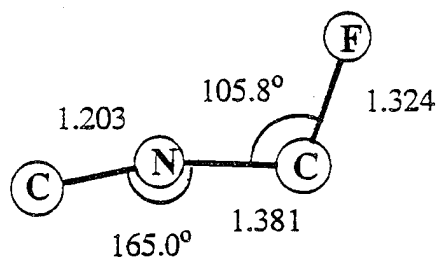
7d, C$_s$: 7.2 kcal/mol
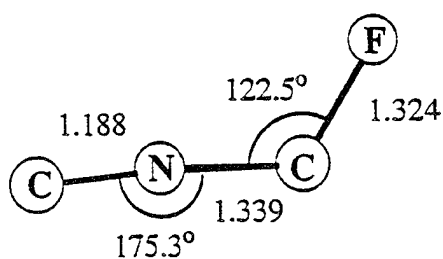
7e, C$_s$ (^{3}A"): 34.0 kcal/mol
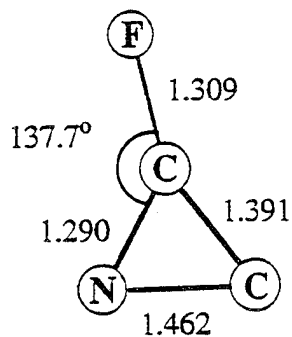
7f, C$_s$: 10.3 kcal/mol
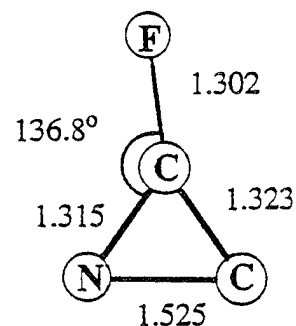
7g, C$_s$ (^{3}A"): 76.5 kcal/mol (MP2)

Scheme R-13

214
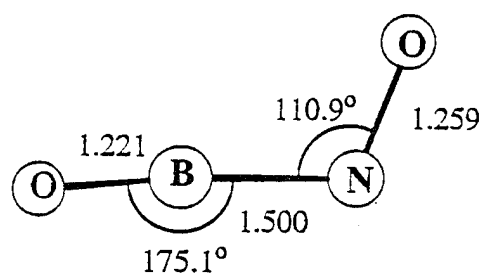
8a, C_s: 0.0 kcal/mol
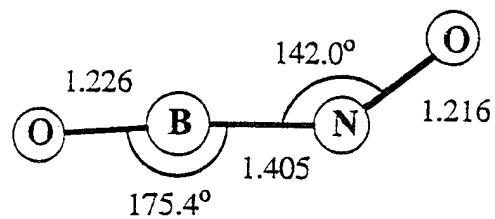
8b, C_s ($^3A''$): 0.4 kcal/mol

Scheme R-14
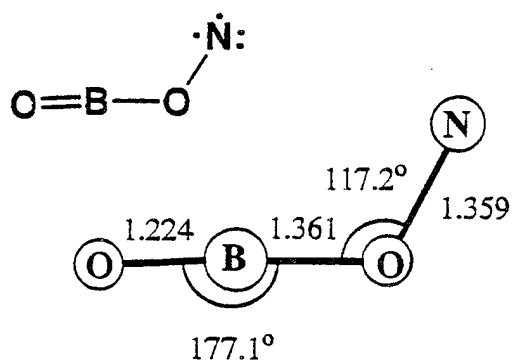
8c, C_s ($^3A''$): 8.7 kcal/mol (MP2)
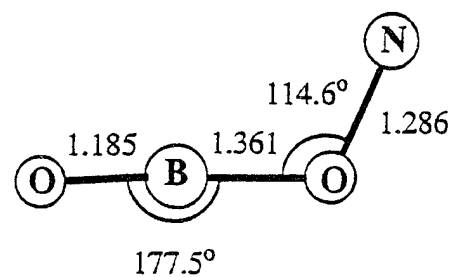
8d, C_s: 22.2 kcal/mol (HF)

Scheme R-15
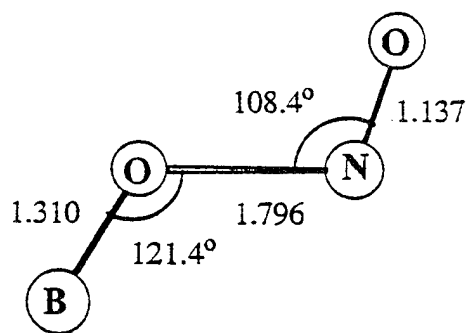
8e, C_s: 55.6 kcal/mol (MP2)
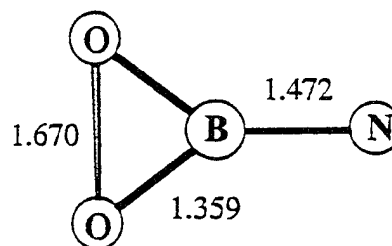
8f, C_{2v} ($^3A_2$): 68.3 kcal/mol (MP2)

Scheme R-16
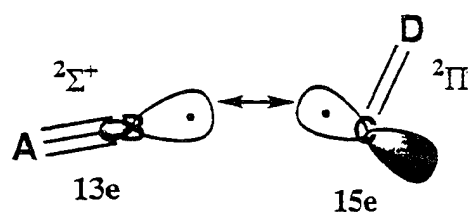
Scheme R-18

215

Photodynamics of O and O_2 isolated in solid $D_2(H_2)$

V. Ara Apkarian
Department of Chemistry
University of California
Irvine CA 92717

The spectroscopy of molecular impurities serve as probes of local energetics and dynamics in quantum hosts, materials of main relevance to the HEDM program of the AFOSR. While this proposition is relatively obvious, the literature on spectroscopic studies of molecular probes in quantum hosts is sparce. We first present a detailed analysis of the spectroscopy of molecular oxygen in solid $D_2(H_2)$, a study that was recently submitted for publication,[1] and subsequently discuss the stability of O atoms isolated in the same.

A) Spectroscopy of O_2 in solid $D_2(H_2)$:

The orbitally forbidden Herzberg III transition, namely $A'(^3\Delta g) - X(^3\Sigma_u)$, is the subject of our investigation. We first state the main conclusions:

a) Only molecules isolated in fcc sites, aligned along the [111] direction are observable by laser-induced-fluorescence.

b) O_2 exclusively isolates in hcp sites in H_2, and only a small fraction isolate in the observable sites in D_2.

c) O_2 does not rotate in D_2. It undergoes harmonic angular oscillations, with a frequency of 25 cm^{-1} in the ground state, and 15 cm^{-1} in the excited A' state. The molecular librations are correlated with the cage motion leading to an effective moment of inertia ~10 that of bare O_2.

d) Both in H_2 and D_2 the first solvation shell is tightly bound to the molecule, and at elevated temperatures the intact cluster, of at least $O_2(D_2)_{12}$, diffuses.

Figure 1 shows excitation spectra of the 0-8 and 0-9 bands of O_2 obtained in different samples: a) in D_2; b) in D_2 overcoated with Xe, after annealing the sample at 27 K; c) in H_2 overcoated with Xe, after annealing at 20 K; d) in N_2. The spectra are recorded by monitoring LIF from the vibrationally relaxed $A' \rightarrow X$

emission. In D_2 clear zero-phonon lines can be seen for only two of the Ω components. In each case further splittings are obvious. Independent of the Ω state accessed, the fluorescence is polarized. This implies that the molecule does not rotate, even after vibrational relaxation from v=9 to v=0. The observed polarization ratio is 1.25±0.05, i.e. the transition dipole, in both absorption and emission, is perpendicular to the molecular axis. Since the ground state is $^3\Sigma_g$, and well decoupled from other excited configurations, then the excited state must be mixed with a state of $^3\Pi_u$ configuration. This mixing is mandated based on the observed enhancement of radiative coupling between A' and X states in matrices. Based on fluorescence decay times, $\tau = 5.4$ μs in D_2, 230 μs in N_2, and in contrast with10-50 s in vacuum, it can be inferred that radiative transition rates are enhanced by ~5 orders of magnitude in matrices. Further noting that spin-orbit splittings remain constant throughout the vibrational progression, and nearly identical to that of the gas phase, electrostatic mixing between the A'($^3\Delta_u$) and the repulsive $^3\Pi_u$ state can be uniquely identified as the source of intensity borrowing. Electrostatic mixing between these two states would activate only $\Omega=1$ and $\Omega=2$ components of the $^3\Delta$ state. Indeed only two components show zero-phonon lines in D_2, and can accordingly be assigned. The $\Omega=3$ component can be clearly identified from its phonon sideband, and there spin-rotation can be an operative mixing mechanism. Somewhat surprisingly, this consideration leads to reassignment of the order of the Ω states, leading the assignment of the A' state to a normal triplet in contrast with the inverted assignment presently accepted in the gas phase.[2]

Given the identity of the configuration mixed in the A' state, it is possible to identify the local electrostatic field that gives rise to the mixing. Noting that the electrostatic field acts only on spatial coordinates, therefore on Λ, and that in the present Hund's case (a) Λ is well preserved, the required V_{el} expanded in spherical harmonics must obey :

$$\langle \Pi | V_{el} | \Delta \rangle = \langle L\Lambda | \sum_{kl} V_{kl}(R)Y_{kl}(\theta,\phi) | L'\Lambda' \rangle$$
$$= \langle 2\pm 1 | \sum_{kl} V_{kl}(R)Y_{kl}(\theta,\phi) | 2\pm 2 \rangle \tag{1}$$

the only acceptable harmonics are those that transform as the totally symmetric representation of the lattice site as well. The algebraic sum of $l = \Lambda + \Lambda'$ imposes

l=±1,±3. Since in the hcp lattice V_{el} must remain invariant with respect to reflection in the α plane, odd values of l are unacceptable. Thus, isolation in hcp sites does not yield the required mixing. The vector sum of k + L + L′, imposes the condition that k ≥4. These requirements are nicely met for the anisotropy: $Y_{4,-3}$ - $Y_{4,3}$, which corresponds to the O_h symmetry of the fcc site with the provision that the z axis, the molecular axis, coincide with the [111] direction.[3] The lowest order irreducible representation for such a site is:

$$V_{el} = V(R)[Y_{40} - (10/7)^{1/2}(Y_{4-3} - Y_{43})] \qquad (2)$$

Thus, O_2 isolated in very specific sites, namely fcc and aligned along [111], where the activation of this orbitally forbidden transition is possible are being observed. This assignment resolves the difficulties in understanding the very weak emission intensities observed in D_2. Based on fluorescence decay times, if we were to assume that they were entirely due radiation, then $O_2(A')$ intensities would be expected to be a factor of 50 larger in D_2 than in N_2, yet experimentally the emission intensities in D_2 are nearly two orders of magnitude weaker than in samples of N_2 prepared and observed under identical conditions. We conclude that only a small fraction of the molecules are being observed, presumably the majority being trapped in hcp sites. As in the case of para impurities in ortho D_2, due to the anisotropy of the O_2-D_2 interactions, the hcp site would be the preferred isolation site. In the absence of the V_{el} mixing, the absorption over these bands would be 5-6 orders of magnitude weaker (τ = 10-50 s).[4] We can now understand the absence of the emission in H_2 and the overcoating experiments. In O_2:H_2 = 1:500 mixtures deposited at 3.6 K, no fluorescence could be observed despite the fact that the sample sticks and the temperature is low enough to isolate the molecules. Upon overcoating with Xe and heat cycling to 27 K, the isolated molecular O_2 spectrum is found (figure 1c). Xe has been chosen for this purpose because the A′→X emission is completely quenched by Xe.[5] The fact that isolated O_2 is observed after the heat cycle, implies that isolated O_2 was present in the H_2 sample prior to overcoating and annealing. The fact that the emission is not quenched, implies that the molecule is protected from the Xe by at least one full shell of H_2. The fact that it becomes observable, with an intensity pattern that is more akin to that observed in heavier rare gases and N_2 (all three Ω components show ZPL's), implies that the site is perturbed by

the vicinity of the Xe overlayer, therefore the molecule must have diffused as a cluster. The same observations are also made in D_2. Although in D_2 we observe the molecules prior to the overcoat, upon overcoating and heat cycling the Xe perturbed spectra completely overwhelm the spectra of the molecules isolated in the solid.

The ZPL splittings can only be interpreted as arising from librational motion. Analysis of these intensities, as one dimensional harmonic librators ($V=1/2\ k_\theta(\theta-\theta_e^2)$), yields an interpretation of intensities of the librational progression in terms of Franck-Condon factors. In this interpretation, the observed librational frequencies in the ground and excited state, 25 cm^{-1} and 15 cm^{-1}, respectively, can be associated with the angular oscillator frequency: $\omega=(k_\theta/I)^{1/2}$. When the bare molecular moment of inertia is used, the zero-point oscillator wavefunction is delocalized. To match with the site potential of eq. 2, it is necessary to use a moment of inertia ~10 times that of the bare molecule. This equivalent to the addition of two nearest neighbor D_2 molecules to the oscillator moment. In effect the cage motion is correllated to the oscillations of the molecule.

The detailed picture that is derived from the above analysis is one of a molecule strongly constrained by the lattice, far from notions of a soft quantum host. The only rationale for this, and the overcoating experimental observations, is that the molecule is strongly interacting with its nearest neighbors, and the system is better described as - an $O_2(o-D_2)_{12}$ cluster isolated in normal D_2. This picture was also verified recently my molecular dynamics simulations of the system using a simple approximate method that relies on representing the quantum particles as frozen Gaussians.[6]

B) Atomic O in solid D_2:

O atoms have been isolated in solid D_2 by two different approaches. Photodissociation of O_2 dimers in solid D_2 with an ArF laser, or photodissociation of O_2-Xe pairs in solid D_2. In both cases the atomic species can be observed by LIF of $O(^1S) \rightarrow O(^1D)$, and its presence can be ascertained by observing thermoluminescence induced by recombination. In the case of O_2-Xe pairs, photodissociation also produces the well known spectra of XeO. Attempts at characterizing the thermal diffusion of O atoms in these solids have failed in yielding any quantitative results. The recombination is always catastrophic,

accompanied by pressure bursts and temperature runaway. The recombination temperatures are however scattered, dependent on exact preparation conditions of the solid. In slow deposits, made at 3.6 K, the thermal burst occurs at 5.5 K. In samples prepared at higher temperature, with faster deposition rates, recombination at temperatures as high as 9 K is observed. In short, recombination is established to be defect induced, and not observed unless there is extensive macroscopic diffusion in the host. These observations imply a simple conclusion, namely: the impurity $O(^3P)$ sites are more stable with respect to diffusion than the pure host -- *O atoms stabilize the lattice.* Simulations indicate a nearly linear increase of the O/Xe density with atom content.

A rather surprising finding in these studies has also been the relative unreactivity of $O(^1D)$ with D_2 in the solid state. The stability of $O(^1D)$ is established by the observation that the $O(^1S \rightarrow ^1D)$ emission does not bleach with irradiation time. This finding has now been verified in two different solids, O_2/D_2 and $O_2:Xe/D_2$. It is difficult to rationalize this finding in view of the known reactivity of $O(^1D)$ with H_2 in the gas phase. The reaction in the gas phase is thought to be barrierless. We suggest that an effective barrier is created due to the many-body stabilization of the reagent potential, $O(D_2)_{12}$, of order ~ 100 cm^{-1}. Such a barrier would be impenetrable at 4 K and could explain the observed stability of the atoms when born with negligible kinetic energy.

In conclusion, it would seem that $O/D_2(H_2)$ meets all of the requirements sought in the HEDM research for a novel propellant. The guests stabilize the lattice, and increase its density, moreover guest sites are more stable than the bulk host.

References:

1. A. V. Danilychev, V. E. Bondybey, V. A. Apkarian, S. Tanaka, H. Kajihara, S. Koda, J. Chem. Phys. (submitted, 1995).
2. P. C. Wraight Chem. Phys. Lett. 71, 127 (1980).
3. H. Watanabe, Operator Methods in Ligand Field Theory, (Prentice Hall, N. J., 1966)
4. T. G. Slanger J. Chem. Phys. 69, 4779 (1978).
5. A. V. Danilychev and V. A. Apkarian *J. Chem. Phys. 99,* 8617 (1993).
6. M. Sterling, Z. Li, and V. A. Apkarian, J. Chem. Phys. (submitted, 1995).
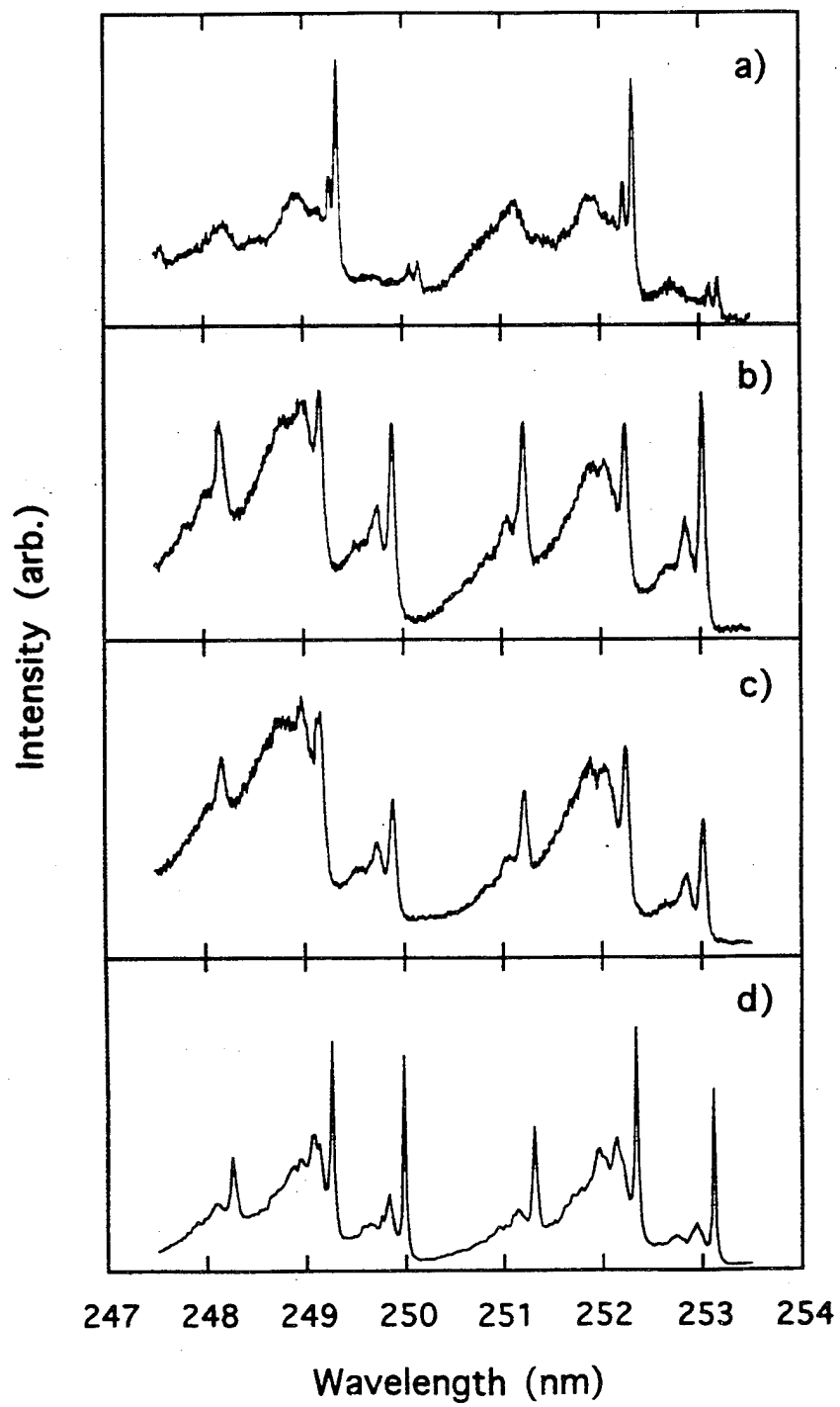
Quantum Molecular Dynamics Simulations of Many-Atom Systems

R.B. Gerber, P. Jungwirth, A.I. Krylov, Z. Li and J. Jung
Department of Chemistry
University of California, Irvine, CA 92717

and

Department of Physical Chemistry
The Hebrew University, Jerusalem 91904, Israel

Abstract

A novel method for time dependent quantum-mechanical simulations of many degrees of freedom is presented. The method is applied to simulations of the dynamics in time following electronic excitation of metal atoms in low temperature clusters or solids. Comparisons are made between two types of systems: (1) Heavy-atom media, e.g. metal atoms in solid Ar and in Ar clusters; (2) Quantum media: Metals in solid H_2 or solid He. The systems studied are in part potential HEDM systems (e.g. Mg in H_2) as high-impulse propellants, or very useful models for realizable HEDM systems.

We report results from simulations of $S \rightarrow P$ state excitations of metal atoms in both "semiclassical" and "quantum" environments. Calculations were realized for systems having up to about 100 degrees of freedom in full dimensionality and for timescales up to a few picoseconds. The P-states of the excited atoms are quasi-degenerate. We compute electronic energy relaxation times; electronic orbital reorientation timescales and the related time-dependent polarization, local structural changes in time, and properties of spectroscopy with ultrafast pulses in these systems. These first Quantum Molecular Dynamics simulations of such realistic systems provide very useful data and understanding of electronically excited atoms in cryogenic media.

I. Introduction

Quantum mechanical description in time of processes in condensed phases is one of the goals of chemical dynamics. A quantum treatment of dynamics is of importance and interest for a wide range of systems, but the problem is crucial in cases that include HEDM materials, such as solid hydrogen doped with light atoms.[1] Quite obviously, the light mass of H_2, the very weak anharmonic interactions between these molecules and the low temperatures of interest, can give rise to very pronounced quantum effects. For calculations of at least certain equilibrium, time-independent properties, well-established many-particle quantum simulations are available. Examples of applications of such methods to systems of HEDM interest include the Feynman Path Integral simulations of Li atoms in solid H_2 and of $Li(H_2)_n$ clusters by Klein and coworkers,[2],[3] and the Diffusion Quantum Monte Carlo simulations of $B(H_2)_n$ clusters by Vegiri et al..[4] These simulations investigated primarily structural properties. The situation is very different for dynamics in time of quantum mechanical systems. In the present state of the art, rigorous, "numerically exact" quantum calculations of the time evolution are limited systems of, say, up to three degrees of freedom. The most effective current methods of this type employ grid representations of the wavepackets.[5] Elegant and powerful as these methods are, the current limitation on the sizes is unlikely to improve greatly, since it follows from grid-size considerations.

We report here on progress in recent work by our group on time-dependent quantum simulations of large systems. These are based on a novel method[6],[7] we developed in the framework of an AF Phillips Laboratory Contract (to RBG). With the new method, results on quantum dynamics for realistic systems having up to ~100 modes are already available, and will be presented here. We anticipate simulations of realistic systems with hundreds of modes in the near future. In our belief, this establishes a tool for simulations of the time evolution of condensed-phase systems in the quantum regime.

Sec. II briefly describes the processes and systems for which applications here are reported. Sec. III gives a brief outline of the method. Sec. IV gives results for the dynamics of electronically excited metal atoms in rare gas clusters, which are models for cryogenic HEDM systems. Sec. V outlines preliminary results for metal atoms in H_2 clusters, which are of HEDM interest.

II. Systems

The applications discussed here are for the dynamics of electronically excited atoms in rare-gas clusters, and in hydrogen clusters. Interest in this problem is motivated by the important work of Fajardo,[8],[9] who has used electronic absorption spectroscopy to characterize Li atoms in solid hydrogen - a potential HEDM system. Calculations of the absorption spectrum as such do not necessarily require time-dependent wavepacket calculations, and indeed time-independent calculations of the spectrum of solid H_2 doped with Li were reported by Klein and coworkers.[3] Our interest here is, however, in the

issue of the dynamics following excitation. This is useful for the characterization of the system, and should provide data on photostability and photodiffusion in the materials considered. Excitations of the metal atoms treated here (Li, Mg, Ba) are to a P-state. The (near) degeneracy of the P-states gives rise to breakdown of the Born-Oppenheimer approximation, and to coupling between electronic and atomic motions. We are particularly interested in the timescales for electronic energy relaxation, and in electronic polarization effects, associated with the re-orientation in time of the p-orbital electrons of the metal. Hitherto, classical Molecular Dynamics simulations were virtually the only tool used to describe the dynamics of *adiabatic* processes in cryogenic solids or large clusters.[10] Semiclassical simulations, based on surface-hopping treatments of electronic transitions,[11] were used in simulations of nonadiabatic processes in solids,[12]-[14] including electronic energy relaxation and orbital reorientation effects. In the present report, such processes, both in rare gas clusters and in hydrogen clusters, are treated for the first time by Quantum Molecular Dynamics simulations, using the method we developed for this purpose.

III. The Method

It will be convenient to describe the method we introduce for many particle quantum dynamics in two stages: First, adiabatic systems only, and then non-adiabatic processes.

(a) *Adiabatic systems*

The method we proposed is the Classically-Based Separable Potential (CSP) approximation and its extensions.[6],[7] In this method, one carries out as a first step a full *classical* Molecular Dynamics simulation of the process of interest. One uses the classical results to construct an effective potential for each degree of freedom. (These potentials are time-dependent, as determined by the classical trajectories). One then calculates for each mode, using the effective potential, a time-dependent quantum wavepacket. The full multi-dimensional wavepacket of the system is constructed from these single mode wavefunctions. This method can work very well even for systems where classical MD itself fails to adequately describe the system, as for quantum solids. For instance, the method works well for electronically excited metal atoms in hydrogen clusters. (The interactions in the excited state are stronger than in the ground state, so the excited state systems are already more "classical" than the ground state quantum clusters). It appears that for nearly all systems, classical dynamics is good enough to calculate mean interactions (the average potentials), even if the detailed behavior given by the trajectories is not adequate. This is the case so long as one deals with atomic (i.e. nuclear) motions, rather than electronic ones - the classical description offers a useful staring point even for systems such as doped solid hydrogen. Consider a systems of coordinates $q_1, \cdots, q_N$. Let the trajectory corresponding to the α-th initial condition be: $q_1^\alpha(t), \cdots, q_N^\alpha(t)$. The effective potential for mode 1, calculated from the classical MD, is defined as

$$\bar{V}_1(q_1, t) = \frac{1}{n_T} \sum_\alpha V(q_1, q_2^\alpha(t), \cdots, q_N^\alpha(t)) \tag{1}$$

where n_T is the number of classical trajectories used. Similarly, the effective potentials $\bar{V}_i(q_i, t)$ for the other modes are defined. A quantum wavepacket for each mode i can now be computed from:

$$i\hbar \frac{\partial \chi_i}{\partial t} = [T_i + \bar{V}(q_i, t)]\chi_i \tag{2}$$

where T_i is the kinetic energy operator of mode i. The total wavefunction of the system is to a first approximation given by

$$\Psi(q_1, \cdots, q_N, t) = \prod_i \chi_i(q_i, t) \tag{3}$$

Note that the effective potentials $\bar{V}_i$ are such that energy transfer between the modes is included in the description. At this level of approximation the method is similar to the Time Dependent Self-Consistent Field (TDSCF) approximation.[15] However, while the new method gives results essentially of the same accuracy as TDSCF, it is computationally vastly simpler. This was demonstrated in test calculations, and also by simulations for realistic systems. The calculation of "nuclear time-dependent orbitals" is so efficient, that in many cases it is practical to compute the multiconfiguration extension of Eq. (3). this leads to wavepackets of the type

$$\Psi_{MC}(q_1, \cdots, q_N, t) = \sum_j C_j(t) \prod_i \chi_i^{(j)}(q_i, t) \tag{4}$$

where the coefficients C_j are time-dependent. Other ways of correcting Ψ of (3) involve perturbation corrections. The approximation deteriorates in time, but the systems considered here it is *very satisfactory*, at least for $t \leq 1 - 2$ps.

(b) *Extension to non-adiabatic processes*

For non-adiabatic systems, the calculation of a multi-configuration wavepacket is essential. The number of configurations must at least equal the number of electronic states. Also *the single-mode nuclear wavefunction must be obtained from effective Hamiltonians that include the effect of nonadiabatic transitions.* For this purpose, one begins the procedure by first computing the semiclassical "surface-hopping" trajectories according to Tully.[11] Then, one uses the trajectories $q_1^\alpha(t), \cdots, q_N^\alpha(t)$ for all initial conditions α to calculate an effective matrix Hamiltonian for each mode (the dimension of the matrix is the number of electronic states). One obtains a set of single-mode nuclear wavefunctions. The total wavefunction is of the form

$$\Psi(r, q_1, \cdots, q_N, t) = \sum_k C_k(t) \phi_k(r, t) \prod_i \chi_i^{(k)}(q_i, t) \tag{5}$$

where the $C_j(t)$ are time-dependent coefficients, and the $\phi_k(r, t)$ are adiabatic electronic wavefunctions, computed at the semiclassical stage. r denotes the electronic coordinates. This approach was used in all the results reported here, with a minimal number of

configurations (=3), corresponding to the number of electronic states involved.

IV. Results

(a) *Photoexcitation dynamics of metal atoms in rare-gas clusters:* $(Ar)_{10}Ba$, $(Ar)_{20}Ba$

Quantum Molecular Dynamics simulations, by the method outlined above, were carried out for the photoexcitation dynamics of $(Ar)_{10}Ba$, $(Ar)_{20}Ba$ using realistic potentials and treating all modes. The heavy atoms of the cluster make this a near classical system. We chose to study such "near-classical" systems in the quantum domain as a useful reference with which the more dramatic quantum effects of metal-hydrogen clusters can be obtained. Very crudely, the Ar atoms in the ground-state of the clusters can be said to form a rough "surface" above (or below) which the Ba atom is located. Excitations $Ba(S) \rightarrow Ba(P)$ of the clusters have Σ and (nearly degenerate) Π components, respectively. Following Σ excitation $Ba(Ar)_{10}$ undergoes dissociation, or "evaporation" of the Ba with a yield of 80%, and in a mostly *direct* process. For $(Ar)_{20}Ba$, only a 20% yield for dissociation is seen over the first few picoseconds. The main reason for this large difference between the two clusters is the higher binding energy of the larger clusters. In any case, in $(Ar)_{20}Ba$ electronic-vibrational relaxation, including nonadiabatic transitions, seems faster in timescale ($t \leq 1.5$ ps) than dissociation. The opposite is true in the smaller cluster, where much of the dissociation occurs directly in the Σ state. Snapshots of the dynamics for $(Ar)_{10}Ba$ are shown in Fig. 1, and for $(Ar)_{10}Ba$ in Fig. 2. In these figures the *mean* positions of the atoms are shown, as is the orientation of the p-orbital of the Ba atom. The quantum fluctuations, associated with the widths of the wavepackets are not shown, but we stress that throughout the process they remain small compared with the interatomic distances. *The atoms retain a high degree of localization during the process*, as expected for a "near classical" system. Despite the extensive energy transfer that occurs, the structural changes in the systems are fairly modest over the simulation period of 1.5 ps. *P-orbital re-orientation is seen to take place in both clusters on a timescale somewhat shorter than 1.5 ps*. The orbital re-orientation processes, driven here by electrostatic interaction between the $Ba(P)$ and the "solvent" Ar atoms are thus quite efficient. The nonadiabatic transition probabilities for $(Ar)_{10}Ba^*$ are shown in Fig. 3. The higher electronic state is depleted by ~12% after 1.5 ps, and the relaxation is mostly to the intermediate electronic state. The lowest state remains hardly populated throughout the 1.6 ps shown. Of special importance is the comparison between our time-dependent quantum simulations, and the semiclassical "surface-hopping" methods.[11] To our knowledge, this is the first time where the "surface-hopping" approximations are tested for a large system. The semiclassical method (Tully's surface hopping approach) was found to be satisfactory on a semiquantitative level, and also for several quantitative aspects. Figure 3 shows the evolution in time of the branching ratios between the different electronic states. The Tully method develops a deviation from the quantum results, that reaches a factor of ~2 at $t = 1.5$ ps. The Tully method is certainly a very useful tool, but can be off quantitatively

by significant factors, even for a "near classical" system. In conclusion, we found that electronic relaxation is faster than dissociation in $(Ar)_{20}Ba$, although the opposite is true in smaller clusters. Both orbital re-orientational and electronic relaxation occur on the picosecond timescale. Quantum effects are modest, but significant, e.g. with regard to quantitative predictions of electronic branching ratios.

(b) *Photoexcitation dynamics of metal atoms in hydrogen clusters:* $Mg(H_2)_{12}$, $Li(H_2)_{12}$

Our calculations on these systems are still not completed. We therefore restrict ourselves to some brief comments as to preliminary results. Both $Mg(H_2)_{12}$ and $Li(H_2)_{12}$ are systems of highly quantum mechanical behavior. The H_2 molecules are strongly delocalized within the cluster, with fluctuations in the relative distances that are of the same order as the distances themselves. In $Li(H_2)_{12}$ a system studied by Klein and coworkers,[2] the metal atom is located outside the "droplet" of H_2 molecules. In $Mg(H_2)_{12}$ the metal atom is inside the cluster, surrounded by an envelope of H_2 molecules. However, the envelope is not spherical. One can refer to the system as an anisotropic quantum liquid droplet. The excitation spectra are broad in both cases. Σ and Π components contribute to the broad absorption spectrum of $Li(H_2)_{12}$. The broad spectrum for $Mg(H_2)_{12}$ is in part due to the anisotropy of the H_2 envelope, which induces a major splitting among the p-levels of the excited Mg atom.

In $Mg(H_2)_{12}$, orbital re-orientation, thus depolarization of the electronic state, occurs on a sub-picosecond timescale. For excitations that populate the highest electronic state initially, significant relaxation to the second electronic state is found within 0.7 ps. For such excitations onset of chemical reactivity $Mg + H_2 \rightarrow MgH + H$ is possible, but was not yet incorporated in our quantum simulations. The semiclassical "surface hopping" method seems to give much larger errors than in the "near classical" clusters considered above. Errors of up to an order to magnitude in the branching ratios can occur for sub-picosecond timescales, and deviations within half an order of magnitude seem typical for this system. The structure changes in this system are much greater than for $(Ar)_nBa$ and correspond to "hot" radial $H_2 - Mg$ vibrations of the clusters. Several H_2 molecules (~2) are ejected from the cluster following excitation at the high side of the absorption spectrum.

In $Li(H_2)_{12}$ an interesting structural change was noted upon excitation - the Li, initially located outside the H_2 droplet is "pulled" inside upon a Π-type excitation and becomes "solvated". This is due to the deep $Li - H_2$ attraction in the B-state of this system. A very hot droplet is formed, in which the most likely configuration of the Li is inside the cluster. The timescale for this process is 100 fs.

In summary, electronic excitation produces drastic structural changes in the quantum cluster studied on a short timescale of 100 fs or so. This is in contrast to the results for the $(Ar)_nBa$ clusters, where the structural changes for the non-dissociated cluster were much more modest.

V. Concluding Remarks

A method for time-dependent quantum mechanical simulations of processes in many atom systems has been developed, and first applications to large, realistic systems in full dimensionality were given. We presented results of simulations of the dynamics following photoexcitation of Ba in $(Ar)_{10}Ba$, $(Ar)_{20}Ba$, and of Mg in $Mg(H_2)_{12}$. The results provide data on the timescales of electronic relaxation and on the mechanisms of such processes in cryogenic materials, on changes of electronic polarization and orbital re-orientation effects in such systems, and on the structural changes in time of the cryogenic systems induced by photoexcitation. The results should be useful for predicting the behavior of low-temperature HEDM systems, and indeed many other systems of chemical interest. A tool for detailed, atomic scale simulations of time-evolution of large poly-atomic and condensed matter has thus been introduced, and we anticipate extensive further applications to both HEDM and other systems.

References

(1) P.G. Carrick and C.R. Brazier, in: Proceedings of the HEDM Contractors Conference, Lancaster, 1992. Edited by M.R. Berman (AFOSR, Air Force Material Command, 1992), p. 8.

(2) D. Scharf, G.J. Martyna and M.L. Klein, J. Chem. Phys. **99**, 8997 (1993).

(3) D. Scharf, G.J. Martyna, D. Li, G.A. Voth and M.L. Klein, J. Chem. Phys. **99**, 9013 (1993).

(4) A. Vegiri, M.H. Alexander, S. Gregurick, A.B. McCoy and R.B. Gerber, J. Chem. Phys. **101**, 2577 (1994).

(5) R. Kosloff, Ann. Rev. Phys. Chem. **45**, 145 (1994).

(6) P. Jungwirth and R.B. Gerber, J. Chem. Phys. **102**, 6046 (1995).

(7) P. Jungwirth and R.B. Gerber, J. Chem. Phys. (in press).

(8) M.E. Fajardo, J. Chem. Phys. **98**, 110 (1993).

(9) M.E. Fajardo, S. Tam, T.L. Thompson and M.E. Cordonnier, Chem. Phys. **189**, 351 (1994).

(10) R. Alimi, R.B. Gerber and V.A. Apkarian, J. Chem. Phys. **89**, 174 (1988); R. Alimi, A. Brokman and R.B. Gerber, J. Chem. Phys. **91**, 1611 (1989); R. Alimi, R.B. Gerber and V.A. Apkarian, Phys. Rev. Lett. **66**, 1295 (1991).

(11) J.C. Tully, J. Chem. Phys. **93**, 1061 (1993).

(12) I.M. Gersonde and H. Gabriel, J. Chem. Phys. **98**, 2094 (1992).

(13) A.I. Krylov, R.B. Gerber and V.A. Apkarian, Chem. Phys. **189**, 261 (1994).

(14) A.I. Krylov and R.B. Gerber, Chem. Phys. Lett. **231**, 395 (1995).

(15) R.B. Gerber and M.A. Ratner, Adv. Chem. Phys. **70**, 97 (1988).

Ba(Ar)₁₀

0 fs

500 fs
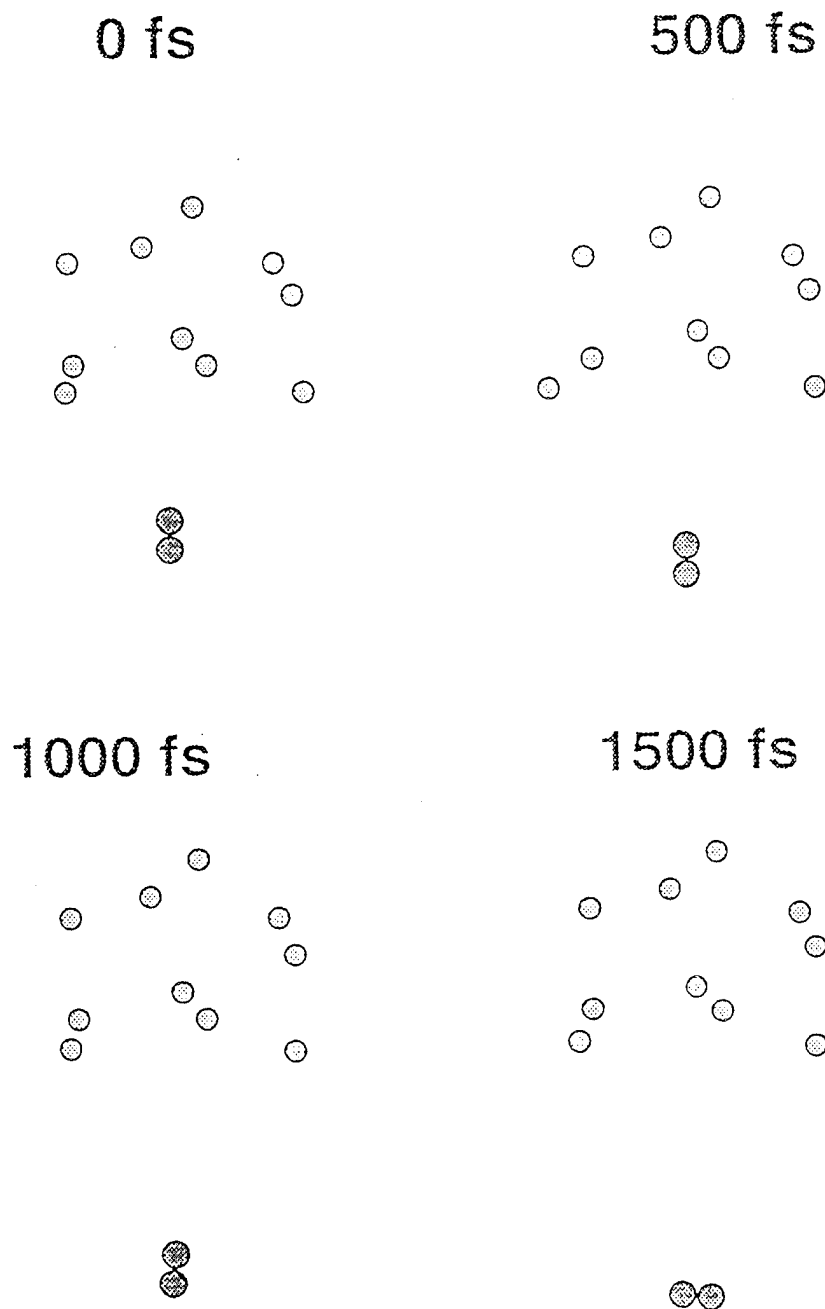
1000 fs

1500 fs

Fig. 1: The time evolution of the mean structure of $(Ar)_{10}Ba$, following photoexcitation.

The mean atomic positions and the p-orbital direction of the Ba are shown. Results are from time-dependent quantum calculations.

Ba(Ar)₂₀

0 fs
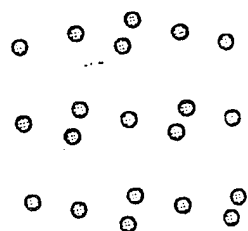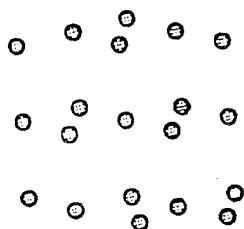
500 fs

1000 fs
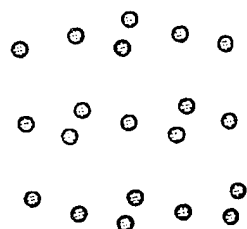
1500 fs
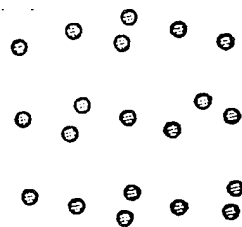
Fig. 2: As in Fig. 1, for the cluster (Ar)₂₀Ba.

Branching Ratios

Ba(Ar)$_{10}$:
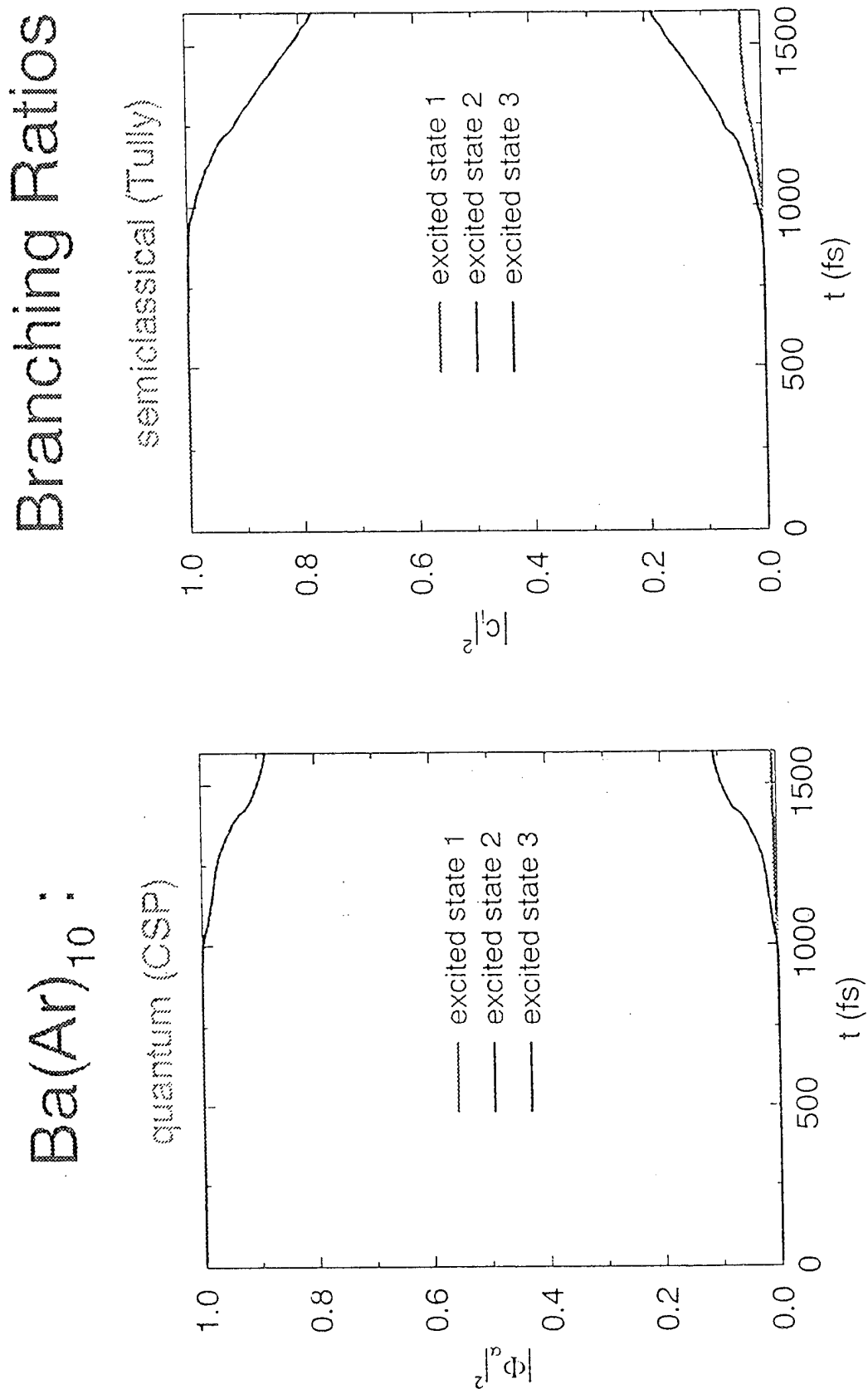
Fig. 3: The branching ratios versus time for the different electronic states of (Ar)$_{20}$Ba. Results of quantum simulations are compared with those of the semiclassical method.

Toward the Production of Measurable Quantities of Highly Doped Solid Hydrogen

High Energy Density Matter Contractors Conference
June 4-7, 1995

Berton Callicoatt, Kenneth C Janda, V. A. Apkarian, R. B. Gerber
Zhiming Li, P. Taborek and J. Rutledge
Advanced Cryogenic Materials Group
University of California
Irvine, California

The goal of this effort is to produce measurable quantities of highly doped (5-10%) solid hydrogen. The desired dopant atoms are C, B, O, and N. Our approach to this material is via the cluster deposition technique, as illustrated in Figure 1. First, a beam of large He clusters (between 10^4 and 10^5 He atoms per cluster) is created following the methods of Toennies[1] and Scoles.[2] Next, the He clusters are passed through a scattering chamber that contains hydrogen molecules and, in the process, "pick-up" between 12 and 20 hydrogen molecules. During the pick up process, sufficient He atoms evaporate for the cluster to maintain a temperature of about 1 K, and the hydrogen is expected to make a small micro-crystal within the He cluster. Next, the He cluster picks up the desired dopant atom. Again, He atoms evaporate to cool the cluster back to 1 K.
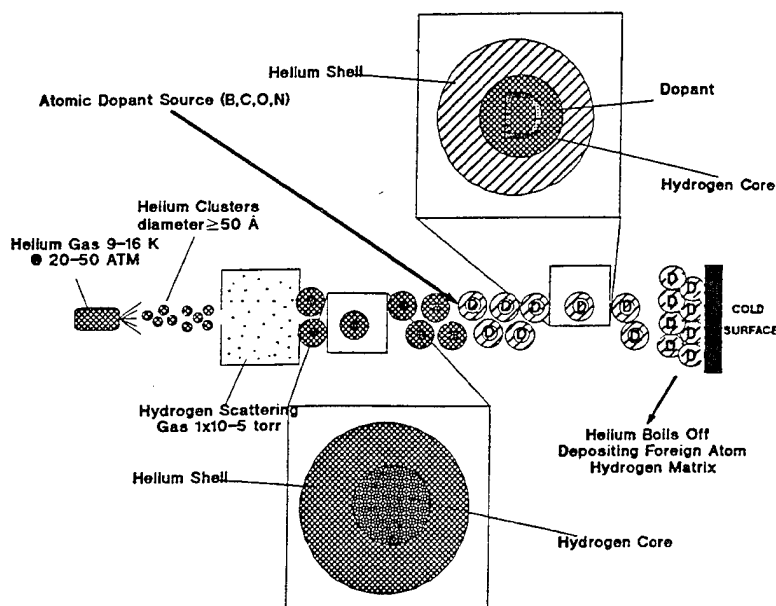
Figure 1. Schematic Diagram for the Deposition of Highly Doped Solid Hydrogen

At these temperatures the dopant atom will not react with the solid hydrogen. Instead, it is expected that the dopant atom and the hydrogen will combine to form an especially stable (at 1 K) micro cluster since the hydrogen molecules are more strongly attracted to the dopant atom than to either other hydrogen molecules or to helium atoms. At this point the clusters are deposited onto a cold surface. The He atoms serve to cushion the impact, and again evaporate in order to keep the temperature of the hydrogen-dopant cluster as low as possible. Once the clusters are deposited on the surface then we can study their stability, and, eventually, their reactivity.

The source for producing large He clusters that contain small hydrogen clusters is shown in Figure 2. It consists of two helium cryostats operated in series. The first cryostat cools the input He gas (at pressures up to 50 atm.) to 12 K. The second cryostat can cool the gas to temperatures as low as 8 K (down to 5 K for lower pressures), at which point it is expanded into the vacuum system through a 5 μm diameter nozzle. He clusters containing between 10^4 and 10^5 atoms are produced during this expansion. The He clusters pass through a 510 μm skimmer orifice into a second chamber that contains hydrogen gas at approximately 10^{-4} torr. Depending on the hydrogen pressure in this chamber, between 0 and 20 hydrogen molecules can be deposited in the He cluster.
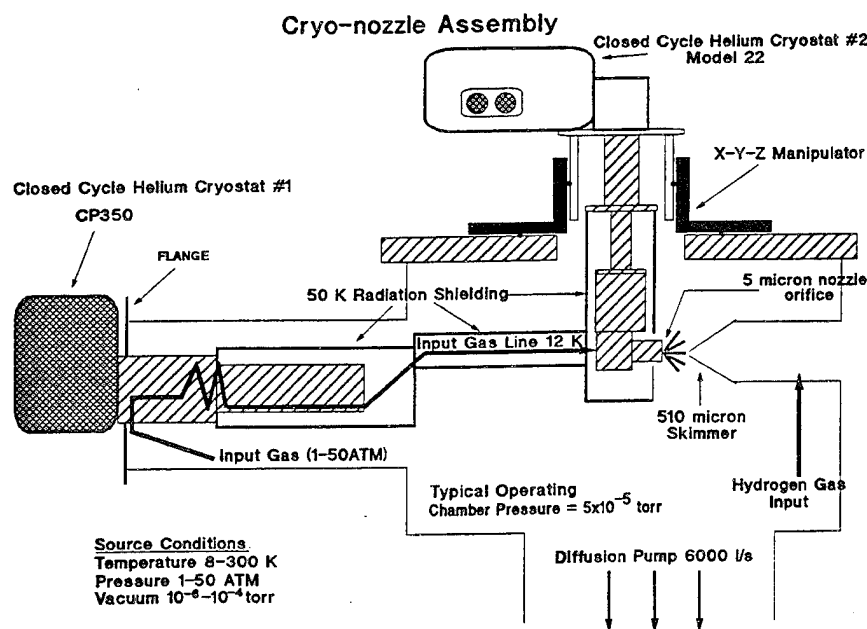
Figure 2: Schematic diagram of the He cluster source and hydrogen pick up region.

Since depositing O, C, N or B atoms into the cluster is one of the most difficult steps of this process, we have begun preliminary tests of the concept by studying the deposition of Br_2. Although Br_2 is not a HEDM material, these

a.

Helium Cluster
Fragments
N=40-48

Mass (amu)

b.

Bromine Pickup In
Helium Clusters

160

158

162

x5

c.

Hydrogen/Bromine Pickup
In Helium Clusters
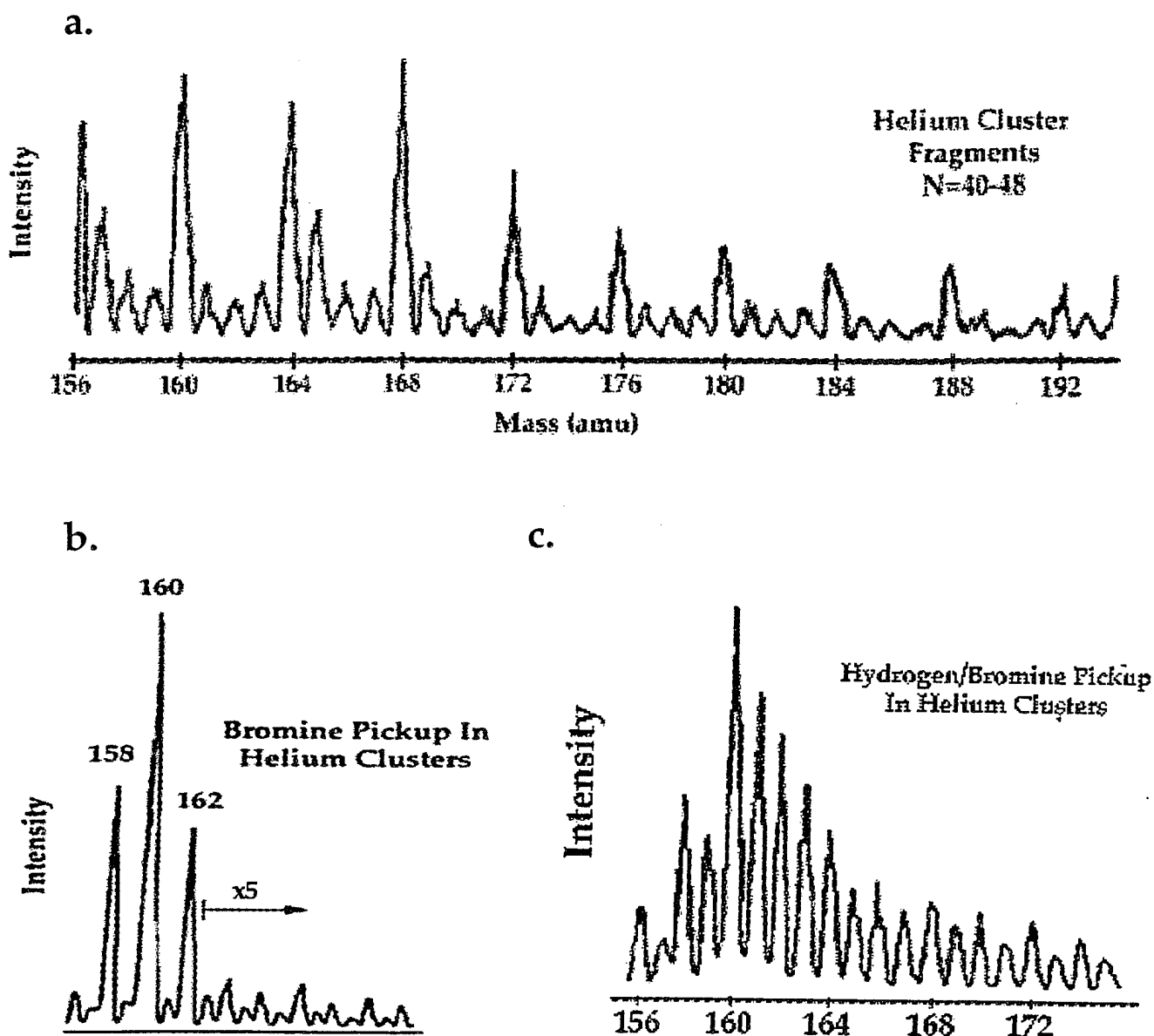
Figure 3. Mass spectra in the range of m/e = 160 obtained under various operating conditions. a. Here only the He cluster beam is on with a nozzle temperature of x and a pressure of y. The mass peaks at m/e = 4n are due to He_n^+. The intervening peaks are due to background gas in the mass spectrometer (pressure = 10^{-8} torr, mostly H_2O). b. When Br_2 is added to the "pick-up" cell, the m/e = 158, 160 and 162 peaks show the highest intensity due to intra-cluster charge transfer from He to Br_2. c. When H_2 is added to the appropriate scattering cell new mass peaks arise. The are assigned to ions of the type $Br_2H_n^+$ ($0 \leq n \leq 14$). This shows that the weak bonds between Br_2 and H_2 molecules survive the ionization process due to the rapid cooling due to evaporation of He. It also shows conclusively that the Br_2 was inside the He cluster and not just dragged into the mass spectrometer by scattering processes.

studies provide valuable insight into how the overall concept will work, and valuable practical experience in running the source and characterizing the clusters with mass spectrometry.

Figure 3 shows a series of three mass spectra in the range of $m/e = 160$ amu. In Fig. 3a only the He cluster source is being operated, and mass peaks are observed every four amu due to He_n^+, with n being in the range of 39-48. The intervening mass peaks are due to background gas. Figure 3b shows part of the same mass region but now the clusters have picked up a Br_2 molecule. Since the IP of Br_2 is 10.5 eV, while that of He is 24.6 eV, any ionization of He in the cluster is quickly transferred to the Br_2, releasing 14 eV of energy into the cluster. This is sufficient energy to evaporate most of the He. Thus the main mass peaks that are observed are the three isotopic Br_2 species at $m/e = 158$, 160 and 162. (If the He beam is turned off, very little Br_2 travels from the scattering cell to the mass spectrometer .) In Figure 3c, H_2 is added to the region behind the skimmer as described above, and the mass peaks between those of Figure 3b are enhanced, as are those for somewhat higher masses. These are due to ions with stoichiometry $Br_2H_n^+$ (n = 0 , 1 , 2...14) that are formed when a cluster that contains He, Br_2 and H_2 is ionized. I Thus we see that even when 14 eV of energy are deposited in the cluster by the ionization process (*vide supra*) the rapid cooling due to He atom evaporation is sufficient to allow the $Br_2(H_2)_n$ core to survive at least partially intact. This gives us reason to hope that the surface deposition process described in the introduction of this abstract has a reasonably high chance of working. We will also present computer simulations which encourage us to believe that the proposed techniques for depostion is viable.

Although the details will not be presented here, we have learned that the cluster beam technique is much more sensitive to operating conditions than might have been imagined. Also, the sensitivity comes in ways that seem non-intuitive. For instance, a He cluster produced with a nozzle temperature of 9.5 K appears to be much less capable of picking up two bromine molecules than is a He cluster produced with a nozzle temperature of 10.0 K. Not only is this temperature dependence extremely sharp, but it goes in the opposite of the expected direction since one would have expected that somewhat larger clusters are produced with lower nozzle temperatures, resulting in a larger cross section for the pick up of Br_2. Another thing that we have learned that will be crucial in a successful demonstration of the cluster deposition technique is that the cold He clusters have a limited ability to pick up the desired amount of H_2, Br_2 (substituting for the desired dopant atoms) and extra He. This limits the flexibility of the design of the experiment in the sense that a seeded pick up beam for the dopant atomsmay not be viable . Finally, we have used, the pick-up probability for residual water in our apparatus to estimate that after the He clusters have picked-up a Br_2 molecule, they are still of the order 50 Å in diameter.

1. H. Buchenau, E. L. Knuth, J. Northby, J. P. Toennies and C. Winkler, *J. Chem. Phys.* **92**, 6875 (1990).

2. F. Stienkemeier, W. E. Ernst, J. Higgins and G. Scoles, *J. Chem. Phys.* **102** 615 (1995).

MONTE-CARLO SIMULATIONS OF THE MAGNETIC CIRCULAR DICHROISM (MCD) SPECTRA OF THE MATRIX-ISOLATED SODIUM/ARGON ^{2}S —> ^{2}P "VIOLET TRIPLET"

John W. Kenney, III
Heidi A. Terrill-Stolper
Chemical Physics Laboratory
Eastern New Mexico University
Portales, NM 88130

Introduction

Alkali metal/rare gas solids (M/Rg solids) constitute an important class of model systems of interest to the U.S. Air Force in simulating the properties of enhanced-performance cryogenic rocket propellants.[1] In particular, the M/Rg systems share many physical, chemical, and spectroscopic characteristics with M/hydrogen systems, where in a potential rocket propulsion application, M is a high energy density material (HEDM); e.g., a low mass alkali metal or Group 13 or 14 element.[2,3] Boatz and Fajardo recently modeled ^{2}S —> ^{2}P electronic absorption spectra in M/Rg systems by using quantum mechanical first-order degenerate perturbation theory in conjunction with a classical Monte Carlo (MC) method to account statistically for the effects of the Rg perturbations on the ^{2}S and ^{2}P terms of the M/Rg systems.[4] Their simulations, while not completely quantitative, do recover many of the key attributes of the electronic absorption spectra of these systems including the characteristic three-peaked or "triplet" absorption band shape. Lawrence and Apkarian take a very similar approach in modeling the ^{2}P terms of halogen atoms doped in cyrogenic matrices.[5] Boatz and Fajardo make the reasonable assumption that spin-orbit coupling represents a small perturbation of the ^{2}P term compared to the Rg perturbation, at least for the lighter alkali metals of interest to them as HEDM rocket propellant dopants, and on this basis justify the exclusion of ^{2}P spin-orbit coupling terms in their model. The Boatz and Fajardo first-order perturbation matrix for the ^{2}P term is, therefore, a 3 x 3 matrix whose matrix elements are defined with respect to a suitable zeroth-order orbital p basis in the angular momentum representation $\{|n/m_l> = |n11>, |n10>, |n1-1>\}$. Spin is not considered. Lawrence and Apkarian do include a ^{2}P spin-orbit term for the halogen in their treatment. They argue convincingly that the large halogen ^{2}P spin-orbit coupling interaction is not greatly affected by the matrix environment; i.e., the use of the atomic spin-orbit coupling constant of the halogen in the formalism represents a good approximation. The

[1](a) Fajardo, M. E.; Carrick, P. G.; Kenney, J. W., III *J. Chem. Phys.* **1991**, *94*, 5812-5825. (b) Fajardo, M. E. *J. Chem. Phys.* **1993**, *98*, 110-118. (c) Tam, S.; Fajardo, M. E. *J. Chem. Phys.* **1993**, *99*, 854-860. (d) Corbin, R. A.; Fajardo, M. E. *J. Chem. Phys.* **1994**, *101*, 2678-2683.

[2]Fajardo, M. E.; Tam, S.; Thompson, T. L.; Cordonnier, M. E. *Chem. Phys.* **1994**, *189*, 361-365.

[3]Carrick, P. G. *Specific Impulse Calculations of High Energy Density Solid Cryogenic Rocket Propellants, I: Atoms in Solid H$_2$, PL-TR-93-3014*; Phillips Laboratory: Edwards AFB, CA, **1993**.

[4]Boatz, J. A.; Fajardo, M. E. *J. Chem. Phys.* **1994**, *101*, 3472-3487.

[5]Lawrence, W. G.; Apkarian, V. A. *J. Chem. Phys.* **1994**, *101*, 1820-1831.

Lawrence and Apkarian ^{2}P perturbation matrix is a 6 x 6 matrix whose individual matrix elements are defined with respect to a suitable zeroth-order Cartesian p basis with spin $\{|n l \text{e} \text{sm}_s> = |n1x \, 1/2 \, 1/2>, |n1y \, 1/2 \, 1/2>, |n1z \, 1/2 \, 1/2>, |n1x \, 1/2 \, -1/2>, |n1y \, 1/2 \, -1/2>, |n1z \, 1/2 \, -1/2>\}$.

Magnetic Circular Dichroism (MCD) spectroscopy, which measures the differential absorption of left circularly polarized (LCP) light vs. right circularly polarized (RCP) light in a sample placed in a magnetic field aligned parallel to the propagation direction of the light, has a long and venerable history of providing insights to the nature of the chemical and physical environment surrounding the MCD-active chromophore.[6] In particular, the MCD-active ^{2}S —> ^{2}P electronic transitions of alkali halide F centers[7] and M/Rg systems[8] have attracted considerable experimental and theoretical attention over the years. The usual approach is to extract parameters such as the g value, the spin-orbit coupling constant, and linear vibrational coupling constants from a moment analysis of the experimental MCD spectrum (or spectra).[6,7b] Only a few full MCD spectral simulations exist in the literature. These simulations of ^{2}S —> ^{2}P MCD spectra rely upon dynamic Jahn-Teller models in which an *a priori* choice is made as to which *specific* interaction vibrational modes will act to lift the degeneracy of the ^{2}P term.[9] This simulation approach is of limited value in modeling the MCD spectra of M atoms trapped in novel and heretofore unobserved sites in Rg matrices for which specific site geometries and lattice mode types are, as yet, unknown. A MC approach for handling Rg perturbation in MCD simulations of M/Rg systems naturally suggests itself. The Monte Carlo-MCD (MC-MCD) simulation method is a first order degenerate perturbation method that straightforwardly extends the MC absorption simulation methods of Boatz and Fajardo[4] and Lawrence and Apkarian[5] by: (a) modeling the interactions of the M/Rg matrix through suitable diatomic potentials and angular momentum coupling algebra; (b) including both first order spin-orbit and Zeeman perturbations in the Hamiltonian of the optically active electron of the alkali metal M; and (c) separately treating the ^{2}S —> ^{2}P electric dipole transitions associated with LCP and RCP light.[10] The MC-MCD perturbation matrix for the ^{2}P term is a 6 x 6 matrix whose individual matrix elements are expressed in terms of a suitable uncoupled angular momentum p basis set with spin $\{|n l m_l \text{sm}_s> = |n11 \, 1/2 \, 1/2>, |n10 \, 1/2 \, 1/2>, |n1\text{-}1 \, 1/2 \, 1/2>, |n11 \, 1/2 \, -1/2>, |n10 \, 1/2 \, -1/2>, |n1\text{-}1 \, 1/2 \, -1/2>\}$. An uncoupled angular momentum representation $\{|n l m_l \text{sm}_s>\}$ for the zeroth-order eigenvectors is chosen,

[6]Piepho, S. B.; Schatz, P. N. *Group Theory in Spectroscopy with Applications to Magnetic Circular Dichroism*; Wiley: New York, **1983**.

[7](a) Luty, F.; Mort, J. *Phys. Rev. Lett.* **1964**, *12*, 45-57. (b) Henry, C. H.; Schnatterly, S. E.; Slichter, C. P. *Phys. Rev.* **1965**, *137*, A583-A602. (c) Mort, J.; Luty, F.; Brown, F. C. *Phys. Rev.* **1965**, *137*, A566-A573. (d) Merle d'Aubinge, Y.; Roussel, A. *Phys. Rev. B* **1971**, *3*, 1421-1427. (e) Osborne, G. A.; Stephens, P. J. *J. Chem. Phys.* **1972**, *56*, 609-618.

[8](a) Hormes, J.; Schiller, J. *Chem. Phys.* **1983**, *74*, 433-439. (b) Lund, P. A.; Smith, D.; Jacobs, S. M.; Schatz, P. N. *J. Phys. Chem.* **1984**, *88*, 31-42. (c) Lund, P. A.; Smith, D.; Williamson, B. E.; Schatz, P. N.; O'Brien, M. C. M. *J. Phys. Chem.* **1986**, *90*, 2608-2615. (d) Samet, C.; Rose, J. L.; Williamson, B. E.; Schatz, P. N. *Chem. Phys. Lett.* **1987**, *142*, 557-561.

[9](a) O'Brien, M. C. M. *J. Phys. C: Solid State Phys.* **1985**, *18*, 4963-4973. (b) O'Brien, M. C. M. *J. Chem. Phys.* **1985**, *82*, 3870-3871.

[10] Kenney, J. W., III *Final Report, 1995 AFOSR SFRP Program*, to be published.

without loss generality, because of the transparent way in which MCD selection rules may be expressed in terms of this representation.[5]

Monte Carlo Simulation of the MCD Spectrum: The full MCD spectrum for a $^2S \longrightarrow \, ^2P$ transition in a M/Rg system in a *specific* Rg configuration is, therefore, a "stick MCD spectrum" consisting of 12 lines (since the ^2S term has two components and the ^2P term has six components in a M/Rg system), appropriately placed on the x (energy) axis at transition energies $h\nu_{fi}$, whose magnitudes and directions (+ or -) on the y ($\Delta A'$) axis are determined by computing the appropriate squared transition moment integrals of each initial ^2S component with respect to each final ^2P state component for both LCP and RCP electric dipole transition operators. To simulate real MCD spectrum, many stick MCD spectra, each arising from a different Rg configuration, are appropriately averaged together using a MC scheme based upon the original Metropolis et al. algorithm[11] exactly as implemented by Boatz and Fajardo for the case of electronic absorption spectroscopy.[4] A MC-MCD simulation begins by choosing an initial Rg configuration, typically representing an idealized trapping site (e.g., a single substitutional site with O_h symmetry). The MC energy optimization scheme operates in the ^2S ground state manifold. At this stage, the very small Zeeman perturbation of the ^2S manifold is neglected. MCD stick spectra arising from more favorable configurations are weighted more heavily in the averaging process than those arising from the less favorable configurations. In actual practice, the LCP and RCP contributions to the MCD spectrum appearing are accumulated and stored separately. This allows both the MCD and the electronic absorption spectra to be recovered from the MC-MCD simulation as the difference and sum of the LCP and RCP absorbances, respectively.

Lattice temperature vs. magnetic temperature in MC-MCD simulations: Temperature effects appear in two distinct places in MC-MCD simulations. A lattice temperature must be specified for the MC simulation process. It may be argued that a proper representation of quantum mechanical zero point vibrational motions of the M/Rg lattice at temperature T requires the classical MC simulation to be carried out at a classical lattice temperature $T' > T$.[5] However, a temperature for the Boltzmann factor of the Zeeman-split ^2S term also must be included. This "magnetic temperature" always should be the actual system temperature T. The MC-MCD simulation code has the option of specifying separate values for the lattice temperature T' and the magnetic temperature T. Lawrence and Apkarian discuss the relationship between T' and T in classical MC simulations of doped Rg systems.[5]

MC-MCD Simulations

The Na/Ar system represents an ideal choice for MC-MCD simulations. Both Na and Ar are small enough systems so that high quality *ab initio* potential surfaces are available (Na-Na, Ar-Ar, and Na-Ar) as the starting point for simulations. However, Na and Ar are sufficiently massive to for a classical MC treatment of vibrational motion to be a reasonable approximation. Na/Ar is also readily accessible experimentally.[1] The following MC-MCD simulations focus on an octahedral (O_h) single subsititutional trapping site, which we

---

[11]Metropolis, N.; Rosenbluth, A. W.; Rosenbluth, M. N.; Teller, A. H.; Teller, E. *J. Chem. Phys.* **1953**, *21*, 1087.

tentatively ascribe to the "violet triplet" absorption feature reported by Tam and Fajardo.[1c] Our primary interest is in modeling the effects of spin-orbit coupling on the simulated MCD spectra and in determining whether or not a MCD spectral band shape arises uniquely from a given set of parameters or if the same general MCD band shape persists over a broad range of parameter variations. The overall goal is, therefore, to move from a simulated MCD spectrum to those specific parameters in the M/Rg system needed to produce a good simulation (e.g., initial trapping site geometry, initial number of host Ar atom vacancies, spin-orbit coupling constant of the optically active M electron, lattice temperature T', and, if applicable, magnetic temperature T). In general, the MC-MCD simulated spectra (and the associated MC-absorption spectra) meet the following criteria: (a) the MCD and absorption band profiles look very similar to the experimental spectra of M/Rg systems and overlay each other in energy; (b) the MCD band profile properly inverts when the direction of the applied magnetic field is changed; (c) the MCD band profile properly increases in amplitude when the magnitude of the magnetic field increases; (d) the simulated MCD and absorption spectra yield proper spin-orbit coupling constants and signs from band moment analyses; (e) are suitably responsive to lattice temperature effects and orientational averaging.[12]

Parameterization Uniqueness and MCD Band Profiles: Shown in the figures below are MC-MCD spectra of Na/Ar at a simulation temperature of 10 K with two different choices of the spin orbit coupling constant magnitude and sign. The key result of this simulation study is that a MC-MCD spectrum in which the sign and magnitude of the atomic ^2P spin-orbit splitting is preserved (+17 cm^{-1} for Na) has the *same overall profile* as a simulated MCD spectrum in which the ^2P spin-orbit coupling splitting is reversed in sign and increased by one order of magnitude (-170 cm^{-1}). This simulation study clearly shows that *caution is in order* in extracting and interpreting parameters from experimental MCD spectra.
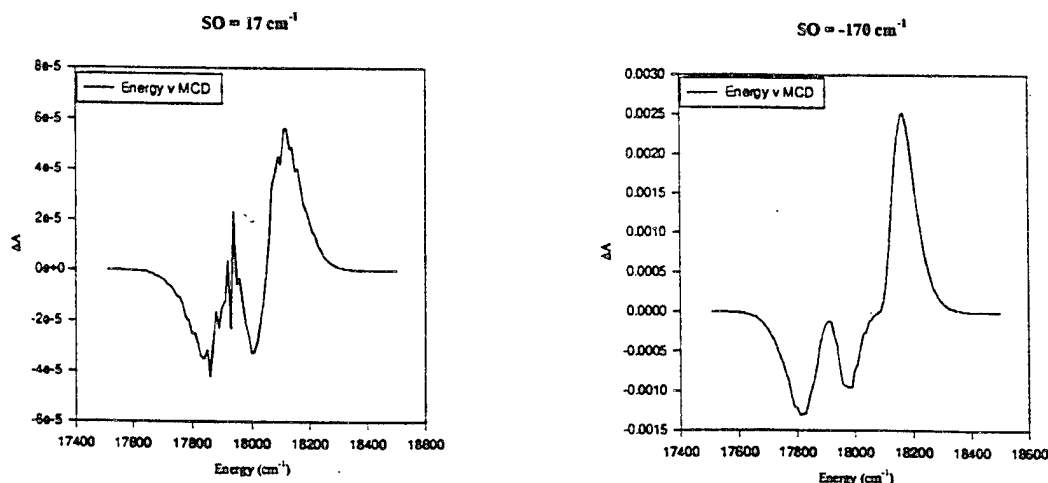
Acknowledgement

It is a pleasure to thank Drs. Jerry Boatz and Mario Fajardo at PL/RKFE their able assistance with all aspects of this project.

---

[12] Terrill-Stolper, H. A. *Final Report, 1995 AFOSR GSRP Program,* to be published.

STRUCTURAL RELAXATION AND SURFACE SELF-DIFFUSION OF QUENCH CONDENSED HYDROGEN FILMS

J. Classen[1], K. Eschenröder[2] and G. Weiss[2]

Universität Heidelberg, Institut für Angewandte Physik,
Albert-Ueberle-Str. 3-5, 69120 Heidelberg, Germany

Surface acoustic (Rayleigh) waves have been used to study the annealing behavior of quench condensed hydrogen films. At temperatures far below the triple point such films undergo drastic structural changes mediated by surface diffusion and form larger crystallites of typically 1 μm diameter. The rearrangement of the film structure could be traced in situ by changes of sound velocity and attenuation arising from scattering of the Rayleigh waves by inhomogeneities. The dominant scattering mechanism appears to be well described by a resonant interaction between surface acoustic waves and elastic eigenmodes of the hydrogen crystallites. From the temperature dependence of the speed of the structural changes we deduce the activation energies for surface self-diffusion as 23 K, 35 K, and 47 K for H_2, HD, and D_2, respectively.

[1]Present address: Department of Physics, Brown University, Providence, Rhode Island 02912, USA.

[2]Present address: Universität Karlsruhe, Physikalisches Institut, Engesserstr. 7, 76128 Karlsruhe, Germany.

VELOCITY SELECTION OF LASER ABLATED METAL ATOMS
BY A NOVEL NON-MECHANICAL TECHNIQUE

MARIO E. FAJARDO AND MICHEL MACLER*
Emerging Technologies Branch, Propulsion Directorate, Phillips Laboratory,
OLAC PL/RKFE, 10 E. Saturn Blvd., Edwards Air Force Base, CA 93524-7680.
*AFMC PL/NRC Post-doctoral Research Associate, now with Hughes STX.

ABSTRACT

We present the results of experiments on velocity selection of fast laser ablated Al, Ga, and In atoms by a novel, non-mechanical, technique. Pulses of atoms with broad velocity distributions are produced by laser ablation of a single component pure metal target in vacuum. After a delay of ~ 1 µs, there exists a strong one-to-one correlation between atomic velocity and distance traveled from the ablated surface. Thus, a second pulsed laser, delayed by ~ 1 µs and crossed at a right angle to the atomic beam, can be used to photoionize only those atoms with unwanted velocities, $i.e.$: atoms moving too fast or too slow to be hidden behind an opaque mask placed ~ 1 cm from the ablated surface. The photoions, and any ions surviving from the ablation event, are subsequently deflected from the beam by a static magnetic field. By a fortunate coincidence, Al, Ga, and In atoms all have very large single photon photoionization cross sections at 193 nm, the output wavelength of the ArF excimer laser; thus, well over 95% of the unwanted atoms can be easily photoionized and rejected. We have demonstrated velocity selected Al, Ga, and In atom fluxes equivalent to $\Phi \sim 10^{11}$ atoms/(cm^2-eV-pulse) at a working distance of 10 cm.

INTRODUCTION

Pulsed laser ablation of solid targets is an increasingly popular technique for the deposition of a wide variety of thin film materials [1]. There are many fundamental and applied studies underway of $e.g.$: laser/surface interactions, plume plasma hydrodynamics, plume composition vis-$à$-vis ions/neutrals/clusters/particulates, internal and kinetic energy content of ablated species, $etc.$, and of how all these factors ultimately affect the processes of thin film deposition and growth. Unfortunately, progress towards this ultimate goal is hampered by the bewildering complexity of the phenomena involved, a predicament that has been likened to studying "a tornado in a garbage can." We believe that any modification of "standard" laser ablation techniques which result in a simplification of this situation, and/or in improved parametric control over deposition conditions, will prove to be highly valuable to the thin film deposition community.

As a case in point: we have been employing pulsed laser ablation of metal targets as a source of metal atoms for matrix isolation spectroscopy (MIS) studies for several years now [2-6]. We prepare our MIS samples by codepositing the products of a laser ablated plume along with a large excess of an inert matrix host gas onto a cryogenically

cooled substrate. These experiments have lead us to hypothesize that the incident kinetic energy (KE) of the ablated metal atoms plays a key role in determining the atomic isolation efficiency of the matrix deposition process, and in the formation of novel metal atom trapping site structures.

However, this hypothesis is largely speculation, as we have not measured *in situ* (in our MIS apparatus) the actual composition of these laser ablated plumes, or the kinetic energy distributions (KEDs) of the ablated atoms. Furthermore, the laser ablation process can produce a mixture of metal atoms, clusters, and ions with rather broad KEDs, in some cases with KEs tailing out to several tens of electron volts. Thus, we undertook an effort to better characterize the chemical identity and KEDs of the laser ablated species produced under our experimental conditions, and to find out if we could gain improved control over these properties [7,8]. This effort culminated last year in our demonstration of velocity selection of fast laser ablated Al atoms by Temporally And Spatially Specific PhotoIonization (TASSPI) [9]; a novel, non-mechanical technique which provides a clean, stable, compact, intense, and tunable source of fast monoenergetic metal atoms for MIS experiments in particular, and thin film depositions in general.

In this manuscript, we briefly describe the TASSPI technique, and present the highlights of our recent results on velocity selection of Ga and In atoms; the interested reader is directed to ref. 9 for details of our Al atom work. A more detailed presentation of all our TASSPI related work is currently in preparation [10].
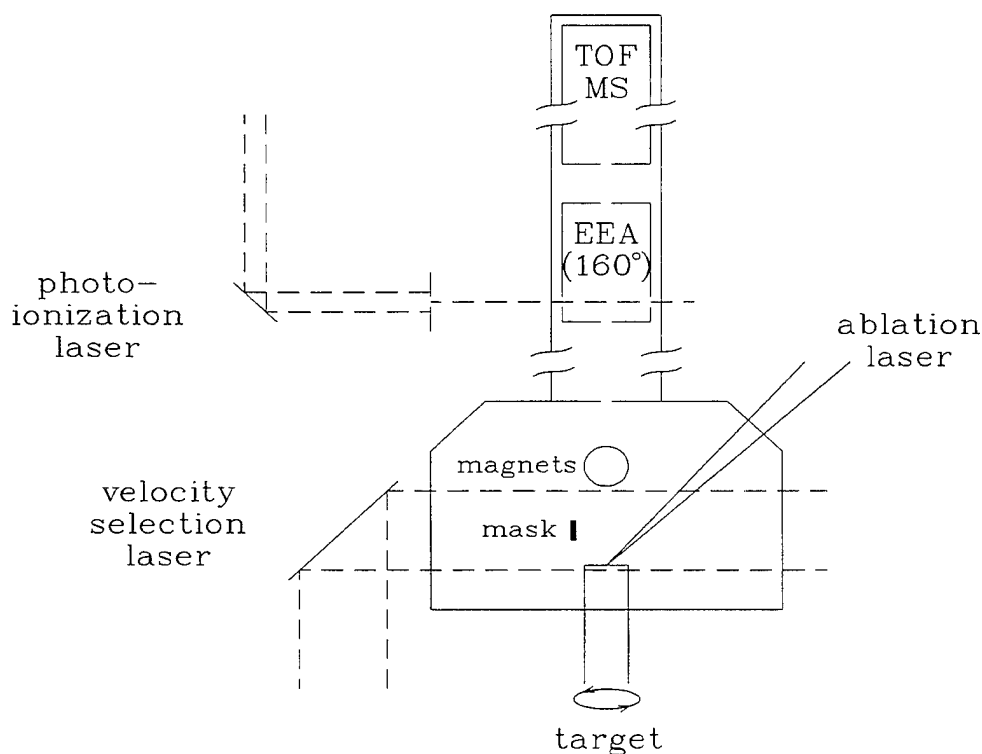
Fig. 1: *TASSPI Experimental Diagram.*

EXPERIMENTAL

Fig. 1 shows a schematic of our experimental setup, as configured for velocity selection by TASSPI. The metal ablation targets are mounted on a rotatable rod within a vacuum chamber pumped directly by a small turbomolecular pump to $\sim 10^{-6}$ Torr. The ablated plumes are generated by an excimer laser beam (XeCl, $\lambda=308$ nm) incident at an angle of $45°$ from the surface normal, and focused to a ≈ 0.003 cm^2 spot so as to cut a circular track on the rotating target. The laser ablated plume products pass through a magnetic field region ($|\mathbf{B}| = 2.8$ kG), located 2.5 cm from the ablation target surface, which deflects ionic species (e.g.: Ga$^+$ and In$^+$ ions with KE ≤ 15 eV) from the atomic beam axis. The beam axis is defined by the ablation spot on the target and a 0.2 cm diameter isolation aperture located ≈ 6 cm from the target surface, from which we estimate the final beam divergence as ≈ 40 mrad.

We characterize the chemical composition and KEDs of the species emerging through the isolation aperture with an electrostatic energy analyzer/time-of-flight mass spectrometer (EEA/TOFMS) system, using pulsed photoionization (ArF, $\lambda=193$ nm) of neutrals [8,9]. As we have discussed before [8,9], the apparent redundancy of this detection scheme (which requires that the time of flight of neutrals from the ablation target surface to the photoionization region be appropriate to the photoion pass energy selected by the EEA) allows us to detect the presence of non-atomic M$^+$ ion precursors in the atomic beam. The photoions which transit the EEA are accelerated to 2.0 keV, separated by mass in a 1 m TOF tube, and detected by a low gain microchannel plate detector.

Velocity selection by TASSPI entails photoionizing those metal atoms with unwanted velocities using another ArF excimer laser ("velocity selection laser" in fig. 1) and rejection of the resulting photoions by the magnetic deflection field. We have previously reported measurements of Al atom KEDs made close to and far from the ablated target surface which demonstrate that, under our mild ablation conditions, the Al atom KEDs are established on a sub 100 ns timescale [7,8]. Thus, after a delay of ~ 1 μs, there exists a strong one-to-one correlation between atomic velocity and distance traveled from the ablated surface (i.e. the atoms have sorted themselves out with the faster atoms traveling farther from the surface). A simple opaque mask of width Δx, placed at a distance x from the target surface, serves to protect those metal atoms hidden behind it at the arrival time of the velocity selection laser (t_{VS}). These metal atoms, with mean velocity $v = x/t_{VS}$, will not be photoionized, and hence will not be deflected from the atomic beam by the magnetic rejection field. The mean velocity can thus be set by adjusting x, and/or by adjusting t_{VS}, within limits set by the requirement that the fastest metal atoms to be rejected still be in the velocity selection region at t_{VS}. The surviving metal atoms have a spread of velocities, Δv (full width at half maximum, FWHM), and a corresponding spread of kinetic energies, ΔKE, all related by:

$$\frac{\Delta KE}{KE} \approx 2\frac{\Delta v}{v} \approx 2\left[\left(\frac{\Delta x}{x}\right)^2 + \left(\frac{\Delta t_{VS}}{t_{VS}}\right)^2\right]^{\frac{1}{2}}$$

in which Δt_{VS} is taken as the sum of the duration of the velocity selection laser pulse and the jitter between the ablation and velocity selection pulses ($\Delta t_{VS} \approx 50$ to 100 ns).

RESULTS AND DISCUSSION

We have previously shown in our Al experiments that maintaining the ablation laser intensity (I_{abl}) below $\approx 1\times10^8$ W/cm^2 greatly reduces the number of metal clusters and particles formed in the ablation process [8,9]. For Ga and In targets, we achieved the same results by keeping I_{abl} below $\approx 4\times10^7$ W/cm^2.

By varying the fluence of the ArF photoionization laser up to about 500 mJ/cm^2 we were able to saturate the intensities of both Ga$^+$ and In$^+$ signals. By fitting these saturation curves we can estimate the atomic photoionization cross sections at 193 nm as $\sigma_{PI}(\text{Ga}) = 2.7(\pm0.6)\times10^{-17}$ cm^2 and $\sigma_{PI}(\text{In}) = 1.7(\pm0.6)\times10^{-17}$ cm^2, in good agreement with previously published values [11]. These measurements confirm the velocity selection laser fluences, F_{VS}, required for efficient implementation of the TASSPI process.

Fig. 2 shows the results of a velocity selection experiment on laser ablated Ga
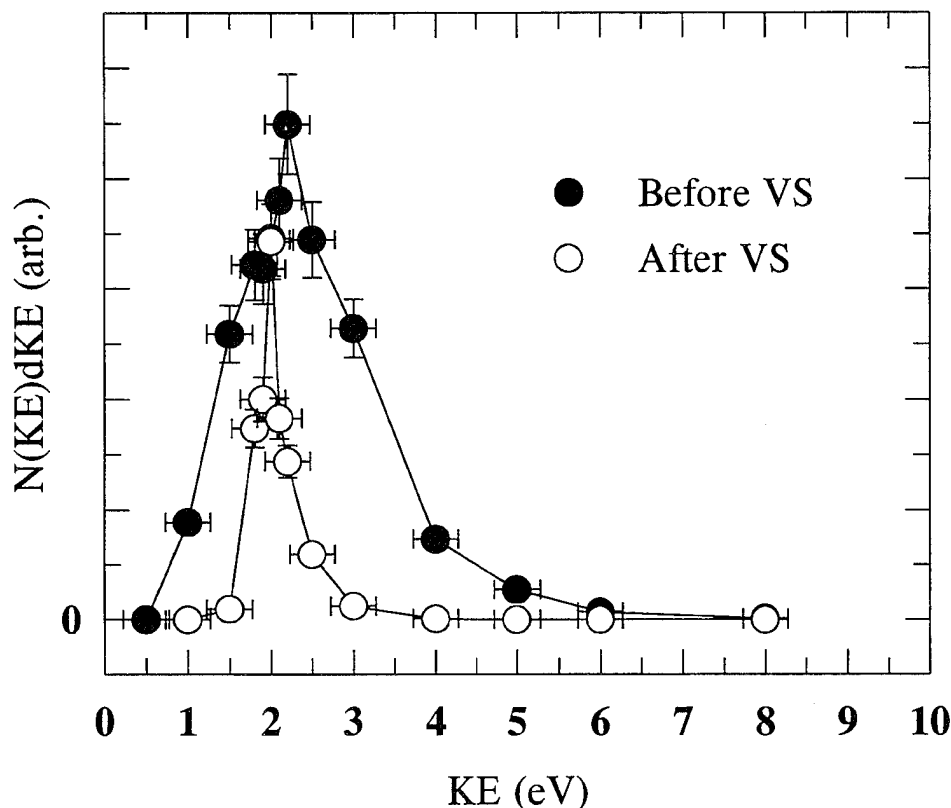
Fig. 2: Velocity Selection of Ga Atoms by TASSPI. The closed circles show the nascent Ga atom KED, the open circles show the TASSPI effect. The error bars represent the estimated ± 1 σ limits. The experimental conditions were: $I_{abl} = 3.4\times10^7$ W/cm^2, $F_{VS} = .500$ mJ/cm^2, x = 0.90 cm, $\Delta x = 0.16$ cm, $t_{VS} = 3.8$ μs.

atoms. The nascent Ga atom KED peaks near 2.2 eV and shows a FWHM of ≈ 1.8 eV. The velocity selected Ga atom KED peaks at 2.0 eV with a FWHM of 0.5 eV. The transmission of the velocity selector at the 2 eV peak is very nearly 100%, and the integrated transmission is ≈ 20 % of the original laser ablated flux. Quartz crystal microbalance (QCM) measurements indicate a velocity selected Ga atom flux of Φ_{Ga} ≈ 8x10^{10} atoms/(cm^2 eV pulse) at a distance of 10 cm from the ablation target surface.

Fig. 3 shows the results of a velocity selection experiment on laser ablated In atoms. The nascent KED peaks near 2.8 eV and shows a FWHM of ≈ 2.4 eV. The velocity selected KED peaks near 3 eV with a FWHM of 0.9 eV. The transmission at the 3 eV peak is very nearly 100%, and the integrated transmission is ≈ 20 % of the original atomic flux. QCM measurements yield a velocity selected In atom flux of Φ_{In} ≈ 6x10^{10} atoms/(cm^2 eV pulse) at a working distance of 10 cm.
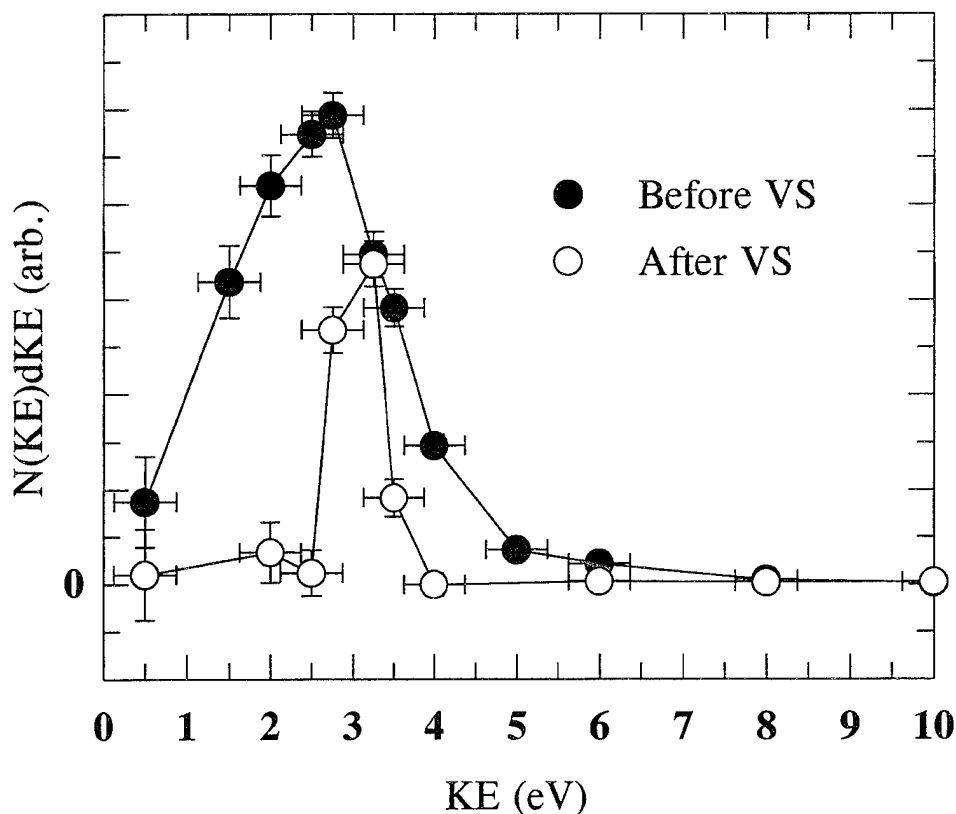
Fig. 3: Velocity Selection of In Atoms by TASSPI. The closed circles show the nascent In atom KED, the open circles show the TASSPI effect. The error bars represent the estimated ± 1 σ limits. The experimental conditions were: I_{abl} = 3.4x10^7 W/cm^2, F_{VS} = 530 mJ/cm^2, x = 0.90 cm, Δx = 0.16 cm, t_{VS} = 4.0 μs.

CONCLUSIONS AND FUTURE DIRECTIONS

We have demonstrated a new, non-mechanical technique for performing velocity selection of fast laser ablated Al, Ga, and In atoms. Actually, the relatively low velocities of the heavy Ga and In atoms allow the use of conventional velocity selection schemes, but we found switching between group IIIB metals very convenient with the TASSPI method.

We are currently pursuing velocity selection of lighter species such as fast Li and B atoms. Unfortunately, the single photon photoionization cross section for Li is smaller than that for Al by over two-orders of magnitude [11], and the ionization potential for B atoms is almost 6.7 eV [12], corresponding to a presently inconvenient photon wavelength of 185 nm. It may be that the implementation of TASSPI in these systems will require the use of multi-photon ionization techniques, perhaps involving tunable pulsed lasers able to effect resonance enhancement via intermediate states [12].

We hope to ultimately apply a TASSPI source to help answer some of the questions arising from our MIS work mentioned above. We will begin with co-depositions of fast Al atoms and molecular hydrogen at 2 K, examining the KE dependence of the atomic isolation efficiency and the formation of Al_xH_y reaction products [6].

We also hope that the TASSPI technique will find its way into other thin film deposition experiments, at least as a research tool. Three simultaneous modifications: increasing the ablation laser spot size while maintaining I_{abl} constant, increasing the diameter of the beam defining aperture, and increasing the magnetic rejection field strength, should allow for pure atomic fluxes of over 10^{12} atoms/(cm^2 eV pulse) at a 10 cm working distance. Excimer lasers operating at ~ 1 KHz repetition rates would then provide $\sim 10^{15}$ atoms/(cm^2 eV s). Ultimately, TASSPI may help elucidate the roles of incident atomic KE, beam composition, etc. in the formation of mixed semiconductors, nonlinear optical materials, and other thin films produced by laser ablation techniques.

REFERENCES

1. Laser Ablation in Materials Processing: Fundamentals and Applications, B. Braren, J.J. Dubowski, and D.P. Norton, eds. (Mater. Res. Soc. Proc. 285, Boston, MA, 1993).
2. M.E. Fajardo, P.G. Carrick, J.W. Kenney III, J. Chem. Phys. 94, 5812 (1991).
3. M.E. Fajardo, J. Chem. Phys. 98, 110 (1993).
4. S. Tam and M.E. Fajardo, J. Chem. Phys. 99, 854 (1993).
5. R.A. Corbin and M.E. Fajardo, J. Chem. Phys. 101, 2678 (1994).
6. M.E. Fajardo, S. Tam, T.L. Thompson, and M.E. Cordonnier, Chem. Phys. 189, 351 (1994).
7. M. Macler and M.E. Fajardo, pp. 105-110 in ref. 1.
8. M. Macler and M.E. Fajardo, Appl. Phys. Lett. 65, 159 (1994).
9. M. Macler and M.E. Fajardo, Appl. Phys. Lett. 65, 2275 (1994).
10. M. Macler and M.E. Fajardo, manuscript in preparation.
11. R.D. Hudson and L.J. Kieffer, Atomic Data 2, 205 (1971).
12. V.S. Letokhov, Laser Photoionization Spectroscopy, (Academic, Orlando, FL 1987).

APPLICATION AND PERFORMANCE REQUIREMENTS FOR HYDROCARBON FUELS

A. WILSON and E.J. WUCHERER
PHILLIPS LABORATORY/HUGHES STX
10 E. SATURN BLVD.
EDWARDS AFB, CA 93524-7680

This effort examines mission applications for hydrocarbon fuels and investigates requirements necessary for various propellants to have an impact on these missions. Hydrocarbon fuels will continue to be required in the traditional role of launch/boost for staged, expendable launch vehicles. For reusable launch, advantages of handling, storage, and vehicle size may allow lower performing LOX/Hydrocarbon systems to supplement the high performance LOX/LH2 combination.

Two most common rocket fuels in use today are liquid hydrogen and the hydrocarbon mixture RP-1. A comparison of the two propellants shows that each has individual characteristics that may be more desirable for a given rocket application depending the mission flight performance parameters. Liquid hydrogen gives the higher performance of the two fuels. Assuming standard conditions of 1000 psi chamber pressure, 14.7 psi nozzle exit pressure, optimum nozzle expansion ratio, and an adiabatic expansion, a LH2/LOX mixture yields a specific impulse (Isp) of 390 seconds and an RP-1/LOX mixture yields an Isp of 300 seconds. However, with the density of RP-1 being three times greater than LH2, RP-1 may have an increased role in future missions. The density of hydrocarbons, along with ease of handling, and implications on vehicle volume suit hydrocarbons well for use in staged expendable launch vehicles where Isp and weight are not as critical because vehicle weight is removed in stages.

Because of its reliability and low cost, hydrocarbon fuels in use in the current ELV stages are seen as a mature technology. However, improvements in hydrocarbon fuels could have a significant mission impact on the systems considered for the Air Force Evolved Expendable Launch Vehicle (EELV) Program. EELV mission impact could be achieved by hydrocarbon fuel improvements of a 5-10% increase in Isp and density while keeping the physical and combustion properties as well as costs similar to RP-1. This requirement also holds true in the concepts of designing a fully reusable shuttle. Two hydrocarbon fuels that may potentially achieve the 5-10% increase in Isp and density are cubane and acetylene. Cubane offers a 6% increase in Isp and a 20% increase in density. Acetylene offers a 10% increase in Isp, but at a 15% decrease in density. A drawback to these compounds is the current costs associated with the production of cubane, and the explosion hazards of pure acetylene.

The criticality of the combination of high Isp and a high thrust/weight ratio to enable a single-stage-to-orbit (SSTO) reusable launch vehicle (RLV) dictates

the use of LOX/LH2 or a tri-propellant LOX/Hydrocarbon/LH2 propulsion system. Hydrocarbons in a tri-propellant propulsion system are being considered in the NASA X-33 Technology Program which will demonstrate the technologies necessary for a SSTO vehicle. Serious consideration of a hydrocarbon reusable vehicle would require a hydrocarbon propellant combination that would achieve an Isp of 350 seconds or greater. This increase in Isp could also greatly benefit staged ELV systems.

Theoretical formulations of molecules similar to the formulas for such fuels as acetylene, pentaborane, UDMH, and hydrazine could yield Isp values of 350 seconds when combusted with LOX. To achieve the Isp of 350 seconds, the heat of formation of the molecule would need to be increased to provide a greater available chemical energy, or heat of reaction. For example, the value of the heat of formation of Hydrazine, $(NH_2)_2$, is 0.4 kcal/gm and a LOX/Hydrazine combustion at standard conditions yields an Isp of 313 seconds. A theoretical formulation of an $(NH_2)_x$ molecule with a heat of formation of 1.52 kcal/gm would yield an Isp of 350 seconds when combusted with LOX.

Additional increases in Isp can also be achieved by using more energetic oxidizers besides LOX. Since most of the propellant mass carried on a launch vehicle is in the oxidizer, increases in Isp due to the oxidizer would have a significant mission impact. The use of liquid fluorine (LF2), liquid ozone (LO3), or combination of LO3 and LOX, all with various fuels, could achieve Isp values greater than 350 seconds. Currently, the hazards of handling LO3 and the toxicity and corrosiveness of LF2 are prohibitive to the use of these oxidizers in launch systems.

This investigation has shown that mission enabling hydrocarbons require heat of formation values of approximately 3.0 kcal/gm, or roughly double the heat of formation value of Cubane. Calculations of several theoretical molecules with greater heat of formation values have yielded mission impact levels of performance. Current hydrocarbon candidates such as Cubane must be reduced in cost to compete with the mature RP-1 propellant. Since the propellant mixture on a vehicle is 60%-70% oxidizer, a significant increase in performance may be best realized by working to apply more energetic oxidizers such as liquid ozone.

SYNTHETIC EFFORTS TOWARDS SUBSTITUTED HOMOPENTAPRISMANE: A NON-PHOTOCHEMICAL APPROACH

Suresh Chander Suri & Stephen L. Rodgers
Hughes STX Corporation, Propulsion Science Division
Phillips Laboratory, 10 East Saturn Blvd.
Edwards Air Force Base, CA 92524-7680

Introduction

[n]-Prismanes belong to a class of polyhedranes having a general formula of $(CH)_{2n}$ where n represents the order of prismane. This class of polyhedrane (prismanes) possesses unusual C-C bond length and bond angles, steric compression, and high strain energy. These unusual properties of [n]-prismanes contribute towards their chemical reactivity. The strategies to synthesize [n]-prismanes (n = 3, 4, 5 or 6) via generating multiple cyclobutane rings [(2+2) photocycloaddition] with stereocontrol have been unsuccessful. For example, hypostrophene (1) fails to undergo (2+2) photocycloaddition to furnish pentaprismane (2). The successful approaches for the synthesis of [n]-prismanes[1] (n = 4, 5) involve [2+2] photocycloaddition in a homologus system and Favorskii ring contraction as key steps.

$$1 \qquad\qquad 2$$
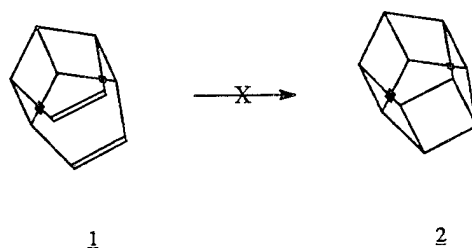
Pentaprismane (2) was synthesized by Eaton et al.[2] by [2+2] photocyclo-addtion of substituted homohypotrophene 3 followed by functionalization of the

$$3 \qquad 4 \qquad 5 \qquad 6$$
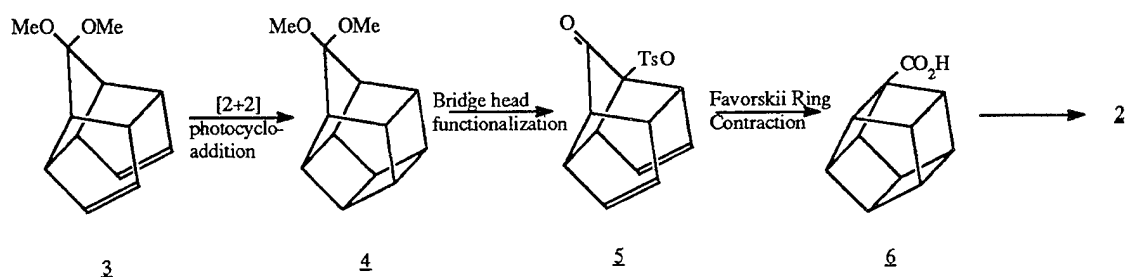
bridge head position of the resulting homopentaprismane $\underline{4}$. The Favorskii ring contraction of the functionalized homopentaprismane $\underline{5}$ furnished pentaprismane derivative $\underline{6}$ which was converted to pentaprismane.

The chemistry of pentaprismane is not developed because of non-availability of bridge head functionalized homopentaprismane in large quantities. We present here our synthetic efforts towards bridge head substituted homopentaprismane from readily available 1,8,10-trichloro-11,11-dimethoxy-3-*exo*-hydroxytetracyclo-$[6.2.1.0^{2,7}.0^{4,10}]$undec-5-ene-9-one[3] ($\underline{7}$).

Results

1,8,10-Trichloro-11,11-dimethoxy-3-*exo*-hydroxytetracyclo$[6.2.1.0^{2,7}.0^{4,10}]$-undec-5-ene-9-one[3] ($\underline{7}$) can be obtained by treating 1,8,9,10-tetrachloro-3,6-*exo*-dihydroxy-11,11-dimethoxytricyclo$[6.2.1.0^{2,7}]$undec-4,9-diene[4] with t-BuOK/t-BuOH. It is obvious that carbon-carbon bond formation between C_3 & C_6 and C_5 & C_9 should lead to functionalized homopentaprismane. Recently, it was demonstrated that C_5 & C_9 bond formation could be achieved via intramolecular ketylolefin reductive coupling to furnish substituted pentacyclo[5.4.0.$0^{2,6}.0^{3,10}.0^{5,9}$]undecane[5] $\underline{8}$. The C_3 & C_6 bond formation was demonstrated by treating the tosylate $\underline{9}$ with lithium aluminum hydride to furnish the corresponding 3-oxahexacyclo[5.5.0.$0^{2,6}.0^{4,11}.0^{5,9}.0^{8,12}$]-dodecane[6] $\underline{10}$ via tandem cyclization.
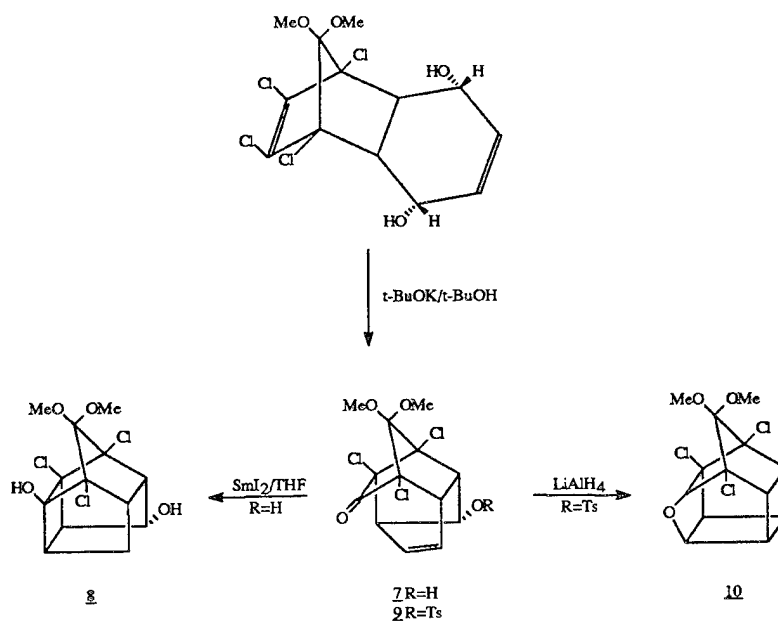
The carbon-carbon bond formation between C_3 & C_6 and C_5 & C_9 simultaneously were unsuccessful. At this point it was decided to join C_3 & C_6 and functionalize C_5 position in $\underline{7}$ using external nucleophile like halogen. The corresponding tosylate $\underline{9}$ was subjected to variety of conditions to furnish functionalized pentacyclic compounds $\underline{10}$ and/or $\underline{11}$.
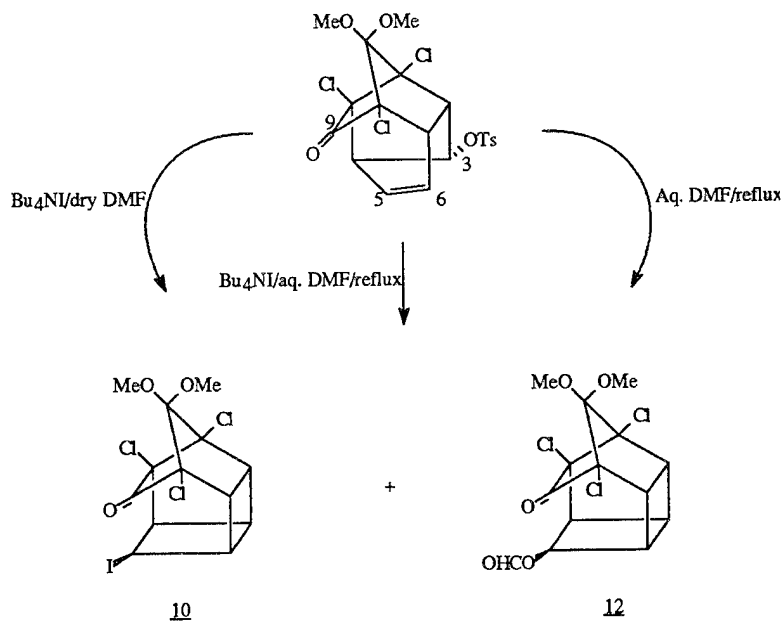
The iodo compound 10 was also obtained directly from alcohol 7 by treating it with Ph3P/imidazole/I2 in refluxing toluene[7]. The formate 11 was treated with Jones' reagent to furnish diketone 12. It is anticipated that compounds 11 & 12 are viable precursors for the synthesis of substituted homopentaprismane.
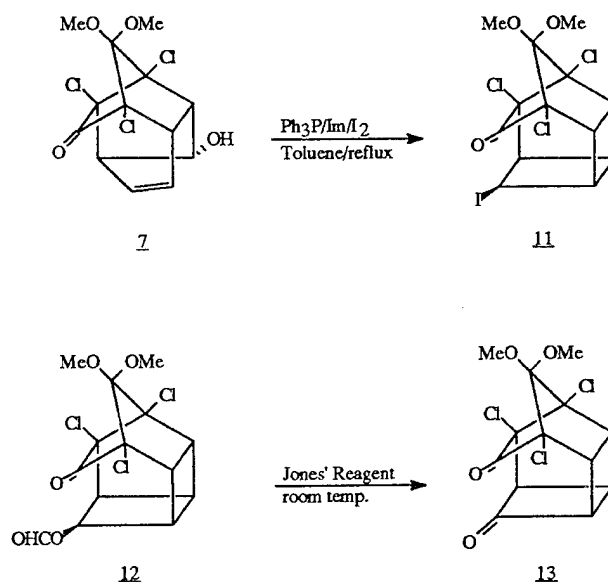
Future Efforts Towards Substituted Homopentaprismane

Intramolecular Alkylation

Molecular mechanics calculations, using Chem-X, were done to examine the relative strain energies, and energy barrier to intermediate formation (Figure 1). These calculations suggest that the intramolecular alkylation reaction on 11 is a facile process to furnish 14.

Figure 1

ΔH -39.64
SE 82.73
MM 104.41

ΔH -44.52
SE 67.74
MM 89.92

ΔH -65.06
SE 94.07
MM 118.04
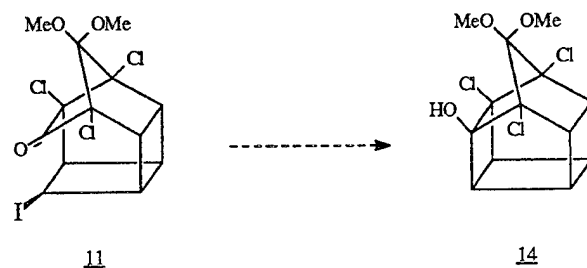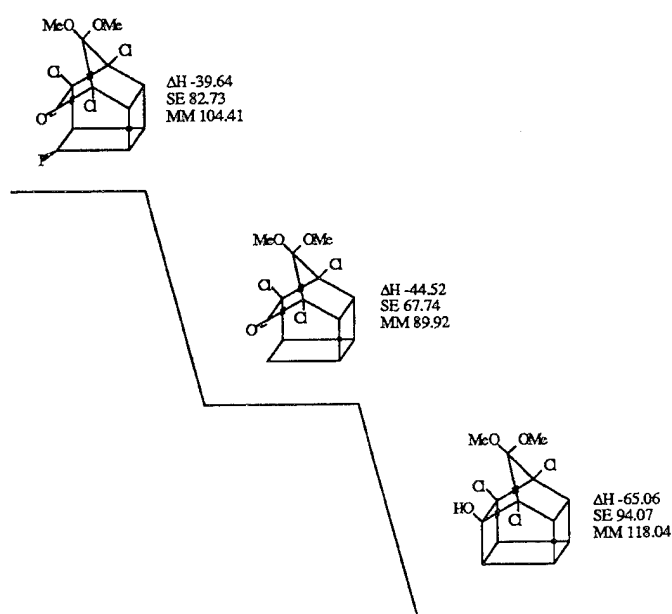
SE - Strain Energy
MM - Molecular Mechanic Energy in Kcal/.
Calculations done using Chem-X

Pinacol Coupling Reaction

Molecular mechanics calculations carried out on 13 reflected the carbonyl carbons distance 2.546 A which is within the range[8] for coupling reaction. It is

13   Coupling Reaction   15
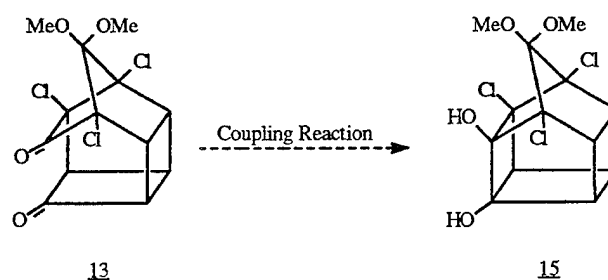
anticipated that when 13 is subjected to variety of coupling reagents it should furnish the corresponding pinacol coupling product 15.

References

1.   For a comprehensive review on prismane: Mehta, G. and Padma, S. in "Carbocyclic Cage Compounds" Ed. by Osawa, E. & Yonemitsu, O.; VCH Publisher, Inc. NY 1992.

2. Eaton, P.E.; Or, Y.S. and Branca, S.J. *J. Am. Chem. Soc.*, 1981, *103*, 2134.

3.   Suri, S.C. *Tetrahedron Lett.*, 1990, *31*, 3695.

4. Marchand, A.P., LaRoe, W.D., Sharma, G.V.M., Suri, S.C. and Reddy, D.S. *J. Org. Chem.*, 1986, *51*, 1622.

5.   Suri, S.C. and Hardcastle, K.I. *J. Org. Chem.* 1992, *57*, 6357.

Emission Spectroscopy of the Triplet System of the BH Radical

C.R. Brazier

Hughes STX

Phillips Lab. /RKS

Edwards AFB, CA 93524-7680

Introduction

The $b^3\Sigma^-$-$a^3\Pi$ transition near 27000 cm^{-1} is the only known triplet system of the BH radical. This system was first observed by Lochte-Holtgreven and van der Vleugel in 1931 (1) and more extensively analyzed and assigned as $^3\Sigma$-$^3\Pi$ by Almy and Horsfall in 1937 (2). They analyzed the 0-0 band and obtained rotational constants and the $^3\Pi$ state spin-orbit splitting graphically. There had been no further spectroscopic observations of the BH triplet system until the present work. Interest in the triplet system of BH has increased recently due to the development of a possible chemical laser based on the $A^1\Pi$-$X^1\Sigma^+$ system of BH (3,4). The BH molecules were excited from the ground $X^1\Sigma^+$ state to the $A^1\Pi$ state, in two steps via the $a^3\Pi$ state, by near resonant energy transfer from excited NF. Accurate characterization of the triplet states of BH is important for understanding the excitation process and for performing reliable diagnostic measurements (4). Theoretical calculations of the radiative decay rate of the $a^3\Pi$ state (5) and radiative and non-radiative decay of the $b^3\Sigma^-$ state (6) have been performed by Pederson et al. to assist in the characterization of the BH excitation scheme. These calculations have also proved useful for comparison with the present experimental observations.

The triplet system of BH was originally recorded as part of a study of boron species that was focussed primarily on B_2 (7-9), with the overall goal of studying species that could be stored in solid hydrogen for use as high energy density rocket fuels (10). Extremely strong spectra of BH were observed and the $\Delta v=0$ sequence of the triplet system was measured at high resolution using the Fourier transform spectrometer at Kitt Peak National Observatory. The weaker off-diagonal bands were subsequently recorded using a 1.3 m monochromator and OMA. We present here a detailed analysis of the observed bands, which extend up to 80% of the dissociation limit in the $a^3\Pi$ state and 75% in the $b^3\Sigma^-$ state. The potential curves derived from these observations are compared with the most recent theoretical results (5). The intensities of the observed lines are compared with the theoretical predictions of predissociation by the $(1)^3\Sigma^+$ state (6).

Experimental

The BH radicals were produced in a corona excited supersonic expansion (CESE) (11) of dilute diborane (B_2H_6) in helium. Detailed experimental information can be found in the earlier work on B_2 (7). The only significant difference for this study was that the BH signal was optimized at slightly lower diborane concentrations, typically 100 ppm. When the discharge was operating correctly a bright purple glow from the strong $A^1\Pi$-$X^1\Sigma^+$ system of BH was visible in the supersonic flow. This glow continued past the shock fronts into the background gas all the way to the electrical ground. The light from the region just beyond the tip of the nozzle was

focussed onto the entrance window of the 1 meter Fourier transform spectrometer at Kitt Peak National Observatory. The use of diborane in a CESE source leads to significant production of solid polymer that tends to clog the nozzle. Consequently a series of short accumulations of data were made, for a total of 10 scans in 20 minutes. The observed linewidth was $0.14\,cm^{-1}$, comprising an instrumental width of $0.07\,cm^{-1}$ and a Doppler spread of $0.12\,cm^{-1}$.

The only available calibration line in the current spectrum is the 3^3P-2^3S helium line at 3888.65 Å. The 3^3P-2^3S line appears in the current spectrum as a partially resolved doublet with one component 8 times as strong as the other. The strong line comprises the unresolved $^3P_2$-^3S and $^3P_1$-^3S components and the weak line the $^3P_0$-^3S component. The $^3P_2$-^3S and $^3P_1$-^3S lines are at $25708.5875(10)\,cm^{-1}$ and $25708.6095(10)\,cm^{-1}$ respectively. The intensity weighted average position for the two overlapped components is $25708.6007(10)\,cm^{-1}$.
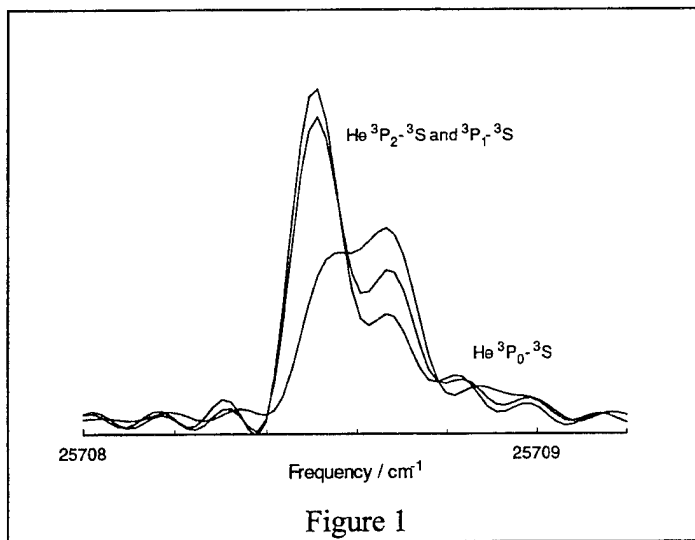
Figure 1

Measurement of the position of the 3^3P-2^3S He line in the BH spectra is complicated by an apparent splitting of both the strong and weak components. The size of the splitting and relative intensities of the two components is different for each of the three scans, as can be seen in Fig. 1. This suggests that the structure on the line is a result of the source. The 3^3P-2^3S He line was found to be red shifted by $0.0440\,cm^{-1}$ and $0.0602\,cm^{-1}$ for the second and third data sets relative to the first one. Comparable shifts were also seen in the BH spectra, for example the 0-0 $P_1(2)$ line exhibits shifts of $0.0443\,cm^{-1}$ and $0.0599\,cm^{-1}$ among the three data sets. The calibration was performed using the sum of the three spectra resulting in a weighted average line position of $25708.5782\,cm^{-1}$. This is a shift of $0.0225\,cm^{-1}$ compared to the known position, which corresponds to a fractional shift of 8.752×10^{-7}. The frequencies of all of the BH lines were adjusted by this factor.

The origin of the structure on the helium line is most likely self absorption in the background gas between the jet and the window of the vacuum system. The 2^3S state of He is metastable with a very long gas phase lifetime in the absence of collisions. The fact that the position of the absorption peak remains fixed, while the emission peak shifts as the alignment of the jet is changed, supports this supposition. The amount of absorption is somewhat different in each scan, but if an average absorption of 40% is assumed then this equates to a population density of He 2^3S of about 3×10^{-6} Torr over the approximate 10 cm path length.

To provide information on the vibrational frequencies in the $a^3\Pi$ and $b^3\Sigma^-$ states, additional BH emission spectra were recorded using a 1.3 m monochromator and OMA. The resolution was lower, about $0.85\,cm^{-1}$, but the sensitivity was much higher. The $\Delta v=+1$ sequence

was observed out to the 8-7 band and some bands in the Δv=+2 and Δv=-1 sequences were also observed. The higher sensitivity also allowed extension of the Δv=0 observations up to the 7-7 band and to higher rotational levels for the previously observed bands. The OMA spectra were calibrated by recording the spectrum of a thorium/neon hollow cathode lamp. The observed thorium and neon lines were compared with those listed in the atlas of Palmer and Engleman (14) and a calibration function for the region of interest generated.

Results

The $b^3\Sigma^-$-$a^3\Pi$ system of BH is a typical Hund's case b to case b $^3\Sigma$-$^3\Pi$ transition with strong P and Q branches and weaker R branches, and with each rotational transition split into three components due to the electron spin. This can be seen clearly in Fig. 2, which shows the origin region of the 0-0 band. The first lines are clearly visible, and as the F_1 component is the strongest, assignment of the branches is straightforward. For low J values there are also a limited number of weak satellite branch lines (ΔJ≠ΔN), which are useful for simultaneously determining the spin structure in both the Σ and Π states. Boron has two naturally occurring isotopes ^{10}B and ^{11}B present in the ratio of 1:4. This results in weak ^{10}BH satellite lines on the side away from the origin for the 0-0 band lines, as can be seen in Fig. 2. Even though the BH molecules were produced in a supersonic expansion the spectrum shows little sign of rotational cooling. The strongest part of the spectrum, near the origin, has a rotational temperature near 300 K, and there is also a weaker high temperature tail extending out to J
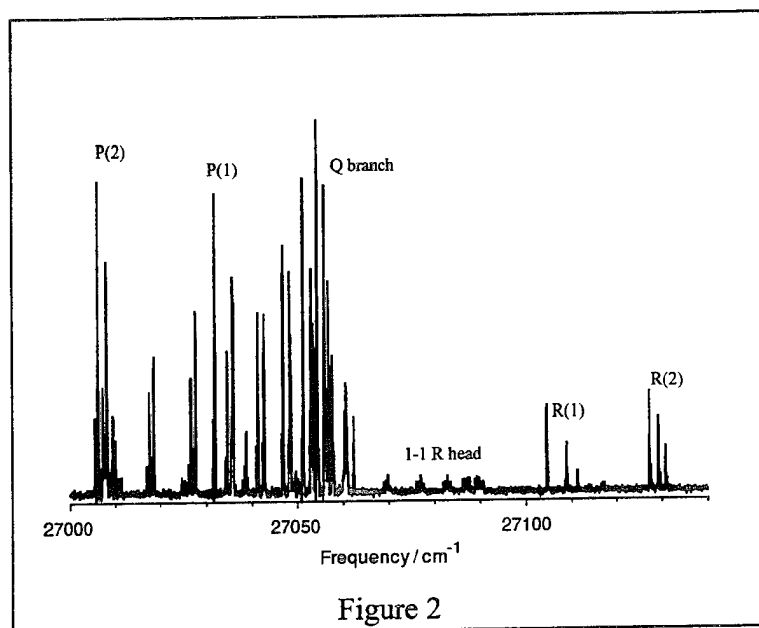
Figure 2

of about 40, which corresponds to a 'temperature' of approximately 4000 K.

A least squares fit of the calibrated BH 0-0 band lines to standard $^3\Pi$ and $^3\Sigma^-$ Hamiltonians was performed. The Hamiltonian and principal matrix elements are given by Brown et al. (15) while explicit matrix elements to high order in centrifugal distortion are given by Brazier et al. (16). The 0-0 band line positions were reproduced to their estimated measurement accuracy. Subsequently the other Δv=0 bands, 1-1, 2-2, 3-3, 4-4, and 5-5 were identified and fitted.

The high resolution FTS data for the Δv=0 bands were supplemented by data recorded at 0.85 cm^{-1} resolution using a monochromator and OMA detector for the off-diagonal bands. The $b^3\Sigma^-$ and $a^3\Pi$ potential curves of BH are very similar so that the off-diagonal bands are expected to be weak. A search was made in both the Δv=+1 and Δv=-1 regions based on theoretical

Table I. Constants for the $b^3\Sigma^-$-$a^3\Pi$ System of BH (in cm^{-1})		
Constant	$a^3\Pi$	$b^3\Sigma^-$
T_e	0	27152.745(29)[a]
ω_e	2625.136(149)	2438.097(85)
$\omega_e x_e$	55.784(149)	55.562(67)
$\omega_e y_e$	-0.201(68)	-0.392(22)
$\omega_e z_e$	-0.1851(157)	0.0129(32)
$\omega_e a_e$	0.01880(177)	-0.00342(16)
$\omega_e b_e$	-0.001798(78)	
A_e	4.3878(15)	
$A(2)$	0.0317(19)	
A_D	0.0000984	
λ_e	-0.0147(11)	0.2406(10)
B_e	12.89309(28)	12.34263(34)
α_e	0.41561(76)	0.43087(100)
$B(3)$	-0.01416(51)	-0.02001(78)
$B(4)$	0.002292(117)	0.006302(252)
$B(5)$	-0.0003820(86)	-0.001079(37)
$B(6)$		0.0000596(20)
D_e	0.00123482(98)	0.00125759(106)
$D(2)$	0.00002223(242)	0.00002116(271)
$D(3)$	-0.00001868(129)	-0.00002073(150)
$D(4)$	0.000003701(142)	0.000003346(161)
$10^7 \times H_e$	1.0001(99)	0.9675(112)
$10^7 \times H(2)$	0.1016(221)	0.1624(264)
$10^7 \times H(3)$	-0.1000(97)	-0.1235(127)
$10^{11} \times L$	-1.402(28)	-1.282(20)
$10^{11} \times L(2)$	0.206(52)	
$10^{11} \times L(3)$	-0.162(20)	
γ_e	0.00144(30)	-0.00669(30)
$\gamma(2)$		0.000820(90)
$10^6 \times \gamma_D$		2.47(14)
o_e	0.40264(93)	
$o(2)$	-0.01242(114)	
p_e	0.005221(93)	
$10^6 \times p_D$	-1.31(28)	
q_e	0.020143(16)	
$q(2)$	-0.000812(29)	
$q(3)$	-0.0000631(110)	
$10^6 \times q_D$	-7.511(40)	
$10^{10} \times q_H$	9.25(33)	

[a] One standard deviation error estimates in parentheses.

estimates of the vibrational frequencies (5). The search was complicated by overlapping BH singlet bands in both regions. The 1-0 band was eventually found, under the main $\Delta v=0$ sequence of the $B^1\Sigma^+$-$A^1\Pi$ system. The higher bands in the $\Delta v=+1$ sequence of the $b^3\Sigma^-$-$a^3\Pi$ system were then traced out all the way from 1-0 through 8-7. The intensities of the bands change very little until the 6-5 band, which is a factor of 4 weaker than the earlier bands. All of the higher bands are relatively weak. With the observation of the 1-0 band the location of the 0-1 band could be predicted exactly. The 0-1 band was found to be extremely weak, and in addition it was overlapped by the 2-1 band of the $A^1\Pi$-$X^1\Sigma^+$ system. No further bands in the $\Delta v=-1$ sequence could be measured. The higher signal-to-noise ratio of the monochromator/OMA data, made possible the extension of the $\Delta v=0$ data set to higher rotational levels. In addition the 6-6 and 7-7 bands were found.

The $\Delta v=+1$ bands were each analyzed separately. The bands could be fitted while constraining the rotational constants to values determined from the $\Delta v=0$ bands. Most of the bands were well behaved and the data could be fitted

using a small number of parameters that varied in a predictable way from band to band. The 6-5 and 6-6 bands, however, were very difficult to reproduce adequately, and the parameters determined were different from those expected based on analysis of the other bands. This is clear evidence of a perturbation in v=6 of the $b^3\Sigma^-$ state. While the $b^3\Sigma^-$ lines were clearly shifted, there was no evidence of extra lines from the perturbing state.

In order to perform a complete analysis of all the bands, a modified fitting program was developed in which all of the parameters in both states could be expanded in Dunham type series in the vibrational quantum number. Since the v=6 level was known to be perturbed, the parameters for this level were allowed to float separately from the Dunham parameters. The individual vibrational bands were added one at a time to the fit, and the number of parameters slowly increased. All of the levels observed, v=0 through v=7 in the $a^3\Pi$ state, and v=0 through v=8 in the $b^3\Sigma^-$ state (except v=6), could be adequately reproduced using a single set of Dunham parameters for each state. The levels above v=6 in the $b^3\Sigma^-$ state show some effects of possible perturbation. In the final fit the parameters for v=8 were allowed to float separately. The equilibrium parameters and their one standard deviation error estimates from the least squares fit are listed in Table I.

Discussion

The equilibrium constants for the triplet states of BH have been determined for the first time. For the 0-0 band that had been observed previously (1,2) the constants are consistent, but much more precise. The equilibrium constants are compared with ab initio predictions (5) in Table II. The transition energy is extremely close, while the equilibrium separations are slightly shorter than predicted. The vibrational frequencies are also slightly higher than predicted for both electronic states, indicating that the binding in the theoretical potential curves is not quite tight enough near equilibrium.

The experimental vibrational energies and rotational constants were inverted by the RKR method to generate experimental potential curves. For the perturbed v=6 level in the $b^3\Sigma^-$ state the calculated energy and

Table II. Comparison with Ab Initio Predictions		
Constant	Experiment	Theory[a]
$a^3\Pi$		
r_e(Å)	1.19000	1.194
ω_e(cm^{-1})	2625.1	2612
$b^3\Sigma^-$		
T_e(cm^{-1})	27152.7	27286
r_e(Å)	1.21625	1.221
ω_e(cm^{-1})	2438.1	2419
[a] From Ref. 5.		

Figure 3

rotational constants from the fit to the other experimental levels were used rather than the observed values.

The two curves lie almost exactly above each other, with the $a^3\Pi$ state being 0.03 Å more tightly bound. As a result the transition is highly diagonal in nature, at least for the lower lying levels. Figure 4 shows the two potential curves shifted so that their minima are both at zero energy. The relative experimental intensities are in agreement with this observation, as can be seen in Table III. For the higher vibrational levels we would expect to see other sequence bands becoming strong. Experimentally the $\Delta v=+1$ sequence is observed to gain rapidly in intensity; in addition the $\Delta v=-1$ and $\Delta v=+2$ were also observed although they were much weaker than the $\Delta v=0$ and $\Delta v=+1$ sequences. A simple Franck-Condon factor calculation did not match the experimental observations. In particular the $\Delta v=-1$ sequence was predicted to become strong for the higher vibrational levels, but experimentally this sequence was observed to be weak and die out at higher v. The tendency towards the $\Delta v=-1$ sequence, or red part of the Franck-Condon parabola, for high v arises from the slight shift of the two potentials that results in preferential overlap for this sequence for the outer lobes of the vibrational wavefunctions. The lack of intensity for this part of the Franck-Condon parabola implies that although the molecules are spending the majority of the time in the outer part of the potential they are not fluorescing while there. This observation is consistent with the theoretical transition dipole moment function of Pederson et al. (5), which, as can be seen in Fig. 4, is strongly peaked toward short internuclear distances. When the transition dipole moment function is included in the Franck-Condon factor calculation, the calculated values match the experimental observations much more closely. If the slope of the transition dipole moment

Figure 4

Table III. Approximate Relative Intensities of the Observed Bands

Band	Intensity	Band	Intensity
0-0	13.2		
1-1	2.9	1-0	0.93
2-2	1.8	2-1	0.60
3-3	0.8	3-2	0.43
4-4	0.25	4-3	0.93
5-5	0.15	5-4	1.08
6-6	0.03	6-5	0.19
7-7	0.025	7-6	0.17
		8-7	0.15

function is adjusted slightly to bring it to zero near 2 Å rather than the calculated 2.5 Å, then the match is exact considering the accuracy of the experimental intensity measurements. The strong peaking of the transition moment to shorter internuclear separations results in emission from the higher vibrational levels occurring when the molecules are near the inner wall of the molecular potential. As the $b^3\Sigma^-$ state has a slightly longer bond length than the $a^3\Pi$ state this favors the blue part of the Franck-Condon parabola and particularly the $\Delta v=+1$ sequence.

The observed vibrational levels in both the $a^3\Pi$ and $b^3\Sigma^-$ states cover a substantial fraction of the bound part of the potential, such that it should be possible to obtain reasonable estimates of the dissociation energy for both states. Recently Leroy (17) has developed a method of direct fitting of the observed vibrational intervals to many functional forms that all extrapolate correctly to dissociation. For Leroy's long range expansion technique to work, an estimate is needed of the leading long range attraction term. As both dissociation limits involve the ^2S state of hydrogen this is the C_6/r^6 term (18). The C_6 terms were estimated from the long range part of the theoretical potential curves (5) for the $a^3\Pi$ and $b^3\Sigma^-$ states. The 15 a_0 (7.9 Å) points were taken as the separated atom limits and the 5 a_0 (2.6 Å) points as representative of the long range region where the C_6/r^6 term is dominant. The values determined are listed in Table IV.

Table IV. Long Range Attraction Parameters		
State	C_6 ($Å^6 cm^{-1}$)	$X_0(6)$ (cm^{-1})
$a^3\Pi$	113000	30.76
$b^3\Sigma^-$	405000	14.05

Following the formula from Leroy (17), for the case n=6 (the leading long range term) and t=1 (next term is C_8/r^8) the vibrational energies are given by,

$$G(v) = D - X_0(6)(v_D - v)^3 \left(\frac{1 + p_2(v_D - v)^2 + p_3(v_D - v)^3 + \cdots + p_{1+L}(v_D - v)^{1+L}}{1 + q_2(v_D - v)^2 + q_3(v_D - v)^3 + \cdots + q_{1+M}(v_D - v)^{1+M}} \right)^s,$$

where D is the dissociation energy, v_D is the effective (non-integer) vibrational level at dissociation and the parameters p_i and q_i are effective fitting constants. The exponent s can be either 1 or 3. The term $X_0(6)$ is readily evaluated from C_6 (19) and is listed in Table IV for both states. The 8 observed $a^3\Pi$ and 9 observed $b^3\Sigma^-$ vibrational energy levels were initially fitted separately to Eq. (1) using different groups of parameters with s=1 or 3. The dissociation energy and v_D were allowed to vary while $X_0(6)$ was held fixed.

Once it had been determined that the two sets of energy levels could be fitted adequately they were combined together. The difference of the $a^3\Pi$ and $b^3\Sigma^-$ dissociation limits can be evaluated from the equilibrium transition energy and the separation of the boron ^2P and ^4P limits, 28867.1 cm^{-1} (13). Subtracting the transition energy gives a difference in the dissociation limits of

Table V. Satisfactory Fits to the Near Dissociation Expansion					
$a^3\Pi$		$b^3\Sigma^-$		Standard	$a^3\Pi$ Dissociation
s	L	M	L	M	Deviation (cm^{-1})	Energy (cm^{-1})
1	0	3	0	4	0.37	19768(17)[a]
1	1	2	1	3	0.43	19770(21)
1	2	1	3	1	0.28	19708(10)
3	0	3	0	4	0.22	19682(6)
3	2	1	3	1	0.15	19631(6)
[a] One standard deviation error in parentheses.					

1714.4 cm^{-1}, with the b$^3\Sigma^-$ state more deeply bound. The same set of fitting parameters p_i, q_i were used for both states, but with one extra term in the longer series for the b$^3\Sigma^-$ state. The results of the 5 fits that adequately reproduced the data are listed in Table V. The five values for D_e for the a$^3\Pi$ state were averaged together, The mean dissociation energy of the a$^3\Pi$ state was found to be 19710 cm^{-1} with a standard deviation of 50 cm^{-1}. The D_e for the b$^3\Sigma^-$ state is then 21420 cm^{-1}. The effect of varying the C_6 long range attraction term was investigated by repeating the fit that had best reproduced the data with either one or both of the C_6 terms either increased or decreased by 30%. The maximum change in dissociation energy in this series of fits was 210 cm^{-1}. The precision of the dissociation energy calculation is estimated to be 1σ=200 cm^{-1}. The experimental dissociation energies are significantly larger than the most recent theoretical calculations (5) (a$^3\Pi$ D_e=18600 cm^{-1}, b$^3\Sigma^-$ D_e=20190 cm^{-1}).

Since the a$^3\Pi$ and X$^1\Sigma^+$ states both dissociate to the same limit, the a$^3\Pi$ dissociation limit can be combined with the ground state dissociation limit (20) (X$^1\Sigma^+$ D_e=29660±170 cm^{-1}) to yield the singlet-triplet energy separation. The value obtained T_e-S_e=9950±270 cm^{-1} is significantly less than the ab initio estimates (5,21) due to the larger experimental value for the dissociation energy of the a$^3\Pi$ state.

Recently Pederson and Yarkony (6) predicted that the v=3 and higher levels of the b$^3\Sigma^-$ state should be significantly predissociated by a crossing with the repulsive (1)$^3\Sigma^+$ state that correlates to the lowest ^{2}P+^{2}S limit. As the predissociation is between a $^3\Sigma^-$ state and a $^3\Sigma^+$ state, the F$_2$ spin level is predissociated at about twice the rate of the other two spin components. This is because the F$_2$ level can couple to two of the $^3\Sigma^+$ spin components while the F$_1$ and F$_3$ levels can only couple to one. The predissociation is predicted to reduce the fluorescence intensity from the v=3, N=3 levels to 78%, 61%, and 72% of the original intensity for the F$_1$, F$_2$ and F$_3$ levels respectively. This corresponds to a drop in relative intensity for the F$_2$ component of 22% compared to the F$_1$ component. Such a change in the relative intensities of the three spin components would be readily observable in the spectrum. This is illustrated in Fig. 5, which shows the 3-3 band Q(3) lines together with calculated intensity profiles, with and without predissociation. Several other low N lines in the 3-3 and 4-4 bands were also sufficiently clear from overlapping transitions for the relative intensities of the spin components to be compared with
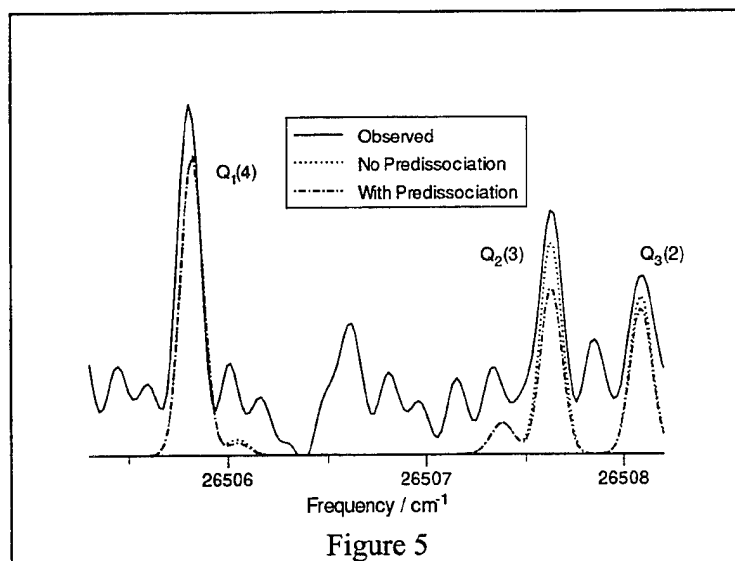
Figure 5

predictions. In no case was a significant loss of intensity for the F$_2$ spin component detected. The strongest predissociation that would be consistent with the observed fluorescence intensities is about a factor of 3 less than predicted.

This discrepancy could come from either the fluorescence or predissociation lifetime calculations. It is possible that the crossing of the $b^3\Sigma^-$ and $(1)^3\Sigma^+$ states occurs higher than the predicted position of just below v=3 in the $b^3\Sigma^-$ state. Using the more deeply bound experimental curve for $b^3\Sigma^-$ and the ab initio curve for $(1)^3\Sigma^+$ shifts the crossing by about 800 cm^{-1} to midway between v=3 and v=4. This reduces the predicted effects of predissociation in the v=3 level (22), but they are still sufficiently large that they should be observable. The effect of the predissociation would also be much less if the fluorescence lifetime was shorter than predicted. Recent experiments by Xin and Dagdigian (23) suggest that the fluorescence lifetime is only about 100 nsec for v=3 compared to the ab initio value of 236 nsec. With both of these effects, the predicted drop in intensity for the F_2 component relative to F_1 for the v=3, N=3 levels of $b^3\Sigma^-$ is reduced from 22% to 9%, which is close to the experimental detection limit.

While no signs of interaction between the $b^3\Sigma^-$ and $(1)^3\Sigma^+$ states were observed, there is clear evidence of a perturbation of the v=6 level for the $b^3\Sigma^-$ state. This level could not be fitted simultaneously with the other $b^3\Sigma^-$ levels. There was also a sharp drop off in emission intensity (see Table III) from the levels v=6 and above, presumably due to loss of population from the $b^3\Sigma^-$ state into the perturbing state. The origin of the v=6 level is shifted up by 0.25 cm^{-1} compared to its predicted position. The rotational constant is also significantly higher than would be expected (9.266 cm^{-1} compared to 9.194 cm^{-1}). The spin-rotation interaction is more than an order of magnitude larger than for the other vibrational levels. The shifts in the origin and rotational constant are consistent with an interaction with a lower lying level for which the crossing occurs below N=0. The N=0 level, observed in the 6-5 P_1(2) line could not be fitted with the other lines from the band, and had a residual deviation of 0.3 cm^{-1}. A calculation of the 6-5 band using the Dunham constants (Table I) showed that the P_1(2) line was exactly where it should be if there was no perturbation. The lack of any interaction for N=0 and the fact that the remaining lines could be fitted with an effective Hamiltonian, although with significantly different constants from the other levels, is consistent with the perturbation being due to a $^3\Pi$ level. If the perturbation of the $b^3\Sigma^-$ state is due to a $^3\Pi$ state then it is presumably the first excited $^3\Pi$ state that correlates to the same $^4P+^2S$ limit as the $b^3\Sigma^-$ state. The dominant configuration for the $a^3\Pi$ state near equilibrium is $1\sigma^2 2\sigma^2 3\sigma^1 1\pi^1$ where the 2σ orbital is primarily σ-bonding and 3σ is primarily non-bonding. The first excited $^3\Pi$ configuration is then $1\sigma^2 2\sigma^1 3\sigma^2 1\pi^1$, which is likely to be at least weakly bound.

References

1. W. Lochte-Holtgreven and E.S. van der Vleugel, Z. Phys. **70**, 188-203 (1931).
2. G.M. Almy and R.B. Horsfall, Jr., Phys. Rev. **51**, 491-500 (1937).
3. D.J. Benard, E. Boehmer, H.H. Michels and J.A. Montgomery, Jr., J. Phys. Chem. **98**, 8952-8958 (1994).
4. E. Boehmer and D.J. Benard, J. Phys. Chem. **99**, 1969-1973 (1995).
5. L.A. Pederson, H. Hettema and D.R. Yarkony, J. Phys. Chem. **98**, 11069-11074 (1994).
6. L.A. Pederson and D.R. Yarkony, Mol. Phys. **84**, 611-618 (1995).
7. C.R. Brazier and P.G. Carrick, J. Chem. Phys. **96**, 8684-8690 (1992).
8. C.R. Brazier and P.G. Carrick, J. Chem. Phys. **100**, 7928-7937 (1994).

9.   M.E. DeRose, P.G. Carrick and C.R. Brazier, J. Mol. Spectrosc. in press.

10.   P.G. Carrick, USAF Technical Report No. PL-TR-93-3014, 1993.

11.   P.C. Engelking, Rev. Sci. Instrum. **57**, 2274-2277 (1986).

12.   W.C. Martin, Phys. Rev. A **36**, 3575-3589 (1987).

13.   NIST Database for Atomic Spectroscopy, ver. 1, National Institute of Standards and Technology, Gaithersberg, MD, 1995.

14.   B.A. Palmer and R. Engleman, Jr., Los Alamos National Laboratory Technical Report No. LA-9615, 1983 (unpublished).

15.   J.M. Brown, I. Kopp, C. Malmberg and B. Rydh, Physica Scripta, **17**, 55-67 (1978).

16.   C.R. Brazier, R.S. Ram and P.F. Bernath, J. Mol. Spectrosc. **120**, 381-402 (1986).

17.   R.J. LeRoy, J. Chem. Phys. **101**, 10217-10228 (1994).

18.   R.J. LeRoy, in "Molecular Spectroscopy," edited by R.F. Barrow, D.A. Long and D.J. Millen (Specialist Periodical Report of the Chemical Society, London, 1973), Vol. 1, p113-176.

19.   R.J. LeRoy and W.-H. Lam, Chem. Phys. Lett. **71**, 544-548 (1980).

20.   C.W. Bauschlicher, Jr., S.R. Langhoff and P.R. Taylor, J. Chem. Phys. **93**, 502-506 (1990).

21.   J. A. Pople and P.v.R. Schleyer, Chem. Phys. Lett. **129**, 279-281 (1986).

22.   L. A. Pederson, personal communication.

23.   Y. Xin, personal communication.

Synthetic Efforts to High Nitrogen-Oxygen Compounds

Mark A. Petrie

Hughes STX, Phillips Laboratory, Edwards AFB, CA

This research concerns the synthesis and characterization of energetic high nitrogen-oxygen liquid oxidizers for use in the Non-Toxic Storable Propellants and HEDM programs. The Non-Toxic Storable program seeks to identify liquid (primarily) and solid oxidants and fuels to replace conventional propellants. These propellants must be non-toxic, non-halogenated, and give greater performance than RP-1 (kerosene), NH_4ClO_4 (AP), and N_2O_4 (NTO). The HEDM Synthetic effort seeks to synthesize very energetic molecules for use as energetic dopants in solid cryogenic matrices of hydrogen or oxygen.

From the more applied perspective, several liquid oxidant candidates were suggested for the Non-Toxic Storable program. These oxidants are based on the known dinitramide, $^-N(NO_2)_2$ and trinitromethanide, $^-C(NO_2)_3$ anions. Various non-aqueous synthetic routes to low-melting ammonium, $HONH_3^+$ and RNH_3^+ salts of these anions are currently being investigated in this laboratory.

Initial basic research in this area included failed attempts to prepare the oxydinitramide, $^-ON(NO_2)_2$ anion. The reaction of Angeli's salt $[M^+]_2[ON=NO_2]$ (M = Cs^+, Na^+) with nitronium, NO_2BF_4 and nitrosonium, $NOBF_4$ salts in acetonitrile produced gases and an intermediate blue-colored solution. In both reactions the sole observed gaseous product was nitrogen oxide (NO) by IR and RGA. Analysis of the solid products was by Raman and IR spectroscopy. The $^+NO_2$ reaction yielded one equivalent of nitrate, $^-NO_3$. Reaction of $^+NO_2$ and $^{-2}ON=NO_2$ may initially form oxydinitramide which then decomposes to $^-NO_2$ and transient blue "$ON-NO_2$" (N_2O_3).

Oxidation of $^-NO_2$ by $ON-NO_2$ to nitrate, $^-NO_3$ would yield two equivalents of nitrogen oxide gas. Reaction involving ^+NO and $^{-2}ON=NO_2$ gave nitrate, $^-NO_3$ with a minor amount of nitrite, $^-NO_2$. In this case, the mixture of products is evidence for a more complex mechanism.

Work in progress towards other unknown energetic anions was described. Nucleophilic substitution reactions at nitrogen of the chlorourethanes, $EtOC(O)NCl_2$, $EtOC(O)N(H)Cl$, and $EtOC(O)N(Na)Cl$ and nitrochlorourethane $EtOC(O)N(NO_2)Cl$ may lead to the novel diazidamides and nitroazidamides. Other areas of current research involve new energetic and oxidizing cations and borate or aluminate oxidizer salts.

Simulations of Quantum Many-Body Systems by Classical Dynamics

Z. Li, M. Sterling, and V. A. Apkarian
Department of Chemistry
University of California
Irvine, CA 92717

Classical molecular dynamics simulations of quantum crystals, using a simple pseudo-potential, are reported. The method is implemented for calculating both equilibrium and dynamical properties. As a test, the radial distribution functions for neat solid H_2 and Li doped solid H_2 are computed, and found to be in excellent agreement with prior results obtained by the variational Einstein model [D. Li and G. A. Voth, J. Chem. Phys. 96, 5340 (1992)]. The method also yields a realistic phonon density of states, which is obtained by normal mode analysis. As an implementation in dynamics, the rotational motions of O_2 isolated in solid D_2 is investigated. In agreement with recent experiments, it is found that O_2 does not rotate in solid D_2. Applications of this method to O doped D_2 crystal and $O/H_2/He$ clusters are also presented.

INTRODUCTION

The most common approach for simulating quantum many-body systems involves the path integral formulation of quantum statistical mechanics.[1] There is a vast literature on realizations of this principle in treatments of quantum hosts: solids, fluids, and clusters, which we do not cite here. We note, though, that these methods are inherently equilibrium calculations. We have tested the utility of a conceptually simple dynamical approach, namely, classical dynamics simulations in which the single particles are represented by spatial Gaussian distributions. To test the method, we carry out simulations of solid para-hydrogen, both neat, and doped with Li. The latter system has recently been scrutinized by path integral Monte Carlo (PIMC) and a variational quantum Einstein model, with which we compare our results.[2,3] Having tested the reliability of the approach in obtaining equilibrium properties, we implement it in dynamical calculations, specifically considering the rotational dynamics of O_2 isolated in solid D_2, a system which was recently scrutinized by experiments.[4]

The method consists of classically propagating the time evolution of the centers of the Gaussians subject to the assumption of pairwise additivity of forces. The equations of motion for the centers obey Ehrenfest's theorem:

$$m\frac{d^2}{dt^2}\bar{r}_i \equiv m\frac{d^2}{dt^2}\langle r_i \rangle = \sum_{j \neq i}\langle -\nabla V(r_i - r_j) \rangle \tag{1}$$

For isotropic pair potentials, functions of internuclear separation $R = |r_i - r_j|$ alone, the average force implied in eq. 1 can be obtained for a pair of Gaussian particles by the convolution integral:

$$\left\langle -\nabla V_{ij}(\overline{R}) \right\rangle \equiv \left\langle -\nabla V(|\overline{r}_i - \overline{r}_j|) \right\rangle = -\int_{-\infty}^{\infty} dr_i \int_{-\infty}^{\infty} dr_j G(r_i - \overline{r}_i) G(r_j - \overline{r}_j) \frac{\partial V(r_i - r_j)}{\partial (r_i - r_j)}$$ (2a)

$$= -\int_{-\infty}^{\infty} dR G_{ij}(R - \overline{R}) \frac{\partial V_{ij}(R)}{\partial R}$$

$$\text{where,} \quad G_{ij}(R - \overline{R}) = \frac{1}{2\sigma\sqrt{\pi}} \exp\left[-\frac{(R - \overline{R})^2}{4\sigma^2} \right]$$ (2b)

While the definition of the average force is sufficient for numerical integration of Newton's equations of motion, it is generally more appealing to define a pseudo-potential, $\tilde{V}_{ij}$, from which the pseudo-force can be obtained. This can be done by taking advantage of the local nature of the Gaussian function, and properties of the convolution integral:

$$\left\langle -\nabla V_{ij}(\overline{R}) \right\rangle = -\frac{\partial}{\partial \overline{R}} \int_{-\infty}^{\infty} dR V_{ij}(R) G_{ij}(R - \overline{R}) = -\frac{\partial}{\partial \overline{R}} \left\langle V_{ij}(\overline{R}) \right\rangle \equiv -\frac{\partial \tilde{V}_{ij}(\overline{R})}{\partial \overline{R}}$$ (3)

In practice $\tilde{V}_{ij}(\overline{R})$ is constructed by convolution of the pair potential, $V_{ij}(R)$, with a $G_{ij}(R)$ which represents the self-consistent pair probability distribution in the extended solid. Noting that at zero K the pseudo-potential represents the sum of potential and zero-point kinetic energy terms, then the self-consistency criterion for the choice of the Gaussian width is that minimization of the lattice sum of the pseudo-potential yield the proper experimental lattice constant at T=0.

$$\frac{d\tilde{U}_{tot}}{dR} = \frac{d}{dR} \frac{1}{2} \sum_{ij} \tilde{V}(\overline{R}_{ij}) = 0$$ (4)

For $\tilde{V}_{ij}(\overline{R})$ given as a function of powers of internuclear separation, the lattice sum can be evaluated and minimized analytically. Given $\tilde{V}_{ij}$, classical molecular dynamics simulations can be carried out according to well established prescriptions.[5] It is however important to note that the simulations are for the centers of the single particle distributions. While most observables can be computed directly, in the case of distributions, the output of the simulation has to be convoluted by the Gaussian once again. Thus, in the case of the radial distribution function, the simulation yields $g(\overline{R})$, and the proper distribution function, $g(R)$, is obtained as:

$$g(R) = \int_{-\infty}^{\infty} dR G(R - \overline{R}) g(\overline{R})$$ (5)

APPLICATION

1. Solid H₂:

For simulations of solid H_2, we use the Silvera-Goldman pair potential as $V_{ij}(R)$.[6] Note, this is an effective pair potential, implicitly incorporating many-body contributions. A Gaussian of width $\sigma = 0.30$ Å in eq. 2b reproduces the lattice constant of solid H_2 (a=3.79 Å), which is nearly constant between T= 0 and 4 K (at T=4.2 K, P = 0, V=23.16 cc/mole).[7] The pair potential, the pseudo-potential, and the Gaussian used are illustrated in figure 1. In the bound region, to within 0.1K, $\tilde{V}_{ij}(\overline{R})$ can be fitted to the functional form (energies in eV and distances in Å):

$$\tilde{V}_{H_2-H_2}(\overline{R}) = -\frac{25369}{\overline{R}^{12}} + \frac{9128.1}{\overline{R}^{10}} - \frac{600.62}{\overline{R}^8} + \frac{1.0585}{\overline{R}^6} \tag{6}$$

which is a convenient form to be used in the numerical simulations (also illustrated in fig. 1). Classical molecular dynamics simulations were carried in the micro-canonical ensemble. A total of 640 p-H_2 molecules arranged on an hcp lattice were included in the simulation box, periodic boundary conditions, and the Verlet algorithm were implemented.[5] The H_2-H_2 radial distribution function, constructed according to eq. 5, is shown in figure 2. Comparison of the radial distribution function with those of Li and Voth shows that the present result is indistinguishable from their converged variational Einstein model,[3] however, both are more structured than the fully converged PIMC simulations. The latter can be regarded as nearly exact.[2,3] Quite clearly, by freezing the zero-point energy in the pseudo-potential the inter-particle correlations are not well reproduced. It is interesting to note that if we do away with the criterion for the choice of the Gaussian width, then the PIMC results can be emulated. If we choose a Guassian width nearly half that obtained by the energy minimization of eq. 4, effectively unfreezing part of the zero-point energy, it is possible to approach the PIMC results. This is illustrated in figure 2 for a Gaussian width of 0.13 Å. However, given the arbitrary nature of this adjustment, we do not further pursue the procedure. The phonon density of states for this system is determined by normal mode analysis, by diagonalizing the force matrix. The results are shown in figure 3. The density of states qualitatively agrees with that of solid H_2.[7,8] However, the computed frequencies are ~10% higher, the implication is that the pseudo-potential created based on the spatial Gaussian distribution yields too stiff a lattice.

2. Li doped H₂:

In the case of solid H_2 doped with a Li impurity atom, a self-consistency criterion does not exist for the choice of a Gaussian to generate the Li-H_2 pseudo-potential. Given the fact that the Li-H_2 pair potential is extremely shallow, we do not expect localization of the H_2 function near the impurity. Moreover, since the solid is expected to anneal around the impurity for low doping densities, we expect that H_2 molecules nearest neighbor to Li will be well represented by their bulk single particle

distributions. Accordingly, we construct the Li-H_2 pseudo-potential using the same pair potential given in reference 3, and the Gaussian determined above for the neat solid.

The classical simulations in this case are carried out by placing the Li atom in a five-fold substitutional site, which is one of the various trapping sites simulated in ref. 3. The computed Li-H_2 pair distribution function is shown in figure 4. As in the case of neat H_2, the present result is indistinguishable from the converged variational Einstein Model, and more structured than the converged PIMC results.[2a]

3. Rotational dynamics of O_2 isolated in solid D_2:

In recent experiments the spectroscopy of O_2 isolated in solid D_2 was investigated.[4] Based on a detailed analysis of the spectra, including polarized laser induced fluorescence measurements, it was established that O_2 molecules isolated in fcc sites of the solid do not rotate. In principle such an issue can be trivially resolved by simulations in classical solids. However, in the case of quantum crystals, strictly classical simulations completely fail. We illustrate in figure 5, the results of simulations by the pseudo-potential approach, where the time evolution of the projection of the molecular axis, $\cos\theta = \hat{R}(t)\cdot\hat{R}(0)$, is shown. When the pseudo-potential approach is used, the lattice is stable, and the molecular rotation is completely frozen as illustrated in figure 5, in agreement with the experiment.

In these simulations the O-D_2 potential was assumed to be that of O-Ne, which has been obtained from scattering data[9]. The pseudo-potentials were generated as in the case of Li/H_2, by using the self-consistent Gaussian width reproduces the lattice constant for neat other-D_2 solid.

4. Other applications:

We also show the results of studies of the structural properties of O doped D_2 crystal and mixed O/H_2/He cluster using the method presented.

CONCLUSIONS

We have described an approach for molecular dynamics simulations of quantum crystals, which despite its simplicity, seems to produce quite realistic results. The method, relies on the assumption of a Gaussian spatial probability distribution for single particles, based on which a pseudo-potential is generated without any adjustable parameters. Strictly classical dynamics is then simulated using these pseudo-potentials, which represents a standard computational task. The radial distribution functions calculated via strictly classical simulations on these pseudo-potentials then yield radial distribution functions that are identical to the variational Einstein model results of Li and Voth,[3] and a realistic phonon spectrum. However, in contrast with Monte Carlo methods, the approach can be implemented in dynamical applications. The latter was demonstrated in calculations of rotational dynamics of O_2 in solid D_2.

In its present formulation, the method described only produces a qualitative picture. The radial distribution functions for example do not match exactly with those of the converged path integral Monte Carlo calculations. This disagreement is clearly due to the complete freezing of zero-point kinetic energy in the pseudo-potential. This suggests obvious possible refinements, in particular, the use of Gaussian wavepackets in the simulations could be expected to produce improved results with little increase in computational effort.[10] Such an implementation is being presently pursued by us.

REFERENCES

1. R. P. Feynman and A. R. Hibbs, Quantum mechanics and path integrals (McGraw-Hill, New York, 1965).
2. a) D. Scharf, G. J. Martyna, D. Li, G. A. Voth, and M. Klein, J. Chem. Phys. 99, 9013 (1993);
   b) D. Scharf, G. J. Martyna, and M. Klein, J. Chem. Phys. 99, 8997, (1993);
3. D. Li and G. A. Voth, J. Chem. Phys. 96, 5340 (1992).
4. A. Danilychev, V. E. Bondybey, V. A. Apkarian, S. Tanaka, H. Kajihara, S. Koda, J. Chem. Phys. (submitted, 1995).
5. M. P. Allen and D. J. Tildesley, Computer Simulations of Liquids, (Clarendon, Oxford, 1987).
6. I. F. Silvera and V. V. Goldman, J. Chem. Phys. 69, 4209 (1978).
7. I. F. Silvera, Rev. Mod. Phys. 52, 393 (1980).
8. V. V. Goldman, J. Low Temp. Phys. 36, 521(1979).
9. V. Aquilanti, R. Candori, and F. Pirani, J. Chem. Phys. 89, 6157 (1988).

10. E. Heller, J. Chem. Phys. 62, 1544(1975); 75, 2923 (1981).

Figure Captions:

Fig. 1: The Silvera-Goldman pair potential for H_2 is shown (thick line) along with the pseudo-potential (thin line) generated by convolution of the Gaussian. The hatch marks are for the analytic fit to the pseudo-potential, eq. 6 of text, which reproduces the numerical potential to within 0.1 K throughout the range of interest.

Fig. 2: Radial distribution function for solid H_2. Solid line is for the self consistent Gaussian width of 0.30 Å, using the pseudo-potential defined in eq. 6. The dashed line corresponds to a Gaussian width of 0.13 Å.

Fig. 3: Li-H_2 radial distribution function with Li occupying a five-fold substitutional site in hcp H_2.

Fig. 4: Normal mode distribution of solid H_2 using the psudo potential of eq. 6 in text.

Fig. 5: Rotational dynamics of O_2 isolated in solid D_2. The time evolution of the O_2 axis is shown as a function of time, using psuedo potentials.
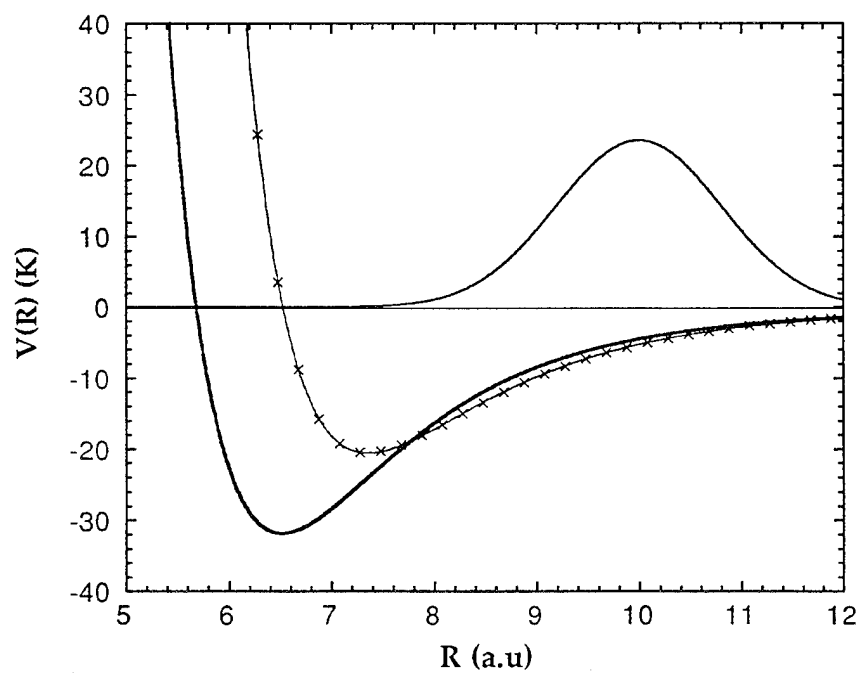
Fig. 1
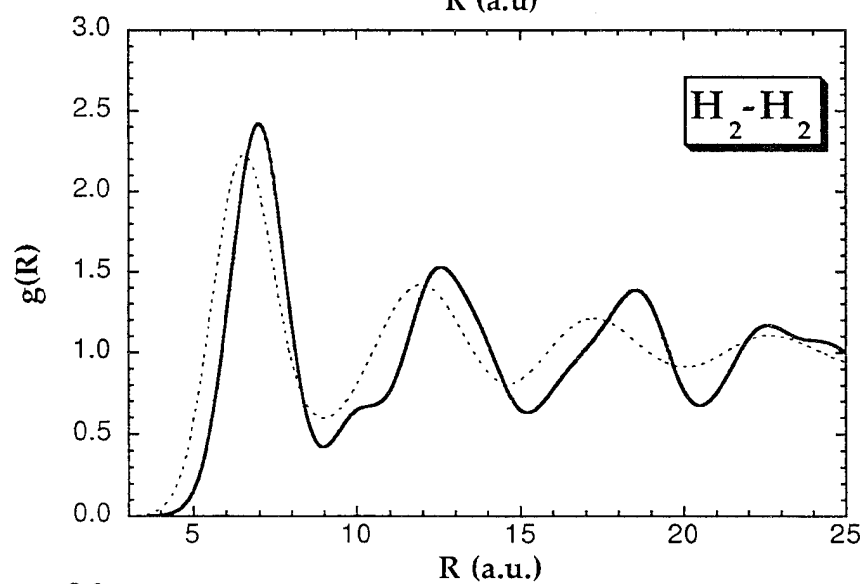
Fig. 2
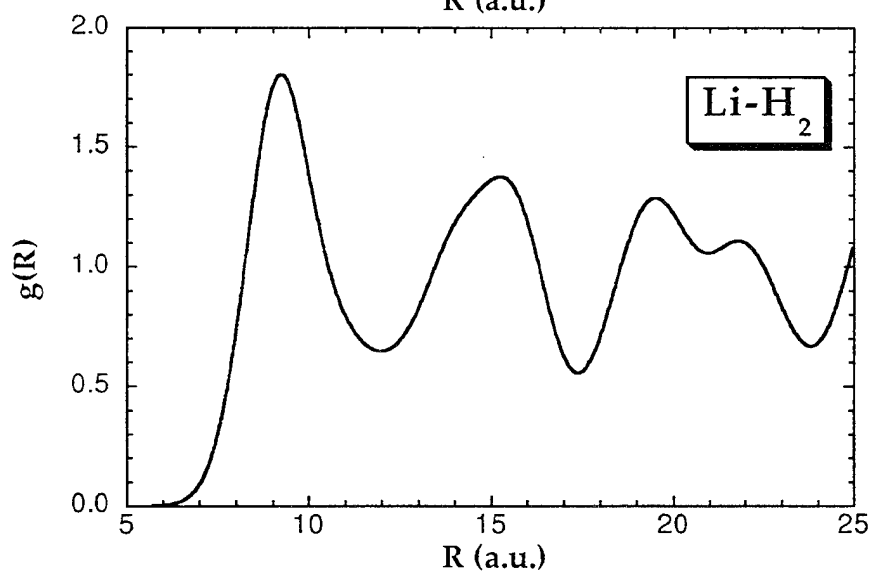
Fig. 3
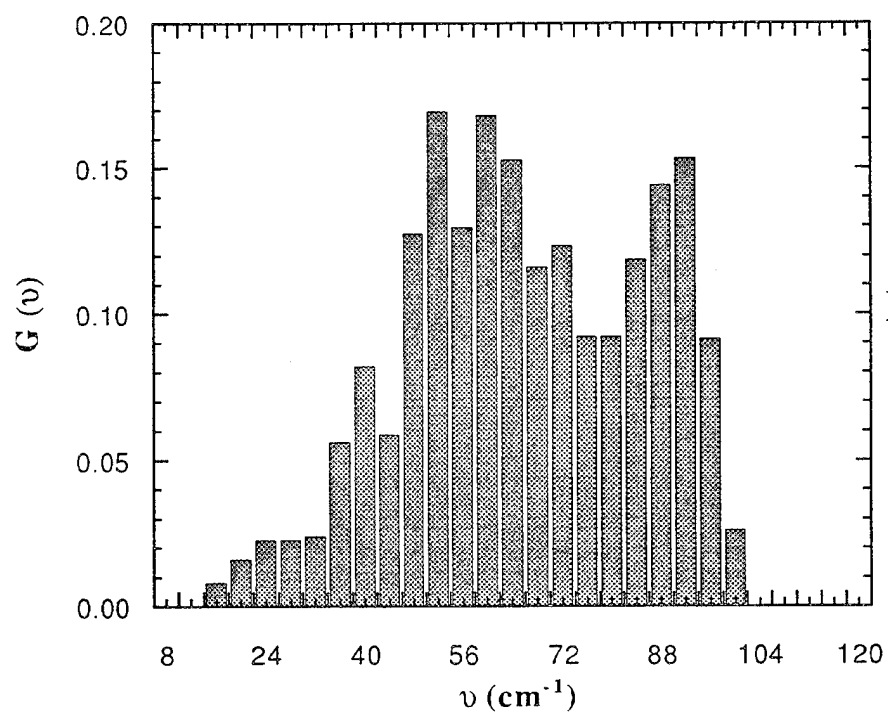
Fig. 4
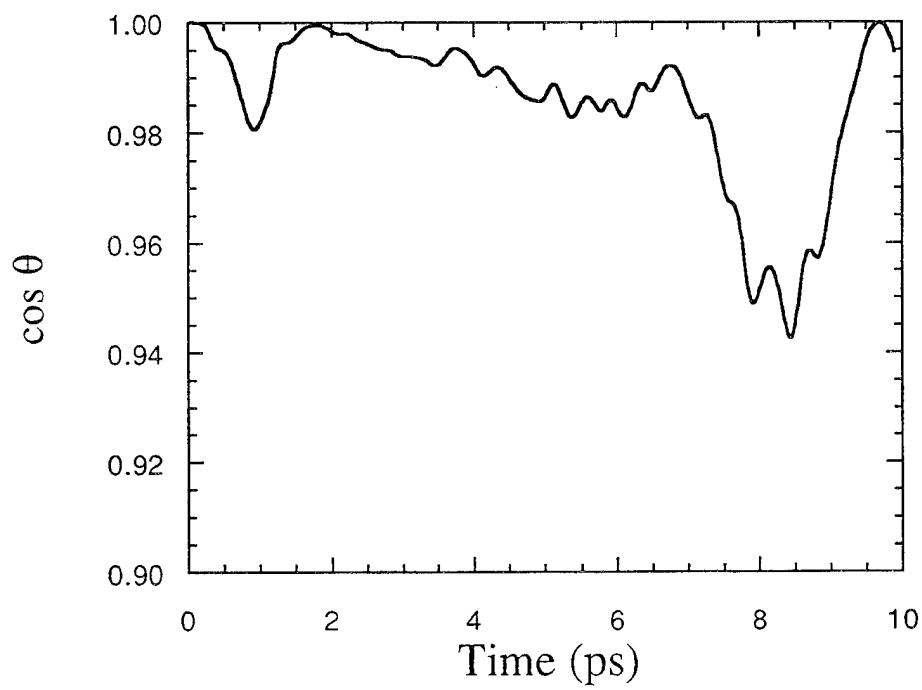
Fig. 5

Spectroscopy of Lithium Boride, A Candidate HEDM Species

Jeffrey A. Sheehy

Hughes STX Corporation

USAF Phillips Laboratory
10 East Saturn Boulevard
Edwards AFB, CA 93524-7680

E-mail: sheehy@helium.ple.af.mil

Introduction

The notion of enhancing the performance characteristics of rockets by employing a frozen fuel or oxidizer that is seeded with particular atoms or small molecules has developed into a major component of the high energy density matter (HEDM) program [1]; it is viewed as a far-term yet potentially feasible means of achieving revolutionary increases in rocket performance. Calculations suggest that certain atomic or molecular additives to solid hydrogen, for example, hold the potential to substantially increase the specific impulse of a solid hydrogen/liquid oxygen hybrid rocket motor [2]. It has been suggested that diatomic molecules might be preferred over atoms because of their assumed lower mobilities in a solid matrix, as well as their smaller propensities for forming aggregates upon encountering like species. A desirable small molecule for these purposes would have a low molecular weight (comprised of first- or second-row atoms), a relatively small dissociation energy, minimal propensities for diffusion and recombination within the matrix, and favorable energetics associated with any products formed from its combustion.

Specific impulse calculations indicate that lithium boride (LiB) would be a particularly useful molecule in this context; five mole percent LiB in solid hydrogen would increase the specific impulse of a hydrogen/oxygen motor from 389 to 496 sec [2]. Little is known about the compound, however, as it has not yet been observed in the laboratory, and it has been the subject of only limited theoretical examination. The aim of the present study is to provide detailed spectroscopic calculations that will aid in the experimental detection and characterization of LiB.

Whereas early self-consistent-field (SCF) calculations on LiB [3-4] assumed a $^1\Sigma^+$ ground state ($1\sigma^2\ 2\sigma^2\ 3\sigma^2\ 4\sigma^2$), more recent results including various electron correlation treatments [5-8] have determined that the ground state is $^3\Pi$, having a predominant $1\sigma^2\ 2\sigma^2\ 3\sigma^2\ 4\sigma\ 1\pi$ electron configuration. Calculations employing fourth-order Møller-Plesset perturbation theory and quadratic single- and double-excitation configuration interaction in 6-311+G* basis sets [8] yield a dissociation energy of 1.18 eV and an equilibrium bond distance of 4.03 a_0, with the $X\,^3\Pi$ state lower in energy that the $(1)^1\Sigma^+$ state by about 6.9 kcal/mol. In the present work, all electronic states dissociating to the first four separated-atom limits are calculated. In addition to the potential-energy curves for these states, spectroscopic constants, transition-moment functions, absorption and emission intensities, and radiative lifetimes are determined.

Present Calculations

The examination of LiB spectroscopy is performed using correlation-consistent valence quadruple-zeta one-particle basis sets [9] supplemented with two additional diffuse s, p, and d functions to yield final basis sets of the form $(14s\ 8p\ 5d\ 2f\ 1g)/[7s\ 6p\ 5d\ 2f\ 1g]$. Several choices of active space for the state-averaged complete-active-space SCF calculations [10] are explored, with the final results distributing the four valence electrons over a (6330) set of active orbitals; the calculations are performed in C_{2v} symmetry. All reference configurations from the wave functions so obtained are used in the ensuing internally contracted multireference configuration-interaction calculations [11]. The electronic structure computations are performed using the MOLPRO-94 program system [12] on IBM RS/6000 work stations.

Electronic states dissociating to the Li ^2S and B ^2P (ground state atoms), Li $(2p)\ ^2P$ + B ^2P, Li $(3s)\ ^2S$ + B ^2P, and Li $(2s)\ ^2S$ + B $(2s2p^2)\ ^4P$ separated-atom limits are examined, encompassing the following states: four $^1\Sigma^+$, four $^3\Sigma^+$, four $^1\Pi$, five $^3\Pi$, one $^5\Pi$, one $^1\Delta$, one $^3\Delta$, one $^1\Sigma^-$, two $^3\Sigma^-$, and one $^5\Sigma^-$. The vibrational spectrum is extracted by solving the radial Schrödinger equation; ω_e and $\omega_e x_e$ are obtained by fitting the computed vibrational levels as a function of $v + \frac{1}{2}$ in a polynomial expansion. Calculated Franck-Condon factors are used along

with the transition moments to obtain absorption and emission intensities for transitions of particular spectroscopic interest; radiative lifetimes of the excited state are also determined.

Results

Potential-energy curves for the singlet, triplet, and quintet manifolds of states are shown in Figs. 1-3, respectively; the minimum of the (ground) $X^3\Pi$ potential function is taken as the zero of energy in each case. Spectroscopic constants derived from the calculated potentials are listed in Tables 1-3. The present calculations are in good accord with recent results [8] for the two lowest triplet and singlet states; there are no previous calculations of the higher states. In addition to the ground state, other states exhibiting significant binding include the $(1)^1\Sigma^+$, $(2)^1\Sigma^+$, $(3)^1\Sigma^+$, $(4)^1\Sigma^+$, $(2)^1\Pi$, $(1)^1\Sigma^+$, $(1)^1\Delta$, $(4)^3\Sigma^+$, $(2)^3\Pi$, $(3)^1\Pi$, and $(1)^3\Sigma^-$ states. Radiative lifetimes of these states are listed in Tables 4 and 5.

The data indicate that although the ground state is a triplet, the singlet manifold provides several states with significant binding (Fig. 1 and Table 1), suggesting that a good opportunity for detecting electronic transitions in excited LiB molecules lies in the singlet band, notwithstanding the experimental obstacles. In the triplet manifold (Fig. 2), unfavorable Franck-Condon factors or weak binding in the various states (Table 2) indicate that spectroscopic detection in absorption or emission might be difficult. The $(1)^3\Sigma^-$ state, although strongly bound with a short equilibrium bond length due to its ion-pair character, has a relatively small transition energy with the $X^3\Pi$ state (Table 2), rendering the transition between these states unsuitable for observation in many experimental implementations.

Summary

Twenty-four electronic states of LiB have been calculated at a high level of *ab initio* theory; results for the lowest few states agree with previous calculations, whereas all other states are previously unknown. Calculated spectroscopic constants, transition moments, and radiative lifetimes, along with intensities in absorption and emission, are expected to aid in experimental efforts to identify and characterize the molecule by examining electronic transitions in absorption

or emission. Theoretical studies of cryogenic propellant performance indicate that even a few mole-percent LiB stabilized in solid hydrogen would be an extremely attractive HEDM fuel.

References

[1] See, for example, *Proceedings of the High Energy Density Matter (HEDM) Contractors Conference*, ed. by T.L. Thompson, June 1994, Crystal Bay, NV, USAF Report PL-TR-94-3036.

[2] P. G. Carrick, *Theoretical Performance of High Energy Density Cryogenic Solid Rocket Propellants*, 31st Joint Propulsion Conference, July 1995, San Diego, CA, AIAA 95-2893.

[3] J. J. Kaufman and L. M. Sachs, J. Chem. Phys. 52 (1970) 645.

[4] P. E. Cade and W. M. Huo, At. Data Nucl. Data Tables 15 (1975) 1.

[5] A. V. Nemukhin, J. Almlöf, and A. Heiberg, Chem. Phys. Lett. 76 (1980) 601.

[6] Z. H. Zhu and J. N. Murrell, Chem. Phys. Lett. 88 (1982) 262.

[7] D. B. Knowles and J. N. Murrell, J. Mol. Struct. 135 (1986) 169.

[8] A. I. Boldyrev, J. Simons, and P. v. R. Schleyer, J. Chem. Phys. 99 (1993) 8793.

[9] T. H. Dunning, Jr., J. Chem. Phys. 90 (1989) 1007.

[10] H.-J. Werner and P. J. Knowles, J. Chem. Phys. 82 (1985) 5053; P. J. Knowles and H.-J. Werner, Chem. Phys. Lett. 115 (1985) 259.

[11] H.-J. Werner and P. J. Knowles, J. Chem. Phys. 89 (1988) 5803; P. J. Knowles and H.-J. Werner, Chem. Phys. Lett. 145 (1988) 514.

[12] MOLPRO is a package of *ab initio* programs written by H.-J. Werner and P. J. Knowles, with contributions from J. Almlöf, R. D. Amos, M. J. O. Deegan, S. T. Elbert, C. Hampel, W. Meyer, K. Peterson, R. Pitzer, A. J. Stone, and P. R. Taylor.

Table 1. Spectroscopic Constants for Singlet States.

State	$R_e\,(a_0)$	$\omega_e\,(\text{cm}^{-1})$	$\omega_e x_e\,(\text{cm}^{-1})$	$T_e\,(\text{cm}^{-1})$
$(1)^1\Sigma^+$	4.52	415	4.45	1749
$(2)^1\Sigma^+$	4.02	488	18.7	13497
$(3)^1\Sigma^+$	4.32	508	5.95	16266
$(4)^1\Sigma^+$	4.73	348	3.22	28297
$(1)^1\Pi$	4.17	454	9.93	6116
$(2)^1\Pi$	4.77	324	0.442	16199
$(3)^1\Pi\,^a$	-----	-----	-----	-----
$(4)^1\Pi\,^b$	4.74	-----	-----	34059
$(1)^1\Delta$	3.77	601	7.58	8822
$(1)^1\Sigma^-\,^a$	-----	-----	-----	-----

Table 2. Spectroscopic Constants for Triplet States.

State	$R_e\,(a_0)$	$\omega_e\,(\text{cm}^{-1})$	$\omega_e x_e\,(\text{cm}^{-1})$	$T_e\,(\text{cm}^{-1})$
$(1)^3\Sigma^+\,^a$	-----	-----	-----	-----
$(2)^3\Sigma^+\,^a$	-----	-----	-----	-----
$(3)^3\Sigma^+\,^b$	4.81	-----	-----	27643
$(4)^3\Sigma^+$	4.98	189	-3.23	32187
$X^3\Pi$	4.17	534	4.97	$1.20^{\,c}$
$(2)^3\Pi$	5.07	222	-1.96	15857
$(3)^3\Pi$	5.22	216	7.78	23184
$(4)^3\Pi\,^a$	-----	-----	-----	-----
$(1)^3\Delta\,^a$	-----	-----	-----	-----
$(1)^3\Sigma^-$	3.73	611	5.52	3780
$(2)^3\Sigma^-$	6.84	198	5.82	27252

[a] State is repulsive.

[b] Binding in this state is extremely weak.

[c] Dissociation energy in eV.

Table 3. Spectroscopic Constants for Quintet States.

State	$R_e\,(a_0)$	$\omega_e\,(\text{cm}^{-1})$	$\omega_e x_e\,(\text{cm}^{-1})$	$T_e\,(\text{cm}^{-1})$
$(1)^5\Pi\ ^a$	-----	-----	-----	-----
$(1)^5\Sigma^-$	3.95	537	4.67	24086

^{a} State is repulsive.

Table 4. Singlet State Radiative Lifetimes
(units of nanoseconds unless otherwise specified).

v'	$(1)^1\Pi\ (\mu s)$	$(1)^1\Delta\ (\mu s)$	$(2)^1\Sigma^+$	$(2)^1\Pi$	$(3)^1\Sigma^+$	$(4)^1\Sigma^+$
0	37.2	1530	367	84.7	20.8	27.0
1	31.0	580	195	88.5	23.0	28.7
2	28.0	303	128	98.5	19.6	27.0
3	27.1	180	95.9	70.1	24.7	24.2
4	27.9	115	89.0	68.2	22.8	26.0
5	30.4	77.1	103	83.5	25.2	27.9

Table 5. Triplet State Radiative Lifetimes.

v'	$(1)^3\Sigma^-\ (\mu s)$	$(2)^3\Pi\ (ns)$	$(3)^3\Pi\ (ns)$	$(4)^3\Sigma^+\ (ns)$
0	413	74.5	40.1	118
1	216	74.3	42.1	86.5
2	136	74.1	44.6	72.3
3	93.4	73.8	47.5	64.8
4	67.6	73.5	51.2	60.8
5	50.7	73.1	55.8	59.0

Figure 1. LiB Singlet Potential-Energy Curves
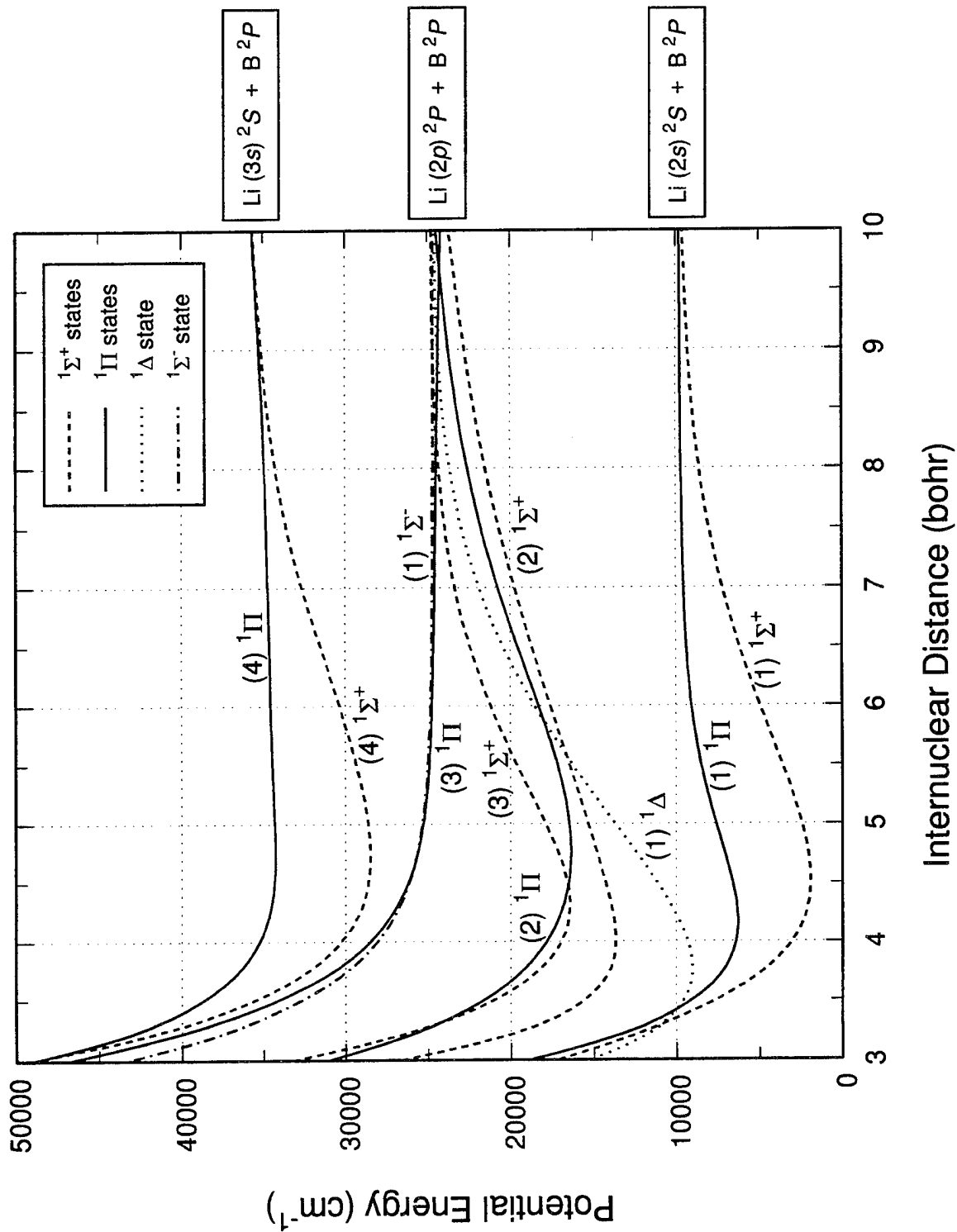
Figure 2. LiB Triplet Potential-Energy Curves

Li ^2S + B $(2s\,2p^2)$ ^4P

Li $(3s)$ ^2S + B ^2P

Li $(2p)$ ^2P + B ^2P

Li $(2s)$ ^2S + B ^2P

Legend:
- $^3\Sigma^+$ states
- $^3\Pi$ states
- $^3\Delta$ state
- $^3\Sigma^-$ states

(4) $^3\Sigma^+$
(2) $^3\Sigma^-$
(3) $^3\Sigma^+$
(4) $^3\Pi$
(2) $^3\Sigma^+$
(1) $^3\Delta$
(3) $^3\Pi$
(2) $^3\Pi$
(1) $^3\Sigma^-$
(1) $^3\Sigma^+$
X $^3\Pi$

Potential Energy (cm^{-1})

50000
40000
30000
20000
10000
0

Internuclear Distance (bohr)

3   4   5   6   7   8   9   10

282
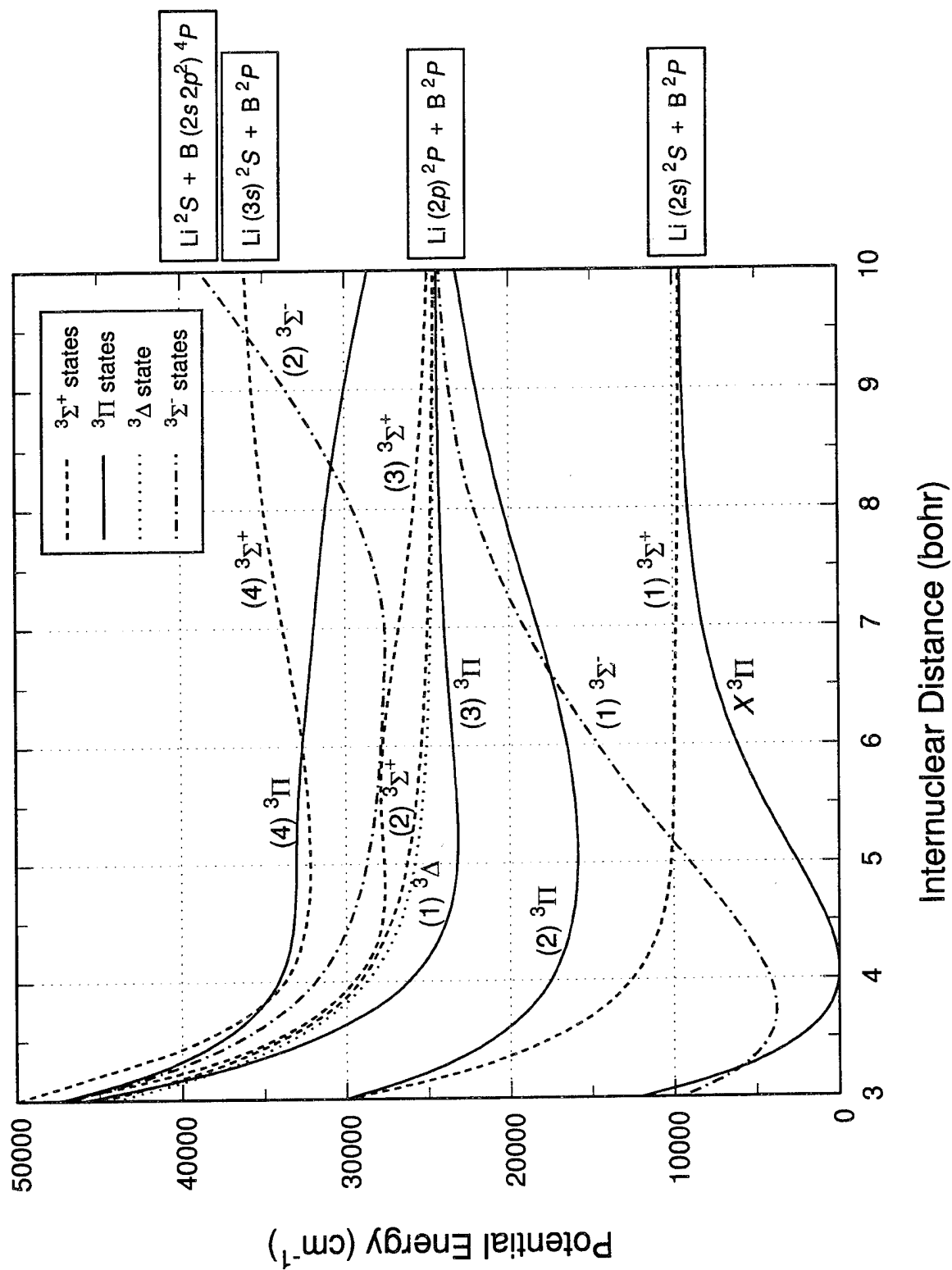
Figure 3. LiB Quintet Potential-Energy Curves
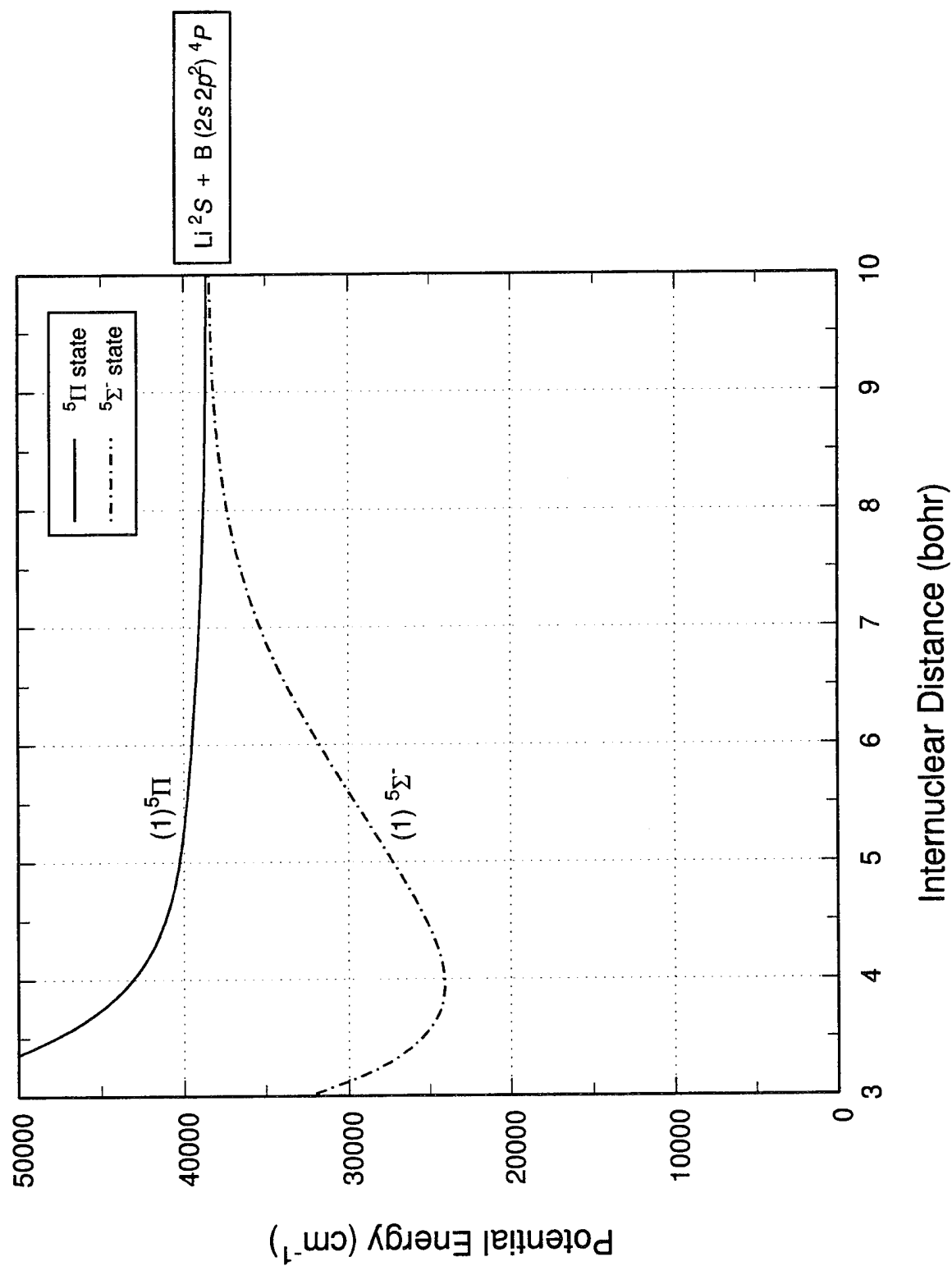
A DFT Study of the B-H_2 Potential Energy Surfaces

Leslie S. Perkins[†] and J.A. Boatz
Propulsion Directorate/RKS, Phillips Laboratory
Edwards Air Force Base, California 93524-7680

Abstract

We have used density functional theory with gradient-corrected electron exchange and correlation functionals to map the ground state interactions between B and H_2. The B-H_2 interactions have been calculated for a variety of H-H distances and B-H_2 distances. Comparisons are made to available *ab initio* data.

Introduction

A long term goal in the understanding of cryogenic HEDM is to construct a general simulation method using molecular dynamics and/or Monte Carlo, that would allow the doping of any type of atom in solid H_2. This method would be computationally efficient for solids and still incorporate the quantum effects associated with hydrogen. Unfortunately, the obstacle to construct such a general simulation method is a quick and efficient way of generating the interactions between atoms for each step of the calculation. The conventional method to determine the potential energy surface (PES) of a system is to use *ab initio* calculations, that require much computational effort. However, when one wishes to study a system that contains 10^2 to 10^4 atoms, as in the doping of condensed phase H_2, it is not temporally or economically feasible to work with the conventional method. Approximations have been used to determine the underlying PES, such as assuming additivity of pairwise potentials. This approach, while suitable for modeling chemically inert systems, such as rare gas clusters and solids, may be inappropriate for modeling of potentially reactive systems, such as $B(H_2)_n$ clusters. Another option is to employ density functional theory.

Density functional theory (DFT) has been used to model extended transition metal surfaces [1], silicon clusters [2], the collisions of cluster of atoms with metallic substrates [3], and the ground state of H_2 [4]. In this study, we will determine if density functional theory can be used to model the relatively weak interactions of the B-H_2 van der Waals complex.

Density Functional Theory

In Kohn-Sham (KS) density functional theory, the ground state energy of a many electron system is obtained as the minimum of the energy functional:

$$E[\rho] = \int \rho(r)\upsilon(r)dr + T_s[\rho] + V_{ee}[\rho] + E_{xc}[\rho] \tag{1}$$

The ground state electron density is the density that minimizes E[ρ], satisfying the Euler equation

$$\mu = \upsilon(r) + \frac{\delta F[\rho]}{\delta\rho(r)} \tag{2}$$

subject to the constraint:

$$\int \rho(r)dr = N \tag{3}$$

The KS orbital equations solved are

$$\left[-\tfrac{1}{2}\nabla_r^2 + \upsilon(r) + \int \frac{\rho(r')}{|(r-r')|}dr' + \upsilon_{xc}(r)\right]\psi_i(r,s) = \varepsilon_i\psi_i(r,s) \tag{4}$$

and

$$\rho(r) = \sum_i^N \sum_s |\psi_i(r,s)|^2 \tag{5}$$

The computational effort to solve the KS equation is roughly equivalent to solving the Hartree equation and less than solving the Hartree-Fock equation.

In these calculations, the local spin density (LSD) approximation is employed since it is a better approximation for systems with significant variations in density, such as open shell systems. The Kohn-Sham LSD equations replace the spinless density [ρ] with the up- and down- spin densities [ρ^α, ρ^β]. The exchange-correlation energy in the LSD approximation in equation (2) is defined to be

$$E_{xc}^{LSD}[\rho] = E_x^{LSD}[\rho^\alpha,\rho^\beta] + E_c^{LSD}[\rho^\alpha,\rho^\beta] \tag{6}$$

Calculations have been performed using MOLPRO [5] and ACESII [6]. Electron densities are calculated from the Hartree-Fock (HF) orbitals from an SCF calculation instead of building the KS orbitals and determining the densities from them. The electronic densities are then calculated and equations (4) and (5) are used to determine the self-consistent energies of the system. Electron exchange energies were described using the Becke gradient-corrected functional [7] and electron correlation energies were described using the Lee-Yang-Parr gradient-corrected functional [8].

Results and Discussion

The interaction between H_2 and B were calculated for bond distances (**r**) of H_2 between 1.0 and 2.6 bohr and an adjusted B and H_2 (**R**) between 2.4 and 4.0 bohr. This **R** bisects the H-H bond distance and is adjusted since it does not include the offset distance of 1.0274 bohr. This distance between the B and the H_2 occurs at the molecular minimum with **r**=4.06 bohr.

The initial set of interactions calculated using both MOLPRO and ACESII was the $^2A_1$ state of the B-H_2 complex. This state has the $2p$ orbital of the B perpendicular to the H_2 bond and the plane of the three atoms. This state was chosen for the first set of calculations since *ab initio* data from Alexander [9] indicates that there is a barrier due to an avoided crossing.

Figures 1 and 2 show the restricted open-shell Hartree-Fock (ROHF) calculations of the $^2A_1$ interaction surface using the two packages. These contours seem reasonable, so the densities from them should be acceptable for use in the proceeding DFT calculations. The DFT contour plots of the interaction energies are found in figures 3 and 4. The ACESII contours bear a close resemblance to the upper left and lower right sections of the interaction energy contours in Alexander's paper. However, the barrier is not found in the ACESII contour since density functional codes are single configuration codes. Therefore, the data will not show any knowledge of any other states. However, the MOLPRO data has completely unphysical results. There is a "minimum" in this graph at approximately **r**=1.4 bohr and **R**=3.5 bohr. This is not the correct molecular minimum for this molecule. The contours do not resemble any part of the CASSCF data from ref. [9].

The next set of figures correspond to the $^2B_2$ state of the B-H_2 complex. In this state, the $2p$ orbital is parallel to the H_2 bond. Again, the ROHF results, found in figures 5 and 6, are reasonable. The ACES II contours in figure 7 are similar in the upper left corner of the contours from the *ab initio* data. But, these do not capture any of the contours in any other area of interest. The MOLPRO DFT results in figure 8 are again very suspect, with a minimum in the surface not corresponding to the correct molecular minimum.

Conclusions

While density functional theory has proven useful for application in strongly bound systems and homogeneous electron systems, it seems that the present implementations of DFT are not suitable for weakly-

bound systems, such as van der Waals complexes. This would seem to call for further developments in the state of density functional codes.

References

1. L.S. Perkins and A.E. DePristo, Surf. Science 325 (1995) 169; L. Hansen, P. Stoltze, K.W. Jacobsen, and J.K. Nørskov, Phys. Rev. B 44 (1991) 6523; C.L. Liu, J.M. Cohen, J.B. Adams, and A.F. Voter, Surf. Sci. 253 (1991) 334.

2. R. Fournier, S.B. Sinnott, and A.E. DePristo, J. Chem. Phys. 97 (1992) 4149.

3. H. Hsieh, R.S. Averback, H. Sellers, and C.P. Flynn, Phys. Rev. B. 45 (1992) 4417.

4. G.S. Painter and F.W. Averill, Phys. Rev. B 28 (1982) 1781.

5. MOLPRO is a set of *ab initio* programs written by H.-J. Werner and P.J. Knowles.

6. ACESII is a set of *ab initio* programs, written by Rodney Bartlett, et al. from the Quantum Theory Project of the University of Florida.

7. A.D. Becke, Phys. Rev. A 38 (1988) 3098.

8. C. Lee, W. Yang, and R.G. Parr, Phys. Rev. B 37 (1988) 785; B. Miehlich, A. Savin, H. Stoll and H. Preuss, Chem. Phys. Lett. 157 (1989) 200.

9. M.H. Alexander, J. Chem. Phys. 99 (1993) 6014.

ROHF calculation
$^2A_1$ - VTZ basis

ROHF calculation
$^2A_1$ state - VTZ basis

Figure 1

Figure 2

DFT-BLYP calculation
$^2A_1$ - VTZ basis

DFT-BLYP calculation
$^2A_1$ state - VTZ basis
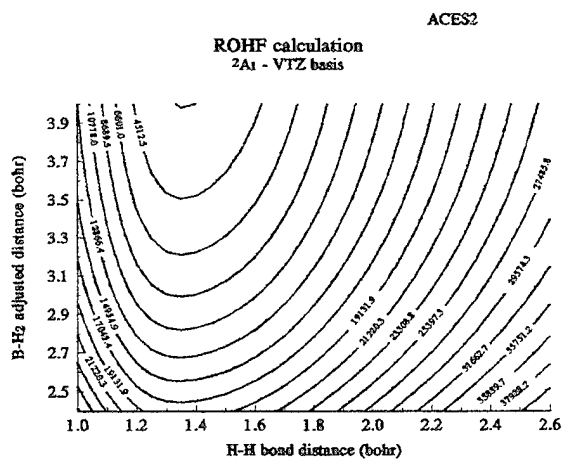
Figure 3
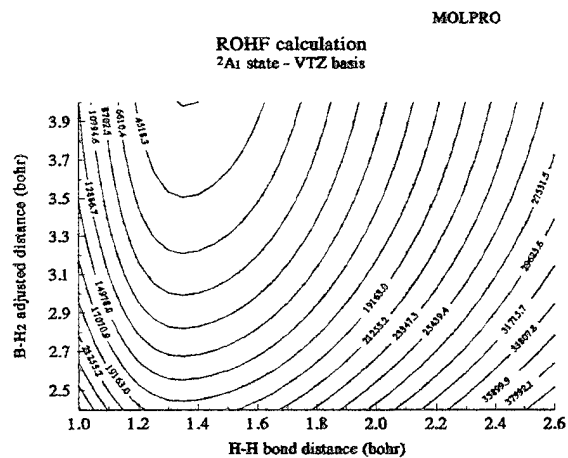
Figure 4
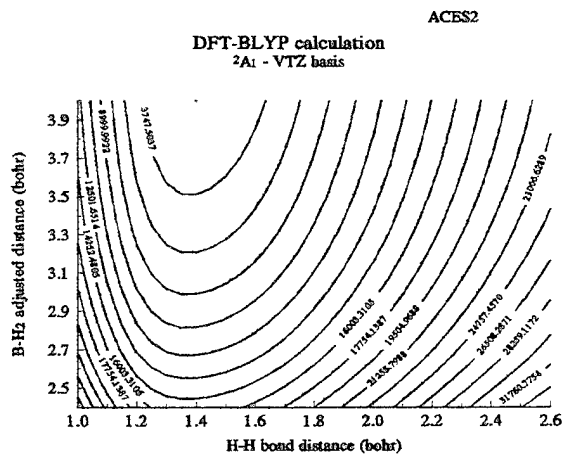
Figure 5
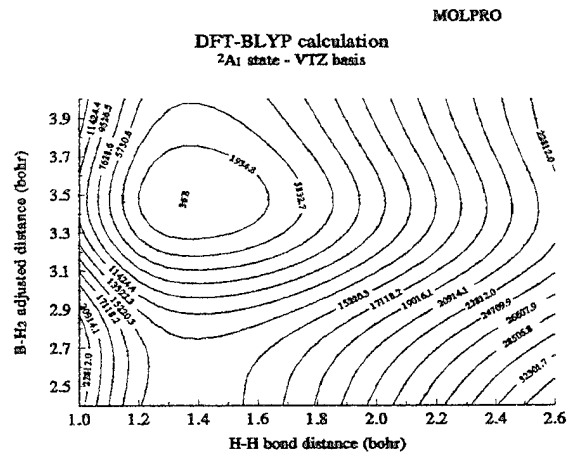
Figure 6

Figure 7

Figure 8

Global Geometry Optimization of B(Ar)$_n$ Clusters using a Modified Genetic Algorithm

Millard H. Alexander and Susan K. Gregurick

Department of Chemistry and Biochemistry, University of Maryland, College Park MD 20742

Bernd Hartke

Institut für Theoretische Chemie, Universität Stuttgart, 70569 Stuttgart, Germany

I. Introduction

We investigate the determination of global minima of weakly-bound molecular clusters. The optimization will become more difficult as the number of dimensions, and thus the number of local minima, grows. A host of complementary optimization methods are available: simulated annealing,[1-4] quantum annealing,[5] potential deformation,[6] hierarchical searching,[7] interval analysis,[8] and genetic algorithms.[9, 10]

Each of these methods has advantages and disadvantages. For example, annealing methods are limited by the cooling schedule, which in some cases can result in extremely long trajectories. Previously, genetic algorithms have been limited by premature or slow convergence. We circumvent these difficulties by introducing gradient information.

II. Genetic Algorithms (GA):

Genetic algorithm methods simulate the genetic learning process of biological species. In the standard GA,[9] the coordinate information of a particular cluster, designated the "individual", is encoded into a binary string, designated the "genome". The potential energy of the cluster is then evaluated and a "fitness parameter" is determined for the individual. Pairs of individuals are selected as parents, one chosen for high fitness and the other chosen randomly. A subsequent generation of children is produced which inherit binary coordinate vectors which are random crosses of those of each parent. To ensure additional randomness, mutations are allowed to occur, in which binary bits in each genome are reversed. The children then become parents and the process is iterated.

Hartke presented[10] a first implementation of this method to the study of (Si)$_4$ clusters. We here extend this investigation by including gradient information into the determination of the fitness parameter. The coordinates of N randomly chosen clusters

(typically $N = 100 - 200$), consisting of n atoms, will be designated collectively $\vec{q}$ and are encoded into a binary vector. The energy fitness parameter, $F(\vec{q})$ of the cluster is defined in terms of the potential energy, $V(\vec{q})$, of the cluster as follows:

$$F(\vec{q}) = exp\left\{ \left[\, V(\vec{q}) - E_{min} \,\right] \big/ E_{min} \right\} \, , \qquad (1)$$

where E_{min} is the estimated global minimum. We define a combined fitness parameter, which will favor both low potential energies and small gradients, as:

$$F_{comb} = F(\vec{q}) \cdot F_{\nabla}(\vec{q}) \, , \qquad (2)$$

where $F(\vec{q})$ is defined by Eq. (1), and the gradient fitness parameter is defined as

$$F_{\nabla}(\vec{q}) = exp(-\left| \nabla V(\vec{q}) \right|) \, . \qquad (3)$$

As in the standard GA method, two parents are selected, the first with a high fitness parameter and the second at random. The number of children is fixed at two, so that the total number of individuals in the population remains constant. Mutations in the genome are allowed to occur at a fixed probability ($0 < P < 0.1$), unchanged from generation to generation.

At each generation the energy of the individual with the highest fitness parameter is recorded. When the change in this reference energy from one generation to the next is smaller than a preset criteria, the GA optimization is halted. The minimum of the cluster can subsequently be located to any precision by using the geometry of the reference individual as a starting point for a conventional conjugate gradient minimization.[4]

In practice, convergence is accelerated by the following global-local optimization procedure: After each mating, a conjugate gradient optimization is invoked to minimize the energy gradient of each individual. This optimization continues until the change in at least one component of the gradient drops below a preset, but relatively high, threshold. This hybrid procedure repositions the children, which are initially redistributed randomly, to be close to local minima or saddle points. We also find that convergence can be accelerated by

prohibiting the dissociation of any n-atom cluster into two (or more) smaller clusters. This is done by restricting all atoms to lie within a sphere of suitably chosen radius.

III. Demonstration Calculation

As a demonstration of the speed and accuracy of our modified GA, we investigated the optimization of clusters of n identical Ar atoms, which interact through pair-wise Lennard-Jones potentials.[11] In Table 1 we list the minimum energy, as a function of cluster size, for these homogenous Lennard-Jones clusters as obtained by our modified GA calculations. The energies are virtually identical to the "exact" values of Hoare and Pal[11] and more precise than the energies, also tabulated, obtained by quantum annealing.[5] Clearly, our implementation of the GA avoids the premature convergence difficulties, which have been observed in some prior applications of GA methods.[12]

Also shown in Table I is a comparison of the cpu times required by the modified and standard GA's.

For the $n = 6$ and $n = 18$ clusters the search for the global minima is complicated by the presence of at least one low-lying local minimum; hence the relatively longer computation time in these cases. Notwithstanding, inclusion of gradient information results in a major savings in computational expense. The cpu times in Table I scale as $n^{4.7}$ (or, if we eliminate the singularly high value at $n = 18$, as $n^{4.5}$). This high power dependence illustrates the difficulty of finding global minima for large clusters.

IV. B(Ar)$_n$ clusters

The interaction of the B atom ($2s^2 2p\ ^2P$) with a spherical atom must be described by *two* potential curves ($^2\Pi$ and $^2\Sigma^+$).[13] We take the orientation of the B $2p$ orbital to define a space-fixed axis system, and place an Ar atom at coordinates $\vec{q} = R,\ \theta,$ and ϕ with respect to the B atom. In the absence of spin-orbit coupling, the three electronic states which describe the BAr system are the roots of the 3×3 Hamiltonian defined by[14]

$$V(\vec{q}) = T(\theta,\phi) \begin{bmatrix} V_\Pi(R) & 0 & 0 \\ 0 & V_\Pi(R) & 0 \\ 0 & 0 & V_\Sigma(R) \end{bmatrix} T(\theta,\phi)^T , \qquad (4)$$

292

where $T(\theta, \phi)$ is the product of the two rotations which define the position of the Ar atom.

Balling and Wright describe the interaction of n Ar atoms with a B atom by a 3×3 Hamiltonian which is a generalization of Eq. (4), namely

$$V(\vec{q}_1, \vec{q}_2, \dots, \vec{q}_n) = \sum_{i=1}^{n} V(\vec{q}_i) + \sum_{i,j>i}^{n} V_{Ar_2}(q_{ij}) \qquad (5)$$

where q_{ij} is the distance between Ar atoms i and j. Again, following Balling and Wright,[14] and unpublished work of Boatz and Fajardo,[15] we assume that the potential energy of the B(Ar)$_n$ cluster is defined by the lowest eigenvalue of $V(\vec{q}_1, \vec{q}_2, \dots, \vec{q}_n)$. In other words

$$V(\vec{q}_1, \vec{q}_2, \dots, \vec{q}_n) = c_1 V c_1^T, \qquad (6)$$

where c_1 denotes the 3 component row vector corresponding to this lowest eigenvalue.

The derivative of $V(\vec{q})$ with respect to any coordinate is given by a similar orthogonal transformation of the derivative of the $V(\vec{q})$ matrix.[16]

We used the *ab initio* BAr V_Π and V_Σ potentials of Hwang *et al.*[13] and the Ar$_2$ potentials of Aziz and Chen.[17] The similarity in well depth and equilibrium distance of the V_Π ($r_e = 3.67$ Å, $D_e = 94.8$ cm^{-1}) and Ar$_2$ potentials ($r_e = 3.757$ Å, $D_e = 97.81$ cm^{-1}), suggests that B may substitute readily for an Ar atom, provided that all the nearest-neighbor Ar atoms lie in (or close to) the plane perpendicular to the occupied B $2p$ orbital.

Table 2 compares the global minima for (Ar)$_n$ and B(Ar)$_{n-1}$ clusters. We find the substitution of B for Ar results in a slight stretching of the unsubstituted (Ar)$_n$ poly–pentagonal cluster, with the B always taking a peripheral position. Only on the periphery is the repulsive (V_Σ) interaction between the B $2p$ orbital and the Ar atoms minimized. We are currently extending our simulations to larger clusters and will report on this at the 1995 meeting.

Table I. Results of demonstration calculations on Lennard-Jones $(Ar)_n$ clusters.

n	Genetic Algorithm [a]			Quantum Annealing [d]	Exact [b]
	cpu time [c]				
	w/o gradient	w gradient	Energies [e]		
2			−1.000	−0.998	−1.000
3			−2.999	−2.999	−3.000
4	292	0.46	−5.999	−5.997	−6.000
5	485	0.15	−9.104	−9.095	−9.104
6	2039 [e]	6.3 [f]	−12.712	−12.710	−12.712
7	4690	4.2	−16.505	−16.505	−16.505
8	6901	3.4	−19.821	−19.794	−19.822
9	9501	8	−24.113	−24.108	−24.113
10	12494	22	−28.422	−28.408	−28.420
11		65	−32.764		−32.765
12		54	−37.966		−37.967
13		35	−44.325		−44.327
14		46	−47.841		−47.845
15		175	−52.318		−52.322
16		144	−56.813		−56.815
17		230	−61.304		−61.307
18		778 [g]	−66.527		−66.531
19		275	−72.657	−72.622	−72.659

a. In all calcualations 30% of the parents were retained in the next generation. A mutation rate of 0.1 was used consistently. To allow more efficient exploration of the larger configuration space accessible to the larger clusters, the number of individuals in the starting population was increased as the cluster size increased.

b. Ref. 11.

c. Cpu seconds on an IBM RS6000/370, FORTRAN code compiled with optimization.

d. Ref. 5.

e. In units of the Lennard-Jones well-depth.

f. The optimization of this structure is complicated by existence of a low-lying local minimum at $E = -12.303$.

g. The optimization of this structure is complicated by existence of a low-lying local minimum at $E = -66.279$ with a poly-pentagonal geometry very similar to the global minimum.

Table 2. Comparison of calculated minima of $(Ar)_n$ and $B(Ar)_{n-1}$ clusters.

n	Cluster Minimum (cm^{-1})	
	$(Ar)_n$	$B(Ar)_{n-1}$
2	−97.82	−96.03
3	−293.45	−289.87
4	−586.90	−532.47
5	−887.46	−818.46
6	−1228.12	−1131.79
7	−1598.70	−1412.68
8	−1913.34	−1713.22

References

1. K. S. Kirkpatrick, C. D. Gelatt, and M. P. Vecchi, Science **220**, 671 (1983).
2. K. S. Kirkpatrick, J. Stat. Phys. **34**, 975 (1984).
3. P. J. M. van Laaarhoven and E. H. L. Aarts, *Simulated Annealing: Theory and Applications* (Reidel, Dordrecht, 1987).
4. W. H. Press, B. P. Flannery, S. A. Teukolsky, and W. T. Vetterling, *Numerical Recipes: The Art of Scientific Computing (FORTRAN Version)*, 2 ed. (Cambridge University Press, Cambridge, UK, 1990).
5. A. B. Finnila, M. A. Gomez, C. Sebenik, C. Stenson, and J. D. Doll, Chem. Phys. Lett. **219**, 343 (1994).
6. L. Piela, J. Kostrowicki, and H. A. Scheraga, J. Phys. Chem. **93**, 339 (1989).
7. L. S. Reid and J. M. Thornton, Proteins **5**, 170 (1989).
8. E. R. Hansen, Numer. Math. **34**, 247 (1980).
9. D. E. Goldberg, *Genetic Algorithms in Search, Optimization, and Machine Learning* (Addison-Wesley, Reading, MA, 1989).
10. B. Hartke, J. Phys. Chem. **97**, 9973 (1993).
11. M. R. Hoare and P. Pal, Adv. Phys. **20**, 161 (1971).
12. *Proc. Fifth Int. Conf. Genetic Algorithms*, ed. S. Forrest (Morgan Kaufmann, San Mateo, CA, 1993).
13. E. Hwang, Y.-L. Huang, P. J. Dagdigian, and M. H. Alexander, J. Chem. Phys. **98**, 8484 (1993).
14. L. C. Balling and J. J. Wright, J. Chem. Phys. **79**, 2941 (1983).
15. J. Boatz and M. Fajardo, abstracts *Proceedings of the High Energy Density Materials Contractor's Conference,* Wood's Hole, MA, 1993, p. .
16. S. Castellano and A. A. Bothner-By, J. Chem. Phys. **41**, 3863 (1964).
17. R. A. Aziz and H. H. Chen, Mol. Phys. **58**, 679 (1986).

Laser Photolysis of Cryogenic Solid Oxygen/Ozone

M. J. Dyer, H. Helm*, R. P. Saxon, and D. L. Huestis
Molecular Physics Laboratory
SRI International
Menlo Park, CA 94025

Introduction

We have begun a series of experiments designed to generate, trap and detect high energy oxygen polyatomics in cryogenic oxygen and oxygen/ozone environments using intense laser photolysis. Polyatomic oxygen molecules possessing higher than three atoms, such as cyclotetraoxygen, have been predicted, and recent experimental evidence exists that identifies the O_4 neutral rectangular (D_{2h}) structure; Seidl and Schaefer[1] analogized polyatomic oxygen rings to sulfur ring systems, such as S_8, known to be relatively stable, and experiments by Helm and Walter[2] indicate that electronically-excited rectangular O_4 is produced after charge transfer in a fast beam of O_4^+ ions. If conditions shown to generate these structures, specifically electronically "hot" reaction environments such as plasmas, can be produced and the products immediately "frozen out" in a cryogenic lattice, it should be possible to store energy in polymeric form within cryogenic solid oxygen.

Method

We are studying highly concentrated cryogenic oxygen and oxy/ozone systems because they offer an environment, when subjected to intense laser irradiation, in which high densities of translationally and electronically excited oxygen may react and form new polyatomics. In high energy or high intensity photolysis of molecular oxygen, significant kinetic energy is carried away by ground state and electronically-excited photofragments. When photolysis occurs in the high density environment of a cryogenic solid, the photofragments can impact and immediately interact with like fragments and parent molecules. The products of these reactions are either condensed and frozen out, or their decomposition processes delayed by the cryogenic environment.

Oxygen-containing rare-gas matrices, in which lasers are used to photodissociate concentrations of oxygen and ozone molecules, have received much attention recently.[3,4,5] In these experiments, subsequent recombination of the products is followed using Fourier-transform infrared (FTIR) and ultraviolet/visible spectroscopies. In such "matrix-isolation" experiments, optical measurements of the photolysed species of interest are typically free from matrix background interferences, but recombination occurs under conditions that appear not to be favorable for the excited state-excited state reactions deemed necessary to form higher order polyatomics. In contrast, pure oxygen/ozone environments offer close proximity for the reactions to occur, but the environment does not permit deep penetration of single-photon photolysis wavelengths nor high detection sensitivity over the parent-host background.

Our approach to generating new oxygen polyatomics is two-fold: to drive excited state reactions in a plasma generated from free-standing cryogenic oxygen using low- and high-photon energy laser light, or to penetrate deep into the oxygen solid with an intense picosecond laser operating in the near UV and visible. The latter technique will rely on multiphoton absorption at

*Current address Albert-Ludwigs Universitat, Freiburg, Germany.

wavelengths where single-photon transparencies are relatively high. In both approaches, the chemistry and reaction products are frozen and cooled either by expansion into a high-vacuum environment or trapping within the cryogenic lattice. Detection of hot reaction products ablated/evaporated from or within the solid will be pursued with ionization/time-of-flight and optical methods to initially detect higher mass polyatomics and to characterize their structures, respectively.

Experimental

Cryogenic Oxygen Sample Generator

Bulk solid oxygen and ozone are difficult to produce with sufficient optical quality to allow photolysis and optical probes deep within the solid's interior. Since part of our interest lies in delivering high intensities to the interior of such materials, we have constructed a cryogenic oxygen sample generator and explored methods to produce good optical quality free-standing oxygen "cubes" with flat surfaces.

Solid cryogenic oxygen samples are generated atop a copper stage cooled by a closed-loop helium refrigerator that has been inverted and sealed to a turbo-pumped high vacuum chamber, which maintains a 10^{-7} Torr base pressure. The top of this copper stage is covered with a 2 mm thick layer of indium. which is flattened to a smooth, even surface. The indium serves as a gasket for the open end of a quartz cuvette in which the sample is formed.

The 5x5x15 mm high fused quartz cuvette is attached with indium solder to the base of a liquid nitrogen-cooled column mounted on a three-axis manipulator above and opposite the cold stage. The bottom of the cuvette is removed with a diamond saw, and the exposed edges are polished to a flat, smooth finish to permit sealing onto the cryogenic stage. Prior to sealing and cooling the apparatus, the cuvette is lowered onto the warm sample stage and pressed into the soft indium in order to conform and produce a very tight seal against the open base of the cuvette. The sample generator is depicted in figure 1.

The cold stage is temperature-controllable from 300 to 10 Kelvin in 0.1 degree increments. Under a vacuum of roughly 10^{-7} Torr, the helium refrigerator cools the sample stage to 10 K and the cuvette column is cooled to 77 K. The column is loaded to exert pressure onto the indium-coated sample stage as the cooled components contract in order to maintain the cuvette-stage seal. Oxygen gas is flowed into the sealed cuvette through a precooling coil in contact with the LN_2-cooled column on its way through the column and into the cuvette. As much as an atmosphere of backing pressure may be used to fill the cuvette without breaching the cuvette-indium seal, but a low-pressure regulator maintains the cuvette typically between 5 and 200 Torr. At 50 Torr, oxygen condenses into the cuvette and forms a solidified volume of 0.14 cm³ after a few hours.
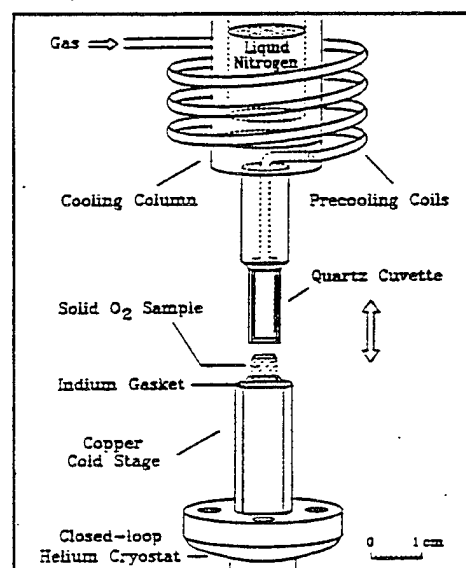
Figure 1   Cryogenic oxygen sample stage.

Careful regulation of the stage temperature to first liquify the gas, then solidify it slowly can produce an optically acceptable volume, but this process is time-consuming and accompanied by large pressure fluctuations, resulting in a visually "layered" sample . We have found that first depositing a volume of oxygen "snow" at 10 K, then isolating the cell from the gas flow and cycling the temperature to melt and resolidify the volume produces a dense, translucent sample. Further improvements in sample homogeneity and the resolidification rate have been found by placing neodymium-iron-boron magnets on either side of the retractable cuvette. As yet, the reasons for these improvements are not entirely understood, and this technique is used only when optical measurements are to be made, because the magnets can not be removed to a distance in the chamber where the magnetic fields do not profoundly influence the time-of-flight ion collection.

Absorptions of Cryogenic O₂

Absorption measurements of cryogenic liquid and solid O_2 were performed on the 5 mm deep samples in order to identify suitable photolysis wavelengths and single-photon absorption depths. The absorption scans shown in figure 2 were taken using a 1/4-meter monochrometer and a deuterium lamp as a light source. The resolution of the measurements was 0.4 nm. Normalization runs were made with an empty cell before and after filling with condensed oxygen.
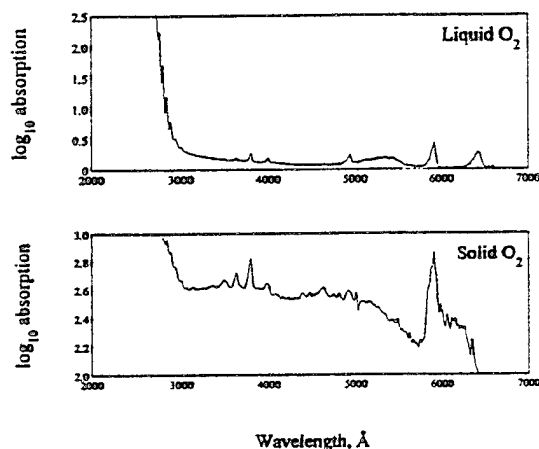
Figure 2 Absorptions of liquid and solid O_2.

In order to minimize exposure of the cryogenic oxygen samples to the lamp's total emission spectrum, and thus minimize any photochemistry that might occur during the course of the measurements, the light was first passed through the monochrometer, imaged into the sample using a calcium fluoride lens, then collected and reimaged onto an apertured UV sensitive photomultiplier.

Assignments of the features shown have been made previously and are attributed to absorptions by O_2 and O_4 complexes[6,7]. The absorption scan of the solid shows a large continuous "background," compared to the liquid. This is in part due to scattering losses in measurements of a solid sample made prior to improvements in the growth process.

Ablation at 1064 nm and Fluorescence of the [O₂(¹Δₐ)]₂ Complex.

O_4 complexes in condensed phases of O_2 absorb at 1060 nm with an extinction coefficient of almost 0.7 cm⁻¹. Huestis et al. [5] measured the fluorescence and quenching rates of $O_2(^1\Delta_g)$ and $[O_2(^1\Delta_g)]_2$ and found that radiative pooling in the reaction:

$$O_2(^1\Delta_g) + O_2(^1\Delta_g) \rightarrow O_2(^3\Sigma_g^-) + O_2(^3\Sigma_g^-) + h\nu$$

produced emissions at 634 and 703 nm.
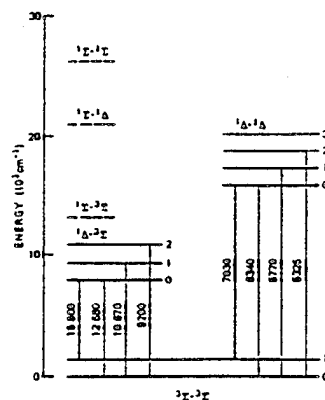
Figure 3 Energy levels for O_4 complex.

Figure 3 illustrates the energy levels involved. We explored this excitation scheme as a promising method for simultaneously removing cryogenic oxygen by ablation at the 1064 nm fundamental of Nd:YAG and monitoring through fluorescence the ablation rate. This wavelength is ideal for producing a dense plume of material in this system, because neither the time-of flight mass spectrometer nor the UV/VIS or FTIR optical measurements will be disturbed by it: 1064 nm light is not energetic enough to generate substantial background ionization from the solid oxygen or surfaces in the vacuum chamber, and the optical instrumentation is not sensitive to it. Photolysis and ionization of the expanding plume created by the 1064 nm pulse may then be carried out using a single or multiple steps.
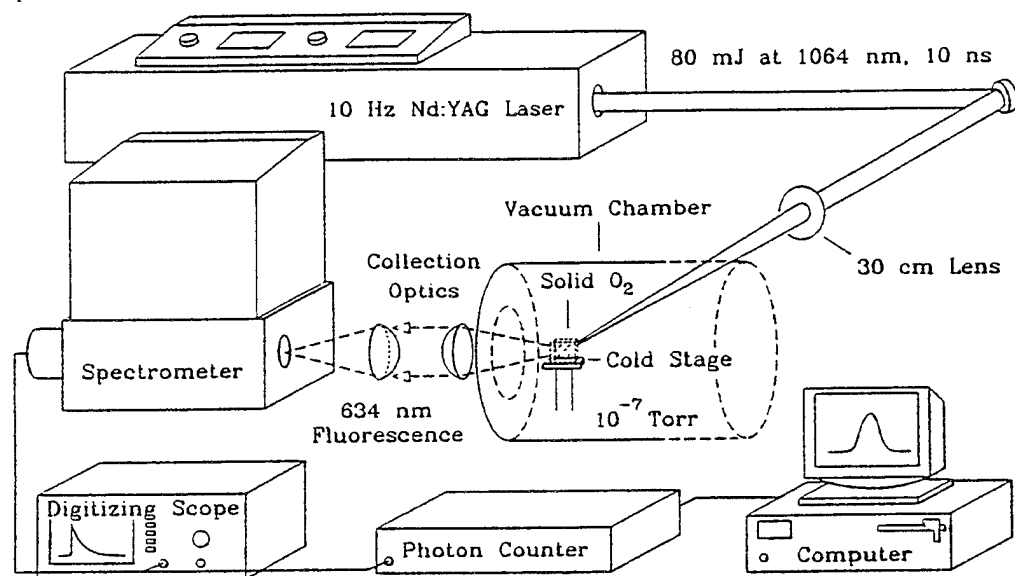
Figure 4 Experimental setup for $[O_2(^1\Delta_g)]_s$ measurements.

We focussed roughly 80 mJ of pulsed 1064 nm light into free-standing solid oxygen at 12 K and detected fluorescence at 643 nm emitted orthogonal to the excitation beam. The experimental setup is shown in figure 4. Removal of material was visually evident under these conditions, but no attempt was made at the time to correlate the quantity of removed material with the disappearance of fluorescence, which occurred over a period of roughly 15 seconds. After moving to fresh material, the fluence was lowered and a photon counter measured the emission for a fluorescence scan, and a digitizing oscilloscope recorded the fluorecence decay of the 643 nm light. The results in figure 5 are comparable to those measured[7] for liquid oxygen at 77 K.
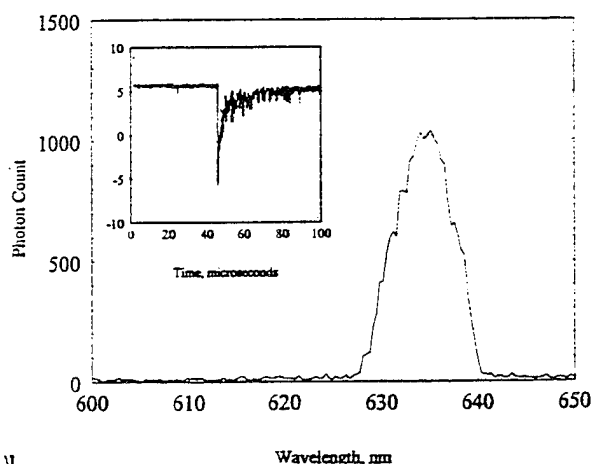
Figure 5 Fluorescence measurements of $[O_2(^1\Delta_g)]_s$

299

Future Research

Experiments currently under development make use of multiple laser sources to ablate, photolyse and ionize plumes of material from solid cryogenic oxygen with a nanosecond pulsed laser and an intense picosecond laser. Figure 6 depicts the heart of the experiment. The solid oxygen is subjected to nanosecond light in the ablation and photolysis steps, followed by picosecond ionization at some later time as the plume expands away from the free-standing sample. Positive ions are then extracted into the drift tube of a time-of flight mass spectrometer using a grid negatively biased relative to the grounded cryogenic stage.
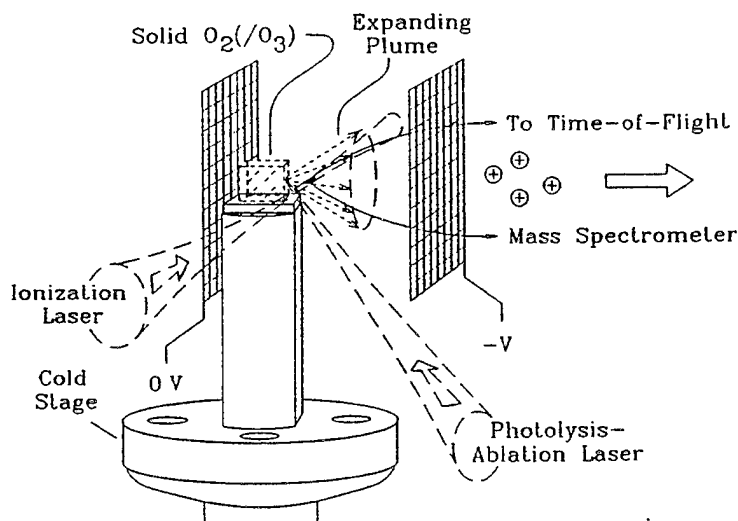
Figure 6 Experimental concept for polymeric oxygen generation.

In a variation on this experiment, the photolysed and ablated materials are recondensed onto a cold thalium bromoiodide window, positioned in place of the negatively-biased ion extraction grid, through which the beam of an FTIR spectrometer passes. It is expected that the polymeric composition of the condensed material can be characterized via predicted characteristic fundamental vibrations[1], for example, and as a function of window temperature[9] in order to understand the formation mechanisms of the photolysed products.

References

1.   E. T. Seidl and H. F. Schaefer III, J. Chem. Phys. **88**, 7043 (1988).

2.   H. Helm and C. W. Walter, J. Chem. Phys. **98**, 1 (1993).

3.   A. V. Danilychev and V. A. Apkarian, J. Chem. Phys. **99**, 8617 (1993).

4.   A. V. Benderskii and C. A. Wight, J. Chem. Phys. **101**, 292 (1994).

5.   E. T. Ryan and E. Weitz, J. Chem. Phys. **99**, 8628 (1993).

6.   V. I. Dianov-Klokov, Opt. Spectrosc. **21**, 233 (1966) and references therein.

7.   H. D. Smith and N. Barton, Trans. Roy. Soc. Canada **39** (III), 25 (1945).

8.   D. L. Huestis, G. Black, S. A. Edelstein, and R. L. Sharpless, J. Chem. Phys **60**, 4471 (1974).

9.   L. Shriver-Mazzuoli, A. de Saxce, C. Lugez, C. Camy-Peyret, and A. Shriver, J. Chem. Phys. **102**, 690 (1994).

THE STRUCTURE AND STABILITY OF M - H_2 VAN DER WAALS COMPLEXES

(M=Li, Be, B, C, Na, Mg, Al, Si).

Galina Chaban and Mark S. Gordon
Department of Chemistry
Iowa State University
Ames, Iowa 50011

Ab initio calculations have been performed for a series of Van der Waals complexes M---H_2 where M=Li, Be, B, C, Na, Mg, Al, and Si. The calculations were done using quadratic configuration interaction method QCISD(T)[1] with Dunning's correlation consistent valence-triple-zeta (cc-pVTZ) basis sets [2]. The Al-H_2 potential surface was also studied at the multi-reference CI level based on a full-valence active space MCSCF(5,6) wavefunction.

Complexes of s-elements.

According to our calculations, s-elements in their ground states (^2S, Li, Na and ^1S, Be, Mg) form only linear complexes with H_2 molecule. The dissociation energies are very small: about 15 cm^{-1} for Li and Na and 30 cm^{-1} for Be and Mg. C_{2v} complexes of these elements correspond to transition states between linear configurations at the level of theory used in this work.

C_{2v} complexes correspond to minima and are very stable for excited states of S-elements (^2P Li,Na and ^3P Be,Mg) due to interactions of occupied p-orbitals with σ^*(H-H). The dissociation energies for $^2B_2$ complexes of Li and Na are 18 and 9 kcal/mol; for $^3B_2$ complexes of Be and Mg the dissociation energies are 20 and 6 kcal/mol. However, these complexes may be unstable kinetically due to crossings with ground state A_1 surfaces. These crossings suggest that sufficiently strong non-adiabatic coupling between the states could result in pre-dissociation of the excited state complexes.

The structural parameters and dissociation energies for complexes of s-elements are shown in Table 1.

Calculations of Be $(H_2)_n$ complexes with n=2-4 have shown that the dissociation energies of these complexes change almost additively with the number of H_2 molecules: 33, 65, 99, and 132 cm^{-1} for n=1, 2, 3, and 4 respectively.

Van der Waals complexes M_2---H_2 (M=Li, Be) are found to be more stable than M---H_2. The Li_2--H_2 complex has T-shaped geometry and D_e= 49 cm^{-1}. Two complexes are found for Be_2--H_2: with linear geometry (58 cm^{-1}) and with parallel orientation of Be_2 and H_2 (122 cm^{-1}).

Complexes of p-elements

P-elements (ground states) form much stronger complexes due to interaction of occupied p-orbital with H_2 molecule (Table 2). P-elements form complexes with both linear and perpendicular geometry. The most stable of these correspond to a perpendicular orientation of the H_2 molecule, with the occupied p-orbital parallel to the H-H bond. Thermodynamic stability of perpendicular complexes increases from B, Al to C, Si. MRCI calculations of the B-H_2 potential surface performed by Alexander[3], and our study of the Al-H_2 system showed that the most stable Van der Waals complexes for these species correspond to a $^2B_2$ state and have dissociation energies of 121 and 204 cm^{-1} respectively. Less stable complexes were found on the $^2B_1$ and $^2\Sigma$ potential energy surfaces of B-H_2 and Al-H_2.

Kinetic stability was studied for C_{2v} complexes, since stable MH_2 compounds with this symmetry exist for M= B, Al, C, Si . Complexes are stable only if barriers to insertion are high enough. Van der Waals complexes and MH_2 compounds have different electronic states, and the energy of their crossing is the upper limit for the barrier of reaction, which can proceed via an avoided crossing.

The Al---H_2 ($^2B_2$) complex is found to be kinetically stable at the QCISD(T) level of theory (see Figure 1). MRCI / MCSCF(5,6) calculations of the $^2B_2$ - $^2A_1$ crossing region showed that

the minimum energy crossing point corresponds to the structure with $R (Al - H_2) = 1.51Å$ and $r (H-H) = 1.682Å$ and is 28.1 kcal/mol above the $^2B_2$ complex. The calculations showed very little interaction between $^2B_2$ and $^2A_1$ states: the distortion to Cs symmetry by changing the angle between the $Al - H_2$ axis and H-H bond from 90 to 80 degrees resulted in only a few cm^{-1} energy lowering of the lower $^2A'$ state at about 89.5 degrees, and then the energies of both states go up. This suggests that the energy of the crossing point can be considered as a good approximation to the height of the barrier for this reaction.

The structures and stabilization energies for several $Al-(H_2)n$ complexes were calculated with n = 1-4 (Figure 4) . As in the case of $Be-(H_2)n$, the addition of H_2 molecules increases the stability of the complex almost additively.

No complex is found on the $^1A_1$ surface for either $C-H_2$ or $Si-H_2$: the insertion of singlet C and Si into H_2 goes with no barrier at all. Although Van der Waals complexes with $D_e=324$ cm^{-1} and 720 cm^{-1} are found for the $^3A_2$ potential surfaces of C ---H_2 and Si---H_2, they are probably unstable kinetically (see Figure 2 and 3). $^3B_1$ crosses $^3A_2$ only 1.5 kcal/mol above the C (^3P) + H_2 dissociation energy. In the case of Si, the $^3A_2$ - $^3B_1$ crossing is in the region of 20 kcal/mol above the $Si-H_2$ complex. However, the $^1A_1$ state crosses $^3A_2$ about 5 kcal above the complex, so the stability of the $Si-H_2$ complex depends on how strong is the interaction between triplet and singlet states near the crossing region.

References:

1. Pople, J. A.; Head-Gordon, M.; Raghavachari, K. J. Phys. Chem. 1987, 87,5968.

2. T.H. Dunning, Jr., J. Chem. Phys. 90, 1007 (1989); R.A. Kendall, T.H. Dunning, Jr., and R.J. Harrison, J. Chem. Phys. 96, 6796 (1992); D.E. Woon and T.H. Dunning, Jr., J. Chem. Phys. 98, 1358 (1993).

3. M. H. Alexander. J. Chem. Phys. 1993, 99, 6014.

Table 1. Characteristics of Van der Waals complexes of Li, Na, Be, and Mg atoms with H_2

M	State	R (M-X[1]), Å	R (H-H), Å	D_e
Li	$^2\Sigma$	5.21	0.743	15 cm^{-1}
	$^2B_2$	1.66	0.84	18.2 kcal/mol
	$^2B_1$	1.89	0.75	7.3 kcal/mol
	$^2\Sigma$	6.27	0.743	27 cm^{-1}
Na	$^2\Sigma$	5.50	0.743	13 cm^{-1}
	$^2B_2$	2.14	0.79	9.2 kcal/mol
	$^2B_1$	2.36	0.75	3.8 kcal/mol
	$^2\Sigma$	7.27	0.743	19 cm^{-1}
Be	$^1\Sigma$	4.21	0.743	33 cm^{-1}
	$^3B_2$	1.36	0.98	20.4 kcal/mol
	$^3B_1$	1.78	0.76	1.9 kcal/mol
	$^3\Sigma$	4.32	0.743	98 cm^{-1}
Mg	$^1\Sigma$	4.66	0.743	30 cm^{-1}
	$^3B_2$	2.01	0.80	5.6 kcal/mol
	$^3B_1$	2.77	0.743	0.7 kcal/mol
	$^3\Sigma$	5.07	0.743	84 cm^{-1}

[1] X - midpoint of H-H bond.

Table 2. Characteristics of Van der Waals complexes of B, Al, C, and Si atoms with H_2 molecule.

M	State	R (M-X[1]), Å	D_e, cm^{-1}	M	State	R (M-X), Å	D_e, cm^{-1}
B	$^2\Sigma$	3.87	93	Al	$^2\Sigma$	4.62	89
	$^2B_2$	3.11	130		$^2B_2$	3.25	204
	$^2B_1$	3.33	78		$^2B_1$	3.60	103
C	$^1\Sigma$	3.61	120	Si	$^1\Sigma$	4.25	112
	$^3\Pi$	3.54	81		$^3\Pi$	4.15	84
	$^3A_2$	2.21 [2]	324		$^3A_2$	2.25 [2]	720

[1] X - midpoint of H-H bond.

[2] Equilibrium distance r(H-H)=0.75 and 0.76Å for C-H_2 and Si-H_2 $^3A_2$ complexes, and 0.743 Å for other complexes.
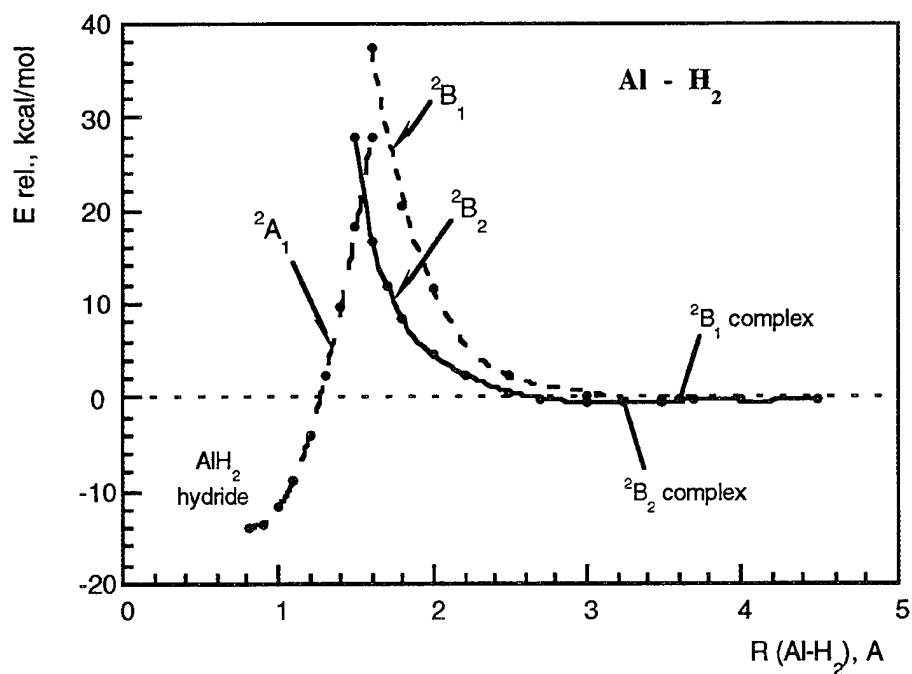
Figure 1. QCISD(T)/aug-pvtz potential energy surfaces for Al-H_2 (C_{2v} symmetry).

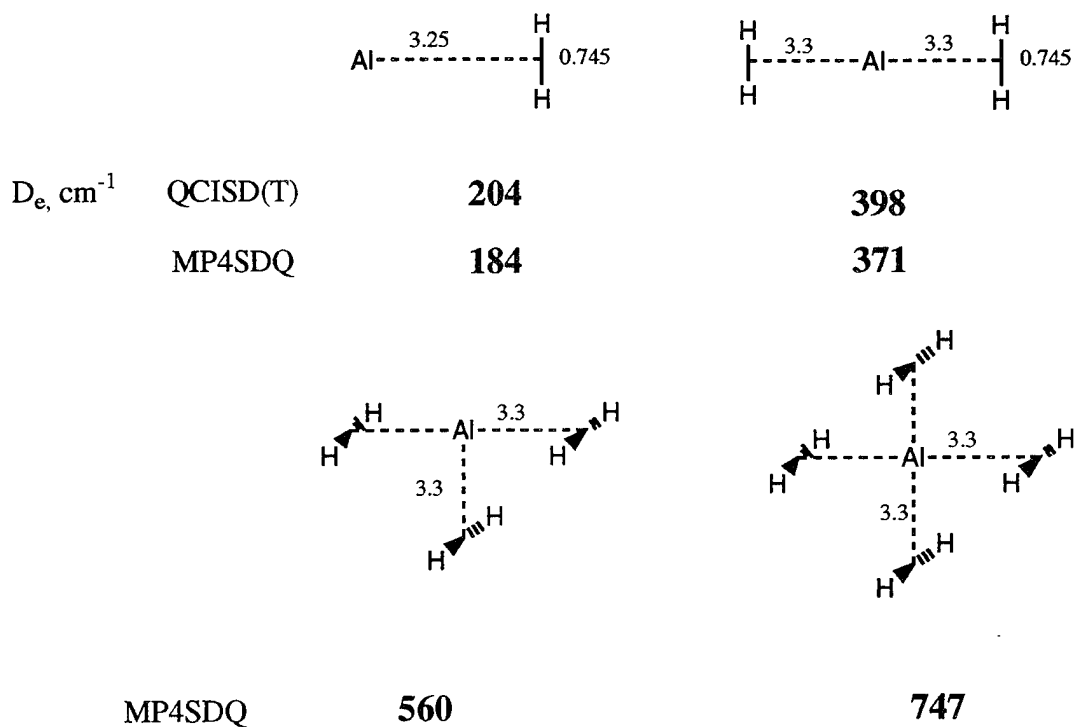| D_e, cm^{-1} | QCISD(T) | 204 | 398 |
| MP4SDQ | 184 | 371 |

| MP4SDQ | 560 | 747 |

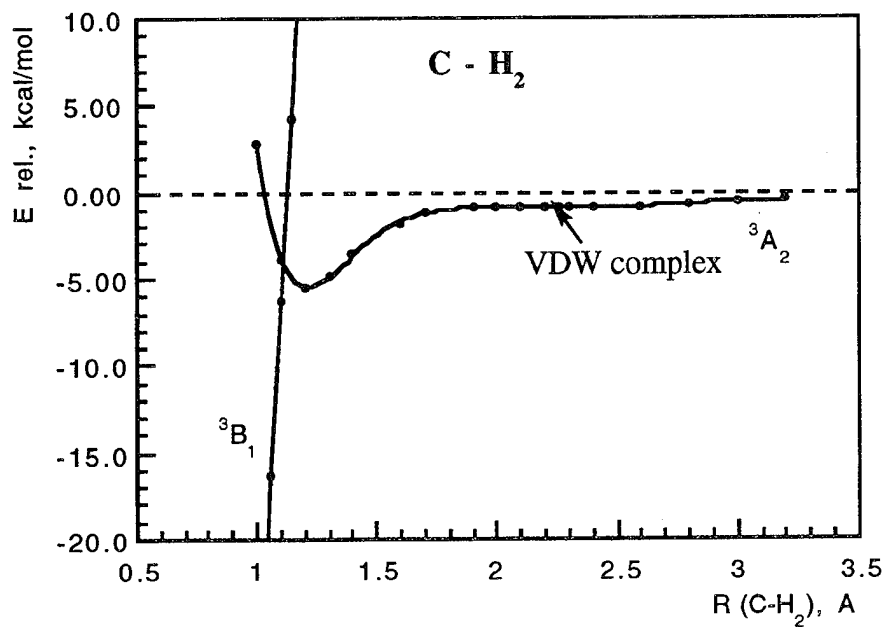Figure 2. Van-der-Waals complexes of Al with H_2 molecules.

Figure 3. QCISD(T)/aug-pvtz potential energy surfaces for C - H₂
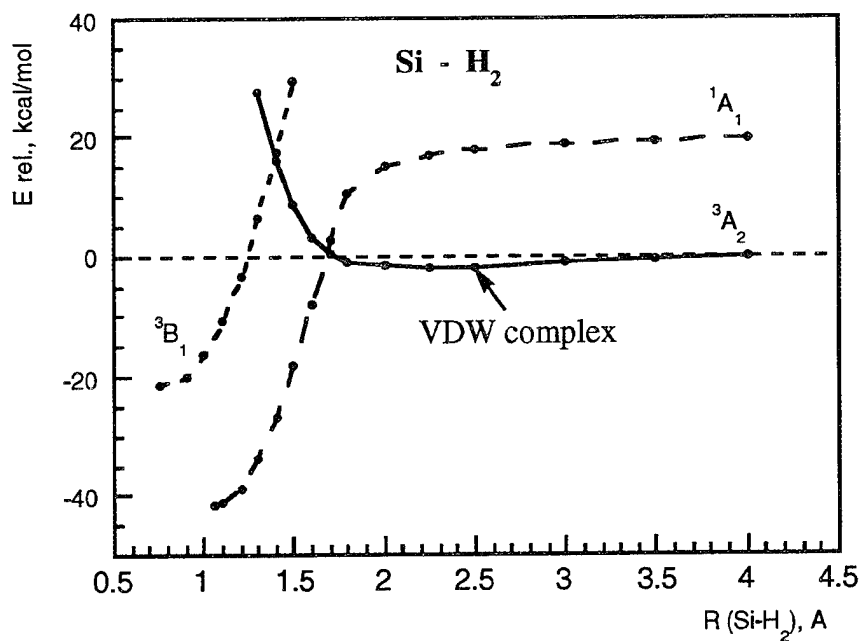(C₂ᵥ symmetry).

Figure 4. QCISD(T)/aug-pvtz potential energy surfaces for Si - H₂
(C₂ᵥ symmetry).

306

Mobilities and Reaction Dynamics of H Atoms in Cryogenic Solids

E. Todd Ryan, Dwayne LaBrake and Eric Weitz

Department of Chemistry
Northwestern University
Evanston, IL 60208-3113

Introduction

The technique of matrix isolation spectroscopy[1] has served as a powerful tool for the study of reactive chemical species. The species of interest can be prepared in various ways. One common technique involves the photolysis of a precursor molecule in the matrix to produce a reactive species directly as a photoproduct. Another technique involves the production of an atom or radical by photolysis which subsequently reacts with some other radical or molecule in the matrix to produce the species of interest.[1,2]

In both of the above techniques, the rates for atomic and molecular mobility in the matrix are of prime importance. If the atom or radical is produced by reaction of two species in the matrix, the timescale for its production will be effected by the diffusion time of the reactant in the matrix. Once a radical is produced, its lifetime will be determined in part by the time that it takes for the atom or radical to diffuse to another reactant in the matrix.

It is also possible that the reactive species can absorb electromagnetic radiation. This radiation can then be degraded into energy in translational and/or internal degrees of freedom. If a significant amount of the initially absorbed energy eventually resides in translational degrees of freedom of the reactive species, the mobility of this species can be enhanced. This processes has been termed "photoinduced mobility".[3-8] This process will occur anytime the absorption of a photon results in the complex residing on the repulsive portion of a barrier-less potential energy surface. Such a process may occur as a result of a simple, direct photodissociation process, or when the reactive species can form an excited state or charge transfer complex with the host material. Under the latter circumstances relaxation of the complex will typically lead to a transition where the constituents of the complex are placed on the repulsive wall of the ground state potential energy surface leading to translational excitation of the species. Such behavior has been reported for F atoms in rare gas solids[6] and we have observed such behavior for XeO complexes.[3] We have also observed this behavior for H atoms and discuss results in this area in this report.

Experimental

The experimental apparatus used in these studies has been reported on in detail previously.[3,4,7,8] The output of an ArF or KrF excimer laser is used to photolyze HBr. The 193 nm output of this laser is also used to excite H atom - xenon exciplexes. These exciplexes have been reported to have an Xe_2H structure, analogous to the Rg_2X structure of rare gas - halogen exciplexes.[6] Pulses of approximately 10 mj/cm^2 are used to photolyze the samples. Significantly reduced energy pulses are used to probe the H atom concentration via Xe_2H emission when it is probed independently of the photodissociation process. The output of a XeF excimer laser is used to probe Br atom concentrations by exciting Xe_2Br emission. The exciplex emission produced upon matrix irradiation, is viewed by a gated optical multichannel analyzer (OMA) (Princeton Instruments

model IRY700) attached to an ISA HR-320 monochromator equipped with a 300 grooves/mm grating blazed at 600 nm. The gate width of the OMA is set to be significantly longer than the fluorescence decay time. The output from the OMA is thus the integrated fluorescence signal over the entire duration of fluorescence which is normalized by the excimer laser energy. In some experiments a phototube is used in place of the OMA.

Results and Discussion

Figures 1, 2, and 3 are of Xe_2H emission produced by irradiating matrices with 7.0 mj/cm^2 ArF laser pulses. Figure 1 is for a matrix that has an approximately 1:100,000 HBr:Xe composition. Since HBr is a very "sticky" gas it was very difficult to make up reproducible mixtures at high dilution. Thus the concentration of a mixture was judged by the relative intensity of the Br atom exciplex emission at a point corresponding to complete photolysis. This emission has been shown to be linear in Br atom concentration.[4] The inset to the Figure is a plot of log $((I_M-I)/I_M)$. The linearity of this plot implies that the data in Figure 1 follows kinetics that are first order in HBr concentration. The matrix in Figure 2 has a composition of 1:10,000 HBr/Xe and the matrix in Figure 3 has a composition of 1:800 HBr/Xe.

Emission from Xe_2Br exciplexes, which can be observed subsequent to photolysis of HBr containing xenon matrices, has already provided an interesting picture of the dynamics of atom motion in condensed phase rare gases.[3] In very dilute matrices the Br atom concentration grows exponentially with the number of laser pulses. This is what is expected for a simple photolysis process which produces non-reactive photofragments. This process can be represented by equation 1.

$$HBr + h\nu_{193/248} \rightarrow H + Br \tag{1}$$

In more concentrated matrices the kinetics of formation of Br atoms changes and becomes second order in the HBr concentration. Similarly the loss of HBr is second order in the HBr concentration. It has been shown that the minimal set of kinetic equations that describes the processes taking place in the system is:[4]

$$
\begin{aligned}
HBr + h\nu_{193/248} &\rightarrow H + Br & k_\theta &= I\sigma_{HBr/\lambda} & (2)\\
H + HBr &\rightarrow H_2 + Br & k & & (3)\\
H + Br &\rightarrow HBr & k & & (4)\\
H + H &\rightarrow H_2 & k & & (5)
\end{aligned}
$$
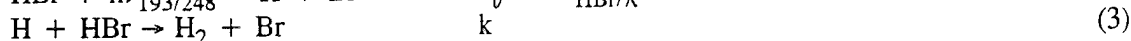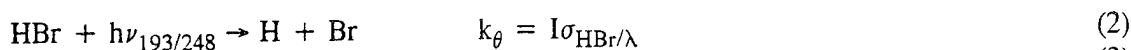
In this formulation I is the laser pulse intensity in photons/cm^2/sec and σ is the effective absorption cross-section in cm^2. As discussed previously in detail,[4] σ can be written as $\sigma_1\phi_1$ where σ_1 is the intrinsic absorption cross-section and ϕ_1 is the cage exit probability.[3] Based only on Br atom data it was not possible to obtain information on the rate constants for equations 3-5 and the rate constants for these equations were assumed to be the same since each reaction is expected to be limited by the mobility of the H atom reactant.

Figure 1: A plot of exciplex emission intensity versus number of ArF laser pulses for an approximately 1:100,000 HBr:Xe matrix at 10 K. The inset is a plot of the log of $(I_m-I)/I_m$ versus number of laser pulses

Figure 2: A plot of exciplex emission intensity versus number of ArF laser pulses for a 1:10,000 HBr:Xe matrix at 10K.
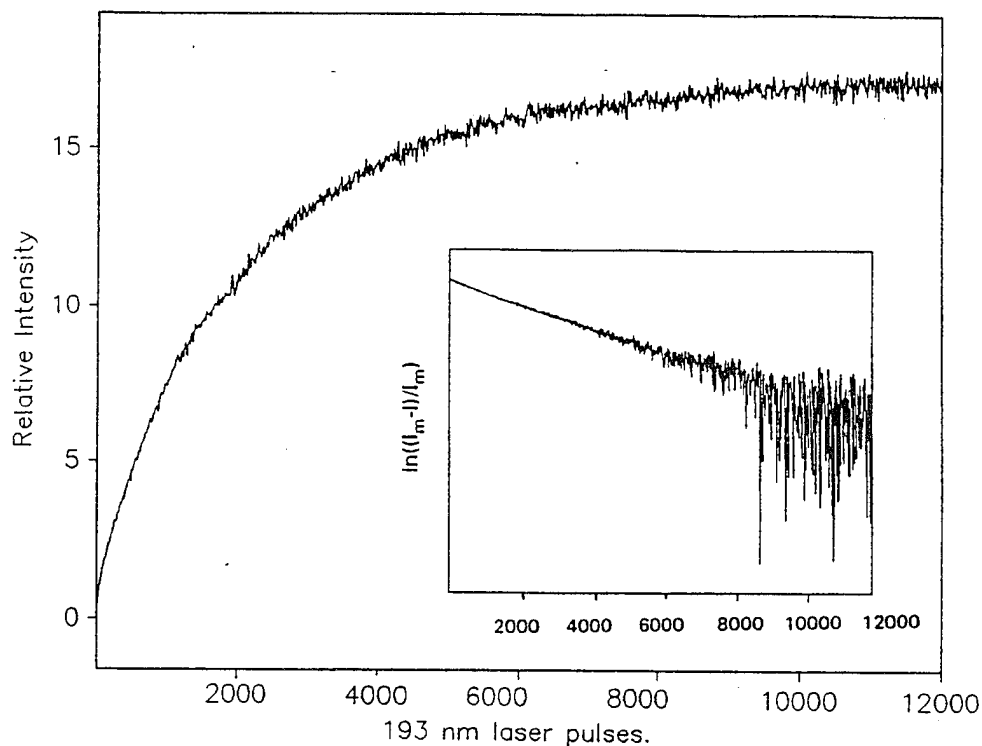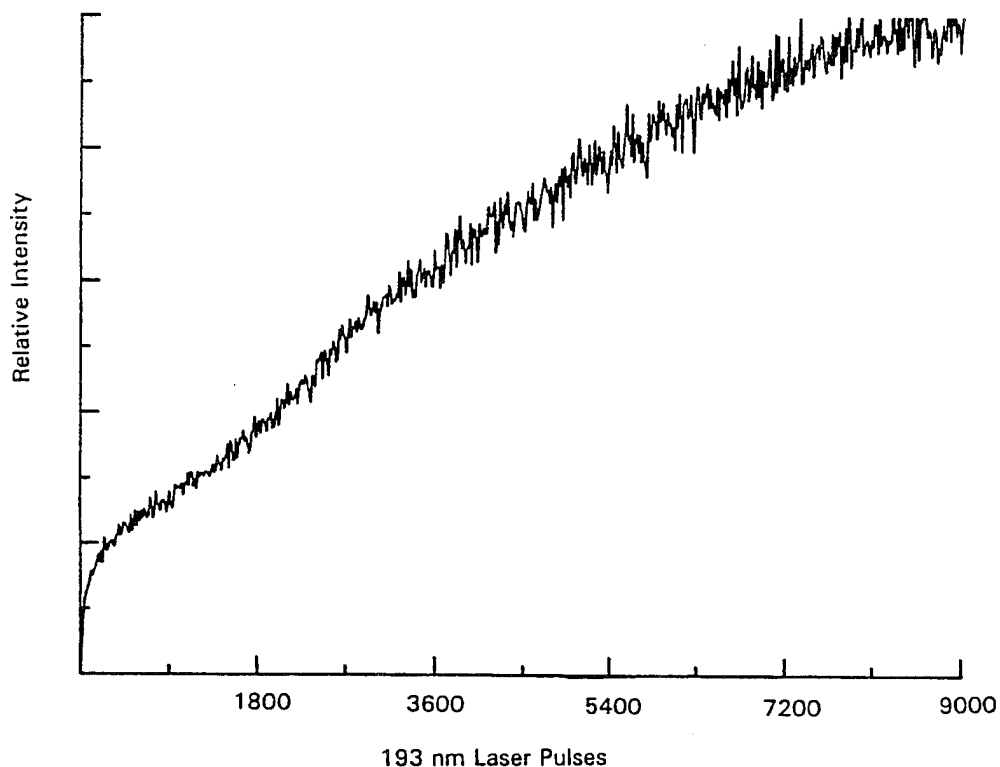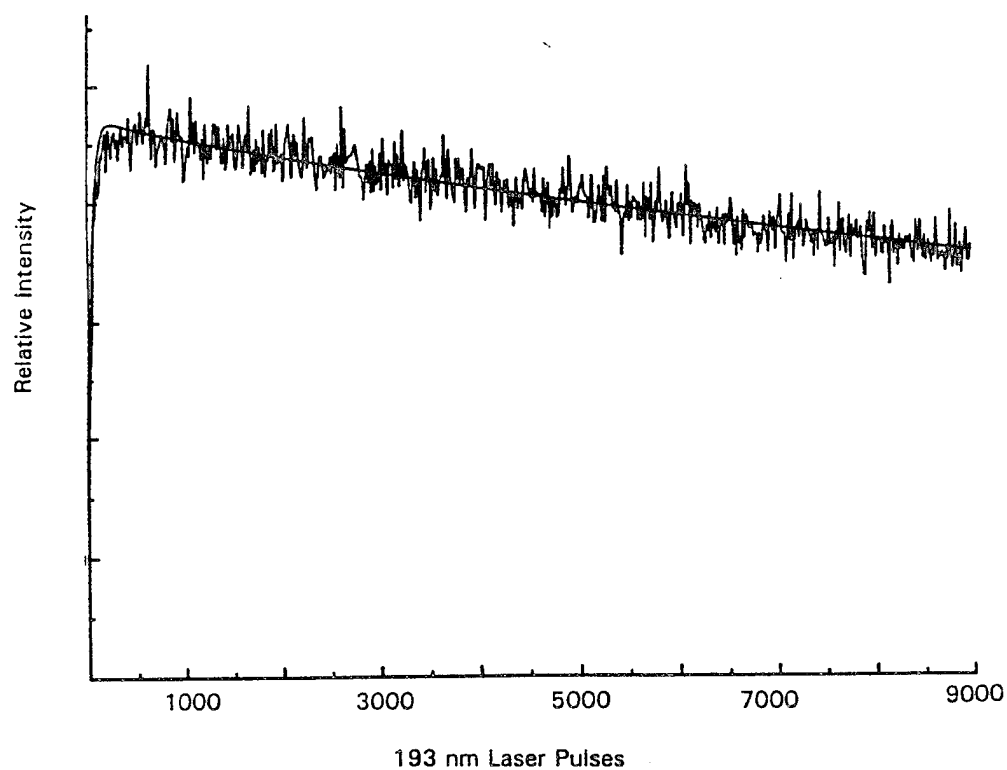
Figure 3: A plot of exciplex emission intensity versus number of ArF laser pulses for a 1:800 HBr:Xe matrix
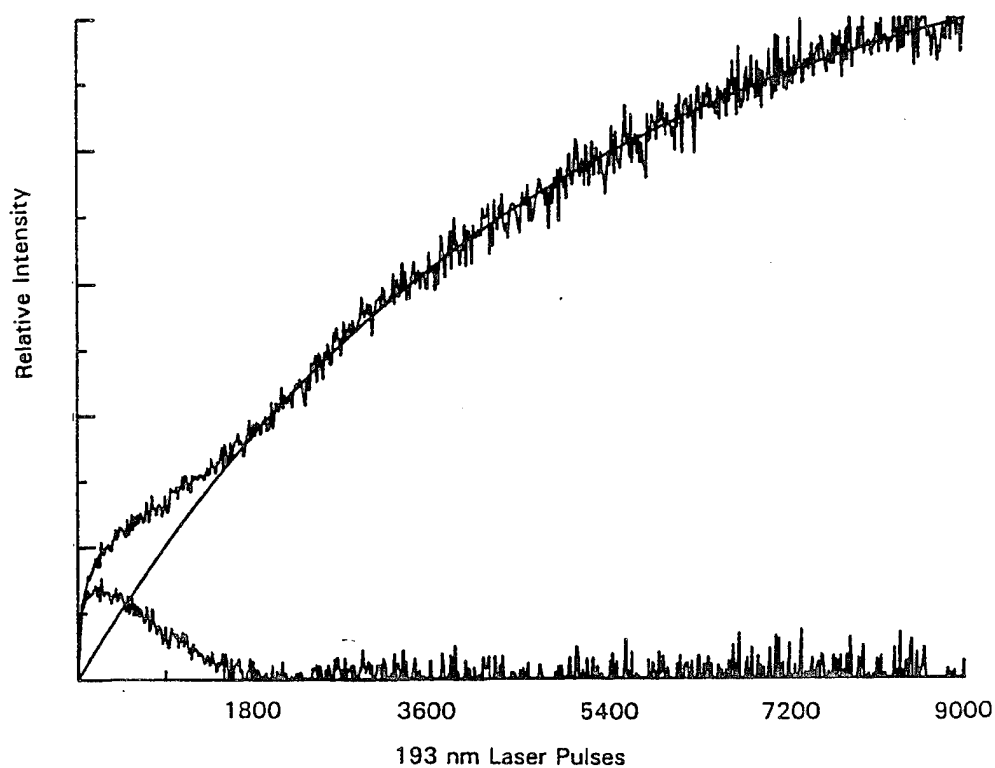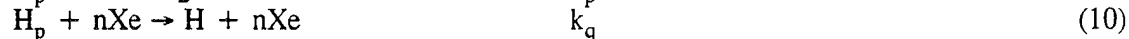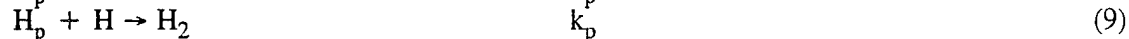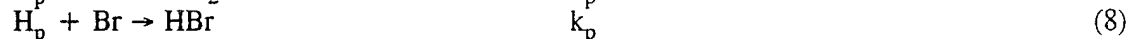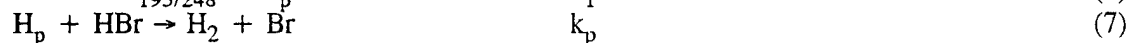

Figure 4: A fit of the data for the 1:10,000 matrix shown in Figure 2 to an exponentially growing signal and a residual.

The availability of data on H atom loss kinetics and concentrations provides more detailed information about the dynamics of H atom motion in this system. As expected, and as shown in Figure 1, in dilute matrices the H atom concentration also evolves with first order kinetics. For a 1:100,000 matrix the mean distance between reaction centers (HBr molecules) is large enough that the probability of a photolytically generated H atom reaching a potential reactant is small. Under these circumstances first order generation of H atoms is expected and observed.

As the HBr concentration becomes more concentrated the distance between H atoms and prospective reactants decreases and the probability of reactive loss of H atoms increases. The data for the 1:10,000 HBr:Xe matrix demonstrates this. In this data, which is shown in Figure 4, deconvoluted into a first order component and a residual, there is an ensemble of HBr molecules that have a large enough mean distance between them that reaction is unlikely. There is another component to the HBr population with a mean spacing such that reaction becomes likely.

As the concentration increases further, the probability of reaction of a photogenerated H atom increases. By the time the concentration reaches 1:800, greater than 99% of the initially generated H atoms react. The kinetics of this system can be modeled over this range of concentrations using a set of differential rate equations. The model was evaluated for Br atom data as well as H atom data. A simultaneous fit to these two sets of data over the indicated concentration range required the following set of equations.

$$HBr + h\nu_{193/248} \rightarrow H_p + Br \qquad \sigma_1 I \qquad (6)$$
$$H_p + HBr \rightarrow H_2 + Br \qquad k_p \qquad (7)$$
$$H_p + Br \rightarrow HBr \qquad k_p \qquad (8)$$
$$H_p + H \rightarrow H_2 \qquad k_p \qquad (9)$$
$$H_p + nXe \rightarrow H + nXe \qquad k_q \qquad (10)$$
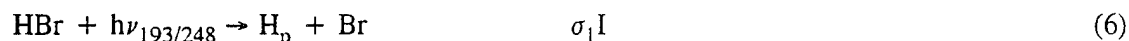
where H_p denotes H atoms mobilized by the photodissociation of HBr. In this development I is the laser fluence (photon/cm^2 pulse) and $\sigma_1 = \sigma_1' \varphi_1$ where σ_1' is the uv absorption cross-section of HBr and φ_1 is the cage exit probability. k_p is the rate constant for reaction of H_p and k_q is the rate constant for translational quenching of the H_p.

A loss mechanism involving mobilization of H atoms as a result of exciplex relaxation is included as follows:

$$H + 2Xe + h\nu_{193} \rightarrow Xe_2H \rightarrow H_e + 2Xe \qquad \sigma_2 I \qquad (11)$$
$$H_e + HBr \rightarrow H_2 + Br \qquad k_e \qquad (12)$$
$$H_e + Br \rightarrow HBr \qquad k_e \qquad (13)$$
$$H_e + H \rightarrow H_2 \qquad k_e \qquad (14)$$
$$H_e + nXe \rightarrow H + nXe \qquad k_{qe} \qquad (15)$$
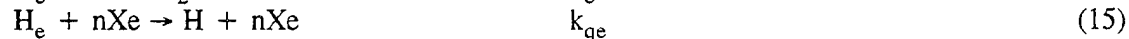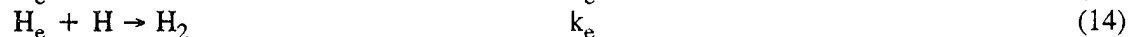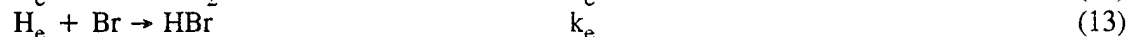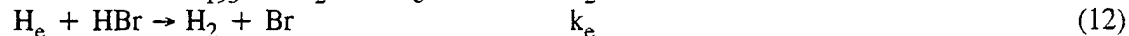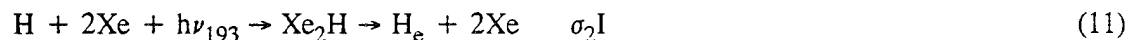
where $\sigma_2 = \sigma_2' \varphi_2$; σ_2' is the exciplex absorption cross-section and φ_2 the cage exit probability on exciplex relaxation and where H_e denotes H atoms mobilized by exciplex relaxation. The details of this kinetic model which provide information about the range of H atom motion in matrices will be elaborated on in a forthcoming publication.[8] Briefly H atom motion is observed to be on the order of 100 Å and there is evidence that the existence of impurity molecules (HBr) can effect the local morphology of the matrix which in turn effects photodissociation cross-sections, presumably through cage exit probabilities, and atom mobilities.

311

References

1.   M. E. Jacox in <u>Chemistry and Physics of Matrix-Isolated Species</u>, L. E. Andrews and M. Moskovits eds., (Elsevier, Amsterdam, 1989).

2.   For example, B. Brocklehurst and G. C. Pimentel, J. Chem. Phys. **36**, 2040 (1962); J. Fournier, C. Lalo, J. Deson and C. Vermiel, J. Chem. Phys. **66**, 2656 (1977); R. N. Perutz, Chem. Rev. **85**, 77 (1985).

3.   E. T. Ryan and Eric Weitz, J. Chem. Phys. **99**, 8628 (1993).

4.   Dwayne LaBrake, E. Todd Ryan and Eric Weitz J. Chem. Phys. **102**, 4112 (1995).

5.   M. E. Fajardo and V. A. Apkarian, J. Chem. Phys. **96**, 5660 (1986).

6.   R. Alimi, R. B. Gerber and V. A. Apkarian, Phys. Rev. Letters **66**, 1295 (1991).

7.   E. T. Ryan and E. Weitz Chemical Physics **189**, 293, (1994).

8.   D. LaBrake, E. T. Ryan and E. Weitz - manuscript in preparation.

THEORY OF LASER INDUCED FLUORESCENCE LINESHAPES: APPLICATIONS TO DOPED CRYOGENIC CLUSTERS[†]

J. D. Mills and P. W. Langhoff

Department of Chemistry
Indiana University
Bloomington, IN 47405-4001

and

Emerging Technology Branch
Phillips Laboratory - OLAC PL/RKFE
Edwards AFB, CA 93523-5000

ABSTRACT

Cross sections are derived from the general (two-photon) Kramers-Heisenberg expression for the electronically inelastic resonant scattering of polarized radiation from a homogeneous isotropic ensemble of doped quantum or classical clusters. Scattered intensities differential in energy, angle and polarization are reported for cases in which the resonant intermediate states in a single doped cluster are homogeneously broadened by (delocalized) electronic band or surface states, (localized) trap or bubble states, or other mechanism giving rise to intrinsic continuum states. Circumstances in which complex (Fano-like) lineshapes in scattering energy can arise are identified, and conditions leading to their observation in the presence of inhomogeneous broadening are described. Comparisons are made with standard two-step interpretations of the resonant inelastic scattering event, in which case the measured LIF signal is proportional to one-photon absorption. Selected applications illustrate possible two-photon, coherent, and homogeneous broadening contributions to the excitation and emission spectra of cryogenic clusters doped with metal radicals, which heretofore have been interpreted largely in the absence of such effects.

Thermoluminescence Studies of N/N$_2$ Condensates

Formed on Liquid Helium II

M.E. DeRose, Y.K. Bae, C.W. Larson, C.R. Brazier and M.E. Fajardo

U.S. Air Force Phillips Laboratory

OL-AC PL/RKS

10 East Saturn Blvd.

Edwards AFB, CA 93524-7680

Abstract

We are examining issues arising from the production, handling, and storage of free radical doped cryogenic solid High Energy Density Matter (HEDM). Currently under investigation is the possible existence of the so-called "Impurity Helium Solid Phase" (IHSP) reported by Gordon et al.[1-3] The IHSP was reported to have at least 2 - 8 % mole percent of atomic impurities which solidify liquid He at 1 atm, and was proposed by Gordon et al. to be composed of clusters with polarizable heavy impurity cores coated by He atoms. We report here our progress to date, including the formation of gram quantities of an N/N$_2$/He condensate formed by deposition of N$_2$/He mixtures discharged in a corona excited supersonic expansion (CESE) source onto the surface of liquid He II, and thermoluminescence studies of the condensates.

Introduction

One proposed High Energy Density Matter (HEDM) concept is the trapping of atomic and molecular species in cryogenic solid hydrogen. Calculations show that adding 5 mole percent energetic atoms or molecules to solid hydrogen can increase the specific impulse (I_{sp}) of the propellant significantly.[4] For example, when 5 mole percent diatomic boron molecules are trapped in solid hydrogen, the calculated I_{sp} increases from 389 seconds (for undoped solid hydrogen) to 492 seconds, an increase of 103 seconds, or 26%, in I_{sp}. In the current stage of these experiments, we are concerned with the production of homogeneous samples of a "model" HEDM made up of a mixture of atomic and molecular nitrogen, characterization of the samples, and handling of the samples. Preliminary successes include the deposition of bulk samples of our model HEDM into superfluid helium.

We are also attempting to reproduce the work of Gordon *et al.* who reported the discovery of a metastable solid phase of helium, the Impurity Helium Solid Phase (IHSP), "consisting mainly of helium atoms and [staying] nevertheless stable and solid out of liquid helium and at temperatures above the helium critical point".[2] Our preliminary experiments verify several of Gordon's experimental observations.

Experiment

A schematic diagram of the apparatus for these experiments is shown in Figure 1. The cryostat is made up of a large (approximately 20 l) liquid helium chamber surrounded by vacuum and liquid nitrogen shields with removable bottom tails. There is a large stainless steel funnel inside the chamber with a 12 mm inside diameter Pyrex tube at the bottom where the sample collects, and through which the deposition and thermoluminescence can be monitored. Underneath the copper bottom plate of the liquid helium chamber is a heater which is used to boil off the liquid helium and to warm the sample; under this same plate and also under the liquid nitrogen shield are silicon diode temperature sensors. A sensor probe enters the cryostat from the top and can be placed directly into the sample region. This probe consists of a silicon diode temperature sensor and fiber optic cables that direct emission to a photodiode detector and photomultiplier tube and which can also be

315

used to manipulate the samples. The corona excited supersonic expansion (CESE) source enters in through one of the top ports of the cryostat and has been described elsewhere[5] with our only change being to lengthen it to approximately 94 cm. A pinhole at the end of the source with a diameter of 90-95 μm seems to work best in this application.

Once the cryostat has been filled with liquid helium, the helium is pumped on to obtain superfluid helium. Samples are produced by expanding a mixture of approximately 1:50 N_2:He through the CESE source. A current of 3 mA @ 3 kV bias through the CESE source serves to dissociate a portion of the N_2 molecules and to excite the product species. The expanded gas is deposited onto the superfluid helium surface where it solidifies and sinks. The solid product is funneled into the glass sample tube. When the deposition is complete, the liquid helium is boiled off and the sample is warmed. Thermoluminescent emission is monitored through the optical ports on the side of the cryostat with CCD video cameras and an optical multichannel analyzer (OMA); temperature and light intensity are recorded through the sample probe.

Results

Within seconds from starting the CESE source, glowing-green sample particles can be observed as they fall slowly through the liquid helium and into the sample tube. The particles have a feathery appearance but can be manually compacted with the sensor probe discussed above or by a nylon rod coming down from the top of the cryostat. At temperatures between 2.2K and 4K, the samples display only a very faint green thermoluminescence. However, after the liquid helium is boiled off and the samples are warmed above 4K, they glow brightly and occasional intense flashes are observed. The flashes propagate through the sample with an apparent velocity of about 10 cm/sec and are often so intense that the cameras and OMA are saturated. The flashing normally occurs between 5K and 7K, but the exact temperature depends on experimental conditions such as sample preparation, heating rate, etc. For example, flashing was observed for all samples

heated at rates of 15 K/hr or faster, but samples heated at 5 K/hr did not flash. The flashing can also be induced by friction such as compressing the sample with the nylon rod.

Figure 2 shows a low resolution spectrum of emission intensity vs. wavelength taken with the OMA of N/N_2 deposited in superfluid liquid helium. The spectrum was taken during sample warm-up at a temperature roughly estimated to be 20K. As can be clearly seen, the N atom emission near 522 nm is the strongest. The molecular emissions appear to originate from fewer excited vibrational levels than seen in traditional N/N_2 matrix studies.[6] The atomic and molecular oxygen emissions are most likely due to air contamination.

Figure 3a shows a phosphorescence spectrum of solid N/N_2 particles during a deposition. The N atom emission between 520 and 526 nm probably arises from excited $N(^2D)$ atoms produced in the discharge, as this emission decays with a lifetime of approximately 30 sec following shutdown of the CESE source. The emission lineshape shows a prominent peak near 521 nm, consistent with Gordon's observations of IHSP samples[3] but in sharp contrast to emissions recorded from conventional N/N_2 matrices.[7]

Figure 3b shows intensity vs. wavelength for a "dry" (meaning the liquid helium has been boiled away) N/N_2 sample at $\approx$ 8K before a flash. This spectrum also resembles that of Gordon's emission spectrum of the nitrogen IHSP.[3] Figure 3c shows intensity vs. wavelength for the same "dry" sample as in figure 3b but after a flash. The peak near 521 nm has almost completely disappeared, and the 523 nm peak is now the strongest. This spectrum more closely resembles the emissions recorded from N/N_2 matrices produced by traditional deposition methods.[7] An example of such a spectrum is shown in Figure 3d, which we recorded in a separate apparatus at roughly 3.6K.

Discussion

Thermoluminescence from N/N_2 matrices is usually explained by the following mechanism:

Detrapping: $$N(^4\Sigma)_{trapped} \xrightarrow{\Delta} N(^4\Sigma)_{mobile}$$

Recombination: $$N(^4S) + N(^4S) \rightarrow N_2(A\,^3\Sigma_u^+) + \Delta E$$

Exciton Movement
in N_2 matrix: $$N_2(A\,^3\Sigma_u^+) + N_2(X\,^1\Sigma_g^+) \rightarrow N_2(X\,^1\Sigma_g^+) + N_2(A\,^3\Sigma_u^+)$$

Energy Transfer: $$N_2(A\,^3\Sigma_u^+) + N(^4S) \rightarrow N_2(X\,^1\Sigma_g^+) + N(^2D) + \Delta E$$

Matrix Perturbed Radiation: $$N(^2D) \rightarrow N(^4S) + h\nu \;(\sim 522\ nm) + \Delta E$$
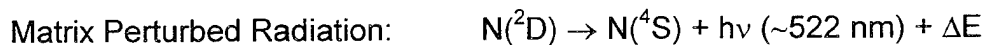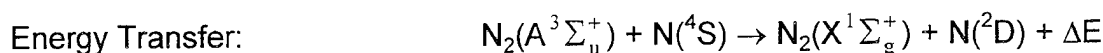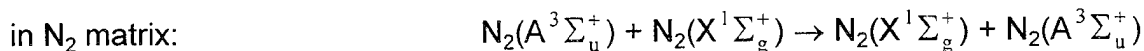
The kinetics of this mechanism is usually discussed in the context of a slowly and uniformly heated thin film sample that is thermally anchored to a much larger substrate. However, the recombination, energy transfer, and radiative steps all involve dissipation of excess energy into the matrix surroundings. Thus, "dry," unsupported N/N_2 condensates can become locally overheated, further increasing the N atom detrapping rate, and ultimately leading to runaway kinetics and the observed "flashing" phenomenon.

Gordon's group has additionally reported the simultaneous flashing and "vaporization" of their nitrogen IHSP samples at T $\approx$ 8.5K,[1] and have interpreted this as evidence for a "phase transition" in the IHSP material. We have produced samples that have undergone partial melting during a flash event, but have never observed the disintegration of a sample. Further, the temperature at which flashing occurs seems to be strongly dependent on sample preparation and heating rate, with slowly heated samples never exhibiting any runaway processes. Thus, we remain unconvinced that the flashes and vaporization of IHSP represent true phase transitions.

Gordon's most convincing evidence that the IHSP samples represent a novel material is the difference in spectral lineshape of the N atom emission between the IHSP and N/N_2 samples, particularly the anomalous intensity of the 521 nm

component. The $N(^2D) \rightarrow N(^4S)$ is both spin and electric dipole forbidden, and the matrix induced perturbations that help break these symmetry rules also alter the transition energies. Hence, the N atom emission lineshape is strongly dependent on the local matrix environment, leading to a pronounced temperature dependence in N_2 matrices[7], and to qualitatively different lineshapes for N atoms trapped in different rare gas matrices. The change in $N(^2D) \rightarrow N(^4S)$ emission lineshape observed following a bright flash thus represents a change in the local environment of the emitting N atoms, and may well be due to the destruction of an IHSP fraction in our samples.

Summary

We have produced gram-quantity N/N_2 condensates by depositing a mixture of atomic and molecular nitrogen discharged in a corona excited supersonic expansion source onto a surface of superfluid helium. The condensates have been spectroscopically investigated and the high-resolution thermoluminescence spectra of the $N(^2D \rightarrow {}^4S)$ line before and after flash events are considerably different from each other, in agreement with the observations by Gordon *et al.* However, we did not observe the disintegration of the samples upon warming as reported by Gordon.

Future plans are to study the transportation of the solid samples from a 4K environment to a room temperature storage chamber, to characterize the CESE source products in detail, and to perform calorimetry studies on the solid samples.

References

1. E.B. Gordon, V.V. Khmelenko, A.A. Pelmenev, E.A. Popov, and O.F. Pugachev, *Chem. Phys. Lett.* **155**, 301 (1989).
2. E.B. Gordon, V.V. Khmelenko, A.A. Pelmenev, E.A. Popov, O.F. Pugachev, and A.F. Shestakov, *Chem. Phys.* **170**, 411 (1993).
3. R.E. Boltnev, E.B. Gordon, V.V. Khmelenko, I.N. Krushinskaya, M.V. Martynenko, A.A. Pelmenev, E.A. Popov, and A.F. Shestakov, *Chem. Phys.* **189**, 367 (1994).
4. P.G. Carrick, in Proceedings of the High Energy Density Matter (HEDM) Contractors Conference, PL-CP-93-3041, ed. by T.L. Thompson (USAF Phillips Laboratory, Edwards AFB, CA, 1993).
5. A.T. Droege and P.C. Engelking, *Chem. Phys. Lett.* **96**, 316 (1983).
6. M.E. Fajardo, S. Tam, T.L. Thompson, and M.E. Cordonnier, Chem. Phys. **189**, 351 (1994).
7. O. Oehler, D.A. Smith, and K. Dressler, *J. Chem. Phys.* **66**, 2097 (1977).
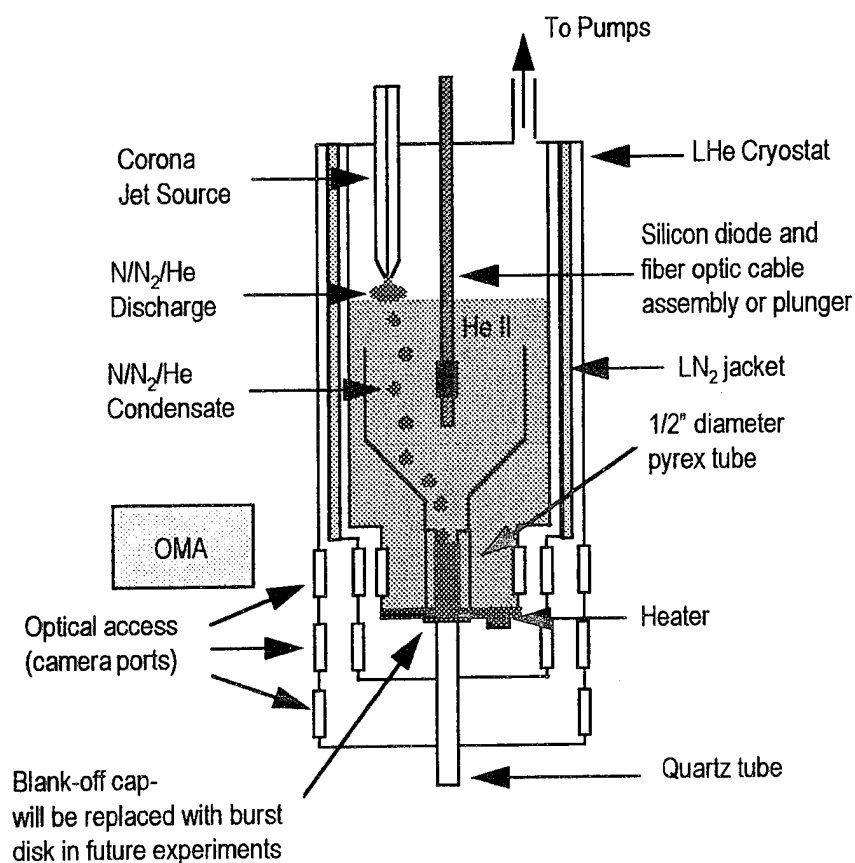
Figure 1. Experimental apparatus for slush cryostat. Diagram is not to scale.
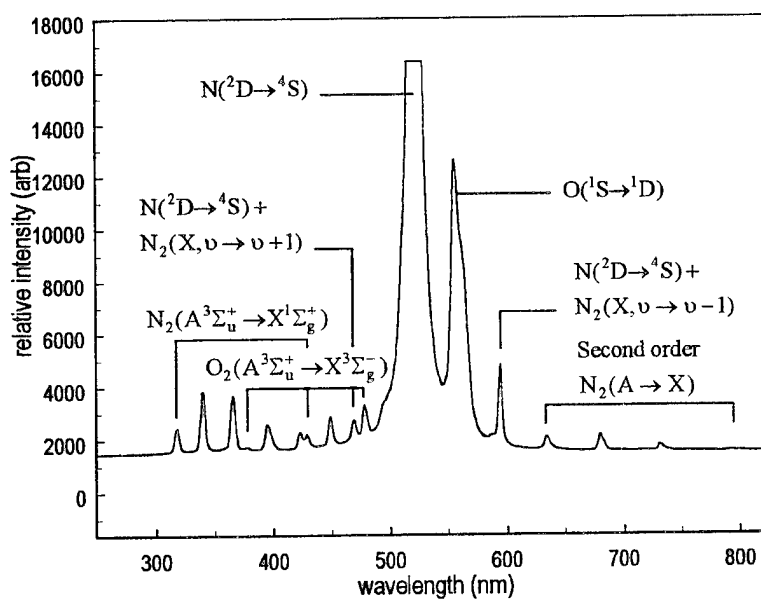
Figure 2. Low resolution emission spectrum taken during sample warmup. The sample temperature was approximately 20K.
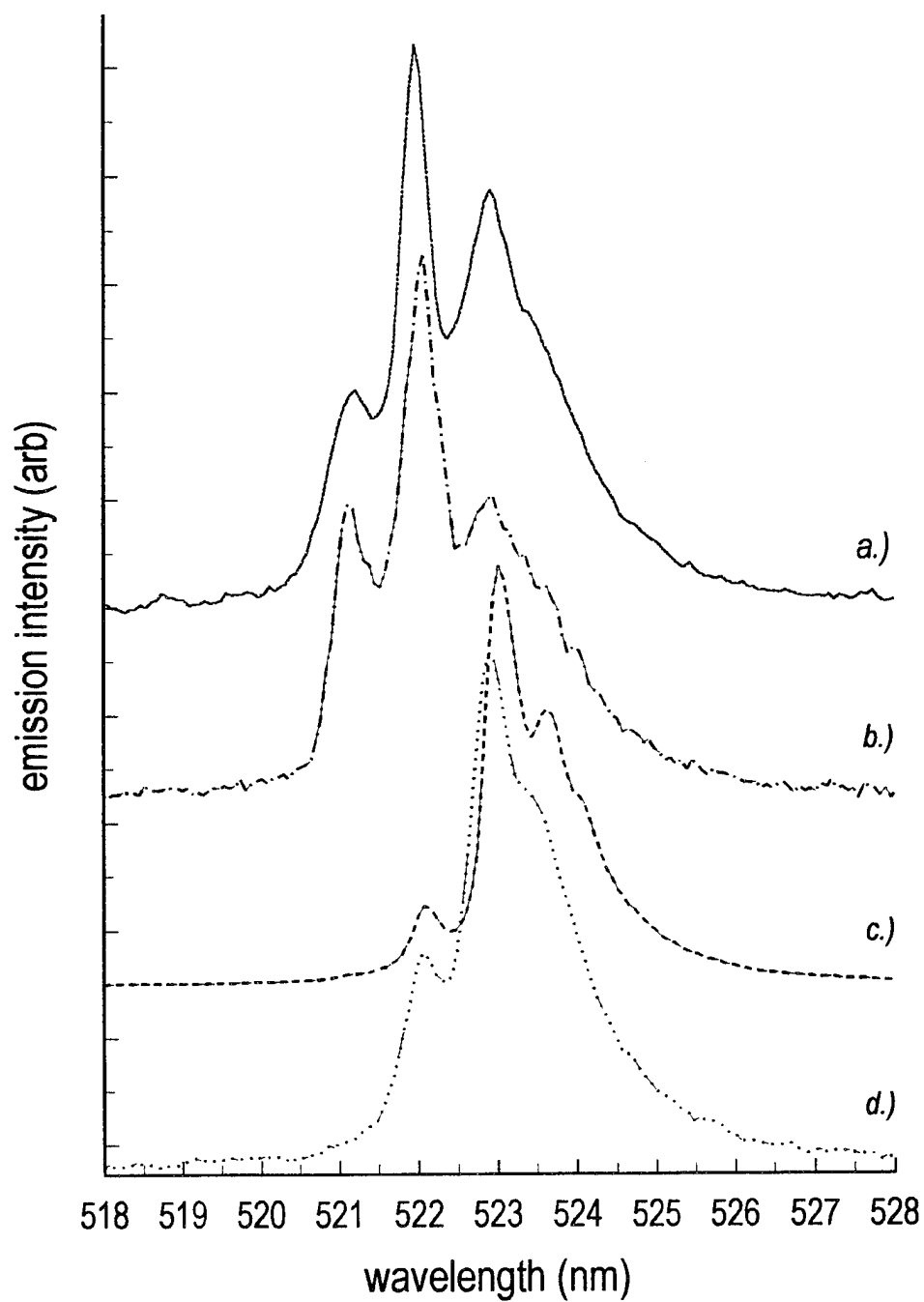
Figure 3. Emission spectra of N/N_2 condensates a.) during deposition, b.) before a flash, c.) after a flash, and d.) N/N_2 matrix.

APPARATUS FOR MEASUREMENTS OF THE THERMAL PROPERTIES OF METAL ATOM-DOPED SOLIDS AT LOW TEMPERATURES

K.S. Ketola, W. Homsi, H.J. Maris, G.M. Seidel

Department of Physics, Brown University, Providence, Rhode Island 02912

I. Overview of Experimental Program

An apparatus is being constructed to measure the specific heat and thermal conductivity of thin films of cryogenic solids containing metal atoms. We will focus our investigations first on solid molecular para hydrogen doped with impurity atoms such as lithium, beryllium, boron, or carbon. The films will be prepared by depositing hydrogen from the vapor onto a substrate held at a temperature below 2 K, while the impurity atoms are co-deposited by laser ablation. Characterization of the films will be carried out using several different experimental probes. The film thickness will be determined by optical interferometry and by a quartz crystal oscillator. Optical transmission measurements will provide information regarding the concentration of metal atoms in the film. The magnetization of the film, as determined by a SQUID magnetometer, can also be used to obtain the concentration of metal atoms. Once the film is prepared and characterized, then the measurements of the thermal conductivity and the specific heat will be made over a temperature range 0.4-3.0 K using the ac technique. Below, we briefly discuss the motivations for doing these experiments, the fundamental goals of the research, and some details of the apparatus and measurement techniques.

II. Motivations and Goals

There is much current interest in the use of solid hydrogen doped with impurity atoms, as a high energy-density material. Knowledge of the thermal properties may be useful in the effort to utilize these materials.

Another motivation is to learn more about the mechanisms underlying the universal behavior of disordered materials. The thermal properties of almost all disordered materials exhibit common features which are very different from those of crystalline materials. The specific heat of disordered materials varies linearly with temperature below 1 K, in contrast to the T^3 dependence of crystalline materials. Also, the thermal conductivity κ of disordered materials is greatly reduced compared to that of crystalline dielectrics and varies with temperature in a qualitatively different way. Below 1 K, κ varies approximately as T^2. Between about 1 K and 10 K, there is a plateau region where κ becomes independent of temperature. Above the temperature range of the plateau region, the thermal conductivity steadily increases all the way up to room temperature.

Some understanding of the thermal properties of disordered materials is provided

by the "two-level" system (TLS) model. This phenomenological theory posits that in any disordered solid there will be atoms or groups of atoms which can tunnel between two configurations of nearly the same energy and that the height of the barrier between the two configurations and the difference in energy of the two states are random quantities distributed over some range of values. The TLS model is able to explain the linear term in the specific heat and the T^2 dependence of the thermal conductivity. However, the nature of the units that compose the two-level systems is not known. Another question is: why do these objects exist with roughly the same characteristics in a very broad range of disordered materials? Also, what is the explanation for features such as the thermal conductivity plateau?

Solid hydrogen doped with impurity atoms represents a novel disordered system with properties outside of the normal range of most other disordered materials, since the system should be highly disordered and quantum effects are important. It will be of interest to see how the thermal properties of the doped H_2 films differ from those of other disordered materials. This should help to provide answers to the many questions surrounding the nature of these materials.

III. Apparatus

The doped H_2 films will be produced and studied within a common-vacuum dewar which has both liquid helium and liquid nitrogen reservoirs (see Figure 1). Optical access to the experimental region is obtained via windows which are in the room temperature, 77 K, and 4 K tail sections of the dewar. The cryostat insert, which has been completed from the room temperature section down to just below the 4 K plate, will be placed inside the dewar as shown in Figure 1. The experimental cell will be placed within the 4 K tail section and will be mounted to the 4 K plate. Electrical leads and the various gases required for the experiment and the refrigeration will be carried from room temperature into the experimental region via the stainless steel tubes of the upper part of the cryostat. The experimental cell has been constructed from a 4.5 inch diameter thin wall stainless steel tube which is 5 inches in length. There are seven optical access ports which have been welded to the 4.5 inch diameter tube, spaced 45 degrees apart around the circumference and halfway along the length of the tube (see Figure 2). There is also an eighth port on the circumference which could be used to mount the deposition cell (see later discussion). Each of the seven optical ports consist of a 1 inch diameter steel tube which has a flange welded to the end so that a window can be sealed into place using an indium o-ring seal. There are also indium o-ring flanges welded to ends of the 4.5 inch diameter tube so that top and bottom plates can be attached. There will be electrical feedthroughs on the top plate as well as tubes to bring hydrogen into the cell for deposition and helium for thermalizing the impurity atoms before they reach the substrate (see later discussion).

A schematic depiction of the apparatus for doing the experiment is shown in Figure 3. The main cell described above is at the center of Figure 3. A deposition cell will also be constructed, which can then be placed at either the bottom, as shown in Figure 3, or the side of the main cell. The deposition cell will consist of a copper ring with a window mounted to one end of the ring and the deposition substrate mounted to the other end, using a low thermal conductivity glue. The interior of the
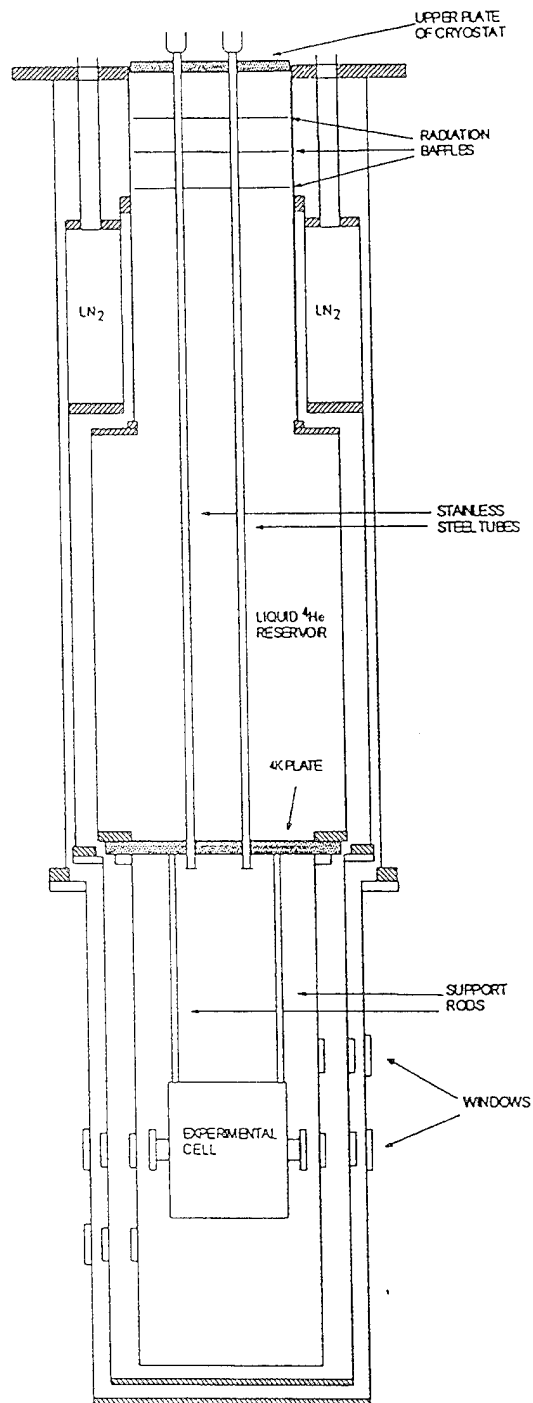
Figure 1: Cross-sectional view of the experimental dewar and parts of the cryostat insert. The upper plate of the cryostat is shown as well as the 4 K plate at the bottom of the liquid helium reservoir. For simplicity, only two of the thin-walled stainless steel tubes of the cryostat are shown. The experimental cell is supported from the 4 K plate.

SIDE VIEW

INDIUM O-RING FLANGE
FOR SEALING WINDOW
TO PORT

INDIUM O-RING FLANGE
TO ALLOW FOR MOUNTING
OF DEPOSITION CELL
ON THE SIDE OF THE CELL

INDIUM O-RING FLANGE FOR
SEALING BOTTOM PLATE TO CELL
(THERE IS ANOTHER FLANGE AT
THE TOP OF THE CELL)

TOP VIEW

DIAMETER=4.5 IN.
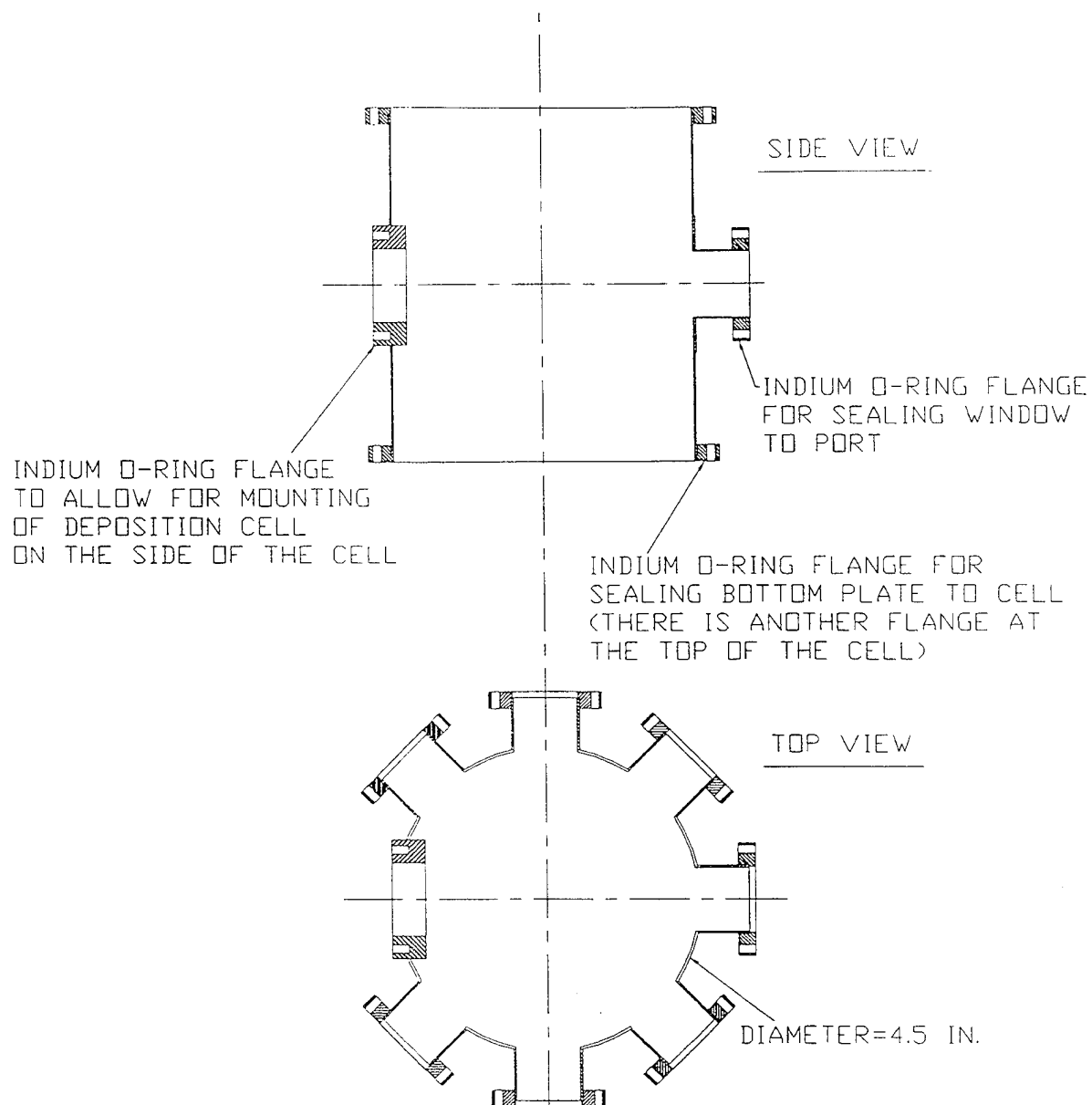
Figure 2: Cross-sectional views of the stainless steel cell. Figure 1 shows how the cell will be oriented within the dewar.
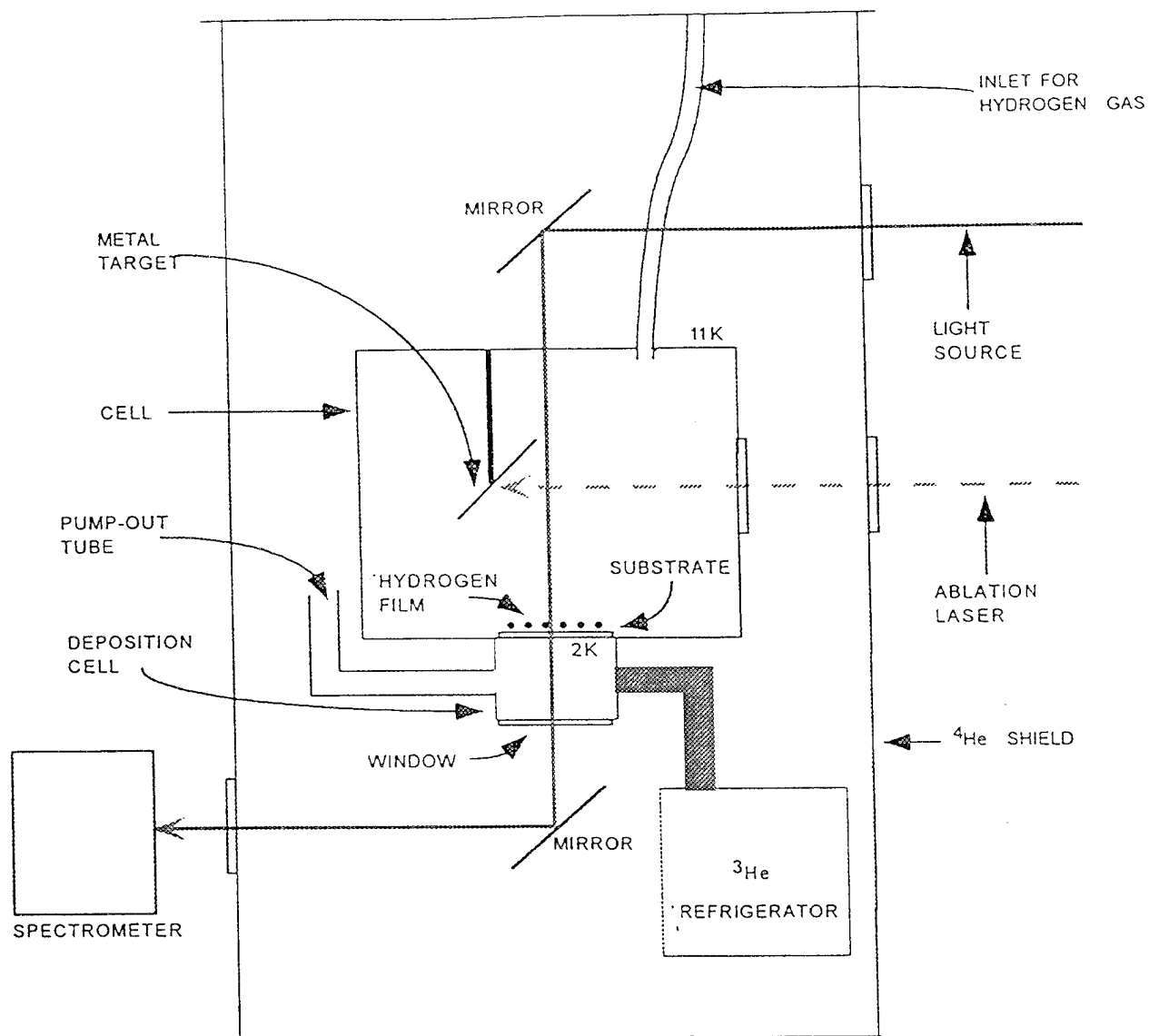
Figure 3: Schematic depiction of the apparatus. See text for discussion.

deposition cell can be filled with helium to transport heat to the refrigerator during the deposition process. When thermal isolation is required for heat capacity measurements, the helium can be removed through a pump-out tube. The ablation target and tube for carrying the H_2 gas into the cell are also shown. During the deposition process, the deposition substrate will be kept at a temperature below 2 K while the temperature at the top of the cell, where the H_2 comes in, will be kept at about 10 K. This temperature gradient will be maintained during the deposition process by having a strong thermal link between the deposition cell and the ^{3}He refrigerator, while applying heat to the top plate of the cell. The wall thickness of the cell is only 0.025 inches so as to reduce the amount of heat that will flow from the top plate to the deposition cell. Once the deposition process is complete, the heater on the top plate will be turned off and the entire cell will then come into thermal equilibrium. In order to thermalize the Li atoms which are ablated from the target, helium buffer gas at an approximate density of 10^{15} cm^{-3} will be maintained within the cell. The gas density will be adjusted so that a Li atom will undergo several collisions with helium atoms before reaching the substrate, but also so that there will be a low probability of colliding with another Li atom in the process.

IV. Measurements

The characterization of the films will obtained via several different experimental probes. As shown in Figure 3, during the deposition process, we will be able to measure optical transmission through the film using a light source and a spectrometer/CCD camera which is interfaced to a computer. This will allow us to measure the concentration of metal atoms in the film. An independent measure of the concentration will be obtained by having a SQUID magnetometer on the deposition substrate. The shift in frequency of a quartz crystal resonator placed near to the deposition substrate will provide the total mass per unit area of the deposited film. Another means of obtaining the thickness of the film is to measure the number of oscillations in the intensity of a laser beam reflected from the surface of the deposition substrate, as the film grows.

The heat capacity and thermal conductivity of the Li/H_2 films will be obtained through ac calorimetry. In this technique, a sinusoidally varying heat input is applied to the film and the amplitude and phase of the temperature variation of the system is measured using lock-in detection. By analyzing the behavior of the amplitude and the phase as a function of the frequency of the heat input, it will be possible to extract the heat capacity and thermal conductivity.

Hydrogen Bridge Bond Stabilization of Azidoborane Structures

E. Boehmer
Rockwell International Science Center
Thousand Oaks, CA 91358

EXTENDED ABSTRACT

Ring and cage structures containing boron and nitrogen are promising HEDM's due to their compact structure, large positive heat of formation and a large specific impulse boost. Production of desired structures such as B-N prismane and three membered BBN and BNN rings has so far been impossible or involved large organic protection groups, which not only add unwanted bulk and weight to the ring, but also hinder ring closures needed for the production of strained BN-ring or cage structures, e.g., B-N prismane. A unique approach to this challenge has been identified at Rockwell Science Center based on the compounds diazidoborane (DAB), tetra-azidodiborane (TADB) and the very recently discovered dimethyl-diazidodiborane.
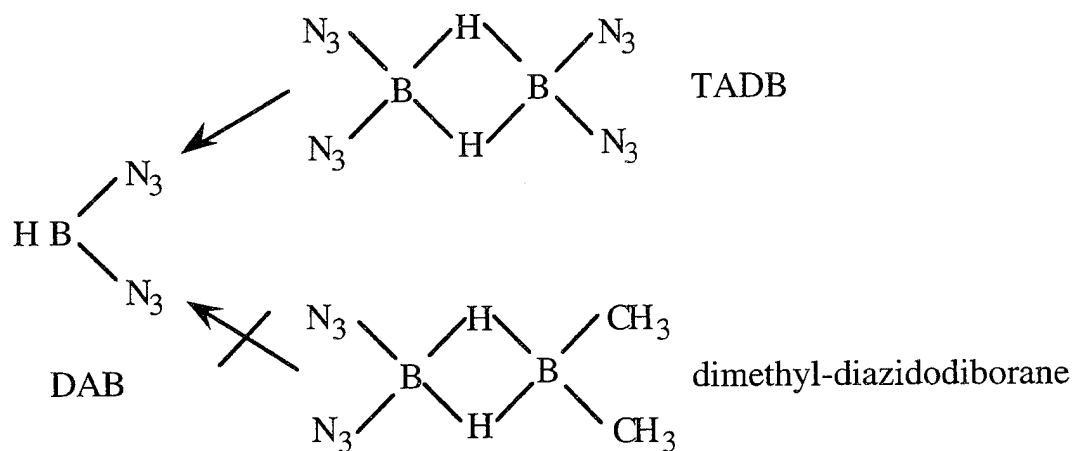
Fig. 1

In limited gas phase studies TADB and dimethyl-diazidodiborane were evaluated as BH sources for visible chemical laser purposes. The stability of

the compound and its usefulness as a BH donor was found to depend critically on the integrity of the hydrogen bridge bond during synthesis and handling. TADB decayed comparatively rapidly into DAB (poor BH source), see Fig.1. This was attributed to the four (pseudo halogens) azide groups which have an electron pulling effect that destabilizes the bridge bonds. In dimethyl-diazidodiborane two adjacent azide groups of TADB were replaced by weakly electron pushing methyl groups in a three step synthesis.

Dimethyl-diborane with two adjacent methyl groups was formed in the gas-solid reaction between dimethylbromoborane diluted in helium and $NaBH_4$, respectively, which proceeded at ~ 300 °C and 500 Torr. The methylated diborane reaction product product was readily characterized with FT-IR spectroscopy. No scrambling of methyl groups was observed, i.e., no cross methylated species was formed.

Step 1   Fig. 2
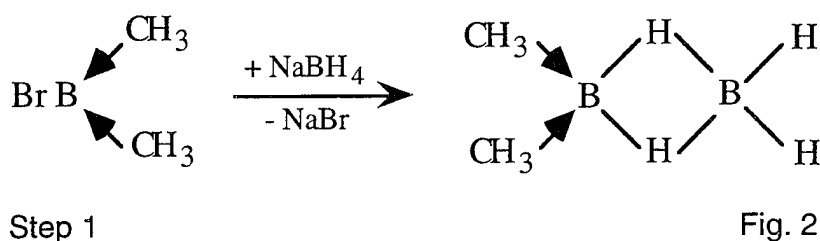
Subsequently, the two peripheral hydrogen atoms in dimethyldiborane were selectively substituted by chlorine in a gas phase reaction of dimethyl-diborane with Cl_2, and these same sites were in turn selectively replaced by azide groups in the reaction of dimethyl-dichlorodiborane with HN_3, see Fig. 3. Both reactions proceeded at ambient temperature and at 500 Torr. Under these conditions molecular chlorine attacked selectively dimethyl-diborane and HN_3 reacted exclusively with the chlorinated intermediate. Step 2 and 3 were therefore processed in parallel. Intermediate dimethyl-dichloroborane and the end product dimethyl-diazidodiborane were characterized with FT-IR spectroscopy. No $HB(N_3)_2$ byproduct or cross substituted chlorinated and azylated species were detected, which indicated that the bridge bond survived under the applied experimental conditions. Dimethyl-diazidodiborane was found to be have a much longer lifetime than TADB. The increased stability makes the compound easier to handle and more amenable to scale-up procedures. However, dimethyl-diazidodiborane is just a representative of a group of azidoboranes which are stabilized by small organic groups and which

may be developed in studies designed to address issues related to HEDM applications.
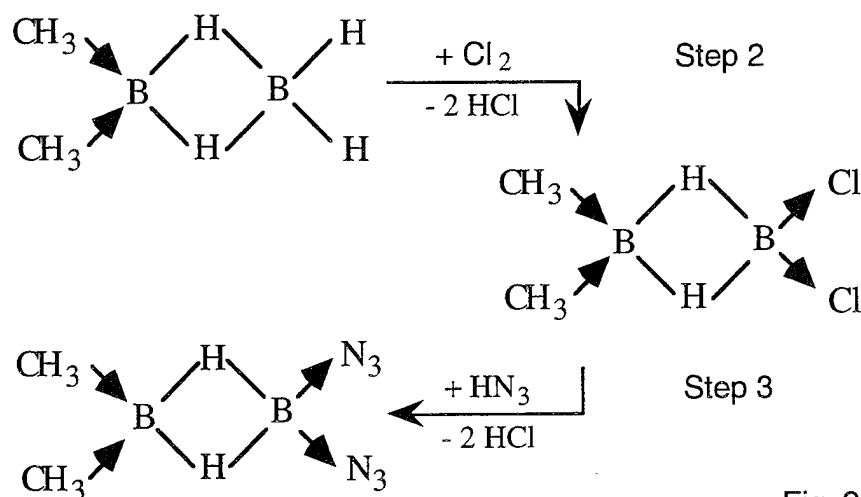
Fig. 3

The ultimate goal is (i) the development of hydrogen bridge bond stabilized azido boranes as BNN ring sources and (ii) the synthesis of cage structures such as B-N prismane. In the near term several issues with respect to scale-up procedures will be addressed in small scale laboratory experiments, e.g., interactions with different solvents and scrambling processes at higher particle densities will be investigated with already existing compounds dimethyl-diazidodiborane or TADB. Long range plans are to synthesize other hydrogen bridge bond stabilized azido compounds and to investigate selective decay pathways of the compounds to BNN rings. For these studies more controlled conditions are required which can be provided by an organic glass or matrix environment. When the decay conditions are established, synthesis of cage compounds will be attempted. Both near and long term goals would profit considerably from *ab initio* support, which is currently only available for TADB.

DESIGN OF HIGH ENERGY DENSITY CAGE AZABORANE FUELS

R. B. King

Department of Chemistry, University of Georgia, Athens, Georgia 30602

A. Cage Boranes as Three-dimensional Aromatic Systems

Methods derived from topology and graph theory indicate that the cage borane dianions $B_nH_n^{2-}$ ($6 \leq n \leq 12$) constructed from B_n deltahedra (Figure 1: a deltahedron is a polyhedron in which all faces are triangles) may be regarded as three-dimensional delocalized aromatic systems in which surface bonding and core bonding correspond to the σ-bonding and π-bonding, respectively, in planar polygonal two-dimensional hydrocarbons $C_nH_n^{(n-6)+}$ (n = 5, 6, 7). Thus first consider benzene as a prototypical planar polygonal aromatic hydrocarbon since other approaches to the bonding in benzene are familiar to many chemists. The four carbon valence orbitals of the sp^3 manifold of a CH vertex in benzene are divided into three sp^2 hybrids and a single p orbital. One of the sp^2 hybrids is bonded to the external hydrogen atom leaving two sp^2 hybrids and the p orbital as internal orbitals. Among the three internal orbitals the two equivalent sp^2 hybrids are twin internal orbitals or *tangential* orbitals whereas the single p orbital is a unique internal orbital or *radial* orbital.

The internal orbitals of the six carbon atoms form the benzene skeletal bonding including the delocalization responsible for its aromaticity. Pairwise overlap of the (2)(6) = 12 twin internal orbitals around the circumference of the hexagon is responsible for splitting these 12 orbitals into 6 σ-bonding and 6 σ^*-antibonding orbitals leading to the so-called σ-bonding of benzene. This σ-bonding of benzene is supplemented by the so-called π-bonding arising from overlap of the six unique internal orbitals, namely the single p orbital on each of the carbon atoms. The total benzene skeleton thus has 9 bonding orbitals (6σ and 3π) which are filled by the 18 skeletal electrons which arise when each of the CH vertices contributes three skeletal electrons. Twelve of these skeletal electrons are used for the σ-bonding and the remaining six electrons for the π-bonding.

Figure 1: The borane deltahedra.

Similar ideas can be used to describe the three-dimensional aromaticity in the boranes $B_nH_n^{2-}$ and carboranes $B_{n-2}C_2H_n^{2-}$ ($6 \leq n \leq 12$) based on deltahedra (Figure 1), with vertices of degrees four and five being strongly favored. Consider the simplest deltahedral borane, namely the octahedral $B_6H_6^{2-}$, as an example of such a deltahedral borane. The four boron valence orbitals of the sp^3 manifold of a BH vertex in $B_6H_6^{2-}$ are divided into two sp hybrids and two extra p orbitals. One of the sp hybrids is bonded to an external hydrogen atom leaving the second sp hybrid and the two extra p orbitals as internal orbitals. Among these three internal orbitals the two equivalent p orbitals are the twin internal orbitals or *tangential* orbitals whereas the single sp hybrid is a unique internal orbital or *radial* orbital.

The internal orbitals of the six boron atoms form the skeletal bonding in $B_6H_6^{2-}$ including the delocalization responsible for its aromaticity. The pairwise overlap of the $(2)(6) = 12$ twin internal orbitals, namely the two p orbitals on each of the six boron atoms, leads to six bonding and six antibonding orbitals over the surface of the polyhedron. This surface bonding in $B_6H_6^{2-}$, which is analogous to the σ-bonding in benzene, is supplemented by *core* bonding arising from overlap of the six unique internal orbitals, which are the single sp hybrids on each of the six boron atoms directed towards the core of the polyhedron. This core bonding, which is analogous to the π-bonding in benzene, leads to a single molecular orbital. The skeletal bonding in $B_6H_6^{2-}$ uses a total of 14 skeletal electrons, namely 12 electrons for the six bonding molecular orbitals of the surface bonding and an additional 2 electrons for the single core bonding molecular orbital. The other deltahedral borane anions, $B_nH_n^{2-}$ ($6 < n \leq 12$) use similar skeletal bonding models with $2n + 2$ skeletal electrons with the delocalized n-center core bonding leading to three-dimensional aromatic stabilization similar to the two-dimensional aromatic stabilization in planar polygonal hydrocarbons such as benzene. Such three-dimensional aromatic stabilization of the deltahedral cage boranes $B_nH_n^{2-}$ as well as the isoelectronic carboranes $C_2B_{n-2}H_n$ makes these compounds much more stable than other borane derivatives.

B. Cage Azaboranes as High Energy Density Fuels

Compounds containing only boron and hydrogen are potential high energy fuels since they oxidize very exothermally according to the following general equation:

$$B_nH_m + (^{3n}/_2 + {}^m/_2)[O] \longrightarrow (^n/_2)B_2O_3 + (^m/_2) H_2O \qquad (1)$$
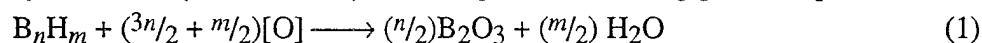
However, the most familiar neutral binary boranes with open structures including B_2H_6, B_5H_9, and $B_{10}H_{14}$ are not attractive as fuels since such boranes have limited thermal stability leading to problems with particulates during combustion processes as well as combustion to the less energetically favorable O=B–OH. Cage boranes containing boron deltahedra (Figure 1) are more promising candidates for high energy fuels since they are much more thermally stable than the boranes with open structures owing to the three-dimensional aromaticity discussed above. In rocket propellants deltahedral boranes thus survive for a longer time before onset of combustion than boranes with open structures so that combustion of cage boranes can occur at higher temperatures to provide a better chance of yielding the thermodynamically most favorable combustion products and hence the highest combustion energy. However, binary deltahedral boranes are only stable as dianions of the type $B_nH_n^{2-}$ ($6 \leq n \leq 12$) and thus must be obtained as salts of lower energy cations. The presence of such cations dilutes the deltahedral borane anions and thus lowers their energy density. The general objective of this project is the development of

high energy boron fuels based on electrically neutral compounds containing boron deltahedra in which the inherent negative charge of such boron deltahedra is balanced by the substitution of a single cage boron atom with a nitrogen atom leading to azaboranes of the general formula B_nH_nNH as well as their substitution products. Of particular interest are N–N bonded dimeric deltahedral cages of the type $B_nH_nN–NB_nH_n$ (Figure 2) because of the possibility of additional energy release from the formation of the stable N_2 during the oxidation process, i.e.

$$B_nH_nN–NB_nH_n + 2n\ O_2 \longrightarrow N_2 + n\ B_2O_3 + n\ H_2O \qquad (2)$$
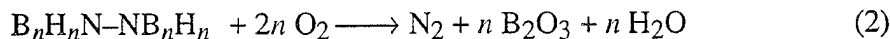
The linked azaborane cages $B_nH_nN–NB_nH_n$ ($n = 9, 11$: Figure 2) thus combine the cage structures of cubanes and other polyhedranes, the exothermic oxidation of boranes, and the energetics of hydrazine oxidation when used as high energy density fuels.

$$B_9H_9N–NB_9H_9 \qquad\qquad B_{11}H_{11}N–NB_{11}H_{11}$$
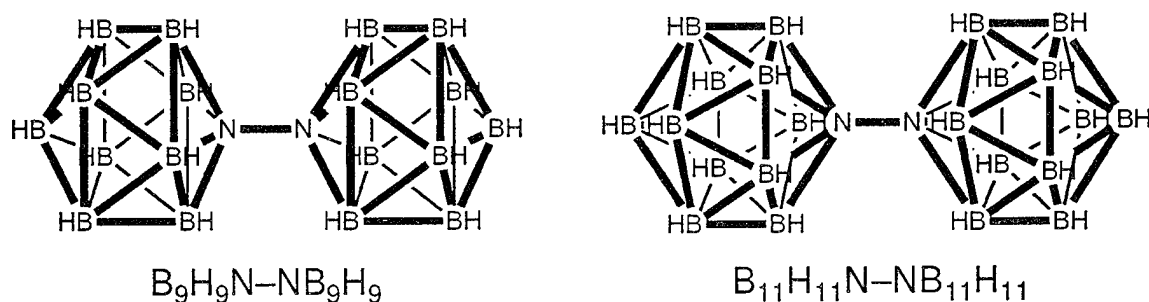
Figure 2: The linked azaborane cages $B_nH_nN–NB_nH_n$ ($n = 9, 11$),

The most stable boron cage *closo* deltahedra are the 10-vertex 4,4-bicapped square pyramid and the 12-vertex regular icosahedron. In both cases the corresponding neutral azaboranes are known.[1] The preferred methods for the synthesis of B_9H_9NH and $B_{11}H_{11}NH$ from decaborane, $B_{10}H_{14}$, are summarized in Figure 3. A promising method for converting B_9H_9NH and $B_{11}H_{11}NH$ to the corresponding N–N dimers (Figure 2) uses the one-electron oxidation of the corresponding $B_nH_nN^-$ anion which is readily formed by deprotonation of B_nH_nNH, i.e.,

$$B_nH_nNH + Et_3N \longrightarrow [Et_3NH][B_nH_nN] \qquad (3a)$$

$$2\ [Et_3NH][B_nH_nN] + [O] \longrightarrow B_nH_nN–NB_nH_n + Et_3N + H_2O \qquad (3b)$$
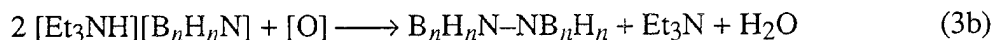
One-electron oxidizing agents such as Fe^{+3}, Cu^{+2}, and Ce^{+4} are particularly interesting oxidants for this reaction. Stable free radicals $B_nH_nN\bullet$ are possible intermediates from the one-electron oxidation of the $B_nH_nN^-$ anions.

[1](a) B_9H_9NH: Arafat, A.; Baer, J.; Huffman, J. C.; Todd, L. J., *Inorg. Chem.*, **1986**, *25*, 3757; (b) $B_{11}H_{11}NH$: Müller, J.; Runsink, J.; Paetzold, P., *Angew. Chem. Int. Ed.*, **1991**, *30*, 175.

$$B_{10}H_{14} \xrightarrow{\text{NaNO}_2/\text{THF}} B_9H_{11}NH \xrightarrow{375-400°C} B_9H_9NH$$

B₁₀H₁₄

B₉H₁₁NH
57% yield

B₉H₉NH
54% yield

3 Me₂S·BH₃/140°C

BH₂SMe₂

$$B_{11}H_{11}NBH_2SMe_2 \xrightarrow{\text{Me}_3\text{CNH}_2} [\text{Me}_3\text{CNH}_3][B_{11}H_{11}N] \xrightarrow{\text{HBF}_4/\text{Et}_2\text{O}} B_{11}H_{11}NH$$

B₁₁H₁₁NBH₂SMe₂
47% yield

[Me₃CNH₃][B₁₁H₁₁N]
96% yield

B₁₁H₁₁NH
~100% yield
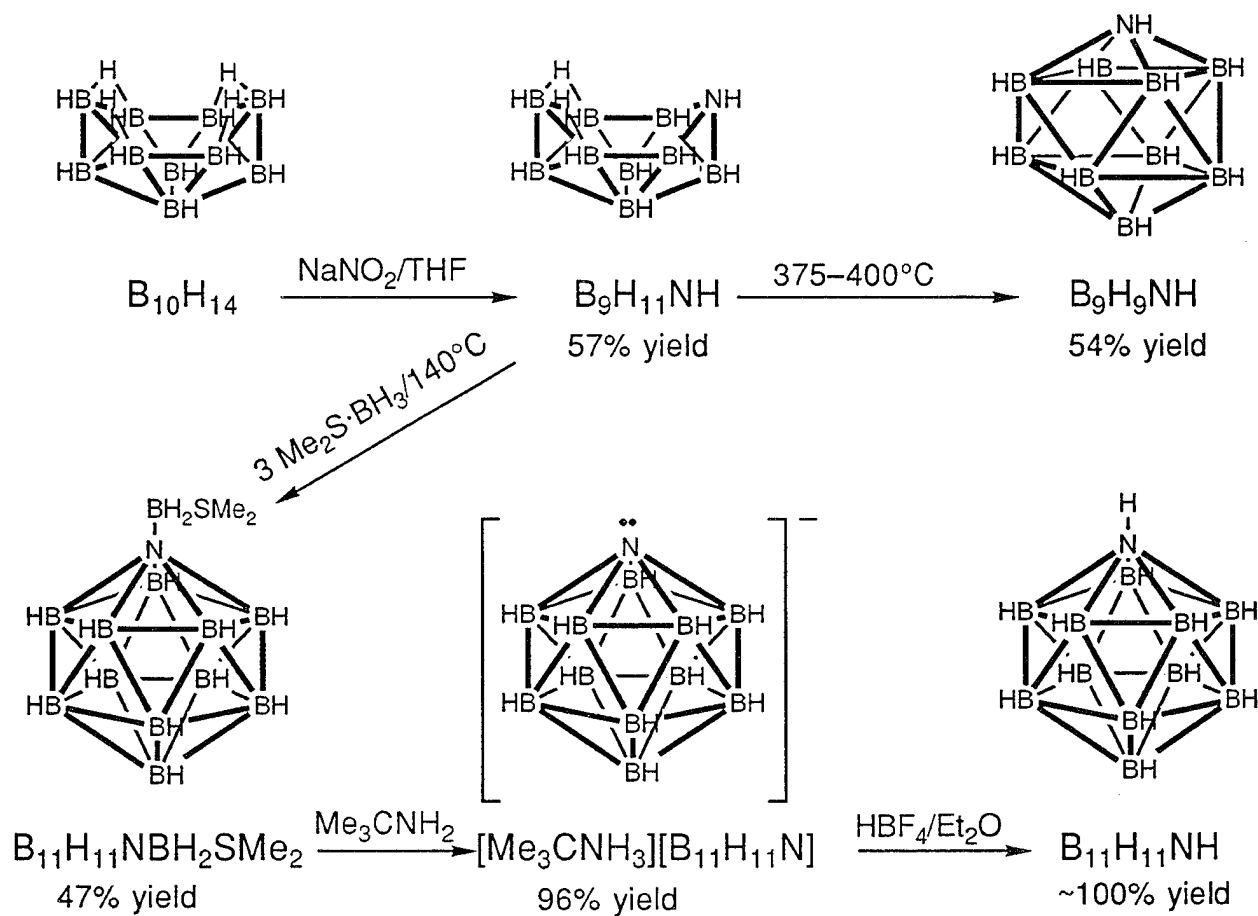
Figure 3: Synthesis of cage azaboranes.

335

IMPROVEMENT OF NF / BiF VISIBLE WAVELENGTH CHEMICAL LASER
BY DONOR PRECOMBUSTION

D. J. Benard
Rockwell International Science Center
P.O. Box 1058, Mail Stop: A/9
Thousand Oaks, CA 91358
805/373-4278

INTRODUCTION

A number of tactical and strategic missions of importance to the DoD require the development of low weight and volume systems which are capable of generating and efficiently projecting large amounts of power over great distances. Short (visible) wavelength laser systems are capable of achieving the necessary beam divergences from transmitting apertures of reasonable size and direct chemical pumping of the required population inversion is a feasible approach to meet the power, size and weight requirements. Chemical reactions, however, are most likely to deposit their energy release into vibrational modes of the product molecules, and powerful infrared (HF/DF) chemical lasers have been developed based on this principle.

Efficient chemical pumping of electronic transitions in the product molecules of chemical reactions is not favored by the density of final states that are accessible, even when reactions are highly exothermic, and can be achieved only if production of the ground electronic state is forbidden by a constraint such as conservation of spin angular momentum. Therefore chemically generated electronically excited states are as a rule metastable with respect to optical transitions because photon emission is also a spin conserving process. Consequently, electronic transition (visible wavelength) chemical lasers also operate on the principle of energy transfer whereby the metastable species are used to collisionally excite resonant electronic states in a molecule with superior photon emission properties. The process of energy pooling,

which involves two-step excitation of an emitting molecule upon sequential energy transfer collisions with two or more metastable species, allows the emitting molecule to reach a more highly excited state before photon emission, and thereby generate laser radiation at shorter wavelength than would otherwise be possible. One of the shortest wavelength chemical lasers demonstrated todate is based on the metastable generation / energy pooling scheme:

$$Heat + FN3 = NF^* + N2 \qquad\qquad Donor = BiF(X) + Byproducts$$

$$2\,NF^* + BiF(X) = 2\,NF + BiF(A) \qquad BiF(A) = BiF(X) + h\nu(471\ nm)$$

Donor Chemistry Produces BiF Radicals
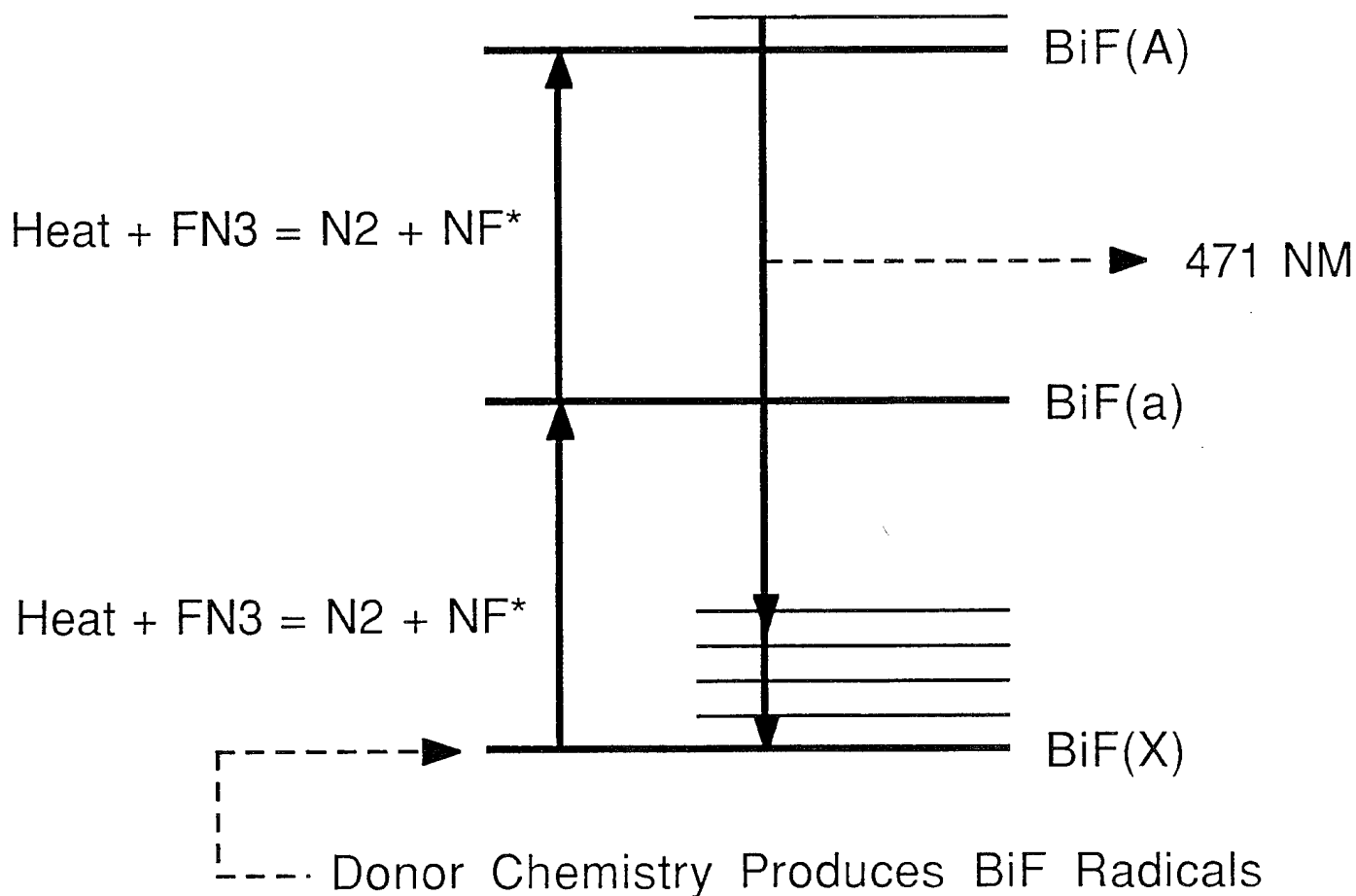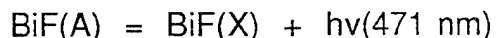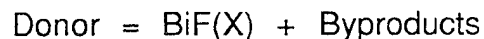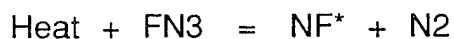
Since the BiF(A-X) transition is fast, relatively high densities of the metastable species (NF*) are required to achieve inversion, and consequently the major source of inefficiency in the system is due to metastable self-annihilation. To combat this loss, the density of emitting molecules (BiF) must be large enough to dominate the decay of NF*. The only volatile Bi-donor (trimethyl bismuth or TMB), however, is a source of byproducts that rapidly relax the metastable energy store by quenching through non-radiative channels. Consequently, efficient optical power extraction cannot be achieved without some form of donor preconditioning.

Precombustion is a concept in which the TMB donor is mixed on-the-fly with a fuel/oxidizer combination that is ignited immediately prior to mixing with FN3 and subsequent thermal dissociation to release the NF*. The purpose of the precombustion reaction is to generate a transient Bi-donor and react all other species to forms that are not effective quenchers of NF*, such as CO_2, CF_4, H_2O or HF. To evaluate the feasibility of this concept for improving the NF/BiF chemical laser we have constructed a tabletop scale shock tube reactor in which an electrically triggered $H_2 + F_2$ explosion is used to launch a M = 2 shock wave that dissociates FN3 upon reflection at the back wall. The TMB / fuel / oxidizer reaction is also independantly triggered by electrical means inside a closely coupled injection manifold about 3 ms ahead of the shock wave. The resulting rapid combustion chemically processes the donor and the corresponding increase in temperature and pressure causes rapid injection of the reaction products into the shock channel where mixing with FN3 preceeds the subsequent chemistry. Requirements for an effective fuel / oxidizer combination include: short time stability when mixed with TMB, facile electrical ignition, rapid combustion velocity, adequate heat release and a favorable spectrum of products including an effective Bi-donor and no severe quenchers of NF*.

Precombustion systems that are potentially able to meet the above criteria include $F_2 + H_2$, $NF_3 + H_2$, $N_2O + CO$ and $C_2N_2 + O_2$. Testing has revealed that the $F_2 + H_2$ system is prone to spontaneous ignition when doped with TMB even in the presence of

338

O2 added as a stabilizer. The NF3 + H2 system is stable but must be run H2 rich to produce useful Bi-atoms rather than inert BiF3 products and, consequently, deleterious spontaneous reaction of the atomic species (both Bi and H) occurs upon injection of the precombusted gases into FN3 in the shock channel. In the oxygen based systems, some H2 must be added as a catalyst to achieve ignition and rapid combustion. The H2 addition can be as low as 2 % in the C2N2 + O2 system provided sufficient electrical energy is used to initiate the reaction, however, use of this precombustion scheme strongly favors Bi-atoms over the desired BiF emitter. It is believed that OBi(CN) is the primary Bi-carrier produced by the precombustion reaction and this species fails to react with the FN3 before it is converted to NF. Consequently, since NF is reducing with respect to Bi-species, only a small yield of active BiF is obtained.

In the N2O + CO system more H2 must be added to facilitate rapid combustion but there is no evidence of BiF chemiluminescence upon injection into the FN3 as in the NF3 + H2 system, and a much higher yield of BiF emission (per TMB molecule) is obtained after the shock converts the FN3 into NF*. In this case, it is believed that the precombustor first generates BiO as the most favored Bi-carrier, and this species in turn reacts to stable FBiO upon contact with FN3 and then (subsequently) reacts with NF to yield BiF and stable ONF as a byproduct. Scaling experiments also revealed that the rapid NF* quenching kinetics associated with use of raw TMB donor have been effectively elemenated. Based on these results, we are now ready to proceed to optical cavity experiments that are capabple of efficiently extracting the chemical energy that was initially stored as FN3 and then converted by shock heating to electronically excited NF* metastables.

Oxidative Chemical Oxygenation of NF$_3$ and Novel Synthesis of NF$_3$O

Karl O. Christe and William W. Wilson

Hughes STX, Phillips Laboratory (Propulsion Directorate), Edwards Air Force Base, CA 93524

ABSTRACT

The first purely chemical, oxidative oxygenation of NF$_3$ to NF$_3$O has been achieved. Using SbF$_5$ and elevated temperature and pressure to activate the normally very inert NF$_3$ and N$_2$O molecules, NF$_2$O$^+$ salts were formed in quantitative yield and converted to NF$_3$O by vacuum pyrolysis in the presence of NaF. These reactions afford a new, simple, high yield synthesis of NF$_3$O from commercially avilable starting materials. Raman spectroscopy was used to show that at room temperature liquid SbF$_5$ does not interact with NF$_3$ and N$_2$O, thus raising interesting questions concerning the mechanism of this reaction. The unusual concept is proposed that a Lewis acid - Lewis base pair interacts at elevated temperature in the gas phase but not in the condensed liquid phase.

DISCUSSION

Nitrogen trifluoride oxide, NF$_3$O, is a fascinating molecule[1-8] which is isoelectronic with NF$_4^+$. Its N-O bond possesses a high degree of double bond character (r_{N-O} = 1.159 Å)[1] and, therefore, it is not a typical amine oxide with a long, semi-polar N-O bond and a negative charge on the oxygen atom. To avoid exceeding 8 valence electrons on nitrogen and to satisfy the high electronegativity of fluorine, the NF$_3$O molecule is best described as an NF$_2$O$^+$ F$^-$ type structure in which the negative charge is evenly distributed over all three

fluorine ligands. This description is supported by the unusally long (1.432 Å)[1] and polar N-F bonds observed for NF_3O.

Since NF_3O possess a N(+V) central atom, its synthesis is difficult and and has been achieved either by the fluorination of an NO-containing molecule, such as FNO, or by oxygenation of NF_3. The oxidative fluorination of FNO has been accomplished using the powerful fluorinating agents, IrF_6,[9] elemental fluorine at temperatures in excess of 260 °C,[10] or N_2F^+ or XeF^+ salts.[11] The oxygenation of NF_3 is much more difficult and has been achieved only by the use of O atoms which were generated by electric glow discharge at low temperatures.[12,13] No evidence could be found in the literature for a purely chemical oxygenation of NF_3 to NF_3O. In a recent paper,[14] Cacace and coworkers have reported the formation of gaseous NF_2O^+ ions from the chemical ionization of NF_3/N_2O mixtures in a mass spectrometer. Based on their observations, they suggested (1), where XF_5 represents a strong Lewis acid, as an alternate route to salts containing the NF_2O^+ cation:

$$NF_3 + XF_5 + O\text{-Donor} \longrightarrow NF_2O^+XF_6^- + Donor \qquad (1)$$
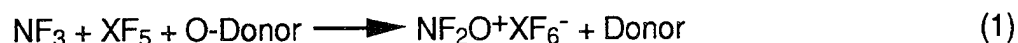
Whereas the formation of free gaseous NF_2^+ cations in a mass spectrometer is facile, their formation in bulk on a preparative scale presents a major problem. Thus, previous studies from other[15] and our[16] laboratories had shown that, even at low temperatures, NF_3 does not form stable adducts with the strong Lewis acids, SbF_5, AsF_5 or BF_3. In spite of these dire prospects, the possibility of chemically oxygenating NF_3 was explored.

Attempts were unsuccessful to prepare the known[17,18] $NF_2O^+AsF_6^-$ salt from NF_3, N_2O and AsF_5 in a Monel cylinder at autogeneous pressures of about 80 atm at temperatures ranging from 100 to 190 °C using a sevenfold excess of NF_3 and N_2O and reaction times of about three days. Only unreacted starting materials were recovered from these experiments. When AsF_5 was replaced by

SbF$_5$, no reaction was observed at 100 °C. When, however, the reaction temperature was raised to 150 °C, a quantitative formation of NF$_2$O$^+$Sb$_2$F$_{11}^-$[17,19] was obtained with the excess NF$_3$ and N$_2$O being recovered unchanged. Raising the reaction tempreature to 190 °C resulted in the formation of a mixture of NF$_2$O$^+$SbF$_6^-$ and NF$_2$O$^+$Sb$_2$F$_{11}^-$ which contained small amounts of NO$^+$[20] and NF$_4^+$[21-24] salts as by-products. When the reaction was carried out at 260 °C, NO$^+$SbF$_6^-$ and NF$_4^+$SbF$_6^-$ became the main products, and the excess NF$_3$ and N$_2$O were again recovered unchanged.

The observed products can be readily explained by scheme (2). The tendency of NF$_3$O and SbF$_5$ to form a salt containing the Sb$_2$F$_{11}^-$ polyanion at 150 °C is in accord with a previous report.[17] With increasing temperature, the formation of NF$_2$O$^+$SbF$_6^-$ is favored, followed by its dissociation to NF$_3$O and SbF$_5$. This is analogous to our previous observations for NF$_4^+$Sb$_2$F$_{11}^-$.[25] At temperatures above 250 °C, NF$_3$O is

$$
\begin{array}{c}
\text{NF}_3 + \text{N}_2\text{O} + 2\text{SbF}_5 \xrightarrow{\;150\ \text{C}\;} \text{NF}_2\text{O}^+\text{Sb}_2\text{F}_{11}^- + \text{N}_2 \\[2mm]
T > 180\ \text{C} \updownarrow \\[2mm]
\text{NF}_3\text{O} + 2\text{SbF}_5 \qquad\qquad (2)\\[2mm]
T > 250\ \text{C} \updownarrow \\[2mm]
\text{FNO} + \text{F}_2 \\[2mm]
\overset{+\ \text{SbF5}}{\swarrow} \qquad \overset{+\ \text{NF3}+\text{SbF5}}{\searrow} \\[2mm]
\text{NO}^+\text{SbF}_6^- \qquad\qquad \text{NF}_4^+\text{SbF}_6^-
\end{array}
$$
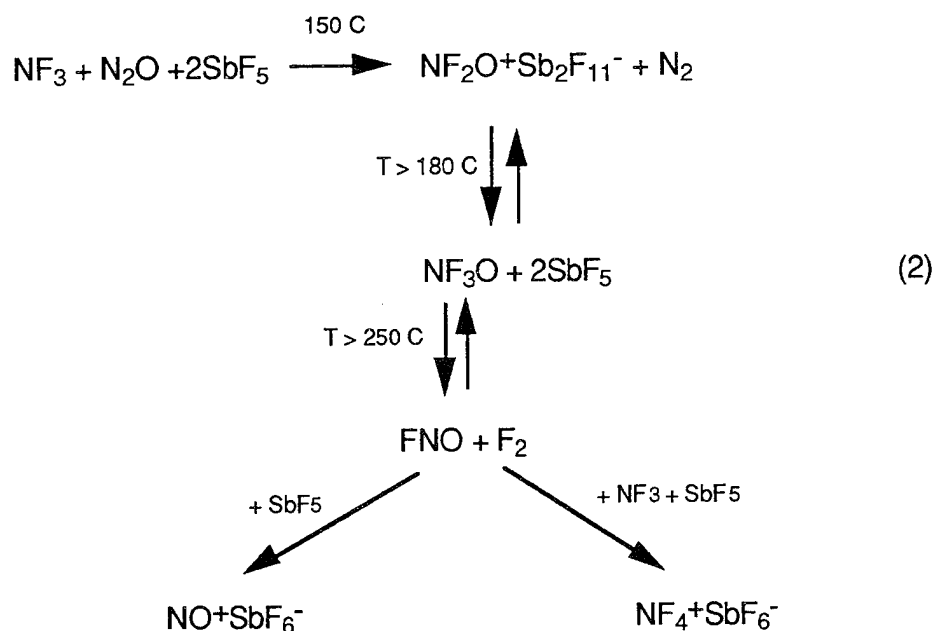
well known[10] to form an equilibrium with FNO and F_2 which, in the presence of SbF_5, is continously shifted to the FNO and F_2 side by the formation of the stable $NOSbF_6$[26] and NF_4SbF_6[25] salts.

The mechanism of the first step of (2) is not as clearcut. Based on the ion-molecule experiment of Cacace[14] and the requirement for SbF_5 in this reaction, it would seem logical to postulate $NF_2{}^+SbF_6{}^-$ as an intermediate in the formation of NF_2O^+. Since previous studies[15,16] had shown no evidence for NF_3 forming an adduct with either BF_3, AsF_5 or SbF_5, further experiments were carried out on the SbF_5-NF_3, SbF_5-N_2O, and SbF_5-NF_3-N_2O systems. Liquid SbF_5 was pressurized with 2 atm of either NF_3, N_2O, or an equimolar mixture of NF_3 and N_2O, and its Raman spectra were recorded. The spectra of the liquid phase showed no detectable frequency shifts for the SbF_5 bands. In addition, weak signals were observed for NF_3 and N_2O dissolved in the liquid SbF_5. The frequencies of these dissolved species were identical to those reported[27] for the free molecules in the gas phase and, hence, liquid SbF_5 does not interact with either NF_3 or N_2O at room temperature.

Since NF_3 and N_2O do not react with each other in the absence of SbF_5 at temperatures as high as 260 °C, as shown by the recovery of the unreacted excess NF_3 and N_2O in our reactions, one might argue that at 150 °C NF_3 and N_2O are in equilibrium with NF_3O and N_2 and that this equilibrium (3) which in the absence of SbF_5 must lie far to the left, is continously shifted to the right by trapping the NF_3O as solid $NF_2O^+SbF_6{}^-$.

$$NF_3 + N_2O \;\rightleftharpoons\; NF_3O + N_2$$

$$\downarrow {\scriptstyle +SbF_5}$$

$$NF_2O^+SbF_6{}^-$$

(3)
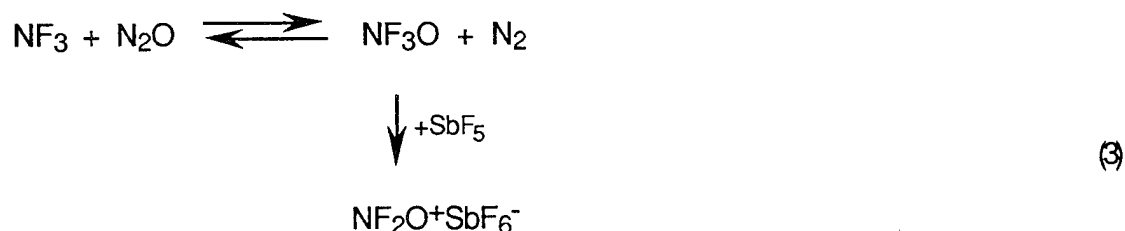
Thermodynamically, (3) is feasible because the $NF_3 + N_2O$ reaction is calculated[28] to be exothermic by about 27 kcal mol^{-1}, and the lattice energy of solid $NF_2O^+SbF_6^-$ should provide an additional driving force. If these assumptions were correct and equilibrium (3) does indeed exist and at 150 to 250 °C is shifted far to the left, NF_3O should react with N_2 at these temperatures to produce NF_3 and N_2O in high yield. This, however, is not the case, and a more plausible mechanism is required for explaining the role of SbF_5 in the first step of (2).

A more appealing, although unprecedented, explanation is that at room temperature SbF_5 does not interact with NF_3 but that at 150 °C it does. This might be possible because at room temperature liquid SbF_5 is highly polymeric and self-associated through fluorine bridges, while above its boiling point (141 °C) in the gas phase it is largely depolymerized. Thus, SbF_5 might be able to interact in the gas phase with NF_3 and polarize it sufficiently to allow its attack by N_2O with the resulting ternary intermediate then undergoing an exothermic intramolecular N_2 elimination reaction with simultaneous formation of solid $NF_2O^+SbF_6^-$ (4).

$$NF_3 + N_2O + SbF_5 \longrightarrow \left[\text{intermediate structure} \right] \longrightarrow NF_2O^+SbF_6^- + N_2 \quad (4)$$
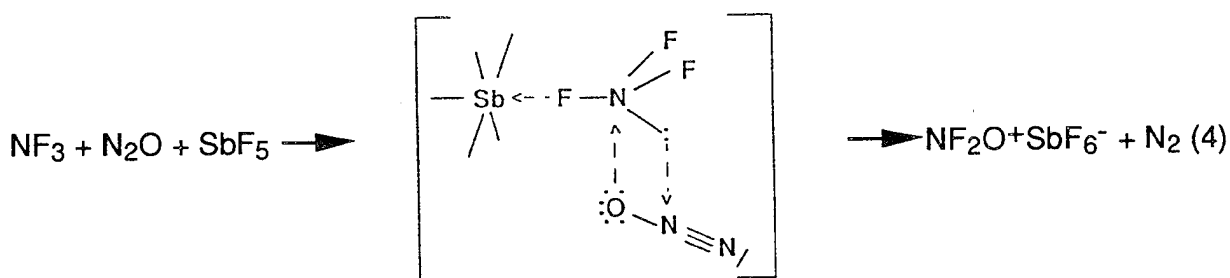
The concept of a Lewis acid - Lewis base pair interacting in the gas phase but not in the condensed liquid phase is highly unusual and will be the subject of a forthcoming ^{18}F radio tracer study.

In order to provide a convenient synthesis for free NF_3O, it was necessary to convert the $NF_2O^+Sb_2F_{11}^-$ salt in an efficient manner to pure NF_3O. This was achieved by vacuum pyrolysis of $NF_2O^+Sb_2F_{11}^-$ at 190 to 230 °C in the presence of excess NaF (5). This process affords pure NF_3O in high yield.

$$NF_2O^+Sb_2F_{11}^- + 2NaF \longrightarrow 2Na^+SbF_6^- + NF_3O \qquad (5)$$
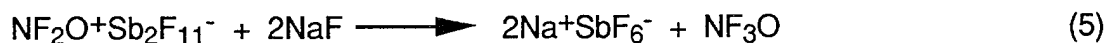
In summary, it has been demonstrated that N_2O, in spite of its high kinetic stability and concomitant unreactivity,[29] can act as a powerful, oxidative oxygenating agent. Using N_2O as the oxygenating agent, the first purely chemical oxygenation of NF_3 to NF_3O has been achieved. This reaction affords a new, simple, high yield synthesis of NF_3O from commercially available starting materials.

Acknowledgement. The author thanks Prof. R. Bau for his numerous attempts to obtain the crystal structure of $NF_2O^+Sb_2F_{11}^-$.

References

(1) Plato, V.; Hartford, W. D.; Hedberg, K. *J. Chem. Phys.* **1970**, *53,* 3488.

(2) Curtis, E. C.; Pilipovich, D.; Moberly, W. H. *J. Chem. Phys.* **1967**, *46*, 2904.

(3) Kirchhoff,W. H.; Lide, D. R. Jr. *J. Chem. Phys.* **1969**, *51, 467*.

(4) Abramowitz, S.; Levin, I. R. *J. Chem. Phys.* **1969**, *51,* 463.

(5) Hirschmann, R. P. ; Harnish, D. F.; Holmes, J. r.; MacKenzie, J. S.; Fox, W. B. *Appl. Spectrosc.* **1969**, *23* ,333.

(6) Frost, D. C.; Herring, F. G.; Mitchell, K. A. R.; Stenhouse, I. R. *J. Am. Chem. Soc.* **1971**, *93,* 1596.

(7) Grein, F.; Lawlor, L. J. *Theoret. Chim. Acta (Berl.)* **1983**, *63,* 161.

(8) Brumm, M.; Frenking, G.; Breidung, J.; Thiel, W. *Chem. Phys. Letters* **1992**, *197,* 330.

(9) Bartlett, N.; Passmore, J.; Wells, E. J. *J. Chem. Soc., Chem. Commun.* **1966**,213.

(10) Bougon, R.; Chatelet, J.; Desmoulin, J. P.; Plurien, P. *C. R. Acad. Sci. Paris Sect. C* **1968**, *266*, 1760.

(11) Minkwitz, R.; Bernstein, D.; Preut, H.; Sartori, P. *Inorg. Chem.*, **1991**, *30*, 2157.

(12) Maya, W. *U.S. Patent* 3,320,147 (1967).

(13) Fox, W. B.; MacKenzie, J. S. *U.S. Patent* 3,323,866 (1967). Fox, W. B.; MacKenzie, J. S.; Vanderkooi, N.; Sukornick, B.; Wamser, C. A.; Holmes, J. R.; Eibeck, R. E.; Stewart, B. B. *J. Am. Chem. Soc.* **1966**, *88*, 2684.

(14) Cacace, F.; Pepi, F.; Grandinetti, F. *J. Phys. Chem.* **1994**, *98*, 8009.

(15) Craig, A. D. *Inorg. Chem.* **1964**, *3*, 1628.

(16) Christe, K. O.; Wilson, R. D.; Goldberg, I. B. *Inorg. Chem.* **1979**, *18*, 2572.

(17) Christe, K. O.; Maya, W. *Inorg. Chem.* **1969**, *8*, 1253.

(18) Wamser, C. A.; Fox, W. B.; Sukornik, B.; Holmes, J. R.; Stewart, B. B.; Juurik, R.; Vanderkooi, N.; Gould, D. *Inorg. Chem.* **1969**, *8*, 1249.

(19) The $NF_2O^+Sb_2F_{11}^-$ salt was identified by its infrared and Raman spectra (ref 17). Single crystals were grown from anhydrous HF solution. Attempts by Prof. R. Bau to solve the crystal structure were unsuccessful due to the poor quality of the crystals.

(20) Geichman, J. R.; Smith, E. A.; Trond, S. S.; Ogle, P. R. *Inorg. Chem.* **1962**, *1*, 661.

(21) Christe, K. O.; Guertin, J. P.; Pavlath, A. E. *Inorg. Nucl. Chem. Letters* **1966**, *2*, 83.

(22) Guertin, J. P.; Christe, K. O.; Pavlath, A. E. *Inorg. Chem.* **1966**, *5*, 1921.

(23) Christe, K. O.; Guertin, J. P.; Pavlath, A. E.; Sawodny, W. *Inorg. Chem.* **1967**, *6*, 533.

(24) Tolberg, W. E.; Rewick, R. T.; Stringham, R. S.; Hill, M. E. *Inorg. Chem.* **1967**, *6*, 1156.

(25) Christe, K. O.; Wilson, R. D.; Schack, C. J. *Inorg. Chem.* **1977**, *16*, 937.

(26) Griffith, J. E.; Sunder, W. A.; Falconer, W. E. *Spectrochim. Acta, Part A* **1975**, *31A,* 1207.

(27) Shimanouchi, T. *Nat. Stand. Ref. Data Ser., Nat. Bur. Stand. (U.S.)* **1972**, *39,* 1.

(28) Chase, M. W. Jr.; Davies, C. A.; Downey, J. R. Jr.; Frurip, D. J.; McDonald, R. A.; Syverud, A. N. *JANAF Thermochem. Tables, Third Edition, J. Phys. Chem. Ref. Data* **1985**, *14,* Suppl. 1.

(29) Greenwood, N. N.; Earnshaw, A. in *Chemistry of the Elements,* Pergamon Press: Oxford, U.K., **1986**.

Spectroscopy of Weakly Bound Aluminum Adducts

James M. Spotts, Matthew S. Johnson, and Mitchio Okumura

Arthur Amos Noyes Laboratory of Chemical Physics
Division of Chemistry and Chemical Engineering
California Institute of Technology
Pasadena, CA 91125

Laser-induced fluorescence (LIF) spectra have been recorded following laser vaporization of Al atoms into a pulsed free jet expansion of H_2O seeded in inert carrier gases. We discuss the possible assignment of a newly observed progression to either insertion products AlOH or HAlOH from the reaction $Al + H_2O$, or to an $Al(H_2O)$ van der Waals complex.

Aluminum-doped solid hydrogen is one of several HEDM candidates with potential for significant I_{sp} improvements over a liquid hydrogen-liquid oxygen propellant. In order to accurately model the behavior of dopants within a cryogenic solid, the intermolecular interactions between a guest Al atom and the surrounding host molecules must be experimentally characterized. A fundamental issue for all such weakly interacting atom/molecule systems is the question of insertion of the atom into a bond. Adducts such as $Al(H_2)$ are all higher in energy than their insertion products, e.g. the dihydride HAlH. Spectroscopic studies of van der Waals complexes provide important tests of the potential energy surfaces predicted by theory, and allow us to explore ground and excited state reactivity.

We have been investigating the spectroscopy of Al-molecule adducts by laser-induced fluorescence. The adducts are formed in a laser vaporization source with the capability for cryogenic operation. We have been investigating the LIF spectra of complexes including $Al(H_2)$, $Al(D_2)$, and $Al(H_2O)$. Here we present results of preliminary spectra obtained studying aluminum/water plasmas and discuss possible assignments of the observed bands.

Aluminum atoms in the presence of water vapor are highly reactive. Previous theoretical and experimental work have concluded that aluminum atoms react with little or no barrier to form products such aluminum hydroxy hydride (HAlOH). Oblath and Gole assigned emission in the range 16,700 cm^{-1} to 28,600 cm^{-1} from aluminum/water plasmas to a chemiluminescent reaction of Al with H_2O to form HAlOH.[1] McClean et al. studied the kinetics of the reaction $Al(^2P_0) + H_2O$ in a high temperature reactor.[2] Margrave and coworkers studied matrices resulting from the codeposition of water vapor with aluminum atoms produced in an oven.[3,4] They observed IR absorptions due to HAlOH, as well as photochemical formation of AlOH but found no evidence for an $Al(H_2O)$ adduct at 15 K. ESR spectra of HAlOH were also obtained from matrix trapped aluminum/water products.[5,6] Early theoretical work supported the notion that HAlOH

formed from the reaction of Al with H_2O with no barrier, with the Al atom approaching perpendicular to the OH bond.[7]

Recent *ab initio* calculations, however, find the Al(H_2O) adduct to be stable relative to insertion and bound by D_e = 9.3 kcal/mol relative to separated monomers.[8] Barrier heights of 8 to 12 kcal/mol have been calculated for insertion to form the HAlOH radical which is stable by 39.8 kcal/mol relative to monomer reactants. It is therefore conceivable that the complex could be formed in the supersonic expansion of highly dilute water/carrier gas mixtures following laser ablation of aluminum.

Previous laser ablation studies have not directly yielded spectroscopic evidence for an Al(H_2O) complex. Duncan and co-workers studied products from laser ablation of aluminum in the presence of water vapor seeded in carrier gas in a Smalley-type laser vaporization source and observed the spectrum of AlOH near 250 nm by two photon resonant ionization.[9] Fuke and coworkers observed Al(H_2O)$_n$ clusters for n = 1 to 10 by ablating an aluminum rod into an expansion of 10 atm of He seeded with water vapor[10] by single photon ionization and time-of-flight mass spectroscopy, but could not determine the actual structure of the neutral complexes.

We have investigated the LIF spectra of aluminum complexes formed in a supersonic jet/laser vaporization source. We searched the region of the spectrum near the aluminum $3^2D \leftarrow 3^2P$ transition at 308.3 nm. This transition lies close to the forbidden $4^2P \leftarrow 3^2P$ transition at 303.4 nm, which becomes allowed in the complex upon breaking spherical symmetry. We hypothesized that adduct electronic states correlating to atomic m_l orbitals with orientations perpendicular to the intermolecular axis would be bound and thus detectable by LIF spectroscopy from the nominally $(3s)^2(3p)\pi$ ground state.

A series of new peaks were observed upon addition of water vapor to the source carrier gas (Ne, N_2, Ar). Three progressions were observed, with harmonic frequencies of 122.3 cm^{-1}, 117.7 cm^{-1}, and 106.6 cm^{-1}. The transitions were relatively weak, similar or slightly weaker in intensity to AlAr when observed in Ar carrier gas.

We have scanned a limited range of approximately 600 cm^{-1}, and therefore have not definitively assigned these bands. We can rule out assignments to expected diatomic species such as AlAr, AlO, AlH, Al_2, and OH, whose spectra are known. The transitions do not match the known spectra of either AlOH or HAlOH, but these species are not as well characterized. Neither the band location nor the excited state frequency agree with the AlOH spectrum observed by Duncan and co-workers at 250 nm, but we cannot rule out the possibility of a new state of AlOH with a bending frequency closer to that of the ground state (155 cm^{-1}). Similarly, the only known band of HAlOH at 450 nm is far to the red, but a transition at 308 nm, if weak, may have been obscured in the matrix work by strong, broadened atomic lines. To account for the observed progressions, at least one of the excited state bending frequencies must be significantly lower than the lowest ground state frequencies of approximately 400 cm^{-1}. Conceivably, the HAlO isomer of

AlOH could also account for the observed spectrum, but this highly energetic, metastable isomer has been predicted but not yet observed.

The proximity of the transition to the atomic line and the observed chemistry is consistent with formation of a complex $Al(H_2O)$. If we are in fact exciting the analogous atomic transition in the complex, then the complex well depth in the excited state must be relatively close to that of the ground state. The observed vibrational spacings are close to those expected for a metal atom-water complex; for example, the harmonic frequencies of the intermolecular stretch are 40 and 173 cm^{-1} in the $Hg(H_2O)$ adduct ground and excited states respectively.[11] The observation of multiple series are analogous to spectra of AlAr observed in this region, which have been assigned as excitations to several closely spaced electronic states originating from different m_l states. One might expect that the $Al(H_2O)$ complex, with a well depth an order of magnitude deeper than that of AlAr, should have significantly higher intensity, but given the relatively low insertion barrier and the high initial Al kinetic energy prior to expansion, it is possible that only a small fraction of the $Al(H_2O)$ complexes survive and do not undergo insertion or photochemical reactions.

The evidence for assignment to the $Al(H_2O)$ complex is at the moment circumstantial, pending further experiments. We are continuing our investigations of the observed spectrum in order to arrive at a definitive assignment. Further scans to the blue, two photon resonant ionization, deuterium substitution, and higher resolution spectra should all aid in this endeavor. Finally, we are studying a number of lines observed in Al/D_2 mixtures which may arise from $Al(D_2)$ complexes.

[1] S. B. Oblath and J. L. Gole, *J. Chem. Phys.* **70**(1), 581 (1979).

[2] R. E. McClean, H. H. Nelson, and M. L. Campbell, *J. Phys. Chem.* **97**, 9673 (1993).

[3] R. H. Hauge, J. W. Kauffman, and J. L. Margrave, *J. Am. Chem. Soc.* **102**(19), 6005 (1980).

[4] M. A. Douglas, R. H. Hauge, and J. L. Margrave, ACS Symposium Series 179, 347, ACS Washington D. C. (1982).

[5] H. A. Joly, J. A. Howard, M. Tomietto, and J. S. Tse, *J. Chem. Soc. Faraday. Trans.* **90**(20), 3145 (1994).

[6] L. B. Knight, Jr., B. Gregory, J. Cleveland, and C. A. Arrington, *Chem. Phys. Lett.* **204**(1,2), 168 (1993).

[7] H. A. Kurtz and K. D. Jordan, *J. Am. Chem. Soc.* **102**(3), 1177 (1980).

[8] S. Sakai, *J. Phys. Chem.* **96**(21), 8369 (1992). S. Sakai, *J. Phys. Chem.* **97**(35), 8917 (1993).

[9] J. S. Pilgrim, D. L. Robbins and M. A. Duncan, *Chem. Phys. Lett.* **202**(3,4), 203 (1993).

[10] F. Misaizu, K. Tsukamoto, M. Sanekata, and K. Fuke, *Suppl. Z. Phys. D.* **26**(S), 177 (1993).

[11] M. C. Duval and B. Soep, *J. Phys. Chem.* **95**, 9075 (1991).

Two-Photon Spectroscopy of the E,F $^1\Sigma_g^+ \leftarrow X^1\Sigma_g^+$ State of Hydrogen

John T. Bahns and William C. Stwalley
Department of Physics
University of Connecticut
Storrs, CT 06269-3046

We have recently begun study of the optical spectroscopy and photochemistry of atoms in solid molecular hydrogen. Initially, two major efforts were undertaken: analysis of previously observed E,F $^1\Sigma_g^+ \leftarrow X^1\Sigma_g^+$ two photon spectra of H_2 in the gas phase; and installation of an improved Alexandrite tunable pulsed laser system for new E,F $^1\Sigma_g^+ \leftarrow X^1\Sigma_g^+$ studies in gaseous and condensed phase H_2.

Previously we have presented E,F $^1\Sigma_g^+ \leftarrow X^1\Sigma_g^+$ two photon spectra of H_2 obtained with our Lambda Physik Excimer-pumped doubled dye laser system. These spectra (Fig. 1 shows Q(0), Q(1), and Q(2) of the E,F $\leftarrow$ X(0,0) band) suffer from excessive laser linewidth and the relatively low pulse energy of the dye laser second harmonic. In particular, the observed linewidths are far in excess of the sub-Doppler values expected (due to a convolution of AC Stark, pressure and natural linewidth). Our new Alexandrite laser system (discussed below) was delivered and with injection seeding from our 899-29 CW ring lasers (either titanium sapphire or LD 700 dye) provides transform-limited pulses with an order of magnitude greater pulse energy at the two-photon wavelengths in Fig. 1 and with a full width half maximum of approximately 10 MHz. This narrow linewidth is critical for deconvolving the true lineshapes in solid H_2 and also for observing weaker lines, e.g. Q(3) of H_2 and Q(0) and Q(1) of HD impurities.

With narrow linewidths, precise frequency calibration becomes important. Fortunately, Prof. Ed Eyler (currently Univ. of Delaware, after September 1, 1995, University of Connecticut) who is perhaps the world's current expert on the electronic spectra of gaseous H_2 has accurately calibrated UV spectra (see attached publication list) which we can use in our work. This was discussed extensively in his March visit and we anticipate he will collaborate in the remainder of this project and its renewal. Thus, we will exploit the accurate shifts as well as widths of solid H_2 spectral lines with respect to gaseous H_2 spectral lines.

The pulsed Alexandrite laser system (Light Age PAL-1) has been installed in our pulsed laser laboratory (Physics 001) and a multicable tube connecting 001 to our CW laser laboratory (Physics 007A) has been installed. One of these cables is a single mode polarization preserving optical fiber; in preliminary experiments a 60 mW titanium sapphire beam has been sent from 007A to 001 with a 20 mW single mode polarized output suitable for injection seeding. We hope to have our injection seeded system working soon with our soon-to-be-delivered crystal for third harmonic generation and our high pressure Raman shifting cell to begin to generate narrow band, high pulse energy output near 200 nm.
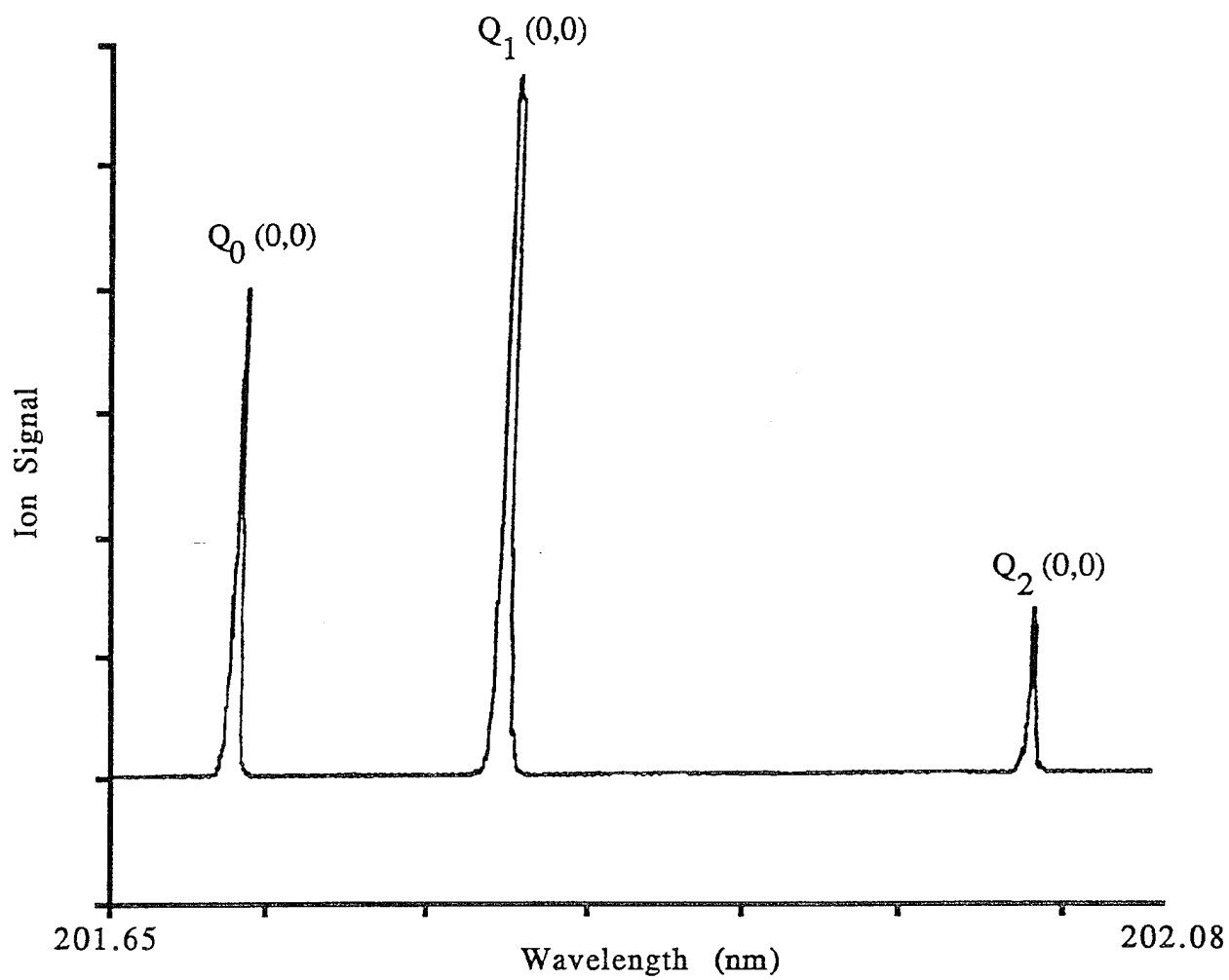
Figure 1.

Recent Publications by Ed Eyler on the E,F $^1\Sigma_g^+ \leftarrow$ X$^1\Sigma_g^+$ States of H$_2$

1. W. Zucker and E. E. Eyler, "Photodissociation Cross Sections from the E<F State of H$_2$", J. Chem. Phys. <u>85</u>, 7180 (1986).

2. E. Eyler, E. McCormack, J. M. Gilligan, A. Nussenzweig and E. Pollack, "Precise Two-Photon Spectroscopy of the E $\leftarrow$ X Intervals of H$_2$", Phys. Rev. A <u>36</u>, 3486 (1987).

3. E. McCormack and E. E. Eyler, "Perturbed Structure of Molecular Hydrogen Near the Second Dissociation Limit", Phys. Rev. Lett. <u>66</u>, 1042 (1991).

4. M. Gilligan and E. E. Eyler, "High Resolution Three-Photon Spectroscopy and Multiphoton Interference in Molecular Hydrogen", Phys. Rev. A <u>43</u>, 6406 (1991).

5. M. Gilligan and E. E. Eyler, "Precise Determinations of Ionization Potentials and E,F -State Energy Levels of H$_2$, HD, and D$_2$", Phys. Rev. A <u>46</u>, 3676 (1992).

6. E. E. Eyler and N. Melikechi, "Near-Threshold Continuum Structure and the Dissociation Energies of H$_2$, HD, and D$_2$", Phys. Rev. A <u>48</u>, R18 (1993).

7. E. Eyler, B. Catching and N. Melikechi, "Structure of Bound and Continuum States Near the Second Dissociation Limits of H$_2$, D$_2$ and HD", in preparation.

8. N. Melikechi, S. Gangopadhyay, J. C. Meiners and E. E. Eyler, "Precise Determination of E,F $^1\Sigma_g^+$ Levels in H$_2$, D$_2$ and HD", in preparation.

A Theoretical Study of High Energy B-N Prismane

Nikita Matsunaga and Mark S. Gordon
Department of Chemistry
Iowa State University
Ames, IA 50011

Our preliminary calculations[1] have shown that the B-N analog of prismane is a high energy minimum on its potential energy surfaces (PES). The relative energy of the B-N prismane with respect to borazine, including zero-point energy correction, is 185.0 kcal/mol at the restricted Hartree-Fock (RHF) level of theory using effective core potential and basis sets of Stevens *et. al* (SBK(d))[2]. The relationship between the B-N prismane and borazine can be thought of as an intramolecular isomerization reaction, in order to attain the maximum energy release from B-N prismane (**Scheme 1**).
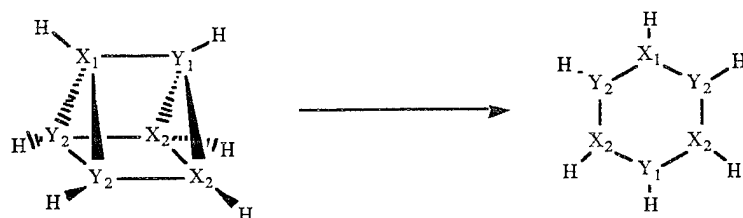
Scheme 1

In this abstract, the potential energy surfaces of the B-N prismane and related molecules are explored in an attempt to achieve the isomerization reaction above.

Computational Approach

The geometries were optimized with the restricted Hartree-Fock (RHF) using GAMESS[3] quantum chemistry programs. The basis sets used here include the Steven-Basch-Krauss-Jasien (SBK) effective core potentials (ECP) and basis sets[2] for all heavy atoms and the

-31G basis[4] for hydroen, also using 6-31G(d,p) basis[4]. All heavy atoms are augumeneted with d-polarizaiton functions[5].

Recation path was followed for each transition state located by using Gonzalez-Schlegel method[6] in order to connect a transition state to the associated two minima.

Due to the fact that the RHF level of theory fails to find a transition state connecting B-N prismane and borazine directly, MCSCF wave function was utiized. For the preliminary results presented here STO-3G[7] basis set was used. Active space of the prismane is consist of the three bonding and anti-bonding orbitals (orbitals that lies on N_1-B_1, N_2-N_2 and B_2-B_2). This 6 electron-6 orbital active space generates 175 configuratin state functions(CSF).

Results

Geometries of the B-N prismane and the related molecules along with the relative energies of each molecule with respect to the B-N prismane are shown in Figure 1. The normal modes correspoinding to the negative eigenvalue of the energy hessian for the transition state found are also shown in Figure 1. The bond lengths of B-N bonds in prismane form is substantially larger than that of the borazine. All the rectangular faces of the B-N prismane possess up to about 5° deviations from the ideal angle of 90°. The two triangular faces deviates less than 4° from the ideal angle, 60°, found in a prismane.

Dewar-benzene analog of borazine is found at the MCSCF/STO-3G level of theory, even though the RHF/SBK(d) failed to do so. The transition state connecting the Dewar-benzene analog and prismane is also found at the MCSCF/STO-3G level. However, the improvement in basis makes these stationary points disappeared.

Bernardi et al.[8] has implied that there is no direct path which connects all carbon prismane and benzene. Also, they have shown that the isomerization reaction of Dewar-benzene to benzene can undergo via non-adiabatic path. The isomerization reaction undergoes a series of cascading through several singlet excited states connected by conical intersections. Such reaction paths might be also important for the B-N prismane.

The bond critical points found for the bonds B_1-N_2 and N_1-B_2 (of **Scheme 1**) are located inside the ring. Especially, the bond critical points of the N_1-B_2 bond can be found close to the ring critical point associated with the ring N_1-B_2-B_2. It means that the ring has small ring strain. One could think of it as a "T-shaped" bond, though the total electron density contour map shows two distinct bond paths. The localized orbitals do not show such characteristics, either. On the other hand, prismane (carbon only) possesses the bond critical points associated with the triangular face are located outside the ring.

Al-N and Ga-N analogs of prismane

There are other possible HEDM candidates. We have found that prismane structures of $(AlH-NH)_3$ and $(GaH-NH)_3$ to be high energy species, 90.7 and 96.4 kcal/mol with respect to the corresponding benzene structures. They are both minima on the PES and the corresponding benzene structures are also minima.

References

[1] N. Matsunaga and M. S. Gordon *J. Ame. Chem. Soc.* **116** (1994) 11407

[2] W. J. Stevens, H. Basch and M. Krauss *J. Chem. Phys.* **81** (1984) 6026

[3] M. W. Schmidt, K. K. Baldridge, J. A. Boatz, S. T. Elbert, M. S. Gordon, J. H. Jensen, S. Koseki, N. Matsunaga, K. A. Nguyen, S. Su, T. L. Windus, M. Dupuis, and J. A. Montgomery *J. Comput. Chem.* **14** (1993) 1347

[4] R. Ditchfield, W. J. Hehre and J. A. Pople *J. Chem. Phys.* **54** (1971) 724

[5] We have used B=0.6 and N=0.8

[6] C. Gonzales and H. B. Schlegel *J. Phys. Chem.* **94** (1990) 5523

[7] W. J. Hehre, R. F. Stewart and J. A. Pople *J. Chem. Phys.* **51** (1969) 2657

[8] M. J. Bearpark, M. A. Robb, H. B. Schlegel *Chem. Phys. Lett.* **223** (1994) 269, reference therein.

1
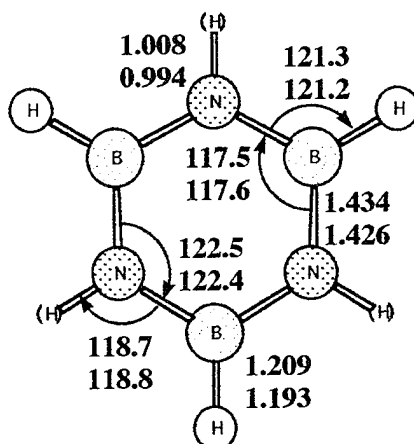
minimum

Relative Energies wrt Prismane:

RHF/SBK(d)//RHF/SBK(d)	**-185.0 kcal/mol**
MP2/SBK(d)//RHF/SBK(d)	**-161.2**
RHF/6-31G(d,p)//RHF/6-31G(d,p)	**-186.0**
MP2/6-31G(d,p)//MP2/6-31G(d,p)	**-**

Vibrational Frequencies:

RHF/6-31G(d,p) vibrational frequencies (in cm^{-1})

295.8	295.8	407.3	555.1	555.1
737.0	737.0	761.8	912.1	991.9
991.9	1003.3	1004.9	1004.9	1022.7
1125.1	1142.8	1142.8	1300.3	1424.8
1495.5	1495.5	1590.6	1590.6	2708.5
2708.5	2722.0	3881.6	3883.1	3883.1

RHF/SBK(d) vibrational frequecies(in cm^{-1}) and intensities (in km/mol)

293.9(0.0)	293.9(0.0)	395.2(55.1)	543.0(0.1)	543.0(0.1)
714.5(0.0)	714.5(0.0)	752.8(98.9)	900.2(0.0)	975.3(0.3)
975.3(0.3)	986.2(0.0)	994.9(0.0)	994.9(0.0)	998.7(296.8)
1095.8(0.0)	1118.5(1.5)	1118.5(1.5)	1288.9(0.0)	1381.6(0.0)
1461.0(58.9)	1461.0(58.9)	1564.8(760.8)	1564.8(760.8)	2716.7(499.2)
2716.7(499.2)	2738.3(0.0)	3792.8(0.0)	3794.7(54.5)	3794.7(54.4)

2

H 1.008 / 0.993
1.509 / 1.500
H
1.200 / 1.184
N
B
1.664 / 1.642
1.622 / 1.632
1.558 / 1.548
1.202 / 1.186
B'
H
1.011 / 0.997
B
N
H
1.680 / 1.671
1.475 / 1.468
H
H

H 129.8 / 130.8
132.4 / 132.3
H
129.1 / 128.6
N
B
127.6 / 127.4
92.8 / 92.6
93.3 / 93.5
56.5 / 56.6
60.9 / 60.4
H
131.7 / 131.7
123.9 / 123.6
B'
B
N
H
H
120.2 / 120.4
86.8 / 87.0
136.8 / 136.8
115.6 / 116.2
H
93.2 / 93.0
84.3 / 84.5
89.6 / 89.3

minimum
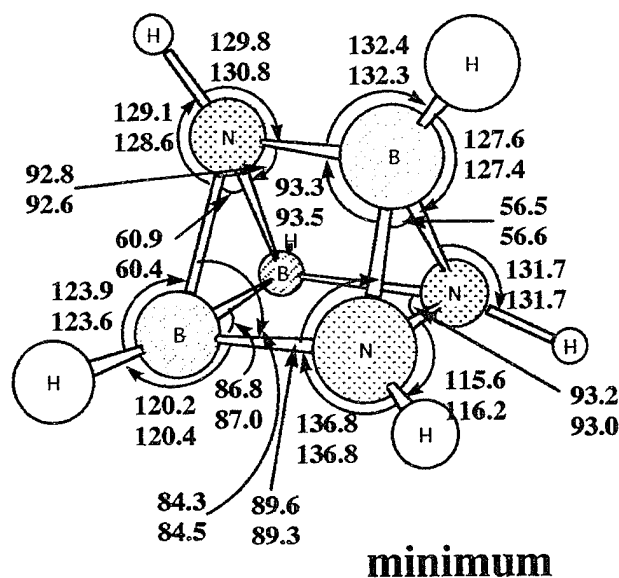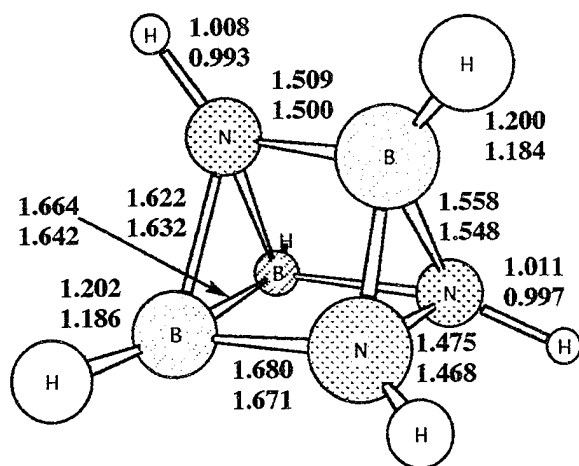
Relative Energies:

RHF/SBK(d)//RHF/SBK(d)	**0.0 kcal/mol**
MP2/SBK(d)//RHF/SBK(d)	**0.0**
RHF/6-31G(d)//RHF/6-31G(d,p)	**0.0**
MP2/6-31G(d)//RHF/6-31G(d,p)	**0.0**

Vibrational Frequencies:

RHF/6-31G(d,p) vibrational frequencies (in cm^{-1})

383.4	478.6	522.8	560.6	628.2
665.5	678.1	690.1	796.9	834.4
892.9	907.3	936.9	950.7	981.2
1024.1	1029.1	1040.1	1125.9	1169.6
1237.7	1250.2	1306.8	1451.8	2736.3
2758.0	2774.9	3858.6	3869.9	3888.3

RHF/SBK(d) vibrational frequencies (in cm^{-1}) and intensities (in km/mol)

370.8(1.6)	462.7(13.4)	483.4(1.9)	546.9(63.4)	623.1(21.5)
655.3(36.4)	664.8(25.4)	665.5(6.4)	767.0(0.1)	814.9(31.5)
879.0(50.6)	894.6(41.8)	916.2(9.2)	935.2(27.4)	960.6(57.9)
1007.2(30.5)	1017.5(132.0)	1020.7(39.7)	1099.2(15.9)	1157.5(96.5)
1205.7(50.2)	1227.1(220.3)	1277.5(114.3)	1425.3(25.3)	2721.1(321.9)
2745.1(186.2)	2763.8(169.7)	3789.3(19.6)	3799.4(19.9)	3805.1(94.8)

3

H
1.208
1.191

1.005   1.409   1.441
0.991   1.400   1.435

B

1.010
0.997

120.0
119.9

123.8   123.6
1.404   123.6   123.5   1.426
1.394   1.417

1.007   123.7   114.3
0.994   123.8   114.4

B

1.213
1.196

1.742
1.720

114.7
114.8

1.400
1.390

1.210
1.194

minimum
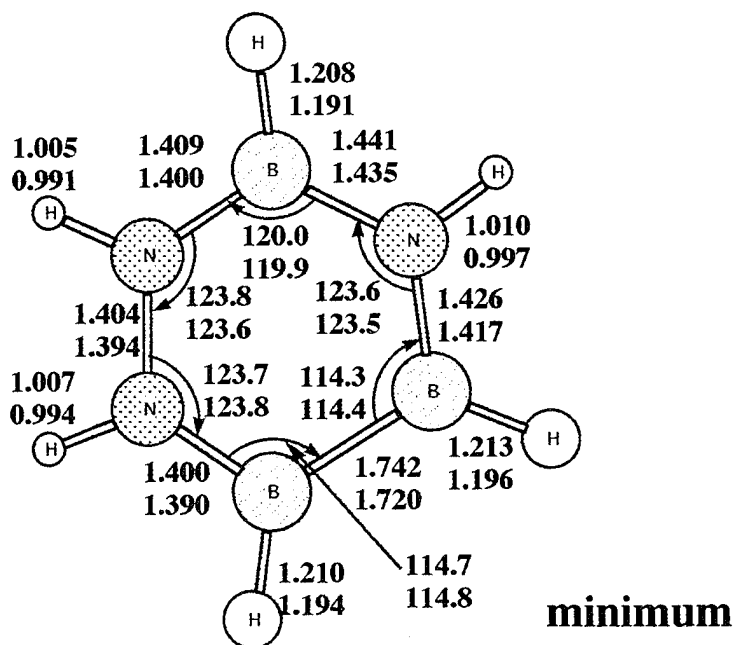
Relative Energies:

RHF/SBK(d)//RHF/SBK(d)	**-86.3kcal/mol**
MP2/SBK(d)//RHF/SBK(d)	**-66.4**
RHF/6-31G(d,p)//RHF/6-31G(d,p)	**-86.8**
MP2/6-31G(d,p)//RHF/6-31G(d,p)	

Vibrational Frequencies:

RHF/6-31G(d,p) vibrational frequencies (in cm^{-1})

152.9	265.7	346.2	482.8	491.6
568.5	592.5	753.1	801.5	913.5
928.2	931.7	987.6	999.0	1005.4
1105.7	1129.9	1277.1	1335.4	1449.1
1512.2	1527.3	1613.3	1718.3	2671.4
2700.9	2730.5	3843.6	3879.7	3922.5

RHF/SBK(d) vibrational frequencies (in cm^{-1}) and intensities (in km/mol)

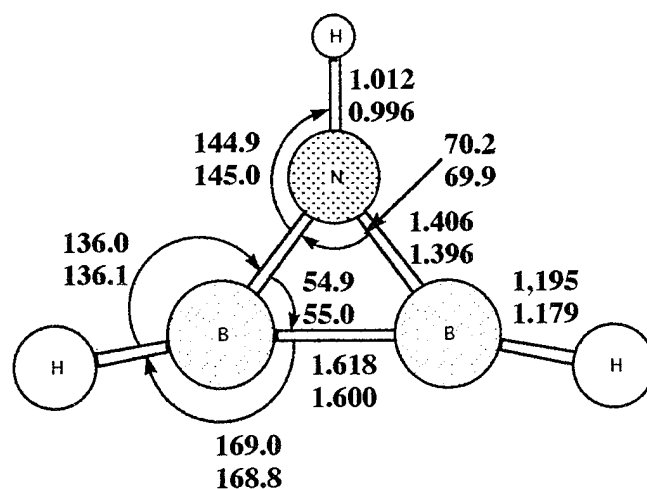|				
103.0(15.6)	245.3(9.8)	331.5(0.0)	475.7(28.7)	476.6(0.9)
556.3(0.8)	579.3(117.6)	739.5(2.1)	798.8(5.2)	895.5(4.0)
911.3(127.3)	919.6(5.0)	974.8(81.7)	982.6(5.4)	988.2(46.1)
1081.6(22.2)	1106.6(1.2)	1251.6(55.4)	1311.7(50.0)	1428.5(61.6)
1474.4(41.6)	1508.6(342.7)	1590.4(40.2)	1679.4(80.3)	2651.4(279.5)
2700.3(560.1)	2710.0(3.6)	3766.6(20.3)	3844.1(15.9)	3880.4(64.6)

5

minimum

Relative Energies:

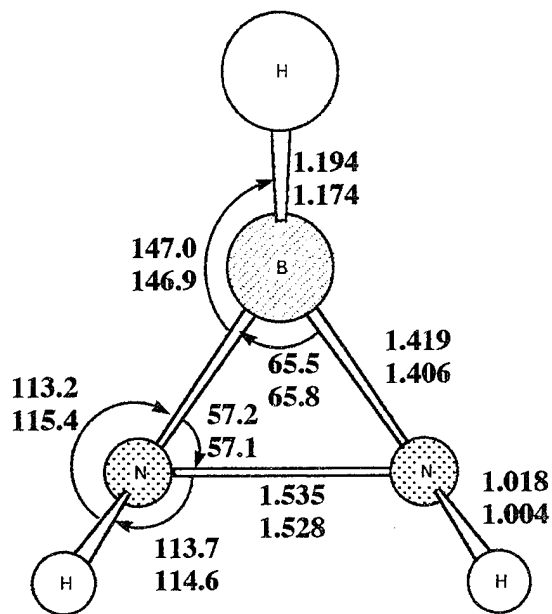RHF/SBK(d,p)//RHF/SBK(d,p)   15.8 kcal/mol
MP2/SBK(d,p)//RHF/SBK(d,p)   22.5

minimum

Relative Energies of 6a + 6b with respect to Prismane:

RHF/SBK(d)//RHF/SBK(d)	**20.7 kcal/mol**
MP2/SBK(d)//RHF/SBK(d)	**30.0**
RHF/6-31G(d,p)//RHF/6-31G(d,p)	**21.5**
MP2/6-31G(d,p)//RHF/6-31G(d,p)	

6b

minimum

Vibrational Frequencies:

RHF/6-31G(d,p) vibrational frequencies (in cm^{-1})

597.7	712.8	819.8	883.2	1054.2
1121.2	1134.1	1443.4	1453.3	2877.7
3729.5	3746.0			

RHF/SBK(d) vibrational frequencies (in cm^{-1}) and intensities (in km/mol)
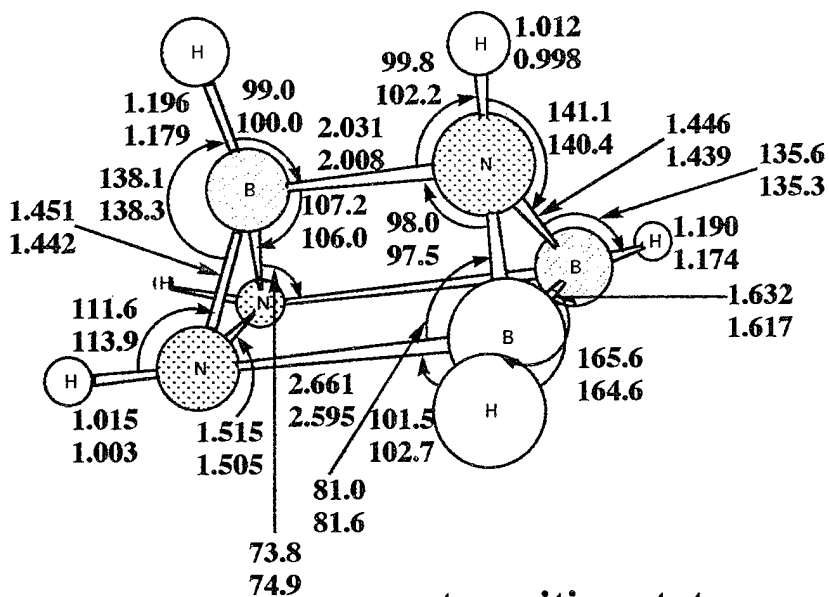
604.5(101.5)	687.8(80.8)	816.4(13.7)	856.1(10.5)	1048.3(115.7)
1081.6(70.6)	1134.8(8.3)	1427.5(102.4)	1432.6(1.8)	2856.8(126.8)
3686.8(0.6)	3703.6(11.3)			

8

minimum
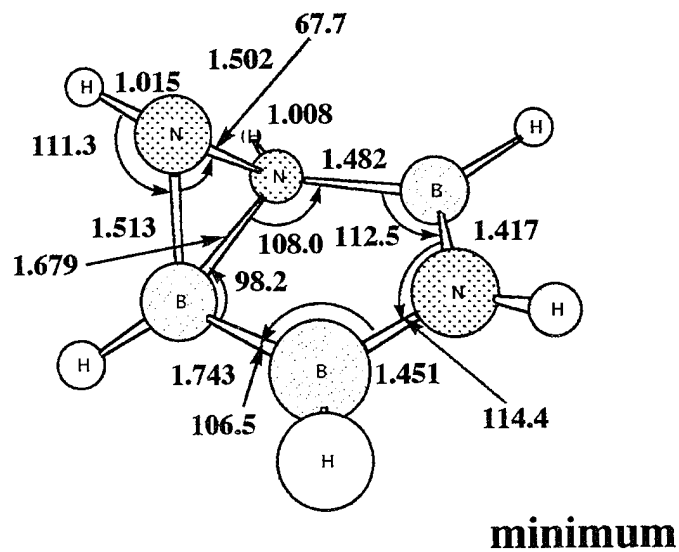
Relative Energies:

RHF/SBK(d)//RHF/SBK(d)	**-53.7 kcal/mol**
MP2/SBK(d)//RHF/SBK(d)	**-36.0**

9

transition state
  i **260.7 cm**$^{-1}$ RHF/SBK(d)
  2i **288.7 cm**$^{-1}$ RHF/6-31G(d,p)

Relative Energies:

RHF/SBK(d)//RHF/SBK(d)   32.1 kcal/mol
MP2/SBK(d)//RHF/SBK(d)   45.1
RHF/6-31G(d,p)//RHF/6-31G(d,p)   30.9
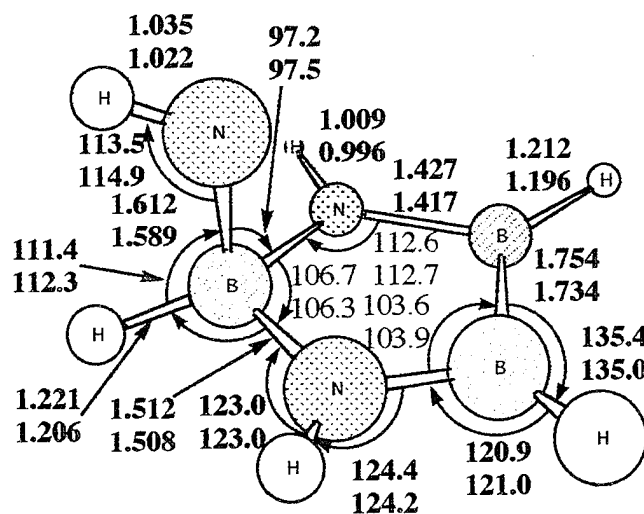
10
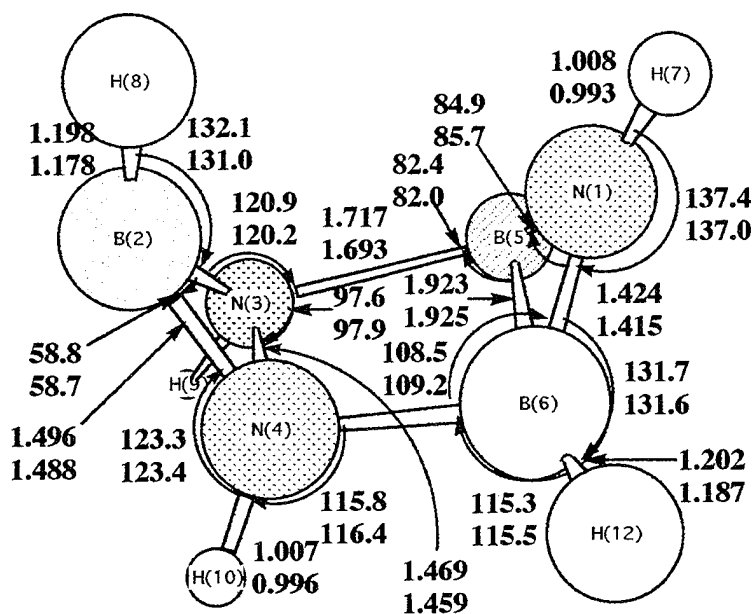
transition state:
i 788.6 cm^{-1} RHF/SBK(d)
i 790.3 cm^{-1} RHF/6-31G(d,p)

Relative Energies:

RHF/SBK(d)//RHF/SBK(d)	72.1 kcal/mol
MP2/SBK(d)//RHF/SBK(d)	43.2
RHF/6-31G(d,p)//RHF/6-31G(d,p)	74.0

11

1.035
1.022

97.2
97.5

1.009
0.996

1.427
1.417

1.212
1.196

113.5
114.9

1.612
1.589

111.4
112.3

112.6

106.7 112.7
106.3 103.6
103.9

1.754
1.734

135.4
135.0

1.221
1.206

1.512
1.508

123.0
123.0

120.9
121.0

124.4
124.2

transition state

i **644.1 cm^{-1}** RHF/SBK(d)
i **685.2 cm^{-1}** RHF/6-31G(d,p)

Relative Energies:

RHF/SBK(d)//RHF/SBK(d)	8.4 kcal/mol
MP2/SBK(d)//RHF/SBK(d)	32.1
RHF/6-31G(d,p)//RHF/6-31G(d,p)	9.1

12
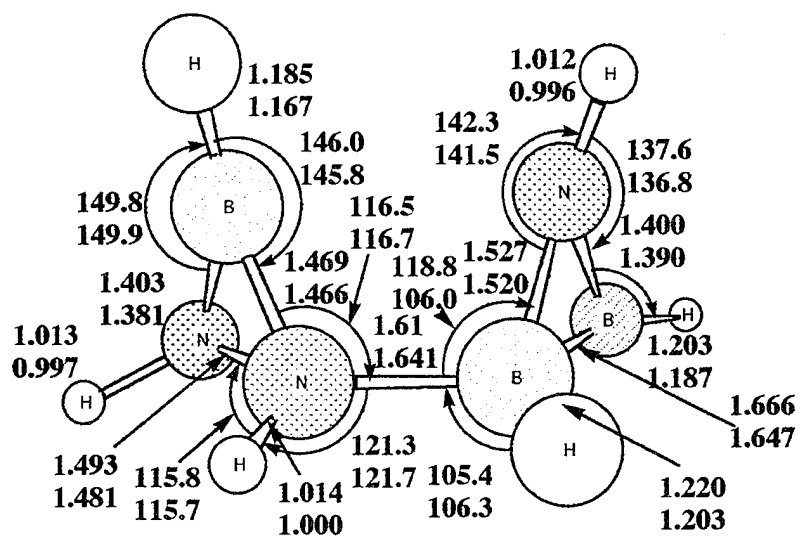
transition state
$i219.8\ \mathrm{cm^{-1}}$ RHF/SBK(d)
$i217.9\ \mathrm{cm^{-1}}$ RHF/6-31G(d,p)

Relative Energies:

RHF/SBK(d)//RHF/SBK(d)	26.4 kcal/mol
MP2/SBK(d)//RHF/SBK(d)	35.3
RHF/6-31G(d,p)//RHF/6-31G(d,p)	23.6

HIGH ENERGY DENSITY MATTER CONTRACTORS CONFERENCE
Wood's Hole, MA 4-7 June 1995

Monte Carlo Simulations of Na Atoms in Dynamically Disordered Ar Systems: Solid, Liquid, and Critical Point Fluid Ar.

Mario E. Fajardo and Jerry A. Boatz

Emerging Technologies Branch, Propulsion Directorate, Phillips Laboratory
(OLAC PL/RKFE Bldg. 8451, Edwards AFB, CA 93524-7680)

ABSTRACT

We present the results of simulations of the structures and optical absorption spectra of Na atoms in solid and liquid Ar at its triple point, and in critical point Ar fluid. The spectral simulations combine a classical Monte Carlo scheme for generating thermally accessible ground state configurations, along with a first order perturbation theory treatment of the interactions between the excited $Na^*(3p\ ^2P)$ atom and the surrounding Ar perturbers [Boatz and Fajardo, J. Chem. Phys. **101**, 3472 (1994)]. These simulations predict a "triplet" (*i.e.* three peaks) absorption lineshape for Na atoms in solid and liquid Ar at its triple point, and an asymmetrical, blue degraded absorption band for Na atoms in critical Ar fluid. We also note and discuss the similarities between the simulated $Na/Ar_{(l)}$ lineshape and an experimental Li/Ar/Xe mixed host matrix spectrum, and the similarities between the simulated spectrum of Na atoms in critical point Ar fluid, and an experimental Li/H_2 matrix absorption spectrum.